Catalyst Development for Selective Ti-Catalyzed Synthesis of Multi-Substituted Pyrroles

A DISSERTATION
SUBMITTED TO THE FACULTY OF THE
UNIVERSITY OF MINNESOTA
BY

Xin Yi See

IN PARTIAL FULFILLMENT OF THE REQUIREMENTS
FOR THE DEGREE OF
DOCTOR OF PHILOSOPHY

Professor Ian A. Tonks

May 2020

Acknowledgements

First, I would like to express my gratitude towards my PhD advisor, Prof. Ian Tonks for his belief in me even before I believed in myself. It has been a great pleasure learning from and alongside him both in and outside of the laboratory. Thank you for giving me the freedom to move around different projects especially when my 'main' project never really took off. With all that I know now, I would still choose to join the Tonks group over again.

Second, I would like to thank the faculty that have served as my committee members throughout the years - Profs. Joseph Topczewski, Daniel Harki and John Ellis. Thank you for sharing with me from your wealth of knowledge and challenging me to think a little deeper every time. My greatest appreciation to Prof. Connie Lu for stepping in at the last minute to be on my committee.

Third, the experience in graduate school was made so much better because of the students in the Tonks group. While the group culture has changed throughout the years, it remains a place where one can depend on for solid support and friendships. To the folks that came and went before me – Peter, Zachary, Abigail, Jimmy, Addison, Gereon and UG Alexander, thank you for answering ALL my questions, especially when I first joined the lab. They have taught me to do good science and not take myself too seriously especially when chemistry goes awry. Rather, hold dear to the memories of blasting music and heartfelt conversations. To my batchmates whom I journeyed/struggled through classes and milestones together – Adam and Robin, thank you for befriending me in those early days when I hardly knew anyone in this foreign land and never made me feel left out. To Evan and Yukun, both of you are brilliant friends I can always count on for a literature reference and crazy ideas. To the rest of the current Tonks group – Janaya, Connor, Steven, Shao Yu, Rachel R. and Rachel D, thank you for tolerating a cranky me while I navigate through job search and graduation. Lastly, I would like to thank Benjamin and Channing for helping me finish up my last project. Ben's curiosity in PCA revived my project out of the grave and taught me so much about statistics. Channing is an immensely brilliant undergraduate whom I owe a lot to in helping me with several challenging synthesis.

Fourth, I am grateful for the friends that I have made in this department. There is always someone whom I can chat with along the corridors when things get a little too crazy

in the Tonks lab. In particular, I am grateful for the amazing women I have met through WISE chemistry, especially Dr. Letitia Yao with whom I had the pleasure to work for as a TA. She has taught me a lot about life beyond graduate school and chemistry. A huge thank you too for all the front office staff who make our lives as graduate students so much easier.

Fifth, I would like to appreciate the chemistry mentors that have inspired me along the way. My mentors from A*, ICES – Martin, James, Ludger, Boon Ying and Buana, thank you for showing me your passion for doing research and telling me there is nothing more logical than doing a PhD. When I was an ignorant undergraduate, they taught me the foundations of doing chemistry and showed me the wonders of organometallic chemistry. In 2018, I had the opportunity to participate in a summer internship at BASF, Germany under the guidance of Dr. Marcel Kienle and his capable team. It was there that I learned about the amazing field of crop protection and more importantly, that I was not sick of chemistry (yet).

Sixth, the support system I have from friends outside of chemistry that has kept me sane. To my friends from Singapore – Sylvia, Ling Xie, Winni, Sarah, Jing Ying, Jorim and Colin, thank you for being only a text away and loving me in your different ways. Despite my lengthy absences, the gatherings we have when I am back home visiting feels just like before. To the friends I have made in Minnesota - Jacquelina, Vivian, Edwin and Lionel, you have been my 'family' away from home and I cherish our game nights, outings and conversations.

Seventh, I would like to thank my family for supporting me even though they understand nothing about what I am doing. I would not be here without their love and concern over the years. To my mama whose love language is cooking up a storm, thank you for travelling across the globe several times just to see and cook for me. To my da jie, thank you for being such an amazing sister to look up to even till today. You inspire me to strive hard for what I believe in and to keep on learning.

Last but certainly not the least, my appreciation to Dexter for always being there for me throughout this rollercoaster ride. Thank you for being my first friend here in Minnesota and now, life partner. I look forward to future adventures together.

Abstract

This thesis broadly covers our catalyst development efforts for selective Ti^{II}/Ti^{IV} redox catalysis towards the synthesis of multi-substituted pyrroles. Chapter 1 provides a literature background on the multitude of ways to access low-valent early transition metals and its application towards group transfer catalysis. Chapter 2 describes the synthesis of pyrroles from the [2+2+1] coupling of alkynes and azides mediated by simple Ti-halide catalysts. Chapter 3 covers the generality of accessing Ti^{II} intermediates, in the absence of strong metal reductants, *via* the coupling of Ti^{IV} imido precatalysts and alkynes. Lastly, Chapter 4 details utilizing iterative supervised principal component analysis as a strategy to aid in rational catalyst design in the Ti-catalyzed regioselective synthesis of pyrroles.

Table of Contents

List of Tables vii

List of Figures ix

Chapter 1: Accessing low-valent early transition metal complexes 1

1.1 Motivation 2

1.2 Classical Reduction Routes 3

1.3 Modern Reduction Routes 5

1.4 Catalytic group transfer 7

1.5 Stoichiometric atom transfer 9

1.6 Thesis outline 10

Chapter 2: : Oxidative nitrene transfer from azides to alkynes *via* Ti(II)/Ti(IV) redox catalysis: formal [2+2+1] synthesis of pyrroles 11

2.1 Overview 12

2.2 Introduction 12

2.3 Results and Discussion 14

2.4 Conclusion 18

2.5 Experimental 19

2.5.1 General considerations 19

2.5.2 General procedure for catalytic reactions 20

2.5.3 Characterization of starting materials in C_6D_5Br 21

2.5.4 Characterization of uncatalyzed triazole products in C_6D_5Br 36

2.5.5 Characterization of cyclotrimerization byproducts in C_6D_5Br 63

2.5.6 NMR analysis of catalytic reactions with internal alkyne substrates (Table 2.1) 73

2.5.7 NMR analysis of catalytic reactions with terminal alkyne substrates (Table 2.2) 104

Chapter 3: : Generation of Ti^{II} Alkyne Trimerization Catalysts in the Absence of Strong Metal Reductants.....122

3.1 Overview 123

3.2 Introduction.....123

3.3 Results and Discussion.....124

3.4 Conclusion 132

3.5 Experimental.....133

3.5.1 General Considerations. 133

3.5.2 Synthesis of compounds.....134

3.5.3 Characterization of substrates and standards in C_6D_5Br.....162

3.5.4 General procedure for catalytic alkyne trimerization 179

3.5.5 Representative Catalytic Spectra 180

3.5.6 Alkyne trimerization mol balance data 182

3.5.7 Preliminary kinetic studies 183

3.5.8 Control reactions.....186

3.5.9 Data for X-ray Structures 187

Chapter 4: : Iterative Supervised Principal Component Analysis-Driven Ligand Design for Regioselective Ti-Catalyzed Pyrrole Synthesis 188

4.1 Overview 189

4.2 Introduction.....190

4.3 Approach 191
4.4 Results and Discussion 194
4.5 Conclusion 212
4.6 Experimental 213
4.6.1 General considerations for experimental work 213
4.6.2 Synthesis of compounds 214
4.6.3 Representative Ti imido catalysts platforms tested 274
4.6.4 Ligand scaffolds attempted 274
4.6.5 General procedure for catalytic pyrrole formation 275
4.6.6 Timepoint studies of catalytic reaction with Precatalyst 4.23 277
4.6.7 Optimization studies with Precatalyst 4.23 279
4.6.8 Isolation attempt of catalytic reaction 279
4.6.9 Data for X-ray Structures 282
4.6.10 General considerations for Principal Component Analysis work 283
4.6.11 Descriptor Set Details methodology 283
4.6.12 Automated Script Details 285
4.6.13 Additional PCA Modelling Data Details 292
4.6.14 General considerations for computational work 301
4.6.15 Computed reaction pathways for catalysts studied 302
4.6.16 Computational Regioselectivity 309

Bibliography 311

List of Tables

Table 2.1 Internal alkyne scope. 16
Table 2.2 Terminal alkyne scope.[a] 18
Table 2.3 Internal alkyne scope triazole yield, trimer yield and mass balance data. 102
Table 2.4 1-azidodecane optimization conditions with 3-hexyne. 103
Table 2.5 Terminal alkyne scope triazole yield, trimer yield and mass balance data. 120
Table 2.6 Azide scope with terminal alkynes. 121
Table 3.1 1-Hexyne trimerization data.[a] 128
Table 3.2 3-Hexyne trimerization data.[a] 131
Table 3.3 Alkyne trimerization mol balance. 182
Table 3.4 Control reactions. 186
Table 3.5 Refined data and cell parameters for X-ray Structures. 187
Table 4.1 Initial computed and tabulated descriptors used in PCA.[254] 198
Table 4.2 Descriptor Contributions to PC1, PC2 and PC3 in optimized ISPCA model 1. 201
Table 4.3 Relative Summed Descriptor Weights from the top 3 components of ISPCA model I. 201
Table 4.4 Relative Summed Descriptor Weights from the top 3 components of weighted ISPCA model II. 207
Table 4.5 DFT-calculated free energies (M06/def2-SVP, SMD $PhCF_3$, 115 °C, $kcalmol^{-1}$) for select catalysts. All TS2 free energies are reported for the *cis*-2 isomer (Figure 4.11). Schematics of the full selectivity manifolds are shown in Figure 4.107-Figure 4.111. 209
Table 4.6 Refined data and cell parameters for X-ray Structures. 282
Table 4.7 List of all descriptors included in initial PCA basis set. 284
Table 4.8 Variable loadings in PC1-PC3 and summed regression coefficients in model IA. 292
Table 4.9 Variable loadings in PC1-PC3 and summed regression coefficients in model IB. 294
Table 4.10 Variable loadings in PC1-PC3 in model IC. 295

Table 4.11 Variable loadings in PC1-PC3 and summed regression coefficients in model IIA.....296
Table 4.12 Variable loadings in PC1-PC3 and summed regression coefficients in model IIB.....297
Table 4.13 Variable loadings in PC1-PC3 and summed regression coefficients in model IIC.....298
Table 4.14 Variable loadings in PC1-PC3 and summed regression coefficients in model IID.....299
Table 4.15 Pairwise Euclidean distances from catalyst 4.1 to all catalysts using different PCA models. 300
Table 4.16 Gibbs free energies calculated by various DFT functionals with def2-TZVPP basis set. 302
Table 4.17 Predicted product ratio using M06/def2-SVP/SMD.....310

List of Figures

Figure 1.1 Relative abundance of the valence states of early transition metal organometallic complexes.[4] 2

Figure 1.2 Classical reduction routes involving strong reductants *via* β-H abstraction and direct metal reduction. 4

Figure 1.3 Representative examples of modern low-valent metal synthesis. a) First reduced Sc complex that reveals end-on N_2 binding. b) Well-defined mononuclear Ti^{II} complexes in the absence of π-accepting ligands with ^3E_g (1.5a) and $^3B_{2g}$ (1.5b) electronic ground state. c) Zero valent isocyanide analogue of the highly unstable $Ta(CO)_6$ prepared by conventional synthesis methods. 5

Figure 1.4 Alternative suite of inner-sphere organosilane reductants for low-valent metal synthesis and catalysis in a salt-free manner. 6

Figure 1.5 Ti^{II}/Ti^{IV} redox catalytic nitrene transfer in oxidative amination catalysis with examples of selected synthesis (left) and proposed mechanism of pyrrole formation (right). 8

Figure 1.6 Nitrene transfer promoted by a *π*-loaded bis(imido)Nb catalyst, which renders the imido fragment more labile than other group 5 imido complexes.....9

Figure 1.7 Reversible oxidative addition and reductive elimination of thiophene from a masked Ti^{II} synthon. 10

Figure 2.1 Formal [2+2+1] synthesis of pyrroles with alkynes and azides mediated by Ti^{IV} imido catalyst. 12

Figure 2.2 Nitrene transfer reactions catalyzed by early transition metal/redox non-innocent ligand systems. 13

Figure 2.3 (1) Initial reaction attempts of 2.1a and 2.2a catalyzed by $Ti(N^tBu)Cl_2py_3$ were marred by azide decomposition (right). (2) More Lewis-acidic catalyst $Ti(NTol)I_2(THF)_3$ formed desired pyrrole product without formation of side products.....14

Figure 2.4 Comparison of rate laws of pyrrole formation with azide versus azobenzene reveal different mechanisms of re-oxidation. 15

Figure 2.5 ^1H NMR spectrum of triphenylmethane in C_6D_5Br. 22

Figure 2.6 ^1H NMR spectrum of (p-tolyl)azide in C_6D_5Br. 23

Figure 2.7 ^{1}H NMR spectrum of 1-azidoadamantane in C_6D_5Br. 24
Figure 2.8 ^{1}H NMR spectrum of 1-azidodecane in C_6D_5Br. 25
Figure 2.9 ^{1}H NMR spectrum of benzylazide in C_6D_5Br. 26
Figure 2.10 ^{1}H NMR spectrum of azidomethyl phenyl sulfide in C_6D_5Br. 27
Figure 2.11 ^{1}H NMR spectrum of trityl azide in C_6D_5Br. 28
Figure 2.12 ^{1}H NMR spectrum of 2-butyne in C_6D_5Br. 29
Figure 2.13 ^{1}H NMR spectrum of diphenylacetylene in C_6D_5Br. 30
Figure 2.14 ^{1}H NMR spectrum of 1-phenyl-1-propyne in C_6D_5Br. 31
Figure 2.15 ^{1}H NMR spectrum of *p*-tolylacetylene in C_6D_5Br. 32
Figure 2.16 ^{1}H NMR spectrum of *t*-butylacetylene in C_6D_5Br. 33
Figure 2.17 ^{1}H NMR spectrum of (trimethylsilyl)acetylene in C_6D_5Br. 34
Figure 2.18 ^{1}H NMR spectrum of 1,7-octadiyne in C_6D_5Br. 35
Figure 2.19 ^{1}H NMR spectrum of 1-(p-tolyl)-4,5-(diethyl)-1,2,3-triazole (2.6aa) in C_6D_5Br. *Taken from XYS04097.* 37
Figure 2.20 Before (bottom, t = 0 h) and after (top, t = 70 h) ^{1}H NMR spectrum of 3-hexyne and (*p*-tolyl)azido reaction in C_6D_5Br. *Taken from XYS04097B.* 37
Figure 2.21 ^{1}H NMR spectrum of 1-adamantyl-4,5-diethyl-1H-1,2,3-triazole (2.6ba) in C_6D_5Br. *Taken from AJP05135B.* 38
Figure 2.22 Before (bottom, t = 0 hr) and after (top, t = 5 days) ^{1}H NMR spectrum of 3-hexyne and 1-azidoadamantane reaction in C_6D_5Br. *Taken from AJP05135B.* 39
Figure 2.23 ^{1}H NMR spectrum of 1-adamantyl-4,5-di(methyl)-1H-1,2,3-triazole (2.6bb) in C_6D_5Br. *Taken from XYS04038A.* 40
Figure 2.24 Before (bottom, t = 0 h) and after (top, t = 16 h) ^{1}H NMR spectrum of 2-butyne and 1-azidoadamantane reaction in C_6D_5Br. *Taken from XYS04038A.* 40
Figure 2.25 ^{1}H NMR spectrum of 1-adamantyl-4,5-diphenyl-1H-1,2,3-triazole (2.6bc) in C_6D_5Br. *Taken from AJP05135A.* 41
Figure 2.26 Before (bottom, t = 0 hr) and after (top, t = 5 days) ^{1}H NMR spectrum of diphenylacetylene and 1-azidoadamantane reaction in C_6D_5Br. *Taken from AJP05135A.* 42

Figure 2.27 ^{1}H NMR spectrum of 1-adamantyl-4-methyl-5-phenyl-1H-1,2,3-triazole and 1-adamantyl-5-methyl-4-phenyl-1H-1,2,3-triazole (2.6bd) in C_6D_5Br. *Taken from AJP05091-2H.* 43
Figure 2.28 Zoom-in ^{1}H NMR spectrum of the alkyl region of 1-adamantyl-4-methyl-5-phenyl-1H-1,2,3-triazole and 1-adamantyl-5-methyl-4-phenyl-1H-1,2,3-triazole (2.6bd) in C_6D_5Br. *Taken from AJP05091-2H.*.....44
Figure 2.29 Before (bottom, t = 0 hr) and after (top, t = 24 h) ^{1}H NMR spectrum of 1-phenyl-1-propyne and 1-azidoadamantane reaction in C_6D_5Br. *Taken from AJP05091-2H.* 45
Figure 2.30 ^{1}H NMR spectrum of 1-adamantyl-4-(*n*-butyl)-1H-1,2,3-triazole and 1-adamantyl-5-(*n*-butyl)-1H-1,2,3-triazole (2.6be) in C_6D_5Br. *Taken from XYS04038_B.* ..46
Figure 2.31 Zoom-in ^{1}H NMR spectrum of 1-adamantyl-4-(*n*-butyl)-1H-1,2,3-triazole and 1-adamantyl-(5-*n*-butyl)-1H-1,2,3-triazole (2.6be) in C_6D_5Br. *Taken from XYS04038_B.* 47
Figure 2.32 Before (bottom, t = 0 h) and after (top, t = 16 h) ^{1}H NMR spectrum of 1-hexyne and 1-azidoadamantane reaction in C_6D_5Br. *Taken from XYS04038_B.*.....47
Figure 2.33 ^{1}H NMR spectrum of 1-adamantyl-4-(*p*-tolyl)-1H-1,2,3-triazole and 1-adamantyl-5-(*p*-tolyl)-1H-1,2,3-triazole (2.6bf) in C_6D_5Br. *Taken from XYS04038_D.*...49
Figure 2.34 Before (bottom, t = 0 h) and after (top, t = 16 h) ^{1}H NMR spectrum of (*p*-tolyl)acetylene and 1-azidoadamantane reaction in C_6D_5Br. *Taken from XYS04038_D.*..49
Figure 2.35 ^{1}H NMR spectrum of 1-(*p*-tolyl)-4-(*t*-butyl)-1H-1,2,3-triazole and 1-(*p*-tolyl)-5-(*t*-butyl)-1H-1,2,3-triazole (2.6ag) in C_6D_5Br. *Taken from XYS04038_F.*.....51
Figure 2.36 Zoom-in ^{1}H NMR spectrum of 1-(*p*-tolyl)-4-(*t*-butyl)-1H-1,2,3-triazole and 1-(*p*-tolyl)-5-(*t*-butyl)-1H-1,2,3-triazole (2.6ag) in C_6D_5Br. *Taken from XYS04038_F*.....51
Figure 2.37 Before (bottom, t = 0 h) and after (top, t = 16 h) ^{1}H NMR spectrum of (*t*-butyl)acetylene and (*p*-tolyl)azido reaction in C_6D_5Br. *Taken from XYS04038_F.*.....52
Figure 2.38 ^{1}H NMR spectrum of 1-adamantyl-4-(trimethylsilyl)-1H-1,2,3-triazole (2.6bh) in C_6D_5Br. *Taken from XYS04038_E.* 53
Figure 2.39 Before (bottom, t = 0 h) and after (top, t = 16 h) ^{1}H NMR spectrum of (trimethylsilyl)acetylene and 1-azidoadamantane reaction in C_6D_5Br. *Taken from XYS04038_E.*.....54

Figure 2.40 ^{1}H NMR spectrum of 1-adamantyl-4-(5-hexyn-1-yl)-1H-1,2,3-triazole (2.6bi) in C_6D_5Br. *Taken from AJP05141*.....55
Figure 2.41 Before (bottom, t = 0 h) and after (top, t = 24 h) ^{1}H NMR spectrum of 1,7-octadiyne and 1-azidoadamantane reaction in C_6D_5Br. *Taken from AJP05141.* 56
Figure 2.42 ^{1}H NMR spectrum of 1-(*n*-decyl)-4,5-(diethyl)-1,2,3-triazole (2.6ca) in C_6D_5Br. *Taken from XYS04097F*. 57
Figure 2.43 Before (bottom, t = 0 h) and after (top, t = 70 h) zoom-in ^{1}H NMR spectrum of 3-hexyne and 1-azidodecane reaction in C_6D_5Br. *Taken from XYS04097F.* 58
Figure 2.44 ^{1}H NMR spectrum of 1-(benzyl)-4,5-(diethyl)-1,2,3-triazole (2.6da) in C_6D_5Br. *Taken from XYS04097C.*.....59
Figure 2.45 Before (bottom, t = 0 h) and after (top, t = 70 h) 1H NMR spectrum of 3-hexyne and benzylazide reaction in C_6D_5Br. *Taken from XYS04097C.*.....60
Figure 2.46 ^{1}H NMR spectrum of 1-(methyl phenyl sulfide)-4,5-(diethyl)-1,2,3-triazole (2.6ea) in C_6D_5Br. *Taken from XYS04097J.* 61
Figure 2.47 Before (bottom, t = 0 h) and after (top, t = 70 h) ^{1}H NMR spectrum of 3-hexyne and azidomethyl phenyl sulfide reaction in C_6D_5Br. *Taken from XYS04097J.* 62
Figure 2.48 Before (bottom, t = 0 h) and after (top, t = 70 h) ^{1}H NMR spectrum of 3-hexyne and trityl azide reaction in C_6D_5Br. *Taken from XYS04097E.* 63
Figure 2.49 ^{1}H NMR spectrum of hexamethylbenzene (2.9b) in C_6D_5Br. *Taken from XYS04019C.* 64
Figure 2.50 Before (bottom, t = 0 h) and after (top, t = 16 h) ^{1}H NMR spectrum of hexamethylbenzene (2.9b) in C_6D_5Br. *Taken from XYS04019C.* 64
Figure 2.51 Post reaction ^{1}H NMR spectrum of diphenylacetylene treated with $TiCl_4$ and Mg* in C_6D_5Br. Major peaks in the aromatic region are identical to diphenylacetylene. *Taken from AJP05145B-1H.*.....65
Figure 2.52 ^{1}H NMR spectrum of 1,2,4-trimethyl-3,5,6-triphenylbenzene and 1,3,5-trimethyl-2,4,6-triphenylbenzene (2.9d) in C_6D_5Br. *Taken from AJP05140A-1H.* 67
Figure 2.53 Zoom-in ^{1}H NMR spectrum of 1,2,4-trimethyl-3,5,6-triphenylbenzene and 1,3,5-trimethyl-2,4,6-triphenylbenzene (2.9d) in C_6D_5Br. *Taken from AJP05140A-1H.* .67
Figure 2.54 ^{1}H NMR spectrum of 1,3,5-tri(*p*-tolyl)benzene (2.9f) in C_6D_5Br. *Taken from XYS03158_3H.* 68

Figure 2.55 ^{1}H NMR spectrum of 1,2,4-tri(*p*-tolyl)benzene (2.9d) in C_6D_5Br. *Taken from XYS03155_4H.* 69
Figure 2.56 ^{1}H NMR spectrum of 1,3,5-tri(*t*-butyl)benzene and 1,2,4-tri(*t*-butyl)benzene (2.9g) in C_6D_5Br. *Taken from XYS04047_B.* 70
Figure 2.57 ^{1}H NMR spectrum of 1,3,5-tris(trimethylsilyl)benzene and 1,2,4-tris(trimethylsilyl)benzene (2.9h) in C_6D_5Br. *Taken from XYS04047_A.* 71
Figure 2.58 ^{1}H NMR spectrum of 1,4-bis(5,6,7,8-tetrahydronaphthalen-2-yl)butane (2.9i) in C_6D_5Br. *Taken from AJP05071*.....73
Figure 2.59 ^{1}H NMR spectrum of 3-hexyne reaction with 1-azidoadamantane in C_6D_5Br. *Taken from AJP05031A-2H.*.....74
Figure 2.60 Zoom-in stacked ^{1}H NMR spectrum of 3-hexyne reaction with 1-azidoadamantane t = 16 h (3), t = 0 h (2) and click reaction (1) in C_6D_5Br. *Taken from AJP05031A & AJP05135B-2H.* 75
Figure 2.61 ^{1}H NMR spectrum of 1-azidoadamantane reaction with 3-hexyne (t = 2 h) in C_6D_5Br. *Taken from XYS04112E*. 76
Figure 2.62 ^{1}H NMR spectrum of 2,3,4,5-tetraethyl-1-adamantyl-1*H*-pyrrole (2.3ba) in $CDCl_3$. *Taken from XYS04116_4H*.....77
Figure 2.63 ^{13}C NMR spectrum of 2,3,4,5-tetraethyl-1-adamantyl-1*H*-pyrrole (2.3ba) in $CDCl_3$. *Taken from XYS04116_1C.*.....78
Figure 2.64 ^{1}H NMR spectrum of 2-butyne reaction with 1-azidoadamantane in C_6D_5Br. *Taken from XYS04017G*.....79
Figure 2.65 Zoom-in stacked ^{1}H NMR spectrum of click reaction (4), 2-butyne reaction with 1-azidoadamantane t = 16 h (3), t = 0 h (2) and trimer reaction (1) in C_6D_5Br. *Taken from XYS04017G.*.....80
Figure 2.66 ^{1}H NMR spectrum of diphenylacetylene reaction with 1-azidoadamantane in C_6D_5Br. *Taken from AJP05033A-2H.* 81
Figure 2.67 Stacked ^{1}H NMR spectrum of diphenylacetylene reaction with 1-azidoadamantane t = 16 h (3), t = 0 h (2) and click reaction (1) in C_6D_5Br. *Taken from AJP05033A and AJP05135A*.....82
Figure 2.68 ^{1}H NMR spectrum of 1-phenyl-1-propyne reaction with 1-azidoadamantane in C_6D_5Br. *Taken from AJP05031C-2H.* 83

Figure 2.69 Zoom-in ^{1}H NMR spectrum of 1-phenyl-1-propyne reaction with 1-azidoadamantane in C_6D_5Br. *Taken from AJP05031C-2H.*.....84
Figure 2.70 ^{1}H-^{13}C NMR spectrum of 1-phenyl-1-propyne reaction with 1-azidoadamantane in C_6D_5Br. *Taken from AJP05089-HC-HMBC.* 84
Figure 2.71 ^{1}H-^{15}N NMR spectrum of 1-phenyl-1-propyne reaction with 1-azidoadamantane in C_6D_5Br. *Taken from AJP05089-HNHMBC.*.....85
Figure 2.72 Zoom-in stacked ^{1}H NMR spectrum of 1-phenyl-1-propyne reaction with 1-azidoadamantane t = 16 h (4), t = 0 h (3), trimerization (2) and click reaction (1) in C_6D_5Br. *Taken from AJP05031C, AJP05140A-1H and AJP05091-2H.*.....86
Figure 2.73 GC/FID trace of 1-phenyl-1-propyne reaction with 1-azidoadamantane in C_6D_5Br. 86
Figure 2.74 ^{1}H NMR spectrum of 1-azidodecane reaction with 3-hexyne in C_6D_5Br. *Taken from XYS04110D.*.....88
Figure 2.75 Stacked ^{1}H NMR spectrum of 1-azidodecane reaction with 3-hexyne t = 2 h (3), t = 0 h (2) and click reaction (1) in C_6D_5Br. *Taken from XYS04097F and XYS04110D.* 88
Figure 2.76 ^{1}H NMR spectrum of 2,3,4,5-tetraethyl-1-decyl-1*H*-pyrrole (2.3ca) in $CDCl_3$. *Taken from XYS04117_4H.*.....90
Figure 2.77 ^{13}C NMR spectrum of 2,3,4,5-tetraethyl-1-decyl-1*H*-pyrrole (2.3ca) in $CDCl_3$. *Taken from XYS04117_1C.*.....91
Figure 2.78 ^{1}H NMR spectrum of benzylazide reaction with 3-hexyne in C_6D_5Br. *Taken from AJP05120B.* 92
Figure 2.79 Zoom-in stacked ^{1}H NMR spectrum of benzylazide reaction with 3-hexyne t = 2 h (3), t = 0 h (2) and click reaction (1) in C_6D_5Br. * Click products highlighted in green. *Taken from AJP0505120B and XYS04097C.*.....93
Figure 2.80 ^{1}H NMR spectrum of 2,3,4,5-tetraethyl-1-benzyl-1*H*-pyrrole (2.3da) in $CDCl_3$. *Taken from AJP05122-2H.* 94
Figure 2.81 Zoom-in ^{1}H NMR spectrum of 2,3,4,5-tetraethyl-1-benzyl-1*H*-pyrrole (2.3da) in $CDCl_3$. *Taken from AJP05122-2H.* 95
Figure 2.82 ^{13}C NMR spectrum of 2,3,4,5-tetraethyl-1-benzyl-1*H*-pyrrole (2.3da) in $CDCl_3$. *Taken from AJP05122-1C.* 95

Figure 2.83 ^{1}H NMR spectrum of (*p*-tolyl)azide reaction with 3-hexyne in C_6D_5Br. *Taken from AJP05120A.* 96
Figure 2.84 Zoom-in stacked ^{1}H NMR spectrum of (*p*-tolyl)azide reaction with 3-hexyne t = 2 h (4), t = 0 h (3), hydroamination of 3-hexyne with *p*-toluidine (2) and click reaction (1). Triazole and hydroamination products are highlighted in green and orange respectively. *Taken from AJP05120A.* 97
Figure 2.85 Zoom-in stacked ^{1}H NMR spectrum of (*p*-tolyl)azido reaction with 3-hexyne t = 2 h (4), t = 0 (3), hydroamination of 3-hexyne with *p*-toluidine (2) and click reaction (1). 98
Figure 2.86 No-D NMR of (*p*-tolyl)azide reaction with 3-hexyne in PhBr. *Taken from AJP05102B.*.....99
Figure 2.87 Stacked ^{1}H NMR spectrum of azidomethyl phenyl sulfide reaction with 3-hexyne t = 2 h (3), t = 0 h (2) and click reaction (1) in C_6D_5Br. *Taken from XYS04110SA and XYS04097J.*.....100
Figure 2.88 Stacked ^{1}H NMR spectrum of tritylazide reaction with 3-hexyne t = 2 h (3), t = 0 h (2) and click reaction (1) in C_6D_5Br. *Taken from XYS04110C and XYS04097E.*..101
Figure 2.89 ^{1}H NMR spectrum of 1-hexyne reaction with 1-azidoadamantane in C_6D_5Br. *Taken from XYS04014_B.* 105
Figure 2.90 Zoom-in ^{1}H NMR spectrum of 1-hexyne reaction with 1-azidoadamantane in C_6D_5Br. *Taken from XYS04014_B.* 105
Figure 2.91 Stacked ^{1}H NMR spectrum of 1-hexyne reaction with 1-azidoadamantane t = 6 h (4), t = 0 h (3), trimerization reaction (2) and click reaction (1) in C_6D_5Br. *Taken from XYS04014_B and XYS04038_B.*.....106
Figure 2.92 ^{1}H NMR spectrum of 1-hexyne reaction with 1-azidoadamantane in $CDCl_3$. *Taken from XYS04036_4H.*.....107
Figure 2.93 ^{15}N-^{1}H HMBC NMR spectrum of 1-hexyne reaction with 1-azidoadamantane in $CDCl_3$. *Taken from XYS04036_1NHMBC.*.....107
Figure 2.94 ^{1}H NMR spectrum of tolylacetylene reaction with 1-azidoadamantane in C_6D_5Br. *Taken from XYS04059_B.* 109

Figure 2.95 Stacked ^{1}H NMR spectrum of tolylacetylene reaction with 1-azidoadamantane t = 6 h (5), t = 0 h (4), 1,2,4-trimer (3), 1,3,5-trimer (2) and click reaction (1) in C_6D_5Br. *Taken from XYS04059_B, XYS03158_3H, XYS03155_4H and XYS04038_D.*.....110

Figure 2.96 ^{1}H NMR spectrum of (*t*-butyl)acetylene reaction with 1-azidoadamantane in C_6D_5Br. *Taken from XYS04014_C.* 111

Figure 2.97 Stacked ^{1}H NMR spectrum of (*t*-butyl)acetylene reaction with 1-azidoadamantane t = 6 h (4), t = 0 h (3), trimer reaction (2) and click reaction (1) in C_6D_5Br. *Taken from XYS04014_C, XYS04047_B and XYS04038_F.*.....112

Figure 2.98 Zoom-in stacked ^{1}H NMR spectrum of (*t*-butyl)acetylene reaction with 1-azidoadamantane t = 6 h (4), t = 0 h (3), trimer reaction (2) and click reaction (1) in C_6D_5Br. *Taken from XYS04014_C, XYS04047_B and XYS04038_F.*.....113

Figure 2.99 Zoom-in stacked ^{1}H NMR spectrum of (t-butyl)acetylene reaction with 1-azidoadamantane t = 6 h (4), t = 0 h (3), trimer reaction (2) and click reaction (1) in C_6D_5Br. *Taken from XYS04014_C, XYS04047_B and XYS04038_F*.....114

Figure 2.100 ^{1}H NMR spectrum of (trimethylsilyl)acetylene reaction with 1-azidoadamantane in C_6D_5Br. *Taken from XYS04015_B.*.....115

Figure 2.101 Stacked ^{1}H NMR spectrum of (trimethylsilyl)acetylene reaction with 1-azidoadamantane t = 6 h (4), t = 0 h (3), trimer reaction (2) and click reaction (1) in C_6D_5Br. *Taken from XYS04015_B, XYS04047A and XYS04038_E.*.....116

Figure 2.102 Zoom-in stacked ^{1}H NMR spectrum of (trimethylsilyl)acetylene reaction with 1-azidoadamantane t = 6 h (4), t = 0 h (3), trimer reaction (2) and click reaction (1) in C_6D_5Br. *Taken from XYS04015_B, XYS04047A and XYS04038_E.* 117

Figure 2.103 ^{1}H NMR spectrum of 1,7-octadiyne reaction with 1-azidoadamantane in C_6D_5Br. *Taken from AJP05034.*.....118

Figure 2.104 Zoom-in ^{1}H NMR spectrum of 1,7-octadiyne reaction with 1-azidoadamantane in C_6D_5Br. *Taken from AJP05034.* 119

Figure 2.105 Stacked ^{1}H spectra of 1,7-octadiyne reaction with 1-azidoadamantane t = 6 h (4), t = 0 h (3), trimer (2) and click reaction (1) in C_6D_5Br. *Taken from AJP05034.*...119

Figure 2.106 Zoom-in stacked ^{1}H spectra of 1,7-octadiyne reaction with 1-azidoadamantane t = 6 h (4), t = 0 h (3), trimer (2) and click reaction (1) in C_6D_5Br. *Taken from AJP05034.*.....120

Figure 3.1 General methodology of obtaining an active Ti^{II} intermediate *via* the coupling of Ti^{IV} imido and 2 alkynes.....123
Figure 3.2 Previously reported Ti^{II}/Ti^{IV} redox catalytic reactions. 124
Figure 3.3 Ti and Zr imido precatalysts investigated for the generality of forming M^{II} intermediate.....125
Figure 3.4 Catalytic alkyne trimerization with Ti^{IV} imido catalysts. 126
Figure 3.5 ^{1}H NMR spectrum of N-(*p*-tolyl)-N,N-bis(trimethylsilyl)amine in C_6D_6. *Taken from ZWG04072.* 136
Figure 3.6 ^{13}C NMR spectrum of N-(*p*-tolyl)-N,N-bis(trimethylsilyl)amine in C_6D_6. *Taken from ZWG04072.* 136
Figure 3.7 ^{1}H NMR spectrum of 3.2 in $CDCl_3$. *Taken from ZWG04081.* 138
Figure 3.8 ^{13}C NMR spectrum of 3.2 in $CDCl_3$. *Taken from ZWG04081.* 138
Figure 3.9 ^{1}H NMR spectrum of 3.3 in $CDCl_3$. *Taken from ZWG04078-C.* 140
Figure 3.10 ^{13}C NMR spectrum of 3.3 in $CDCl_3$. *Taken from ZWG04078-C.* 140
Figure 3.11 50 % thermal ellipsoid drawing of 3.3. Hydrogen atoms are omitted for clarity. 141
Figure 3.12 ^{1}H NMR spectrum of 3.4 in C_6D_6. *Taken from JAL01063.* 143
Figure 3.13 ^{13}C NMR spectrum of 3.4 in C_6D_6. *Taken from JAL01063.* 143
Figure 3.14 ^{1}H NMR spectrum of 3.5 in C_6D_6. *Taken from JAL01064-Xtal.*.....145
Figure 3.15 ^{13}C NMR spectrum of 3.5 in C_6D_6. *Taken from JAL01064-13C.*.....145
Figure 3.16 ^{1}H NMR spectrum of 3.6 in $CDCl_3$. *Taken from TAW01150.*.....147
Figure 3.17 ^{13}C NMR spectrum of 3.6 in $CDCl_3$. *Taken from TAW01150.*.....148
Figure 3.18 ^{1}H NMR spectrum of 3.7 in $CDCl_3$. *Taken from TAW01151.*.....149
Figure 3.19 ^{1}H NMR spectrum of 3.12 in C_6D_6. *Taken from XYS02069_3H.*.....151
Figure 3.20 ^{13}C NMR spectrum of 3.12 in C_6D_6. *Taken from XYS02069_1C.*.....151
Figure 3.21 ^{1}H NMR spectrum of **3.13** in C_6D_6. *Taken from XYS02038_2H.*.....153
Figure 3.22 ^{13}C NMR spectrum of 3.13 in C_6D_6. *Taken from XYS02038_1C.*.....153
Figure 3.23 50 % thermal ellipsoid drawing of 13. Hydrogen atoms are omitted for clarity. 154
Figure 3.24 ^{1}H NMR spectrum of 3.14 in C_6D_6. *Taken from XYS02026_2H.*.....155
Figure 3.25 ^{13}C NMR spectrum of 3.14 in C_6D_6. *Taken from XYS02026.* 156

Figure 3.26 50 % thermal ellipsoid drawing of 3.14. Hydrogen atoms are omitted for clarity. 156
Figure 3.27 ^{1}H NMR spectrum of 3.15 in C_6D_6. *Taken from XYS02053_2H.* 158
Figure 3.28 ^{13}C NMR spectrum of 3.15 in C_6D_6. *Taken from XYS02053_1C.* 158
Figure 3.29 50 % thermal ellipsoid drawing of 3.15. Hydrogen atoms are omitted for clarity. 159
Figure 3.30 ^{1}H NMR spectrum of 3.16 in $CDCl_3$. *Taken from EPB02010.* 160
Figure 3.31 ^{13}C NMR spectrum of 3.16 in $CDCl_3$. *Taken from EPB02010.* 161
Figure 3.32 ^{1}H NMR spectrum of 1,3,5-trimethoxybenzene in C_6D_5Br. 162
Figure 3.33 ^{1}H NMR spectrum of 3-hexyne in C_6D_5Br. 163
Figure 3.34 ^{1}H NMR spectrum of 1-hexyne in C_6D_5Br. 164
Figure 3.35 ^{1}H NMR spectrum of 5,7-dodecadiyne in C_6D_5Br. 165
Figure 3.36 ^{1}H NMR spectrum of the mixture of 1,3,5-tri-*n*-butyl-benzene (3a) and 1,2,4-tri-*n*-butyl-benzene (3b) in C_6D_5Br. *Taken from XYS02044_2H.* 166
Figure 3.37 ^{1}H NMR spectrum of hexaethylbenzene (3f) in C_6D_5Br. Taken from *XYS02045_2H.* 168
Figure 3.38 ^{1}H NMR spectrum of 2,5-di-*n*-butyl-1-tolyl-1*H*-pyrrole (3d) in C_6D_5Br. *Taken from XYS02154_3H.* 169
Figure 3.39 Zoom-in ^{1}H-^{1}H COSY NMR spectrum of 2,5-di-*n*-butyl-1-tolyl-1*H*-pyrrole (3d) in C_6D_5Br. *Taken from XYS02154_1COSY.* 170
Figure 3.40 ^{1}H NMR spectrum of 2,4-di-*n*-butyl-1-*p*-tolyl-1*H*-pyrrole (3c) in C_6D_5Br. *Taken from XYS02041_3H.* 171
Figure 3.41 Zoom-in ^{1}H-^{1}H COSY NMR spectrum of 2,4-di-*n*-butyl-1-*p*-tolyl-1*H*-pyrrole (3c) in C_6D_5Br. *Taken from XYS02041_1COSY.* 172
Figure 3.42 ^{1}H NMR spectrum of 2,5-di-*n*-butyl-1-phenyl-1*H*-pyrrole (3d) in C_6D_5Br. *Taken from XYS02149_5H.* 173
Figure 3.43 Zoom-in ^{1}H-^{1}H COSY NMR spectrum of 2,5-di-*n*-butyl-1-phenyl-1*H*-pyrrole (3d) in C_6D_5Br. *Taken from XYS02149_5H_1COSY.* 174
Figure 3.44 ^{1}H NMR spectrum of 2,4-di-*n*-butyl-1-phenyl-1*H*-pyrrole (3c) in C_6D_5Br. *Taken from XYS02129_3H.* 175

Figure 3.45 ^{1}H NMR spectrum of 2,4-di-*n*-butyl-1-(*t*-butyl)-1*H*-pyrrole (3c) in C_6D_5Br. *Taken from XYS02121_2H.*.....176
Figure 3.46 ^{1}H NMR spectrum of 2,3,4,5-tetraethyl-1-(*p*-tolyl)-1*H*-pyrrole (3g) in C_6D_5Br. *Taken from XYS02042_2H.*.....177
Figure 3.47 ^{1}H NMR spectrum of 2,3,4,5-tetraethyl-1-phenyl-1*H*-pyrrole (3g) in C_6D_5Br. *Taken from XYS02091_3H.*.....178
Figure 3.48 ^{1}H NMR spectrum of 2,3,4,5-tetraethyl-1-(*t*-butyl)-1*H*- pyrrole (3g) in C_6D_5Br. *Taken from XYS02119_2H.*.....179
Figure 3.49 Representative zoom-in ^{1}H NMR spectrum of a 1-hexyne catalytic run in C_6D_5Br (115 °C/16 h/Precatalyst 3.2). *Taken from ZWG04123D.* 180
Figure 3.50 Representative zoom-in ^{1}H NMR spectrum of a 1-hexyne catalytic run in C_6D_5Br (115 °C/16 h/Precatalyst **3.2**). *Taken from ZWG04123C.*.....181
Figure 3.51 Representative zoom-in ^{1}H NMR spectrum of a 3-hexyne catalytic run in C_6D_5Br (115 °C/16 h/Precatalyst 3.2). *Taken from ZWG04123C.*.....181
Figure 3.52 ln[Hex] *vs.* time for a 3-hexyne catalytic run in C_6D_5Br (RT/Precatalyst 3.3). 183
Figure 3.53 ln[Hex] *vs.* time for a 1-hexyne catalytic run in C_6D_5Br (RT/Precatalyst 3.5). 184
Figure 3.54 ln[Hex] *vs.* time for a 1-hexyne catalytic run in C_6D_5Br (RT/Precatalyst 3.10). 185
Figure 4.1 Application of ISPCA towards rational catalyst design for a Ti-catalyzed formal [2+2+1] cycloaddition reaction with phenyl propyne and azobenzene. 189
Figure 4.2 Examples of analysis approaches commonly employed in chemical catalysis. 191
Figure 4.3 Graphical outline of the iterative supervised PCA (ISPCA) strategy. 192
Figure 4.4 Top: Ti-catalyzed [2+2+1] synthesis of regioisomeric pyrroles from PhCCMe. Bottom: computed reaction pathways calculated at M06/6-311G(d,p)/SMD at 110 °C, highlighting rate- and selectivity-determining 2nd alkyne insertion (TS 2, maroon) is nonselective with standard catalysts. L_n = Cl_2py. Calculated transition-state and intermediate free energies (kcalmol^{-1}) are presented below each structure. Species labels

and calculated product ratios are taken from prior mechanistic work.[82] Experimental ratios are taken from initial discovery.[79] 195
Figure 4.5 Initial catalyst screen (experimental and predicted selectivity) for selective [2+2+1] pyrrole formation from phenylpropyne. The most selective catalysts are drawn in orange. Predicted values are calculated from ISPCA model 1. Conditions: 0.5 mmol phenyl propyne, 0.1 mmol azobenzene, 10 mol % [Ti], 0.5 mL $PhCF_3$, 115 °C, 16 h, average of 2-3 runs. 197
Figure 4.6 Principal component map constructed from the top 3 components of ISPCA model I and populated by the catalyst training set. Coloring is set by a dynamic k-means clustering algorithm (see SI for additional details). 199
Figure 4.7 Unoptimized (black) and ISPCA (blue) model predictions versus experimental plots of reaction selectivity delivered by the catalyst training set.....200
Figure 4.8 Schematic representation of steric effects on the imido-Ti-N_{py} angle.....202
Figure 4.9 Second-generation catalysts predicted and synthesized using ISPCA model I and third-generation catalyst predicted and synthesized using weighted ISPCA model II that incorporates catalysts 4.1-4.22. The most selective catalysts are drawn in orange. Conditions: 0.5 mmol phenyl propyne, 0.1 mmol azobenzene, 10 mol % [Ti], 0.5 mL $PhCF_3$, 115 °C, 16 h, average of 2-3 runs.....204
Figure 4.10 Example catalysts deemed not different enough to warrant synthesis *via* prediction from ISPCA model I. 206
Figure 4.11 Possible isomers of TS2 ($TS2_{BF}$ shown) highlighting different positions of the pyridine ligand—either *trans* to the incoming alkyne (*trans-1*) or *cis* to the incoming alkyne (*cis*-1 and *cis*-2). In all cases the *cis*-2 isomer is lowest in free energy.....208
Figure 4.12 Sterically-encumbered pyridine ligands disfavor $TS2_{BE}$, leading to selective formation of 4C through $TS2_{BF}$.....210
Figure 4.13 Electron-rich, bulky pyridines favor coordinated selective species, while solely sterically encumbered pyridines decoordinate, eroding selectivity. 211
Figure 4.14 ^{1}H NMR spectrum of 4.2 in $CDCl_3$. *Taken from XYS0054B_1H.*.....215
Figure 4.15 ^{1}H NMR spectrum of 4.3 in $CDCl_3$. *Taken from XYS-2019-183_1H.*.....216
Figure 4.16 ^{13}C NMR spectrum of 4.3 in C_6D_6. *Taken from XYS-2019-183_2C.* 217
Figure 4.17 ^{19}F NMR spectrum of 4.3 in $CDCl_3$. *Taken from XYS-2019-183_1F.*.....217

Figure 4.18 ^{1}H NMR spectrum of 4.4 in $CDCl_3$. *Taken from XYS-2020-007_1H.*.....219
Figure 4.19 ^{1}H NMR spectrum of 4.4 in $CDCl_3$ at 320K. *Taken from XYS-2020-007_320K.* 219
Figure 4.20 ^{13}C NMR spectrum of 4.4 in $CDCl_3$. *Taken from XYS-2020-007_1C.*.....220
Figure 4.21 ^{1}H NMR spectrum of 4.5 in $CDCl_3$. *Taken from XYS-2019-174B_1H.*.....221
Figure 4.22 ^{1}H NMR spectrum of 4.6 in $CDCl_3$. *Taken from XYS05013-2H.* 222
Figure 4.23 ^{13}C NMR spectrum of 4.6 in $CDCl_3$. *Taken from XYS05013-1C.* 223
Figure 4.24 ^{1}H NMR spectrum of 4.7 in $CDCl_3$. *Taken from XYS-2019-185-7H.*.....224
Figure 4.25 ^{13}C NMR spectrum of 4.7 in $CDCl_3$. *Taken from XYS-2019-185-3C.*.....225
Figure 4.26 Zoom-in ^{1}H-^{1}H COSY NMR spectrum of 4.7 in $CDCl_3$. *Taken from XYS-2019-185-COSY.*.....225
Figure 4.27 ^{1}H-^{1}H NOESY NMR spectrum of 4.7 in $CDCl_3$. *Taken from XYS-2019-185-NOESY.* 226
Figure 4.28 DOSY NMR spectrum of 4.7 in $CDCl_3$. *Taken from XYS-2019-185-DOSY6.* 226
Figure 4.29 Stacked ^{1}H NMR spectrum of 4.7 at 380 K (2) and room temperature (1) in C_6D_5Br. *Taken from XYS-2019-185_380K.* 227
Figure 4.30 50 % thermal ellipsoid drawing of 4.7. Hydrogen atoms are omitted for clarity. 227
Figure 4.31 ^{1}H NMR spectrum of 4.9 in $CDCl_3$. *Taken from AJP-2019-0003-2H.*.....229
Figure 4.32 ^{1}H NMR spectrum of 4.10 in $CDCl_3$. *Taken from XYS-2019-179-2H.*.....230
Figure 4.33 ^{13}C NMR spectrum of 4.10 in $CDCl_3$. *Taken from XYS-2019-179-1C.*.....231
Figure 4.34 ^{1}H NMR spectrum of 4.11 in $CDCl_3$. *Taken from XYS-2019-151B-2H.* 232
Figure 4.35 ^{13}C NMR spectrum of 4.11 in $CDCl_3$. *Taken from XYS-2019-151B-1C.* ...233
Figure 4.36 ^{1}H NMR spectrum of 4.12 in C_6D_6. *Taken from XYS-2019-162_4H.* 234
Figure 4.37 ^{13}C NMR spectrum of 4.12 in C_6D_6. *Taken from XYS-2019-162_1C.*.....235
Figure 4.38 50 % thermal ellipsoid drawing of 4.12. Hydrogen atoms are omitted for clarity. 235
Figure 4.39 ^{1}H NMR spectrum of 4.13 in C_6D_6. *Taken from XYS-2019-159B_5H.* 237
Figure 4.40 ^{13}C NMR spectrum of 4.13 in C_6D_6. *Taken from XYS-2019-159B_1C.* 237
Figure 4.41 ^{1}H NMR spectrum of 4.14 in $CDCl_3$. *Taken from XYS-2019-115C_4H.* ...239

Figure 4.42 ^{13}C NMR spectrum of 4.14 in $CDCl_3$. *Taken from XYS-2019-115C_2C.*....239
Figure 4.43 50 % thermal ellipsoid drawing of 4.14. Hydrogen atoms are omitted for clarity. 240
Figure 4.44 ^{1}H NMR spectrum of 4.15 in $CDCl_3$. *Taken from XYS-2020-020B_1H.*.....241
Figure 4.45 ^{1}H NMR spectrum of 4.16 in $CDCl_3$. *Taken from XYS-2019-174A_1H.*.....242
Figure 4.46 ^{13}C NMR spectrum of 4.16 in $CDCl_3$. *Taken from XYS-2019-123A_1C.*....243
Figure 4.47 ^{1}H NMR spectrum of 4.17 in $CDCl_3$. *Taken from XYS-2019-165A_1H.*.....244
Figure 4.48 ^{13}C NMR spectrum of 4.17 in $CDCl_3$. *Taken from XYS-2019-165A_1C.*....245
Figure 4.49 ^{1}H NMR spectrum of 2,6-dimethyl-4-dimethylaminopyridine in $CDCl_3$. *Taken from CKK-2020-011_12H.* 246
Figure 4.50 ^{1}H NMR spectrum of 4.18 in $CDCl_3$. *Taken from XYS-2020-012A_1H.*.....248
Figure 4.51 Stacked variable temperature ^{1}H NMR spectra of 4.18 in C_6D_5Br. *Taken from XYS-2020-012A_VT.*.....248
Figure 4.52 Zoom-in stacked variable temperature ^{1}H NMR spectra of 4.18 in C_6D_5Br. *Taken from XYS-2020-012A_VT.* 249
Figure 4.53 ^{1}H-^{13}C HSQC NMR spectrum of 4.18 in $CDCl_3$. *Taken from XYS-2020-012A_HSQC.*.....249
Figure 4.54 ^{1}H-^{13}C HMBC NMR spectrum of 4.18 in $CDCl_3$. *Taken from XYS-2020-012A_C HMBC.*.....250
Figure 4.55 ^{1}H NMR spectrum of 4.19 in $CDCl_3$. *Taken from XYS-2019-161_1H.* 251
Figure 4.56 ^{13}C NMR spectrum of 4.19 in $CDCl_3$. *Taken from XYS-2019-161_1C.* 251
Figure 4.57 ^{1}H NMR spectrum of 4.20 in $CDCl_3$. *Taken from XYS-2019-140A_5H.*.....253
Figure 4.58 ^{13}C NMR spectrum of 4.20 in $CDCl_3$. *Taken from XYS-2019-140A_1C.*....253
Figure 4.59 ^{1}H NMR spectrum of 4.21 in C_6D_6. *Taken from XYS-2019-159_3H.* 255
Figure 4.60 ^{13}C NMR spectrum of 4.21 in C_6D_6. *Taken from XYS-2019-169_1C.*.....255
Figure 4.61 ^{19}F NMR spectrum of 4.21 in C_6D_6. *Taken from XYS-2019-169_3F.* 256
Figure 4.62 ^{1}H NMR spectrum of 4.22 in C_6D_6. *Taken from XYS-2019-178_2H.* 257
Figure 4.63 ^{13}C NMR spectrum of 4.22 in C_6D_6. *Taken from XYS-2019-178_1C.*.....258
Figure 4.64 ^{19}F NMR spectrum of 4.22 in C_6D_6. *Taken from XYS-2019-178_2F.* 258
Figure 4.65 ^{1}H NMR spectrum of 4.23 in $CDCl_3$. *Taken from XYS-2020-002_quantH.* 260

Figure 4.66 Stacked variable temperature ^{1}H NMR spectra of 4.23 in C_6D_5Br. *Taken from XYS-2020-002_VT.* 260
Figure 4.67 Zoom-in stacked variable temperature ^{1}H NMR spectrum of 4.23 in C_6D_5Br. *Taken from XYS-2020-002_VT.*.....261
Figure 4.68 ^{13}C NMR spectrum of 4.23 in $CDCl_3$. *Taken from XYS-2020-002_3C.* 261
Figure 4.69 ^{1}H-^{13}C HSQC NMR spectrum of 4.23 in $CDCl_3$. *Taken from XYS-2020-002_HSQC.* 262
Figure 4.70 ^{1}H-^{13}C HMBC NMR spectrum of 4.23 in $CDCl_3$. *Taken from XYS-2020-002_C HMBC.*.....262
Figure 4.71 ^{1}H NMR spectrum of 4.a in C_6D_6. *Taken from XYS-2019-160_2H.* 264
Figure 4.72 ^{13}C NMR spectrum of 4.a in C_6D_6. *Taken from XYS-2019-160_1C.*.....264
Figure 4.73 ^{1}H NMR spectrum of 4.b in C_6D_6. *Taken from XYS-2019-138_3H.* 266
Figure 4.74 ^{13}C NMR spectrum of 4.b in C_6D_6. *Taken from XYS-2019-138_1C.* 266
Figure 4.75 ^{1}H NMR spectrum of 4.d in $CDCl_3$. *Taken from XYS-2019-135B_4H*.....268
Figure 4.76 ^{13}C NMR spectrum of 4.d in $CDCl_3$. *Taken from XYS-2019-135B_1C.*.....269
Figure 4.77 ^{31}P NMR spectrum of 4.d in $CDCl_3$. *Taken from XYS-2019-135B_4P*. 269
Figure 4.78 50 % thermal ellipsoid drawing of 4.d. Hydrogen atoms are omitted for clarity. 270
Figure 4.79 ^{1}H NMR spectrum of 4.e in C_6D_6. *Taken from XYS04078B_3H*.....271
Figure 4.80 ^{13}C NMR spectrum of 4.e in C_6D_6. *Taken from XYS-2020-024A_1C.* 272
Figure 4.81 ^{1}H NMR spectrum of 4.f in C_6D_6. *Taken from XYS-2019-123C_2H.* 273
Figure 4.82 ^{13}C NMR spectrum of 4.f in C_6D_6. *Taken from XYS-2019-123C_1C.* 273
Figure 4.83 Representative ligand scaffolds common in literature tested in catalytic pyrrole formation with PhCCMe. See main text for conditions. 274
Figure 4.84 Ligand scaffolds that were unsuccessful in coordinating to Ti. 274
Figure 4.85 Representative stacked catalytic 1H NMR spectra at t = 16 h (2) and t = 0 h (1) in $PhCF_3$ (115 °C/ Precatalyst 4.1). *Taken from XYS-2020-004F*. 275
Figure 4.86 Representative zoom-in catalytic ^{1}H NMR spectra at t = 16 h in $PhCF_3$ (115 °C/ Precatalyst 4.1). *Taken from XYS-2020-004F.*.....276
Figure 4.87 Representative catalytic ^{1}H-^{15}N HMBC NMR spectra at t = 16 h in $PhCF_3$ (115 °C/ Precatalyst 4.1). *Taken from XYS-2020-004F_N HMBC.* 277

Figure 4.88 Yield of pyrrole *vs.* time for a catalytic reaction with precatalyst 4.23. 278
Figure 4.89 Regioselectivity of pyrroles (left axis) and total percent yield of pyrroles (right axis) *vs.* time for a catalytic reaction with precatalyst 4.23. 278
Figure 4.90 ^{1}H NMR spectrum of isolation attempt of product 4C in $CDCl_3$. *Taken from XYS-2020-022C_Column_F24-51*.....280
Figure 4.91 ^{13}C NMR spectrum of isolation attempt of product 4C in $CDCl_3$. *Taken from XYS-2020-022C_Column_F24-51_C.* 281
Figure 4.92 ^{1}H-^{15}N NMR spectrum of isolation attempt of product 4C in $CDCl_3$. *Taken from XYS-2020-022C_Column_F24-51_N HMBC.* 281
Figure 4.93 Pearson variable correlation matrix (left) and univariate analysis (right); from Figure 1 of *PCA4U2*. 288
Figure 4.94 Variable Scree-type plot; from Figure 2 of *PCA4U2*. 289
Figure 4.95 PCA-space biplot colored using dynamic k-means clustering; from Figure 3 of *PCA4U2*. 289
Figure 4.96 Regression fit using linear least squares fitting; from Figure 4 of *PCA4U2*. 290
Figure 4.97 3D PCA map colored according to linear regression between catalyst PCA scores and corresponding observable values; from Figure 5 of *PCA4U2*. 290
Figure 4.98 2D PCA map projection showing principal component 1 *vs.* 2, colored according to catalyst selectivity; from Figure 6 of *PCA4U2*. 291
Figure 4.99 "Molecular ruler" plot constructed from pairwise Euclidean distances between catalyst PCA scores and catalyst selectivity; from Figure 7 of *PCA4U2*.....291
Figure 4.100 Predicted *vs.* experimental selectivity determined by PCA model IA. 293
Figure 4.101 Predicted *vs.* experimental selectivity determined by PCA model IB. 294
Figure 4.102 Comparison of predicted *vs.* experimental selectivity plots calculated by ISPCA (red) and PLSR model (blue). 295
Figure 4.103 Predicted *vs.* experimental selectivity determined by PCA model IIA. 296
Figure 4.104 Predicted *vs,* experimental selectivity determined by PCA model IIB. 297
Figure 4.105 Predicted *vs.* experimental selectivity determined by PCA model IIC. 298
Figure 4.106 Predicted *vs.* experimental selectivity determined by PCA model IID. 299

Figure 4.107 Calculated transition state barriers (TS1 and TS2) and intermediate free energies (IM3 and IM5) in kcalmol^{-1} for catalyst 4.16 at *trans*- (blue), *cis*-1 (red) and *cis*-2 (black) configurations. Dissociation energies of pyridine at IM3 are given in the dashed box. 303
Figure 4.108 Calculated transition state barriers (TS1 and TS2) and intermediate free energies (IM3 and IM5) in kcalmol^{-1} for catalyst 4.18 at *trans*- (blue), *cis*-1 (red) and *cis*-2 (black) configurations. Dissociation energies of pyridine at IM3 are given in the dashed box. 304
Figure 4.109 Calculated transition state barriers (TS1 and TS2) and intermediate free energies (IM3 and IM5) in kcalmol^{-1} for catalyst 4.23 at *trans*- (blue), *cis*-1 (red) and *cis*-2 (black) configurations. Dissociation energies of pyridine at IM3 are given in the dashed box. 305
Figure 4.110 Calculated transition state barriers (TS1 and TS2) and intermediate free energies (IM3 and IM5) in kcalmol^{-1} for catalyst 4.1 at *trans*- (blue), *cis*-1 (red) and *cis*-2 (black) configurations. Dissociation energies of pyridine at IM3 are given in the dashed box. 306
Figure 4.111 Calculated transition state barriers (TS1 and TS2) and intermediate free energies (IM3 and IM5) in kcalmol^{-1} for Ti(NPh)X_2 (X = Cl, Br, I) at *trans*- (blue), *cis*-1 (red) and *cis*-2 (black) configurations.....308

Chapter 1: Accessing low-valent early transition metal complexes

Reproduced in part with permission from:

Beaumier, E. P.; Pearce, A. J.; See, X. Y.; Tonks, I. A.*,
Modern applications of low-valent early transition metals in synthesis and catalysis.
Nat. Rev. Chem. **2019,** *3,* 15-34.

1.1 Motivation

Early transition metals are excellent candidates for the design and implementation of new catalytic reactions: they are earth abundant, often highly reactive and frequently exhibit different structures and orthogonal reactivity compared to late transition metals.[1-2] However, owing to their electropositive, oxophilic[3] nature, the organometallic chemistry of early transition metals has historically been dominated by complexes in high-valent states (Figure 1.1).[4] In contrast, there are considerably fewer examples of the application of low-valent early transition metals: such complexes are often highly reducing and require strong stabilizing ligands such as strong π-acceptors or bulky cyclopentadienyls.

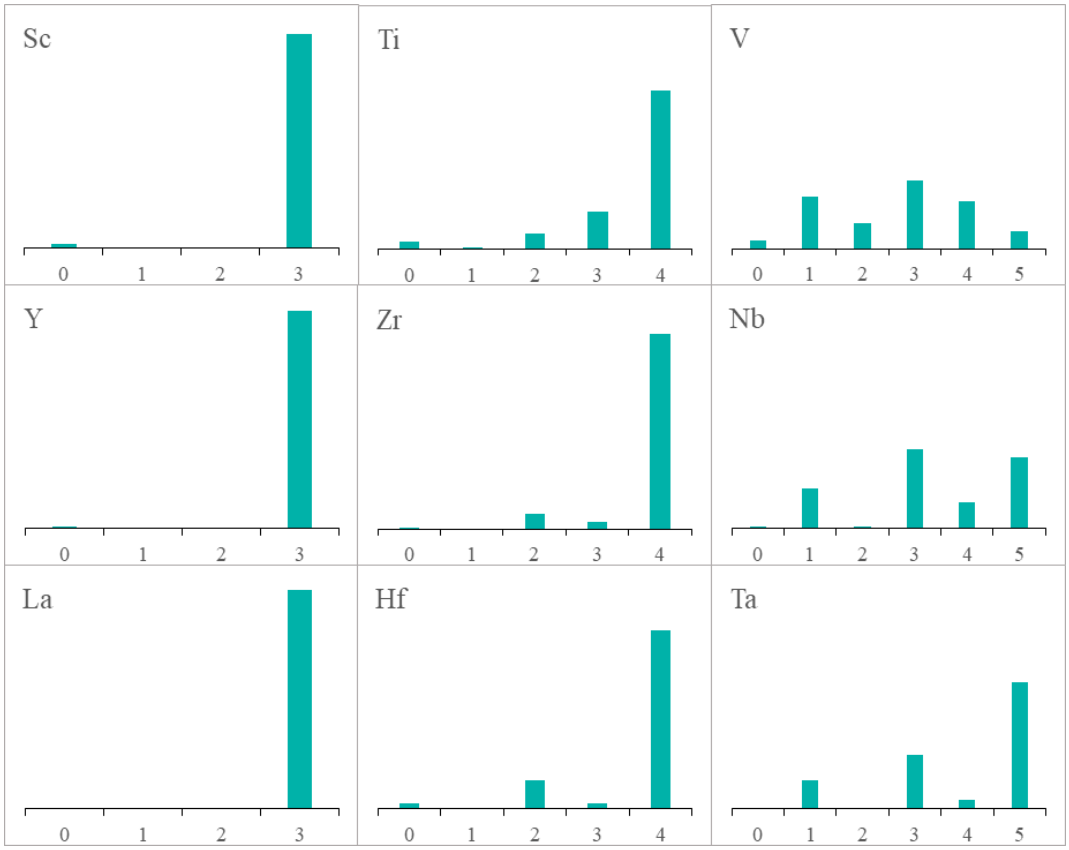

Figure 1.1 Relative abundance of the valence states of early transition metal organometallic complexes.[4]

Nonetheless, there is great interest in harnessing the highly reactive nature of low-valent early transition metals for practical synthesis and catalysis. There are myriad elegant examples of stoichiometric N_2 activation,[5-8] reductive coupling,[9-11] and radical reactions[12-

[14] mediated by low-valent early transition metals. The majority of this reactivity is dependent on the fact that highly reduced early metals can activate otherwise unreactive molecules, wherein metal oxidation and the formation of strong metal–ligand bonds provides a large thermodynamic driving force.

The focus of this introduction is to give a general overview on the various ways to access low-valent early transition metals and its application towards group transfer catalysis. Low-valent early transition metals[4] are classified here as groups 3-5, excluding V because it does not predominantly exist in its highest oxidation state. There has been a resurgence in the field over the past few years to find alternative routes to access these challenging intermediates enabled by new ligand designs, reagents and approaches. The Tonks group in particular is interested in developing Ti-based redox catalysis for the construction of heterocycles and we seek to continually draw inspiration from the field to guide our work in this promising area.

1.2 Classical Reduction Routes

The most common routes for generating low-valent early transition metal complexes are reduction of metal halides with strong alkali metals,[15-20] reduction with other (often weaker) reducing metals such as Mg,[21-22] Mn,[23] Al[24-25] or Zn[26] (providing more functional group tolerance), or through β-H abstraction[27-31] from a metal alkyl (Figure 1.2). Many of these reductions can be performed *in situ* to directly generate reactive low-valent intermediates or in the presence of π-accepting ligands to generate isolable or transiently stable "masked" species that can liberate a reactive low-valent metal fragment upon loss of the π-accepting ligand. For example, the Negishi reagent, $Cp_2Zr(\eta^2\text{-butene})$ (**1.1**), is synthesized by treatment of Cp_2ZrCl_2 with ^{n}BuLi or ^{n}BuMgBr, wherein the $Cp_2Zr^nBu_2$ intermediate undergoes β-H abstraction to liberate one equivalent of butane along with the product.[32-34] $Cp_2Ti(TMS_2C_2)$ (**1.2**) (TMS_2C_2 = bistrimethylsilylacetylene) and related Ti and Zr analogues can be synthesized by reduction of the corresponding high-valent chlorides with Mg in the presence of the π-accepting alkyne TMS_2C_2,[35] while substituted hafnocene analogues have been synthesized using Li as a reductant.[36-37]

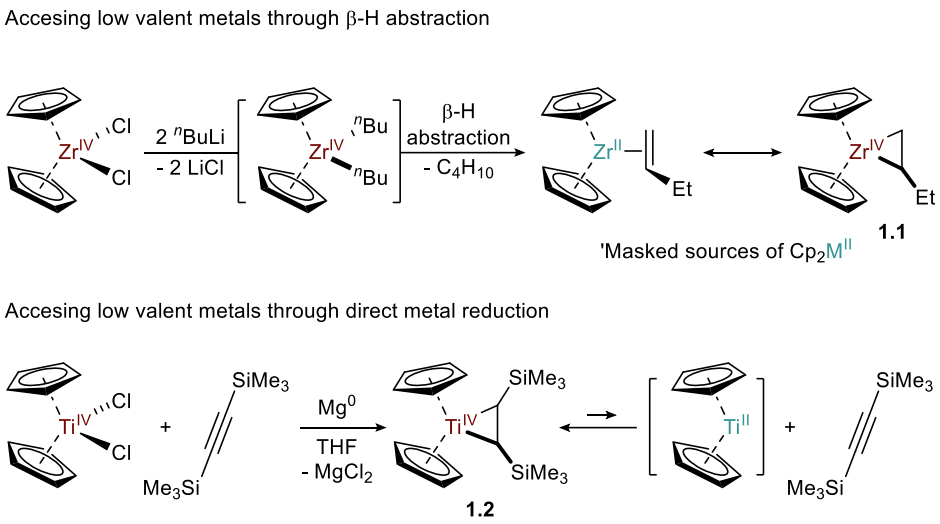

Figure 1.2 Classical reduction routes involving strong reductants *via* β-H abstraction and direct metal reduction.

Stable low-valent coordination complexes of the early transition metals that lack strongly stabilizing ligands are uncommon. However, examples continue to emerge that challenge the limits of stability (Figure 1.3). For example, a suite of divalent Group 3 amides has recently been reported,[38-41] including the first crystallographically characterized Sc^{II} compound,[40] extending the chemistry of low-valent Sc and Y beyond metallocene derivatives.[42-43] The Sc^{II} amide complex **1.3**, exhibits remarkably different reactivity from other reduced group 3 and lanthanide complexes, for the first time revealing end-on, reversible binding of N_2 to form the bridged bimetallic **1.4**.[41] Bulky aromatic heterocycles derived from phosphaalkynes, which are much poorer donors than Cp-based ligands, can also stabilize Sc^{II} complexes.[44] Improved syntheses and full electronic characterization of $TiCl_2py_4$ **1.5a**[45] and $TiCl_2(tmeda)_2$ **1.5b**,[46] rare examples of Ti^{II} coordination complexes, have recently been reported, building upon earlier studies by several groups.[47-48] The chemistry of low-valent early transition metal isocyanide[49-51] and arene complexes[52-53] has also continued to expand, including the recent synthesis of the formally Ta^0 complex **1.6**.[49]

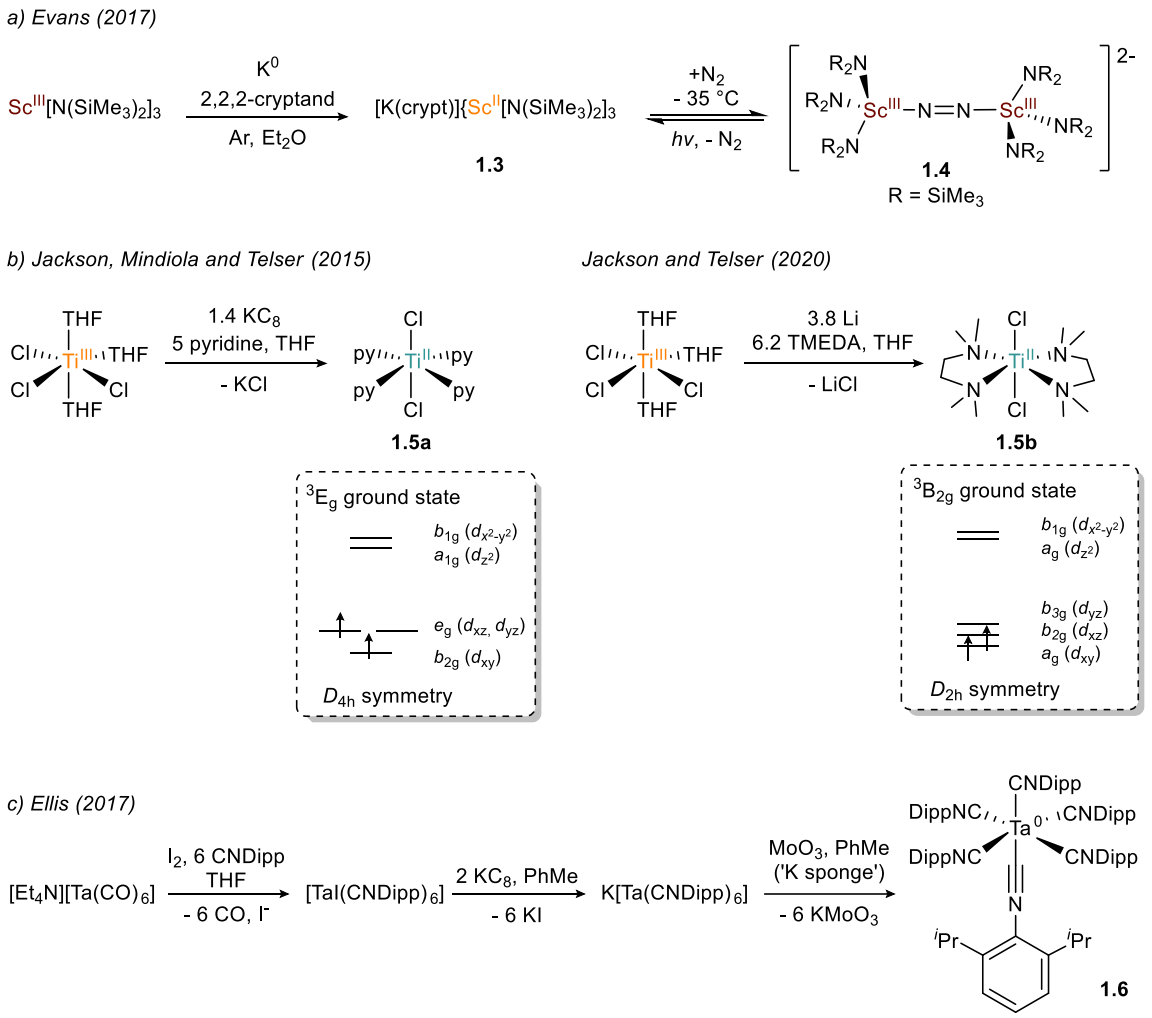

Figure 1.3 Representative examples of modern low-valent metal synthesis. a) First reduced Sc complex that reveals end-on N_2 binding. b) Well-defined mononuclear Ti^{II} complexes in the absence of π-accepting ligands with ^3E_g (**1.5a**) and $^3B_{2g}$ (**1.5b**) electronic ground state. c) Zero valent isocyanide analogue of the highly unstable $Ta(CO)_6$ prepared by conventional synthesis methods.

1.3 Modern Reduction Routes

The high reactivity of strong alkali metal reductants places an inherent restriction on the solvent and reagent compatibility of reactions that employ them as reductants. Considerable progress has been made in designing new reactions and reductants that overcome this challenge. One creative workaround that was recently introduced is to reduce compounds by passing them through columns of KC_8, limiting (or at least fine

tuning) the contact time of the reagent and solvent with the strong reductant[54]. Another strategy is to use inner-sphere reductants that are less prone to over-reduction. In this context, Tsurugi and Mashima have promoted the use of organosilicon reductants, such as 3,6-bis(trimethylsilyl)-1,4-cyclohexadiene[55-57] (**1.7**) and 1,4-bis(trimethylsilyl)-1,4-dihydropyrazine[58-60] derivatives (for example, **1.8**), to reduce group 4 and group 5 metal halides for homogeneous catalytic applications (Figure 1.4). In the case of **1.8**, the steric bulk of the tetramethylpyrazine by-product prevents its coordination to the reduced metal catalyst, which is critical for productive chemistry. These organosilicon reductants derive their reduction potential (ranging from + 0.83 V to − 0.40 V versus Cp_2Fe) from the aromatization of the 1,4-diene core. These reductants have been used by the broader

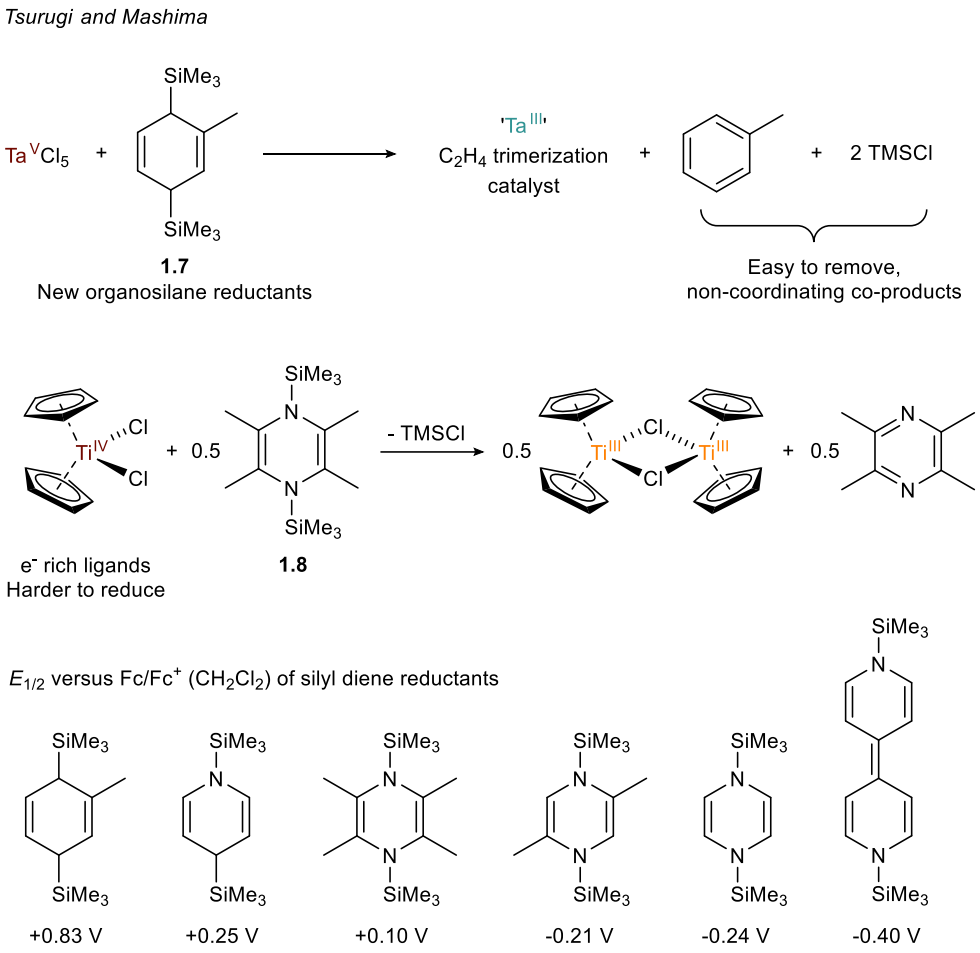

Figure 1.4 Alternative suite of inner-sphere organosilane reductants for low-valent metal synthesis and catalysis in a salt-free manner.

community for wide-ranging applications, from the in situ reduction of Ti precursors in chemical vapor deposition[61] to the in situ generation of Ti^{III} for reductive umpolung reactions.[62] Similarly, commercially available tris(trimethylsilyl)silane has been used to generate Nb^{III} cyclotrimerization catalysts in situ.[63] A major advantage of these silicon-based reductants is that the by-products are simple to remove: Me_3SiCl is less likely than alkali metal halides to coordinate to electrophilic metals and the aromatic by-products can be removed *in vacuo*. Metal salt by-products are often difficult and/or tedious to remove and may interfere with productive chemistry of the reduced complex; thus, these procedures offer an important advancement for applications of reduced early metal chemistry.

Alternative reduction methods of early transition metals include single-electron transfers from weak reductants such as citrate[64] or benzylamine.[65] Hydrogenolysis of metal alkyls has also been used to synthesize low-valent Nb[66] and Zr[67] arene complexes. Redox non-innocent ligands can also engender redox reactivity with early transition metals without formally changing the metal oxidation state.[56-57, 68-71]

1.4 Catalytic group transfer

As is the case with small molecule activation reactions, engendering catalytic reactivity in group transfer reactions is particularly challenging due to the strength of M=E multiple bonds. Classical examples such as methylene transfer in the Tebbe olefination result in the formation of strong Ti=O bonds, precluding practical turnover. Nonetheless, there have been several significant advances toward catalytic oxidative group transfer reactions, in particular nitrene transfer. Most of the catalytic early transition metal nitrene transfer reactions involve oxidative amination of unsaturated organic functional groups, which stands in contrast to late transition metal-catalysed nitrene transfers, which often perform C–H insertions[72-75] or aziridinations.[76-78]

In contrast to examples of overt ligand redox non-innocence in nitrene transfer reactions (covered in more details in Chapter 2), the Tonks group has found success over the past few years in developing formally Ti^{II}/Ti^{IV}-catalyzed oxidative nitrene transfer reaction to access multi-substituted pyrroles from the coupling of alkynes and azobenzene (Figure 1.5).[79-82] The crux of this system is that cooperative metal–ligand effects can also

stabilize low-valent metals through backbonding (classical redox non-innocence) into the reagents (alkynes and diazenes) or products (pyrroles), allowing for otherwise challenging reductive events, such as the reductive elimination from **1.12** to **1.13**, to occur with relative ease. This strategy has also been extended to other oxidative amination reactions such as *α*,*β*-unsaturated imines (**1.15**) and *α*-iminocyclopropanes (**1.16**) from the coupling of alkynes, alkenes and azobenzene[83] and unsymmetrical carbodiimides (**1.17** and **1.18**) from the coupling of isocyanides and nitrenes.[84]

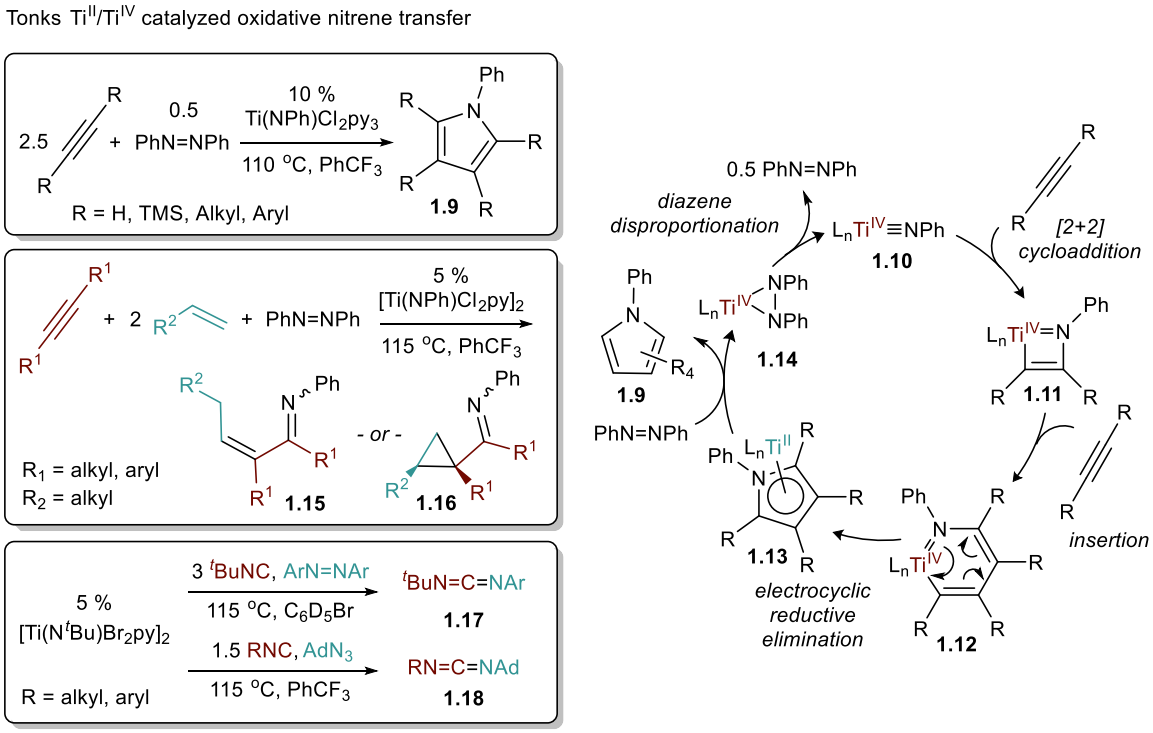

Figure 1.5 Ti^{II}/Ti^{IV} redox catalytic nitrene transfer in oxidative amination catalysis with examples of selected synthesis (left) and proposed mechanism of pyrrole formation (right).

In contrast to group 4 metals, group 5 metal imidos tend to be considerably less reactive. To counteract this, efforts have been made to synthesize group 5 systems that electronically saturate the metal *d* orbitals (*π*-loading), thereby increasing the polarizability of the imido bonds.[85] The *π*-loaded *β*-diketiminate (BDI) Nb bis(imido) complex **1.19** can thus perform a formally Nb^{III}/Nb^{V}-catalyzed nitrene transfer reaction to generate asymmetric dialkylcarbodiimides from azides and isocyanides.[86]

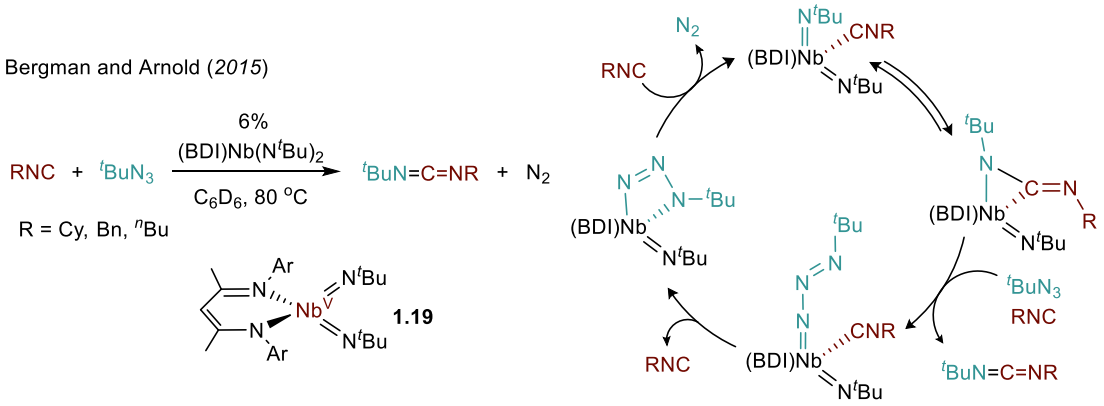

Figure 1.6 Nitrene transfer promoted by a π-loaded bis(imido)Nb catalyst, which renders the imido fragment more labile than other group 5 imido complexes.

1.5 Stoichiometric atom transfer

Outside of catalytic nitrene transfer, there are also many examples of stoichiometric atom-transfer reactions (As_4,[87] S_8[88-89] and P_4[90]). For example, reaction of either P_4 or As_4 with activated zirconocene derivatives results in pnictogen–silicon analogues of benzene[91] and carbon–phosphorous cage compounds[92]. The Cummins group has also extensively studied P_4 transformations[93] and synthesized phosphorous-rich organic clusters mediated by a Nb^{III}/Nb^{V} couple.[94]

Fortier has recently described the synthesis of a masked Ti^{II} synthon **1.20** that undergoes classic two-electron chemistry with N_2O, chalcogen transfer reagents and organoazides to generate the corresponding Ti^{IV} complexes.[95] This complex was subsequently found to also participate in an exceedingly rare reversible two-electron redox cycling with thiophene (Figure 1.7).[96] Oxidative addition (OA) of a thiophene substrate readily gives the ring-opened thiotitanocycle complex **1.21** at room temperature while reductive elimination (RE) occurs under ambient light conditions to regenerate **1.20** and free thiophene. Critically, this OA/RE process is non-substrate induced and stands in contrast to the Tonks group Ti-pyrrole chemistry, where RE of aromatic pyrrole is thermodynamically favored (*vide supra*).

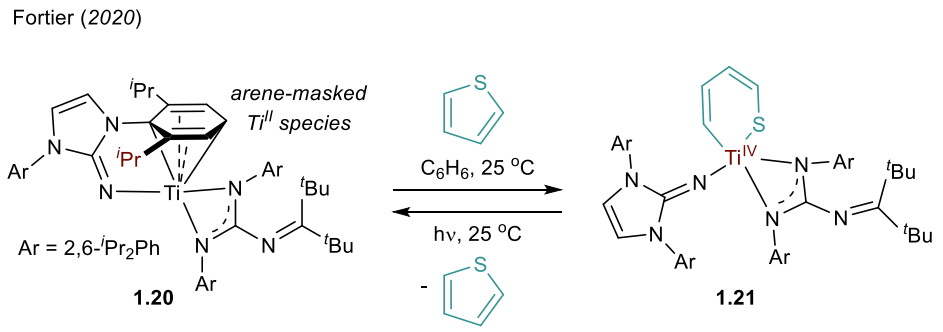

Figure 1.7 Reversible oxidative addition and reductive elimination of thiophene from a masked Ti^{II} synthon.

1.6 Thesis outline

The objective of this thesis is to explore the author's efforts towards the further development of Ti^{II}/Ti^{IV} catalyzed pyrrole chemistry. In chapter 2, the synthesis of pyrroles from the [2+2+1] coupling of alkynes and azides will be discussed. By extending to other nitrene sources, the notion that diazenes was a critical agent for the re-oxidation process from Ti^{II} to Ti^{IV} in the catalytic process was negated. Chapter 3 details the generality of generating low-valent Ti^{II} species *via* the reaction of Ti^{IV} imido precatalysts with alkynes without the use of strong metal reductants. The reactivity of the *in-situ* formed Ti^{II} species towards alkyne cyclotrimerization chemistry offered an insight into how different ligands affects reactivity at the metal center. Finally, chapter 4 covers the efforts in utilizing iterative supervised principal component analysis (ISPCA) as a strategy for rational catalyst design. ISPCA is a general statistical method that helps winnow down important descriptors that affect an aspect of a chemical reaction. In this chapter we have applied it towards identifying key catalyst descriptors towards the Ti-catalyzed regioselective synthesis of pyrroles.

Chapter 2: Oxidative nitrene transfer from azides to alkynes *via* Ti(II)/Ti(IV) redox catalysis: formal [2+2+1] synthesis of pyrroles

Reproduced in part with permission from:

Pearce, A. J.; See, X. Y.; Tonks, I. A.*,
Oxidative nitrene transfer from azides to alkynes *via* Ti(ii)/Ti(iv) redox catalysis: formal [2+2+1] synthesis of pyrroles.
Chem. Commun. **2018,** *54*, 6891-6894.

2.1 Overview

Catalytic oxidative nitrene transfer reactions with organic azides and early transition metals are rare and require the aid of redox non-innocent ligands. In this report, we have developed a formal [2+2+1] coupling of azides and alkynes *via* a Ti^{II}/Ti^{IV} redox catalysis utilizing simple Ti halide imido pre-catalysts. Through this multi-component coupling, poly-substituted N-alkyl pyrroles can be obtained, including *N*-benzyl protected pyrroles and highly electron-rich all alkyl substituted pyrroles that are difficult to synthesize otherwise. Mechanistic studies reveal that changing the nitrene source from azobenzene to bulky azides in these [2+2+1] reactions lead to different mechanistic features.

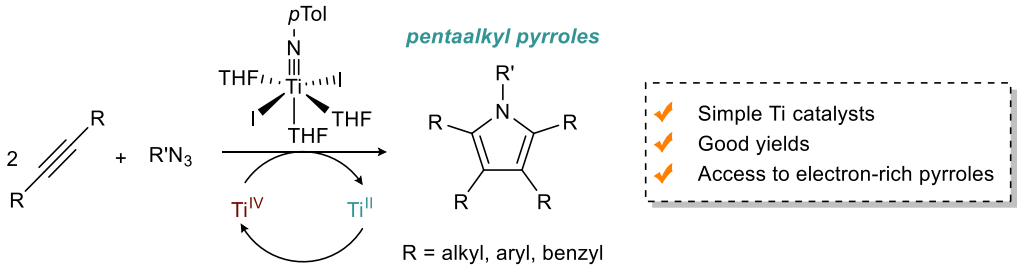

Figure 2.1 Formal [2+2+1] synthesis of pyrroles with alkynes and azides mediated by Ti^{IV} imido catalyst.

2.2 Introduction

Metal-mediated nitrene transfer reactions to unsaturated substrates are effective methods to synthesize C-N bonds that are pervasive in many natural and bioactive synthetic products. Typically, late transition metals with various nitrene sources have been employed to this end in alkene aziridinations[76-78] and C-H functionalisations.[72-74, 97]

However with early transition metals, the lack of an accessible two-electron redox couple at the metal center has limited nitrene transfer reactivity[98] and they are predominantly stoichiometric.[69] In order to circumvent this challenge, the Heyduk[69, 99-101] and Wolczanski[71] groups have utilized redox non-innocent (RNI) ligands with d^0 early transition metals where multi-electron redox changes are now ligand-centered. Both groups have successfully performed catalytic oxidative group transfers with organic azides to functionalize small molecules (Figure 2.2).

In 2016, the Tonks group reported on the first example of a Ti-catalyzed nitrene transfer reaction with the multi-component coupling of alkynes and aryl diazenes to give penta- and tri-substituted pyrroles in high yields.[79] Computational and experimental studies into this mechanism have proposed that in the absence of ancillary RNI ligands, low-valent Ti^{II} intermediates are stabilized through back-donation into substrates and/or products and by solvent effects.[82] Encouraged by the successes of the Wolczanski and Heyduk groups in utilizing RNI-ligands to promote catalytic oxidative nitrene transfer with organic azides and group 4 metals, we looked into using azides for our [2+2+1] synthesis of pyrroles without using a RNI ligand (Figure 2.2).

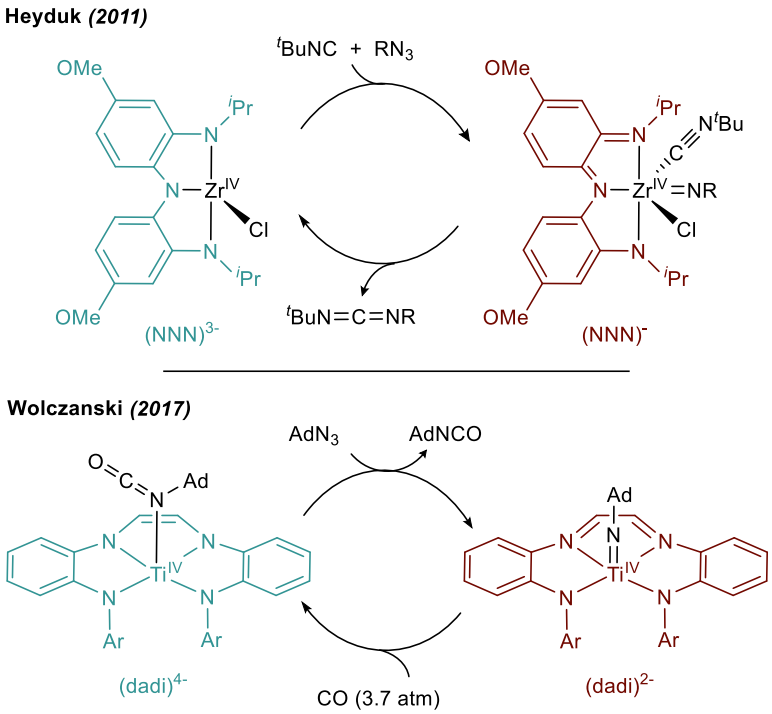

Figure 2.2 Nitrene transfer reactions catalyzed by early transition metal/redox non-innocent ligand systems.

A potential issue we envisioned that can happen with using organic azides in our system is the facile Huisgen cycloadditions between alkynes and azides to form triazoles, both thermally[102] and in the presence of metal catalysts.[103-104] However, we hypothesized that the reduction of azides with highly reactive Ti^{II} intermediates should occur at a rate competitive to that of this potential background reaction. Additionally, there are several

advantages of using organic azides over diazenes. For example, *N*-alkyl pyrroles can be easily accessed by using alkyl azides as they are typically stable beyond our reaction temperature of 115 ˚C, thereby allowing installation of N-protecting groups on pyrroles.[105] This gives us access to penta-alkyl pyrroles which are rare structure motifs as they are oxidatively unstable and difficult to synthesize.[106-108] Alkyl diazenes on the other hand, decompose easily into radicals upon heating.[109] Furthermore, a wide variety of organic azides can be obtained with simple substitution chemistry and many diazenes are in fact synthesized from azides.[100, 110-112] Therefore, utilizing azides directly would prove to be a more economical and straightforward route to access complex *N*-substituted pyrroles.[113-114] Herein, we report that the Ti-catalyzed formal [2+2+1] pyrrole synthesis and related oxidative multi-component alkyne animation reactions can be realized with organic azides to give access to *N*-alkyl functionalized pyrroles which was previously unattainable using diazenes.[79]

2.3 Results and Discussion

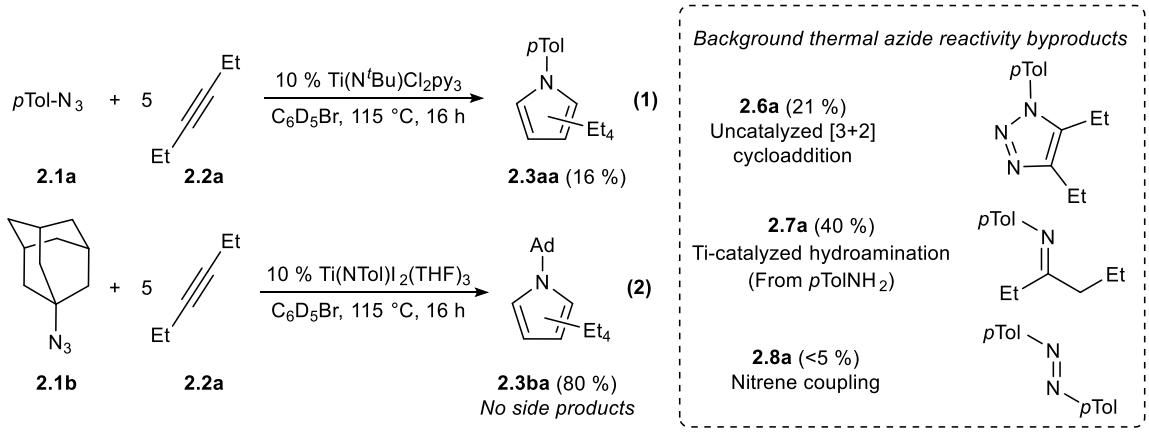

Figure 2.3 (1) Initial reaction attempts of **2.1a** and **2.2a** catalyzed by Ti(N^{t}Bu)Cl$_2$py$_3$ were marred by azide decomposition (right). (2) More Lewis-acidic catalyst Ti(NTol)I$_2$(THF)$_3$ formed desired pyrrole product without formation of side products.

Initial attempts with *p*-tolyl azide (**2.1a**), 3-hexyne (**2.2a**) and 10% Ti(N^{t}Bu)Cl$_2$py$_3$ in C$_6$D$_5$Br at 115 ˚C gave the desired pyrrole product, 2,3,4,5-tetraethyl-*N*-(*p*-tolyl)pyrrole (**2.3aa**) in 16 % yield (Figure 2.3, eqn 1). However, this reaction is hindered by significant side-reactions attributed to thermal azide decomposition (Products **2.6a-2.8a**).[115-116]

Gratifyingly, moving on to adamantyl azides with a Lewis acidic $Ti(NTol)I_2(THF)_3$ catalyst, which binds to ligands more strongly, forms the desired pyrrole product (**3ba**) in 80 % yield without noticing any azide decomposition (Figure 2.3, eqn 2).

Mechanistic analysis of the $Ti(NTol)I_2(THF)_3$-catalyzed reaction of **2.1b** and **2.2a** with variable time normalization analysis revealed a rate law that is 1st order with respect to catalyst and 2nd order to **2.2a** (Figure 2.4). The 1st order dependence of [Ti] and zero-order dependence of **2.1b** indicates that the sterically bulky **2.1b** prevents Ti dimerization and does not competitively bind to Ti, whereas azobenzene does. Substituting **2.1b** for a sterically smaller *n*-decN$_3$ (**2.1c**) gives a rate law that is 0.5 order in [Ti] and - 0.5 order in [*n*-decN$_3$], further supporting the notion that the rate law observed with **2.1b** is due to its steric bulk.

[AdN$_3$] (2.1b): rate $\propto$ $[Ti][EtCCEt]^2$ **[DecN$_3$] (2.1c):** rate $\propto$ $[Ti]^{0.5}[EtCCEt]^2[n\text{-}DecN_3]^{-0.5}$

PhNNPh: rate $\propto$ $[Ti]^{0.5}[EtCCEt]^2[PhNNPh]^{-1}$

Figure 2.4 Comparison of rate laws of pyrrole formation with azide versus azobenzene reveal different mechanisms of re-oxidation.

Following that, the scope of internal alkynes and azides were investigated (Table 2.1). Simple alkynes (**2.2a, 2.2b** and **2.2d**) gave high yields while sterically bulky diphenylacetylene (**2.2c**) gave no product. The azide scope of this system was also investigated with 3-hexyne (**2.2a**) as our model alkyne in the hope of accessing *N*-protected pyrroles. Primary alkyl azides such as *n*-decN$_3$ (**2.1c**) are challenging substrates to harness because primary metal imidos tend to dimerize.[117] Moreover, they are also stronger nucleophiles that could coordinate to Ti and hinder productive chemistry, similar to the role that primary alkyl amines play in hydroamination reactions.[118] Nonetheless, **2.1c** performed moderately in our system to yield penta-alkyl pyrroles (entries 6-9). Upon closer inspection of this reaction, we noticed a small amount of 1-iododecane forming alongside product **2.3ca**. We believe this product is formed *via* a S_N2 reaction of the azide by iodide, with the formation of a titanium azido complex which is unreactive. Reacting $TMSN_3$ with Ti halide catalysts similarly yields TMS-halides and unreactive Ti azido species. Given

these observations, we propose that the lower yields of **2.1c** were a result of catalyst death; no additional product was formed when an additional equivalent of **2.1c** was added to the reaction after the initial reaction period. Rather, decreasing the concentration and reaction time, along with using excess **2.2a** led to an improvement in yields with respect to **2.1c** (entry 9).

Table 2.1 Internal alkyne scope.

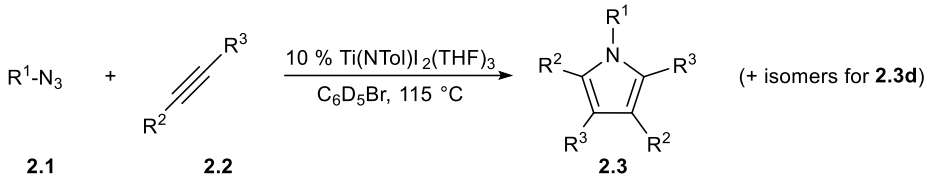

Entry	Azide	Alkyne	Alkyne equiv	t (h)	% Yield (NMR)[a]
1[b]	Ad **2.1b**	Et—≡—Et **2.2a**	5	16	(80)
2[c]	Ad **2.1b**	Et—≡—Et **2.2a**	5	2	23 (59)
3[b]	Ad **2.1b**	Me—≡—Me **2.2b**	5	16	(94)
4[b]	Ad **2.1b**	Ph—≡—Ph **2.2c**	5	16	trace
5[b]	Ad **2.1b**	Ph—≡—Me **2.2d**	5	16	(70)[d]
6[ce]	*n*-dec **2.1c**	Et—≡—Et **2.2a**	3	6	(37)
7[cf]	*n*-dec **2.1c**	Et—≡—Et **2.2a**	3	6	(35)
8[c]	*n*-dec **2.1c**	Et—≡—Et **2.2a**	3	6	(42)
9[c]	*n*-dec **2.1c**	Et—≡—Et **2.2a**	5	2	48 (64)
10[c]	Bn **2.1d**	Et—≡—Et **2.2a**	5	2	59 (62)
11[c]	Tol **2.1a**	Et—≡—Et **2.2a**	5	2	(30)
12[g]	Tol **2.1a**	Et—≡—Et **2.2a**	8	3	(52)

13[c]	$PhSCH_2$ **2.1e**	Et—≡—Et **2.2a**	5	2	0
14[c]	Ph_3C **2.1f**	Et—≡—Et **2.2a**	5	2	0

[a]NMR yield calculated with respect to **2.1** with Ph_3CH internal standard. [b]Conditions: 0.2 mmol **2.1b**, 1.0 mmol **2.2**, 10 mol % $Ti(NTol)I_2(THF)_3$, 115˚C, 16 h, 0.5 mL C_6D_5Br, average of 2 runs. [c]Conditions: 0.1 mmol **2.1**, **2.2a** (x equiv), 10 mol % $Ti(NTol)I_2(THF)_3$, 115 ˚C, 2 h, 0.5 mL C_6D_5Br, average of 2-3 runs. [d]1.6 : 1.0 : 0 ratio of **2.3bd** : **2.4bd** : **2.5bd** [e]Conducted at 80 ˚C. [f]Conducted at 100 ˚C. [g]Conditions: 0.1 mmol **2.1a**, 0.8 mmol **2.2a**, 10 mol % $Ti(NTol)I_2(THF)_3$, 115˚C, 16 h, 0.5 mL C_6D_5Br, single run.

Moderate yields were achieved in the coupling of benzyl azide (**2.1d**) and **2.2a** potentially giving access to N*H* pyrroles *via* the removal of the benzyl protecting group (entry 10). In contrast, the yields remained poor with aryl azides even upon increased alkyne and catalyst loading (entries 11-12). This is attributed to the facile thermal decomposition and uncatalyzed [3+2] Huisgen cycloaddition pathways with aryl azides.

In the presence of terminal alkynes that are less sterically hindered, we had to return to using the less active $Ti(N^tBu)Cl_2py_3$ as the Lewis acidic $Ti(NTol)I_2(THF)_3$ catalyst cyclotrimerizes terminal alkynes rapidly (Table 2.2).[119] Using a 2 : 1 alkyne : azide ratio, simple ^{n}Bu (**2.2e**) and *p*-tolyl (**2.2f**) acetylene achieved moderate pyrrole yields and < 20 % yield of cyclotrimerized product. This is in contrast to using azobenzene as a nitrene source where a 1 : 4 alkyne : azobenzene ratio is necessary to suppress trimerization. Being a stronger nucleophile, azides are more capable of intercepting the Ti^{II} intermediate than azobenzene, thereby affording post rate-determining-step chemoselectivity for pyrrole formation over alkyne trimerization.

Three regiosomeric tri-substituted pyrrole products **2.3**, **2.4** and **2.5** are expected with a terminal alkyne substrate. However, due to the size of the adamantyl azide group, the formation of the 2,5-substituted pyrrole **2.5** was not observed in all cases. Notably in entry 2, a 1 : 1 mixture of **2.3bf : 2.4bf** was observed with *p*-tolylacetylene substrate. This is in contrast to the 4 : 1 mixture of **2.3** : **2.4** with phenylacetylene substrate and azobenzene as the nitrene source.[79] This further demonstrates that bulky alkyl imidos bias the reaction selectivity towards the product **2.4** where substituents are pointed away from nitrogen.

When a bulky alkyne substrate such as *t*-butylacetylene (**2.1g**) was used with **2.1b**, no reaction was observed. With a less bulky *p*-tolyl azide (**2.1a**) and **2.1g**, pyrrole formation was observed in low yield, albeit with significant nitrene decomposition (*vide supra*). Similarly, low pyrrole yields were observed with bulky (trimethylsilyl)acetylene (**2.2h**) substrate as Huisgen cycloaddition and cyclotrimerization of alkynes outcompete productive pyrrole chemistry.

Table 2.2 Terminal alkyne scope.[a]

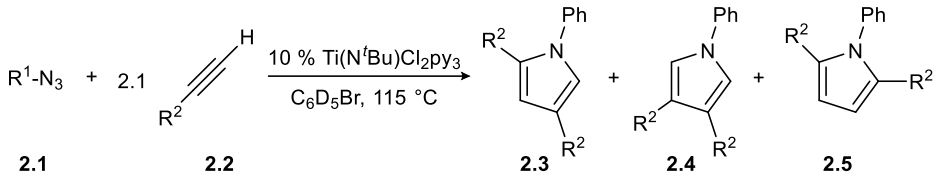

Entry	R^1	Alkyne	% Yield 2.3 – 2.5 (2.3 : 2.4 : 2.5)
1	Ad **2.1b**	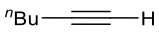 **2.2e**	65 (1.0 : 0.2 : 0)
2	Ad **2.1b**	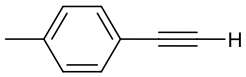 **2.2f**	66 (1.0 : 1.0 : 0[b])
3	Tol **2.1a**	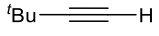 **2.2g**	7 (1.0 : 0 : 0)
4	Ad **2.1b**	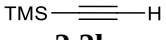 **2.2h**	34 (1.0 : 0 : 0)
5[c]	Ad **2.1b**	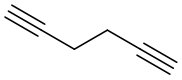 **2.2i**	38 n/a

[a]Conditions: 0.2 mmol **2.1 (**1 equiv), 0.42 mmol **2.2** (2.1 equiv), 10 mol % Ti(N^{t}Bu)Cl$_2$py$_3$, 115 °C, 6 h, 0.5 ml C_6D_5Br, average of 2 runs. [b]Product ratio determined by quantitative GC-FID. [c]0.21 mmol **2i**.

2.4 Conclusion

In conclusion, we have demonstrated the 2nd example of Ti-catalyzed nitrene transfer reactions with azides to generate pyrroles in a formal [2+2+1] manner with alkynes and azides. This is also a rare example of a group 4 metal undergoing 2-electron redox catalysis. Unlike previous examples of group 4 catalyzed oxidative nitrene transfer

reactions from azides, this reaction utilizes simple Ti halide catalysts and does not require redox non-innocent ligands. The Ti^{II} intermediate generated in situ is stabilized by "classical" redox non-innocence *via* π back-bonding into substrates and products. However, this reaction requires higher reaction temperature compared to systems with redox non-innocent ligands.

Furthermore, this system is complementary to our previously reported Ti-catalyzed [2+2+1] pyrrole syntheses with diazenes, which were limited to *N*-aryl pyrroles, by providing access to *N*-alkyl pyrrole derivatives. Highly substituted *N*-alkyl pyrroles, such as atorvastatin, are found widely in bioactive molecules and pharmaceutical products.[120] Mechanistically, nitrene transfer reactions with azides differ in several aspects from using diazenes. The differences include i) outcompeting alkyne cyclotrimerization even with reactive terminal alkynes and ii) re-oxidation of Ti can occur through a monomeric species, therefore changing the rate dependence of catalyst concentration in comparison to reactions using diazenes. These mechanistic insights can serve to allow future development of Ti-catalyzed oxidative amination reactions.

2.5 Experimental

2.5.1 General considerations

All air- and moisture-sensitive reactions were carried out in a nitrogen-filled glovebox. Solvents for air- and moisture-sensitive reactions were i) deoxygenated by sparging with N_2 and dried by passing through activated alumina columns of a Pure Process Technology solvent purification system (PhMe), degassed, filtered through basic alumina and stored over molecular sieves prior to use (PhBr) and iii) vacuum transferred from CaH_2 ($CDCl_3$). C_6D_5Br was synthesized following literature procedure,[121] degassed, dried over CaH_2 and filtered through basic alumina prior to use.

$Ti(N^tBu)Cl_2py_3$[122] and $Ti(NTol)I_2(THF)_3$[119] were synthesized according to literature procedure. Liquid alkynes, azides and other reagents were freeze-pump-thaw degassed three times and passed through activated basic alumina prior to use.

^1H and ^{13}C NMR spectra were recorded on Bruker Avance III HD 400 and 500 MHz spectrometers. Chemical shifts were referenced to the residual protio-solvent impurity for ^1H (s, 7.26 for $CHCl_3$; s 7.30 ppm, 7.02 ppm and 6.94 ppm for C_6D_4HBr) and solvent

carbons for ^{13}C (t, 77.2 ppm for $CDCl_3$). Qualitative GC MS spectra were recorded on a Agilent GC6890N-MSD5975 gas chromatograph-mass spectrometer fitted with a 7683 auto sampler. A HD-5 column (5% diphenyl siloxane in the polymer) was used in the gas chromatograph and electron ionization technique was used for mass spectrometry detection. GC chromatographs were collected on Agilent 7890B GC system equipped with the HP-5 column (30 m, 0.32 mm, 0.25 µm, 7 inch cage), a oxidation-methanation reactor (Polyarc® System, Activated Research Company) and a FID detector for quantitative carbon detection.

2.5.2 General procedure for catalytic reactions

For all reactions, 0.5 ml of the respective stock solution and the required reagents were added to a Teflon tape lined screw-cap NMR tube in a N_2-filled glovebox. This was then sealed with a Teflon screw cap and heated at 80/115 °C for 2 to 16 h (internal alkyne scope, Table 2.1) and 6 h (terminal alkyne scope, Table 2.2). Quantitative ^1H NMR spectra of the catalytic mixture were taken before and after heating on the Bruker Avance III HD 400 and 500 MHz spectrometers (Acquisition time = 5 s; delay time = 30 s; dummy scans = 0; number of scans = 8). Three different stock solutions were prepared with C_6D_5Br and triphenylmethane acting as an internal standard.

Internal alkyne screen

In each reaction, internal alkyne (1.0 mmol, 5 equiv) and 0.5 ml of stock solution were added. Stock solution were prepared by adding $Ti(NTol)I_2(THF)_3$ (10 mol %, 0.02 mmol), triphenylmethane (10 mol %, 0.02 mmol) and 1-azidoadamantane (0.2 mmol, 1.0 equiv) to C_6D_5Br.

Azide screen

In each reaction, $Ti(NTol)I_2(THF)_3$ (10 mol %, 0.01 mmol), azide (0.1 mmol, 1.0 equiv) and 0.5 ml of stock solution were added. Reagents have to be added in this particular sequence to prevent trimerization from occurring prematurely. Stock solution was prepared by adding 3-hexyne (0.5 mmol, 5 equiv) and triphenylmethane (20 mol %, 0.02 mmol) to C_6D_5Br.

Terminal alkyne screen

In each reaction, terminal alkyne (0.42 mmol, 2.1 equiv), 1-azidoadamantane or (*p*-tolyl)azide (0.2 mmol, 1.0 equiv) and 0.5 ml of stock solution were added. Stock solution was prepared by adding $Ti(N^tBu)Cl_2py_3$ (10 mol %, 0.02 mmol), triphenylmethane (10 mol %, 0.02 mmol) to C_6D_5Br.

2.5.3 Characterization of starting materials in C_6D_5Br

Characterization of 3-Hexyne (**2.2a**) and 1-Hexyne (**2.2e**) in C_6D_5Br were reported previously.[119]

Triphenylmethane

^{1}H NMR (500 MHz, C_6D_5Br): δ 7.15 (t, $^{4}J_{HH}$ = 7.5 Hz, 6H, Ar-*H*), 7.10 – 7.06 (m, 9H, Ar-*H*), 5.45 (s, 1H, C-*H*).

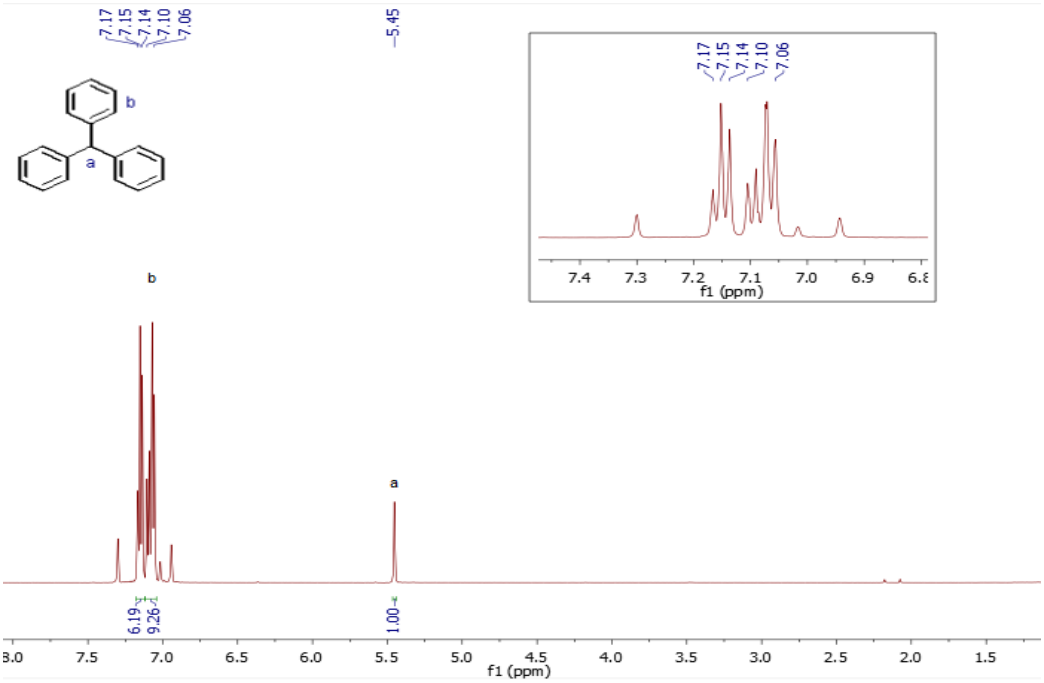

Figure 2.5 ^{1}H NMR spectrum of triphenylmethane in C_6D_5Br.

(*p*-tolyl)azide (2.1a)

(*p*-tolyl)azide was synthesized according to literature procedures.[123]

^{1}H NMR (500 MHz, C_6D_5Br): δ 6.89 (d, $^3J_{HH}$ = 7.9 Hz, 2H, *o*-Tol-*H*), 6.74 (d, $^3J_{HH}$ = 8.1 Hz, 2H, *m*-Tol-*H*), 2.11 (s, 3H, CH_3).

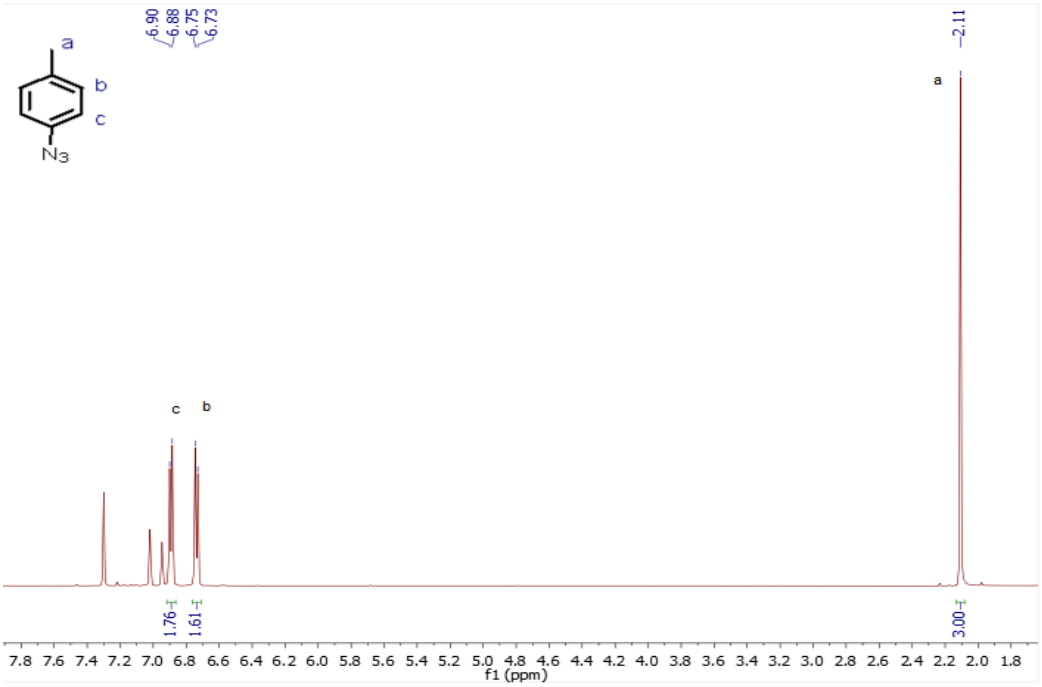

Figure 2.6 ^{1}H NMR spectrum of (p-tolyl)azide in C_6D_5Br.

1-azidoadamantane (2.1b)

^{1}H NMR (500 MHz, C_6D_5Br): δ 1.90 (br s, 3H, C-*H*), 1.64 (m, 6H, CH_2), 1.45 (app q, $^{3}J_{HH}$ = 12.4 Hz, $^{3}J_{HH}$ = 15.8 Hz 6H, CH_2).

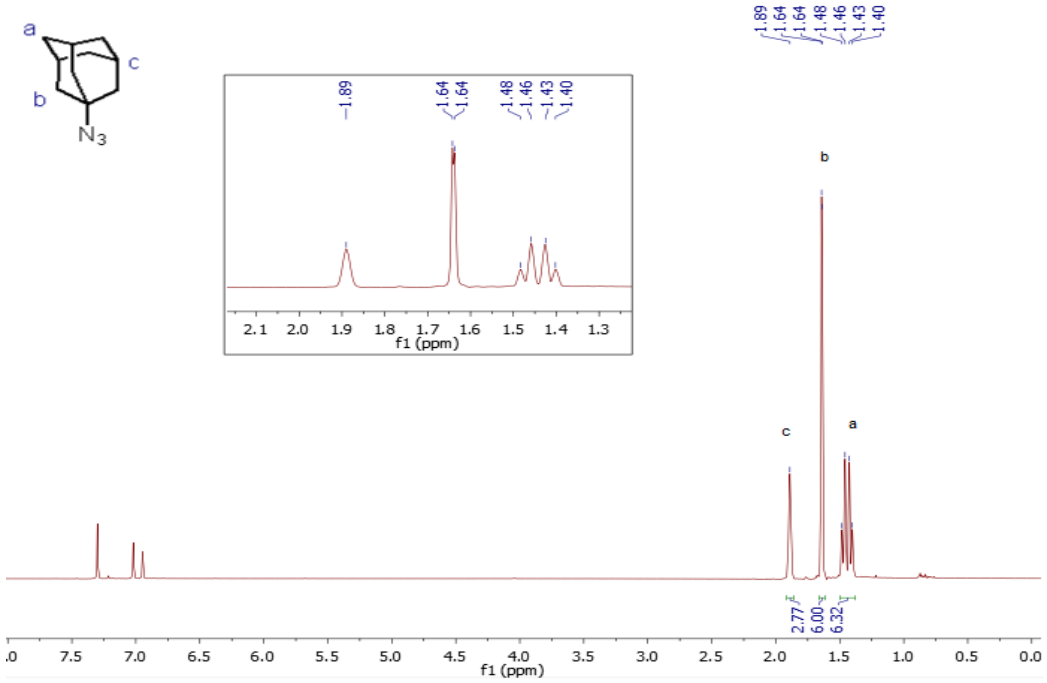

Figure 2.7 ^{1}H NMR spectrum of 1-azidoadamantane in C_6D_5Br.

1-azidodecane (2.1c)

1-azidodecane was synthesized according to literature procedures.[124]

^{1}H NMR (500 MHz, C_6D_5Br): δ 2.96 (t, 2H, $H_3C(CH_2)_8$-C*H*$_2$-N_3), 1.39 – 1.34 (m, 2H, $H_3C(CH_2)_7$-C*H*$_2$-CH_2N_3), 1.29 – 1.25 (m, 2H, $H_3C(CH_2)_6$-C*H*$_2$-$(CH_2)_2N_3$), 1.21 – 1.15 (m, 12H, H_3C-(C*H*$_2$)$_6$- $(CH_2)_3N_3$), 0.88 (t, 3H, *H*$_3$C-$(CH_2)_9N_3$).

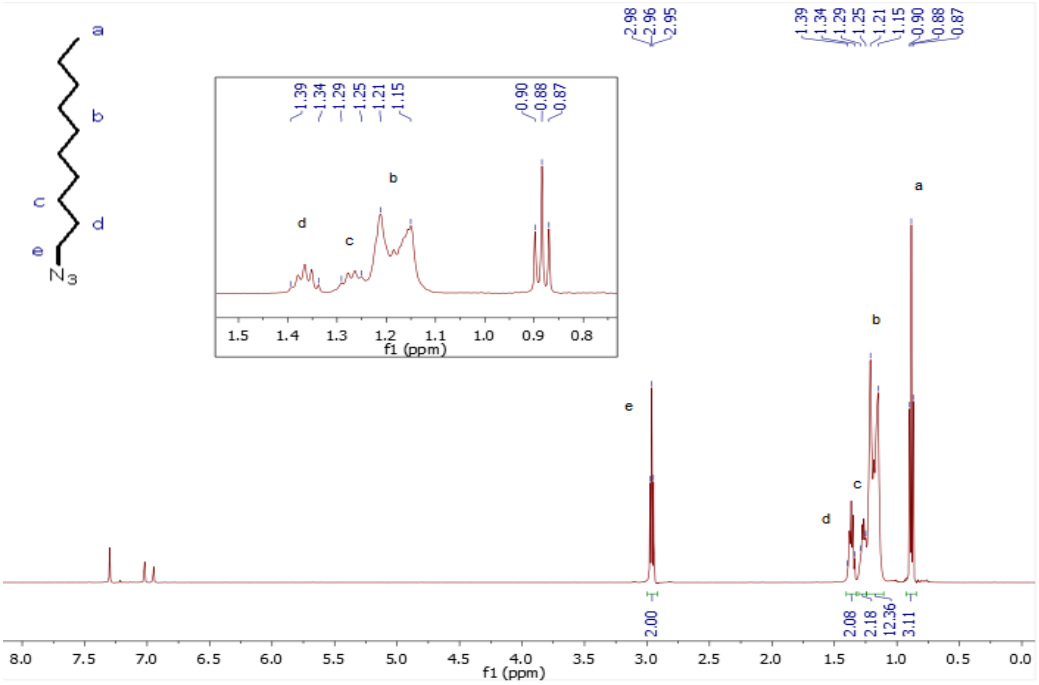

Figure 2.8 ^{1}H NMR spectrum of 1-azidodecane in C_6D_5Br.

Benzylazide (2.1d)

Benzylazide was synthesized according to literature procedures.[125]

^{1}H NMR (500 MHz, C_6D_5Br): δ 7.18 – 7.13 (m, 3H, Ph-*H*), 7.07 – 7.06 (m, 2H, Ph-*H*), 3.99 (s, 2H, C*H*$_2$).

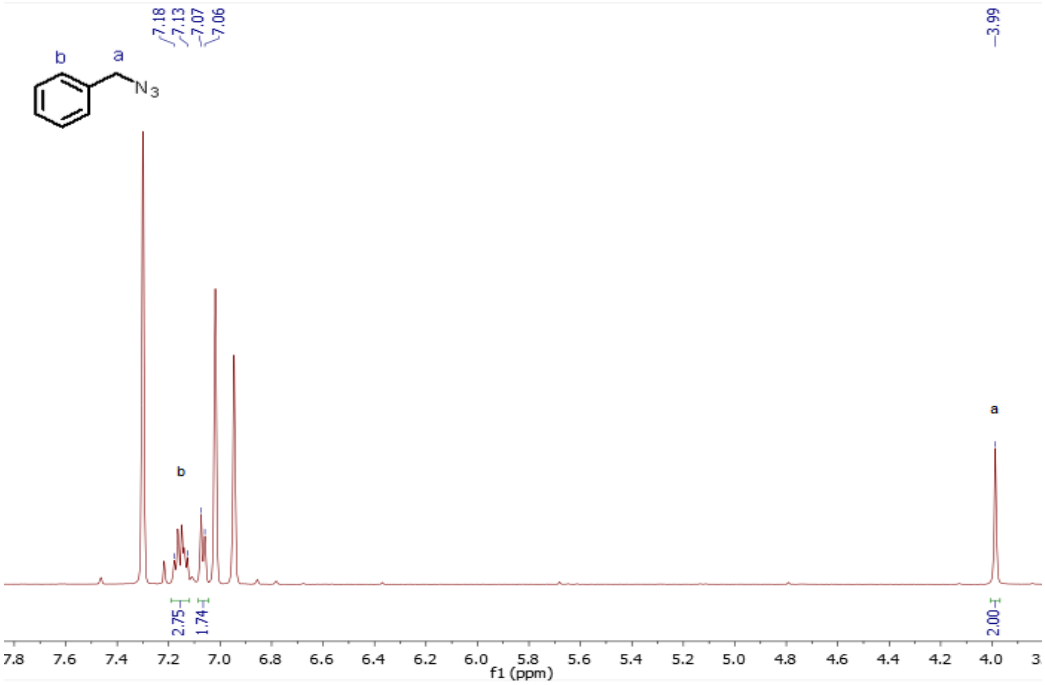

Figure 2.9 ^{1}H NMR spectrum of benzylazide in C_6D_5Br.

Azidomethyl phenyl sulfide (2.1e)

^{1}H NMR (500 MHz, C_6D_5Br): δ 7.33 (d, $^3J_{HH}$ = 7.4 Hz, 2H, *o*-Ph-*H*), 7.11 – 7.05 (m, 3H, *m*-Ph-*H* and *p*-Ph-*H*), 4.17 (s, 2H, CH_2).

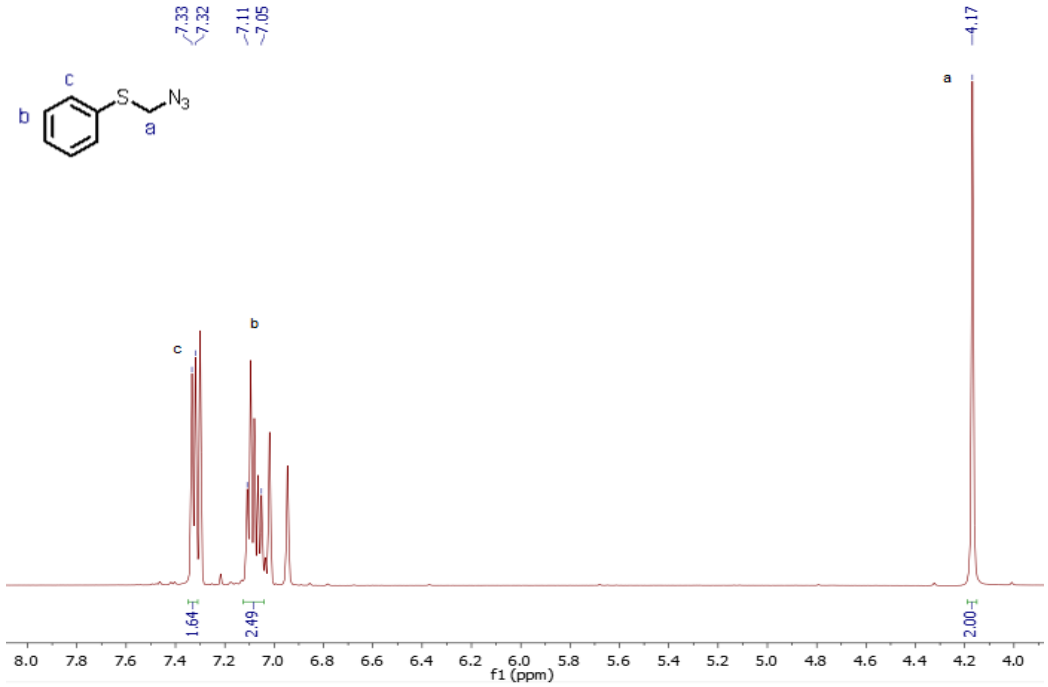

Figure 2.10 ^{1}H NMR spectrum of azidomethyl phenyl sulfide in C_6D_5Br.

Trityl azide (2.1f)

Trityl azide was synthesized according to the literature procedure[126] and used directly without any further purification.

^{1}H NMR (500 MHz, C_6D_5Br): δ 7.27 (d, $^3J_{HH}$ = 7.6 Hz, 6H, *o*-Ph-*H*), 7.18 – 7.10 (m, 9H, *m*-Ph-*H* and *p*-Ph-*H*).

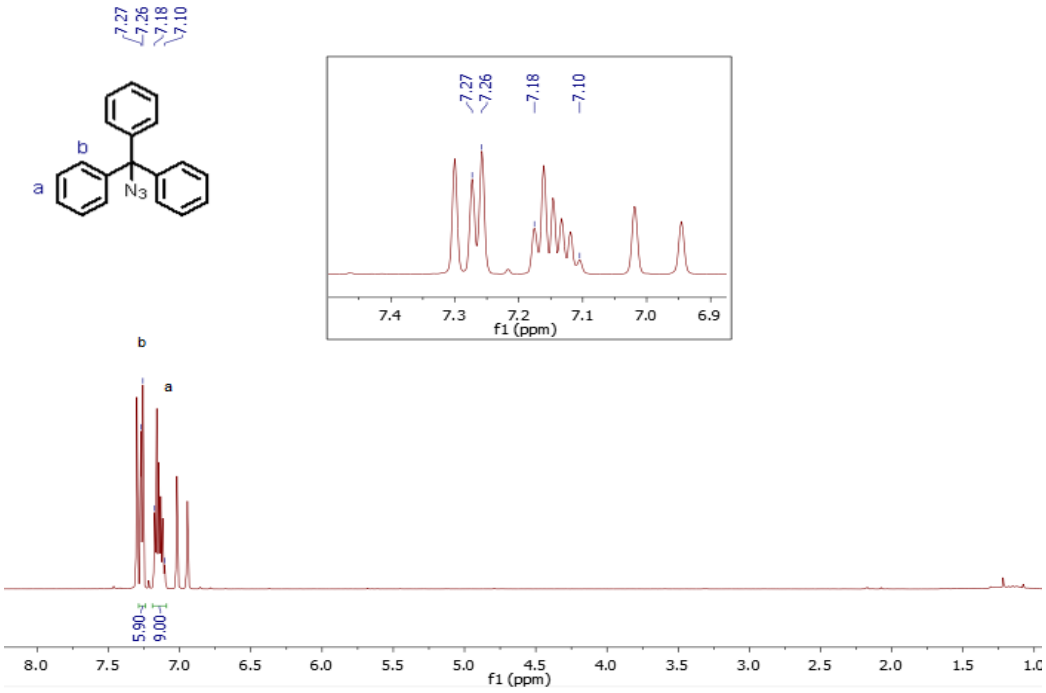

Figure 2.11 ^{1}H NMR spectrum of trityl azide in C_6D_5Br.

2-butyne (2.2b)

^{1}H NMR (500 MHz, C_6D_5Br): δ 1.60 (s, 6H, CH_3).

The other peaks in the spectrum belong to 1-azidoadamantane.

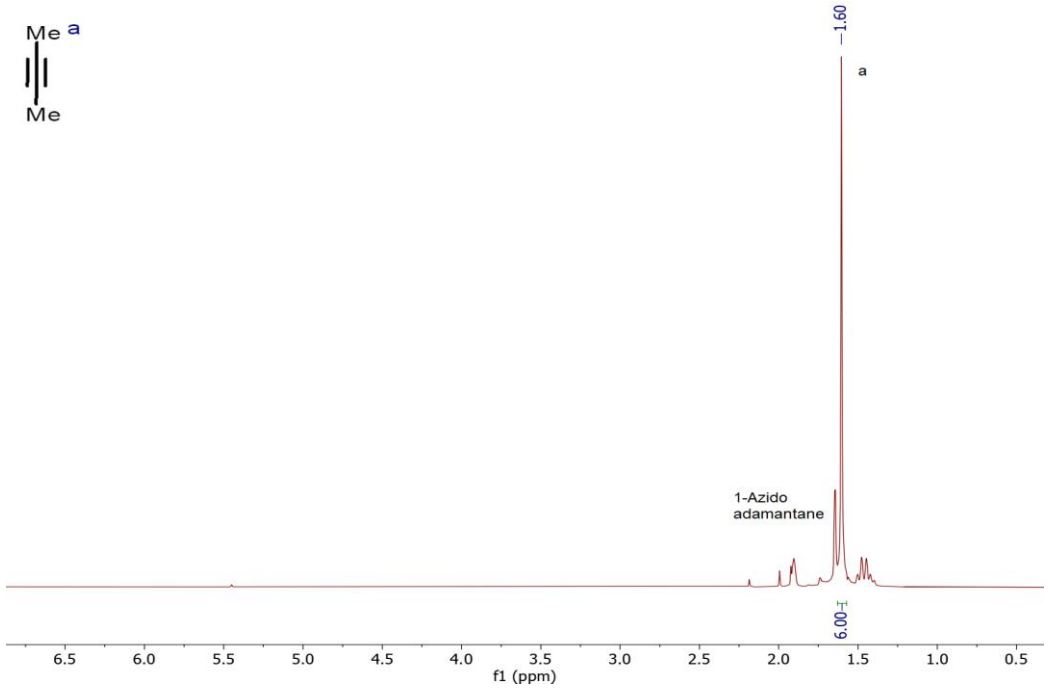

Figure 2.12 ^{1}H NMR spectrum of 2-butyne in C_6D_5Br.

Diphenylacetylene (2.2c)

^{1}H NMR (500 MHz, C_6D_5Br): δ 7.51 (d, $^{3}J_{HH}$ = 7.2 Hz, 4H, *o*-Ph-*H*), 7.18 – 7.12 (m, 6H, *m*-Ph-*H* and *p*-Ph-*H*).

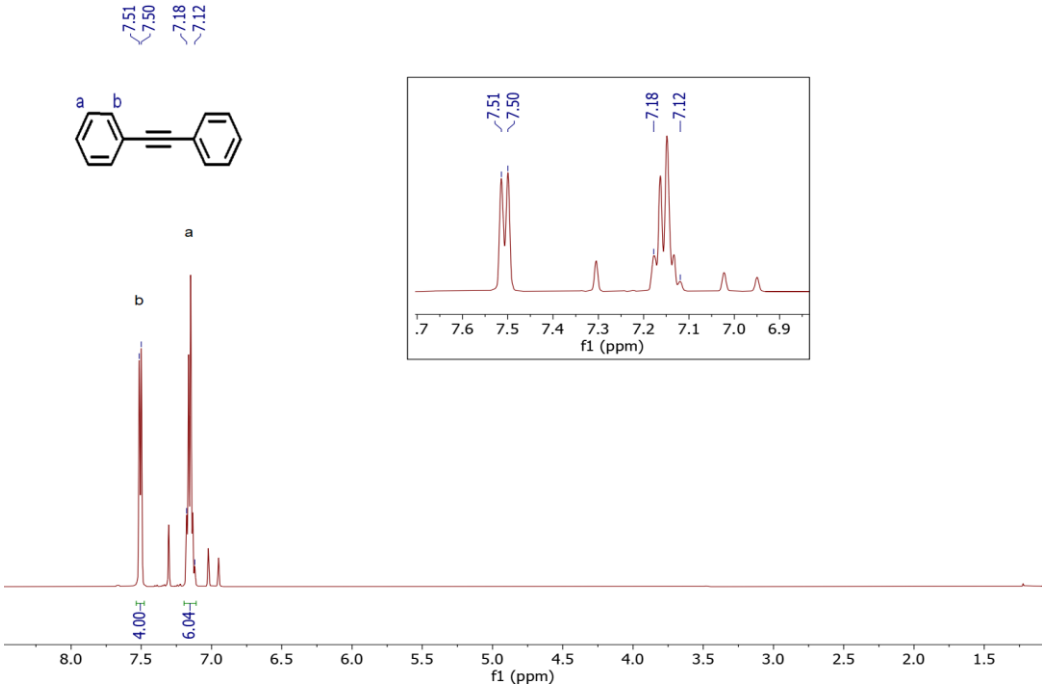

Figure 2.13 ^{1}H NMR spectrum of diphenylacetylene in C_6D_5Br.

1-Phenyl-1-propyne (2.2d)

^{1}H NMR (500 MHz, C_6D_5Br): δ 7.41 (d, $^{3}J_{HH}$ = 6.8 Hz, 2H, *o*-Ph-*H*), 7.13 – 7.09 (m, 3H, *m*-Ph-*H* and *p*-Ph-*H*), 1.84 (s, 3H, CH_3).

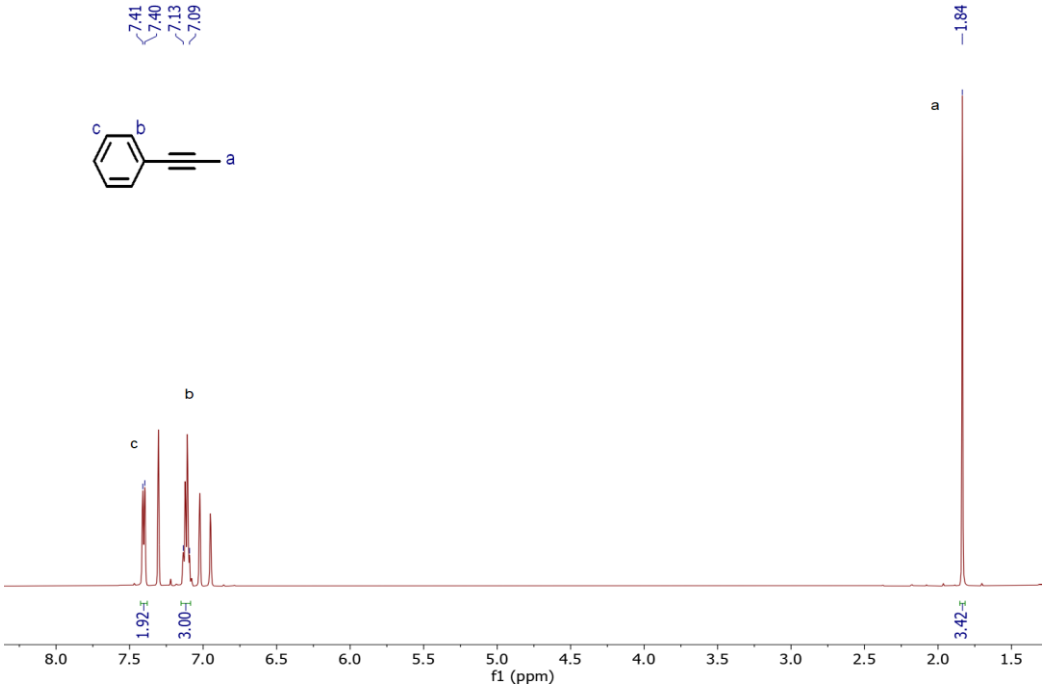

Figure 2.14 ^{1}H NMR spectrum of 1-phenyl-1-propyne in C_6D_5Br.

(*p*-tolyl)acetylene (2.2f)

^{1}H NMR (400 MHz, C_6D_5Br): δ 7.32 (d, $^3J_{HH}$ = 8.1 Hz, 1H, *m*-Tol-*H*), 6.88 (d, $^3J_{HH}$ = 8.2 Hz, 1H, *o*-Tol-*H*), 2.95 (s, 1H, Tol≡*H*), 2.10 (s, 2H, Ar-CH_3).

The other peaks in the spectrum belong to 1-azidoadamantane.

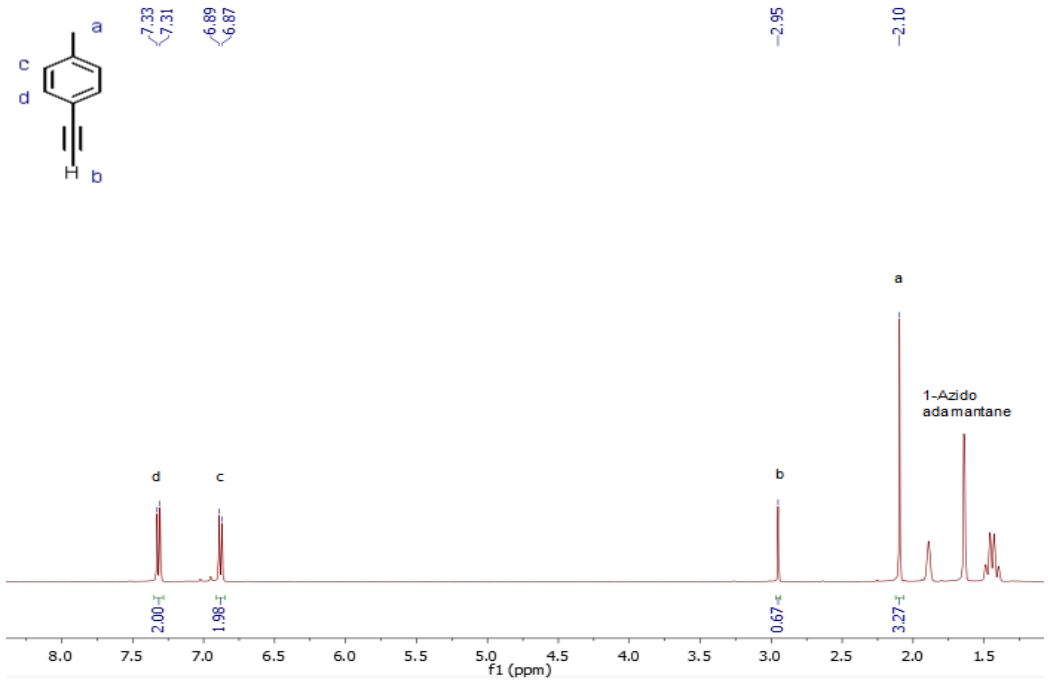

Figure 2.15 ^{1}H NMR spectrum of *p*-tolylacetylene in C_6D_5Br.

(*t*-butyl)acetylene (2.2g)

^{1}H NMR (500 MHz, C_6D_5Br): δ 2.02 (s, 1H, ^{t}Bu≡*H*), 1.16 (s, 9H, ^{t}Bu).

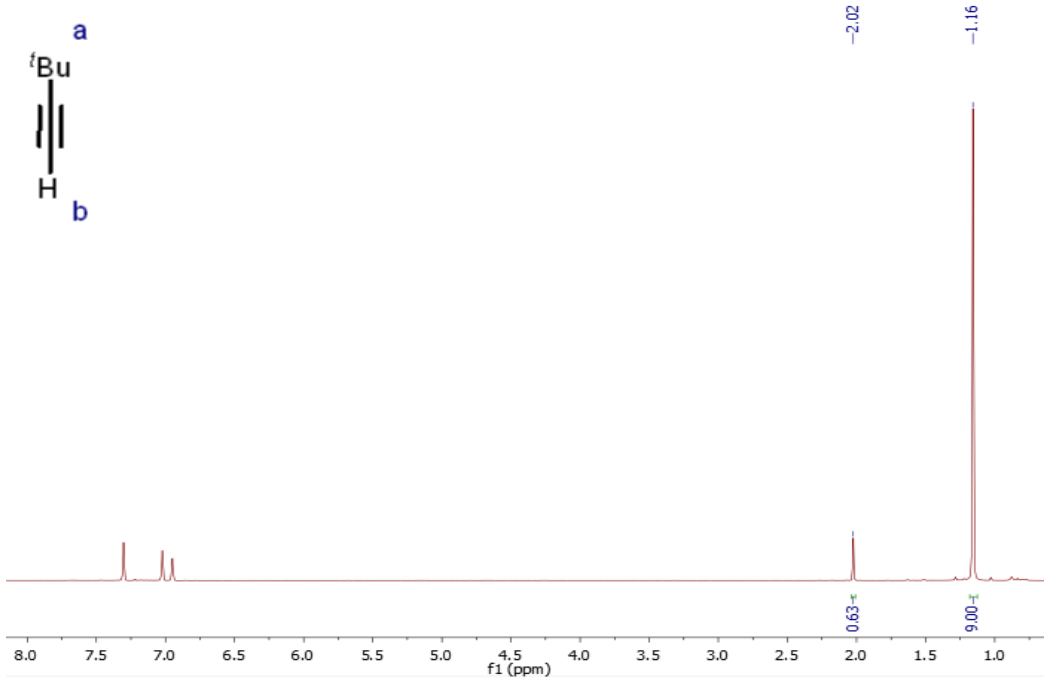

Figure 2.16 ^{1}H NMR spectrum of *t*-butylacetylene in C_6D_5Br.

(Trimethylsilyl)acetylene (2.2h)

^{1}H NMR (400 MHz, C_6D_5Br): δ 2.30 (s, 1H, C-*H*), 0.14 (s, 9H, Si(C*H*$_3$)$_3$).

The other peaks in the spectrum belong to 1-azidoadamantane.

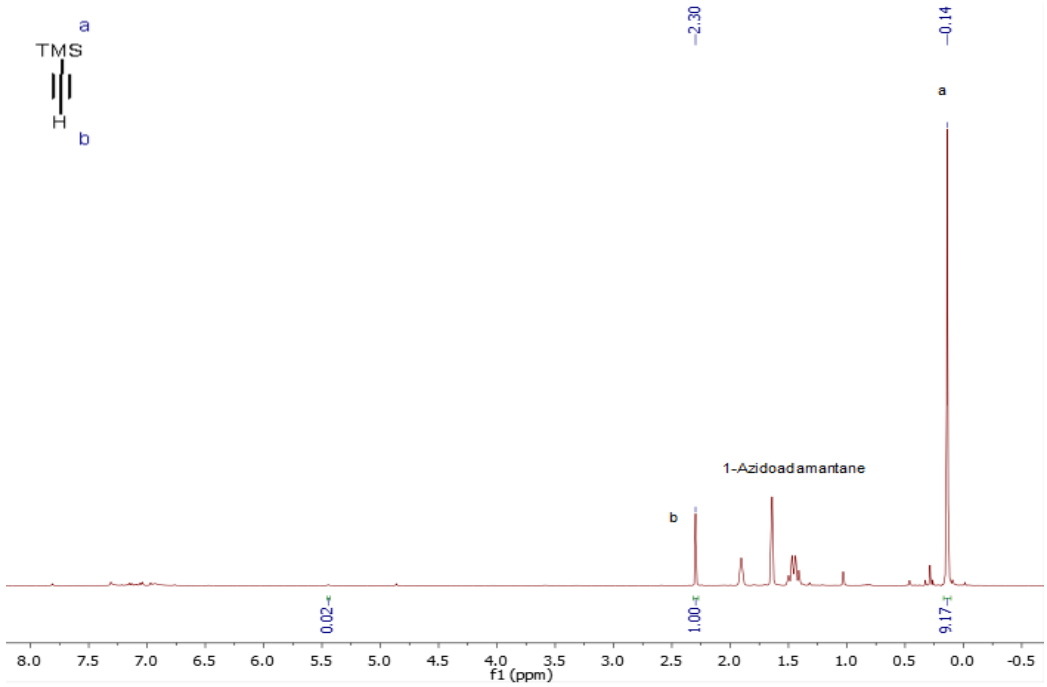

Figure 2.17 ^{1}H NMR spectrum of (trimethylsilyl)acetylene in C_6D_5Br.

1,7-octadiyne (2.2i)

^{1}H NMR (500 MHz, C_6D_5Br): δ 1.99 (s, 4H, HC≡C(C*H*$_2$)(CH$_2$)$_2$(C*H*$_2$)C≡CH), 1.88 (s, 2H, *H*C≡C(CH$_2$)(CH$_2$)$_2$(CH$_2$)C≡C*H*), 1.45 (s, 4H, HC≡C(CH$_2$)(C*H*$_2$)$_2$(CH$_2$)C≡CH).

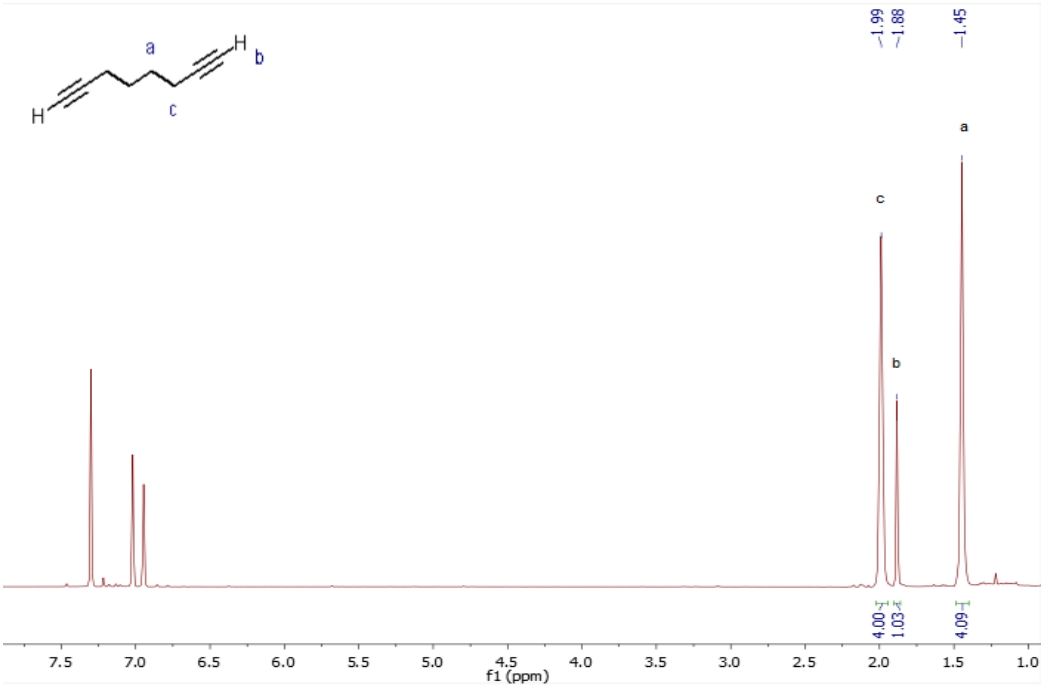

Figure 2.18 ^{1}H NMR spectrum of 1,7-octadiyne in C_6D_5Br.

2.5.4 Characterization of uncatalyzed triazole products in C_6D_5Br

1-(p-tolyl)-4,5-(diethyl)-1,2,3-triazole (2.6aa)

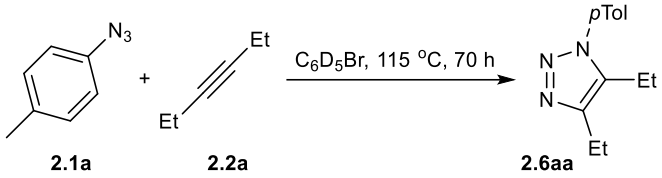

3-hexyne (16 mg, 0.1 mmol, 1.0 equiv), (*p*-tolyl)azide (13 mg, 0.1 mmol, 1.0 equiv) and 0.5 mL of C_6D_5Br were added to a NMR tube in a N_2-filled glovebox. The tube was sealed and heated at 115 °C for 70 h. After which, the reaction mixture was analyzed by ^{1}H NMR without any further work-up to give a mixture of title compound, leftover starting reagents and side products originating from (*p*-tolyl)azide such as *p*-toluidine and 1,2-di-*p*-tolyldiazene

^{1}H NMR (500 MHz, C_6D_5Br): δ 7.14 (d, $^3J_{HH}$ = 8.1 Hz, 2H, *o*-Tol-*H*), 7.01 (d, $^3J_{HH}$ = 8.1 Hz, 2H, *m*-Tol-*H*), 2.65 (q, $^3J_{HH}$ = 7.6 Hz, 2H, 4-CH_2CH$_3$), 2.44 (q, $^3J_{HH}$ = 7.6 Hz, 2H, 5-CH_2CH$_3$), 2.16 (s, 3H, Tol-CH_3), 1.35 (t, $^3J_{HH}$ = 7.6 Hz, 3H, 4-CH$_2$CH_3), 0.85 (t, $^3J_{HH}$ = 7.6 Hz, 3H, 5-CH$_2$CH_3).

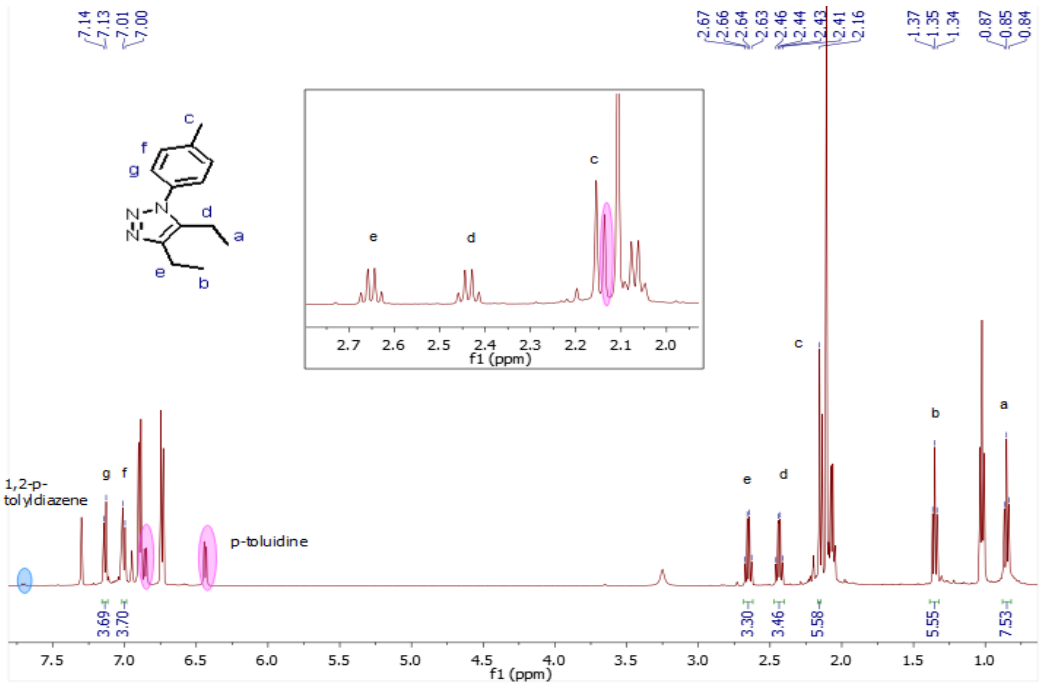

Figure 2.19 ^{1}H NMR spectrum of 1-(p-tolyl)-4,5-(diethyl)-1,2,3-triazole (**2.6aa**) in C_6D_5Br. *Taken from XYS04097.*

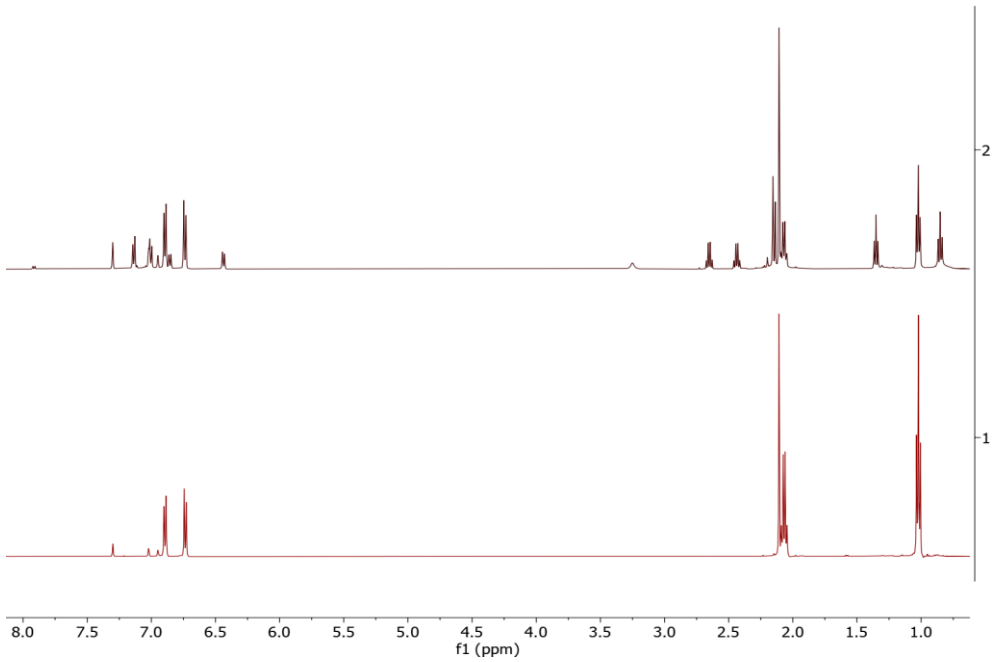

Figure 2.20 Before (bottom, t = 0 h) and after (top, t = 70 h) ^{1}H NMR spectrum of 3-hexyne and (*p*-tolyl)azido reaction in C_6D_5Br. *Taken from XYS04097B.*

1-adamantyl-4,5-di(ethyl)-1H-1,2,3-triazole (2.6ba) (partial)

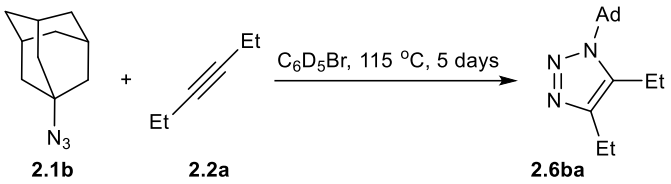

2.1b **2.2a** **2.6ba**

3-hexyne (45 µL, 0.39 mmol, 2.1 equiv), 1-Azidoadamantane (33 mg, 0.19 mmol, 1 equiv) and 0.5 mL of C_6D_5Br were added to a NMR tube in a N_2-filled glovebox. The tube was sealed and heated at 115 °C for 5 days. After which, the reaction mixture was analyzed by ^1H NMR without any further work-up to give the title compound and leftover starting reagents.

^{1}H NMR (500 MHz, C_6D_5Br): δ 2.65 (q, $^3J_{HH}$ = 7.5 Hz, 2H, C(4)-CH_2), 2.55 (q, $^3J_{HH}$ = 7.5 Hz, 2H, C(5)-CH_2), 2.21 (d, $^3J_{HH}$ = 3 Hz, 6H, N-C-(CH_2)$_2$), 2.01 (s (br), 3H, Ad-methine), 1.58 (s (br), 6H, Ad), 1.32 (t, $^3J_{HH}$ = 7.5 Hz, 2H, C(4)-CH$_2$-CH_3).
This is a partial line list; remaining methyl groups are hidden beneath 3-hexyne methyl group.

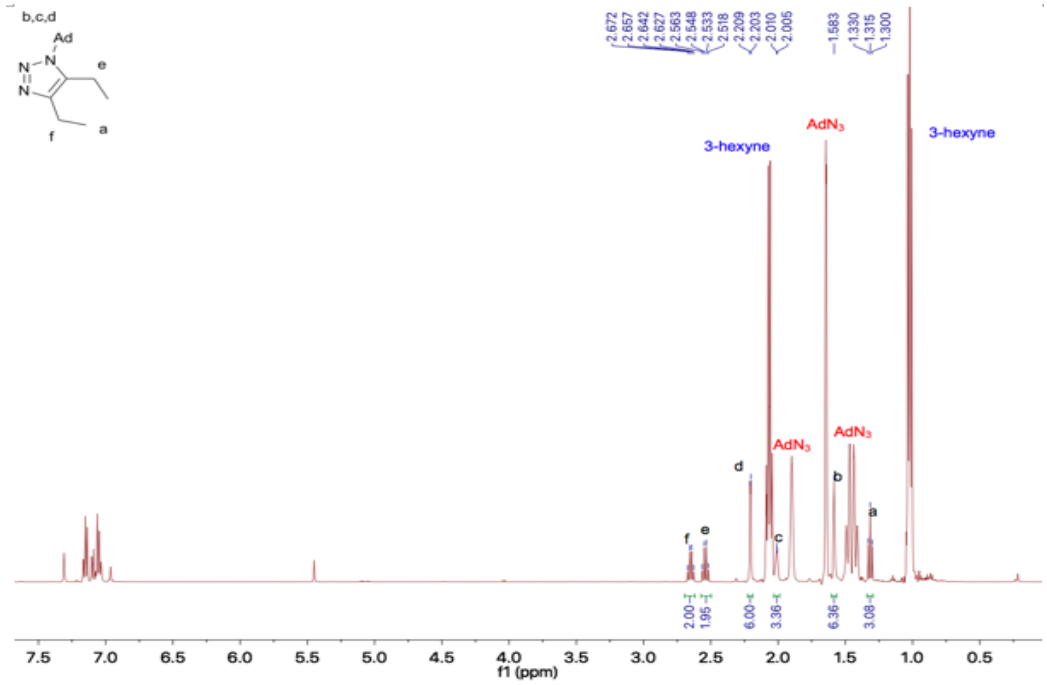

Figure 2.21 ^{1}H NMR spectrum of 1-adamantyl-4,5-diethyl-1H-1,2,3-triazole (**2.6ba**) in C_6D_5Br. *Taken from AJP05135B.*

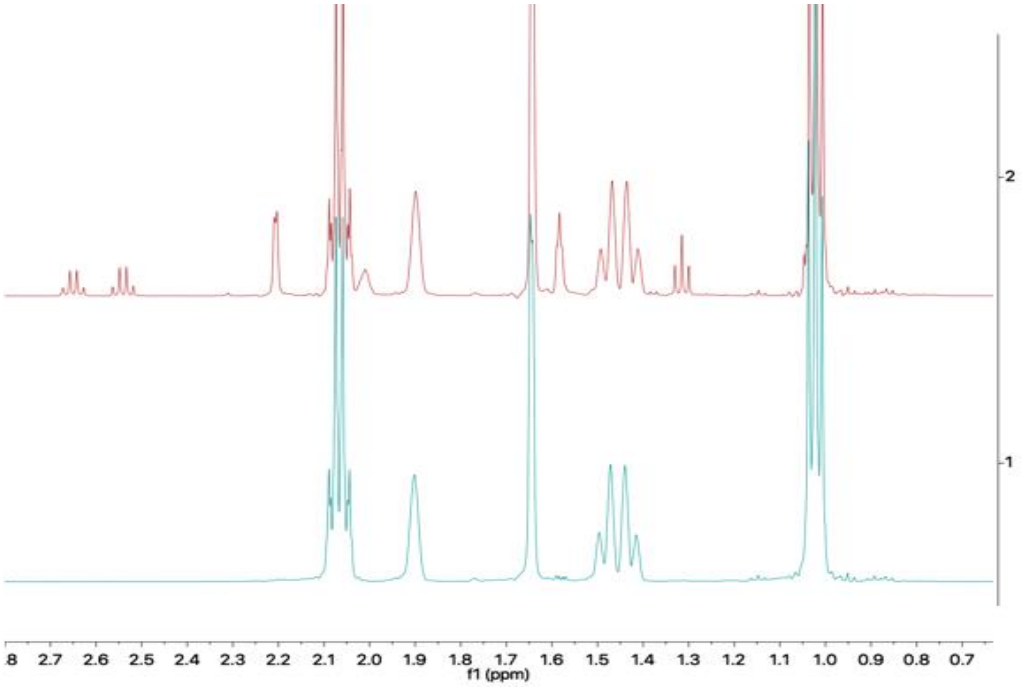

Figure 2.22 Before (bottom, t = 0 hr) and after (top, t = 5 days) ^{1}H NMR spectrum of 3-hexyne and 1-azidoadamantane reaction in C_6D_5Br. *Taken from AJP05135B.*

1-adamantyl-4,5-di(methyl)-1H-1,2,3-triazole (2.6bb) (partial)

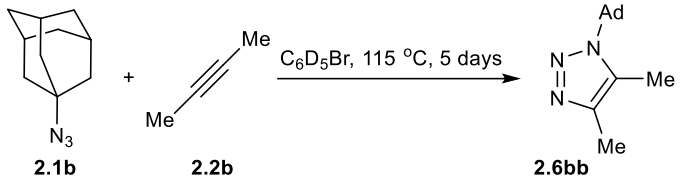

2.1b **2.2b** **2.6bb**

2-butyne (14 mg, 0.26 mmol, 1.7 equiv), 1-azidoadamantane (27 mg, 0.15 mmol, 1.0 equiv) and 0.5 mL of C_6D_5Br were added to a NMR tube in a N_2-filled glovebox. The tube was sealed and heated at 115 °C for 16 h. After which, the reaction mixture was analyzed by ^{1}H NMR without any further work-up to give the title compound and leftover starting reagents.

^{1}H NMR (400 MHz, C_6D_5Br): δ 2.17 – 2.16 (m, 6H, Ad-C*H*$_2$), 2.15 (s, 3H, C4-C*H*$_3$), 2.09 (s, 3H, C5-C*H*$_3$).

This is a partial NMR line list, the remaining adamantyl peaks are buried under the peaks for the starting reagents.

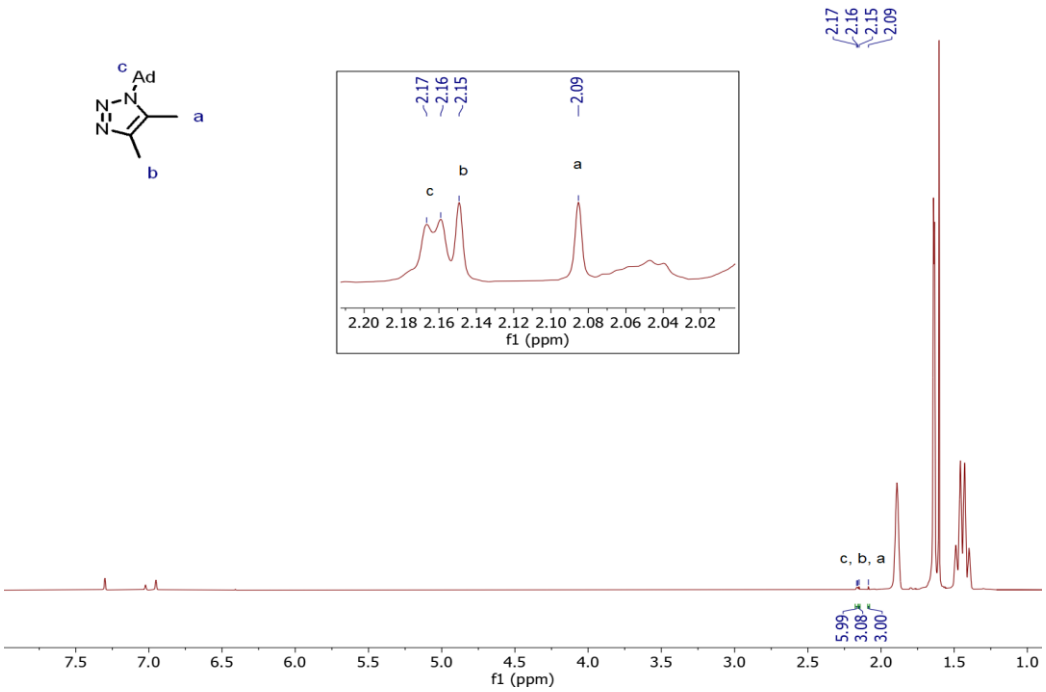

Figure 2.23 ^{1}H NMR spectrum of 1-adamantyl-4,5-di(methyl)-1H-1,2,3-triazole (**2.6bb**) in C_6D_5Br. *Taken from XYS04038A.*

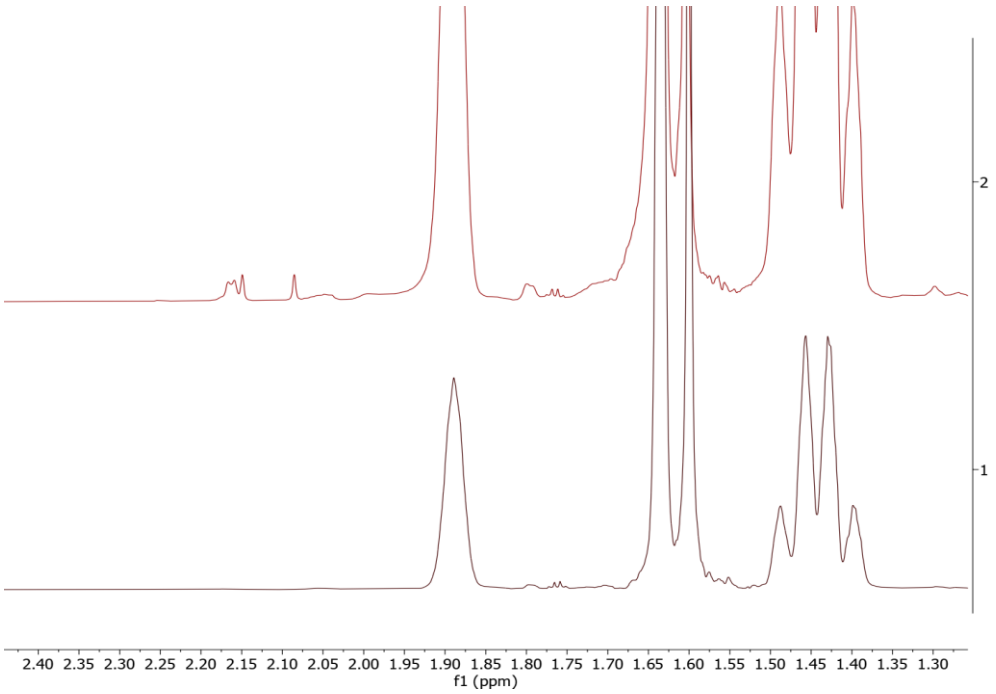

Figure 2.24 Before (bottom, t = 0 h) and after (top, t = 16 h) ^{1}H NMR spectrum of 2-butyne and 1-azidoadamantane reaction in C_6D_5Br. *Taken from XYS04038A.*

1-adamantyl-4,5-di(phenyl)-1H-1,2,3-triazole (2.6bc) (partial)

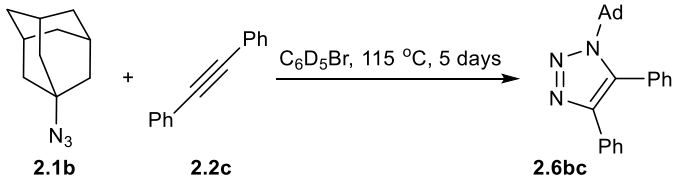

2.1b **2.2c** **2.6bc**

Diphenylacetylene (38 mg, 0.21 mmol, 1.1 equiv), 1-azidoadamantane (33 mg, 0.19 mmol, 1 equiv) and 0.5 mL of C_6D_5Br were added to a NMR tube in a N_2-filled glovebox. The tube was sealed and heated at 115 °C for 5 days. After which, the reaction mixture was analyzed by ^1H NMR without any further work-up to give the title compound and leftover starting reagents.

^1H NMR (500 MHz, C_6D_5Br): δ 7.66 (d, $^3J_{HH}$ = 7.0 Hz, 2H, Ar-*H*) 7.23 (m, 3H, Ar-*H*), 2.18 (d, $^3J_{HH}$ = 3 Hz, 6H, N-C-(C*H*$_2$)$_3$).

This is a partial NMR line list, the remaining adamantyl and aryl peaks are buried under the peaks for the starting reagents.

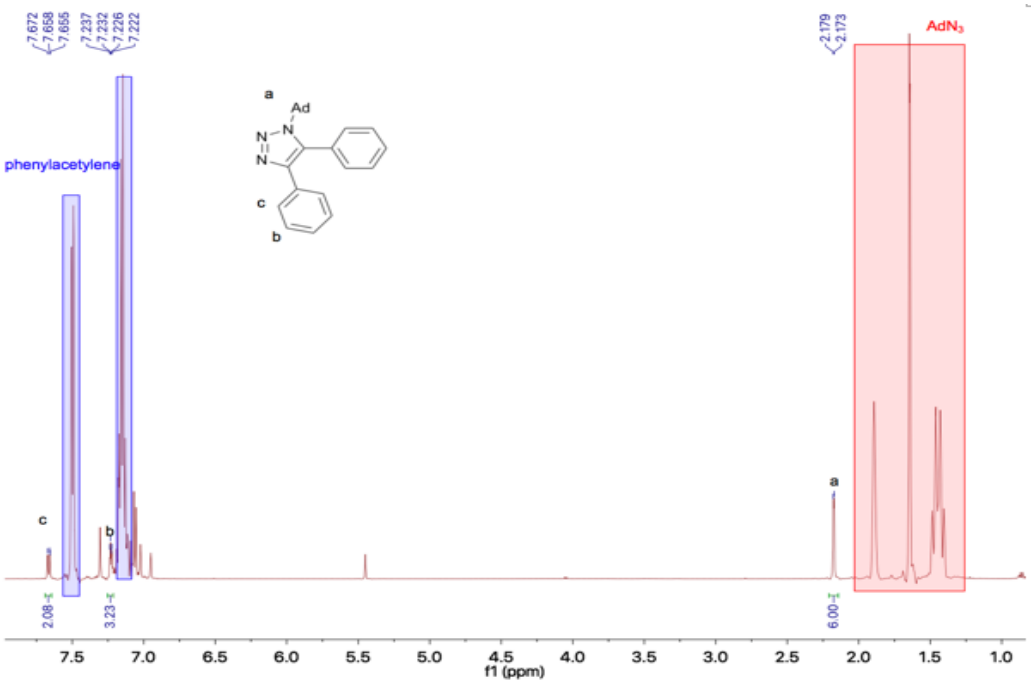

Figure 2.25 ^1H NMR spectrum of 1-adamantyl-4,5-diphenyl-1H-1,2,3-triazole (**2.6bc**) in C_6D_5Br. *Taken from AJP05135A.*

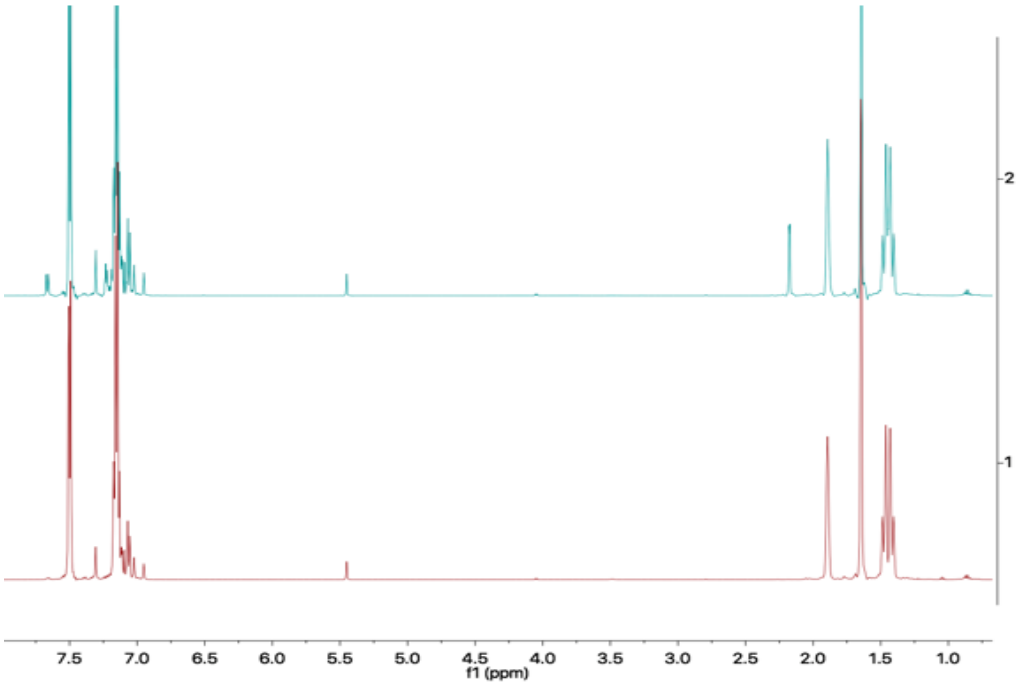

Figure 2.26 Before (bottom, t = 0 hr) and after (top, t = 5 days) ^{1}H NMR spectrum of diphenylacetylene and 1-azidoadamantane reaction in C_6D_5Br. *Taken from AJP05135A.*

1-adamantyl-4-methyl-5-phenyl-1H-1,2,3-triazole and 1-adamantyl-5-methyl-4-phenyl-1H-1,2,3-triazole (2.6bd)

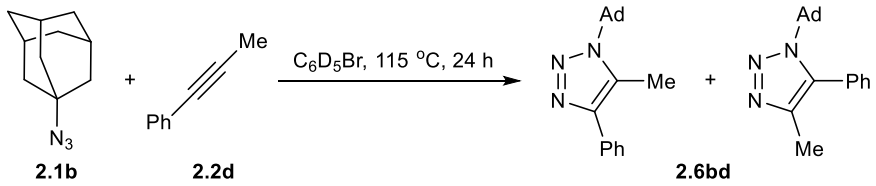

2.1b **2.2d** **2.6bd**

1-Phenyl-1-propyne (75 µL, 0.59 mmol, 2.6 equiv), 1-azidoadamantane (40 mg, 0.11 mmol, 1.0 equiv) and 0.5 mL of C_6D_5Br were added to a NMR tube in a N_2-filled glovebox. The tube was sealed and heated at 115 °C for 24 h. After which, the reaction mixture was analyzed by ^{1}H NMR without any further work-up to give a mixture of both title compounds and leftover starting reagents.

1-adamantyl-4-methyl-5-phenyl-1*H*-1,2,3-triazole

^{1}H NMR (500 MHz, C_6D_5Br): δ 7.73 (d, $^{3}J_{HH}$ = 6.5, 2H, *o*-Ar-*H*), 7.35 (t, $^{3}J_{HH}$ = 7.5, 2H, *m*-Ar-*H*), 2.35 (s, 3H, C(4)-C*H*$_3$), 2.22 (d, $^{3}J_{HH}$ = 3.0 Hz, 6H, N-C-(C*H*$_2$)$_3$), 2.02 (s (br), 3H, Ad-methine), 1.59 (s (br), 6H, Ad).

This is a partial NMR line list; *p*-aryl C-H is hidden behind the peaks for starting materials

1-adamantyl-5-methyl-4-phenyl-1*H*-1,2,3-triazole

^{1}H NMR (500 MHz, C_6D_5Br): δ 7.23 (t, $^{3}J_{HH}$ = 7.0 Hz, 2H, *m*-Ar-*H*), 2.15 (d, $^{3}J_{HH}$ = 3.0 Hz, 6H, N-C-(CH_2)$_3$), 2.07 (s, 3H, C(5)-CH_3).

This is a partial NMR line list; Remaining peaks are hidden behind starting materials**.**

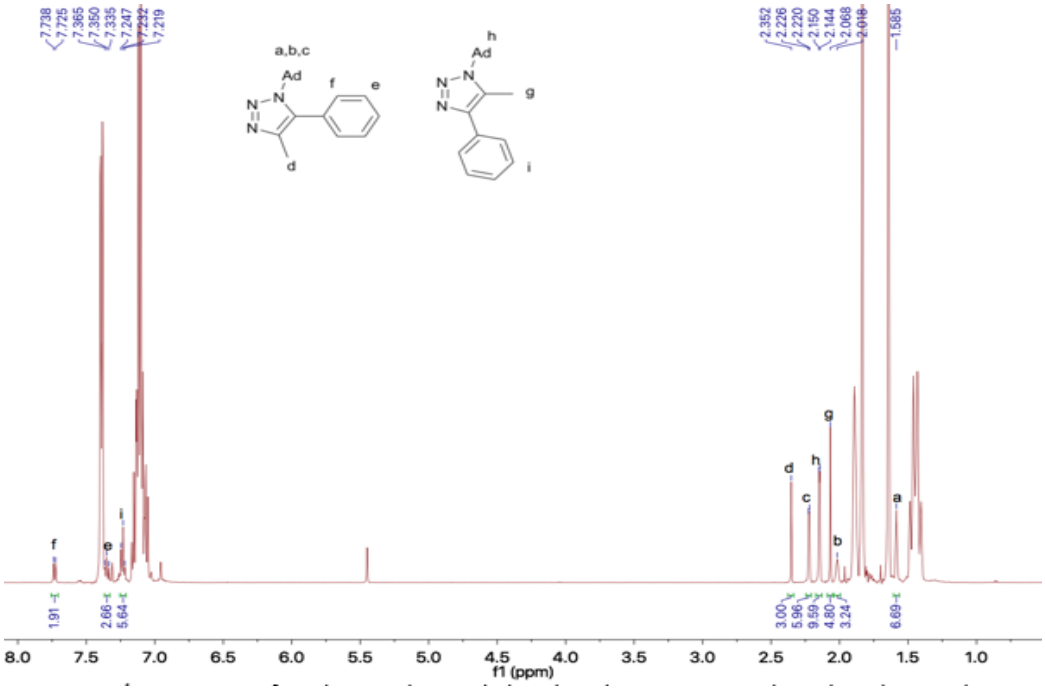

Figure 2.27 ^{1}H NMR spectrum of 1-adamantyl-4-methyl-5-phenyl-1H-1,2,3-triazole and 1-adamantyl-5-methyl-4-phenyl-1H-1,2,3-triazole (**2.6bd**) in C_6D_5Br. *Taken from AJP05091-2H.*

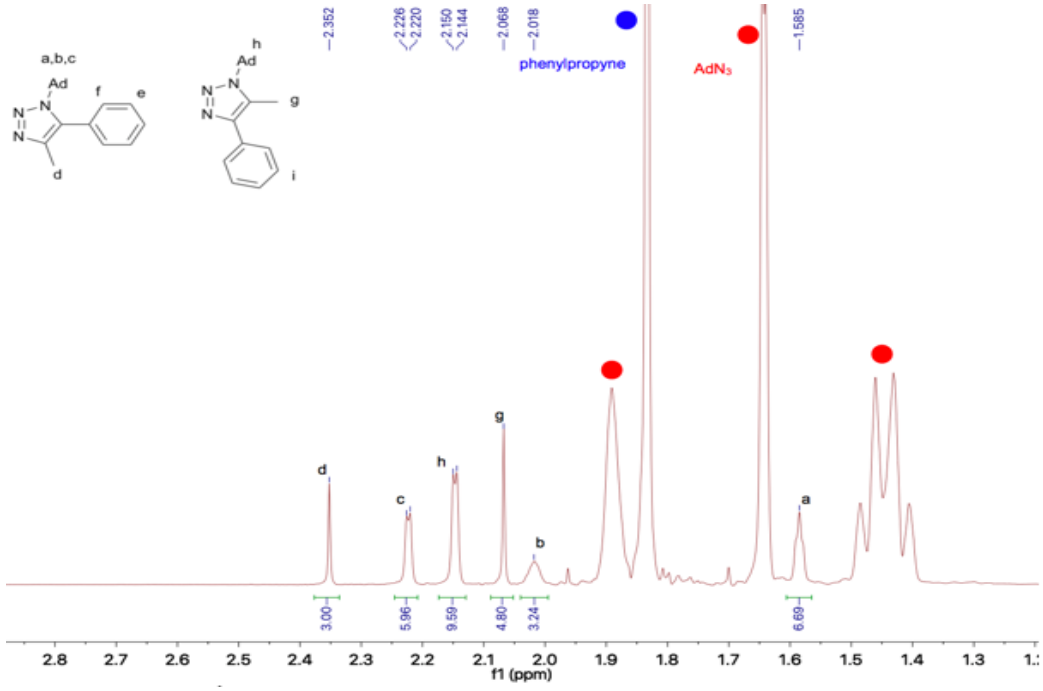

Figure 2.28 Zoom-in ^{1}H NMR spectrum of the alkyl region of 1-adamantyl-4-methyl-5-phenyl-1H-1,2,3-triazole and 1-adamantyl-5-methyl-4-phenyl-1H-1,2,3-triazole (**2.6bd**) in C_6D_5Br. *Taken from AJP05091-2H.*

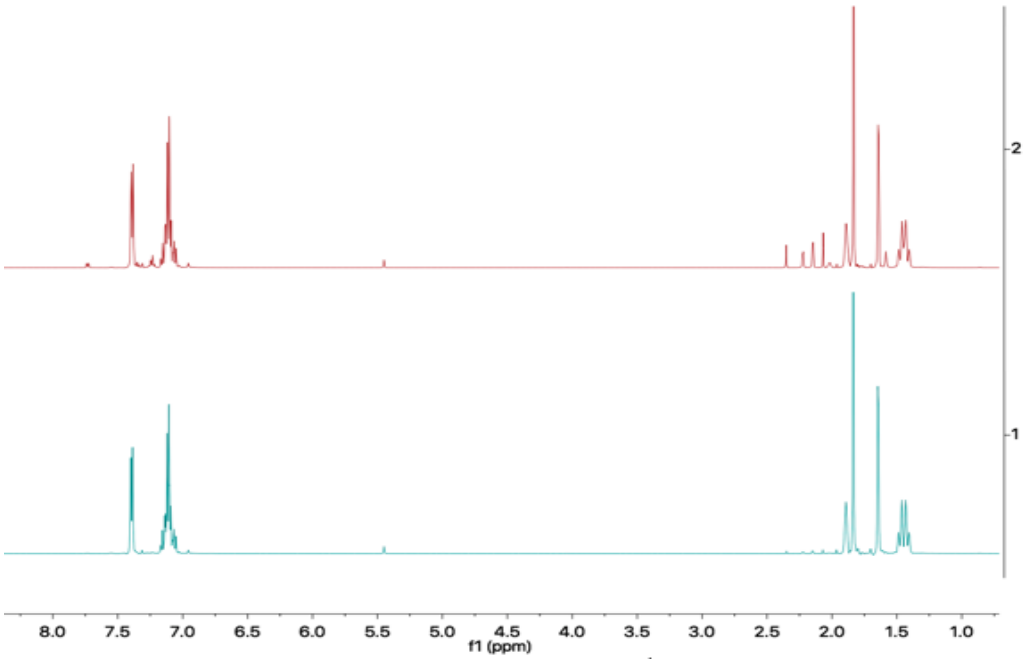

Figure 2.29 Before (bottom, t = 0 hr) and after (top, t = 24 h) ^{1}H NMR spectrum of 1-phenyl-1-propyne and 1-azidoadamantane reaction in C_6D_5Br. *Taken from AJP05091-2H.*

1-adamantyl-4-(*n*-butyl)-1H-1,2,3-triazole and 1-adamantyl-5-(*n*-butyl)-1H-1,2,3-triazole (2.6be) (partial)

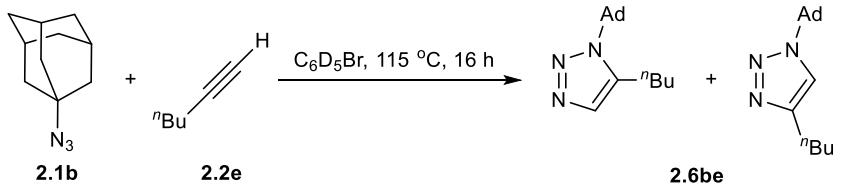

1-hexyne (15 mg, 0.18 mmol, 1.6 equiv), 1-azidoadamantane (20 mg, 0.11 mmol, 1.0 equiv) and 0.5 mL of C_6D_5Br were added to a NMR tube in a N_2-filled glovebox. The tube was sealed and heated at 115 °C for 16 h. After which, the reaction mixture was analyzed by ^{1}H NMR without any further work-up to give a mixture of both title compounds and leftover starting reagents.

1-adamantyl-4-(*n*-butyl)-1H-1,2,3-triazole (partial)

^{1}H NMR (400 MHz, C_6D_5Br): δ 7.12 (s, 1H, Ar-C*H*), 2.71 (t, $^{3}J_{HH}$ = 7.8 Hz, 2H, C*H*$_2$CH$_2$CH$_2$CH$_3$), 2.04 (m, 6H, Ad-C*H*$_2$), 1.98 (m, 3H, Ad-C*H*), 1.56 (m, 6H, Ad-C*H*$_2$), 0.88 (t, $^{3}J_{HH}$ = 7.4 Hz, 3H, CH$_2$CH$_2$CH$_2$C*H*$_3$).

Singlet at δ 2.04 is partially overlapped by the 1-hexyne substrate. This is a partial NMR line list, the remaining peaks for the *n*-butyl chain are overlapping with other peaks.

1-adamantyl-5-(*n*-butyl)-1H-1,2,3-triazole (partial)

^{1}H NMR (400 MHz, C_6D_5Br): δ 7.44 (s, 1H, Ar-C*H*), 2.64 (t, $^{3}J_{HH}$ = 7.8 Hz, 2H, CH_2CH$_2$CH$_2$CH$_3$), 2.22 – 2.21 (m, 6H, Ad-CH_2).

Triplet peak for CH$_2$CH$_2$CH$_2$CH_3 is buried under the other regioisomer at δ 0.86. This is a partial NMR line list, the remaining peaks for the adamantyl group and *n*-butyl chain are overlapping with other peaks.

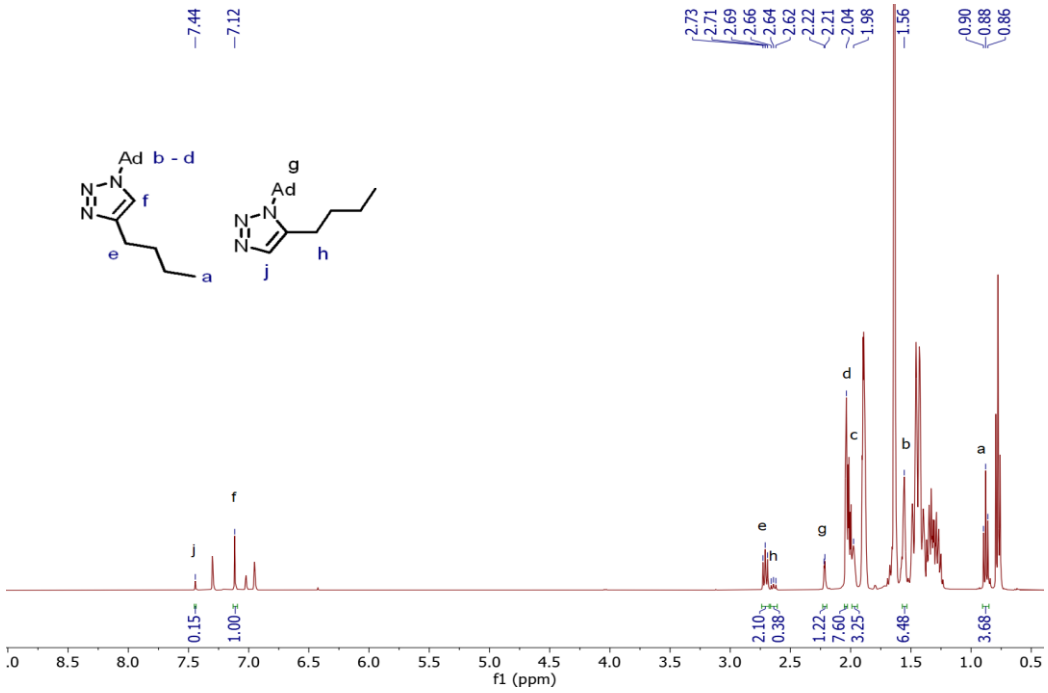

Figure 2.30 ^{1}H NMR spectrum of 1-adamantyl-4-(*n*-butyl)-1H-1,2,3-triazole and 1-adamantyl-5-(*n*-butyl)-1H-1,2,3-triazole (**2.6be**) in C_6D_5Br. *Taken from XYS04038_B.*

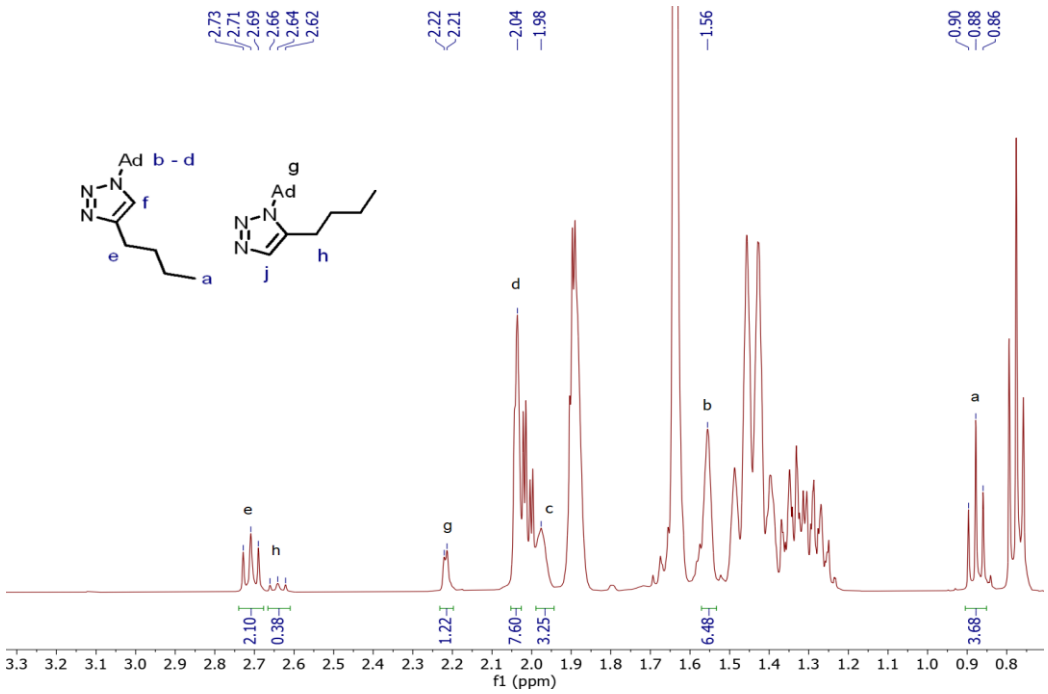

Figure 2.31 Zoom-in ^{1}H NMR spectrum of 1-adamantyl-4-(*n*-butyl)-1H-1,2,3-triazole and 1-adamantyl-(5-*n*-butyl)-1H-1,2,3-triazole (**2.6be**) in C_6D_5Br. *Taken from XYS04038_B.*

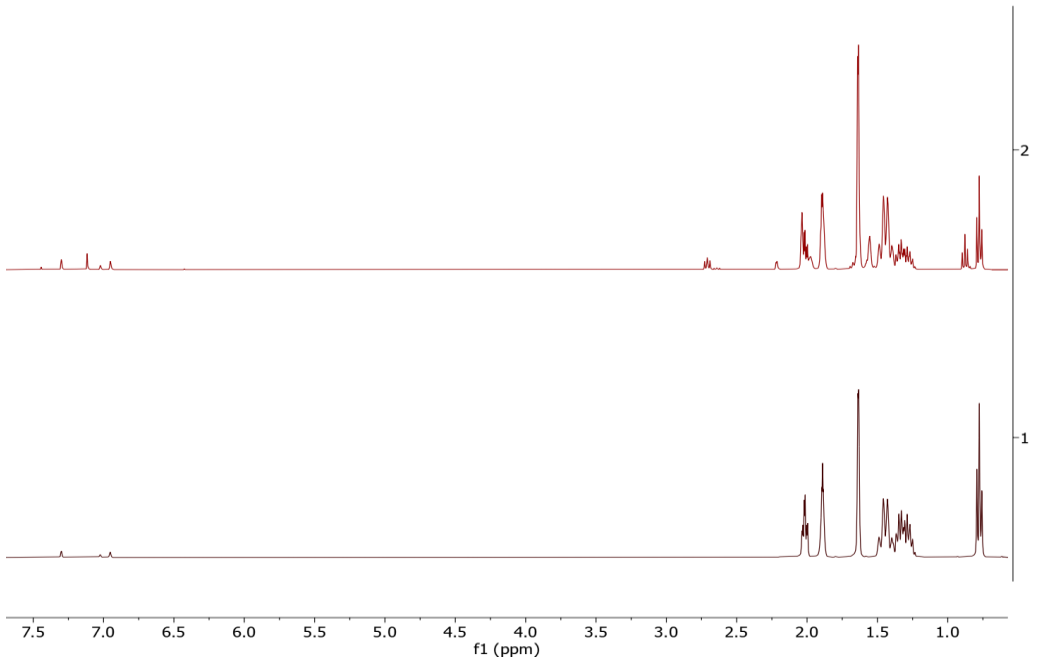

Figure 2.32 Before (bottom, t = 0 h) and after (top, t = 16 h) ^{1}H NMR spectrum of 1-hexyne and 1-azidoadamantane reaction in C_6D_5Br. *Taken from XYS04038_B.*

1-adamantyl-4-(*p*-tolyl)-1H-1,2,3-triazole and 1-adamantyl-5-(*p*-tolyl)-1H-1,2,3-triazole (2.6bf) (partial)

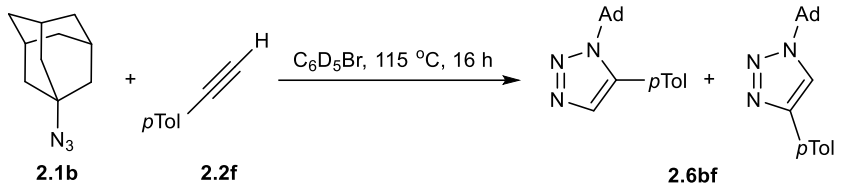

2.1b **2.2f** **2.6bf**

(*p*-tolyl)acetylene (15 mg, 0.13 mmol, 1.4 equiv), 1-azidoadamantane (16 mg, 0.09 mmol, 1.0 equiv) and 0.5 mL of C_6D_5Br were added to a NMR tube in a N_2-filled glovebox. The tube was sealed and heated at 115 °C for 16 h. After which, the reaction mixture was analyzed by ^{1}H NMR without any further work-up to give a mixture of title compounds and leftover starting reagents.

1-adamantyl-4-(*p*-tolyl)-1H-1,2,3-triazole

^{1}H NMR (400 MHz, C_6D_5Br): δ 7.88 (d, $^3J_{HH}$ = 8.1 Hz, 2H, *o*-Tol-*H*), 7.87 (s, 1H, Ar-*H*), 7.13 (d, $^3J_{HH}$ = 7.9 Hz, 2H, *m*-Tol-*H*), 2.23 (s, 3H, Tol-CH_3), 2.07 – 2.06 (m, 6H, Ad-CH_2), 2.00 (br s, 3H, Ad-C*H*), 1.57 (m, 6H, Ad-CH_2).

1-adamantyl-5-(*p*-tolyl)-1H-1,2,3-triazole (partial)

^{1}H NMR (400 MHz, C_6D_5Br): δ 7.53 (s, 1H, Ar-*H*), 7.10 (d, $^3J_{HH}$ = 8.0 Hz, 2H, *o*-Tol-*H*), 7.02 (d, $^3J_{HH}$ = 7.7 Hz, 2H, *m*-Tol-*H*), 2.17 (m, 9H, Tol-CH_3 and Ad-CH_2).

m-Tol-*H* peak at δ 7.02 ppm overlaps with C_6D_5Br solvent peak. This is a partial NMR line list, the remaining peaks for the adamantyl group are overlapping with other peaks.

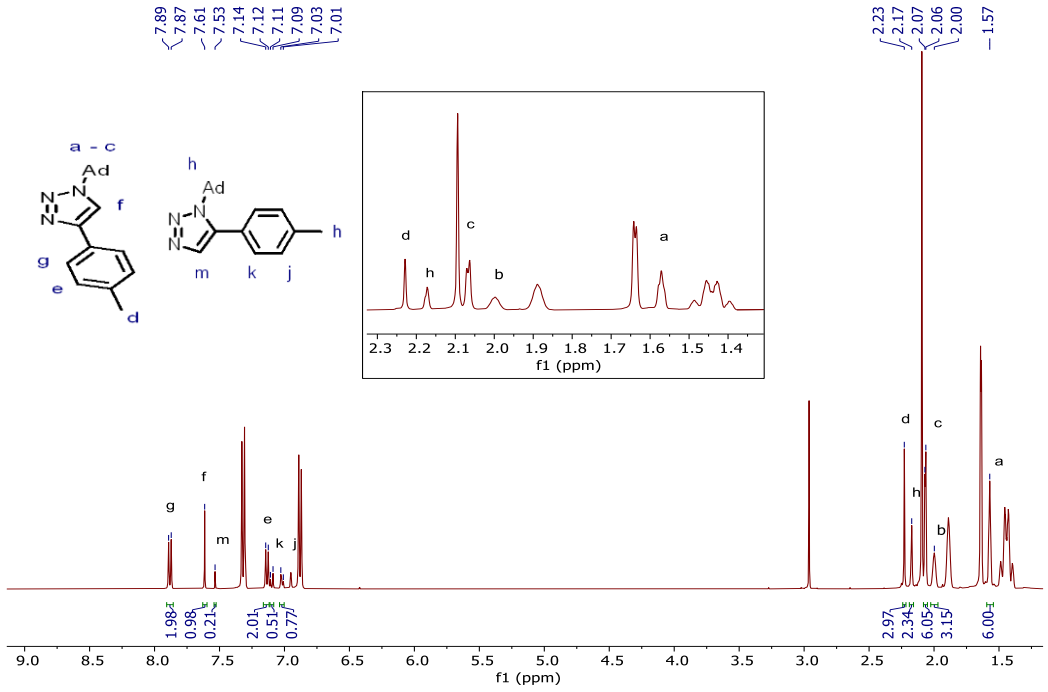

Figure 2.33 ^{1}H NMR spectrum of 1-adamantyl-4-(*p*-tolyl)-1H-1,2,3-triazole and 1-adamantyl-5-(*p*-tolyl)-1H-1,2,3-triazole (**2.6bf**) in C_6D_5Br. *Taken from XYS04038_D.*

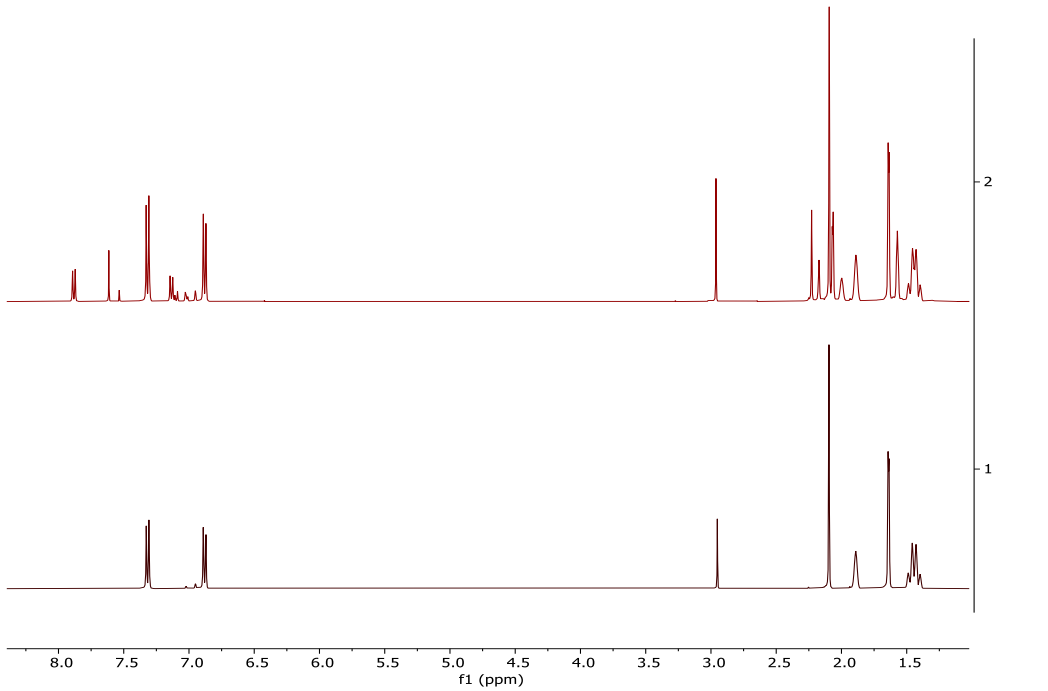

Figure 2.34 Before (bottom, t = 0 h) and after (top, t = 16 h) ^{1}H NMR spectrum of (*p*-tolyl)acetylene and 1-azidoadamantane reaction in C_6D_5Br. *Taken from XYS04038_D.*

1-(*p*-tolyl)-4-(*t*-butyl)-1H-1,2,3-triazole and 1-(*p*-tolyl)-5-(*t*-butyl)-1H-1,2,3-triazole (2.6ag) (partial)

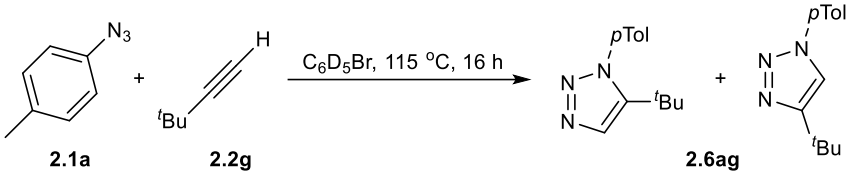

(*t*-butyl)acetylene (15 mg, 0.18 mmol, 1.1 equiv), (*p*-tolyl)azide (21 mg, 0.16 mmol, 1.0 equiv) and 0.5 mL of C_6D_5Br were added to a NMR tube in a N_2-filled glovebox. The tube was sealed and heated at 115 °C for 16 h. After which, the reaction mixture was analyzed by ^{1}H NMR without any further work-up to give a mixture of title compounds, leftover starting reagents and side products originating from (*p*-tolyl)azido such as *p*-toluidine and 1,2-di-*p*-tolyldiazene.

1-(*p*-tolyl)-4-(*t*-butyl)-1H-1,2,3-triazole

^{1}H NMR (400 MHz, C_6D_5Br): δ 7.46 (s, 1H, Ar-*H*), 7.44 (d, $^3J_{HH}$ = 8.4 Hz, 2H, *o*-Tol-*H*), 7.00 (d, $^3J_{HH}$ = 8.1 Hz, 2H, *m*-Tol-*H*), 2.15 (s, 3H, Tol-CH_3), 1.40 (s, 9H, ^{t}Bu).

1-(*p*-tolyl)-5-(*t*-butyl)-1H-1,2,3-triazole (partial)

^{1}H NMR (400 MHz, C_6D_5Br): δ 7.50 (s, 1H, Ar-*H*), 1.03 (s, 9H, ^{t}Bu).

This is a partial NMR line list, the remaining peaks cannot be positively identified from the other degradation impurities.

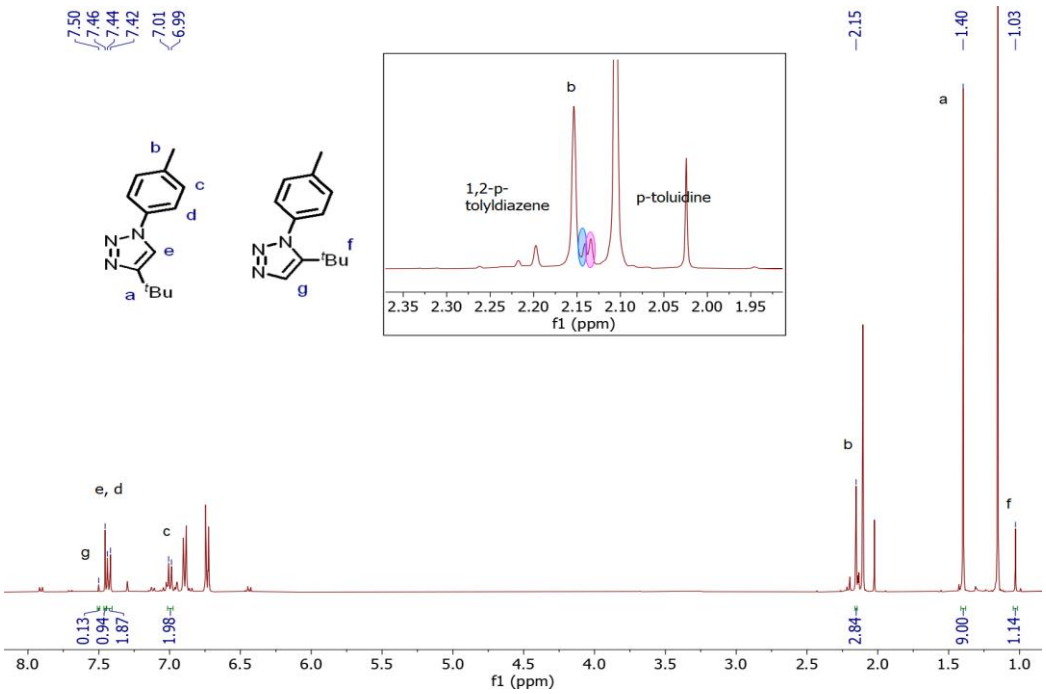

Figure 2.35 ^{1}H NMR spectrum of 1-(*p*-tolyl)-4-(*t*-butyl)-1H-1,2,3-triazole and 1-(*p*-tolyl)-5-(*t*-butyl)-1H-1,2,3-triazole (**2.6ag**) in C_6D_5Br. *Taken from XYS04038_F.*

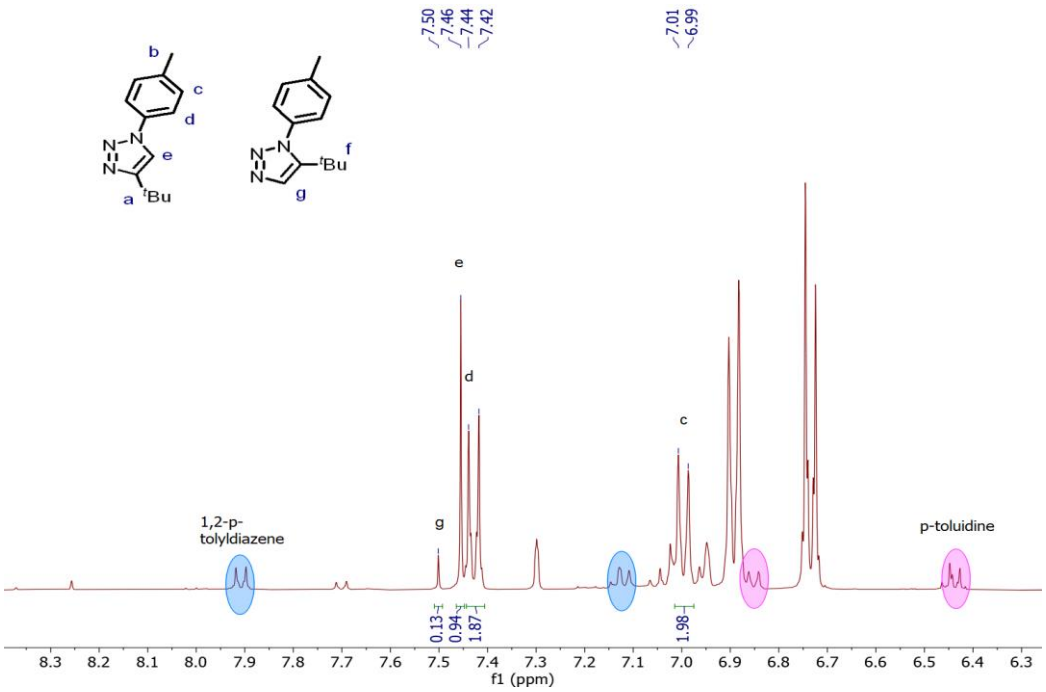

Figure 2.36 Zoom-in ^{1}H NMR spectrum of 1-(*p*-tolyl)-4-(*t*-butyl)-1H-1,2,3-triazole and 1-(*p*-tolyl)-5-(*t*-butyl)-1H-1,2,3-triazole (**2.6ag**) in C_6D_5Br. *Taken from XYS04038_F.*

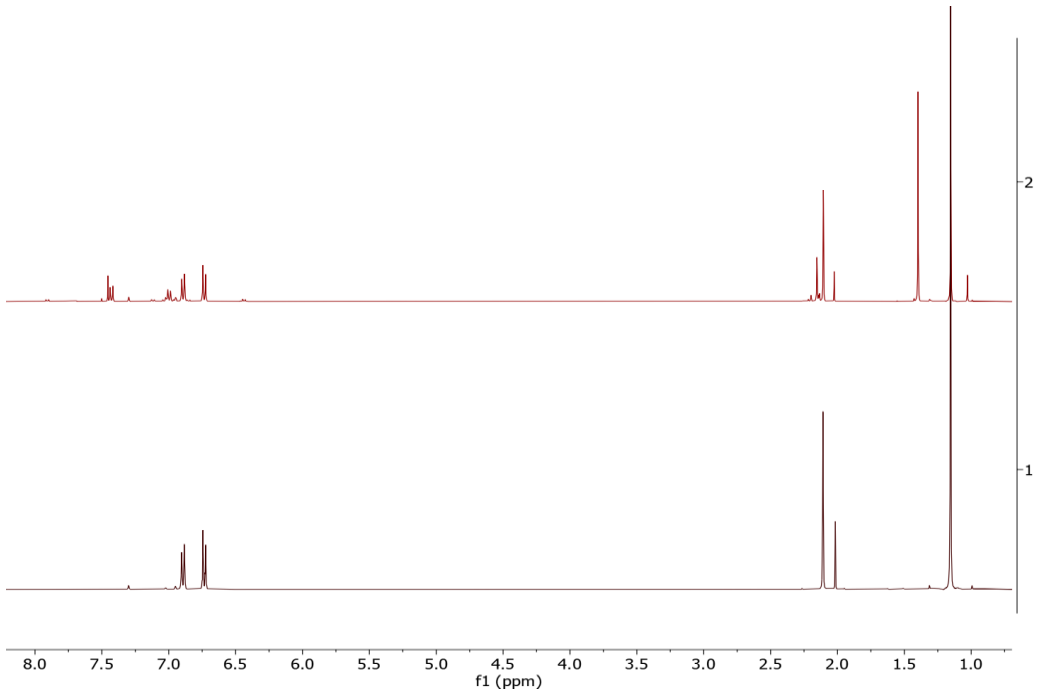

Figure 2.37 Before (bottom, t = 0 h) and after (top, t = 16 h) ^{1}H NMR spectrum of (*t*-butyl)acetylene and (*p*-tolyl)azido reaction in C_6D_5Br. *Taken from XYS04038_F*.

1-adamantyl-4-(trimethylsilyl)-1H-1,2,3-triazole (2.6bh)

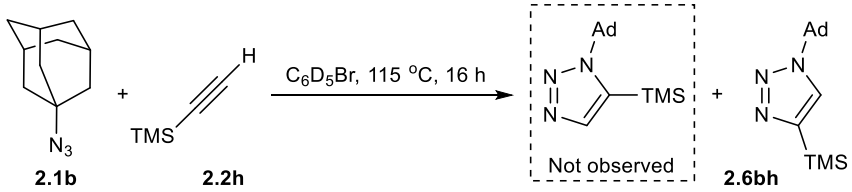

(Trimethylsilyl)acetylene (16 mg, 0.16 mmol, 1.7 equiv), 1-azidoadamantane (16 mg, 0.09 mmol, 1.0 equiv) and 0.5 mL of C_6D_5Br were added to a NMR tube in a N_2-filled glovebox. The tube was sealed and heated at 115 °C for 16 h. After which, the reaction mixture was analyzed by ^{1}H NMR without any further work-up to give a mixture of title compound and leftover starting reagents.

^{1}H NMR (400 MHz, C_6D_5Br): δ 7.56 (s, 1H, Ar-*H*), 2.03 (m, 6H, Ad-CH_2), 1.96 (br s, 3H, Ad-C*H*), 1.54 (br s, 6H, Ad-CH_2), 0.38 (s, 9H, Si(CH_3)$_3$).

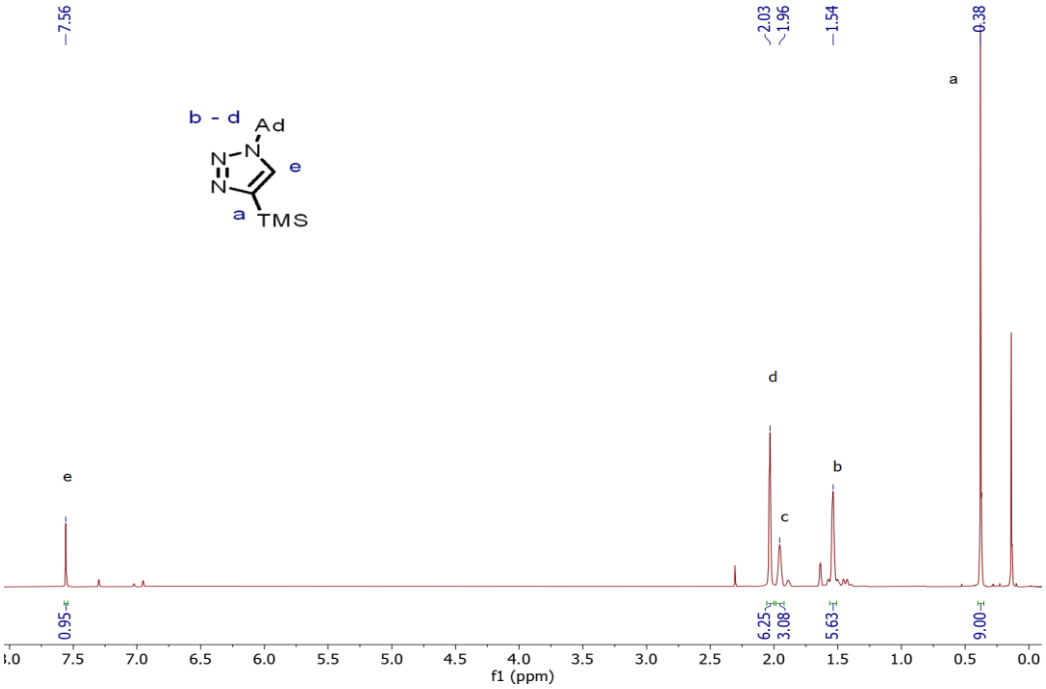

Figure 2.38 ^{1}H NMR spectrum of 1-adamantyl-4-(trimethylsilyl)-1H-1,2,3-triazole (**2.6bh**) in C_6D_5Br. *Taken from XYS04038_E.*

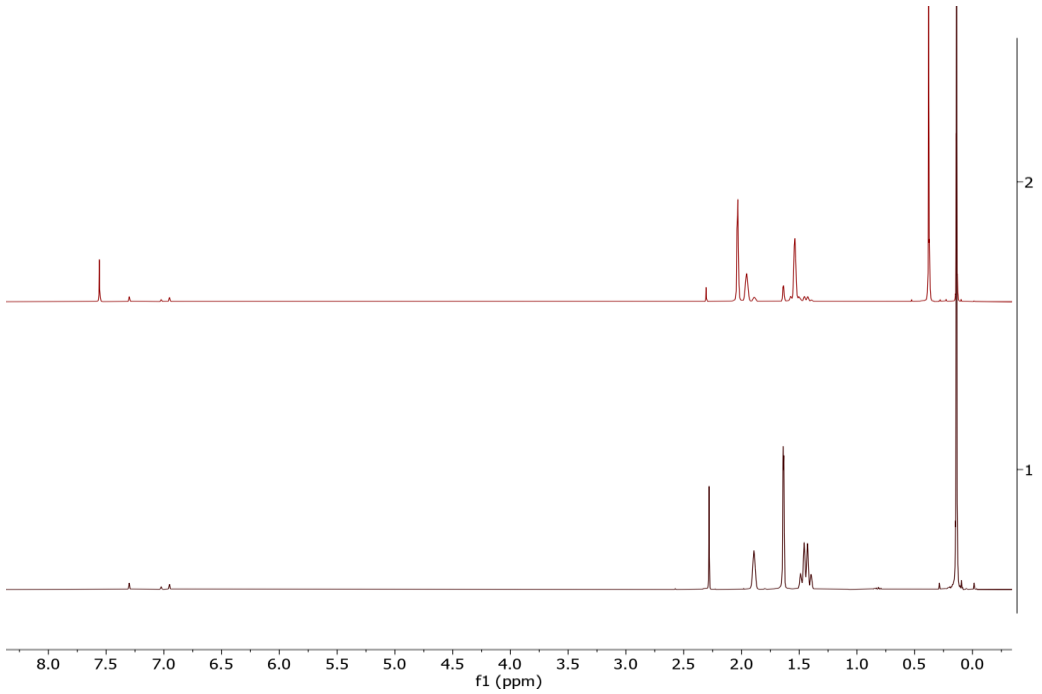

Figure 2.39 Before (bottom, t = 0 h) and after (top, t = 16 h) ^{1}H NMR spectrum of (trimethylsilyl)acetylene and 1-azidoadamantane reaction in C_6D_5Br. *Taken from XYS04038_E.*

1-adamantyl-4-(5-hexyn-1-yl)-1H-1,2,3-triazole (2.6bi)

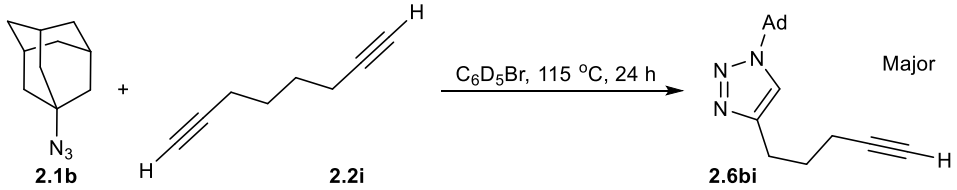

1,7-octadiyne (11 mg, 0.10 mmol, 0.43 equiv), 1-azidoadamantane (40. mg, 0.23 mmol, 1 equiv) and 0.5 mL of C_6D_5Br were added to a NMR tube in a N_2-filled glovebox. The tube was sealed and heated at 115 °C for 24 h. After which, the reaction mixture was analyzed by ^{1}H NMR without any further work-up to give a mixture of title compound and leftover starting reagents.

^{1}H NMR (500 MHz, C_6D_5Br): δ 7.10 (s, 1H, Ar-*H*), 2.67 (t, $^{3}J_{HH}$ = 8.0 Hz, 2H, Ar-CH_2), 2.07 (td, $^{3}J_{HH}$ = 7.0 Hz, $^{4}J_{HH}$ = 2.5 Hz, 2H, HC≡C-CH_2) 2.02 (d, $^{3}J_{HH}$ = 7.5 Hz, 6H, N-C-(CH_2)$_2$ of Ad group), 1.56 (m, 6H, Ad).

This is a partial NMR line list, the remaining peaks for the hexynyl chain and adamantyl group are overlapping with other peaks.

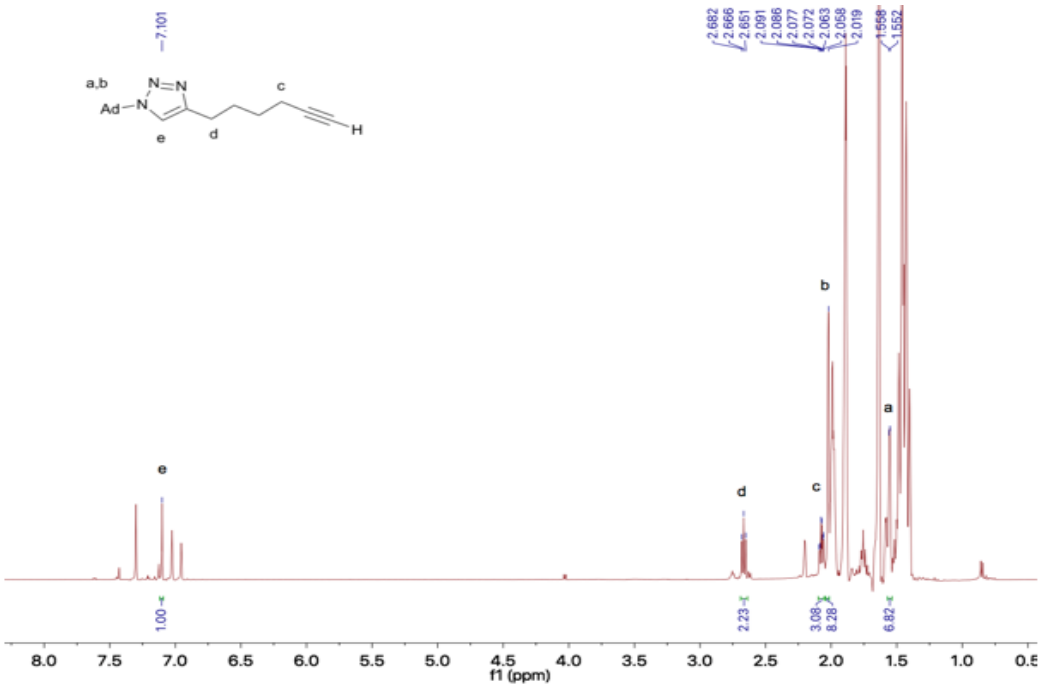

Figure 2.40 ^{1}H NMR spectrum of 1-adamantyl-4-(5-hexyn-1-yl)-1H-1,2,3-triazole (**2.6bi**) in C_6D_5Br. *Taken from AJP05141*.

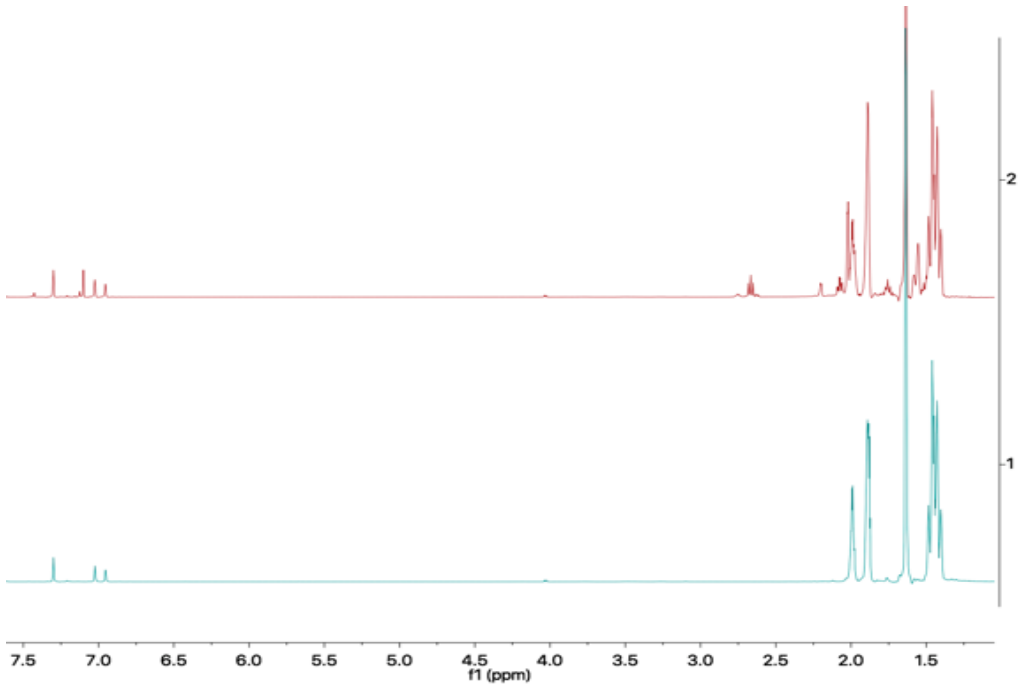

Figure 2.41 Before (bottom, t = 0 h) and after (top, t = 24 h) ^{1}H NMR spectrum of 1,7-octadiyne and 1-azidoadamantane reaction in C_6D_5Br. *Taken from AJP05141*.

1-(*n*-decyl)-4,5-(diethyl)-1,2,3-triazole (2.6ca) (partial)

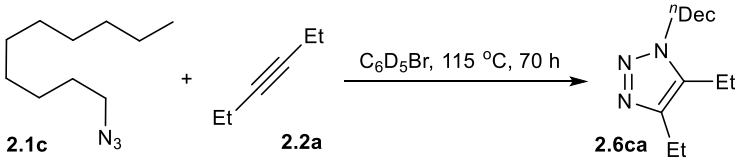

3-hexyne (16 mg, 0.1 mmol, 1.0 equiv), 1-azidodecane (19 mg, 0.1 mmol, 1.0 equiv) and 0.5 mL of C_6D_5Br were added to a NMR tube in a N_2-filled glovebox. The tube was sealed and heated at 115 °C for 70 h. After which, the reaction mixture was analyzed by ^{1}H NMR without any further work-up to give a mixture of title compound and leftover starting reagents.

^{1}H NMR (500 MHz, C_6D_5Br): δ 3.92 (t, $^{3}J_{HH}$ = 7.3 Hz, 2H, $H_3C(CH_2)_8$-CH_2-N), 2.57 (q, $^{3}J_{HH}$ = 7.6 Hz, 2H, 4-CH_2CH$_3$), 2.35 (q, $^{3}J_{HH}$ = 7.6 Hz, 2H, 5-CH_2CH$_3$), 1.71 – 1.68 (m, 2H, $H_3C(CH_2)_7$-CH_2-CH_2N), 0.95 (t, $^{3}J_{HH}$ = 7.6 Hz, 3H, 5-CH_2CH_3).

This is a partial NMR line list, the remaining peaks are buried under the starting reagents.

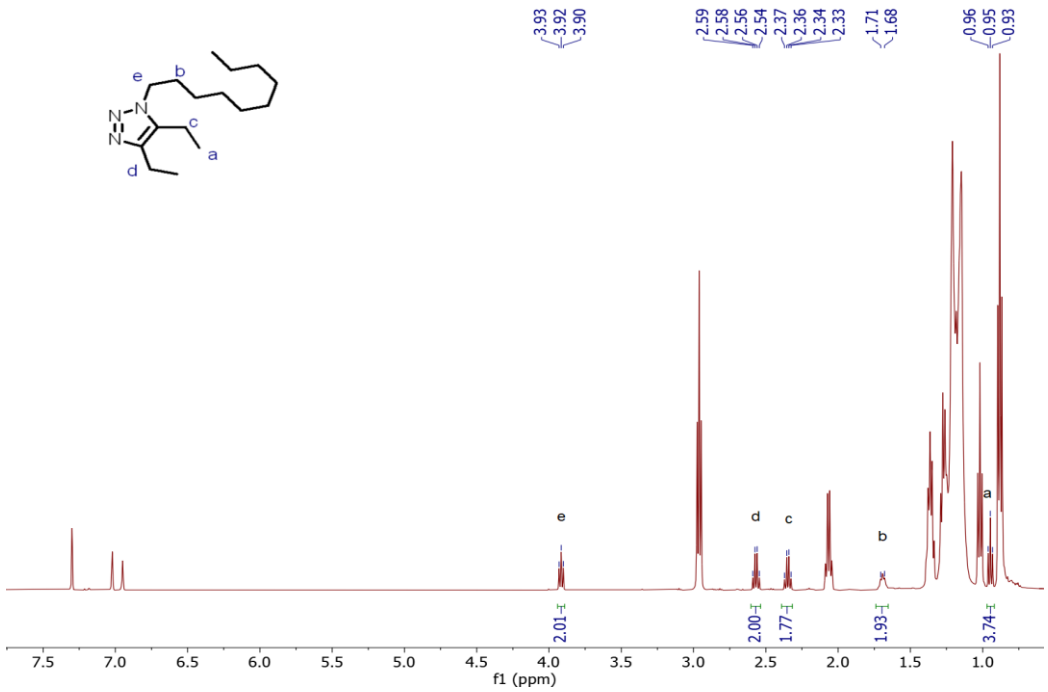

Figure 2.42 ^{1}H NMR spectrum of 1-(*n*-decyl)-4,5-(diethyl)-1,2,3-triazole (**2.6ca**) in C_6D_5Br. *Taken from XYS04097F*.

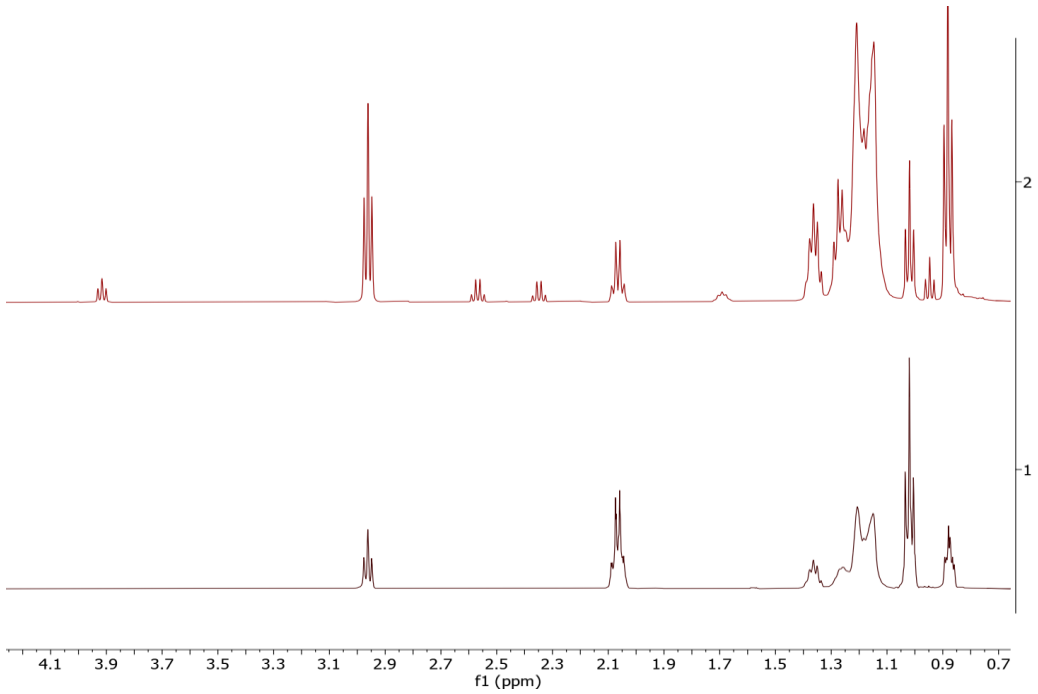

Figure 2.43 Before (bottom, t = 0 h) and after (top, t = 70 h) zoom-in ^{1}H NMR spectrum of 3-hexyne and 1-azidodecane reaction in C_6D_5Br. *Taken from XYS04097F*.

1-(benzyl)-4,5-(diethyl)-1,2,3-triazole (2.6da) (partial)

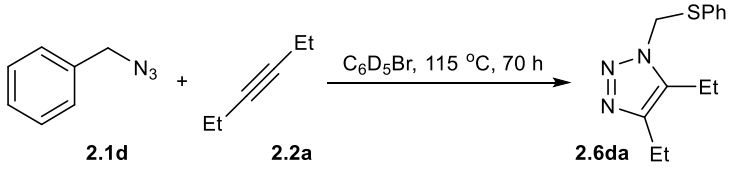

3-hexyne (16 mg, 0.1 mmol, 1.0 equiv), benzylazide (14 mg, 0.1 mmol, 1.0 equiv) and 0.5 mL of C_6D_5Br were added to a NMR tube in a N_2-filled glovebox. The tube was sealed and heated at 115 °C for 70 h. After which, the reaction mixture was analyzed by ^{1}H NMR without any further work-up to give a mixture of title compound and leftover starting reagents.

^{1}H NMR (500 MHz, C_6D_5Br): δ 6.98 – 6.97 (m, 2H, Ar-*H*), 5.17 (s, 2H, Ar-CH_2), 2.54 (q, $^{3}J_{HH}$ = 7.6 Hz, 2H, 4-CH_2CH$_3$), 2.23 (q, $^{3}J_{HH}$ = 7.6 Hz, 2H, 5-CH_2CH$_3$), 1.26 (t, $^{3}J_{HH}$ = 7.6 Hz, 3H, 4-CH$_2$CH_3), 0.71 (t, $^{3}J_{HH}$ = 7.6 Hz, 3H, 5-CH$_2$CH_3).

This is a partial NMR line list, the remaining aryl peaks are buried under the starting reagents.

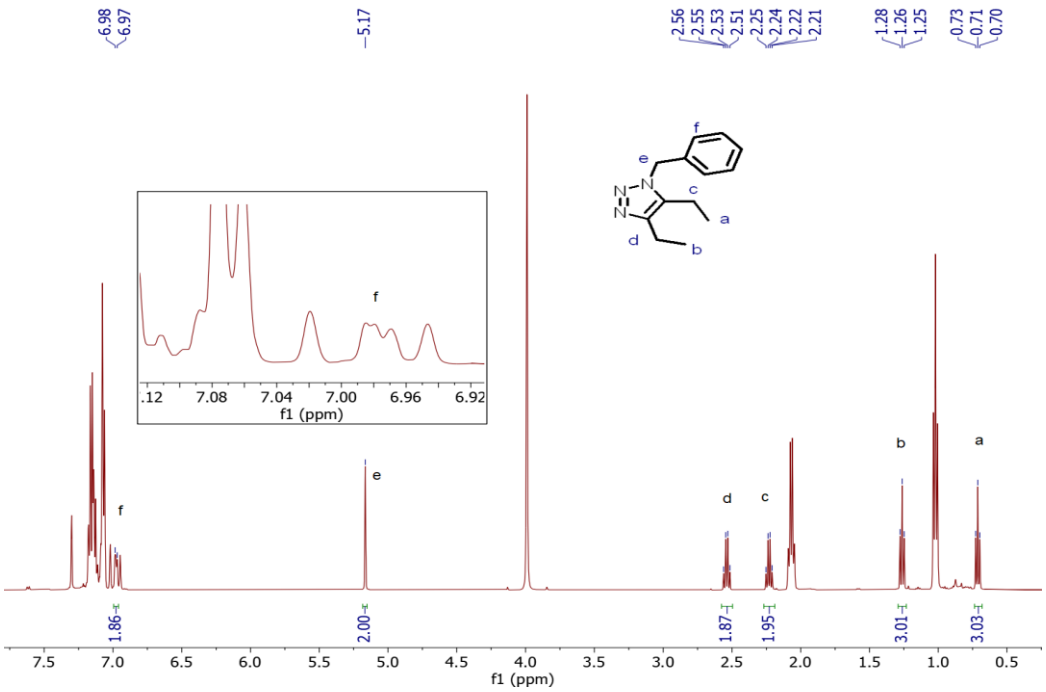

Figure 2.44 ^{1}H NMR spectrum of 1-(benzyl)-4,5-(diethyl)-1,2,3-triazole (**2.6da**) in C_6D_5Br. *Taken from XYS04097C.*

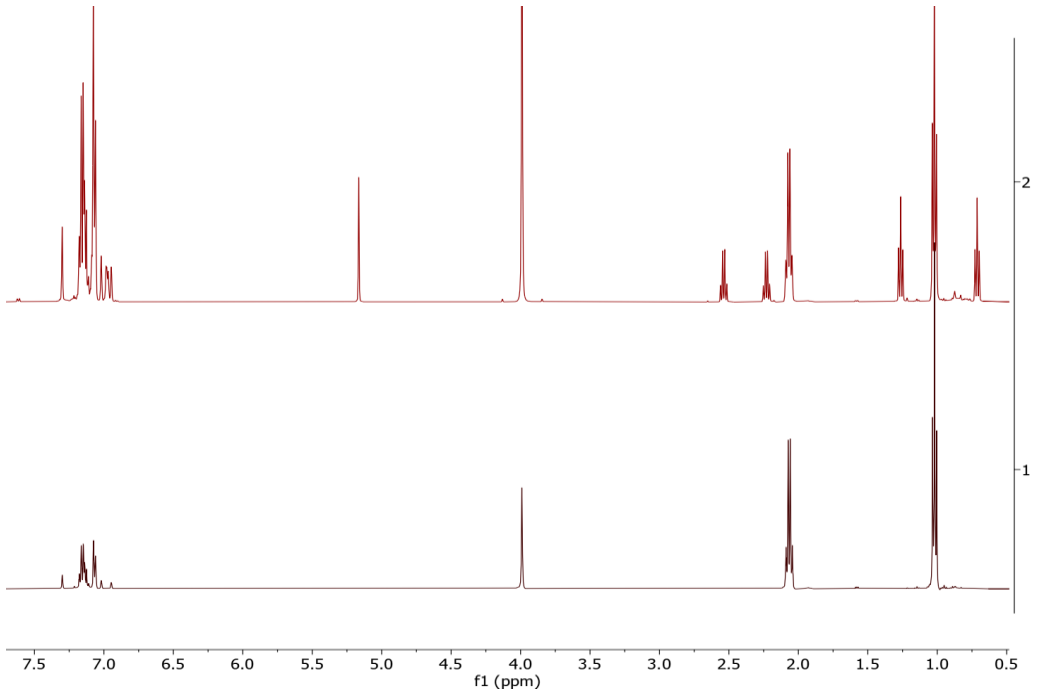

Figure 2.45 Before (bottom, t = 0 h) and after (top, t = 70 h) 1H NMR spectrum of 3-hexyne and benzylazide reaction in C_6D_5Br. *Taken from XYS04097C.*

1-(methyl phenyl sulfide)-4,5-(diethyl)-1,2,3-triazole (2.6ea) (partial)

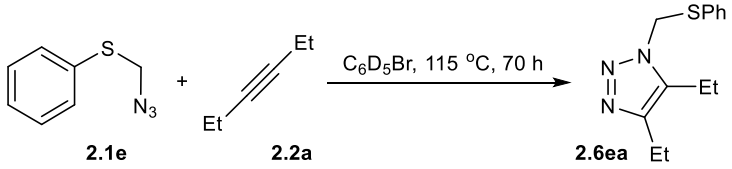

3-hexyne (16 mg, 0.1 mmol, 1.0 equiv), azidomethyl phenyl sulfide (18 mg, 0.1 mmol, 1.0 equiv) and 0.5 mL of C_6D_5Br were added to a NMR tube in a N_2-filled glovebox. The tube was sealed and heated at 115 °C for 70 h. After which, the reaction mixture was analyzed by ^{1}H NMR without any further work-up to give a mixture of title compound and leftover starting reagents.

^{1}H NMR (500 MHz, C_6D_5Br): δ 5.28 (s, 2H, PhS-CH_2), 2.49 (q, $^3J_{HH}$ = 7.6 Hz, 2H, 4-CH_2CH$_3$), 2.33 (q, $^3J_{HH}$ = 7.6 Hz, 2H, 5-CH_2CH$_3$), 1.21 (t, $^3J_{HH}$ = 7.6 Hz, 3H, 4-CH$_2$CH_3), 0.93 (t, $^3J_{HH}$ = 7.6 Hz, 3H, 5-CH$_2$CH_3).

This is a partial NMR line list, the decomposition peaks are overlapping with the aryl peaks.

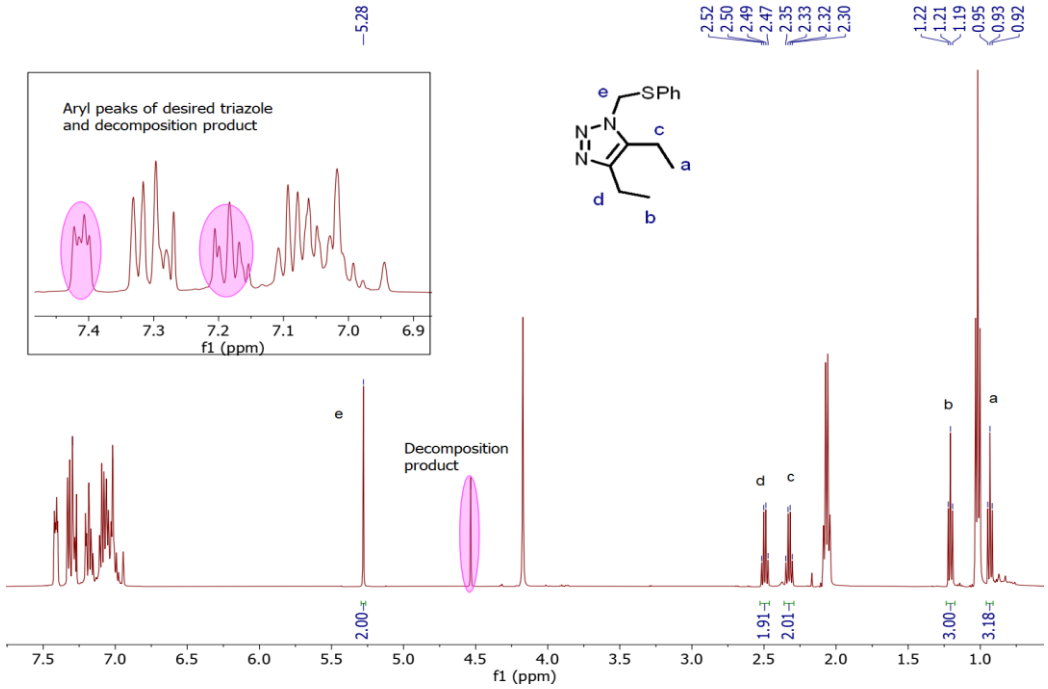

Figure 2.46 ^{1}H NMR spectrum of 1-(methyl phenyl sulfide)-4,5-(diethyl)-1,2,3-triazole (**2.6ea**) in C_6D_5Br. *Taken from XYS04097J.*

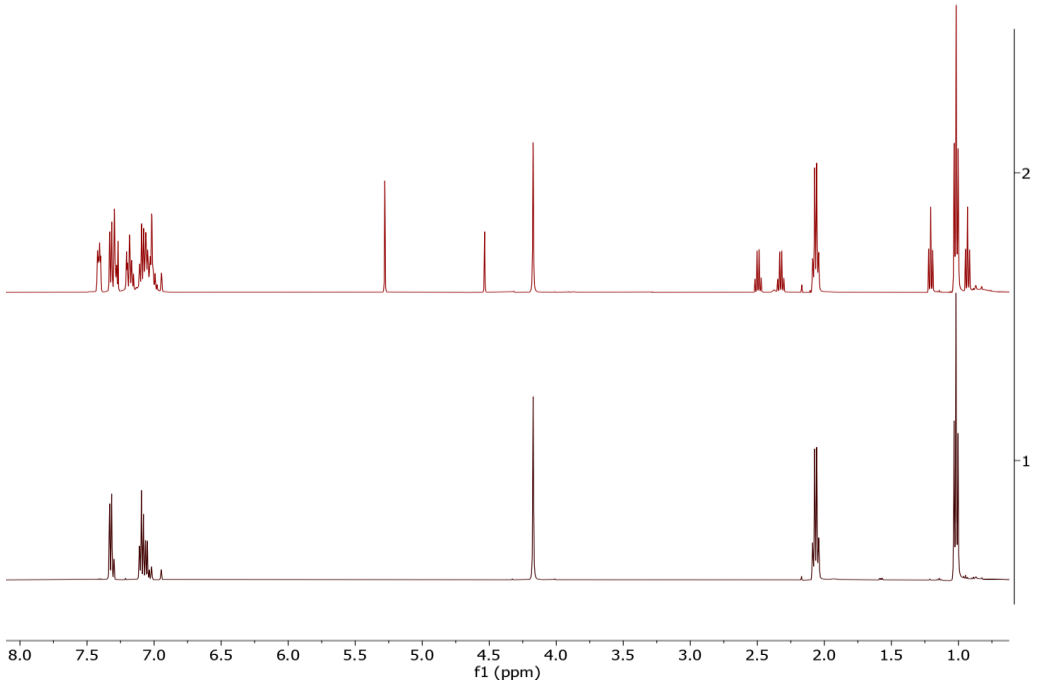

Figure 2.47 Before (bottom, t = 0 h) and after (top, t = 70 h) ^{1}H NMR spectrum of 3-hexyne and azidomethyl phenyl sulfide reaction in C_6D_5Br. *Taken from XYS04097J.*

Attempted reaction of trityl azide and 3-hexyne (2.6fa) in C_6D_5Br

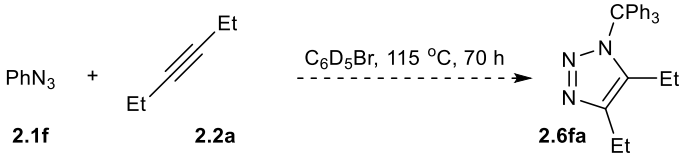

3-hexyne (16 mg, 0.1 mmol, 1.0 equiv), trityl azide (28 mg, 0.1 mmol, 1.0 equiv) and 0.5 mL of C_6D_5Br were added to a NMR tube in a N_2-filled glovebox. The tube was sealed and heated at 115 °C for 70 h. After which, the reaction mixture was analyzed by ^{1}H NMR without any further work-up to give leftover starting reagents, degradation products and a small new quartet peak that we cannot positively attribute as the desired product.

In light of the slow/no reactivity, we do not think that this by-product formation will be significant in our catalytic reaction.

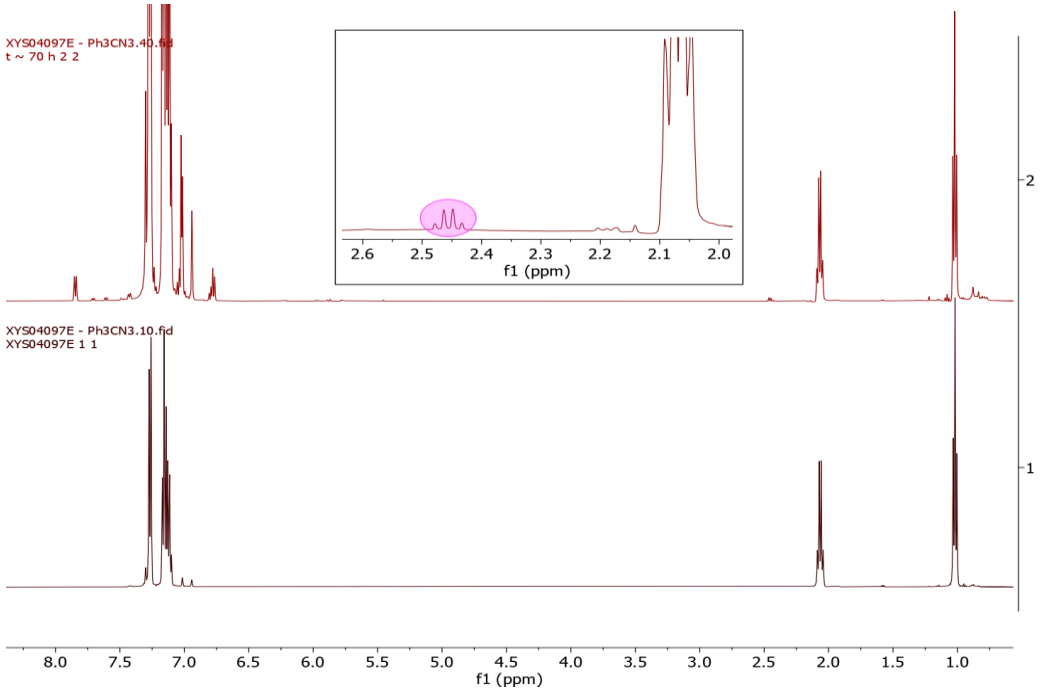

Figure 2.48 Before (bottom, t = 0 h) and after (top, t = 70 h) ^{1}H NMR spectrum of 3-hexyne and trityl azide reaction in C_6D_5Br. *Taken from XYS04097E.*

2.5.5 Characterization of cyclotrimerization byproducts in C_6D_5Br

Characterization of hexaethylbenzene (**2.9a**), 1,3,5-tri-*n*-butyl-benzene (**2.9e**) and 1,2,4-tri-*n*-butyl-benzene (**2.9e**) in C_6D_5Br were reported previously.[119]

Hexamethylbenzene (2.9b)

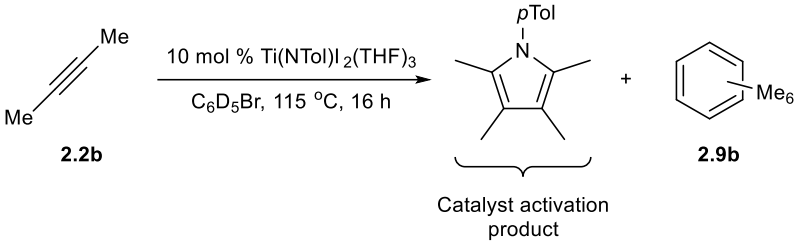

2-butyne (13 mg, 0.24 mmol, 1.0 equiv), $Ti(NTol)I_2(THF)_3$ (11 mg, 0.02 mmol, 10 mol %) and 0.5 mL of C_6D_5Br were added to a NMR tube in a N_2-filled glovebox. The tube was sealed and heated at 115 °C for 16 h. After which, the reaction mixture was analyzed by ^{1}H NMR without any further work-up to give a mixture of the title compounds.

^{1}H NMR (500 MHz, C_6D_5Br): δ 2.11 (s, 18H, CH_3).

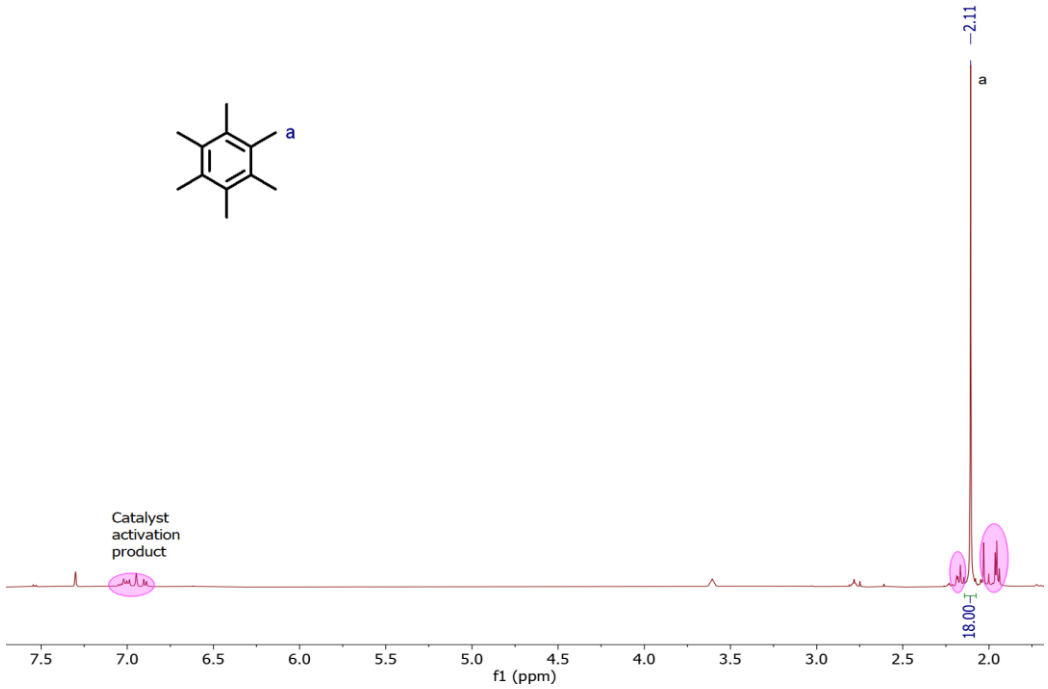

Figure 2.49 ^{1}H NMR spectrum of hexamethylbenzene (**2.9b**) in C_6D_5Br. *Taken from XYS04019C*.

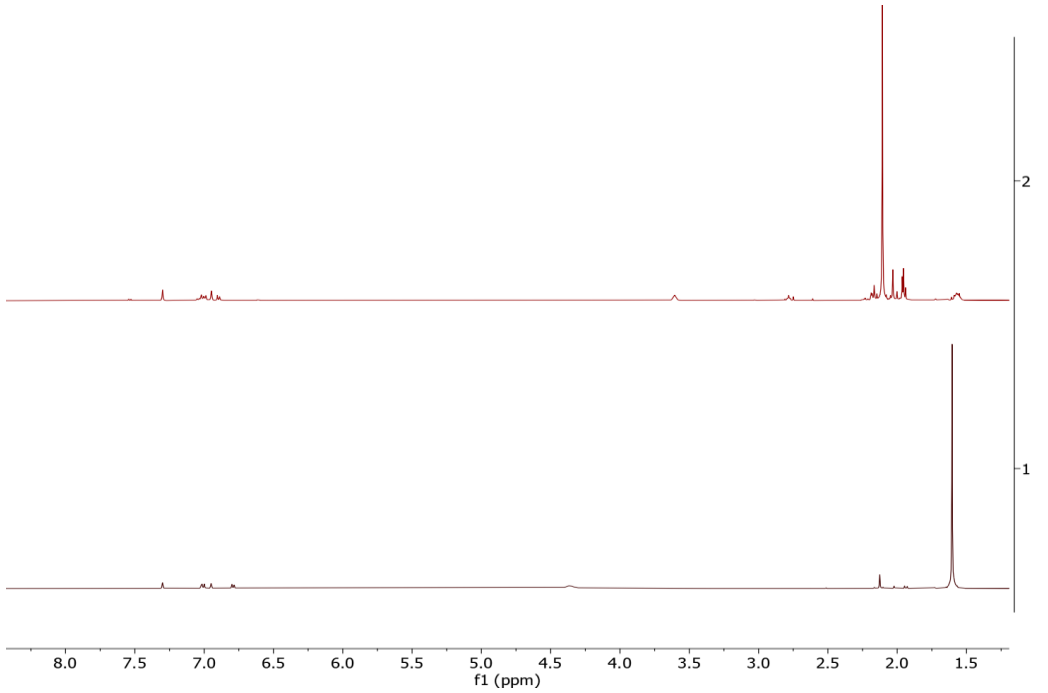

Figure 2.50 Before (bottom, t = 0 h) and after (top, t = 16 h) ^{1}H NMR spectrum of hexamethylbenzene (**2.9b**) in C_6D_5Br. *Taken from XYS04019C.*

Attempted cyclotrimerizaton of diphenylacetylene (2.9c)

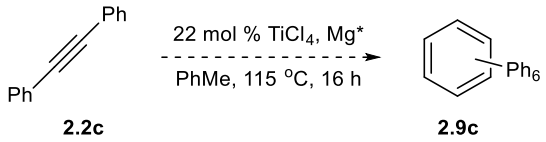

2.2c **2.9c**

Diphenylacetylene (128 mg, 0.72 mmol, 1 equiv), $TiCl_4$ (30 mg, 0.16 mmol, 22 mol %), Mg* (41 mg, 0.098 mmol, 14 mol %) and 0.5 mL of toluene were added to a 20 mL scintillation vial equipped with a small stir bar in a N_2-filled glovebox. This was then sealed with a Teflon screw cap and heated at 115 °C for 24 h. After which, the reaction mixture was concentrated *in vacuo* to dryness before dissolving in minimal C_6D_5Br. The mixture was filtered through celite before analysis to give a mixture of mostly starting materials and residual toluene. In light of the slow/no reactivity, we do not think that this by-product formation will be significant in our catalytic reaction.

*Anthracene peaks

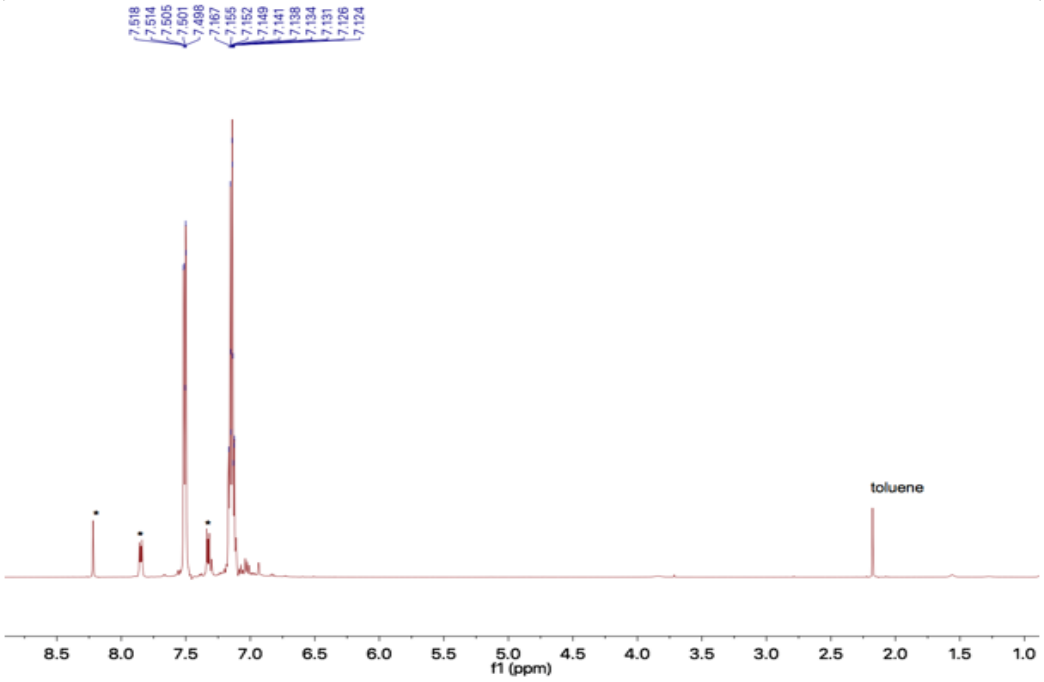

Figure 2.51 Post reaction ^1H NMR spectrum of diphenylacetylene treated with $TiCl_4$ and Mg* in C_6D_5Br. Major peaks in the aromatic region are identical to diphenylacetylene. *Taken from AJP05145B-1H.*

1,2,4-trimethyl-3,5,6-triphenylbenzene and 1,3,5-trimethyl-2,4,6-triphenylbenzene (2.9d) (partial)

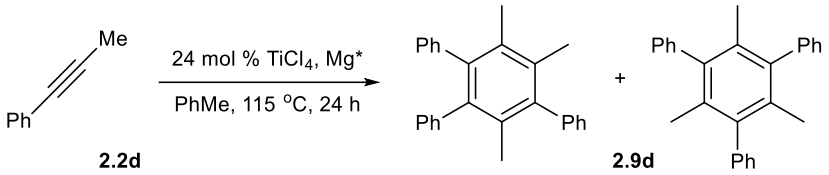

1-phenyl-1-propyne (78 mg, 0.67 mmol, 1 equiv), $TiCl_4$ (30 mg, 0.16 mmol, 24 mol %), Mg* (31 mg, 0.07 mmol, 10 mol %) and 0.5 ml PhMe were added to a 20 mL scintillation vial equipped with a small stir bar in a N_2-filled glovebox. This was then sealed with a Teflon screw cap and heated at 115 °C for 24 h. After which, the reaction mixture was concentrated *in vacuo* to dryness before dissolving in minimal C_6D_5Br. The mixture was filtered through celite before analysis to give a mixture of the two products, starting material and residual anthracene peaks from Mg*.

1,2,4-trimethyl-3,5,6-triphenylbenzene

^{1}H NMR (500 MHz, C_6D_5Br): δ 2.08 (s, 3H, C1-CH_3), 2.05 (s, 3H, C2-CH_3 or C4-CH_3) , 1.90 (s, 3H, C2-CH_3 or C4-CH_3).

This is a partial NMR line list, the aromatic region is unable to be differentiated from the other isomer and starting material.

1,3,5-trimethyl-2,4,6-triphenylbenzene

^{1}H NMR (500 MHz, C_6D_5Br): δ 1.88 (s, 9H, Ar-CH_3).

This is a partial NMR line list, the aromatic region is unable to be differentiated from the other isomer and starting material.

*Anthracene peaks. ** Integration of the aryl region is consistent with the integration of two trimerization isomers and remaining 1-phenyl-1-propyne.

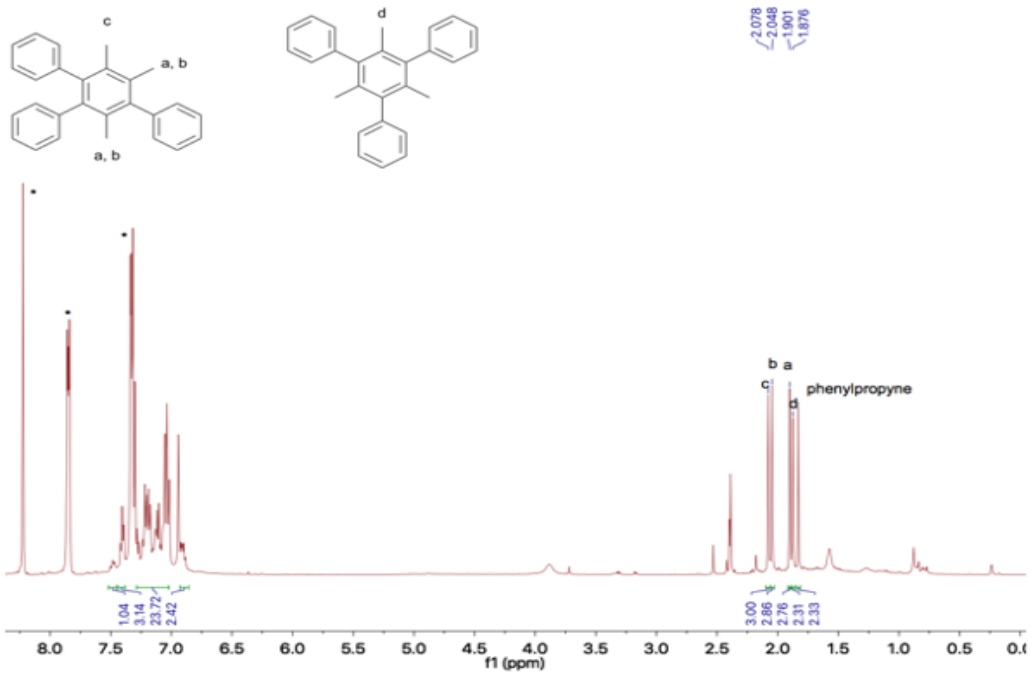

Figure 2.52 ^{1}H NMR spectrum of 1,2,4-trimethyl-3,5,6-triphenylbenzene and 1,3,5-trimethyl-2,4,6-triphenylbenzene (**2.9d**) in C_6D_5Br. *Taken from AJP05140A-1H.*

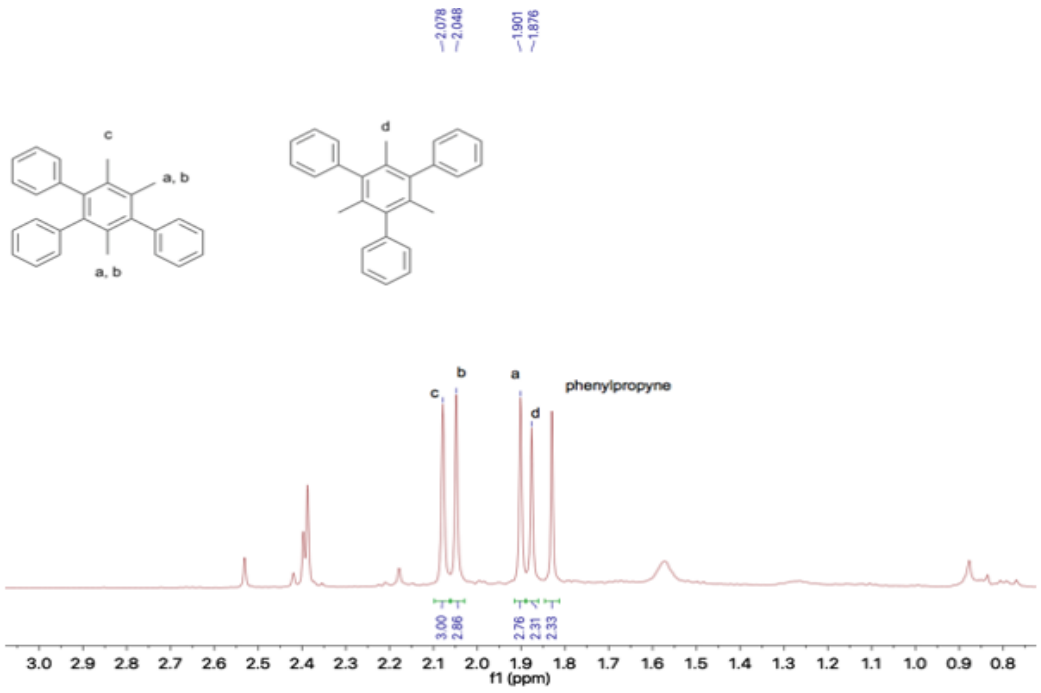

Figure 2.53 Zoom-in ^{1}H NMR spectrum of 1,2,4-trimethyl-3,5,6-triphenylbenzene and 1,3,5-trimethyl-2,4,6-triphenylbenzene (**2.9d**) in C_6D_5Br. *Taken from AJP05140A-1H.*

1,3,5-tri(*p*-tolyl)benzene (2.9f)[127]

Title compound was synthesized following literature procedure and purified with a silica column using pure hexanes as eluent.

^{1}H NMR (400 MHz, C_6D_5Br): δ 7.80 (s, 3H, Ar-*H*), 7.57 (d, $^3J_{HH}$ = 7.9 Hz, 6H, *m*-Tol-*H*), 7.18 (d, $^3J_{HH}$ = 7.9 Hz, 6H, *o*-Tol-*H*), 2.28 (s, 9H, CH_3).

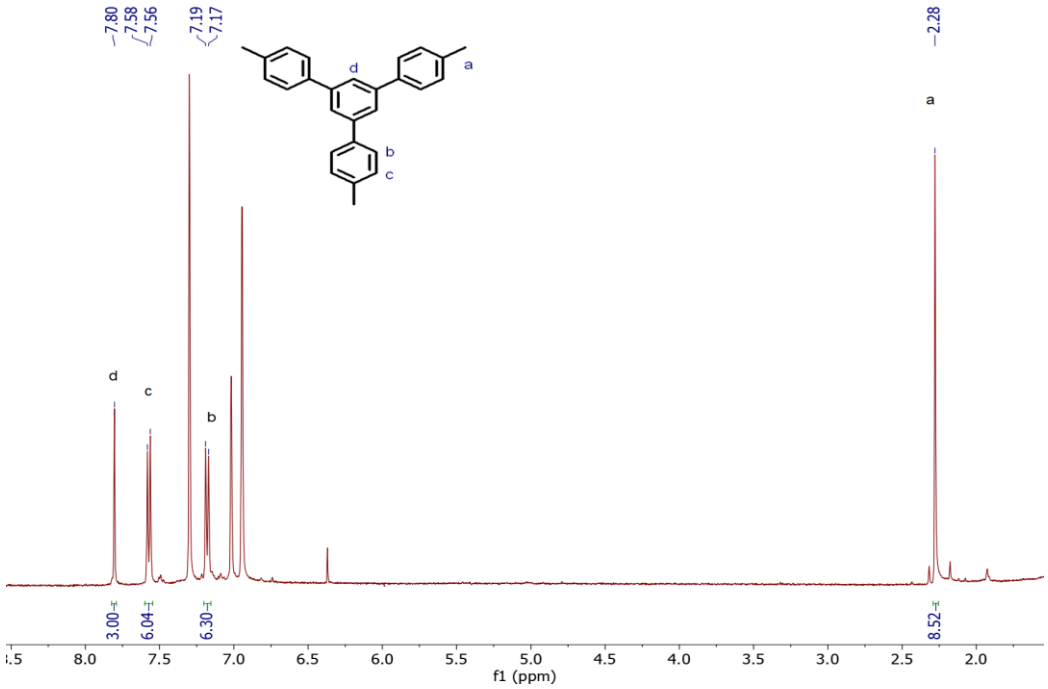

Figure 2.54 ^{1}H NMR spectrum of 1,3,5-tri(*p*-tolyl)benzene (**2.9f**) in C_6D_5Br. *Taken from XYS03158_3H.*

1,2,4-tri(*p*-tolyl)benzene (2.9f)[128]

Title compound was synthesized following literature procedure and purified further with an alumina plug (pure hexanes eluent).

^{1}H NMR (400 MHz, C_6D_5Br): δ 7.70 – 7.69 (m, 1H, Ar-*H*), 7.60 – 7.46 (m, 4H, Ar-*H* and Tol-*H*), 7.16 – 7.14 (m, 6H, Tol-*H*), 6.93 – 6.91 (m, 4H, Tol-*H*), 2.27 (s, 3H, Tol-CH_3), 2.12 (s, 6H, Tol-CH_3).

Multiplet between δ 6.93 – 6.91 is partially overlapped by C_6D_5Br solvent peak.

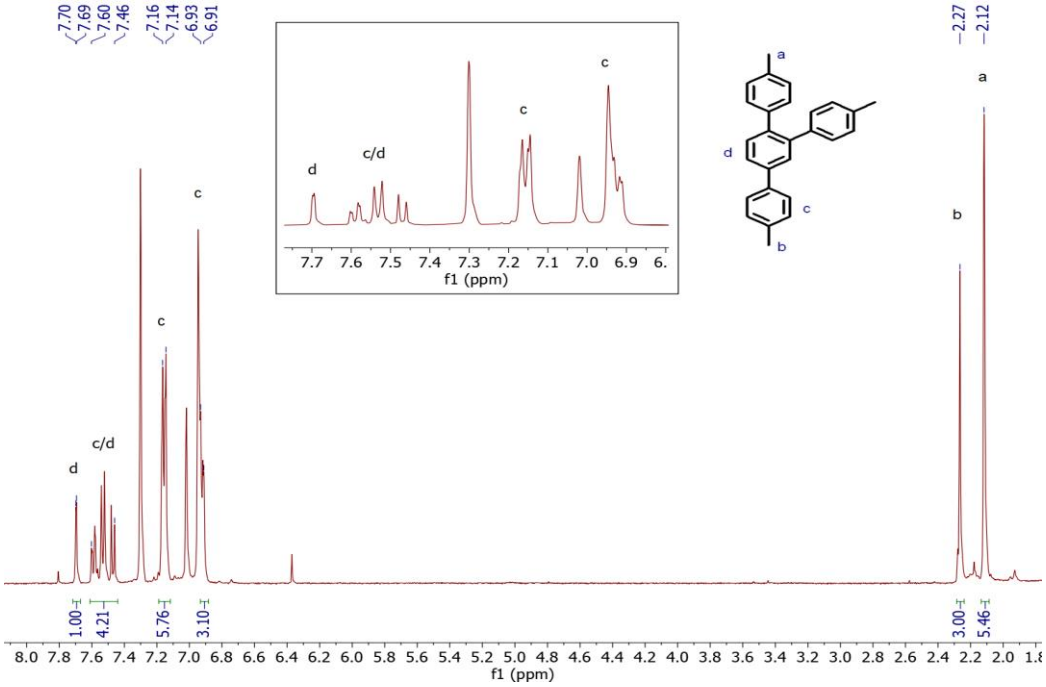

Figure 2.55 ^{1}H NMR spectrum of 1,2,4-tri(*p*-tolyl)benzene (**2.9d**) in C_6D_5Br. *Taken from XYS03155_4H.*

1,3,5-tri(*t*-butyl)benzene and 1,2,4-tri(*t*-butyl)benzene (2.9g)

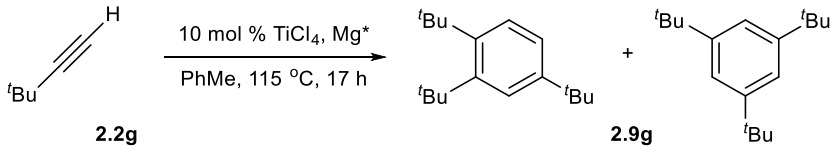

(*t*-butyl)acetylene (56 mg, 0.69 mml, 1 equiv), $TiCl_4$ (13 mg, 0.07 mmol, 10 mol %), Mg* (30 mg, 0.07 mmol, 12 mol %) and 0.5 ml PhMe were added to a 4 mL scintillation vial equipped with a small stir bar in a N_2-filled glovebox. This was then sealed with a Teflon screw cap and heated at 115 °C for 17 h. After which, the reaction mixture was concentrated *in vacuo* to dryness before dissolving in minimal C_6D_5Br. The mixture was filtered through celite before analysis to give a mixture of the two products and the residual anthracene peaks from Mg*.

1,3,5-tri(*t*-butyl)benzene

^{1}H NMR (500 MHz, C_6D_5Br): δ 7.34 (s, 3H, Ar-*H*), 1.33 (s, 27H, ^{t}Bu).

1,2,4-tri(*t*-butyl)benzene

^{1}H NMR (500 MHz, C_6D_5Br): δ 7.66 (d, $^4J_{HH}$ = 2.0 Hz, 1H, C3-Ar-*H*), 7.50 (d, $^3J_{HH}$ = 8.5 Hz, 1H, C5 or C6-Ar-*H*), 7.10 (dd, $^3J_{HH}$ = 8.5 Hz and $^4J_{HH}$ = 2.1 Hz, 1H, C5 or C6-Ar-*H*), 1.52 (s, 9H, ^{t}Bu), 1.48 (s, 9H, ^{t}Bu), 1.27 (s, 9H, ^{t}Bu)

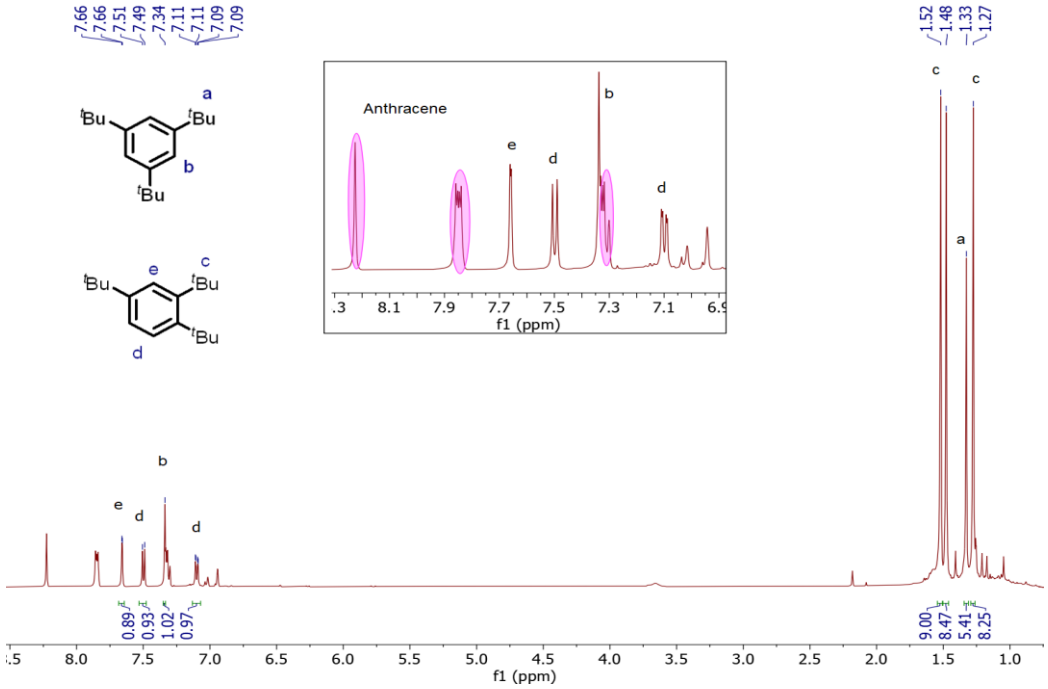

Figure 2.56 ^{1}H NMR spectrum of 1,3,5-tri(*t*-butyl)benzene and 1,2,4-tri(*t*-butyl)benzene (**2.9g**) in C_6D_5Br. *Taken from XYS04047_B.*

1,3,5-tris(trimethylsilyl)benzene and 1,2,4-tris(trimethylsilyl)benzene (2.9h)

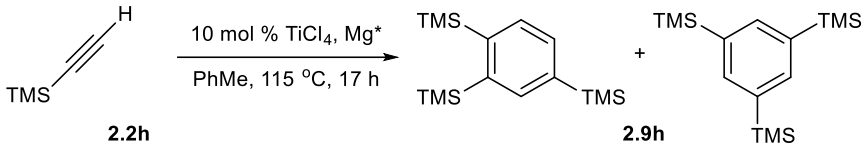

2.2h **2.9h**

(Trimethylsilyl)acetylene (60 mg, 0.61 mml, 1 equiv), $TiCl_4$ (12 mg, 0.06 mmol, 10 mol %), Mg* (30 mg, 0.07 mmol, 12 mol %) and 0.5 ml PhMe were added to a 4 mL scintillation vial equipped with a small stir bar in a N_2-filled glovebox. This was then sealed with a Teflon screw cap and heated at 115 °C for 17 h. After which, the reaction mixture was concentrated *in vacuo* to dryness before dissolving in minimal C_6D_5Br. The mixture was

filtered through celite before analysis to give a mixture of the two products and the residual anthracene peaks from Mg*.

1,3,5-tris(trimethylsilyl)benzene

^{1}H NMR (400 MHz, C_6D_5Br): δ 7.85 (s, 3H, Ar-*H*), 0.30 (s, 27 H, Si(C*H*$_3$)$_3$). Singlet at δ 7.85 is partially overlapped by residual anthracene peak.

1,2,4-tris(trimethylsilyl)benzene

^{1}H NMR (400 MHz, C_6D_5Br): δ 7.95 (s, 1H, C3-Ar-*H*), 7.67 (d, $^3J_{HH}$ = 7.4 Hz, 1H, C5 or C6-Ar-*H*), 7.47 (d, $^3J_{HH}$ = 7.4 Hz, 1H, C5 or C6-Ar-*H*), 0.38 (s, 9H, Si(C*H*$_3$)$_3$), 0.37 (s, 9H, Si(C*H*$_3$)$_3$), 0.27 (s, 9H, Si(C*H*$_3$)$_3$).

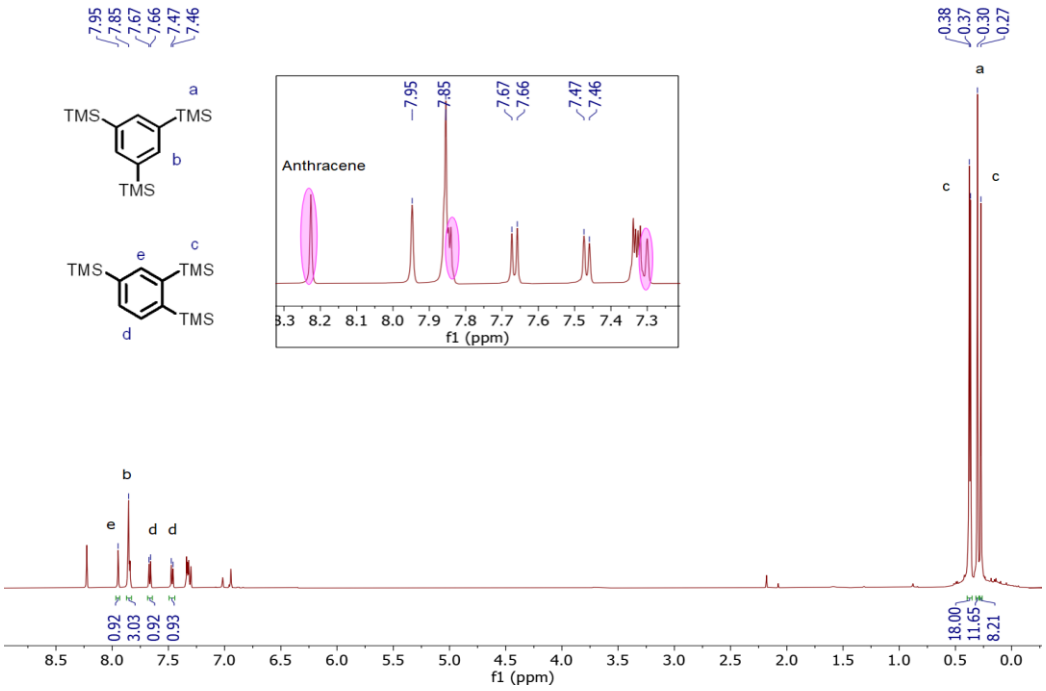

Figure 2.57 ^{1}H NMR spectrum of 1,3,5-tris(trimethylsilyl)benzene and 1,2,4-tris(trimethylsilyl)benzene (**2.9h**) in C_6D_5Br. *Taken from XYS04047_A.*

1,4-bis(5,6,7,8-tetrahydronaphthalen-2-yl)butane (2.9i)

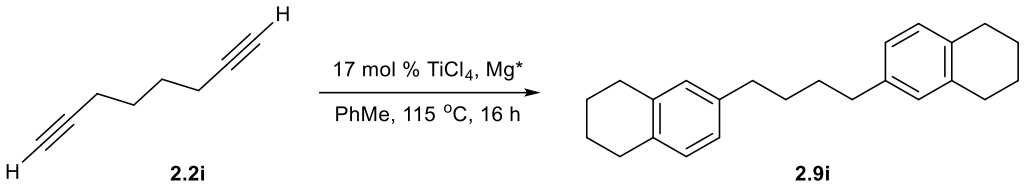

2.2i **2.9i**

1,7-Octadiyne (81 mg, 0.76 mmol, 1 equiv), $TiCl_4$ (24 mg, 0.13 mmol, 17 mol %), Mg* (29 mg, 0.069 mmol, 9 mol %) and 0.5 ml PhMe were added to a 20 mL scintillation vial equipped with a small stir bar in a N_2-filled glovebox. This was then sealed with a Teflon screw cap and heated at 115 °C for 16 h. After which, the reaction mixture was concentrated *in vacuo* to dryness before dissolving in minimal C_6D_5Br. The mixture was filtered through celite before analysis to the product, starting material and residual anthracene peaks from Mg*.

^{1}H NMR (500 MHz, C_6D_5Br): δ 7.02-6.78 (m (br), 6H, Ar-*H*), 2.62-2.60 (m (br), 8H, Ar-C*H*$_2$), 2.52 (m (br), 4H, Ar-C*H*$_2$), 1.62 (m (br), 12H, CH_2-C*H*$_2$C*H*$_2$-CH_2).

* Anthracene peaks

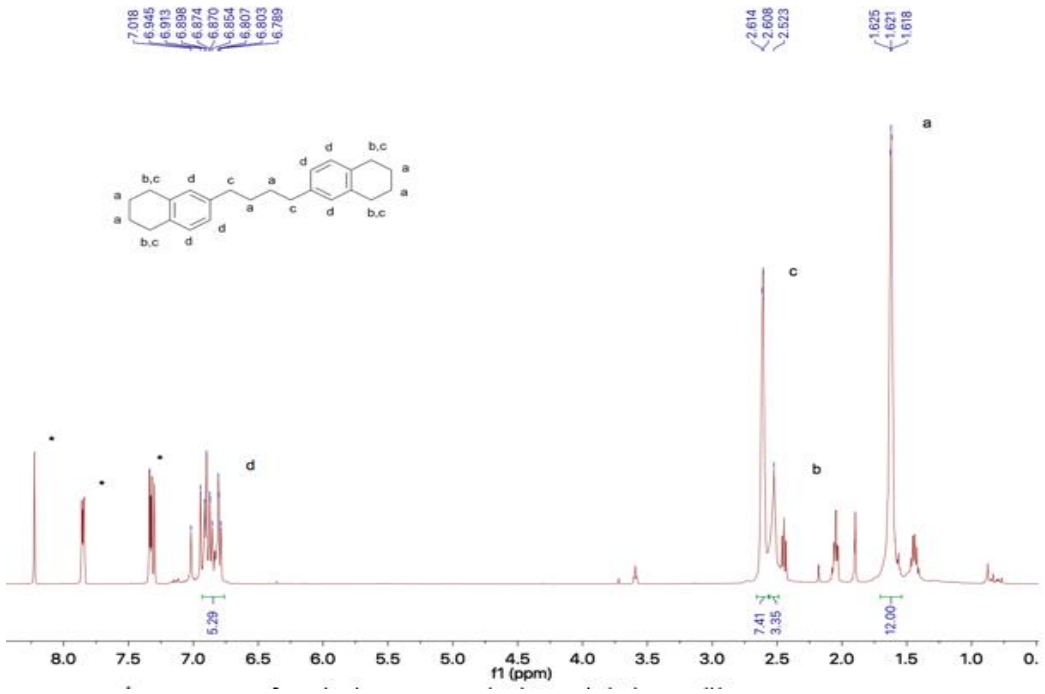

Figure 2.58 ^{1}H NMR spectrum of 1,4-bis(5,6,7,8-tetrahydronaphthalen-2-yl)butane (**2.9i**) in C_6D_5Br. *Taken from AJP05071*.

2.5.6 NMR analysis of catalytic reactions with internal alkyne substrates (Table 2.1)

NMR analysis of 3-hexyne and 1-azidoadamantane reaction (Table 2.1, Entry 1)

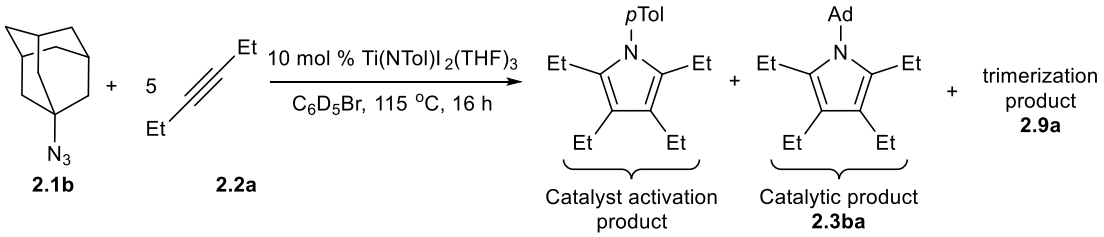

A standard catalytic run with 2-butyne (79 μL, 1.0 mmol) and 0.5 mL of stock solution (internal alkyne screen) was conducted. The catalytic mixture was analyzed directly without any further purification and the products were identified *in situ* to give a mixture of products shown above and leftover starting materials.

2,3,4,5-tetraethyl-1-adamantyl-1*H*-pyrrole

^{1}H NMR (400 MHz, C_6D_5Br): δ 2.83 (q, $^{3}J_{HH}$ = 7.0 Hz, 4H, C3-CH_2), 2.39 (q, $^{3}J_{HH}$ = 7.0 Hz, 4H, C2-CH_2), 2.28 (d, $^{3}J_{HH}$ = 3 Hz, 6H, N-C-(CH_2)$_3$), 2.02 (s (br), 3H, Ad-methine), 1.59 (m, 6H, Ad), 1.15 (t, $^{3}J_{HH}$ = 7.0 Hz, 6H, C3-CH$_2$-CH_3).

Peaks at δ 2.39, 2.02, 1.59 and 1.15 overlap with activation product, 3-hexyne, 1-azidoadamantane, trimerization byproduct and 3-hexyne respectively.

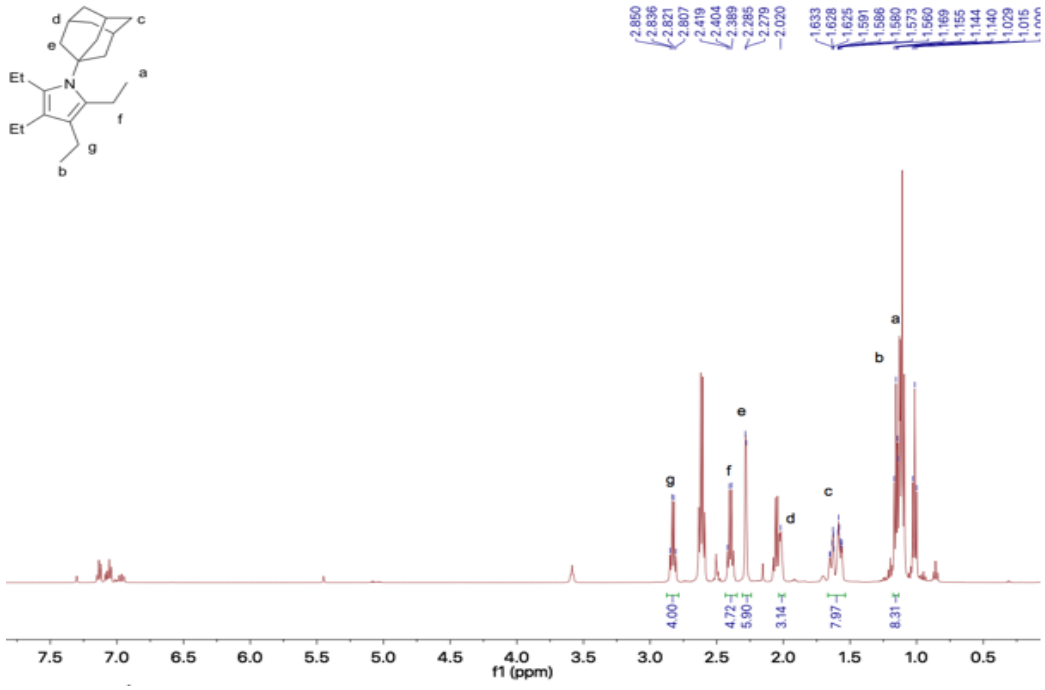

Figure 2.59 ^{1}H NMR spectrum of 3-hexyne reaction with 1-azidoadamantane in C_6D_5Br. *Taken from AJP05031A-2H*.

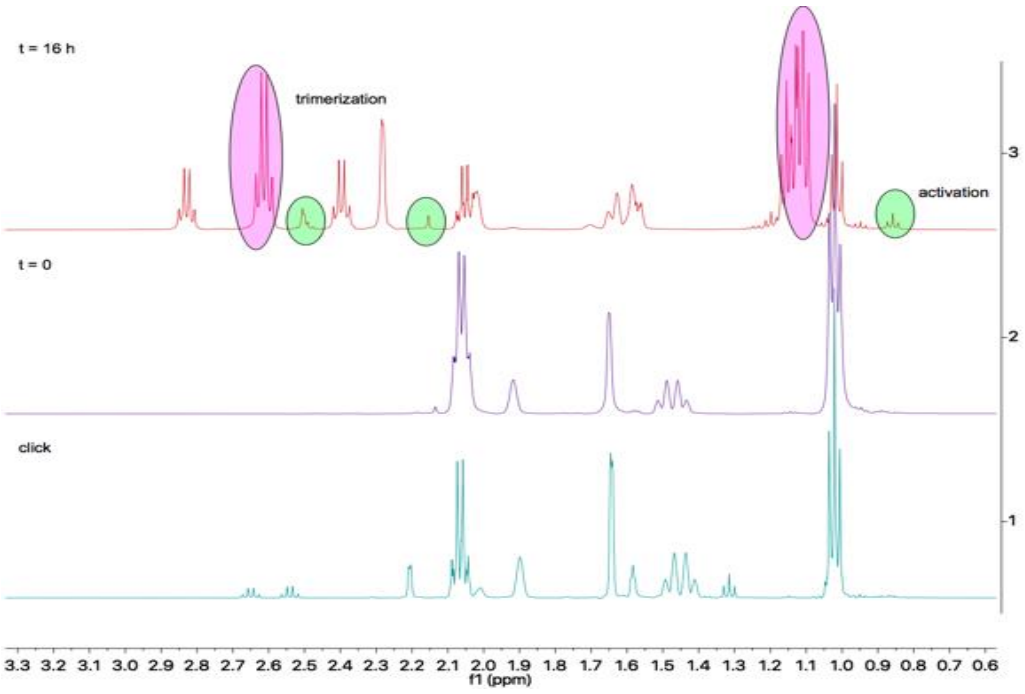

Figure 2.60 Zoom-in stacked ^{1}H NMR spectrum of 3-hexyne reaction with 1-azidoadamantane t = 16 h (3), t = 0 h (2) and click reaction (1) in C_6D_5Br. *Taken from AJP05031A & AJP05135B-2H.*

* Trimerization and activation pyrrole peaks are obtained from literature values[119] and highlighted in pink and green respectively.

NMR analysis of 1-azidoadamantane and 3-hexyne reaction (Table 2.1, Entry 2)

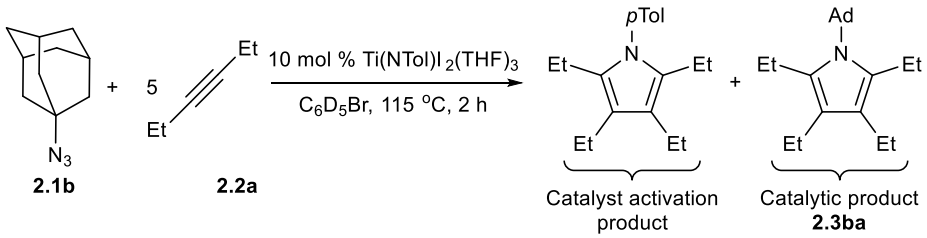

A standard catalytic run with [Ti] (6 mg, 0.01 mmol), 1-azidoadamantane (18 mg, 0.1 mmol, 1 equiv) and 0.5 mL of stock solution (azide screen) was prepared and the reaction mixture was heated for 2 h. The catalytic mixture was analyzed directly without any further purification and the products were identified *in situ* to give a mixture of products shown above and leftover starting materials.

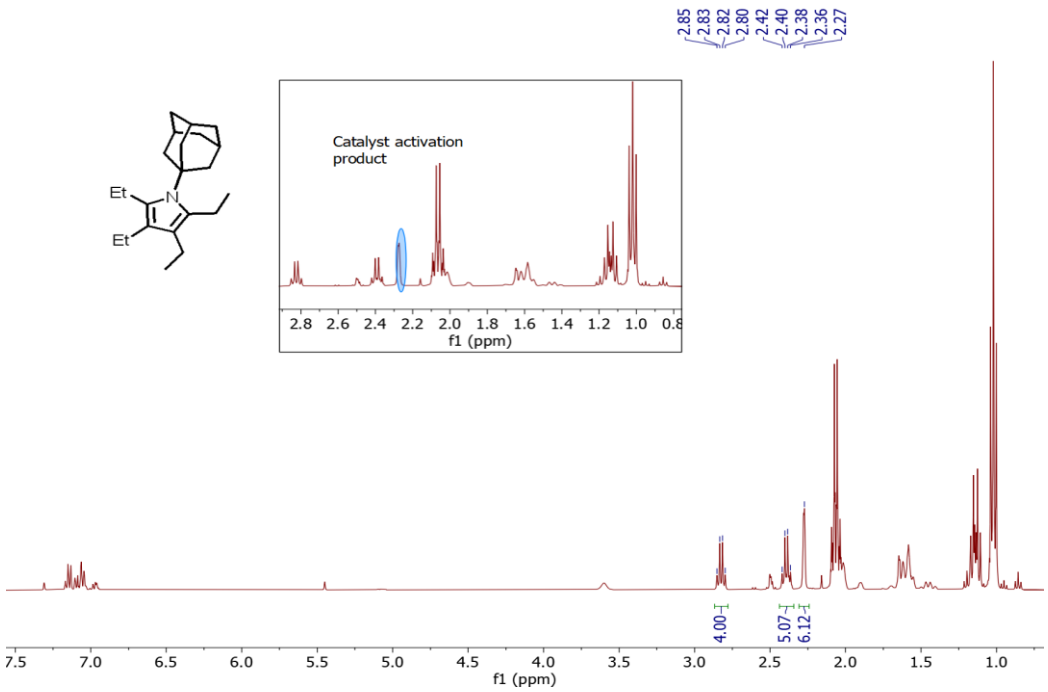

Figure 2.61 ^{1}H NMR spectrum of 1-azidoadamantane reaction with 3-hexyne (t = 2 h) in C_6D_5Br. *Taken from XYS04112E*.

Isolation of 2,3,4,5-tetraethyl-1-adamantyl-1*H*-pyrrole (2.3ba)

To a 7 ml scintillation vial equipped with a stir bar was added $Ti(NTol)I_2(THF)_3$ (35 mg, 0.056 mmol, 10 mol %), 1-azidoadamantane (101 mg, 0.56 mmol, 1 equiv), 2.8 ml C_6H_5Br and 3-hexyne (0.32 ml, 231 mg, 2.82 mmol, 5 equiv) in the following order in a N_2-filled glovebox. The vial was then sealed and heated at 115 °C for 2 h. After which, the reaction mixture was transferred into a 20 ml scintillation vial and dried *in vacuo* while heated to 50 °C for several hours to give a black oil. The oil was taken up in minimal petroleum ether and purified over a silica column using an eluent of 3 % ethyl acetate / petroleum ether. The desired product elutes after the activation product (2,3,4,5-tetraethyl-1-tolyl-1*H*-pyrrole).

Due to a contamination by silicon oil during the column purification, the desired product was taken up again in ~ 1 ml petroleum ether and loaded onto a small silica plug in a pipette. ~ 1 ml of petroleum ether was first used to remove the impurities before washing the rest of the plug with ~ 2ml ethyl acetate. A light orange eluent was collected and dried *in vacuo*

to give the desired product as a pale orange solid with some grease impurities (40 mg, 23 % yield).

^{1}H NMR (400 MHz, $CDCl_3$): δ 2.84 (q, $^{3}J_{HH}$ = 7.3 Hz, 4H, *o*-N-pyr-C*H*$_2$CH$_3$), 2.40 – 2.34 (m, 10H, *m*-N-pyr-C*H*$_2$CH$_3$ and Ad-C*H*$_2$), 2.18 (br s, 3H, Ad-C*H*), 1.74 (q, $^{3}J_{HH}$ = 12.2 Hz, 6H, Ad-C*H*$_2$), 1.19 (t, $^{3}J_{HH}$ = 7.3 Hz, 6H, *o*-N-pyr-CH$_2$C*H*$_3$), 1.11 (t, $^{3}J_{HH}$ = 7.5 Hz, 6H, *o*-N-pyr-CH$_2$C*H*$_3$).

^{13}C NMR (101 MHz, $CDCl_3$): δ 130.5, 121.8, 60.5, 43.4, 36.5, 30.6, 21.7, 18.1, 17.5, 16.8.

GC-HRMS (m/z): calcd. for $C_{22}H_{35}N$, 313.2770 ; found, 313.2756.

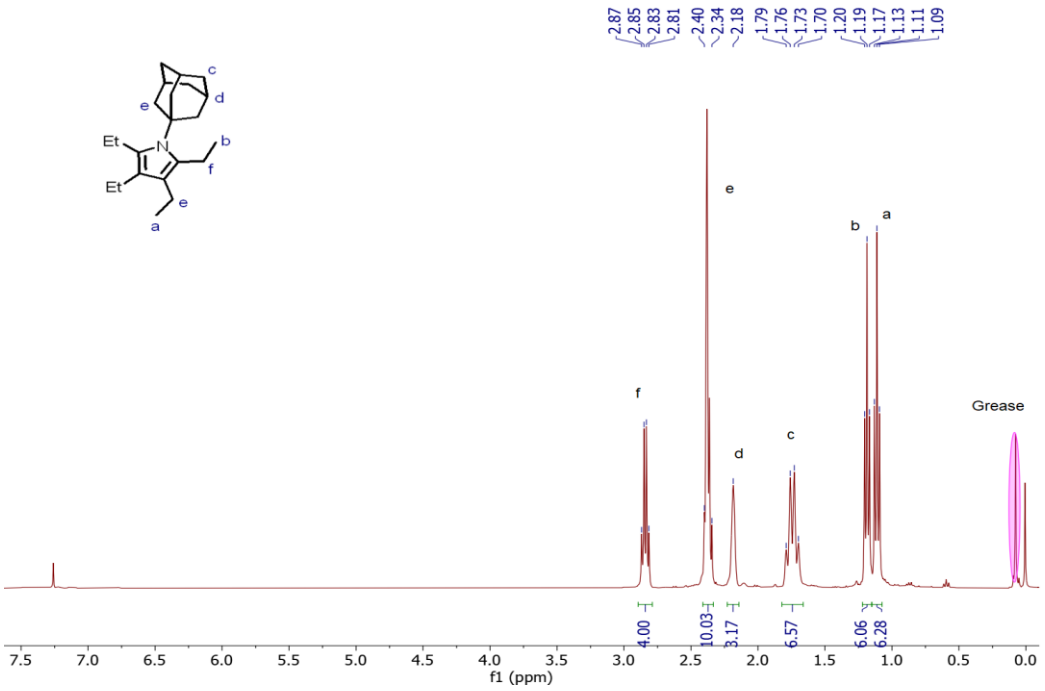

Figure 2.62 ^{1}H NMR spectrum of 2,3,4,5-tetraethyl-1-adamantyl-1*H*-pyrrole (**2.3ba**) in $CDCl_3$. *Taken from XYS04116_4H*.

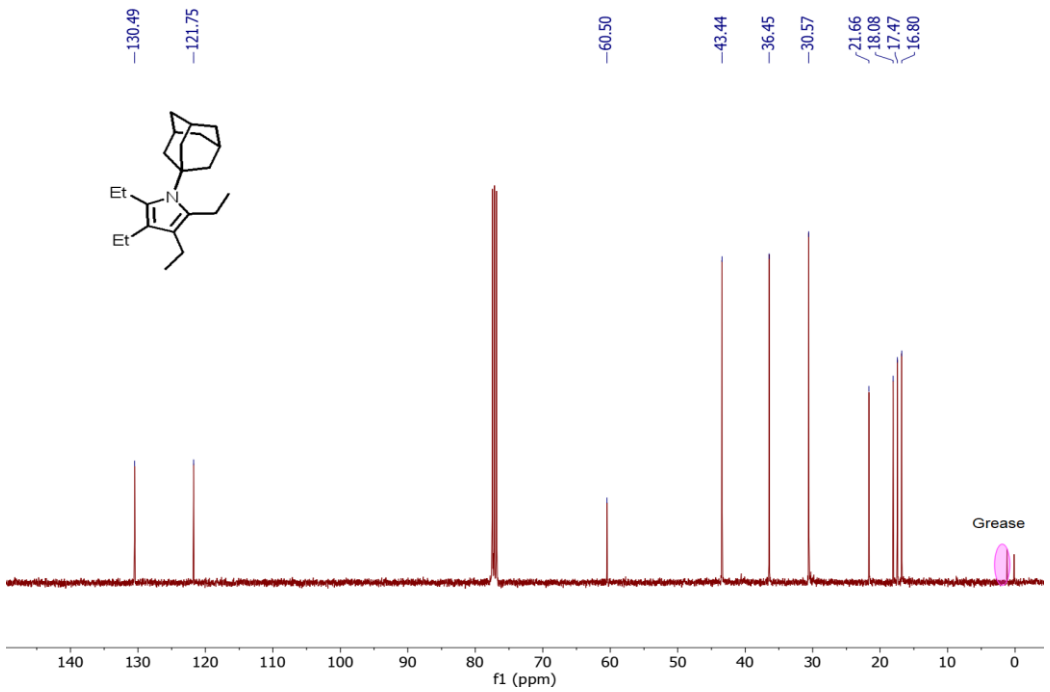

Figure 2.63 ^{13}C NMR spectrum of 2,3,4,5-tetraethyl-1-adamantyl-1*H*-pyrrole (**2.3ba**) in $CDCl_3$. *Taken from XYS04116_1C.*

NMR analysis of 2-butyne and 1-azidoadamantane reaction (Table 2.1, Entry 3)

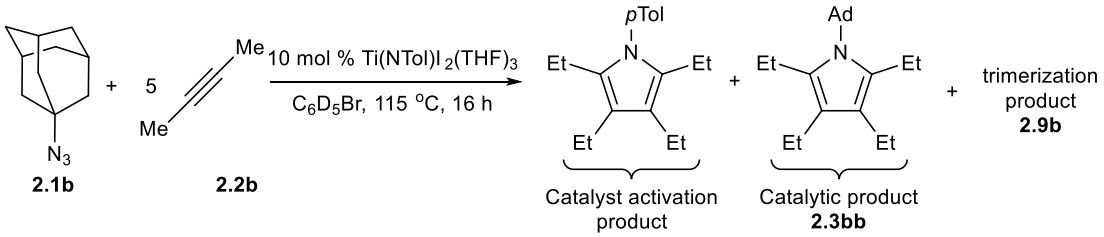

A standard catalytic run with 2-butyne (79 μL, 1.0 mmol) and 0.5 mL of stock solution (internal alkyne screen) was conducted. The catalytic mixture was analyzed directly without any further purification and the products were identified *in situ* to give a mixture of products shown above and leftover starting materials.

2,3,4,5-tetramethyl-1-(adamantyl)-1*H*-pyrrole (2.3bb) (partial)

^{1}H NMR (400 MHz, C_6D_5Br): δ 2.35 (s, 6H, *o*-N-pyr-C*H*$_3$), 2.25 – 2.24 (m, 6H, Ad-C*H*$_2$), 1.92 (s, 6H, *m*-N-pyr-C*H*$_3$), 1.63 – 1.55 (m, 6H, Ad-C*H*$_2$).

Peaks at δ 1.63 – 1.55 overlap with the 2-butyne starting reagent and the Ad-C*H* peak cannot be positively identified from the reaction mixture.

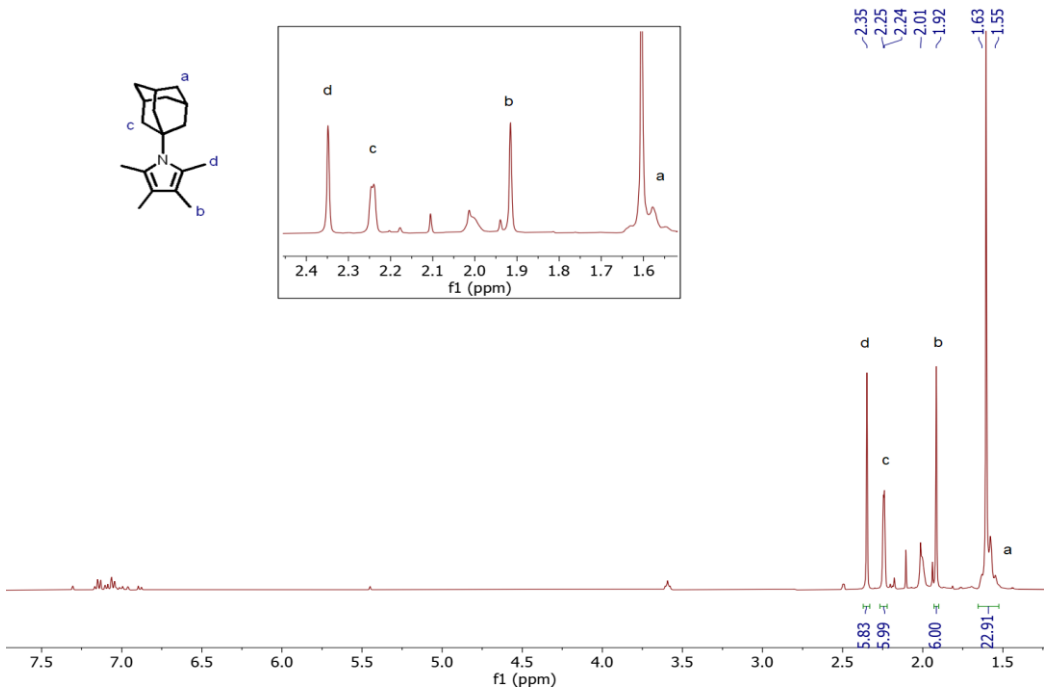

Figure 2.64 ^{1}H NMR spectrum of 2-butyne reaction with 1-azidoadamantane in C_6D_5Br. *Taken from XYS04017G.*

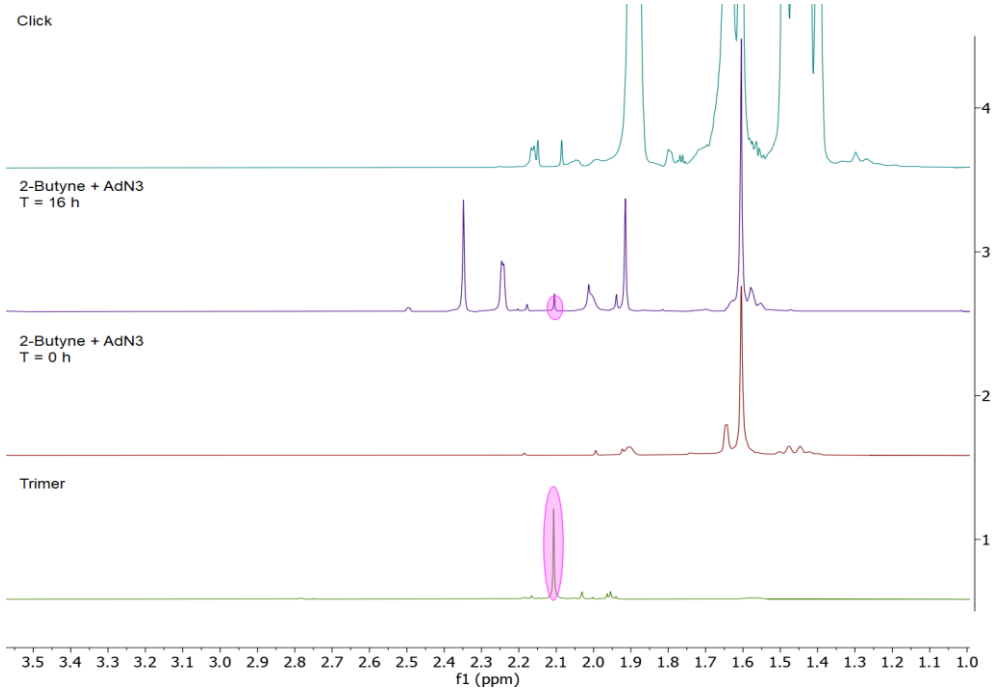

Figure 2.65 Zoom-in stacked ^{1}H NMR spectrum of click reaction (4), 2-butyne reaction with 1-azidoadamantane t = 16 h (3), t = 0 h (2) and trimer reaction (1) in C_6D_5Br. *Taken from XYS04017G.*

NMR analysis of diphenylacetylene and 1-azidoadamantane reaction (Table 2.1, Entry 4)

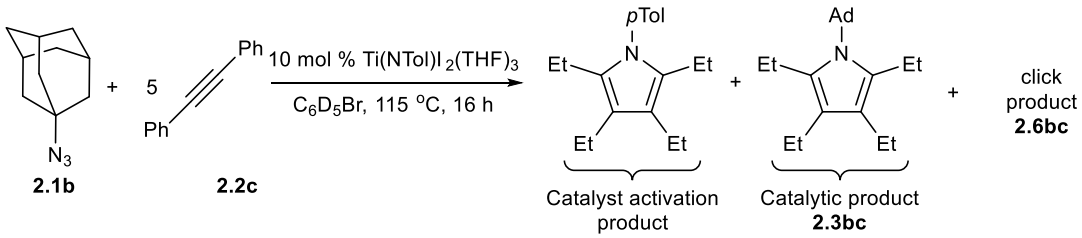

A standard catalytic run with diphenylacetylene (174 mg, 1.0 mmol) and 0.5 mL of stock solution (internal alkyne screen) was conducted. The catalytic mixture was analyzed directly without any further purification and the products were identified *in situ* to give a mixture of products shown above and leftover starting materials.

2,3,4,5-tetraphenyl-1-adamantyl-1*H*-pyrrole (2.6bc)

^{1}H NMR (500 MHz, C_6D_5Br): δ 2.50 *or* 2.20 (d, $^{3}J_{HH}$ = 3.0 Hz, 6H, N-C-(C*H*$_2$)$_3$).

The rest of the peaks are buried beneath starting materials. A definitive assignment of peaks from product could not be made. Maximum product yield based on generated peaks after reaction is < 5%.

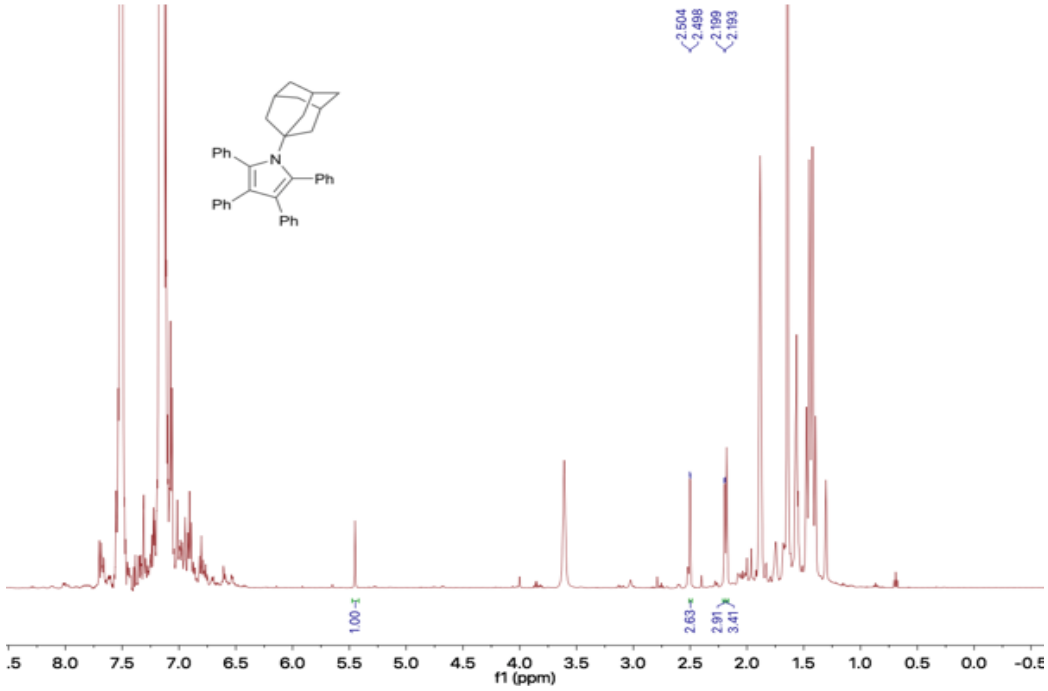

Figure 2.66 ^{1}H NMR spectrum of diphenylacetylene reaction with 1-azidoadamantane in C_6D_5Br. *Taken from AJP05033A-2H.*

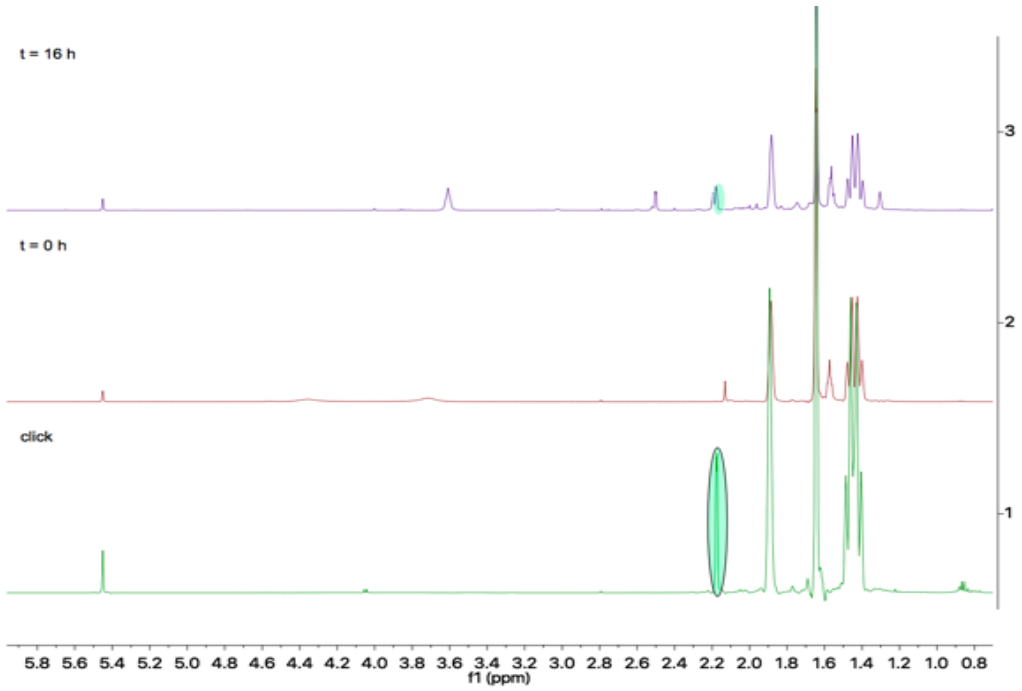

Figure 2.67 Stacked ^{1}H NMR spectrum of diphenylacetylene reaction with 1-azidoadamantane t = 16 h (3), t = 0 h (2) and click reaction (1) in C_6D_5Br. *Taken from AJP05033A and AJP05135A.*

NMR analysis of 1-phenyl-1-propyne and 1-azidoadamantane reaction (Table 2.1, Entry 5)

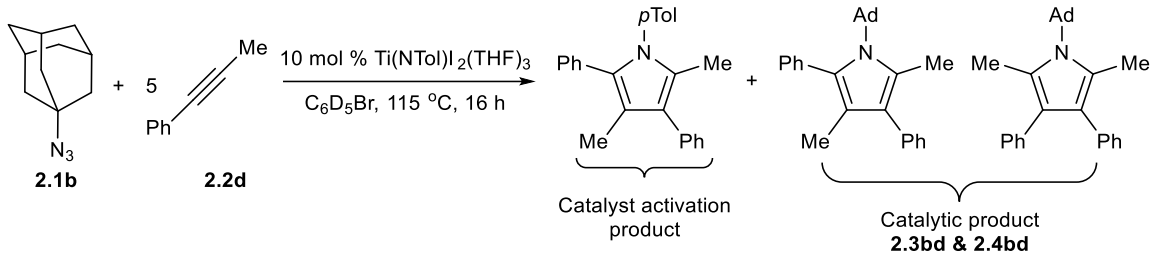

A standard catalytic run with 1-phenyl-1-propyne (125 µL, 1.0 mmol, 5.0 equiv) and 0.5 mL of stock solution (internal alkyne screen) was conducted. The catalytic mixture was analyzed directly without any further purification and the products were identified *in situ* to give a mixture of products shown above and leftover starting materials.

2,4-dimethyl-3,5-diphenyl-1-adamantyl-1*H*-pyrrole (2.3bd)

^{1}H NMR (500 MHz, C_6D_5Br): δ 2.55 (s, 3H, C(2)-CH_3), 2.17 (d, $^3J_{HH}$ = 3.0 Hz, 6H, N-C-(CH_2)$_3$), 1.77 (s, 3H, C(4)-CH_3).

This is a partial line list, aromatic peaks and remaining adamantyl peaks are buried beneath starting materials or could not be determined

2,5-dimethyl-3,4-diphenyl-1-adamantyl-1*H*-pyrrole (2.4bd)

^{1}H NMR (500 MHz, C_6D_5Br): δ 2.50 (s, 3H, C(2)-CH_3), 2.15 (d, $^3J_{HH}$ = 3.0 Hz, 6H, N-C-(CH_2)$_3$), 1.99 (s, 3H, C(5)-CH_3).

This is a partial line list; aromatic peaks and remaining adamantyl peaks are buried beneath starting materials or could not be determined. NMR evidence suggests a breach in symmetry for this molecule. This could occur through arene interactions with solvent or hindered rotation of the adamantyl group.

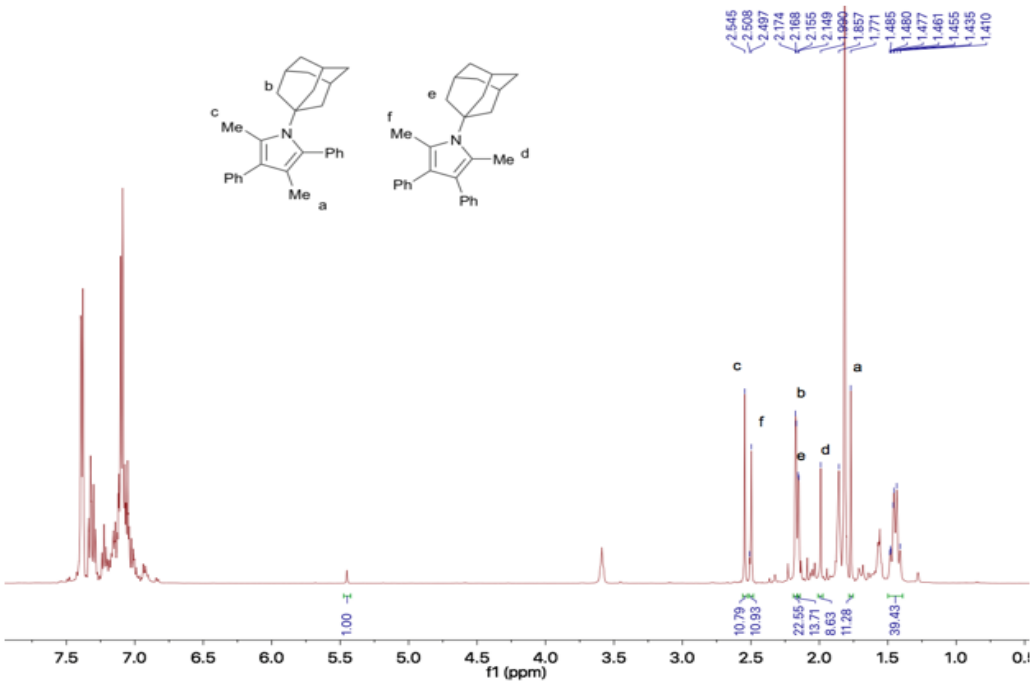

Figure 2.68 ^{1}H NMR spectrum of 1-phenyl-1-propyne reaction with 1-azidoadamantane in C_6D_5Br. *Taken from AJP05031C-2H.*

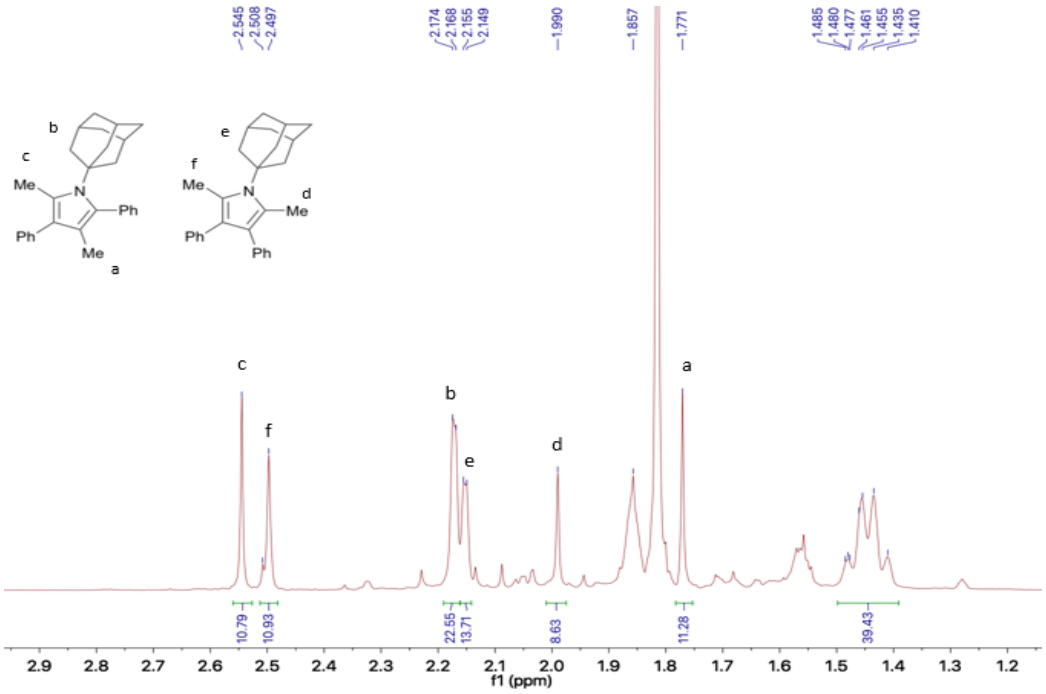

Figure 2.69 Zoom-in ^{1}H NMR spectrum of 1-phenyl-1-propyne reaction with 1-azidoadamantane in C_6D_5Br. *Taken from AJP05031C-2H.*

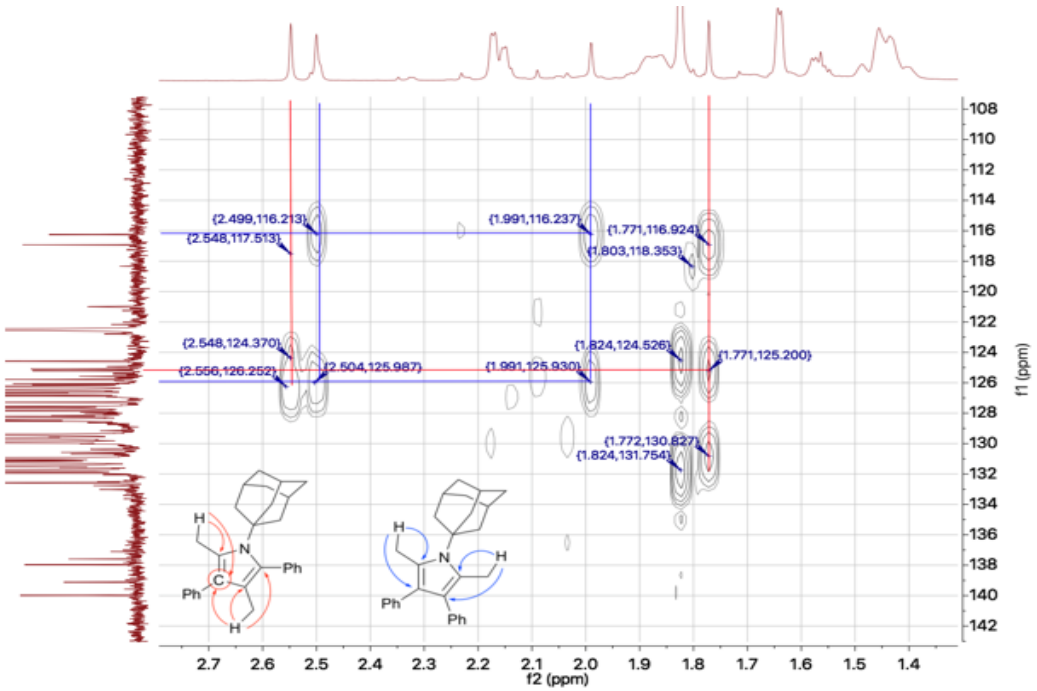

Figure 2.70 ^{1}H-^{13}C NMR spectrum of 1-phenyl-1-propyne reaction with 1-azidoadamantane in C_6D_5Br. *Taken from AJP05089-HC-HMBC.*

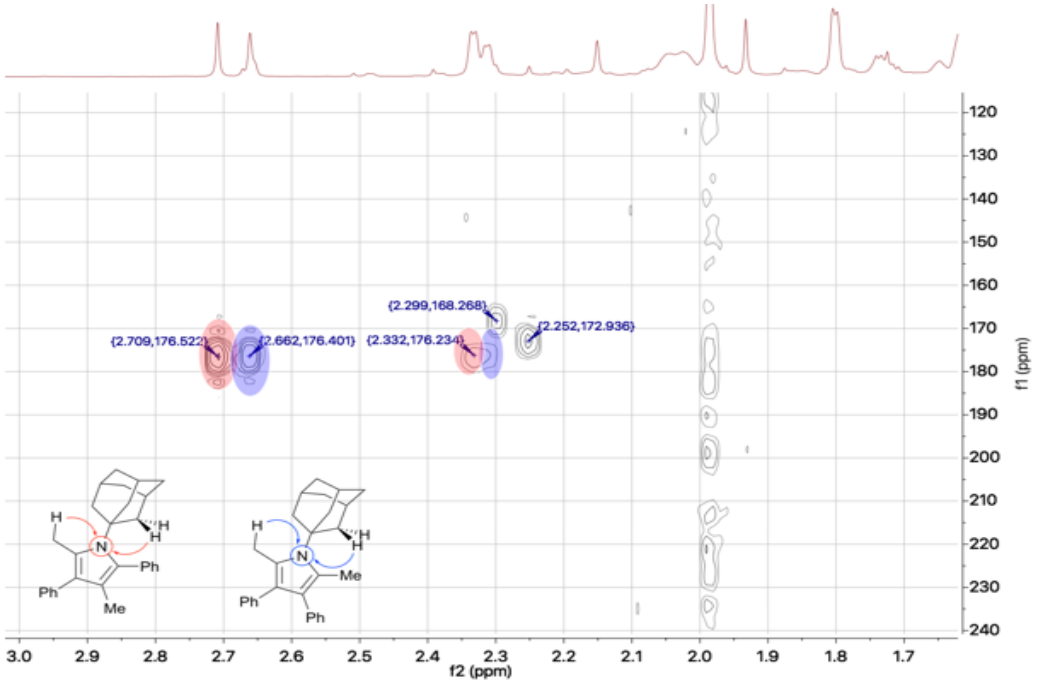

Figure 2.71 ^{1}H-^{15}N NMR spectrum of 1-phenyl-1-propyne reaction with 1-azidoadamantane in C_6D_5Br. *Taken from AJP05089-HNHMBC.*

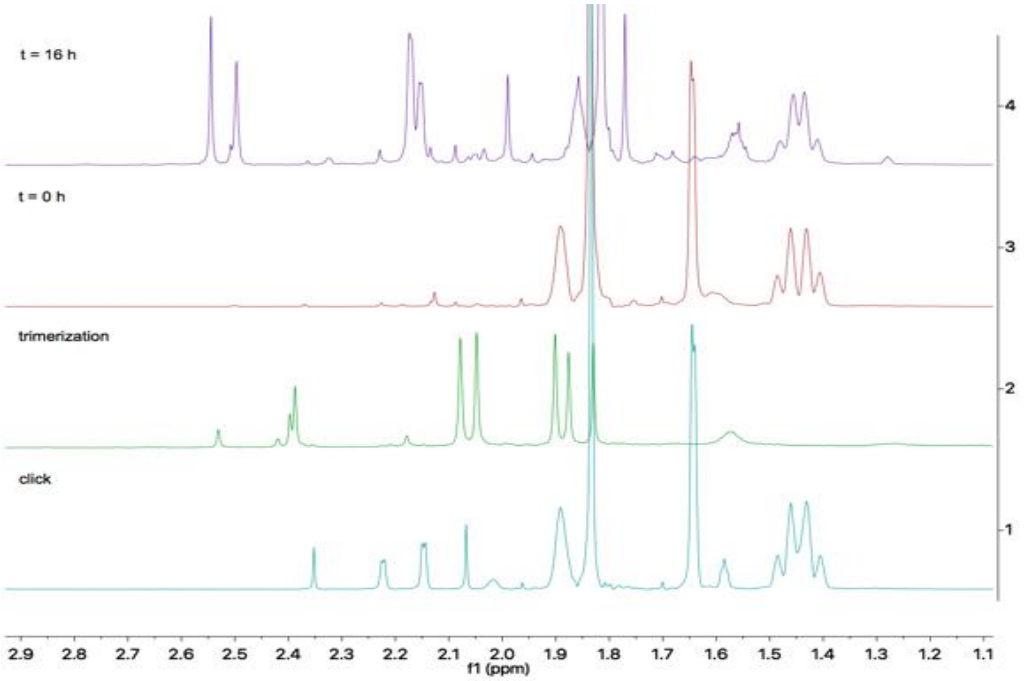

Figure 2.72 Zoom-in stacked ^{1}H NMR spectrum of 1-phenyl-1-propyne reaction with 1-azidoadamantane t = 16 h (4), t = 0 h (3), trimerization (2) and click reaction (1) in C_6D_5Br. *Taken from AJP05031C, AJP05140A-1H and AJP05091-2H.*

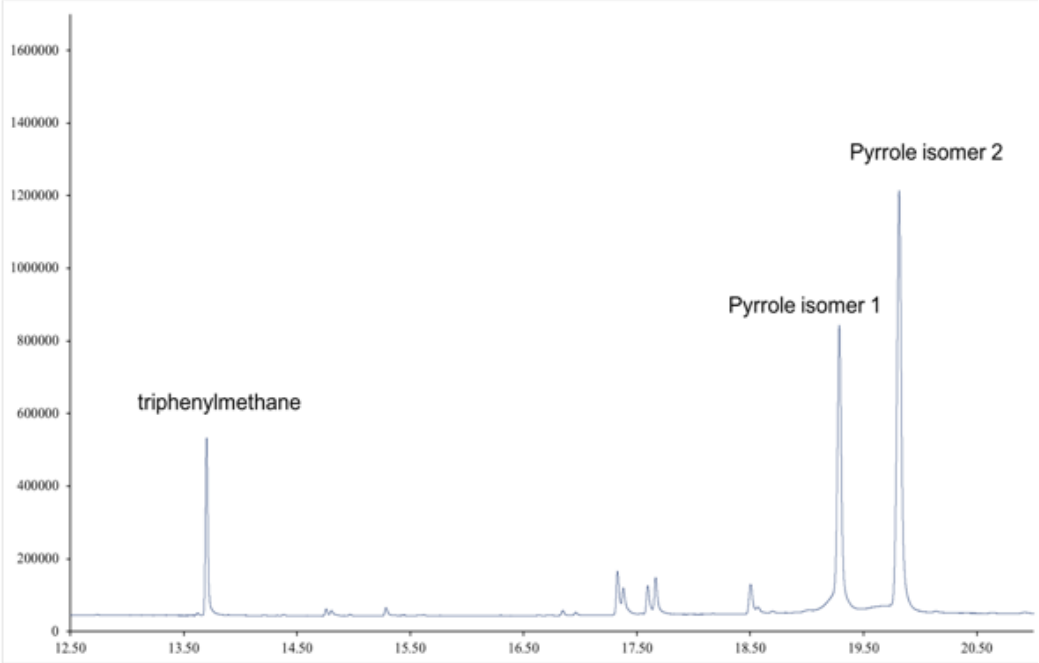

Figure 2.73 GC/FID trace of 1-phenyl-1-propyne reaction with 1-azidoadamantane in C_6D_5Br.

NMR analysis of 1-azidodecane and 3-hexyne reaction (Table 2.1, Entry 9)

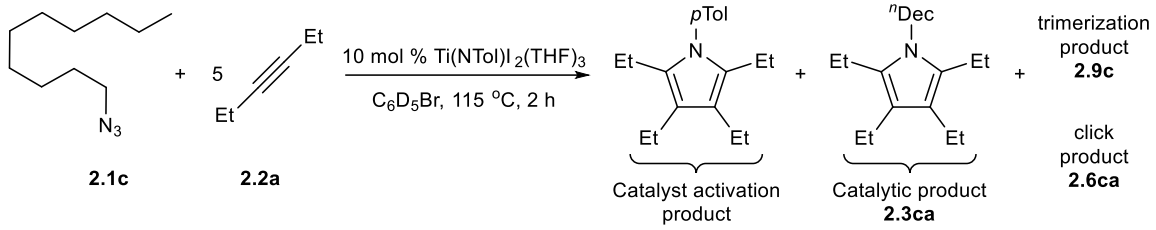

A standard catalytic run with [Ti] (6 mg, 0.01 mmol), 1-azidodecane (19 mg, 0.1 mmol, 1 equiv) and 0.5 mL of stock solution (azide screen) was prepared and the reaction mixture was heated for 2 h. The catalytic mixture was analyzed directly without any further purification and the products were identified *in situ* to give a mixture of products shown above and leftover starting materials.

2,3,4,5-tetraethyl-1-decyl-1*H*-pyrrole (2.3ca) (partial)

^{1}H NMR (400 MHz, C_6D_5Br): δ 3.62 – 3.58 (m, 2H, $H_3C(CH_2)_8$-C*H*$_2$-N), 2.51 (q, $^{3}J_{HH}$ = 7.5 Hz, 4H, *o*-C*H*$_2$-CH_3), 2.43 (q, $^{3}J_{HH}$ = 7.5 Hz, 4H, *m*-C*H*$_2$-CH_3), 0.88 (t, $^{3}J_{HH}$ = 6.9 Hz, 3H, *H*$_3$C-$(CH_2)_9$N).

The peak at δ 3.62 – 3.58 and 0.88 overlaps with THF from the catalyst and other alkyl impurities respectively. This is a partial NMR line list, the remaining peaks cannot be positively identified.

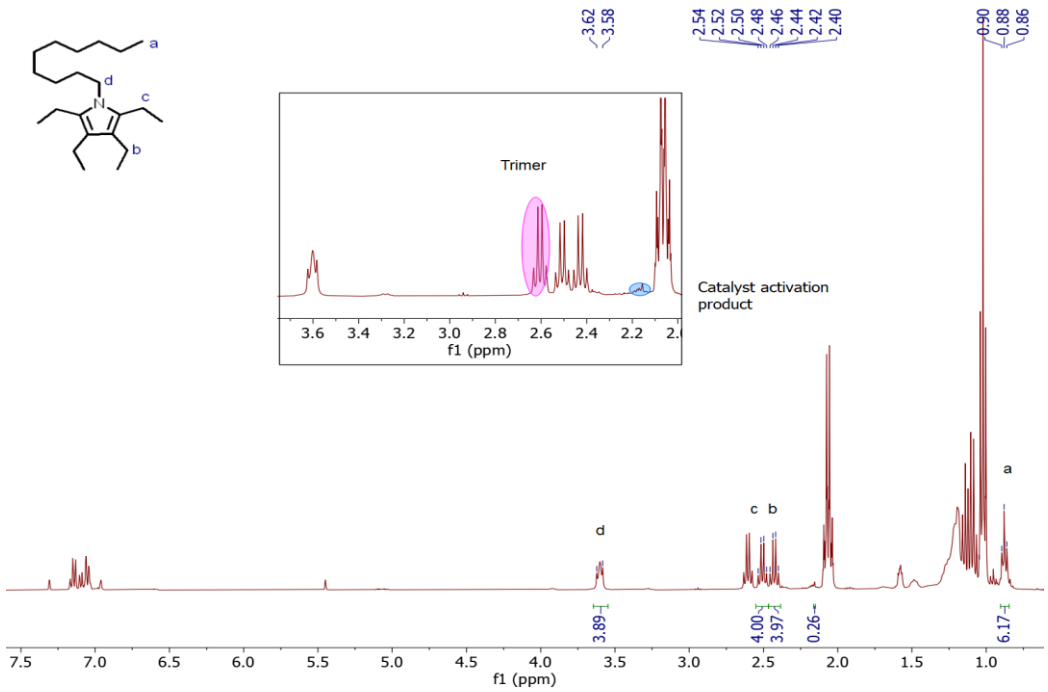

Figure 2.74 ^{1}H NMR spectrum of 1-azidodecane reaction with 3-hexyne in C_6D_5Br. *Taken from XYS04110D.*

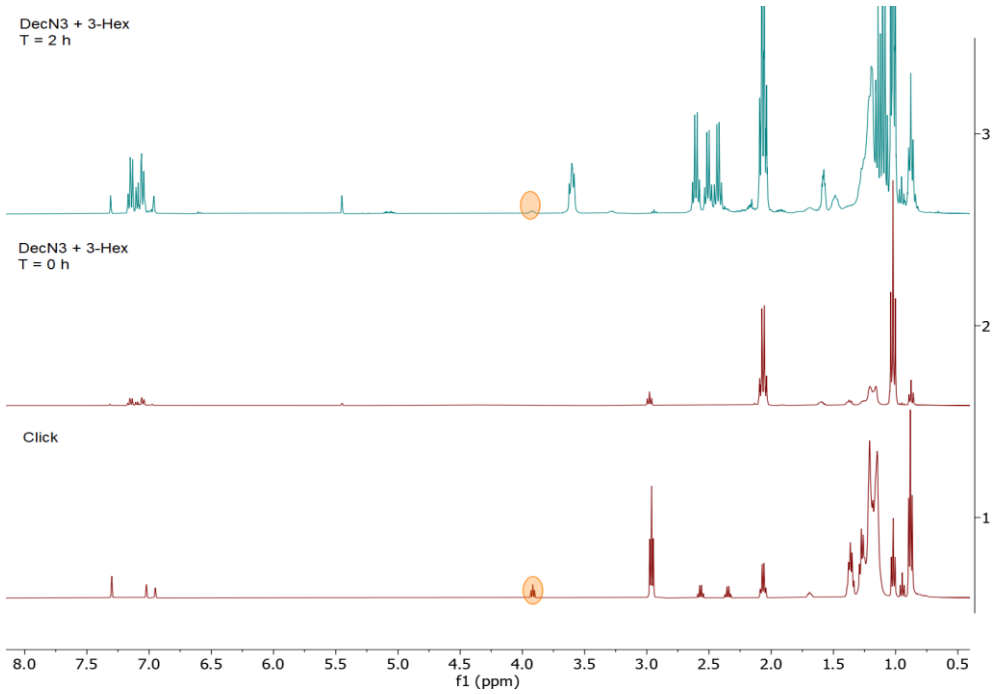

Figure 2.75 Stacked ^{1}H NMR spectrum of 1-azidodecane reaction with 3-hexyne t = 2 h (3), t = 0 h (2) and click reaction (1) in C_6D_5Br. *Taken from XYS04097F and XYS04110D.*

Isolation of 2,3,4,5-tetraethyl-1-decyl-1*H*-pyrrole

To a 7 ml scintillation vial equipped with a stir bar was added $Ti(NTol)I_2(THF)_3$ (35 mg, 0.056 mmol, 10 mol %), 1-azidodecane (103 mg, 0.57 mmol, 1 equiv), 2.5 ml C_6H_5Br and 3-Hexyne (0.32 ml, 231 mg, 2.82 mmol, 5 equiv) in the following order in a N_2-filled glovebox. The vial was then sealed and heated at 115 °C for 2 h. After which, the reaction mixture was transferred into a 20 ml scintillation vial and dried *in vacuo* while heated to 50 °C for several hours to give a black oil. The oil was taken up in minimal dichloromethane and purified over a silica column using an eluent of 3 % ethyl acetate / petroleum ether. The desired product elutes before the activation product (2,3,4,5-tetraethyl-1-tolyl-1*H*-pyrrole).

Two fractions were collected that contained the desired product with small amount of trimerization and activation product present. (83 mg, 46 % corrected yield).

^{1}H NMR (400 MHz, $CDCl_3$): δ 3.69 (m, 2H, N-C*H*$_2$-$(CH_2)_8CH_3$), 2.54 (q, $^3J_{HH}$ = 7.5 Hz, 4H, *o*-N-pyr-C*H*$_2$$CH_3$), 2.40 (q, $^3J_{HH}$ = 7.5 Hz, 4H, *m*-N-pyr-C*H*$_2$$CH_3$), 1.65 – 1.60 (m, 2H, NCH_2-C*H*$_2$-$(CH_2)_7CH_3$), 1.33 – 1.27 (m, 14H, $N(CH_2)_2$-(C*H*$_2$)$_7$-CH_3), 1.15 (t, $^3J_{HH}$ = 7.5 Hz, 6H, *o*-N-pyr-CH_2C*H*$_3$), 1.11 (t, $^3J_{HH}$ = 7.5 Hz, 6H, *o*-N-pyr-CH_2C*H*$_3$), 0.89 (t, $^3J_{HH}$ = 7.5 Hz, 3H, N(C*H*$_2$)$_9$-C*H*$_3$).

^{13}C NMR (101 MHz, $CDCl_3$): δ 128.1, 119.0, 43.7, 32.5, 32.0, 29.7, 29.5, 27.4, 22.8, 18.0, 17.9, 17.3, 16.1, 14.3.

GC-HRMS (m/z): calcd. for $C_{22}H_{35}N$, 319.3239 ; found, 319.3247.

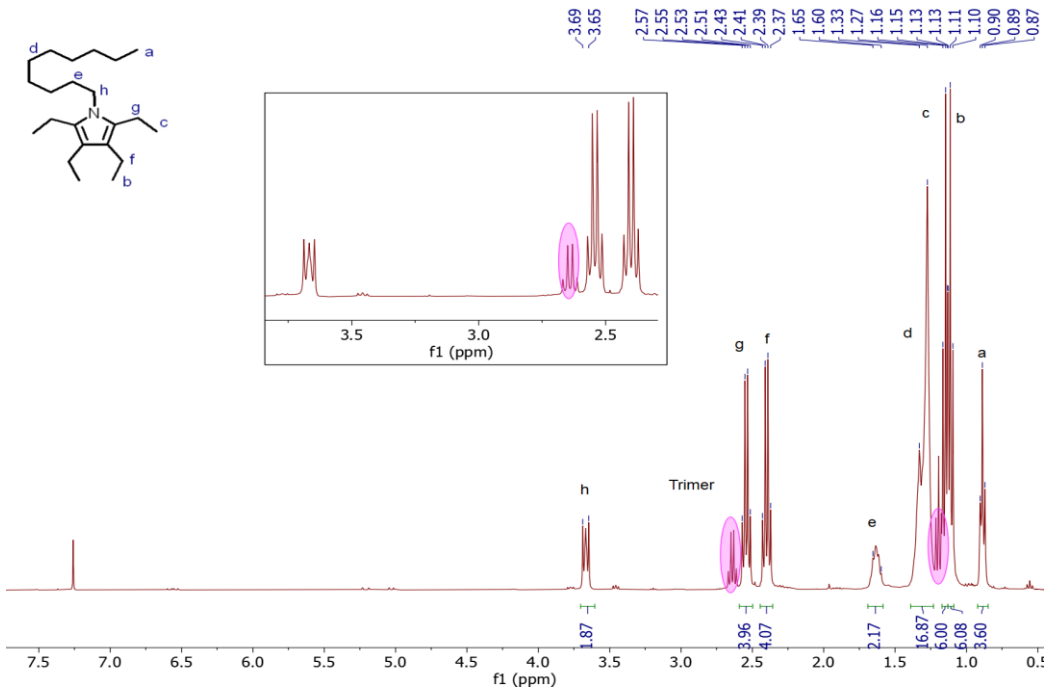

Figure 2.76 ^{1}H NMR spectrum of 2,3,4,5-tetraethyl-1-decyl-1*H*-pyrrole (**2.3ca**) in $CDCl_3$. *Taken from XYS04117_4H.*

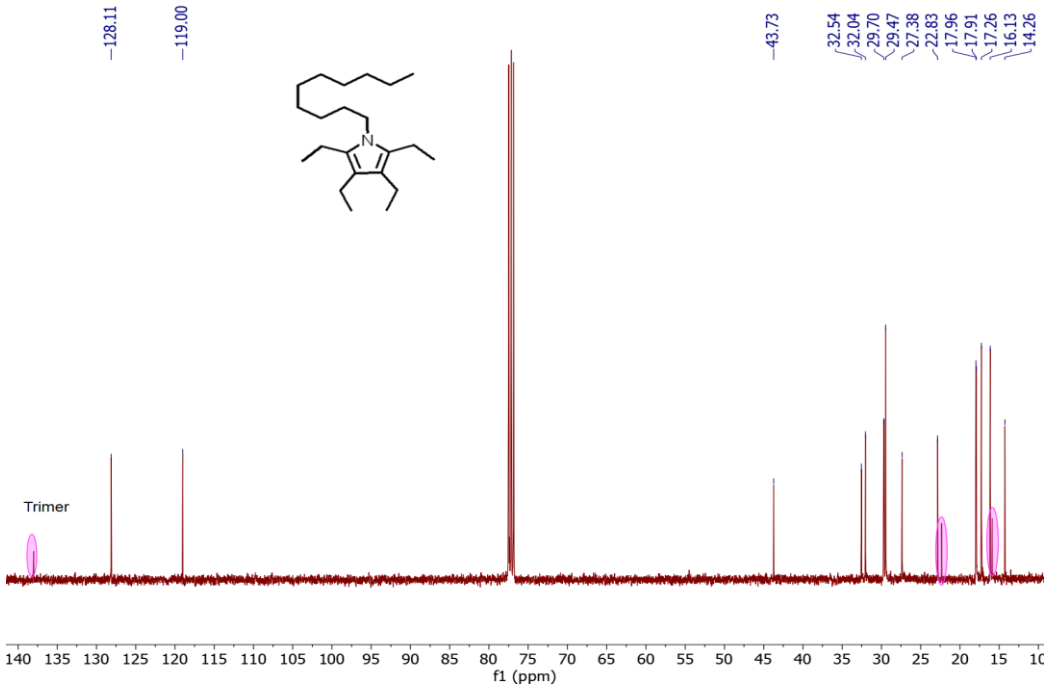

Figure 2.77 ^{13}C NMR spectrum of 2,3,4,5-tetraethyl-1-decyl-1*H*-pyrrole (**2.3ca**) in $CDCl_3$. *Taken from XYS04117_1C.*

NMR analysis of benzylazide and 3-hexyne reaction (Table 2.1, Entry 10)

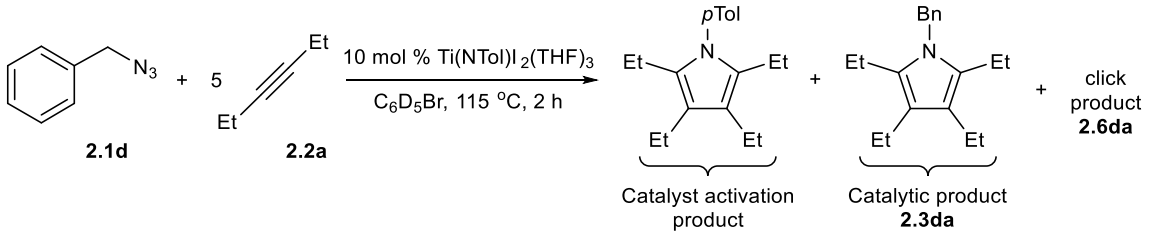

A standard catalytic run with [Ti] (7 mg, 0.01 mmol), benzylazide (13 mg, 0.1 mmol, 1 equiv) and 0.5 mL of stock solution (azide screen) was prepared and the reaction mixture was heated for 2 h. The catalytic mixture was analyzed directly without any further purification and the products were identified *in situ* to give a mixture of products shown above and leftover starting materials.

2,3,4,5-tetraethyl-1-benzyl-1*H*-pyrrole (2.3da)

^{1}H NMR (500 MHz, C_6D_5Br): δ 6.76 (d, $^3J_{HH}$ = 7.0 Hz, 2H, *o*-Ar-*H*), 4.88 (s, 2H, Ar-C*H*$_2$), 2.44 (q, $^3J_{HH}$ = 7.5 Hz, 4H, pyr-C*H*$_2$), 2.36 (q, $^3J_{HH}$ = 7.5 Hz, 4H, pyr-C*H*$_2$) 1.15 (t, $^3J_{HH}$ = 7.5 Hz, 6H, pyr-CH$_2$-C*H*$_3$), 0.91 (t, $^3J_{HH}$ = 7.5 Hz, 6H, pyr-CH$_2$-C*H*$_3$).

Remaining aromatic peaks are hidden behind the internal standard or starting material.

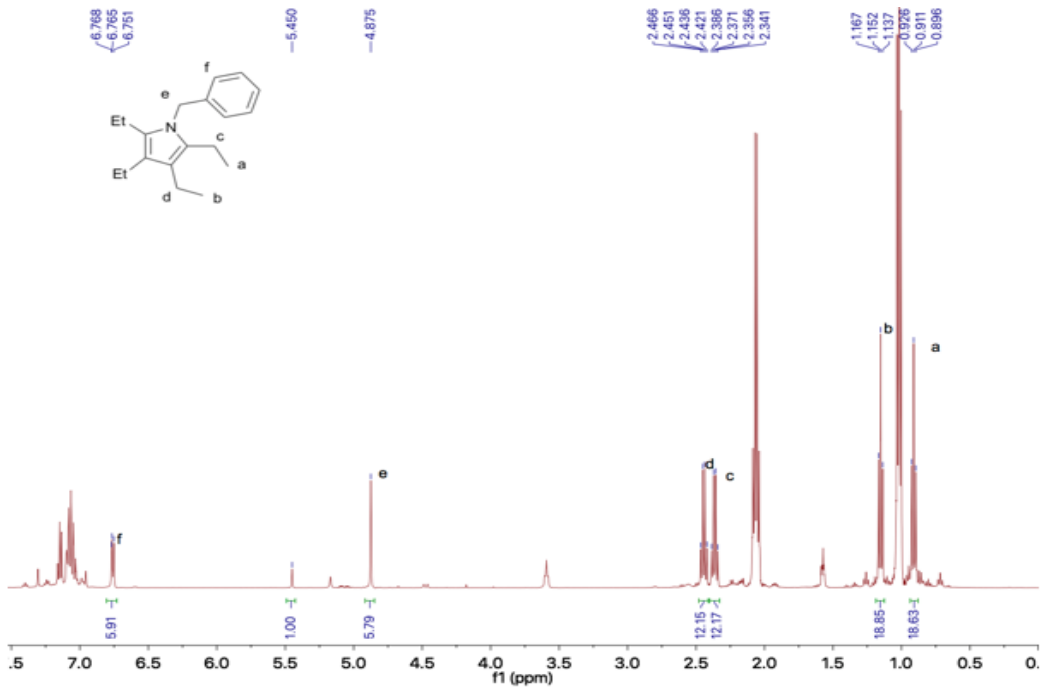

Figure 2.78 ^{1}H NMR spectrum of benzylazide reaction with 3-hexyne in C_6D_5Br. *Taken from AJP05120B.*

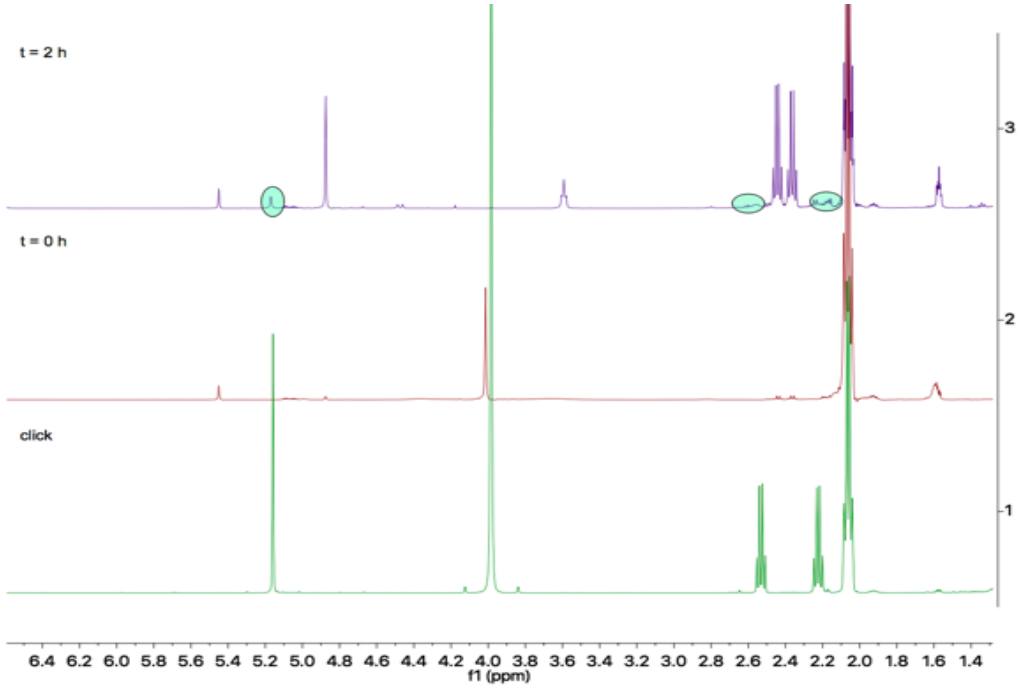

Figure 2.79 Zoom-in stacked ^{1}H NMR spectrum of benzylazide reaction with 3-hexyne t = 2 h (3), t = 0 h (2) and click reaction (1) in C_6D_5Br. * Click products highlighted in green. *Taken from AJP0505120B and XYS04097C.*

Isolation of 2,3,4,5-tetraethyl-1-benzyl-1*H*-pyrrole

To a 20 mL vial equipped with a magnetic stir bar, $Ti(NTol)I_2(THF)_3$ (37 mg, 0.059 mmol, 10 mol %) and benzyl azide (79 mg, 0.59 mmol, 1 equiv) were dissolved in 2 mL of bromobenzene. To this solution was added 3-hexyne (350 µL, 3.1 mmol, 5.2 equiv) and the vial was sealed with a teflon cap, removed from the glovebox and heated at 115 ˚C for 2 hours. The vial was allowed to cool to 40˚C, at which point the cap was removed under air and the volatiles were removed *in vacuo*. This residue was purified by column chromatography (SiO_2, Hexanes : EtOAc 19 : 1 R_f = 0.5) to give the title compound (76 mg, 59% yield).

^{1}H NMR (400 MHz, $CDCl_3$): δ 7.26 (t, $^{3}J_{HH}$ = 7.4 Hz, 2H, *m*-Ar-*H*), 7.19 (t, $^{3}J_{HH}$ = 7.6 Hz, 1H, *p*-Ar-*H*), 6.84 (d, $^{3}J_{HH}$ = 6.8 Hz, 2H, *o*-Ar-*H*), 5.01 (s, 2H, Ar-C*H*$_2$), 2.44 (q, $^{3}J_{HH}$ = 7.6 Hz, 4H, pyr-C*H*$_2$-CH$_3$), 2.43 (q, $^{3}J_{HH}$ = 7.6 Hz, 4H, pyr-C*H*$_2$-CH$_3$), 1.13 (t, $^{3}J_{HH}$ = 7.4 Hz, 3H, pyr-CH$_2$-C*H*$_3$), 0.97 (t, $^{3}J_{HH}$ = 7.6 Hz, 3H, pyr-CH$_2$-C*H*$_3$).

^{13}C NMR (101 MHz, $CDCl_3$): δ 140.2, 128.8, 128.6, 126.8, 125.8, 119.6, 46.6, 18.0, 17.9, 17.4, 16.0.

GC-HRMS (m/z): calcd. for $C_{19}H_{27}N$, 269.2143 ; found, 269.2148.

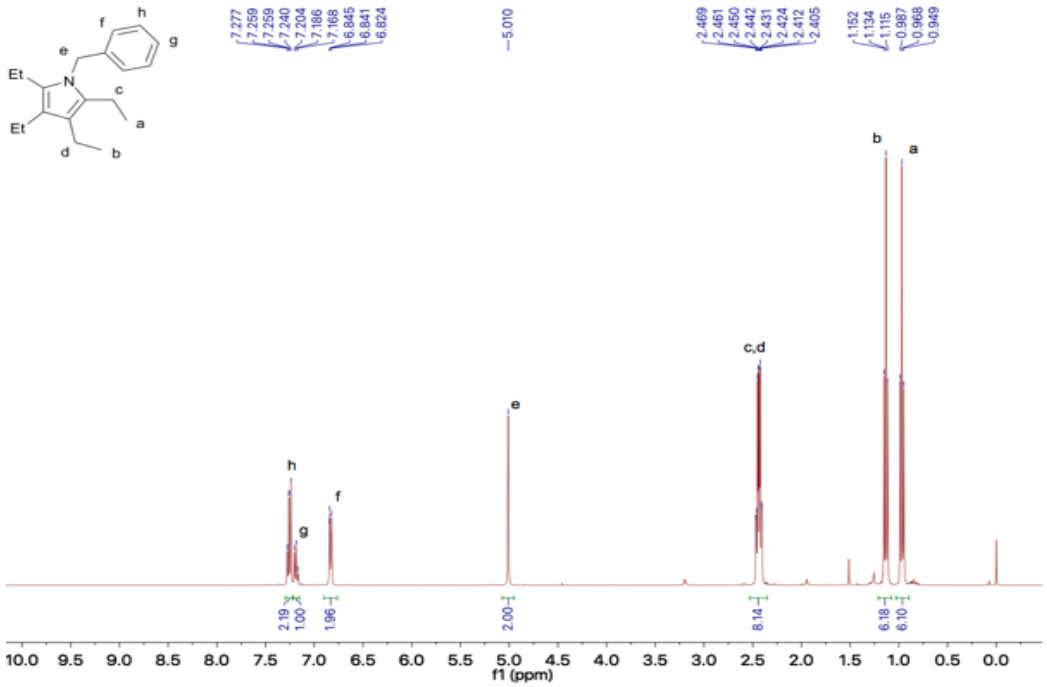

Figure 2.80 ^{1}H NMR spectrum of 2,3,4,5-tetraethyl-1-benzyl-1*H*-pyrrole (**2.3da**) in $CDCl_3$. *Taken from AJP05122-2H.*

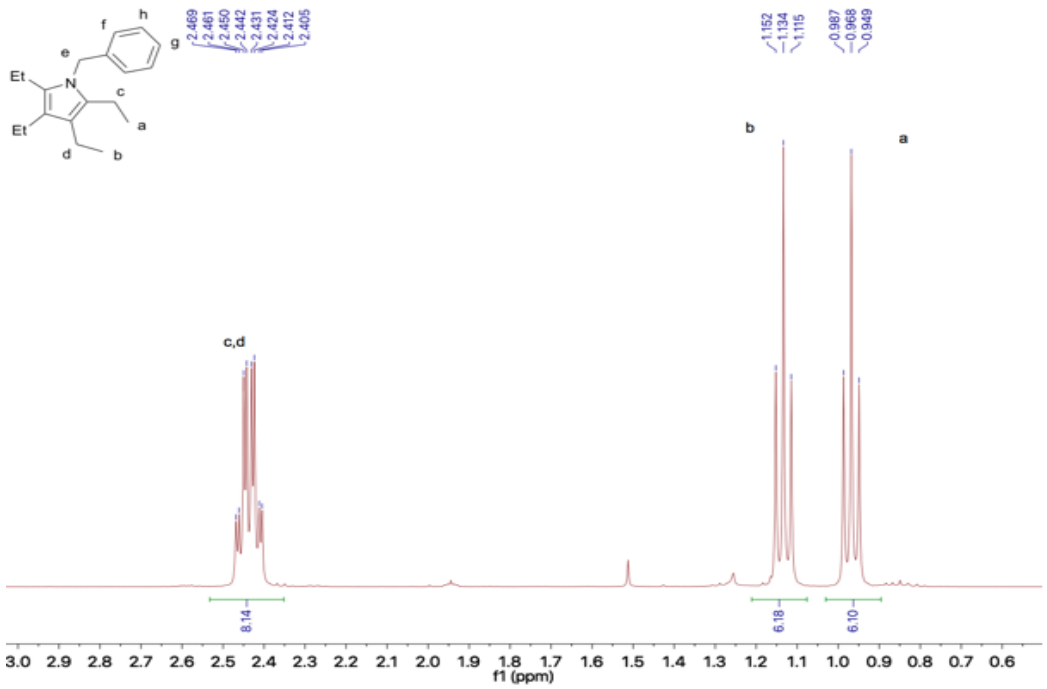

Figure 2.81 Zoom-in ^{1}H NMR spectrum of 2,3,4,5-tetraethyl-1-benzyl-1*H*-pyrrole (**2.3da**) in $CDCl_3$. *Taken from AJP05122-2H.*

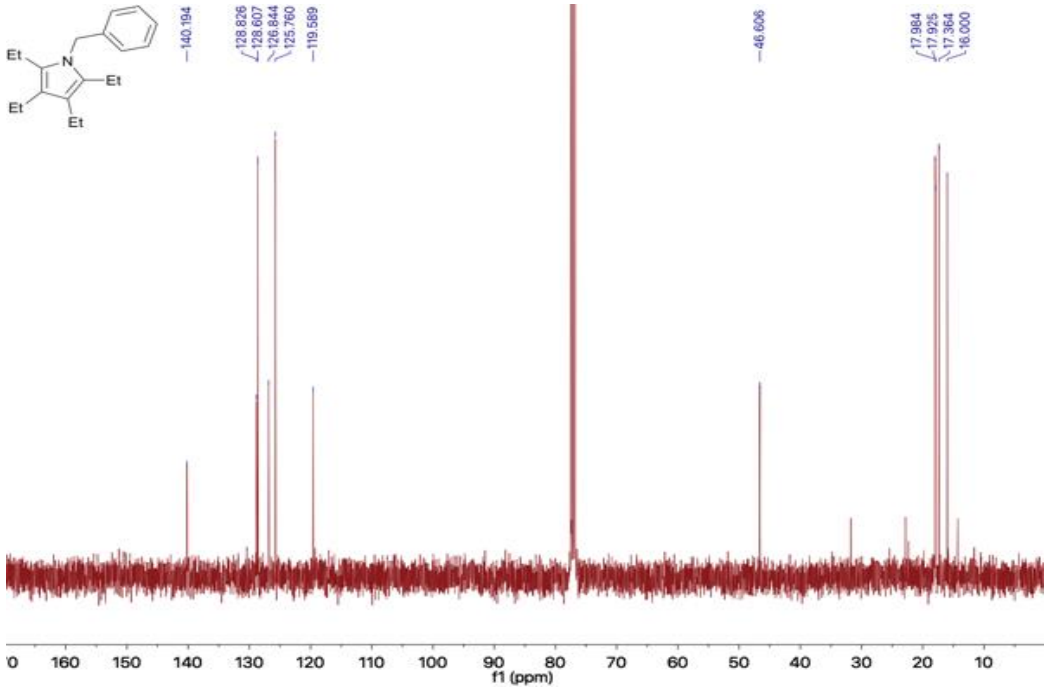

Figure 2.82 ^{13}C NMR spectrum of 2,3,4,5-tetraethyl-1-benzyl-1*H*-pyrrole (**2.3da**) in $CDCl_3$. *Taken from AJP05122-1C.*

NMR analysis of (*p*-tolyl)azide and 3-hexyne reaction (Table 2.1, Entry 11)

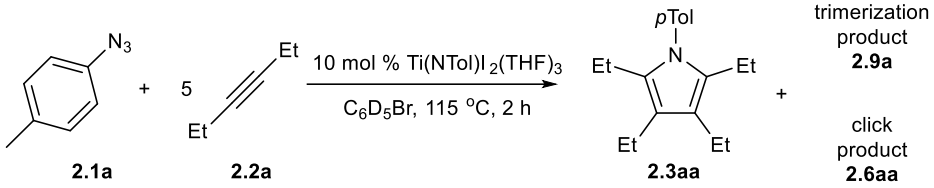

A standard catalytic run with [Ti] (7 mg, 0.01 mmol), (*p*-tolyl)azide (14 mg, 0.1 mmol, 1 equiv) and 0.5 mL of stock solution (azide screen) was prepared and the reaction mixture was heated for 2 h. The catalytic mixture was analyzed directly without any further purification and the products were identified *in situ* to give a mixture of products shown above and leftover starting materials. Characterization of this pyrrole product was done previously.[119]

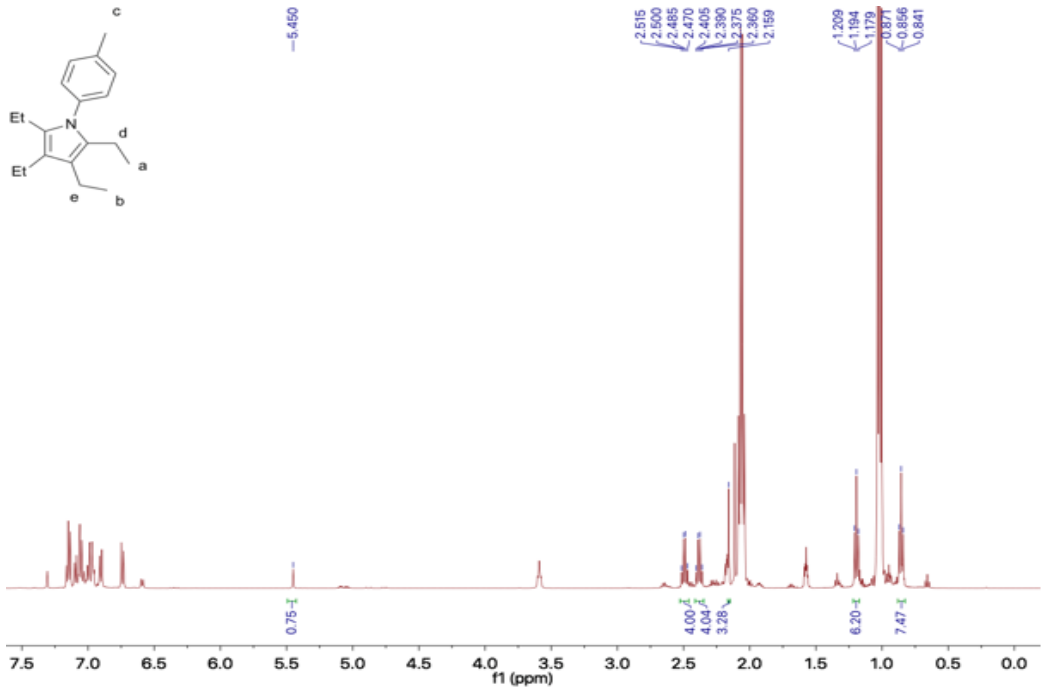

Figure 2.83 ^{1}H NMR spectrum of (*p*-tolyl)azide reaction with 3-hexyne in C_6D_5Br. *Taken from AJP05120A.*

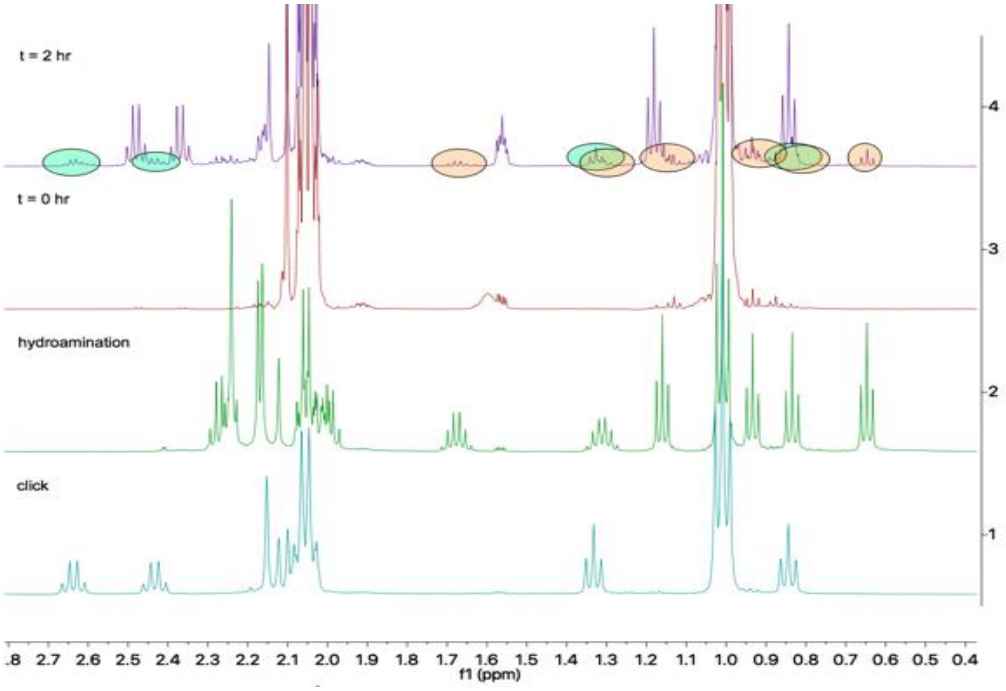

Figure 2.84 Zoom-in stacked ^{1}H NMR spectrum of (*p*-tolyl)azide reaction with 3-hexyne t = 2 h (4), t = 0 h (3), hydroamination of 3-hexyne with *p*-toluidine (2) and click reaction (1). Triazole and hydroamination products are highlighted in green and orange respectively. *Taken from AJP05120A.*

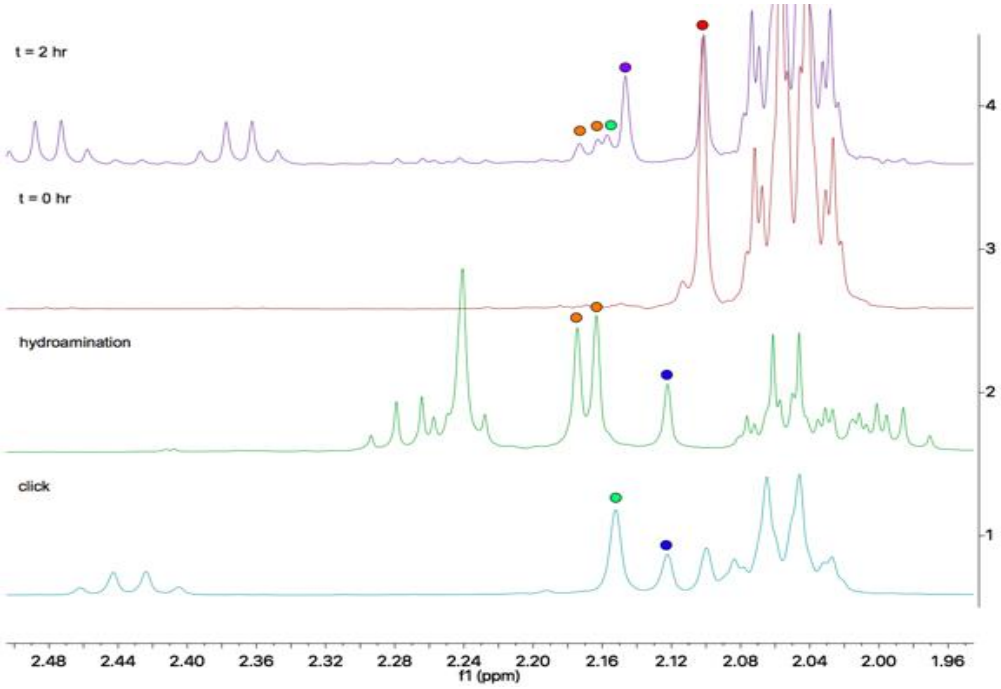

Figure 2.85 Zoom-in stacked ^{1}H NMR spectrum of (*p*-tolyl)azido reaction with 3-hexyne t = 2 h (4), t = 0 (3), hydroamination of 3-hexyne with *p*-toluidine (2) and click reaction (1).

* The p-tolyl peaks from various groups are marked with colored dots (red = (*p*-tolyl)azido; blue = *p*-toluidine; purple = 2,3,4,5-tetraethyl-1-(*p*-tolyl)-1H-pyrrole; green = 4,5-diethyl-1-(p-tolyl)-1H-1,2,3-triazole; orange = N-(p-tolyl)hexan-3-imine (mixture of E and Z isomers)). *Taken from AJP05120A.*

NMR analysis of (*p*-tolyl)azide and 3-hexyne reaction (Table 2.1, Entry 12)

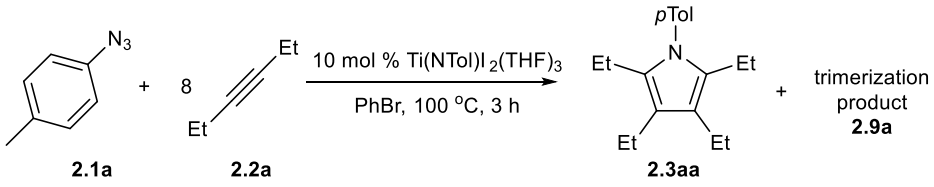

21.6 mg of Ph_3CH was dissolved in 2 mL of bromobenzene (0.044 M Ph_3CH). 0.5 mL of this solution was then used to dissolve $Ti(NTol)I_2(THF)_3$ (6 mg, 0.01 mmol, 10 mol %) and (*p*-tolyl)azide (13.6 mg, 0.102 mmol, 1 equiv) that had been massed out in a screw-cap NMR tube. 3-hexyne (94 µL, 0.83 mmol, 8.3 equiv) was subsequently added and the NMR tube was sealed and inverted to mix. The tube was heated at 100˚C in an oil bath for 3 hours. The catalytic mixture was analyzed directly without any further purification and the

products were identified *in situ* to give a mixture of products shown above and leftover starting materials.

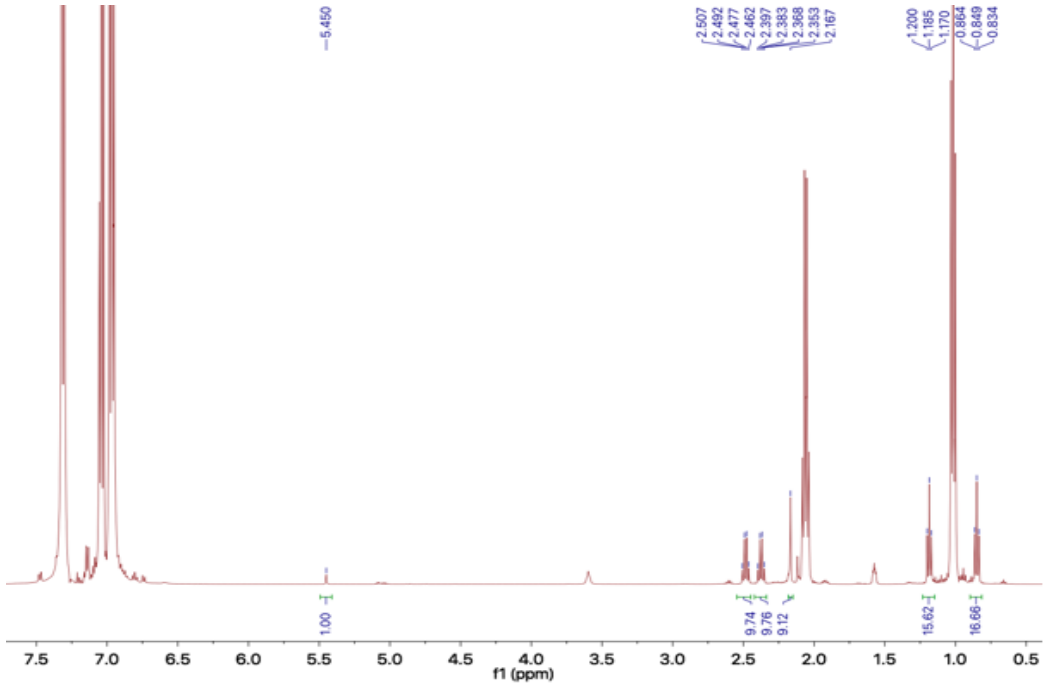

Figure 2.86 No-D NMR of (*p*-tolyl)azide reaction with 3-hexyne in PhBr. *Taken from AJP05102B.*

NMR analysis of azidomethyl phenyl sulfide and 3-hexyne reaction (Table 2.1, Entry 13)

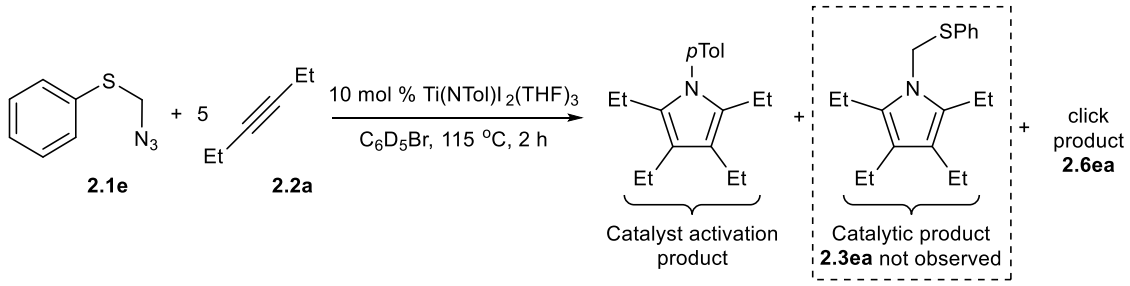

A standard catalytic run with [Ti] (6 mg, 0.01 mmol), azidomethyl phenyl sulfide (19 mg, 0.1 mmol, 1 equiv) and 0.5 mL of stock solution (azide screen) was prepared and the reaction mixture was heated for 2 h. The catalytic mixture was analyzed directly without any further purification and the products were identified *in situ* to give a mixture of

products shown above and leftover starting materials. The catalytic product was not observed although we do observe some unexplainable quartets in the spectrum.

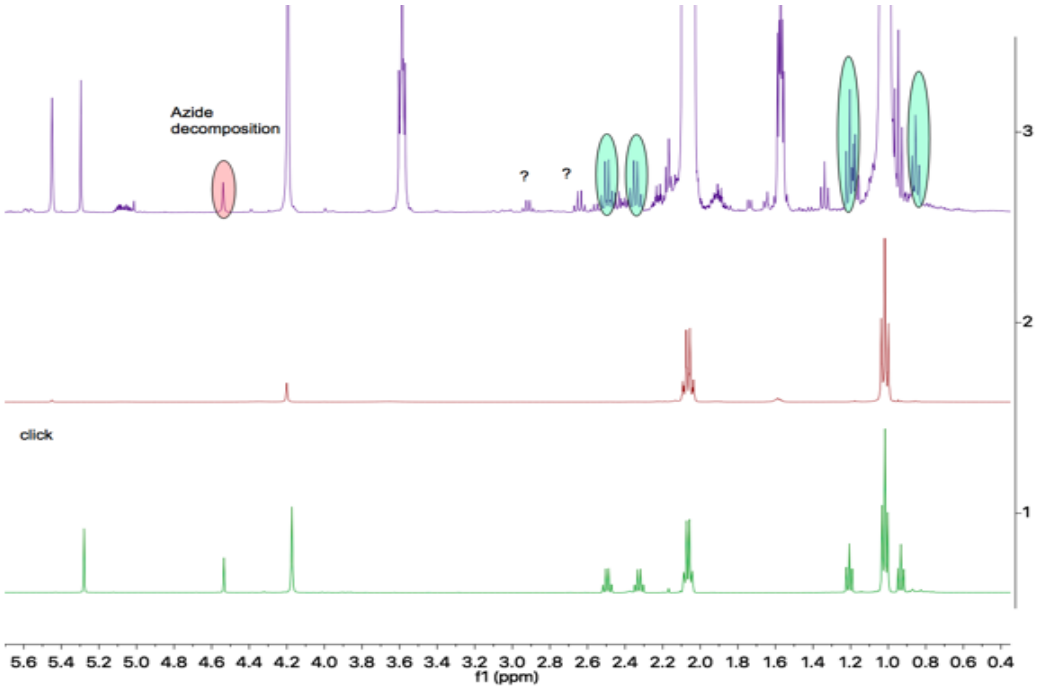

Figure 2.87 Stacked ^{1}H NMR spectrum of azidomethyl phenyl sulfide reaction with 3-hexyne t = 2 h (3), t = 0 h (2) and click reaction (1) in C_6D_5Br. *Taken from XYS04110SA and XYS04097J.*

NMR analysis of trityl azide and 3-hexyne reaction (Table 1, Entry 14)

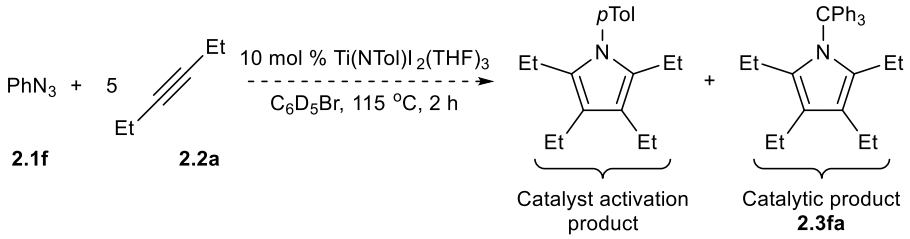

A standard catalytic run with [Ti] (6 mg, 0.01 mmol), trityl azide (30 mg, 0.1 mmol, 1 equiv) and 0.5 mL of stock solution (azide screen) was prepared and the reaction mixture was heated for 2 h. The catalytic mixture was analyzed directly without any further purification and were identified *in situ* to not contain the desired products. Poor mass balances were also observed for both starting reagents.

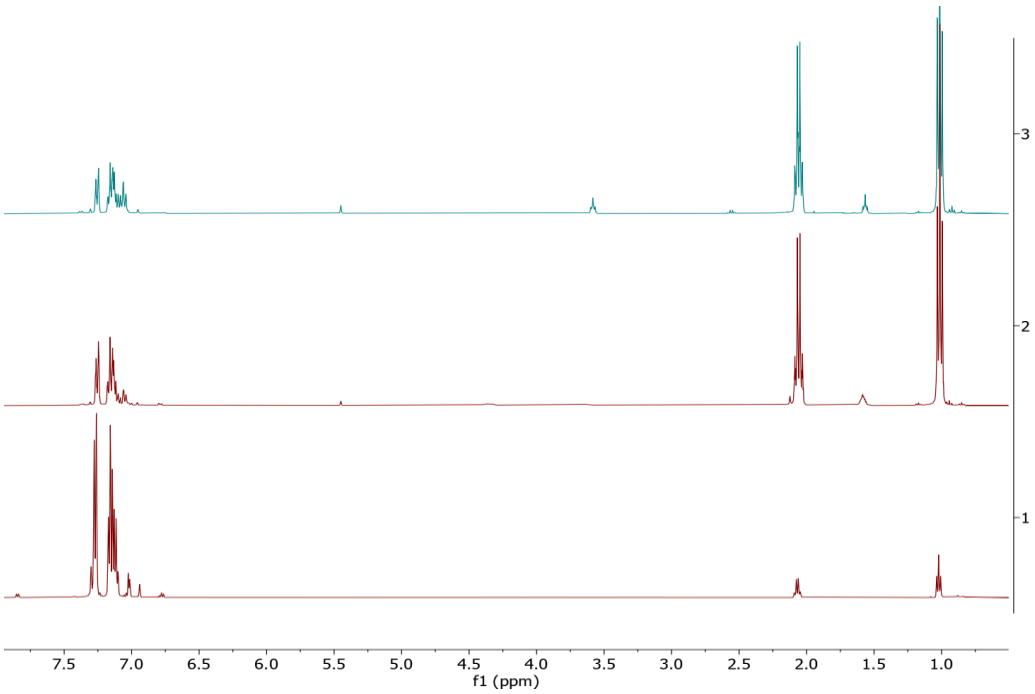

Figure 2.88 Stacked ^{1}H NMR spectrum of tritylazide reaction with 3-hexyne t = 2 h (3), t = 0 h (2) and click reaction (1) in C_6D_5Br. *Taken from XYS04110C and XYS04097E*.

Table 2.3 Internal alkyne scope triazole yield, trimer yield and mass balance data.

Table 2.1, Entry #	**Azide**	**Alkyne**	**Triazole yield (%) 6**	**Trimer yield (%)[g] 9**	**Azide mass balance (%)**	**Alkyne mass balance (%)**
1[a]	Ad **1b**	3-Hexyne **2a**	0	45	80	84
2[b]	Ad **1b**	3-Hexyne **2a**	0	1	85	89
3[a]	Ad **1b**	2-butyne **2b**	0	2	71	90
4[a]	Ad **1b**	Diphenyl-acetylene **2c**	0	0	*	*
5[a]	Ad **1b**	Phenyl propyne **2d**	0	0	*	92
6[d]	*n*-Dec **1c**	3-Hexyne **2a**			-	
7[e]	*n*-Dec **1c**	3-Hexyne **2a**			-	
8[b]	*n*-Dec **1c**	3-Hexyne **2a**			-	
9[b]	*n*-Dec **1c**	3-Hexyne **2a**	7	6	74	95
10[b]	Bn **1d**	3-Hexyne **2a**	11	0	70	89
11[b]	Tol **1a**	3-Hexyne **2a**	10	0	82	92
12[f]	Tol **1a**	3-Hexyne **2a**			-	

13[b]	$PhSCH_2$ **1e**	3-Hexyne **2a**	0	0	65	96
14[b]	Ph_3C **1f**	3-Hexyne **2a**	0	0	44	53

[a]Conditions: 0.2 mmol **1b** (1 equiv), **2** (5 equiv), 10 mol % $Ti(NTol)I_2(THF)_3$ 115 ˚C, 0.5 mL C_6D_5Br, average of 2 runs. [b]Conditions: 0.1 mmol **1** (1 equiv), **2a** (*x* equiv), 10 mol % $Ti(NTol)I_2(THF)_3$, 115 ˚C, 0.5 mL C_6D_5Br, average of 2-3 runs. [d]Conducted at 80 ˚C. [e]Conducted at 100 ˚C. [f]Conditions: 0.1 mmol **1a** (1 equiv), 0.8 mmol **2** (8 equiv), 10 mol % $Ti(NTol)I_2(THF)_3$, 115 ˚C, 0.5 mL C_6D_5Br, single run. [g]Trimer yields are calculated with respect to alkyne. *Overlap of peaks in NMR spectra makes positive identification difficult. - Data unavailable in non-quantitative NMR.

Table 2.4 1-azidodecane optimization conditions with 3-hexyne.

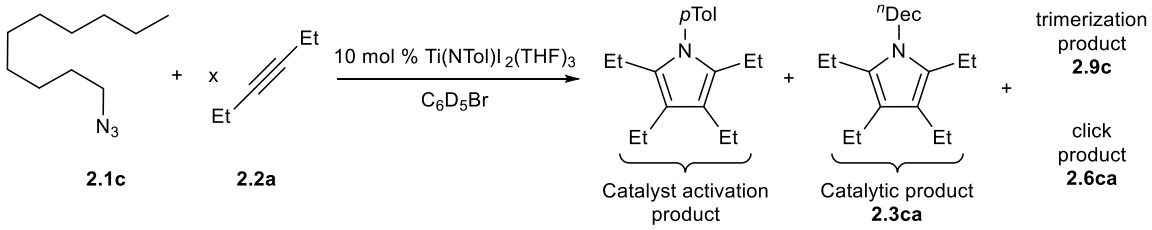

Entry #	3-hexyne equiv (*x*)	Time (h)	Temp (˚C)	Catalytic pyrrole yield (%) 3
1	3	6	80	37
2	3	6	100	35
3	3	6	115	34
4	0.5	3	115	5
5	4.5	3	115	45
6	8	3	115	74

Conditions: 0.1 mmol **1c** (1 equiv), **2a** (*x* equiv), 10 mol % $Ti(NTol)I_2(THF)_3$, 0.5 mL C_6D_5Br, single run.

2.5.7 NMR analysis of catalytic reactions with terminal alkyne substrates (Table 2.2)

NMR analysis of 1-hexyne and 1-azidoadamantane reaction (Table 2.2, Entry 1)

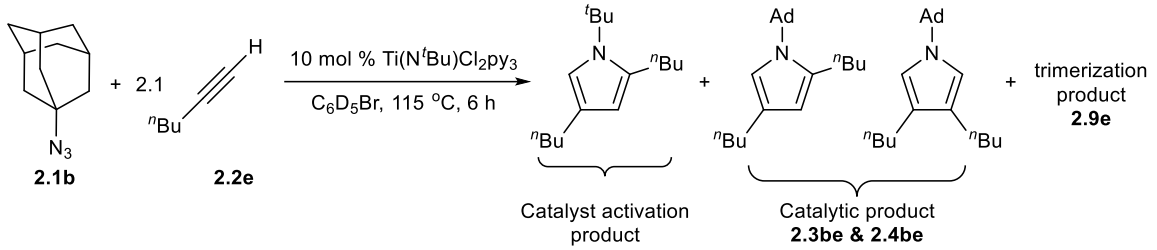

A standard catalytic run with 1-hexyne (48.5 μL, 0.42 mmol, 2.1 equiv), 1-azidoadamantane (35 mg, 0.2 mmol, 1.0 equiv) and 0.5 mL of stock solution (terminal alkyne screen) was conducted. The catalytic mixture was analyzed directly without any further purification and the products were identified *in situ* to give a mixture of products shown above and leftover 1-azidoadamantane.

2,4-di-*n*-butyl-1-(adamantyl)-1*H*-pyrrole (2.3be) (partial)

^{1}H NMR (400 MHz, C$_6$D$_5$Br): δ 6.58 (app m, 1H, *o*-N-pyr-*H*), 5.96 (s, 1H, *m*-N-pyr-*H*), 2.82 – 2.78 (m, 2H, *o*-C*H*$_2$CH$_2$CH$_2$CH$_3$), 2.54 – 2.50 (m, 2H, *m*-C*H*$_2$CH$_2$CH$_2$CH$_3$), 2.07 (s, 6H, Ad-C*H*$_2$), 1.99 (s, 3H, Ad-C*H*), 1.57 (s, 6H, Ad-C*H*$_2$).

This is a partial NMR line list, the remaining *n*-butyl peaks are hidden under other peaks.

3,4-di-*n*-butyl-1-(adamantyl)-1*H*-pyrrole (2.4be) (partial)

^{1}H NMR (400 MHz, C$_6$D$_5$Br): δ 6.58 (app m, 2H, *o*-N-pyr-*H*), 2.70 – 2.66 (m, 2H, *m*-C*H*$_2$CH$_2$CH$_2$CH$_3$).

This is a partial NMR line list, the remaining adamantyl and *n*-butyl peaks are hidden under other peaks.

The pyr-*H* peak for both regioisomers overlap at δ 6.58 ppm in C$_6$D$_5$Br. In CDCl$_3$, the peaks appear as two overlapping peaks that correlate to two N peaks in ^{15}N-^{1}H HMBC. To obtain the spectra in CDCl$_3$, the catalytic reaction was ran as described above in the absence of internal standard (Ph$_3$CH). Following which, the reaction was dried *in vacuo* and retaken up in CDCl$_3$ without any further purification.

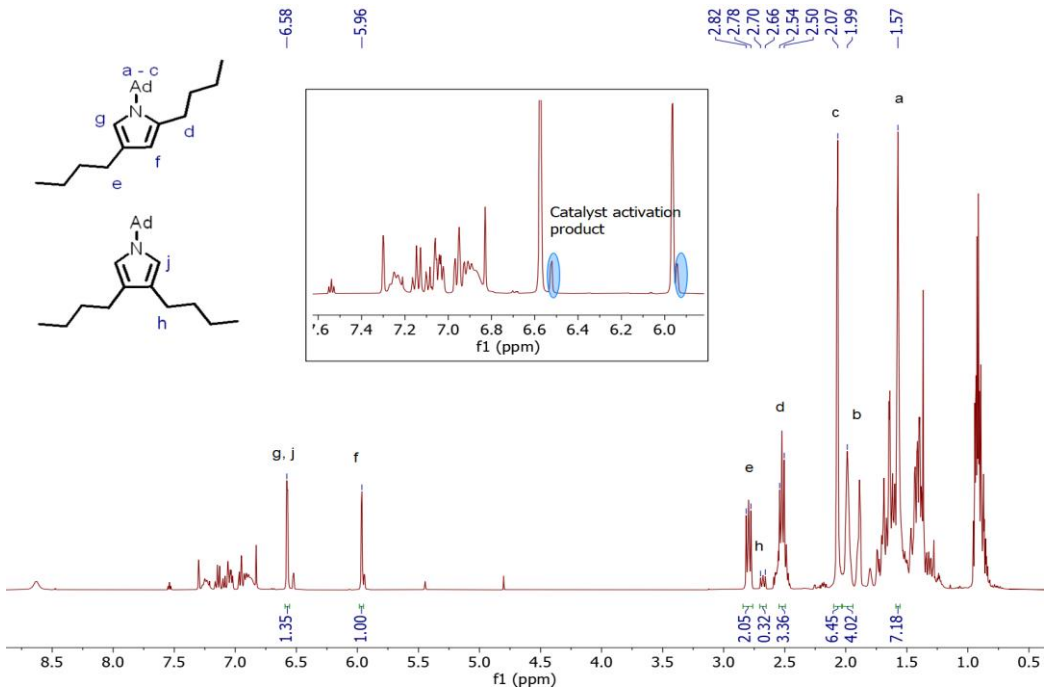

Figure 2.89 ^{1}H NMR spectrum of 1-hexyne reaction with 1-azidoadamantane in C_6D_5Br. *Taken from XYS04014_B.*

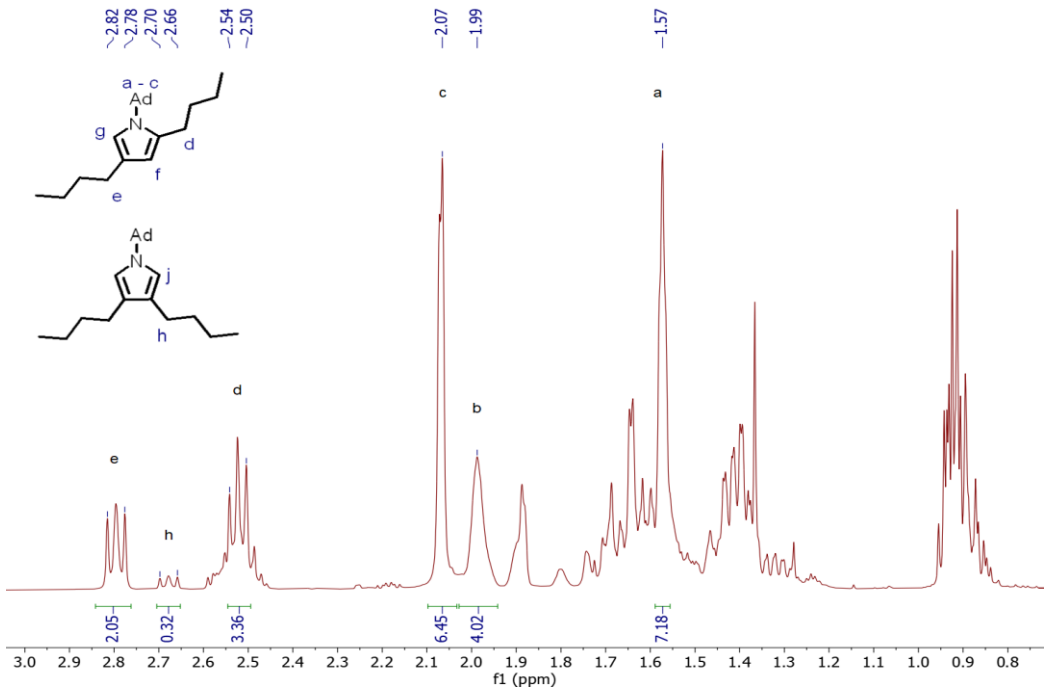

Figure 2.90 Zoom-in ^{1}H NMR spectrum of 1-hexyne reaction with 1-azidoadamantane in C_6D_5Br. *Taken from XYS04014_B.*

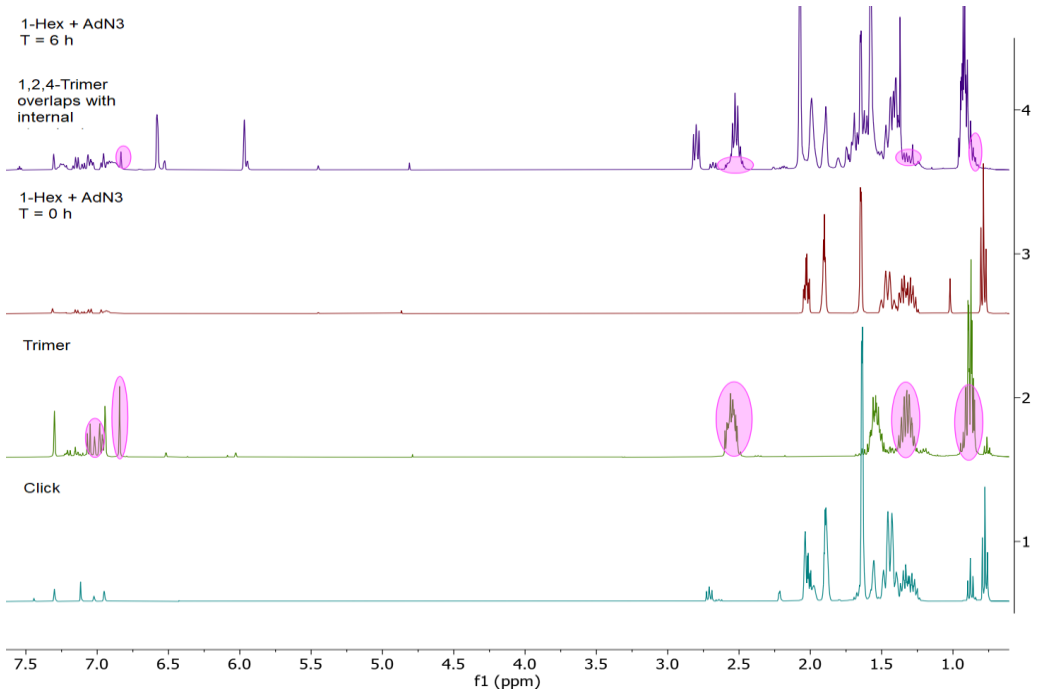

Figure 2.91 Stacked ^{1}H NMR spectrum of 1-hexyne reaction with 1-azidoadamantane t = 6 h (4), t = 0 h (3), trimerization reaction (2) and click reaction (1) in C_6D_5Br. *Taken from XYS04014_B and XYS04038_B.*

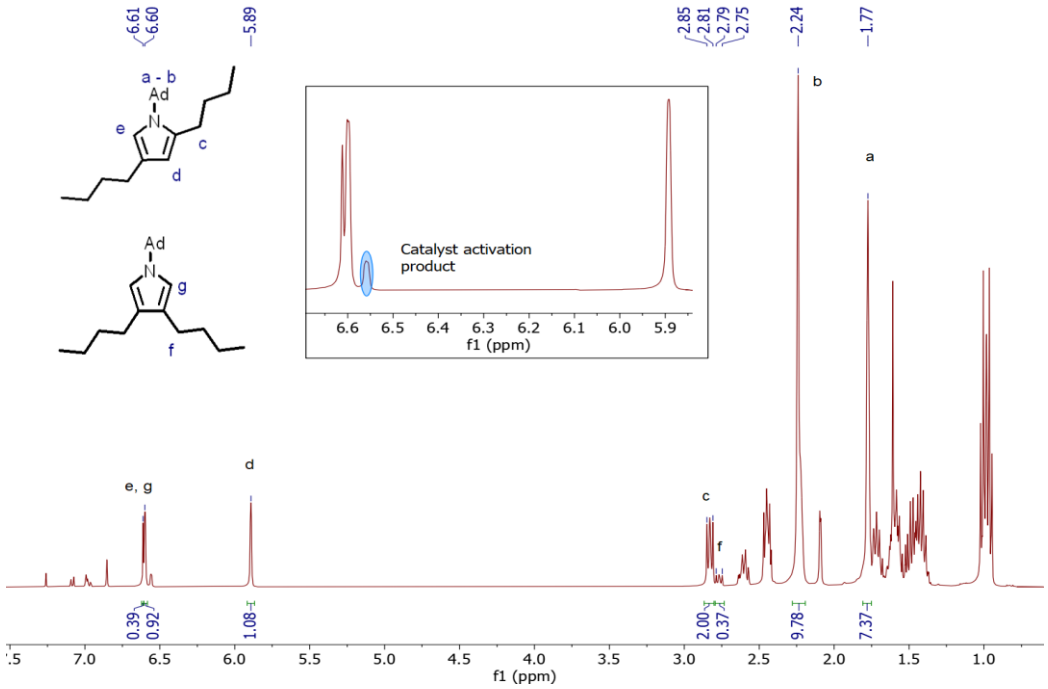

Figure 2.92 ^{1}H NMR spectrum of 1-hexyne reaction with 1-azidoadamantane in $CDCl_3$. *Taken from XYS04036_4H.*

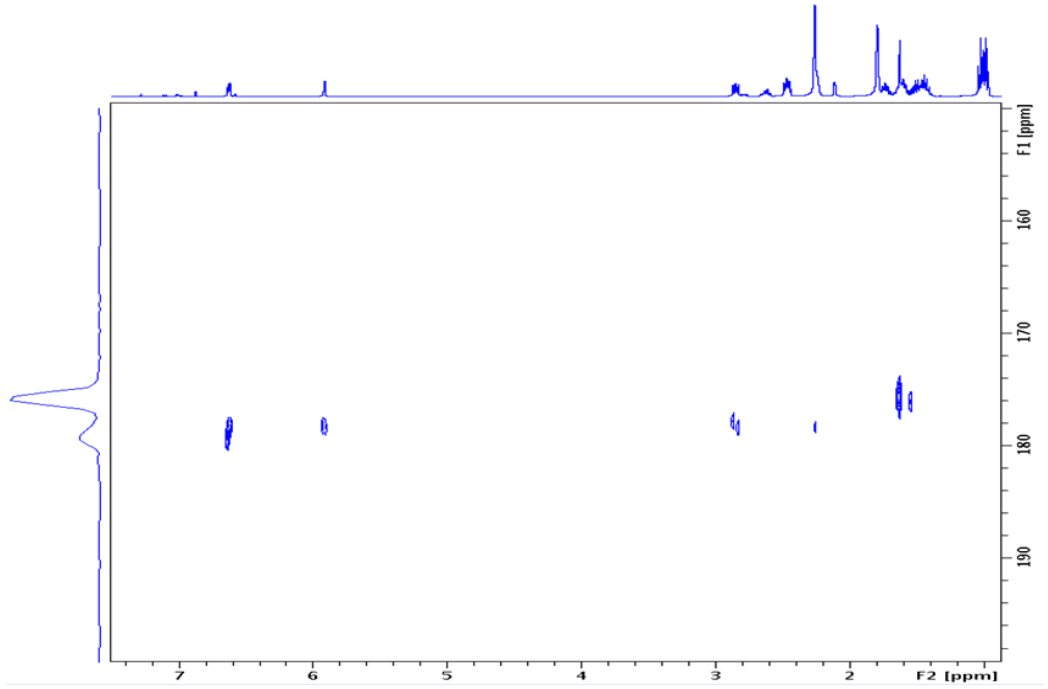

Figure 2.93 ^{15}N-^{1}H HMBC NMR spectrum of 1-hexyne reaction with 1-azidoadamantane in $CDCl_3$. *Taken from XYS04036_1NHMBC.*

NMR analysis of *p*-tolylacetylene and 1-azidoadamantane reaction (Table 2.2, Entry 2)

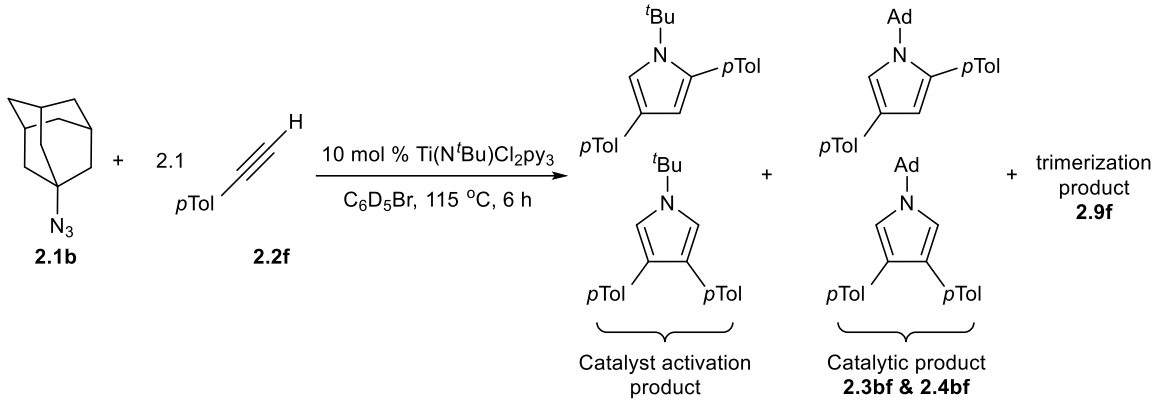

A standard catalytic run with *p*-tolylacetylene (53.5 μL, 0.42 mmol, 2.1 equiv), 1-azidoadamantane (36 mg, 0.2 mmol, 1.0 equiv) and 0.5 mL of stock solution (terminal alkyne screen) was conducted. The catalytic mixture was analyzed directly without any further purification and the products were identified *in situ* to give a mixture of products shown above and leftover starting materials.

2,4-di-*p*-tolyl-1-(adamantyl)-1*H*-pyrrole (2.3bf) (partial)

^{1}H NMR (500 MHz, C$_6$D$_5$Br): δ 2.24 (s, 3H, *o*-C$_6$H$_4$-C*H*$_3$), 2.21 (s, 6H, *m*-N-pyr-C$_6$H$_4$-C*H*$_3$), 1.92 (m, 6H, Ad-C*H*$_2$), 1.65 – 1.64 (m, 6H, Ad-C*H*$_2$).

The peak at δ 2.21 overlaps with that of the other pyrrole regioisomer. This is a partial NMR line list, the remaining peaks are either buried under other products or cannot be positively identified in the reaction mixture.

3,4-di-*p*-tolyl-1-(adamantyl)-1*H*-pyrrole (2.4bf) (partial)

^{1}H NMR (500 MHz, C$_6$D$_5$Br): δ 6.93 (s, 2H, *o*-N-pyr-*H*), 2.21 (s, 6H, *o*-N-pyr-C$_6$H$_4$-C*H*$_3$), 2.05 – 2.04 (m, 6H, Ad-C*H*$_2$), 2.00 (br s, 3H, Ad-C*H*), 1.44 (s, 6H, Ad-C*H*$_2$).

The peak at δ 2.21 overlaps with that of the other pyrrole regioisomer. This is a partial NMR line list, the remaining peaks are either buried under other products or cannot be positively identified in the reaction mixture.

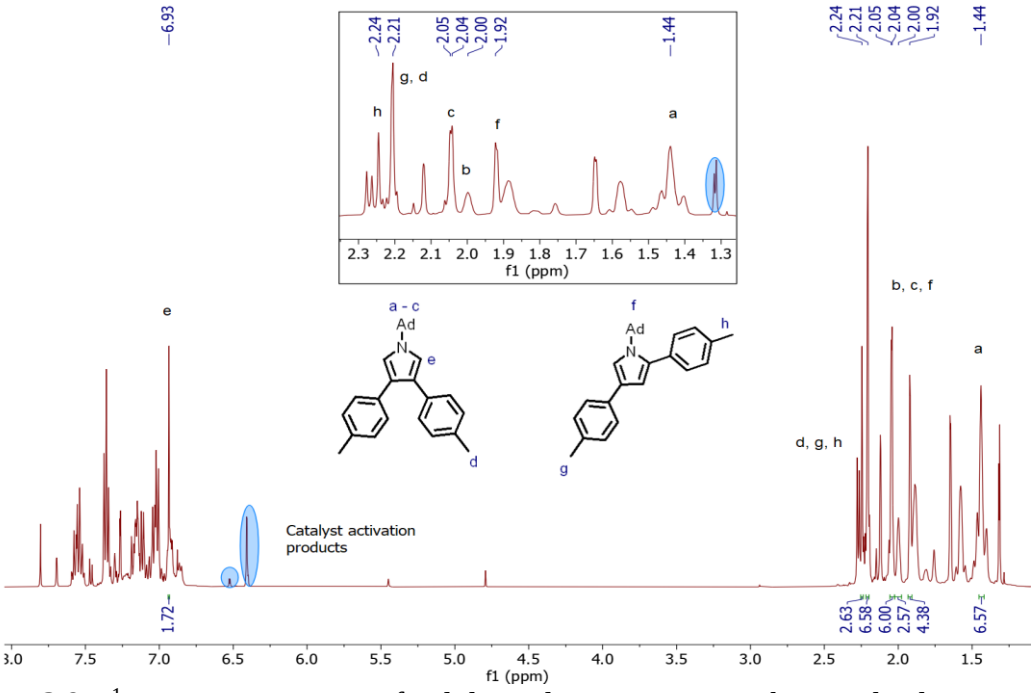

Figure 2.94 ^{1}H NMR spectrum of tolylacetylene reaction with 1-azidoadamantane in C_6D_5Br. *Taken from XYS04059_B.*

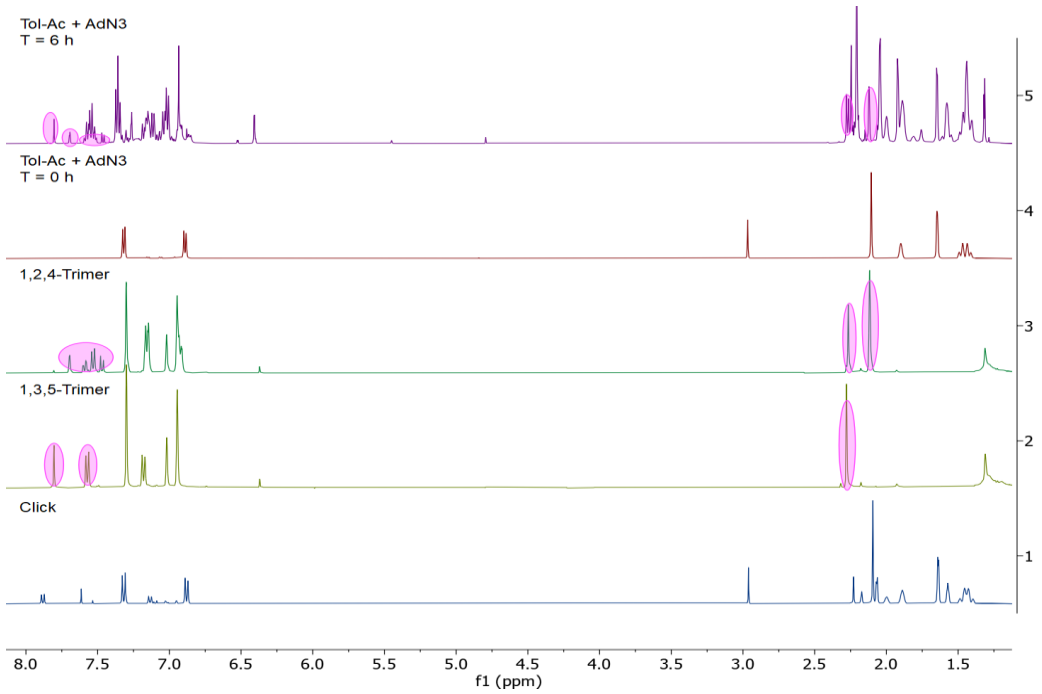

Figure 2.95 Stacked ^{1}H NMR spectrum of tolylacetylene reaction with 1-azidoadamantane t = 6 h (5), t = 0 h (4), 1,2,4-trimer (3), 1,3,5-trimer (2) and click reaction (1) in C_6D_5Br. *Taken from XYS04059_B, XYS03158_3H, XYS03155_4H and XYS04038_D.*

NMR analysis of (*t*-butyl)acetylene and (*p*-tolyl)azide reaction (Table 2, Entry 3)

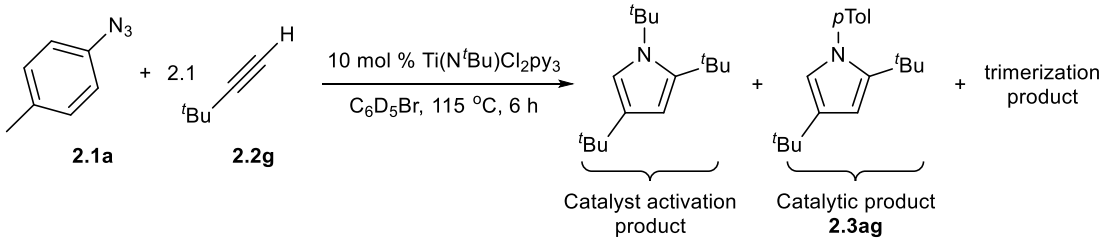

A standard catalytic run with (*t*-butyl)acetylene (54 µL, 0.44 mmol, 2.1 equiv), (*p*-tolyl)azide (28 mg, 0.21 mmol, 1.0 equiv) and 0.5 mL of stock solution (terminal alkyne screen) was conducted. The catalytic mixture was analyzed directly without any further purification and the products were identified *in situ* to give a mixture of products shown above, leftover starting materials and azide decomposition products.

2,4- di-(*t*-butyl)-1-(*p*-tolyl)-1*H*-pyrrole (2.3ag) (partial)

^{1}H NMR (400 MHz, C_6D_5Br): δ 6.14 (d, $^{4}J_{HH}$ = 2.1 Hz, 1H, *m*-N-pyr-*H*), 2.17 (s, 3H, NC_6H_4-CH_3), 1.30 (s, 9H, *o*-N-pyr-^{t}Bu), 1.16 (s, 9H, *m*-N-pyr-^{t}Bu).

The peak at δ 1.16 overlaps with the remaining starting material, (*t*-butyl)acetylene. This is a partial NMR line list, the remaining aromatic peaks cannot be positively identified in the reaction mixture.

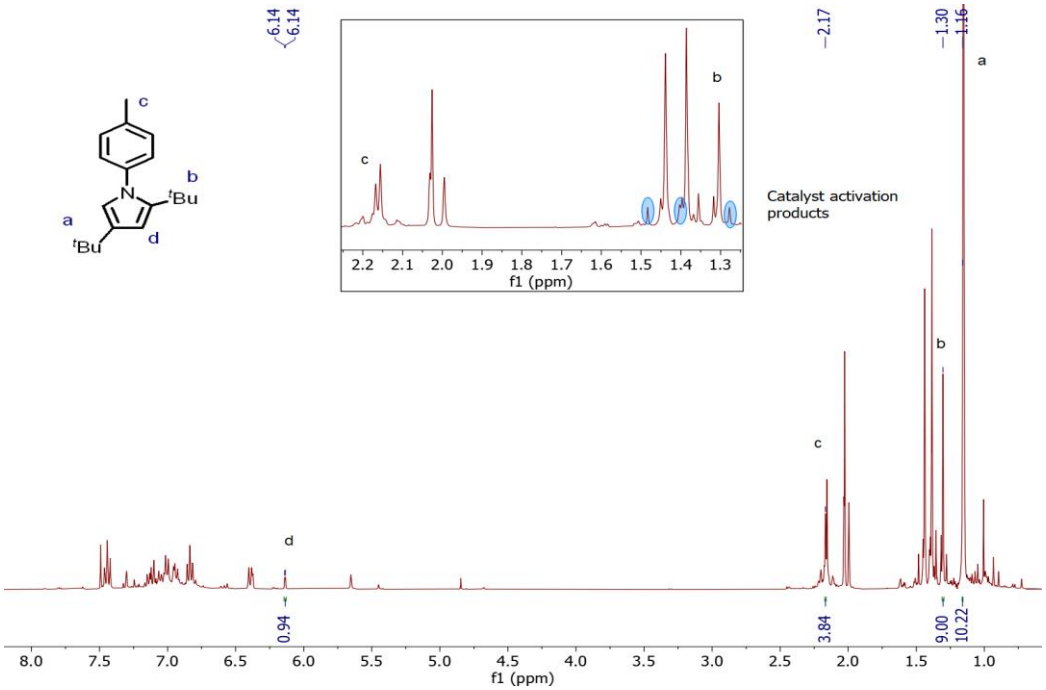

Figure 2.96 ^{1}H NMR spectrum of (*t*-butyl)acetylene reaction with 1-azidoadamantane in C_6D_5Br. *Taken from XYS04014_C.*

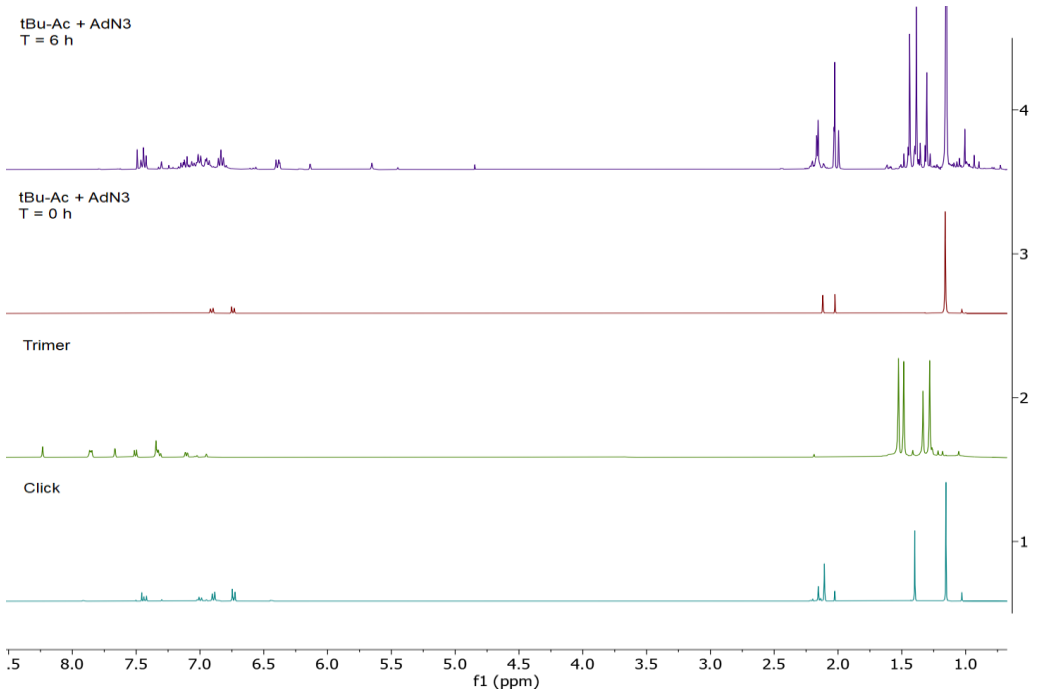

Figure 2.97 Stacked ^{1}H NMR spectrum of (*t*-butyl)acetylene reaction with 1-azidoadamantane t = 6 h (4), t = 0 h (3), trimer reaction (2) and click reaction (1) in C_6D_5Br. *Taken from XYS04014_C, XYS04047_B and XYS04038_F*.

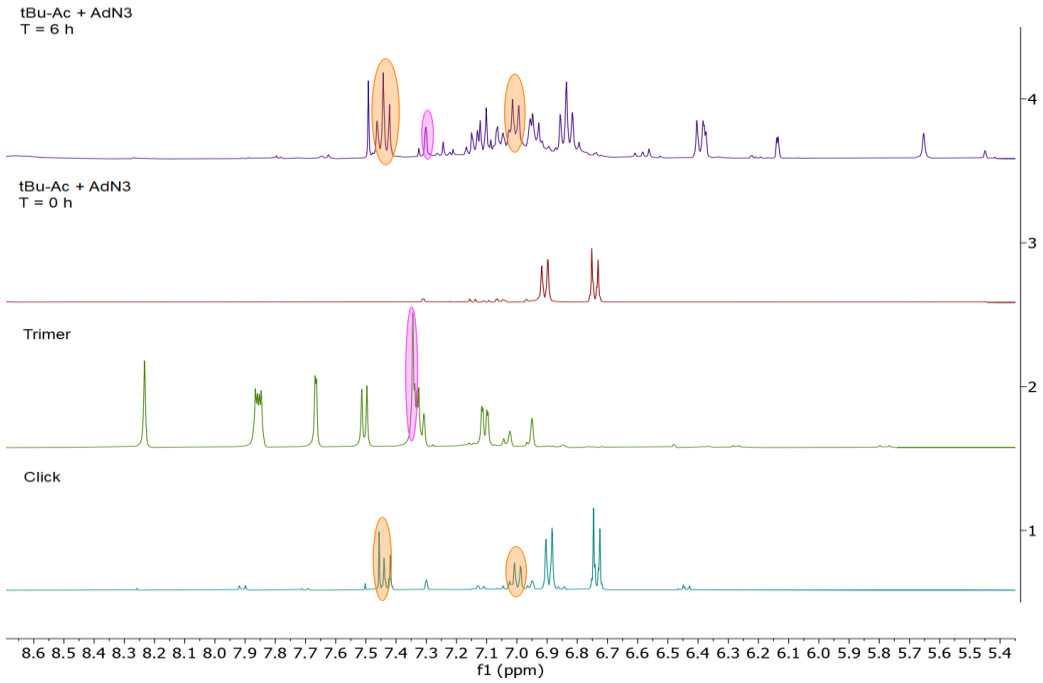

Figure 2.98 Zoom-in stacked ^{1}H NMR spectrum of (*t*-butyl)acetylene reaction with 1-azidoadamantane t = 6 h (4), t = 0 h (3), trimer reaction (2) and click reaction (1) in C_6D_5Br. *Taken from XYS04014_C, XYS04047_B and XYS04038_F*.

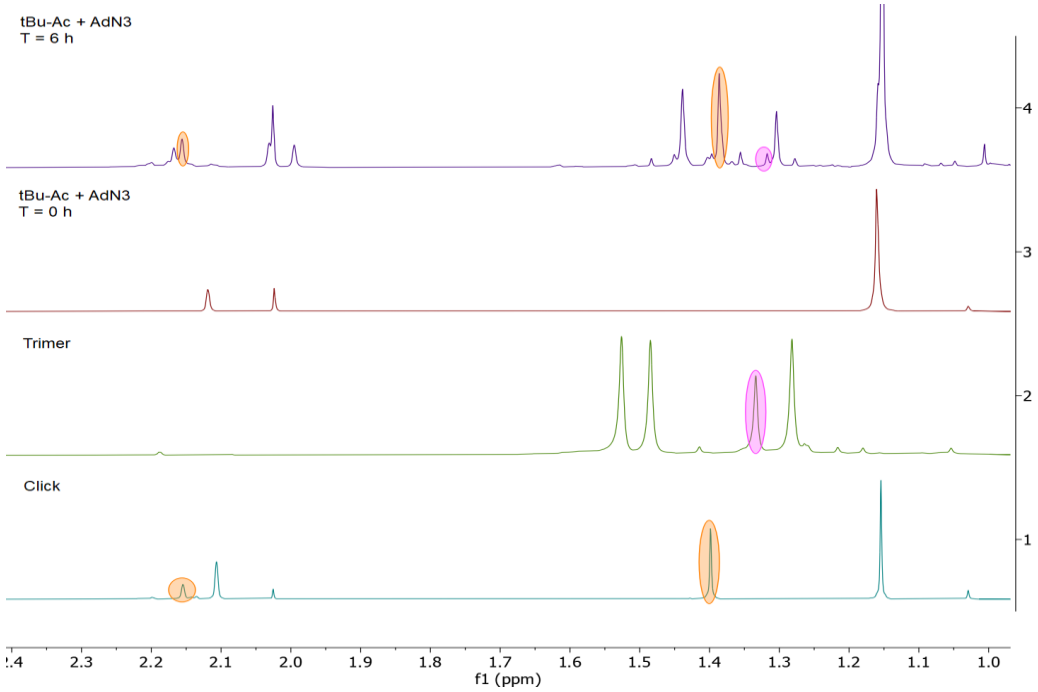

Figure 2.99 Zoom-in stacked ^{1}H NMR spectrum of (t-butyl)acetylene reaction with 1-azidoadamantane t = 6 h (4), t = 0 h (3), trimer reaction (2) and click reaction (1) in C_6D_5Br. *Taken from XYS04014_C, XYS04047_B and XYS04038_F.*

NMR analysis of trimethylsilylacetylene and 1-azidoadamantane reaction (Table 2.2, Entry 4)

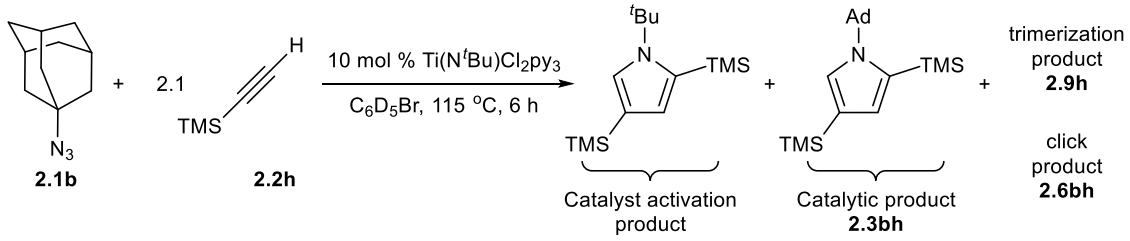

A standard catalytic run with (trimethylsilyl)acetylene (58 µL, 0.42 mmol, 2.1 equiv), 1-azidoadamantane (35 mg, 0.2 mmol, 1.0 equiv) and 0.5 mL of stock solution (terminal alkyne screen) was conducted. The catalytic mixture was analyzed directly without any further purification and the products were identified *in situ* to give a mixture of products shown above and leftover starting materials.

2,4-bis-(trimethylsilyl)-1-(adamantyl)-1*H*-pyrrole (2.3bh) (partial)

^{1}H NMR (400 MHz, C_6D_5Br): δ 7.30 (d, $^{4}J_{HH}$ = 1.6 Hz, 1H, *o*-N-pyr-*H*), 6.82 (d, $^{4}J_{HH}$ = 1.6 Hz, 1H, *m*-N-pyr-*H*), 2.04 (m, 6H, Ad-CH_2), 1.58 (br s, 6H, Ad-CH_2), 0.38 (s, 9H, N-pyr-C2-Si(CH_3)$_3$), 0.29 (s, 9H, N-pyr-C4-Si(CH_3)$_3$).

The peak at δ 2.04 overlaps with that of the click product. This is a partial NMR line list, the remaining adamantyl peak is buried under other products.

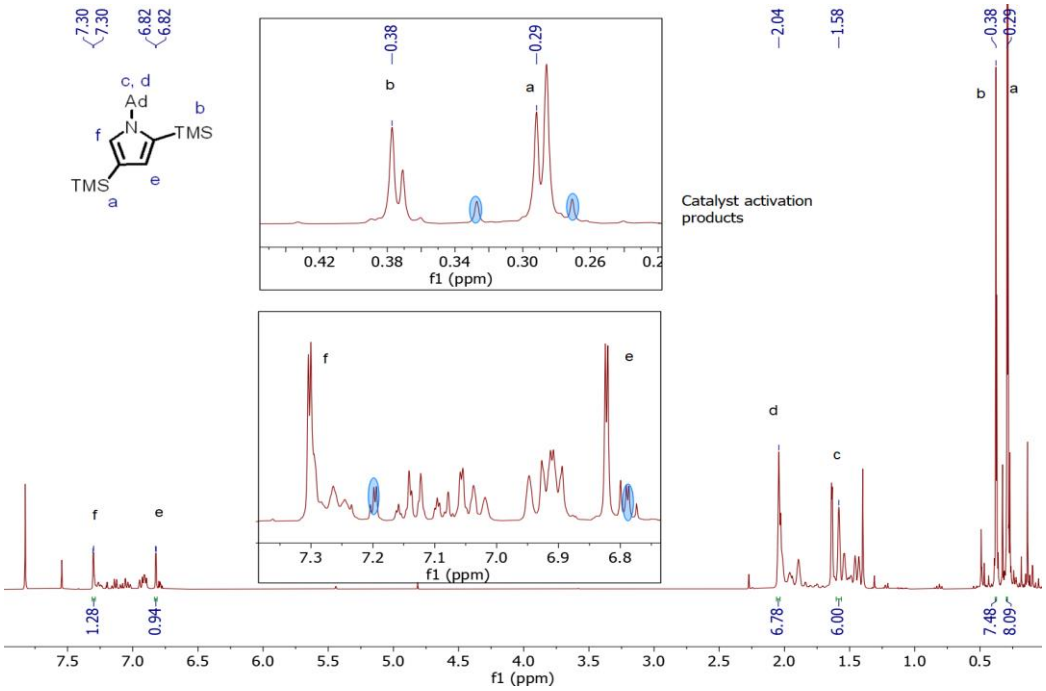

Figure 2.100 ^{1}H NMR spectrum of (trimethylsilyl)acetylene reaction with 1-azidoadamantane in C_6D_5Br. *Taken from XYS04015_B.*

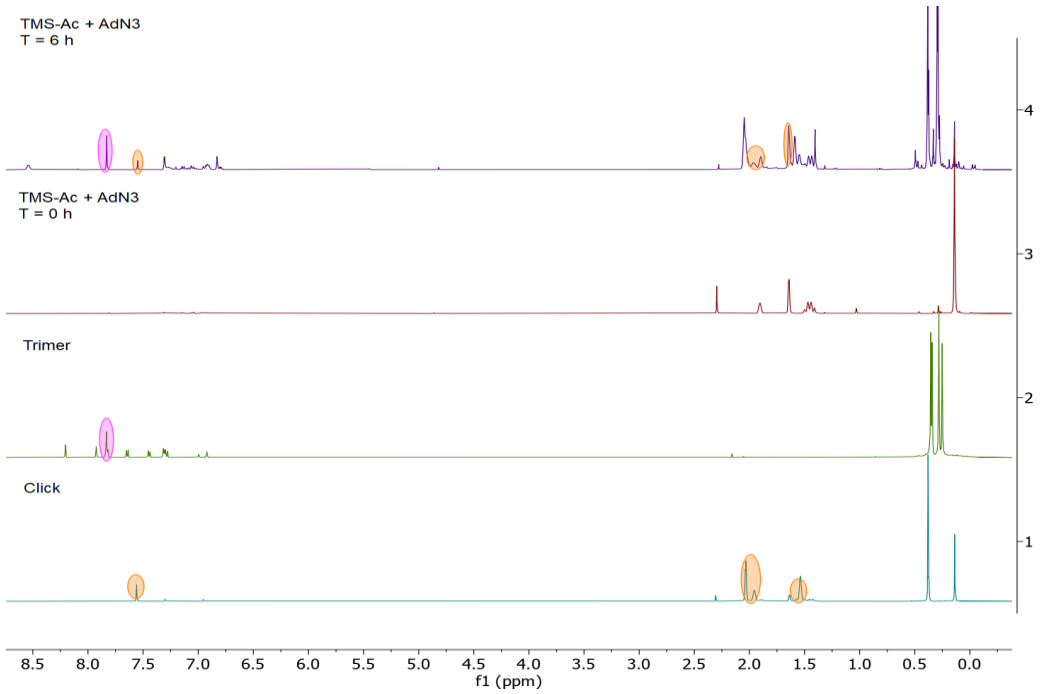

Figure 2.101 Stacked ^{1}H NMR spectrum of (trimethylsilyl)acetylene reaction with 1-azidoadamantane t = 6 h (4), t = 0 h (3), trimer reaction (2) and click reaction (1) in C_6D_5Br. *Taken from XYS04015_B, XYS04047A and XYS04038_E.*

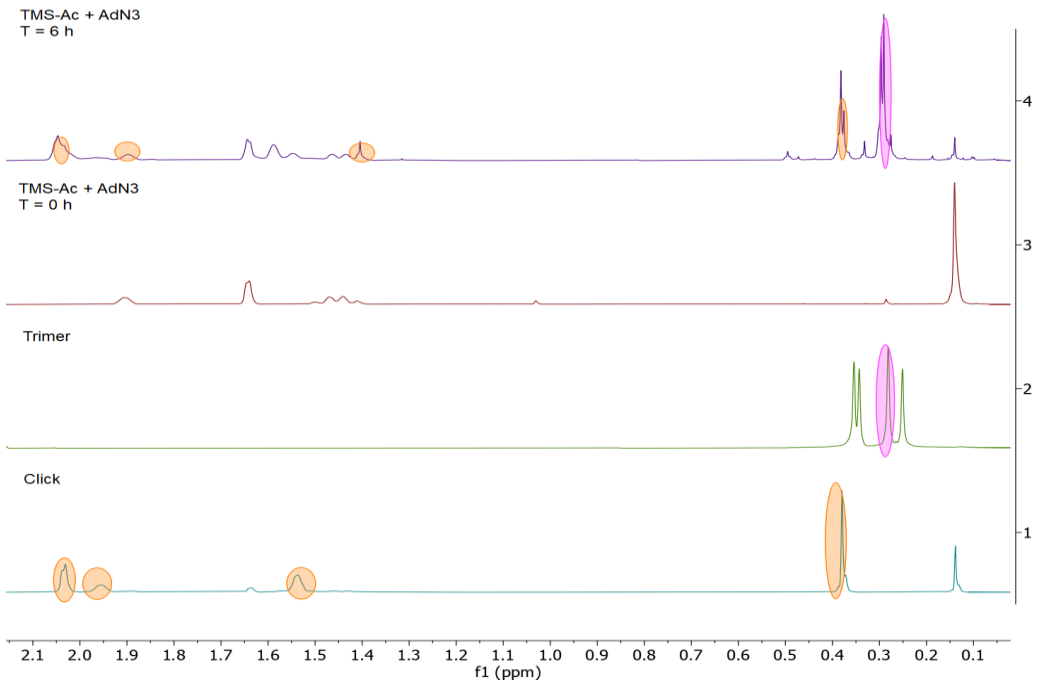

Figure 2.102 Zoom-in stacked ^{1}H NMR spectrum of (trimethylsilyl)acetylene reaction with 1-azidoadamantane t = 6 h (4), t = 0 h (3), trimer reaction (2) and click reaction (1) in C_6D_5Br. *Taken from XYS04015_B, XYS04047A and XYS04038_E.*

NMR analysis of 1,7-octadiyne and 1-azidoadamantane reaction (Table 2.2, Entry 5)

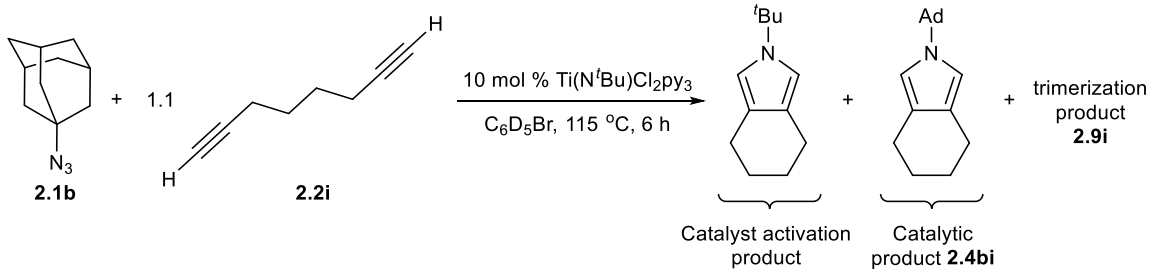

A standard catalytic run with 1,7-octadiyne (28 µL, 0.21 mmol, 1.1 equiv), 1-azidoadamantane (35 mg, 0.20 mmol, 1.0 equiv) and 0.5 mL of stock solution (terminal alkyne screen) was conducted. The catalytic mixture was analyzed directly without any further purification and the products were identified *in situ* to give a mixture of products shown above and leftover starting materials.

2-adamantyl-4,5,6,7-tetrahydro-2*H*-isoindole (2.4bi) (partial)

^{1}H NMR (500 MHz, C_6D_5Br): δ 6.47 (s, 2H, pyr-*H*), 2.64 (m, 4H, pyr-CH_2), 1.97 (s (br), 3H, Ad), 1.87 (d, $^{3}J_{HH}$ = 3.0 Hz, 6H, N-C-(CH_2)$_3$) 1.70 (m, 4H, pyr-CH_2-CH_2).

All peaks other than the aromatic peak at δ 6.47 have some degree of overlap with starting material or trimerization.

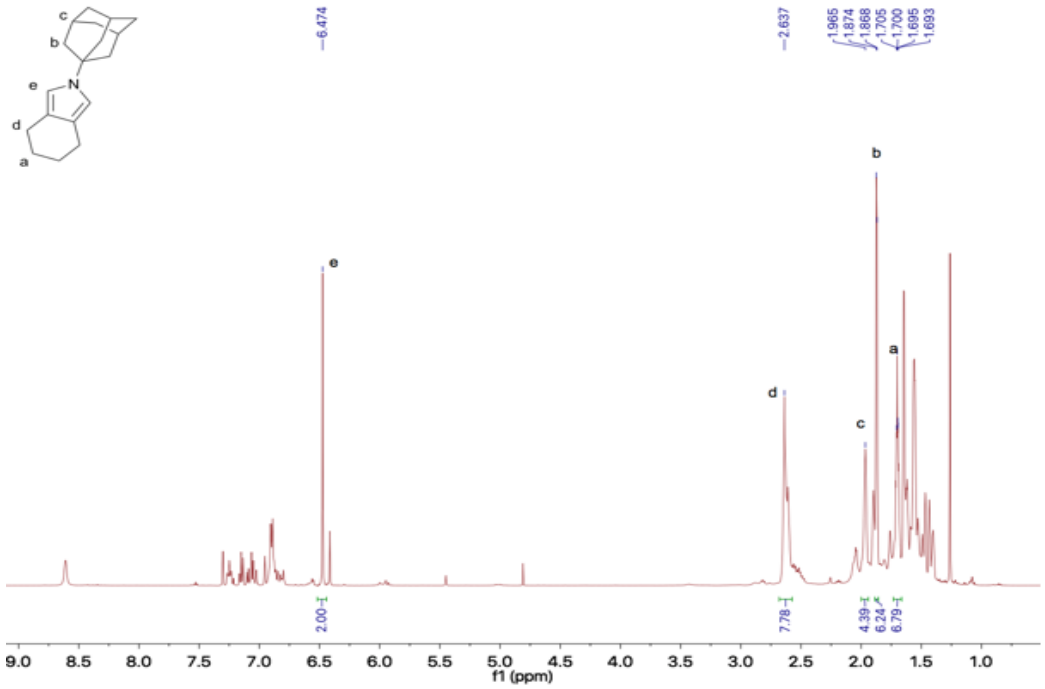

Figure 2.103 ^{1}H NMR spectrum of 1,7-octadiyne reaction with 1-azidoadamantane in C_6D_5Br. *Taken from AJP05034.*

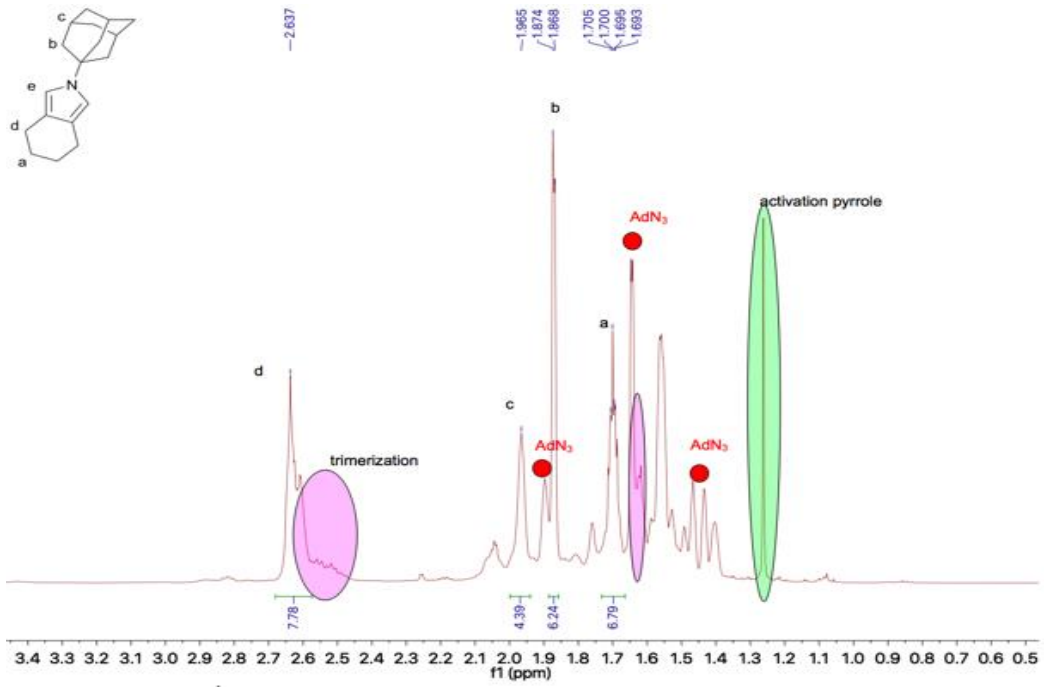

Figure 2.104 Zoom-in ^{1}H NMR spectrum of 1,7-octadiyne reaction with 1-azidoadamantane in C_6D_5Br. *Taken from AJP05034.*

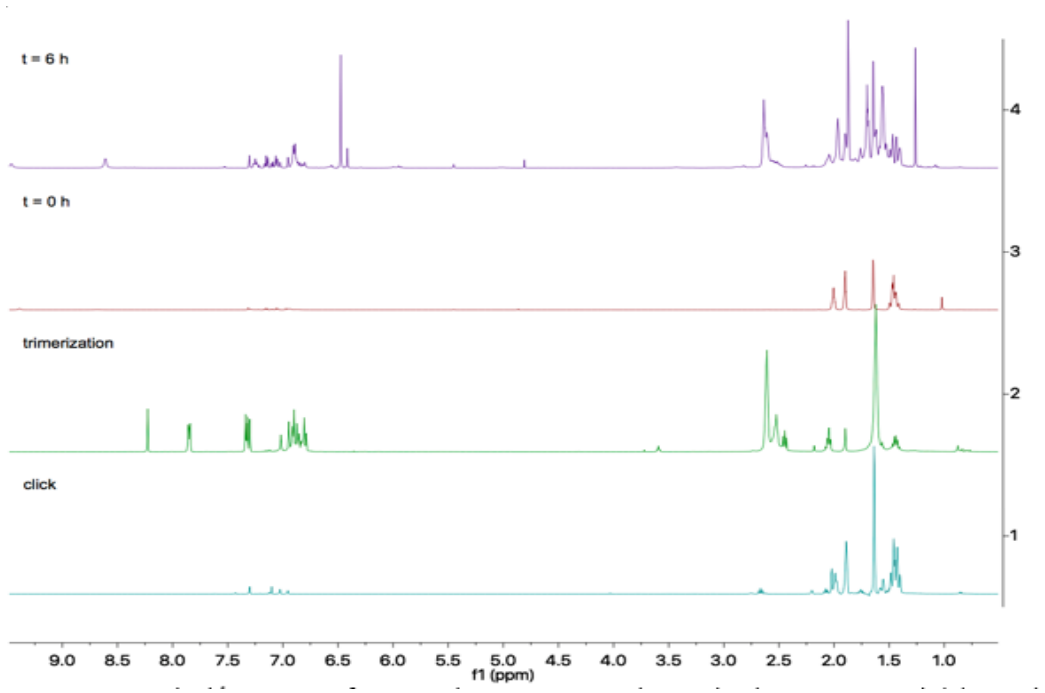

Figure 2.105 Stacked ^{1}H spectra of 1,7-octadiyne reaction with 1-azidoadamantane t = 6 h (4), t = 0 h (3), trimer (2) and click reaction (1) in C_6D_5Br. *Taken from AJP05034.*

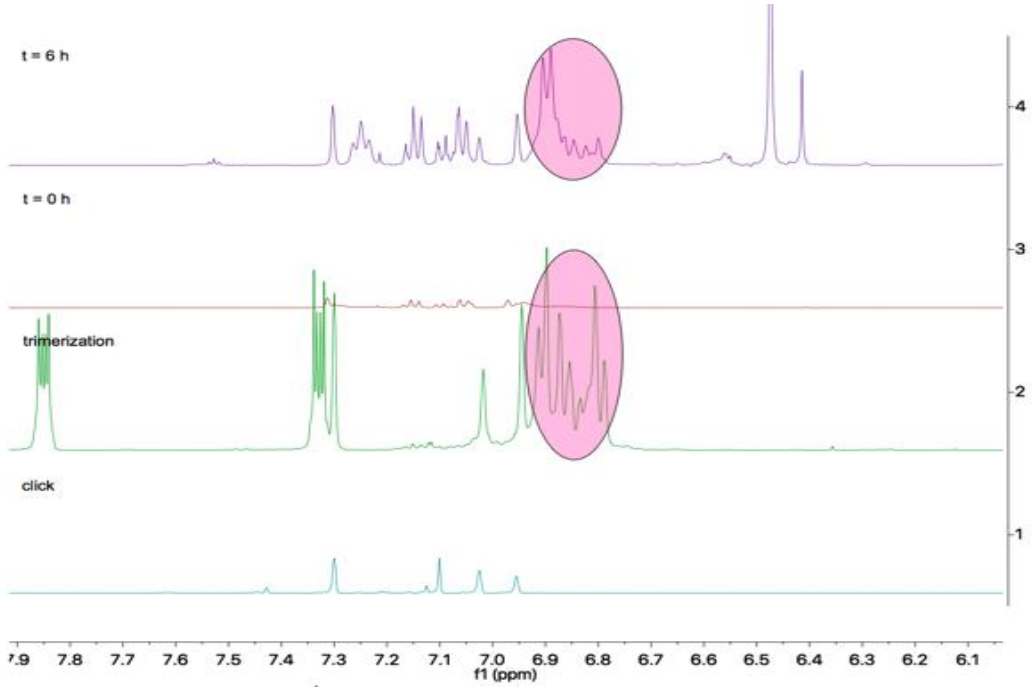

Figure 2.106 Zoom-in stacked ^{1}H spectra of 1,7-octadiyne reaction with 1-azidoadamantane t = 6 h (4), t = 0 h (3), trimer (2) and click reaction (1) in C_6D_5Br. *Taken from AJP05034.*

Table 2.5 Terminal alkyne scope triazole yield, trimer yield and mass balance data.

Table 2, Entry #	Alkyne	Triazole yield (%) 6	Trimer yield (%)[b] 9	Azide mass balance (%)	Alkyne mass balance (%)
1	1-Hexyne **2e**	10	24[c]	quant.	quant.
2	(*p*-tolyl)acetylene **2f**	0	26	87	96
3	(*t*-butyl)acetylene **2g**	12	1	20	53
4	(trimethylsilyl)-acetylene **2h**	20	30	93	95
5[a]	1,7-octadiyne **2i**	0	56	68	97

Conditions: AdN_3 (0.2 mmol, 1 equiv), alkyne (0.42 mmol, 2.1 equiv), 10 mol % $Ti(N^tBu)Cl_2py_3$, 115 °C, 6 h, 0.5 ml C_6D_5Br, average of 2 runs. [a]For **2i** (0.21 mmol, 1.05 equiv) was used. [b]Trimer yields are calculated with respect to alkyne. [c]1,2,4-trimer peak overlaps with the internal standard on NMR, results were supplemented by GC-FID.

Table 2.6 Azide scope with terminal alkynes.

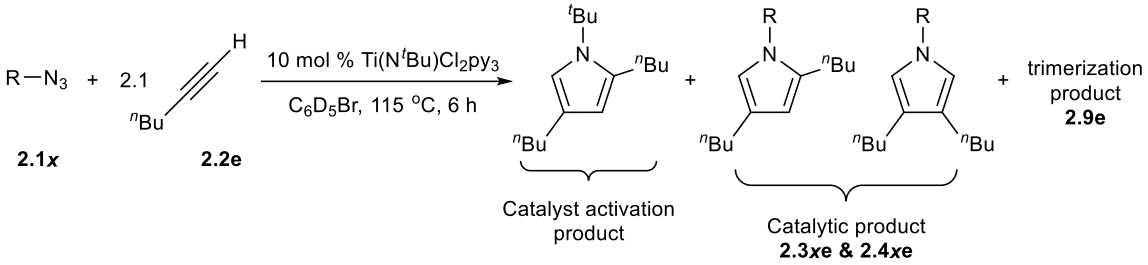

Entry #	Azide	Catalytic pyrrole yield (%)[a] 3	Trimer yield (%)[b] 9
1	Ad **1b**	65	8
2	Ph	38	8
3	Tol **1a**	40	8
4	*n*-Dec **1c**	7	32
5	Bn **1d**	0	20

Conditions: Azide (0.2 mmol, 1 equiv), 1-hexyne (0.42 mmol, 2.1 equiv), 10 mol % $Ti(N^tBu)Cl_2py_3$, 115 °C, 6 h, 0.5 ml C_6D_5Br. [a]Pyrrole yields are calculated with respect to azide. [b]Trimer yields are calculated with respect to alkyne.

Chapter 3: Generation of Ti^{II} Alkyne Trimerization Catalysts in the Absence of Strong Metal Reductants

Reproduced in part with permission from:

See, X. Y.; Beaumier, E. P.; Davis-Gilbert, Z. W.; Dunn, P. L.; Larsen, J. A.; Pearce, A. J.; Wheeler, T. A.; Tonks, I. A.*, Generation of Ti^{II} Alkyne Trimerization Catalysts in the Absence of Strong Metal Reductants. *Organometallics* **2017,** *36*, 1383-1390.

3.1 Overview

Low-valent Ti^{II} species have typically been synthesized by the reaction of Ti^{IV} halides with strong metal reductants. Herein we report that Ti^{II} species can be generated simply by reacting Ti^{IV} imido complexes with 2 equivalents of alkyne, yielding a metallacycle that can reductively eliminate pyrrole while liberating Ti^{II}. In order to probe the generality of this process, Ti^{II}-catalyzed alkyne trimerization reactions were carried out with a diverse range of Ti^{IV} precatalysts.

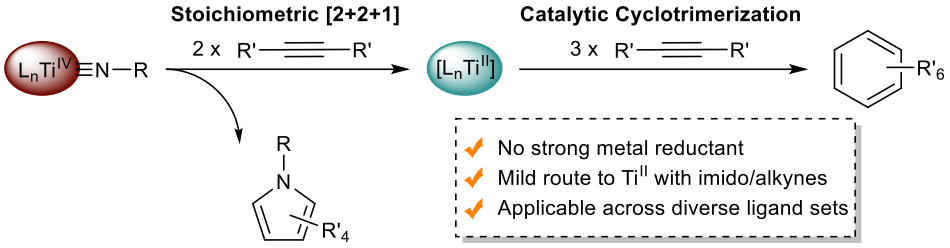

Figure 3.1 General methodology of obtaining an active Ti^{II} intermediate *via* the coupling of Ti^{IV} imido and 2 alkynes.

3.2 Introduction

Low-valent Ti reagents have played an important role in many molecular transformations over the past 50 years.[22, 129-131] In particular, Ti^{II} intermediates have been invoked in a rich and varied range of stoichiometric and catalytic reactions: N_2 fixation,[7, 132-133] McMurry coupling,[130, 134-135] alkyne cyclotrimerization,[22, 136-138] Pauson−Khand cycloaddition,[139-141] cyclopropanation,[142-143] and oxidative addition reactions with many other electrophiles.[45, 144-145] Formally, Ti^{II} coordination complexes are fairly uncommon because of the extremely high thermodynamic stability of the Ti^{IV} oxidation state. Nevertheless, discrete Ti^{II} complexes have been isolated and characterized across diverse ligand sets: cyclopentadienyl,[133, 146] calixarene,[136-138, 147] isocyanide,[51] porphyrin,[144, 148] pyridine,[45] and 1,2-bis(dimethylphosphino)ethane.[149-150] Similarly, "masked" Ti^{II} complexes have also been reported in which the low-valent state is stabilized by strong π-acceptors such as alkyne,[151-153] alkene,[154-156] and carbonyl.[157]

Given that they are highly reducing, Ti^{II} reagents have typically been formed from the reaction of Ti^{IV} halide precursors with powerful reductants: KC_8,[7, 45, 132-133] $LiAlH_4$,[148]

Na/Hg,[158] and Mg.[159-160] Recently, we have reported several catalytic oxidative C-N bond forming reactions that proceed through a formal Ti^{II}/Ti^{IV} redox couple (Figure 3.2). These reactions presumably generate a Ti^{II} intermediate in the absence of a strong metal reductant by coupling a Ti^{IV} imido unit with two alkynes (or an alkyne and an alkene).[79, 83]

Intrigued by this unusual and mild route to form Ti^{II} species *in situ*, we have set out to demonstrate the generality of forming Ti^{II} species from the reaction of alkynes with Ti^{IV} imido complexes. These transient Ti^{II} complexes were then examined for their competency as catalysts for alkyne trimerization. Herein we report that many diverse Ti imido precatalyst structures are capable of generating Ti^{II} intermediates and subsequently trimerizing alkynes. By comparing structurally similar catalyst classes, we have drawn several qualitative conclusions and empirical trends.

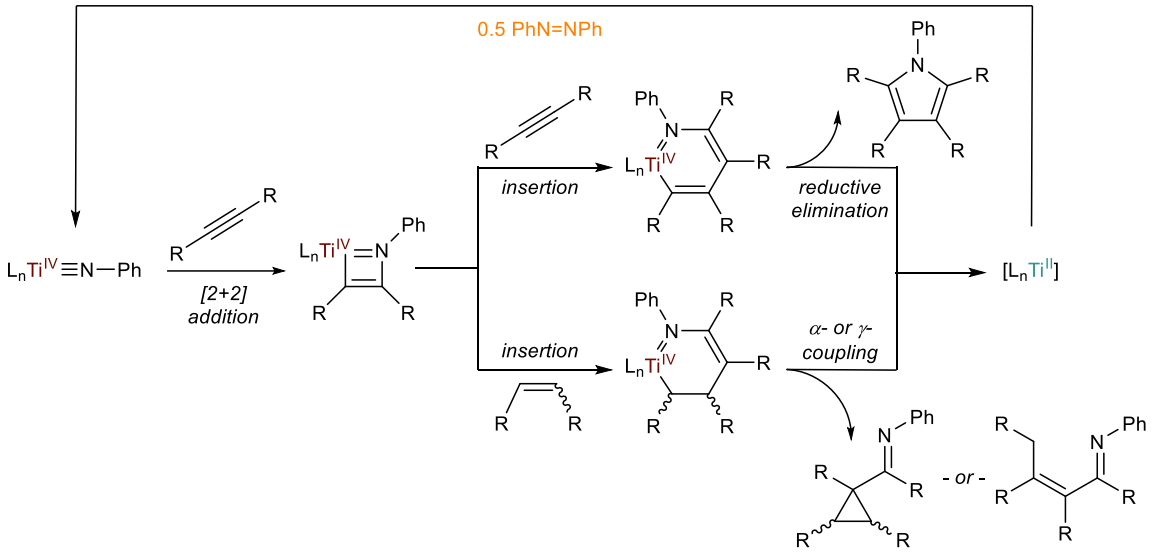

Figure 3.2 Previously reported Ti^{II}/Ti^{IV} redox catalytic reactions.

3.3 Results and Discussion

We began our investigation by synthesizing a diverse set of Ti imido complexes based mostly on ligand architectures that are well-established in titanium-catalyzed hydroamination and polymerization reactions (Figure 3.3). These ligands can be divided into several categories: first, complexes varying in simple monoanionic X-type ligands: halides (**3.1-3.3**),[122] pyrrolides (**3.4-3.5**),[161-162] and aryloxides (**3.6-3.7**);[163-164] second, polyhapto ligands: 1,4-bis(trimethylsilyl)cyclooctatetraene (**3.8**),[165] cyclopentadienyl Cp

(**3.9-3.10**),[166] and pentamethylcyclopentadienyl Cp* (**3.11**);[166] third, LX-type bidentate ligands: amidate (**3.12**),[167-168] phenoxyimino (**3.13**),[169] and amidinate (**3.14-3.15**)[170-171] that may be hemilabile; and last, a Zr analogue (**3.16**) included in the series to allow for reactivity comparison within the group 4 triad. In contrast to titanium, Zr^{II} is considerably harder to access.[8, 67, 172-173]

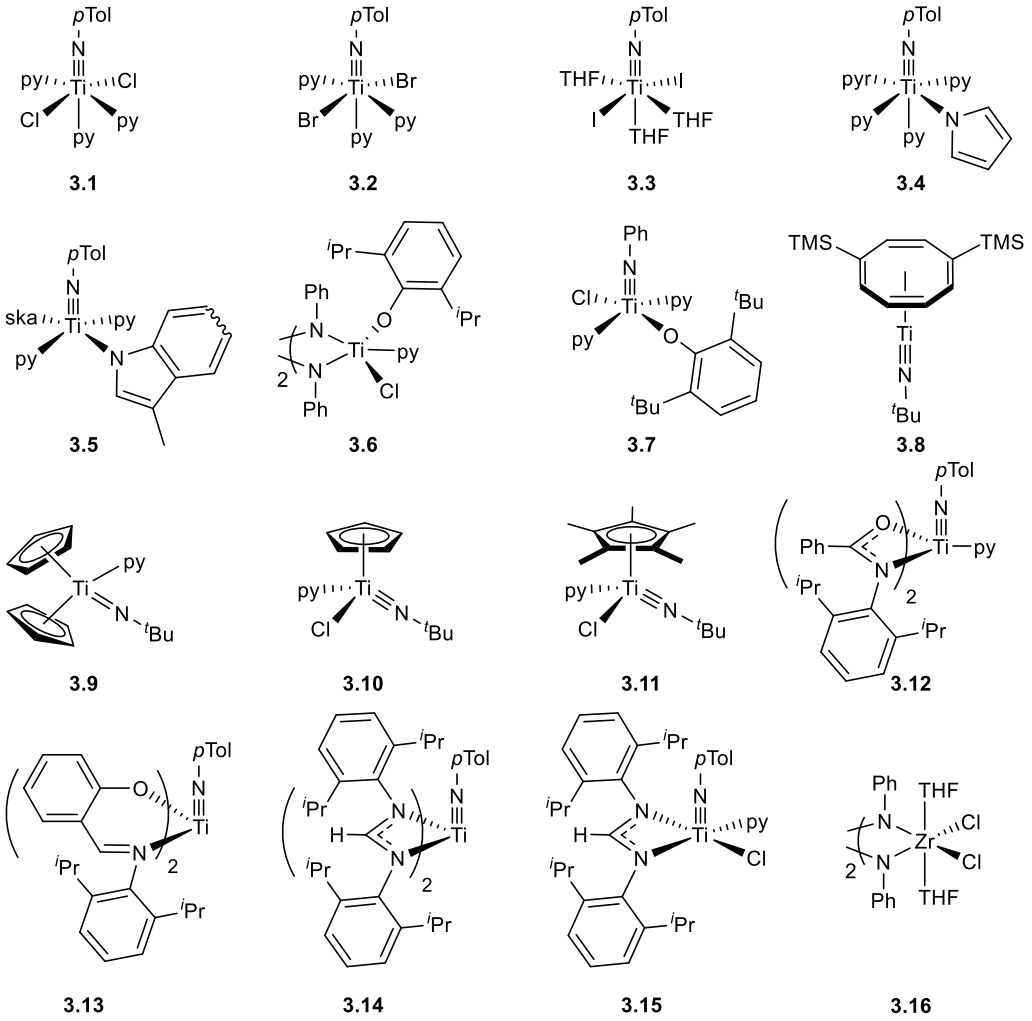

Figure 3.3 Ti and Zr imido precatalysts investigated for the generality of forming M^{II} intermediate.

Based on our previous mechanism for Ti^{II}/Ti^{IV} redox catalysis, Ti^{II} species capable of alkyne trimerization can be generated by the coupling of 2 alkynes with a Ti^{IV} imido and

subsequent elimination of one equivalent of pyrrole per Ti (Figure 3.4, top).[79] This activation process occurs through a [2+ 2] cycloaddition[174] of the Ti^{IV} imido with an alkyne (**3.17**), followed by insertion of the second alkyne into the metallacycle (**3.18**)[175] and finally reductive elimination of pyrrole to yield the Ti^{II} trimerization catalyst.[176] While there may be catalyst-to-catalyst variation in the mechanistic details of trimerization catalysis, Ti^{II} is generally understood[177-179] to trimerize alkynes by first oxidatively coupling two alkynes to yield a metallacyclopentadiene (**3.19**) that can then undergo [4 + 2] cycloaddition with a third alkyne to yield a titananorbornadiene intermediate (**3.20**), which is then displaced by alkyne to liberate the trimerized product (Figure 3.4, bottom). Alternately, the metallacyclopentadiene could insert the third equivalent of alkyne to produce a metallacycloheptatriene (**3.21**), which upon reductive elimination yields the trimerized product. In general, the [4 + 2] mechanism appears to be more broadly invoked,[136] although a universal mechanism for trimerization is unlikely given the diverse range of molecular structures capable of catalyzing this reaction.

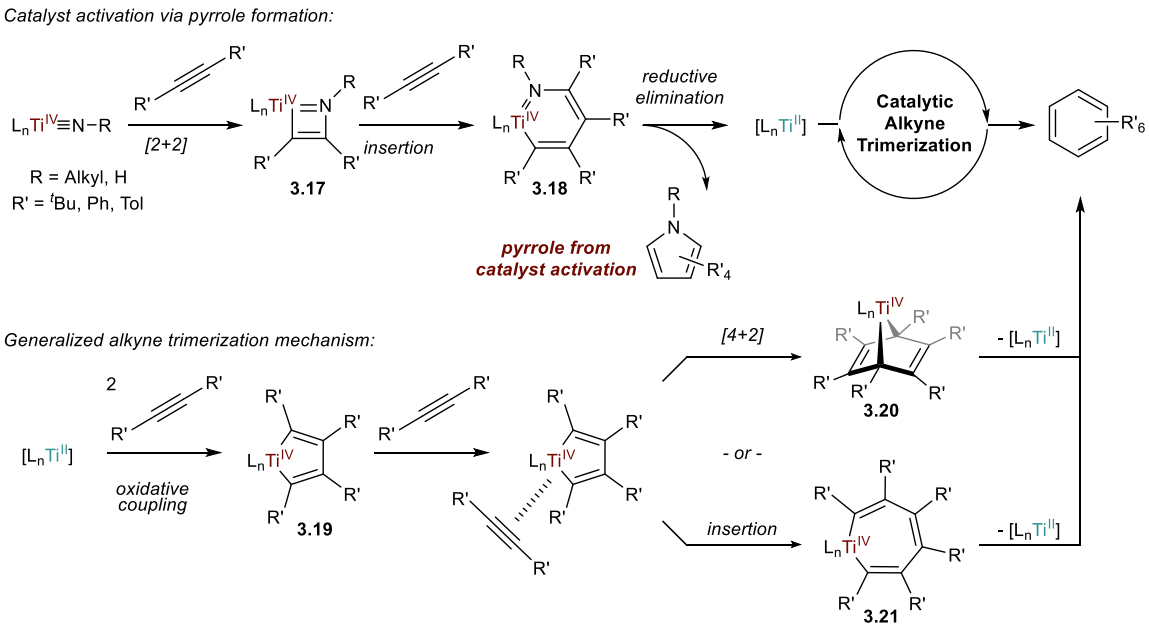

Figure 3.4 Catalytic alkyne trimerization with Ti^{IV} imido catalysts.

Catalytic alkyne trimerization reactions were carried out with 5 mol % of each Ti imido precatalyst and either 1-hexyne or 3-hexyne in C_6D_5Br at 115 °C for 16 h.

Unsymmetrical 1-hexyne can yield two alkyne trimer regioisomers (1,3,5- and 1,2,4-tri-*n*-butylbenzene **3a** and **3b**, respectively) and three pyrrole regioisomers (2,4-, 2,5- and 3,4-di-*n*-butylpyrrole, **3c-3e**, respectively) (Table 3.1). The expected statistical distribution between the two alkyne trimer products is 1 : 3 (**3a : 3b**),[179] while the distribution of pyrrole products is 2 : 1 : 1 (**3c : 3d : 3e**). The 2,4- (**3c**) and 2,5-disubstituted (**3d**) pyrroles were the major products in the reactions reported herein and no significant additional ^{1}H NMR peaks that could plausibly be assigned as the 3,4-regioisomers were observed in any of the catalytic experiments. Where possible, the pyrrole regioisomers were independently synthesized *via* alternate routes to confirm their characterization, although some are inaccessible using modern synthetic techniques (See Table 3.1 and Section 3.5.3 for details). 3-Hexyne can only yield hexaethylbenzene **3f** and 2,3,4,5-tetraethylpyrrole **3g** (Table 3.2).

Given that the pyrrole byproduct formation is stoichiometric with respect to Ti^{II} formation, the amount of Ti^{IV} activated toward catalysis can be determined by quantifying the amount of pyrrole formed in a given reaction. Additionally, control experiments with structurally analogous Ti^{IV} halide precatalysts yield no trimerization (see Table 3.4), indicating that a Lewis acid mechanism for trimerization can be ruled out and that all productive catalysis most likely occurs through Ti^{II}. As a result, one can gain further insight into catalyst activity by calculating a "real" TON for each catalyst: the amount of trimer generated per activated Ti center. While this number may not truly reflect actual turnover given that catalyst dis-/comproportionation or ligand redistribution may occur, it is nonetheless instructive in qualitatively comparing catalyst systems.

All precatalysts examined were active for trimerization catalysis with 1-hexyne, albeit with starkly different degrees of activation and rates of catalysis (Table 3.1), demonstrating the generality of accessing a Ti^{II} intermediate from a Ti^{IV} imido unit. Most of the catalysts examined did not deviate significantly from the statistical distribution of alkyne trimers, although the ratio of pyrrole byproduct regioisomers varied widely. In general, precatalysts with poor to moderate trimerization yields were observed to have poor mass balances that may be a result of alkyne oligomerization,[180-182] catalyst decomposition, or off-cycle/arrested alkyne-bound Ti complexes (metallacyclopropene,

metallacyclopentadiene and η^6-arene)[183-185] that were either incapable of or slower at catalytic turnover.

Table 3.1 1-Hexyne trimerization data.[a]

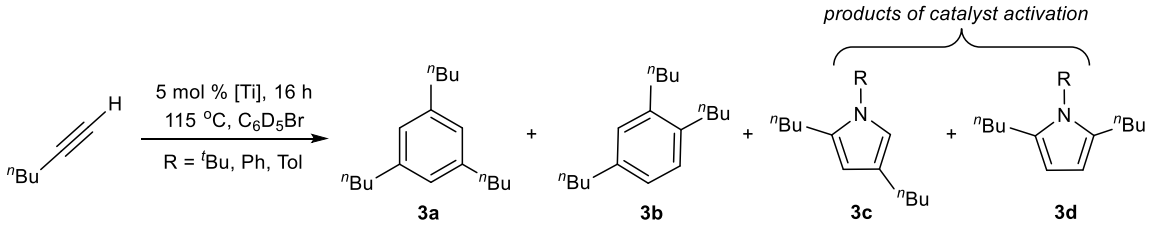

[Ti]	% Trimer yield (3a + 3b)	3a:3b	% [Ti] Activated[b]	3c:3d	% Conversion	TON[c]
1	quant.	27:73	37 ± 4	86:14	100 ± 0	18 ± 2
2	87 ± 1	35:65	6 ± 2	78:23	89 ± 3	94 ± 31
3[d]	94 ± 4	39:61	5 ± 1	100:0	98 ± 2	132 ± 38
4	61 ± 5	24:76	32 ± 3	75:25	93 ± 4	12 ± 2
5	85 ± 2	39:61	20 ± 10	60:40	100 ± 0	28 ± 14
6	quant.	31:69	30 ± 4	86:14	100 ± 0	21 ± 4
7	41 ± 8	37:63	31 ± 8	65:35	64 ± 16	9 ± 4
8	62 ± 4	33:67	36 ± 9	100:0[e]	100 ± 0	11 ± 4
9	53 ± 2	34:66	11 ± 1	100:0[e]	91 ± 3	32 ± 4
10	71 ± 2	27:73	61 ± 3	100:0[e]	100 ± 0	7 ± 0
11	50 ± 4	37:62	33 ± 4	100:0[e]	75 ± 4	10 ± 1
12	34 ± 9	15:85	57 ± 19	37:63	64 ± 7	4 ± 2
13	40 ± 5	17:83	15 ± 2	69:31	55 ± 14	17 ± 3
14	18 ± 3	39:61	7 ± 1	31:69	56 ± 13	17 ± 4
15	65 ± 5	21:79	38 ± 1	65:35	76 ± 12	11 ± 1
16	24 ± 2	42:58	0 ± 0	-	53 ± 5	-

[a]Conditions: 5 mol % [Ti], 0.4 M 1-hexyne, C_6D_5Br, 16 h, 115 °C, average of 2 – 4 runs. Quantitation determined by *in situ* ^{1}H NMR. [b]% Ti activated = (yield of **3c + 3d**)/$[Ti]_{tot}$. [c]TON = (yield of **3a + 3b**)/Ti activated. [d]< 5 min, room temperature. [e]**3d** (R = N^{t}Bu)

could not be independently synthesized/characterized, although raw spectra indicate only formation of **3c**.

Results with catalysts bearing simple monoanionic ligands (**3.1**-**3.3**) indicate that electron-poor metal centers with weaker donor ligands (as measured by Odom *via* ligand donor parameterization) are better for 1-hexyne trimerization: I (**3.3**) > Br (**3.2**) > Cl (**3.1**).[186-187] The apparent TON also increases as the metal center becomes more electron-poor. Most strikingly, even though only 5% of **3.3** was activated, it yielded 94 % trimerization at room temperature in less than 5 min. In contrast, **3.2** slowly trimerized at room temperature, while **3.1** (and others) required high temperatures for productive catalysis to occur. The regioselectivity of both 1-hexyne trimerization and pyrrole formation trends toward sterically favored products **3a** and **3c** as the electrophilicity of the catalyst increases.

Catalyst **3.6** and **3.7** allow for a direct comparison of steric effects on activation and catalysis. While the amount of precatalyst activated is approximately the same for both, catalysis with more sterically encumbered **3.7** is incomplete under standard conditions, yielding significantly less trimerization product than that with **3.6**. Intriguingly, although there are marginal differences in the regioselectivity of trimerization between both, **3.6** is significantly more selective than **3.7** for 2,4-disubstituted pyrrole activation product **3a**. In fact, the overall activation and catalytic profile of catalyst **3.6** are very similar to those of **3.1**. This similarity may indicate that some ligand redistribution/disproportionation occurs in these monoaryloxide complexes.

Varying the substituents on cyclopentadienyl-supported Ti catalysts **3.9**-**3.11** significantly affected both the amount of catalyst activated and the degree of alkyne trimerization. Cp_2-substituted **3.9** exhibits the lowest amount of catalyst activation but has the highest apparent TON of all three Cp-substituted catalysts, indicating that the bulkier and more electron-rich Cp_2Ti^{II} active species may be more long-lived and/or more reactive than the monoligated analogues. More sterically encumbered Cp* derivative **3.11** has a lower degree of activation than Cp counterpart **3.10**, although the apparent TONs for both are similar, indicating that in these systems the initial activation of the Ti(N^{t}Bu)Cp

fragment by incoming alkynes is more sensitive to sterics than alkyne trimerization by a putative $CpTi^{II}$ species.

Catalysts **3.12-3.15**, supported by bidentate, potentially hemilabile ligands, did not react to full conversion under standard catalytic conditions. Similar to Cp derivatives **3.9-3.11**, bis-ligated bidentate ligands undergo lower catalyst activation but have higher apparent TONs, indicating that although mono ligation may aid in catalyst activation due to the steric sensitivity of [2+2+1] pyrrole formation it may also lead to less stable and/or less active trimerization catalysts. Unfortunately, there is no correlation between selectivity in pyrrole activation and 1-hexyne trimerization in any of these systems.

Remarkably, catalysts **3.12** and **3.14** show preference for the selective formation of 2,5-disubstituted pyrrole activation product **3d**, which results from a Markovnikov [2 + 2] addition of 1-hexyne to the Ti(NTol) fragment followed by 2,1-insertion of 1-hexyne into the resulting azametallacycle. This regioselectivity is surprising given that hydroamination of terminal aliphatic alkynes with aniline[168, 188] by catalyst **3.12** favors the opposite [2 + 2] products, in a ratio of approximately 1.6 : 1 anti-Markovnikov to Markovnikov. While these results are apparently contradictory, they are likely a result of different rate-determining steps of catalysis (for example, in Schafer's hydroamination report, [2 + 2] addition is reversible and protonolysis by aniline is rate determining) or a function of a change in catalyst speciation. In hydroamination catalysis, there is a large excess of Lewis basic amine present that may coordinate to Ti throughout the catalytic cycle;[188] however, in these trimerization experiments, no such strong Lewis base exists.

Given successful catalysis with a diverse range of Ti catalysts, we synthesized and tested a Zr imido analogue, **3.16**. Interestingly, catalyst **3.16** trimerized 1-hexyne in poor yield in the absence of any detectable pyrrole activation byproduct. This result leads to one of two possible conclusions: (1) Trimerization by Zr occurred through a Lewis acid mechanism such as that reported by Floriani *et al.*[189] for $ZrCl_4$. (2) Small amounts of Zr(NPh) were activated in a quantity undetectable by ^1H NMR and GC/MS and catalysis occurred in a manner similar to Ti. While $ZrCl_4$ is known to trimerize alkynes through the Lewis acid pathway, control experiments with $ZrCl_4$ under our specific reaction conditions yielded no alkyne trimerization. (Arene coordination to $ZrCl_4$, both from C_6D_5Br and 1,3,5-

trimethoxybenzene, inhibits Lewis acid catalysis. See Table 3.4.) Thus, neither pathway can be fully ruled out.

Table 3.2 3-Hexyne trimerization data.[a]

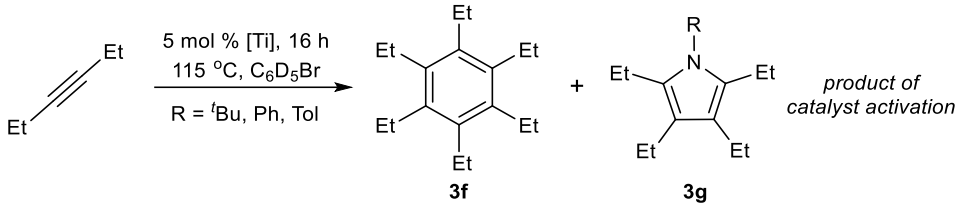

[Ti]	% Trimer yield (3e)	% [Ti] Activated[b]	% Conversion	TON[c]
1	62 ± 13	80 ± 12	73 ± 17	4 ± 2
2	55 ± 21	57 ± 12	77 ± 12	5 ± 2
3[d]	83 ± 6	17 ± 7	81 ± 3	35 ± 14
4	24 ± 8	33 ± 18	54 ± 16	5 ± 3
5	6 ± 5	42 ± 6	15 ± 0	1 ± 1
6	38 ± 2	48 ± 11	72 ± 18	5 ± 1
7	3 ± 3	70 ± 9	49 ± 11	0 ± 0
8	68 ± 7	74 ± 14	87 ± 2	6 ± 1
9	1 ± 0	8 ± 2	12 ± 0	1 ± 0
10	0 ± 0	1 ± 0	7 ± 2	0 ± 0
11	3 ± 0	41 ± 7	49 ± 8	1 ± 0
12	0 ± 0	7 ± 4	42 ± 13	0 ± 0
13	0 ± 0	0 ± 0	42 ± 11	-
14	2 ± 2	6 ± 4	20 ± 15	2 ± 2
15	1 ± 0	25 ± 1	22 ± 6	0 ± 0
16	1 ± 0	0 ± 0	35 ± 4	-

[a]Conditions: 5 mol % [Ti], 0.4 M 3-hexyne, C_6D_5Br, 16 h, 115 °C, average of 2 – 4 runs. Quantitation determined by *in situ* ^{1}H NMR. [b]% Ti activated = (yield of **3g**)/$[Ti]_{tot}$. [c]TON = (yield of **3f**)/Ti activated. [d]Room temperature.

With an internal alkyne such as 3-hexyne, alkyne trimerization becomes more challenging (Table 3.2). In all cases examined, the apparent TON and yield of hexaethylbenzene (**3f**) were lower than those in the 1-hexyne reactions. Interestingly, the amount of pyrrole formed *via* [2+2+1] of 3-hexyne was typically higher than the reactions with 1-hexyne. This is likely the result of the relative rates of activation versus trimerization: In most 1-hexyne reactions, trimerization rapidly depletes the amount of alkyne available for further catalyst activation, whereas with 3-hexyne, catalyst activation can effectively compete with slower alkyne trimerization.

Trends in catalyst activity similar to those observed in 1-hexyne reactions can also be observed in the 3-hexyne reactions. For example, the most electron-deficient simple halide **3.3** substantially outperforms other monoanionic analogues **3.1**, **3.2**, **3.4** and **3.5** despite a lower degree of catalyst activation. Increasing the steric profile of monoligated complexes also suppresses productive catalysis, as catalyst **3.6** gives moderate yields of hexaethylbenzene while the bulkier **3.7** only yields trace product. Disappointingly, catalysts with bidentate ligands **3.9-3.15** yielded no productive catalysis despite some pyrrole production and instead led to poor mass balances.

3.4 Conclusion

In summary, we have demonstrated the generality of obtaining a reduced "Ti^{II}" intermediate by the coupling of a Ti^{IV} imido and 2 equivalence of alkyne, generating a stoichiometric amount of pyrrole as a byproduct. Remarkably, a very diverse range of catalyst structures are reasonably efficient at generating Ti^{II} intermediates *via* [2+2+1]. The degrees of catalyst activation and catalyst activity are highly dependent on the structure of the Ti complex. In general, electron-poor Ti complexes, such as those derived from $Ti(NTol)I_2(THF)_3$ precatalyst **3.3**, are far superior for alkyne trimerization compared to other electron-rich and/or multi-dentate ligands. Additionally, while most precatalysts predominantly generated 2,4-disusbstituted pyrroles (**3c**) on activation with 1-hexyne, hemilabile ligand scaffolds such as catalysts **3.12** and **3.14** demonstrated selectivity toward 2,5-disubstituted pyrroles (**3d**).

More generally, these trimerization reactions illustrate an important design principle for early transition metal catalysis involving redox at the metal: stabilization of

low-valent states. While there have been significant recent advances in the use of redox non-innocent ancillary ligands[69, 71, 101] to modulate similar transformations, one may also consider that redox non-innocent reactants or products can play a similar role; in this case, π-backdonation from Ti^{II} into arenes and alkynes is certainly critical to accessing low-valent states and for catalysis. Similarly, π-backdonation into CO in Pauson−Khand reactions,[139-141] alkenes in the Kulinkovich reaction,[142-143] and azobenzene in [2+2+1] pyrrole syntheses[79, 83] is integral for productive reactivity and catalyst stability. This research will provide new potential access points to carry out various other stoichiometric and catalytic reactions with low-valent Ti under mild conditions and a future platform for new catalyst development toward selective pyrrole syntheses.

3.5 Experimental

3.5.1 General Considerations.

All air- and moisture-sensitive reactions were carried out in a nitrogen-filled glovebox. Standard solvents for air- and moisture-sensitive reactions were either deoxygenated by sparging with N_2 and dried by passing through activated alumina columns of a Pure Process Technology solvent purification system (benzene, ether, pentanes, hexanes, THF, or CH_2Cl_2) or vacuum-transferred from Na/Ph_2CO (C_6D_6) or CaH_2 ($CDCl_3$). C_6D_5Br was synthesized following a literature procedure,[190] degassed, dried over CaH_2 and filtered through basic alumina prior to use. Commercial $PhCF_3$ was vacuum transferred from CaH_2 and filtered through basic alumina prior to use.

Ti(N^{t}Bu)Cl_2py_3,[122] precatalysts **3.1**,[122] **3.8**[165] and **3.9**-**3.11**[166] were synthesized according to literature procedures. Dimeric $[Ti(NPh)Cl_2py_2]_2$ was prepared by extended heating of $Ti(NPh)Cl_2py_3$[122] under vacuum. Liquid alkynes and other reagents were freeze−pump−thawed, degassed three times and passed through activated basic alumina prior to use. 1,2-di(*p*-tolyl)diazene[191] and 5,7-dodecadiyne[192] were prepared following literature procedures. Azobenzene[193] was purified *via* recrystallization and sublimation prior to use.

^1H and ^{13}C NMR spectra were recorded on Bruker Avance III HD 400 and 500 MHz spectrometers. Chemical shifts were referenced to the residual protio-solvent impurity for ^1H (s, 7.16 ppm for C_6D_5H; s, 7.26 for $CHCl_3$; s 7.30, 7.02 and 6.94 ppm for

C_6D_4HBr)[194] and solvent carbons for ^{13}C (t, 128.1 ppm for C_6D_6; t, 77.2 ppm for $CDCl_3$). X-ray data were collected using a Bruker Photon 100 CMOS diffractometer for data collection at 123(2) K using Cu Kα radiation (normal parabolic mirrors). The data intensity was corrected for absorption and decay (SADABS). Final cell constants were obtained from least-squares fits of all measured reflections and the structure was solved and refined using SHELXL-2014/7.[195] Details regarding refined data and cell parameters are available in Table 3.5. CCDC entries 1524349−1524352 contain the supplementary crystallographic data for this paper. These data can be obtained free of charge *via* http://www.ccdc.cam.ac.uk/conts/retrieving.html, Cambridge Crystallographic Data Center, 12 Union Road, Cambridge CB2 1EZ, United Kingdom, fax: (+44) 1223-336-033, or e-mail:deposit@ccdc.cam.ac.uk

3.5.2 Synthesis of compounds

Synthesis of N-(*p*-tolyl)-N,N-bis(trimethylsilyl)amine

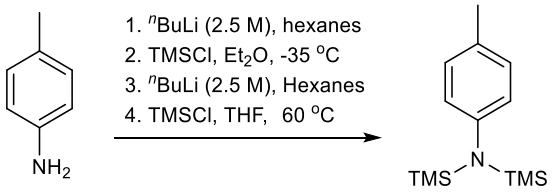

p-toluidine (4.26 g, 39.8 mmol, 1.0 equiv) and 20 mL hexanes were added to a 250 mL round-bottom flask equipped with a stir bar and cooled to - 35 °C in a N_2-filled glovebox. ^{n}BuLi (2.5 M, 16 mL, 40.0 mmol, 1.0 equiv) was then added dropwise to the reaction mixture with stirring. This was allowed to warm up to room temperature and stirred for 30 min. The resulting yellow/white precipitate (Li-NH-C_6H_4-CH_3) was filtered and washed with 20 mL hexanes. The solids were dissolved in 30 mL Et_2O and cooled to - 35 °C before the dropwise addition of TMSCl (5.05 mL, 39.8 mmol, 1.0 equiv). This was allowed to warm up to room temperature and stirred for 1 h, during which LiCl precipitate was formed. After which, the mixture was filtered through a celite plug and washed with 10 mL hexanes. The filtrate was concentrated *in vacuo* to remove ether before diluting with 20 mL hexanes. The hexane mixture was then transferred to a separate 250 mL round-bottom flask and *at room temperature* ^{n}BuLi (2.5 M, 16 mL, 40.0 mmol, 1.0 equiv) was added in 3 portions (6 mL, 5 mL and 6 mL). During the addition, the solution refluxes, highlighting the necessity

of using a sufficiently large flask (best results were obtained when this reaction was allowed to reflux from a fast ^{n}BuLi addition; slow or cold additions have complicated work-up). After stirring for 1 h, the mixture was filtered through a sintered glass frit, collecting approximately 7 g of the Li-(TMS)N- C_6H_4-CH_3 intermediate. The solid was diluted in 20 mL of THF in a 100 mL round-bottom flask to give a yellow solution. TMSCl (6.0 mL, 47.2 mmol, 1.2 equiv) was added dropwise *at room temperature* to the solution (caution: will exotherm). The mixture was heated overnight at 60 – 70 °C to give a clear, nearly colorless solution with white LiCl precipitate. This was cooled to room temperature, diluted with 20 mL hexanes, filtered through a plug of celite and concentrated *in vacuo* to give a cloudy suspension. The suspension was diluted with 5 mL hexanes, passed through a pipette plug of celite to remove residual LiCl and then concentrated *in vacuo* to give a nearly colorless oil of the title compound that should solidify at - 35 °C (7.11 g, 71 % yield). If the solution remains cloudy after concentrating, there may be residual LiCl, further dilution with hexanes and filtering will remove this. If the oil fails to solidify at - 35 °C, then there may be residual solvents.

^{1}H-NMR (400 MHz, C_6D_6): δ 6.91 (d, $^{3}J_{HH}$ = 8.1 Hz, 2H, *m*-NTol-*H*), 6.81 (d, $^{3}J_{HH}$ = 8.1 Hz, 2H, *o*-NTol-*H*), 2.12 (s, 3H, NC_6H_4-C*H*$_3$), 0.12 (s, 18H, -Si(C*H*$_3$)).

^{13}C-NMR (126 MHz, C_6D_6): δ 145.3, 133.3, 130.3, 129.6, 20.9, 2.3.

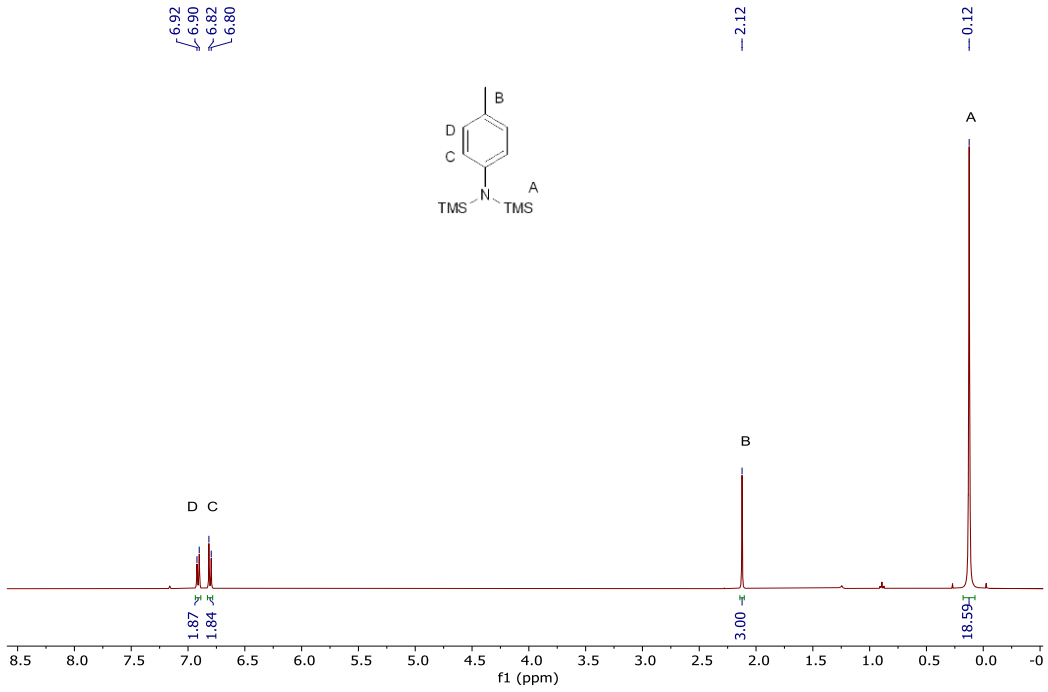

Figure 3.5 ^{1}H NMR spectrum of N-(*p*-tolyl)-N,N-bis(trimethylsilyl)amine in C_6D_6. *Taken from ZWG04072.*

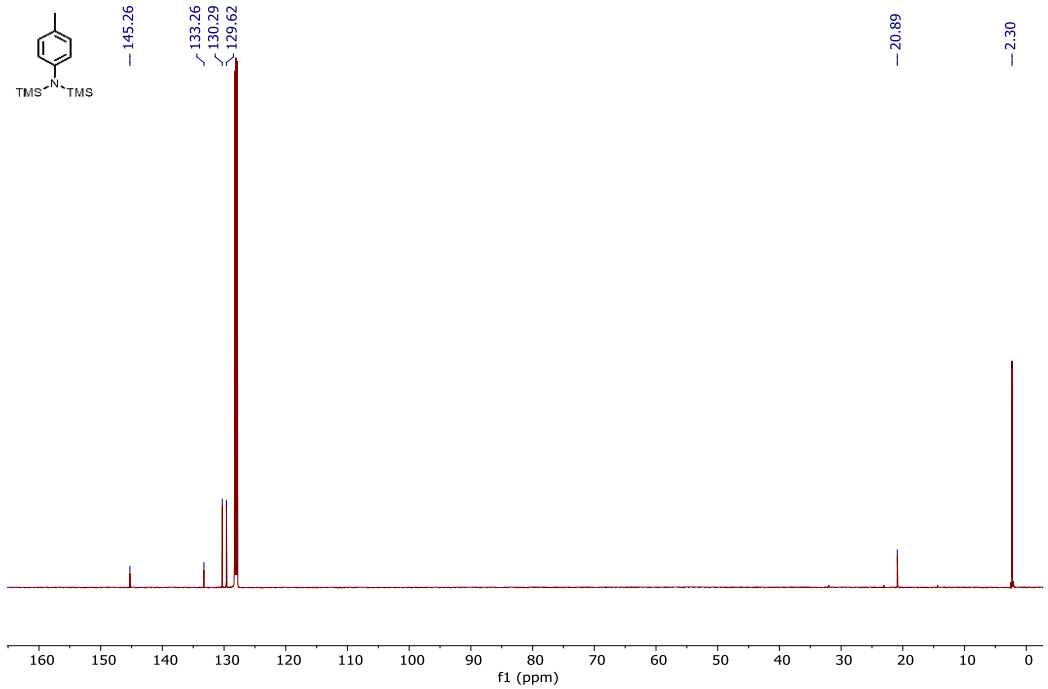

Figure 3.6 ^{13}C NMR spectrum of N-(*p*-tolyl)-N,N-bis(trimethylsilyl)amine in C_6D_6. *Taken from ZWG04072.*

Synthesis of 3.2

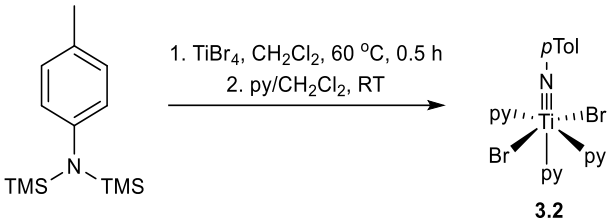

3.2

$TiBr_4$ (604 mg, 1.64 mmol, 1.0 equiv), N-(p-tolyl)-N,N-bis(trimethylsilyl)amine (404 mg, 1.61 mmol, 1.0 equiv) and 8 mL of CH_2Cl_2 were added to a 20 mL scintillation vial equipped with a small stir bar in a N_2-filled glovebox. This was then sealed with a Teflon screw cap, heated to 60 °C and stirred for 0.5 h. After cooling to room temperature, the mixture was left to stir for 1.5 h before diluting with 5 mL of hexanes. The reaction mixture was then filtered through a medium frit and washed with hexanes (3 × 3 mL). The resulting solid was then dissolved with 4 mL of pyridine and 2 mL of CH_2Cl_2. After stirring for 15 min, the solution was further diluted with 10 mL of CH_2Cl_2, filtered through a plug of celite, layered with hexanes and placed in a - 35 °C freezer overnight. The resulting tan/green solid was collected and washed with hexanes to give **3.2** (356 mg, 40% yield). Elemental analysis was not attempted as complex decomposition would occur under prolonged drying on the vacuum line.

^{1}H NMR (400 MHz, $CDCl_3$): δ 9.14 (br s, 4H, *o*-py-*H*), 8.86 (br s, 2H, *axial o*-py-*H*), 7.84 (t, $^3J_{HH}$ = 7.6 Hz, 2H, *p*-py-*H*), 7.72 (t, $^3J_{HH}$ = 7.6 Hz, 1H, *axial p*-py-*H*), 7.36 (t, $^3J_{HH}$ = 6.7 Hz, 4H, *m*-py-*H*), 7.26 (br s, 2H, *axial m*-py-*H*), 6.99 (d, $^3J_{HH}$ = 7.8 Hz, 2H, *m*-NTol-*H*), 6.88 (d, $^3J_{HH}$ = 8.0 Hz, 2H, *o*-NTol-*H*), 2.25 (s, 3H, NC_6H_4-C*H*$_3$).

^{13}C NMR (101 MHz, $CDCl_3$): δ 152.1, 151.3 (br), 138.8, 137.1 (br), 132.3, 128.8, 124.2, 124.1, 123.9 (br, 2C), 21.2 (NC_6H_4-*C*H_3).

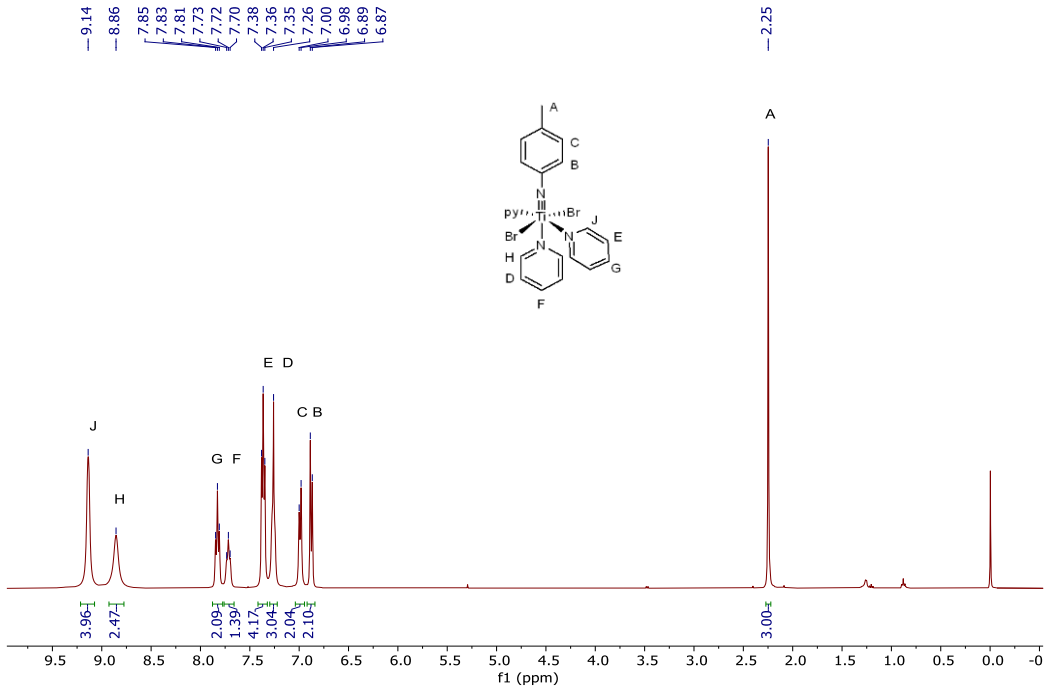

Figure 3.7 ^{1}H NMR spectrum of **3.2** in $CDCl_3$. *Taken from ZWG04081*.

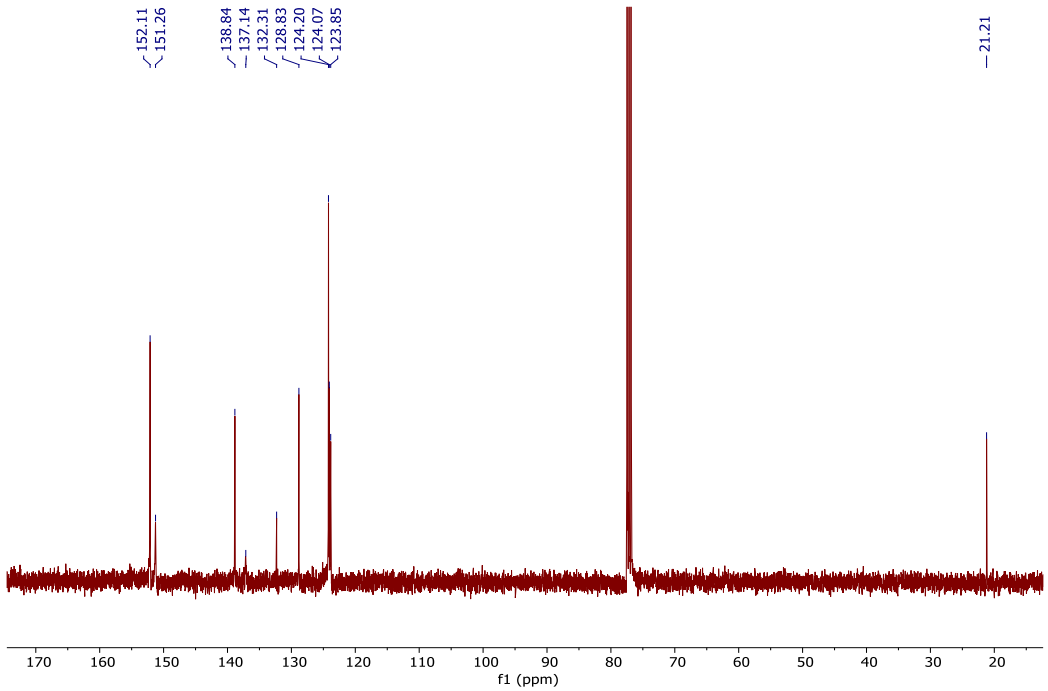

Figure 3.8 ^{13}C NMR spectrum of **3.2** in $CDCl_3$. *Taken from ZWG04081*.

Synthesis of 3.3

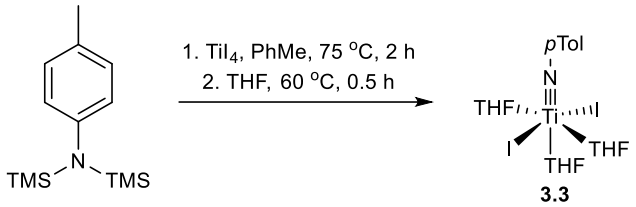

3.3

TiI_4 (442 mg, 0.796 mmol, 1.0 equiv), N-(*p*-tolyl)-N,N-bis(trimethylsilyl)amine (200 mg, 0.795 mmol, 1.0 equiv) and 5 mL PhMe were added to a 20 mL scintillation vial equipped with a small stir bar in a N_2-filled glovebox. This was then sealed with a Teflon screw cap, heated to 75 °C and stirred for 2 h. After cooling to room temperature, the mixture was diluted with 5 mL hexanes. The reaction mixture was then filtered through a medium frit and washed with 3 x 2 mL hexanes. The solid was collected, treated with 5 mL THF and heated to 60 °C until all the solids dissolved to give a red solution. The solution was then layered with 5 mL hexanes and placed in a - 35 °C freezer overnight to give **3** as X-ray quality red block crystals which were washed with cold hexanes (165 mg, 33 % yield). Elemental analysis was not attempted as complex decomposition would occur under prolonged drying on the vacuum line.

^{1}H NMR (400 MHz, $CDCl_3$): δ 6.93 (d, $^3J_{HH}$ = 8.3 Hz, 2H, *m*-NTol-*H*), 6.84 (d, $^3J_{HH}$ = 8.1 Hz, 2H, *o*-NTol-*H*), 4.54 (br s, 8H, 2,5-THF-*H*), 3.77 (br s, 4H, *axial* 2,5-THF-*H*), 2.25 (s, 3H, NC_6H_4-C*H*$_3$), 2.13 (br s, 8H, 3,4-THF-*H*) , 1.85 (br s, 4H, *axial* 3,4-THF-*H*).

^{13}C NMR (101 MHz, $CDCl_3$): δ 160.3, 133.7, 128.8, 123.6, 76.6 (br-s, 1C), 68.4 (br-s, 1C), 25.5 (br-s, 1C), 21.2 (NC_6H_4-*C*H_3).

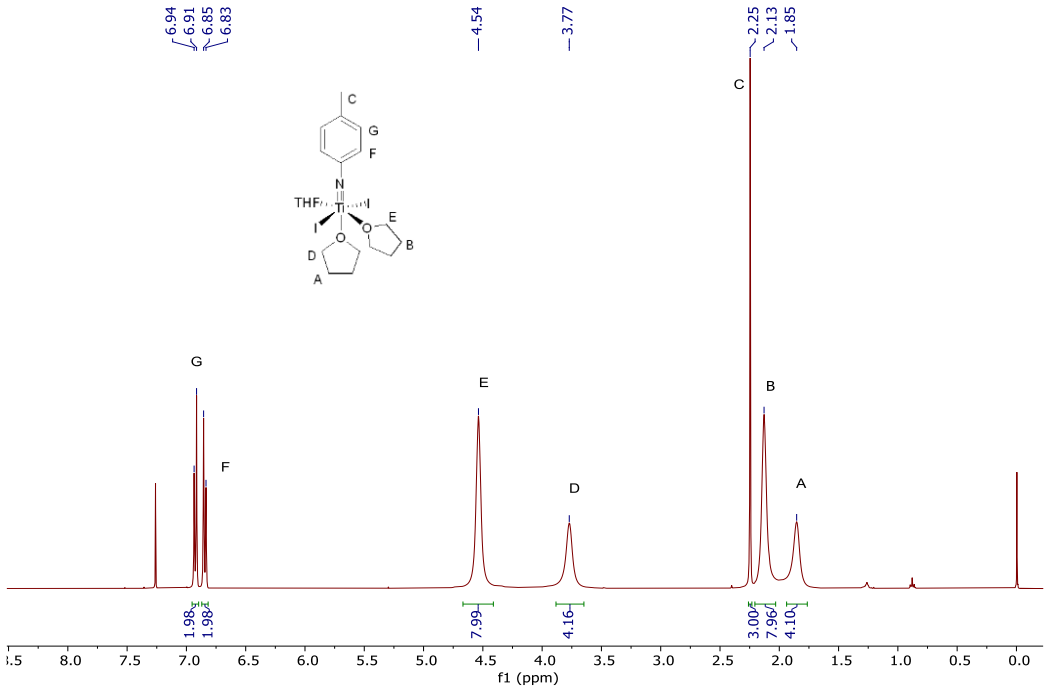

Figure 3.9 ^{1}H NMR spectrum of **3.3** in $CDCl_3$. *Taken from ZWG04078-C.*

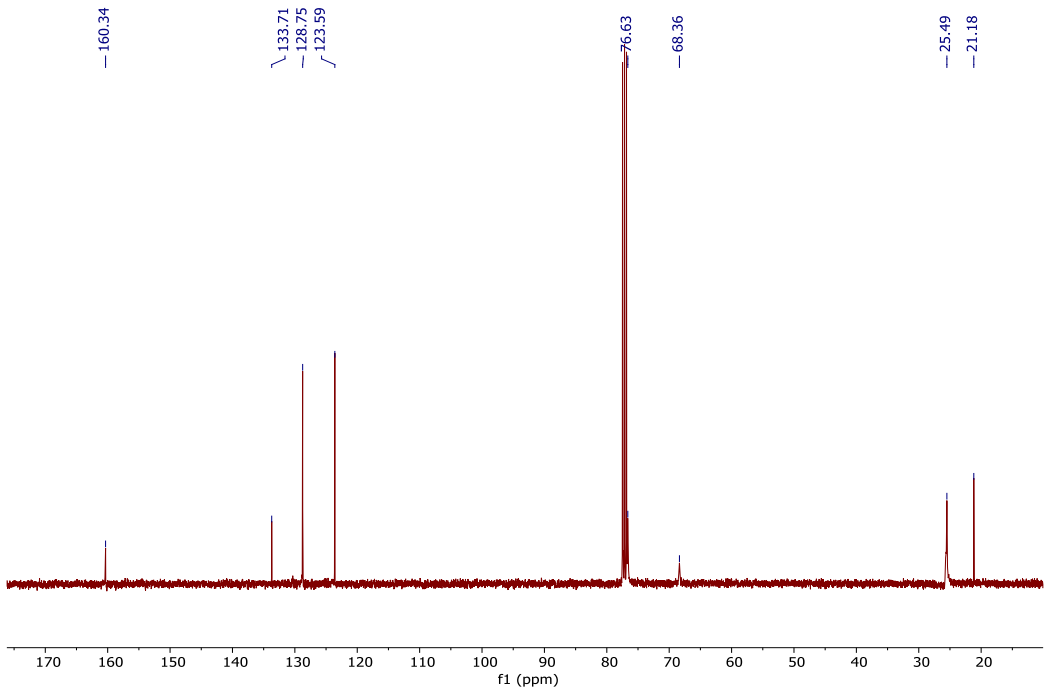

Figure 3.10 ^{13}C NMR spectrum of **3.3** in $CDCl_3$. *Taken from ZWG04078-C.*

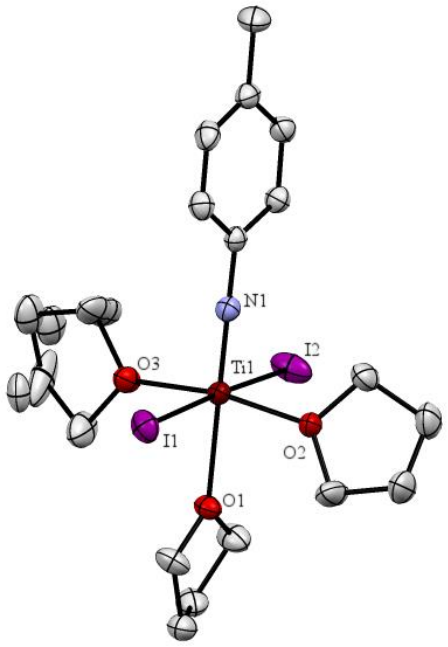

Figure 3.11 50 % thermal ellipsoid drawing of **3.3**. Hydrogen atoms are omitted for clarity.

Synthesis of 3.4

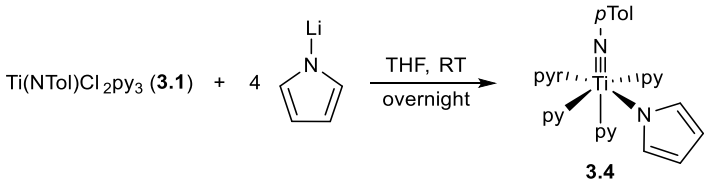

Pyrrole (2.50 g, 37.3 mmol, 1.0 equiv) and 10 mL PhMe were added to a 20 mL scintillation vial equipped with a small stir bar in a N_2-filled glovebox. This was then cooled in the glovebox coldwell to -75 °C. ^{n}BuLi (2.5 M, 18 mL, 44.7 mmol, 1.2 equiv.) was added dropwise to the vial over 15 min. The reaction was allowed to stir while warming to room temperature. Afterwards, excess hexanes was added to precipitate out the lithium pyrrolide salt, which was collected on a medium frit, washed with more hexanes and dried overnight under vacuum to ensure removal of toluene. Solid was used without further purification.

Lithium pyrrolide (200 mg, 2.77 mmol, 4.0 equiv), **3.1** (318 mg, 0.69 mmol 1.0 equiv) and 2 mL THF were added to a 20 mL scintillation vial equipped with a small stir bar in a N_2-filled glovebox. This was then sealed with a Teflon screw cap and stirred overnight at room temperature. The reaction mixture changed to a dark red color over this period of time.

Solvent was removed *in vacuo* and the remaining solid was dissolved in benzene and filtered through celite. The filtrate was lyophilized to give **3.4** (350 mg, 92 % yield).

Elemental analysis (calcd, found; for $C_{30}H_{30}N_6Ti$): C (68.97, 68.88), H (5.79, 5.79), N (16.09, 16.02).

^{1}H NMR (400 MHz, C_6D_6): δ 8.34 (br s, 2H, *axial o*-py-*H*), 8.13 (br s, 4H, *o*-py-*H*), 7.53 (br s, 4H, *o*-NC_5H_4-*H*), 6.96 (d, $^3J_{HH}$ = 7.8 Hz, 2H, *m*-NTol-*H*), 6.88 (br s, 1H, *axial p*-py-*H*), 6.82 (d, $^3J_{HH}$ = 7.8 Hz, 2H, *o*-NTol-*H*), 6.76 (br s, 4H, *m*-NC_5H_4-*H*), 6.59 – 6.56 (m, 4H, *axial m*-py-H and *p*-py-*H*), 6.31 (br s, 4H, *m*-py-*H*), 2.06 (s, 3H, NC_6H_4-C*H*$_3$).

^{13}C NMR (101 MHz, C_6D_6): δ 151.0, 138.1, 130.6, 129.2, 128.6, 127.2, 124.4, 123.4, 108.8, 21.0 (NC_6H_4-*C*H_3).

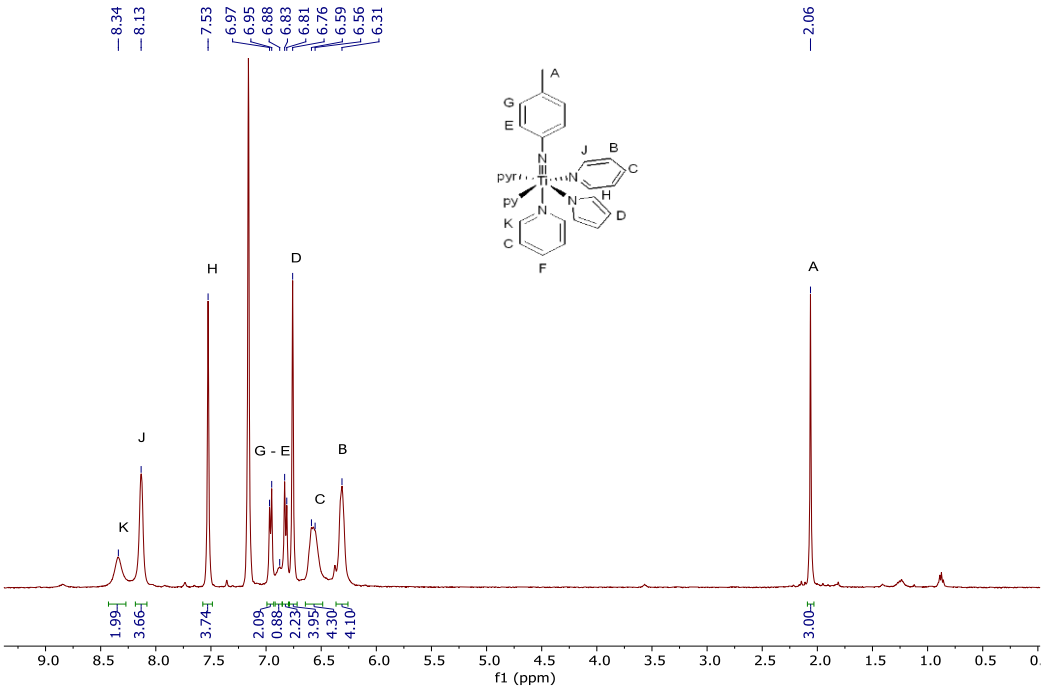

Figure 3.12 ^{1}H NMR spectrum of **3.4** in C_6D_6. *Taken from JAL01063.*

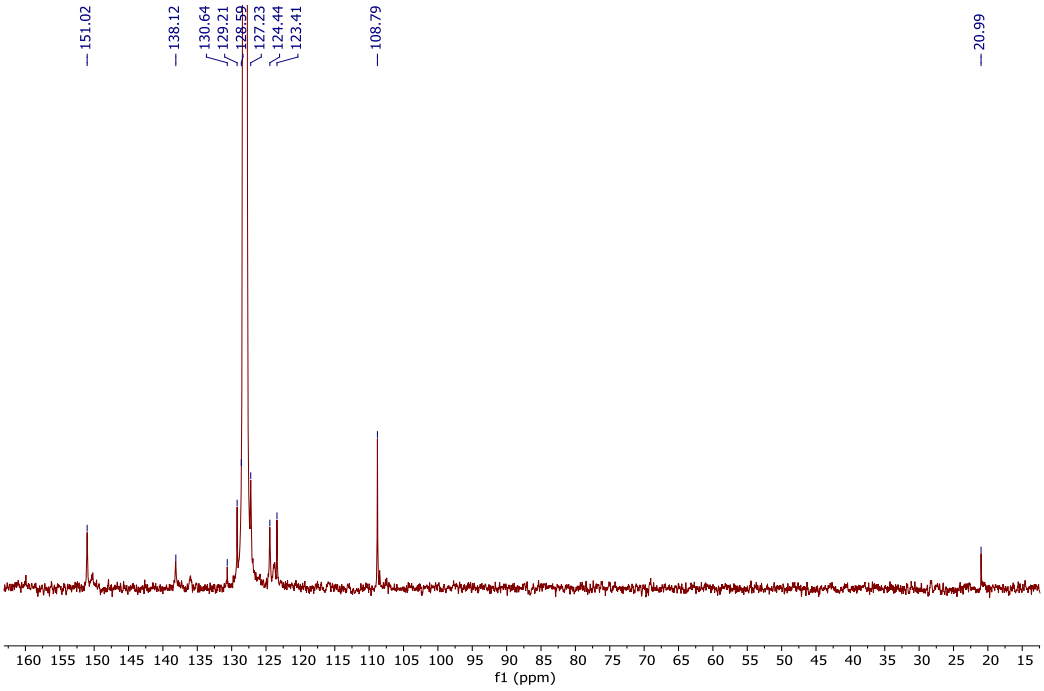

Figure 3.13 ^{13}C NMR spectrum of **3.4** in C_6D_6. *Taken from JAL01063.*

Synthesis of 3.5

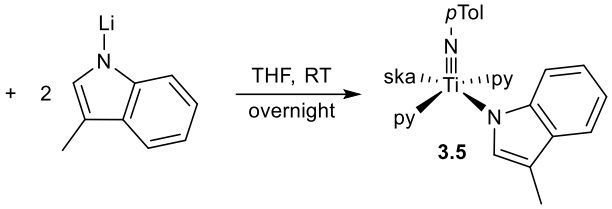

Skatole (2.50 g, 19.1 mmol, 1.0 equiv) and 10 mL PhMe were added to a 50 mL round-bottom flask equipped with a stir bar in a N_2-filled glovebox. This was then cooled in the glovebox coldwell to - 75 °C. ^{n}BuLi (2.5 M, 9 mL, 22.9 mmol, 1.2 equiv) was added dropwise to the round-bottom flask over 15 min. The reaction was allowed to stir while warming to room temperature. Afterwards, excess hexanes was added to precipitate out the lithium skatolide salt which was collected on a medium frit, washed with more hexanes and dried overnight under vacuum to ensure removal of toluene. Solid was used without further purification.

Lithium skatolide (100 mg, 0.729 mmol, 2.2 equiv), **3.1** (150 mg, 0.325 mmol, 1.0 equiv) and 2 mL THF were added to a 20 mL scintillation vial equipped with a small stir bar in a N_2-filled glovebox. This was then sealed with a Teflon screw cap and stirred overnight at room temperature. The reaction mixture changed to a dark red colour over this period of time. The solvent was removed *in vacuo* and the resulting solid was dissolved in benzene, filtered through celite and the filtrate was lyophilized to give **3.5** as an oily red solid (130 mg, 70 % yield).

^{1}H NMR (400 MHz, C_6D_6): δ 8.15 (d, $^3J_{HH}$ = 5.0 Hz, 4H, *o*-py-*H*), 7.84 – 7.82 (m, 2H, Ar-*H*), 7.32 – 7.31 (m, 4H, Ar-*H*), 7.13 (d, $^3J_{HH}$ = 8.2 Hz, 2H, *m*-NTol-*H*), 6.89 (d, $^3J_{HH}$ = 8.1 Hz, 2H, *o*-NTol-*H*), 6.39 (t, $^3J_{HH}$ = 7.6 Hz, 2H, *p*-py-*H*), 5.99 (t, $^3J_{HH}$ = 6.7 Hz, 4H, *m*-py-*H*), 2.53(s, 6H, -C*H*$_3$), 2.09 (s, 3H, NC_6H_4-C*H*$_3$).

^{13}C NMR (126 MHz, C_6D_6): δ 161.1, 150.4, 138.3, 130.9, 130.5, 129.4, 128.4, 124.5, 122.9, 121.6, 119.6, 118.6, 111.7, 21.0 (NC_6H_4-*C*H_3), 10.5 (-*C*H_3).

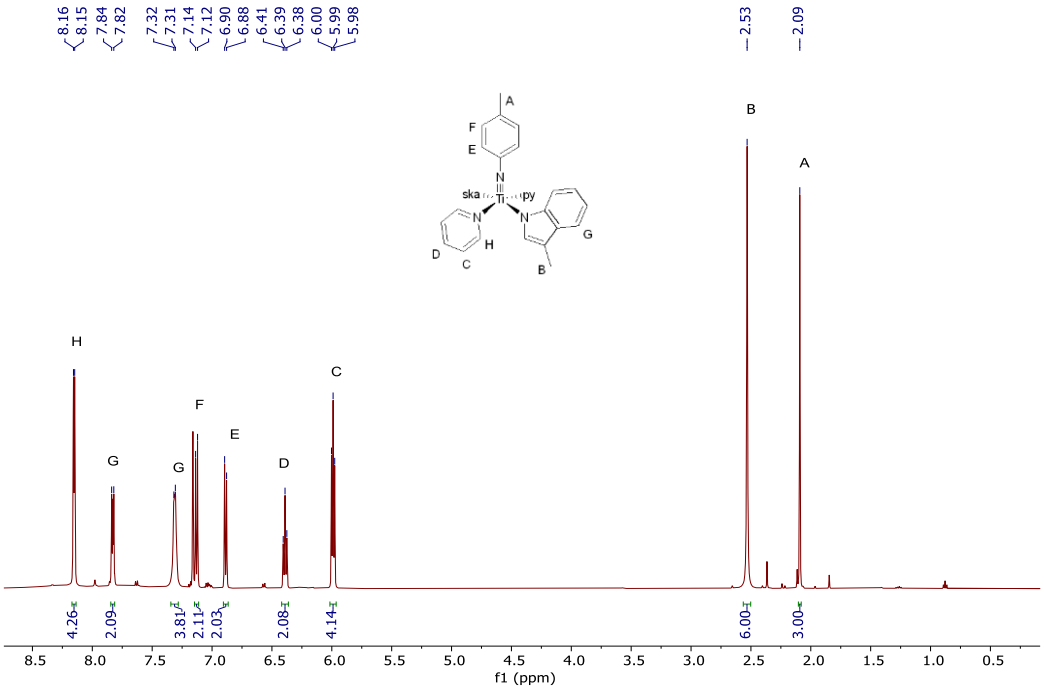

Figure 3.14 ^{1}H NMR spectrum of **3.5** in C_6D_6. *Taken from JAL01064-Xtal.*

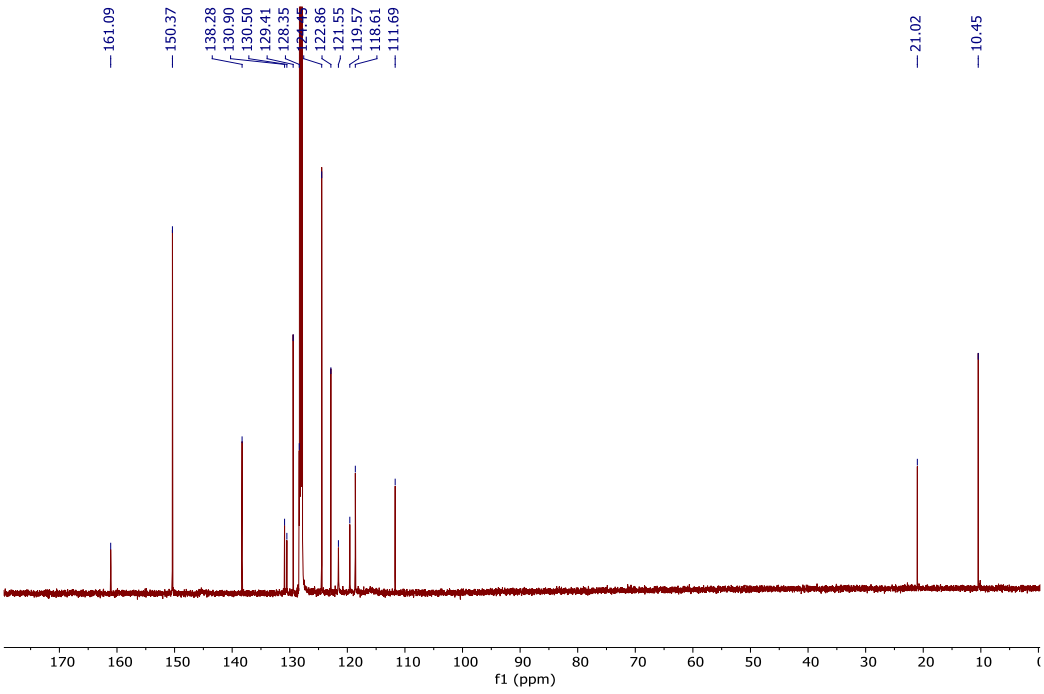

Figure 3.15 ^{13}C NMR spectrum of **3.5** in C_6D_6. *Taken from JAL01064-13C.*

Synthesis of 3.6

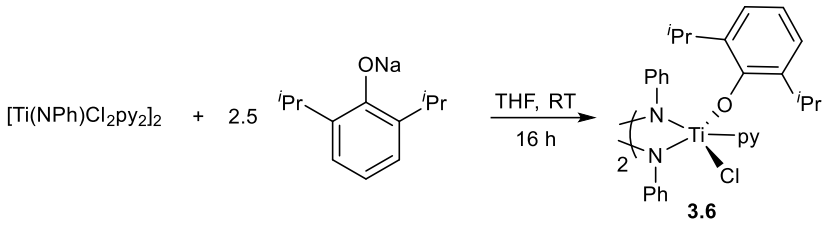

3.6

This procedure was adapted from that used for synthesis of a similar compound with a different imido substituent.[163] 2,6-Diisopropylphenol (17.4 g, 97.6 mmol, 1.0 equiv) and 40 mL of THF were added to a 100 mL round-bottom flask equipped with a stir bar in a N_2-filled glovebox and cooled in the glovebox freezer to - 35 °C. Solid NaH (2.66 g, 111 mmol, 1.1 equiv) was added slowly to the stirring cooled solution. ***Caution:*** *This reaction will exotherm.* The mixture turned deep green in color. Upon full addition, the mixture was warmed to room temperature and stirred for 2 h. The mixture was then filtered through a celite plug, washed with THF and the filtrate solvents were removed *in vacuo* to give the sodium salt as a white solid. Solid was used without further purification.

2,6-$^{i}Pr_2$PhONa (700 mg, 3.50 mmol, 2.5 equiv) was dissolved in 6 mL of THF in a 20 mL scintillation vial in a N_2-filled glovebox. The solution was then added dropwise to a suspension of $[Ti(NPh)Cl_2py_2]_2$ (1.03 g, 1.40 mmol, 1.0 equiv) in 2 mL of THF in a separate 20 mL scintillation vial equipped with a stir bar. This was then sealed with a Teflon screw cap and stirred at room temperature for 16 h before removal of solvents *in vacuo*. The solids were extracted into 5 mL of CH_2Cl_2, filtered through a celite plug to remove NaCl, layered with 5 mL of hexanes and cooled in a - 35 °C freezer. The dark red/black crystalline material was collected and washed with hexanes to give **3.6** (470 mg, 48% yield).

^{1}H NMR (400 MHz, $CDCl_3$): δ 8.57 (d, $^{3}J_{HH}$ = 4.9 Hz, 4H, *o*-py-*H*), 7.47 (t, $^{3}J_{HH}$ = 7.6 Hz, 2H, *p*-py-*H*), 7.10 (d, $^{3}J_{HH}$ = 7.6 Hz, 4H, Ar-*H*), 7.01−6.95 (m, 6H, Ar-*H*), 6.77 (t, $^{3}J_{HH}$ = 7.8 Hz, 4H, Ar-*H*), 6.54−6.49 (m, 6H, Ar-*H*), 3.76 (br s, 4H, $^{i}Pr_2$C-*H*), 1.17 (d, $^{3}J_{HH}$ = 6.8 Hz, 24H, ^{i}Pr-*H*).

^{13}C NMR (101 MHz, $CDCl_3$): δ 163.3, 161.4, 149.8, 138.3, 138.1, 127.6, 124.2, 123.2, 122.7, 122.0, 118.8, 26.8, 23.9.

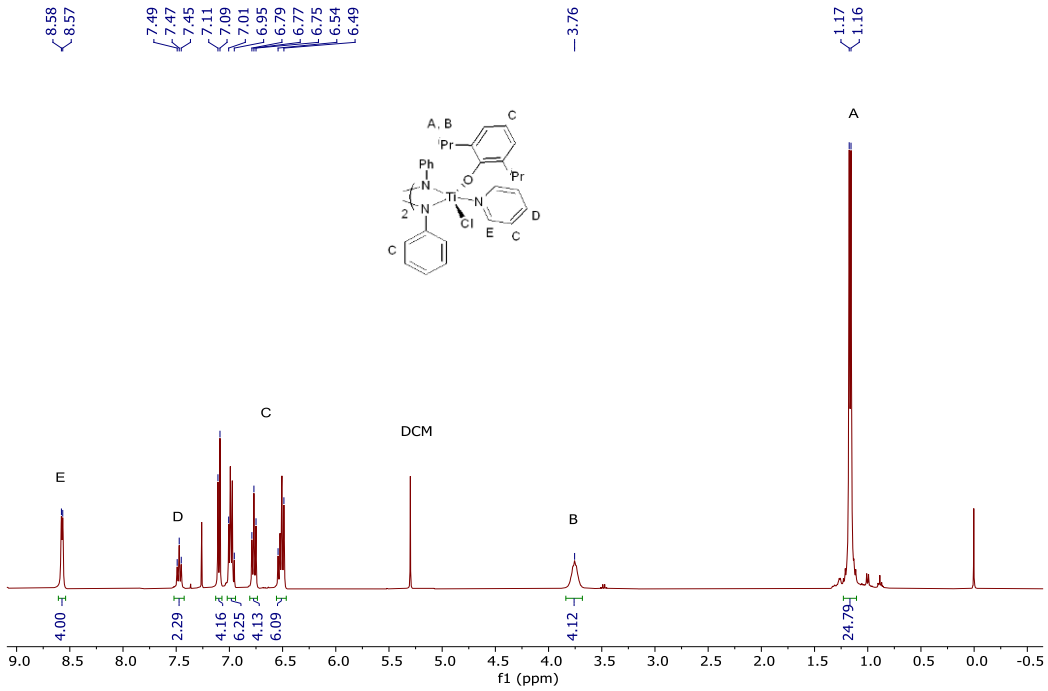

Figure 3.16 ^{1}H NMR spectrum of **3.6** in $CDCl_3$. *Taken from TAW01150.*

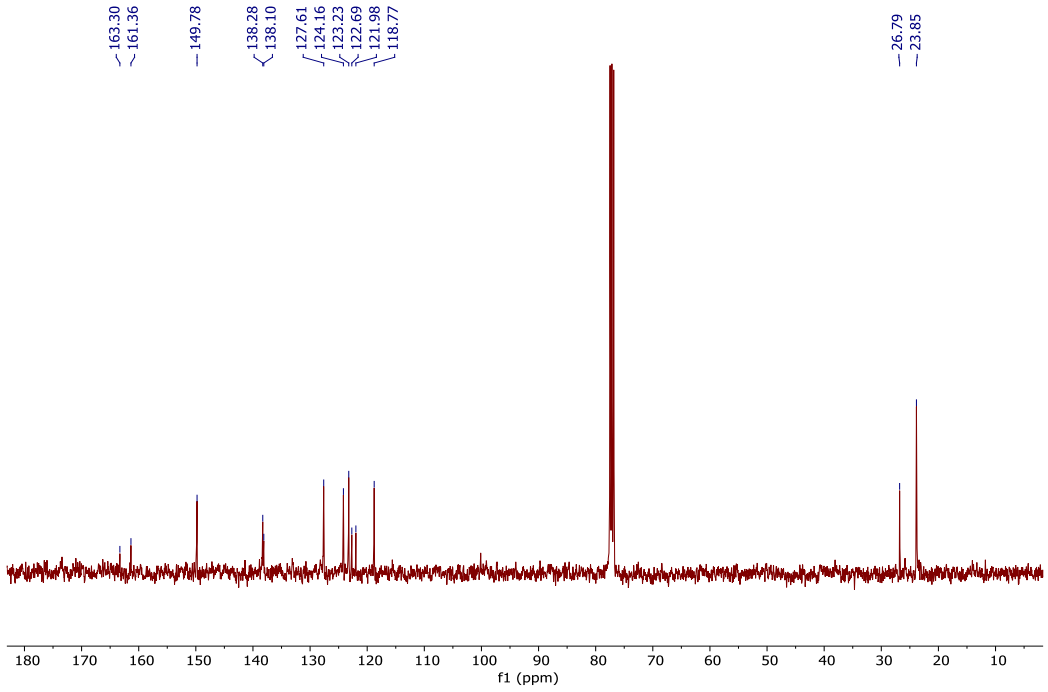

Figure 3.17 ^{13}C NMR spectrum of **3.6** in $CDCl_3$. *Taken from TAW01150.*

Synthesis of 3.7

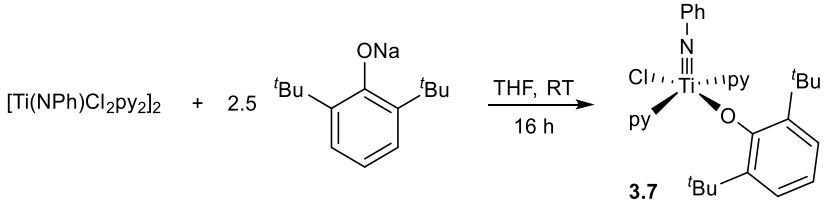

This procedure was adapted from that used for synthesis of a similar compound with a different imido substituent.[163] 2,6-Di-tert-butylphenol (1.00 g, 4.85 mmol, 1.0 equiv) and 10 mL of THF were added to a 20 mL scintillation vial equipped with a small stir bar in a N_2-filled glovebox. ***Caution:*** *This reaction will exotherm.* Solid NaH (150 mg, 6.25 mmol, 1.3 equiv) was added slowly to the solution and the resulting mixture was left to stir uncapped for 30 min to allow for the evolution of H_2. This was then sealed with a Teflon screw cap and stirred at room temperature for 16 h. Afterward, the mixture was filtered through a celite plug to remove residual NaH and dried *in vacuo* to give the sodium salt as a white solid. Solid was used without further purification.

2,6-^{t}Bu$_2$PhONa (227 mg, 0.994 mmol mmol, 2.4 equiv) was dissolved in 6 mL of THF in a 20 mL scintillation vial in a N$_2$-filled glovebox. This solution was added dropwise to a suspension of [Ti(NPh)Cl$_2$py$_2$]$_2$ (305 mg, 0.414 mmol, 1.0 equiv) in 2 mL of THF in a separate 20 mL scintillation vial equipped with a small stir bar. This was then sealed with a Teflon screw cap and stirred at room temperature for 16 h followed by removal of solvents *in vacuo*. The solids were extracted into 5 mL of CH_2Cl_2, filtered through a celite plug to remove NaCl, layered with 5 mL of hexanes and cooled in a - 35 °C freezer. The globular solids were collected, crushed and dried *in vacuo* to yield **3.7** (150 mg, 48% yield).

^{1}H NMR (400 MHz, CDCl$_3$): δ 9.27 (br s, 4H, *o*-py-*H*), 7.86 (br s, 2H, *p*-py-*H*), 7.44 (br s, 4H, *m*-py-*H*), 7.32 (d, $^{3}J_{HH}$ = 7.7 Hz, 1H, *m*-C$_6$H$_3$^{t}Bu$_2$-*H*), 6.92 (t, $^{3}J_{HH}$ = 7.6 Hz, 2H, *o*-NPh-*H*), 6.85 (t, $^{3}J_{HH}$ = 7.8 Hz, 1H, *p*-C$_6$H$_3$^{t}Bu$_2$-*H*), 6.64 (t, $^{3}J_{HH}$ = 7.2 Hz, 1H, *p*-NPh-*H*), 6.36 (d, $^{3}J_{HH}$ = 8.0 Hz, 2H, *m*-NPh-*H*), 1.53−1.21 (m, 18H, ^{t}Bu-*H*).

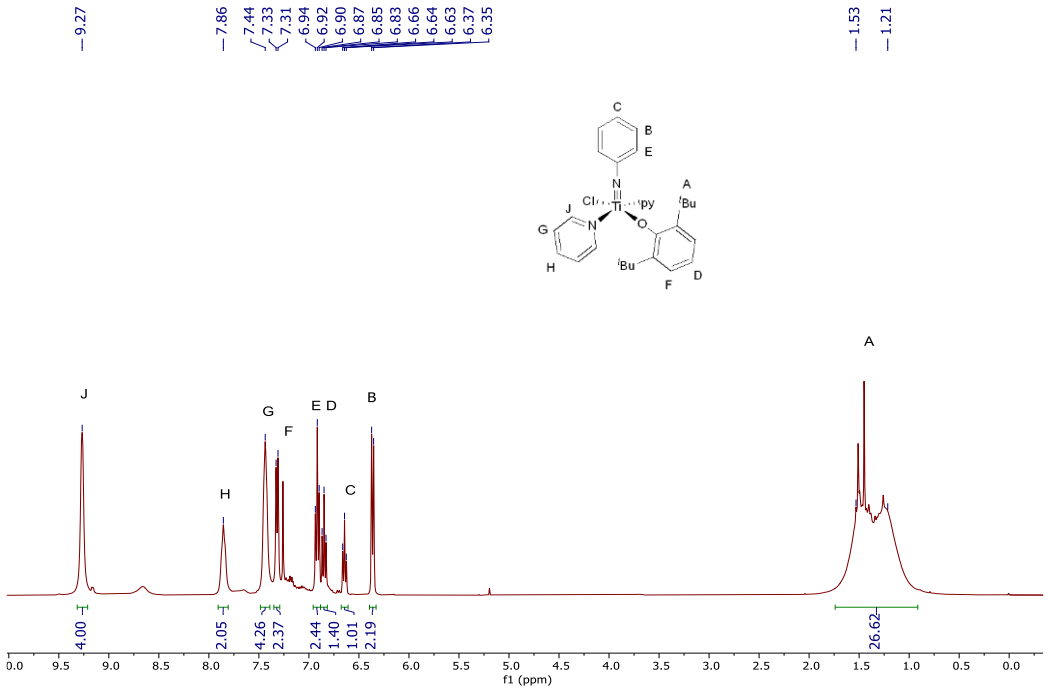

Figure 3.18 ^{1}H NMR spectrum of **3.7** in CDCl$_3$. *Taken from TAW01151.*

Synthesis of 12

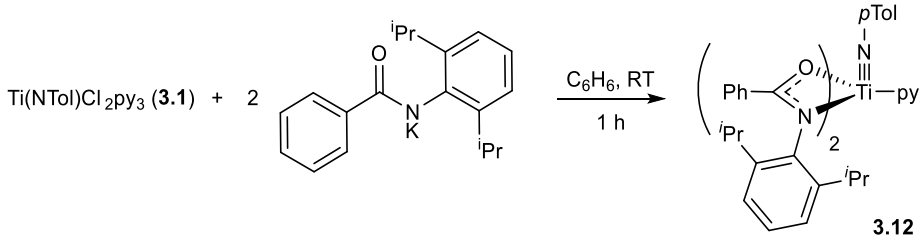

N-(2',6'-diisopropylphenyl)(phenyl)(amide)[196] (186 mg, 0.661 mmol, 2.2 equiv), KBn (86 mg, 0.660 mmol, 2.2 equiv) and 2 mL benzene were added to a 20 mL scintillation vial equipped with a small stir bar in a N_2-filled glovebox. This was stirred at room temperature for 10 min until a colorless solution formed. The colorless solution was added directly into a suspension of **3.1** (139 mg, 0.301 mmol, 1.0 equiv) and 8 mL benzene in a separate 20 mL scintillation vial equipped with a small stir bar. This was then sealed with a Teflon screw cap, stirred at room temperature for 1 h before passing through a plug of celite and drying the filtrate *in vacuo* to give a brown solid. The crude product was dissolved in 10 mL ether and filtered through a glass fiber filter paper fitted in a pipette. 10 mL of hexanes was then layered onto the ether solution and the mixture was placed in a - 35 °C freezer to yield **3.12** as brown crystals. (132 mg, 55 % yield). Elemental analysis was not attempted as complex decomposition would occur under prolonged drying on the vacuum line.

^{1}H NMR (400 MHz, C_6D_6): δ 9.34 (d, $^3J_{HH}$ = 4.4 Hz, 2H, *o*-py-*H*), 7.86 (d, $^3J_{HH}$ = 7.2 Hz, 4H, Ar-*H*), 7.23 (br s, 4H, Ar-*H*), 7.19 (br s, 2H, Ar-*H*), 6.96 – 6.87 (m, 6H, Ar-*H*), 6.74 (d, $^3J_{HH}$ = 8.1 Hz, 2H, *m*-NTol-*H*), 6.70 (t, $^3J_{HH}$ = 7.6 Hz, 1H, *p*-py-*H*), 6.59 (d, $^3J_{HH}$ = 8.2 Hz, 2H, *o*-NTol-*H*), 6.41 (t, $^3J_{HH}$ = 6.4 Hz, 2H, *m*-py-*H*), 4.19 (br s, 2H, ^{i}Pr$_2$C-*H*), 3.59 (br s, 2H, ^{i}Pr$_2$C-*H*), 2.02 (s, 3H, NC_6H_4-C*H*$_3$), 1.29 – 1.19 (m, 12H, ^{i}Pr-*H*), 1.12 – 1.10 (m, 6H, ^{i}Pr-*H*), 0.78 (br s, 6H, ^{i}Pr-*H*).

^{13}C NMR (101 MHz, C_6D_6): δ 158.0, 151.6, 143.1, 142.1, 139.1, 133.5, 131.4, 130.3, 129.7, 128.9, 128.0, 125.8, 125.0, 124.2, 124.1, 28.6, 28.2, 24.6, 23.9, 21.0 (NC_6H_4-*C*H$_3$).

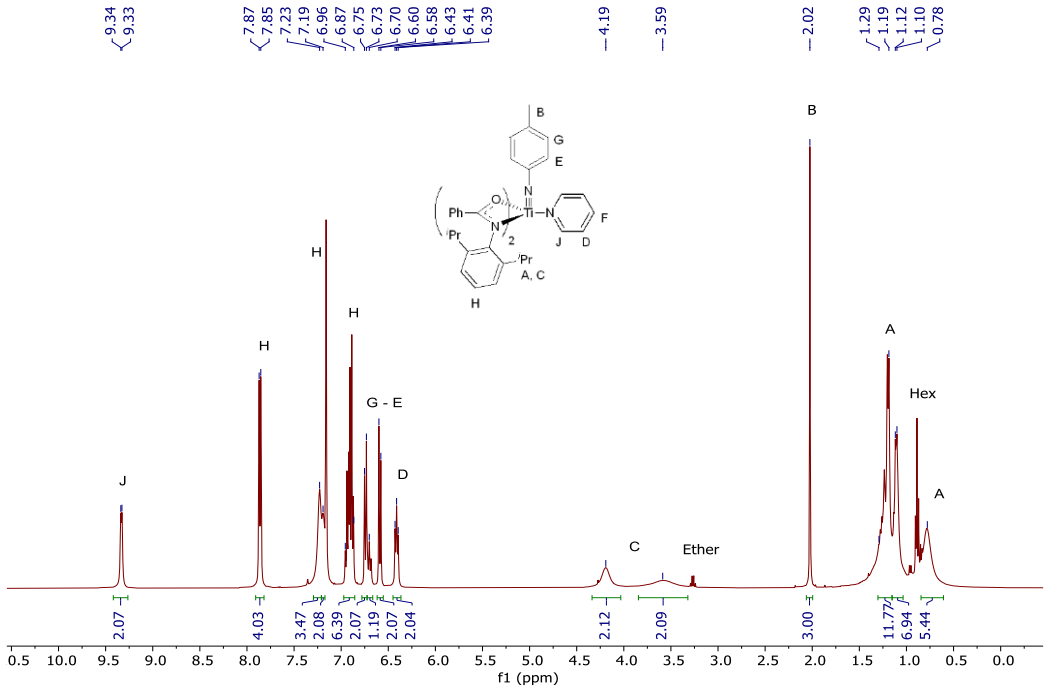

Figure 3.19 ^{1}H NMR spectrum of **3.12** in C_6D_6. *Taken from XYS02069_3H.*

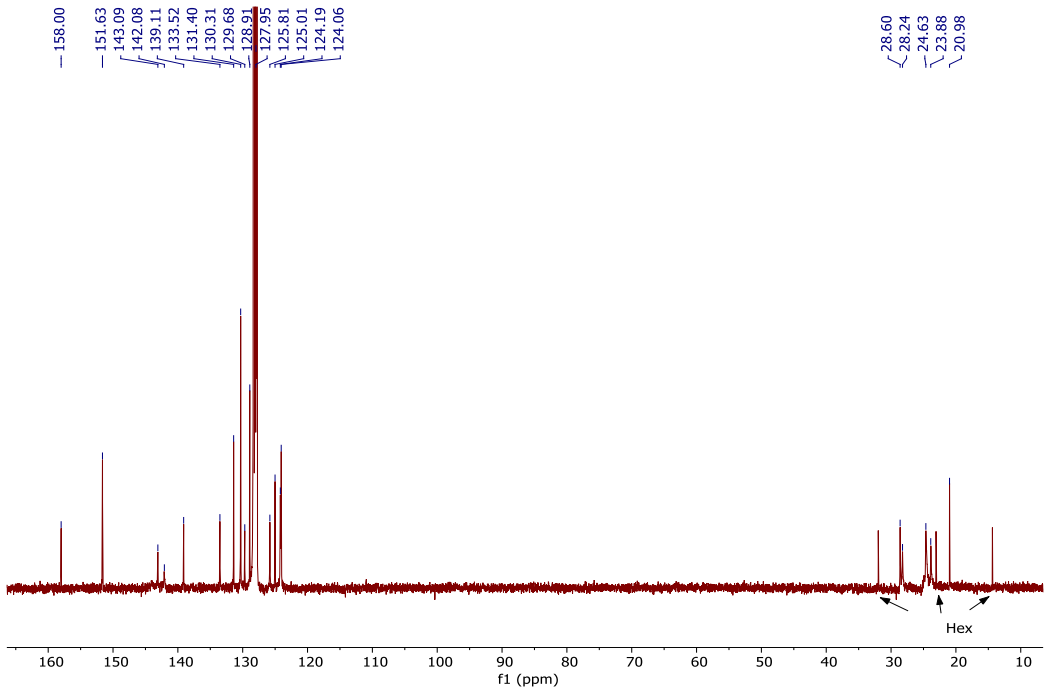

Figure 3.20 ^{13}C NMR spectrum of **3.12** in C_6D_6. *Taken from XYS02069_1C.*

Synthesis of 3.13

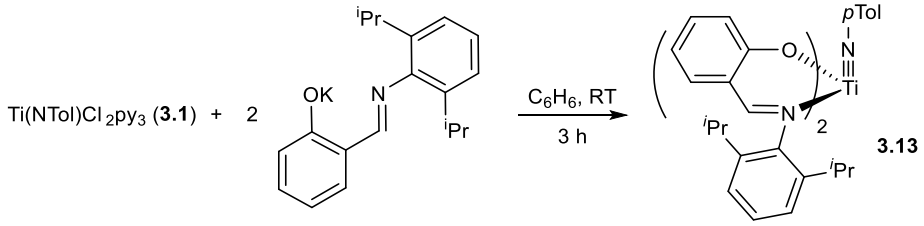

2,6-^{i}Pr$_2$Ph-salycilaldimine[197] (170 mg, 0.604 mmol, 1.2 equiv), KBn (79 mg, 0.607 mmol, 1.2 equiv) and 4 mL benzene were added to a 20 mL scintillation vial equipped with a small stir bar in a N_2-filled glovebox. This was stirred at room temperature for 15 min until a yellow solution formed. The yellow solution was added dropwise to a suspension of **3.1** (234 mg, 0.507 mmol, 1.0 equiv) and 10 mL benzene in a separate 20 mL scintillation vial equipped with a small stir bar. This was then sealed with a Teflon screw cap, stirred at room temperature for 3 h before filtering through a plug of celite and drying the filtrate *in vacuo*. The orange-red solid was dissolved in 15 mL ether and filtered through a glass fiber filter paper fitted in a pipette. The ether filtrate was concentrated to 2.5 mL, layered with 2.5 mL hexanes and placed in a - 35 °C freezer to yield **3.13** as a mixture of X-ray quality orange crystals and powder (160 mg from three crops of recrystallization, 45% yield).

Elemental analysis (calcd, found; for $C_{45}H_{51}N_3O_2Ti$): C (75.72, 74.12), H (7.20, 6.96), N (5.89, 5.69).

^{1}H NMR (400 MHz, C_6D_6): δ 8.15 (s, 2H, *H*-C=N), 7.34 – 7.27 (m, 4H, Ar-*H*), 7.18 (d, $^3J_{HH}$ = 2.1 Hz, 1H, Ar-*H*), 7.16 (br s, 1H, Ar-*H*), 7.11 (dd, $^3J_{HH}$ = 7.0 Hz, $^4J_{HH}$ = 1.7 Hz, 1H, Ar-*H*, 7.09 (dd, $^3J_{HH}$ = 6.9 Hz, $^4J_{HH}$ = 1.6 Hz, 1H, Ar-*H*), 7.04 (dd, $^3J_{HH}$ = 7.8 Hz, $^4J_{HH}$ = 1.7 Hz, 2H, Ar-*H*), 6.56 (d, $^3J_{HH}$ = 7.9 Hz, 4H, Ar-*H*), 6.46 (d, $^3J_{HH}$ = 8.3 Hz, 2H, *m*-NTol-*H*), 6.22 (d, $^3J_{HH}$ = 8.1 Hz, 2H, *o*-NTol-*H*), 3.89 (hept, $^3J_{HH}$ = 6.7 Hz, 2H, ^{i}Pr$_2$C-*H*), 2.60 (hept, $^3J_{HH}$ = 6.8 Hz, 2H, ^{i}Pr$_2$C-*H*), 1.95 (s, 3H, NC$_6$H$_4$-*CH$_3$*), 1.15 (d, $^3J_{HH}$ = 6.9 Hz, 6H, ^{i}Pr), 1.11 and 1.10 (d, $^3J_{HH}$ = 6.9 Hz, 12H, ^{i}Pr), 0.95 (d, $^3J_{HH}$ = 6.9 Hz, 6H, ^{i}Pr).

^{13}C NMR (101 MHz, C_6D_6): δ 168.9, 167.5, 160.1, 149.6, 142.4, 141.5, 136.0, 134.3, 129.7, 126.9, 124.5, 124.0, 123.3, 122.3, 120.3, 117.7, 29.5, 28.3, 25.3, 24.9, 23.8, 22.9, 21.0 (NC$_6$H$_4$-*C*H$_3$).

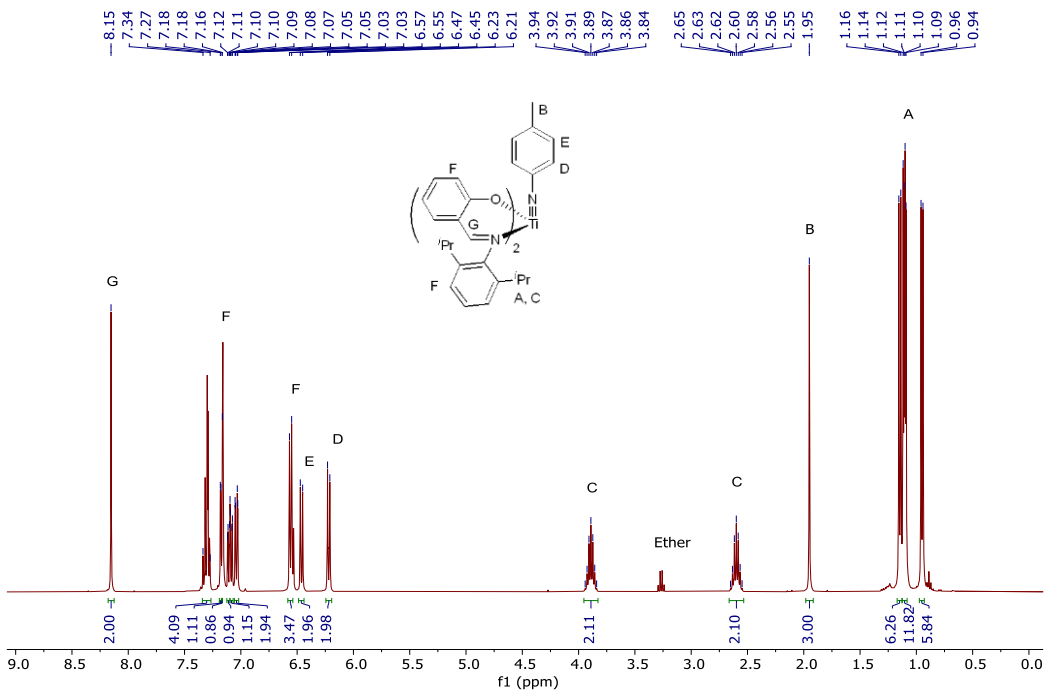

Figure 3.21 ^{1}H NMR spectrum of **3.13** in C_6D_6. *Taken from XYS02038_2H.*

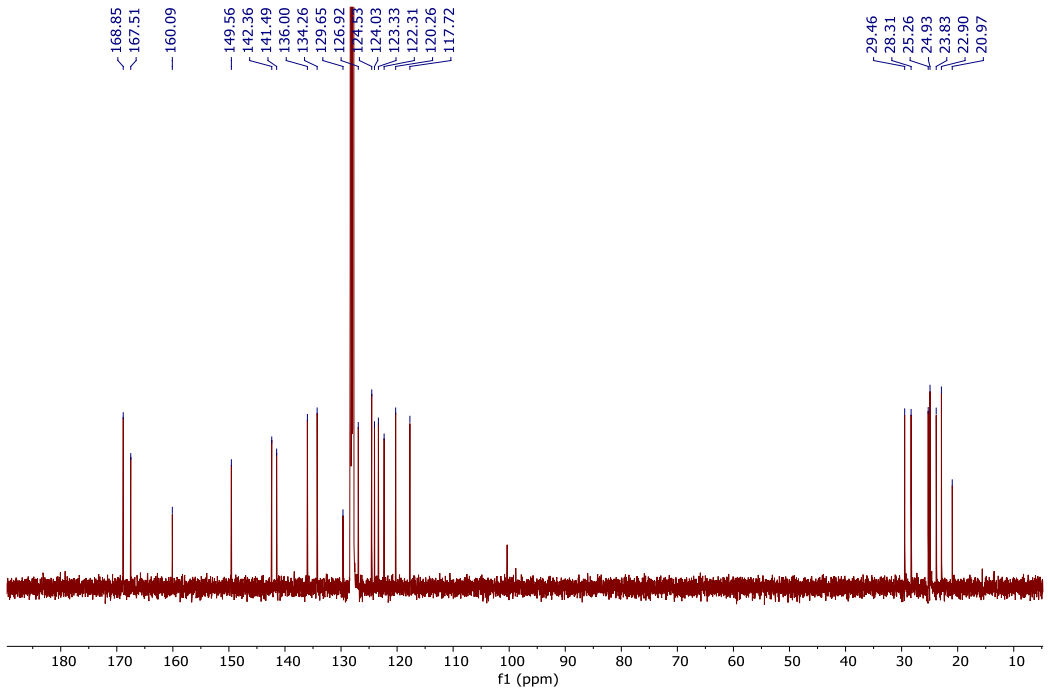

Figure 3.22 ^{13}C NMR spectrum of **3.13** in C_6D_6. *Taken from XYS02038_1C.*

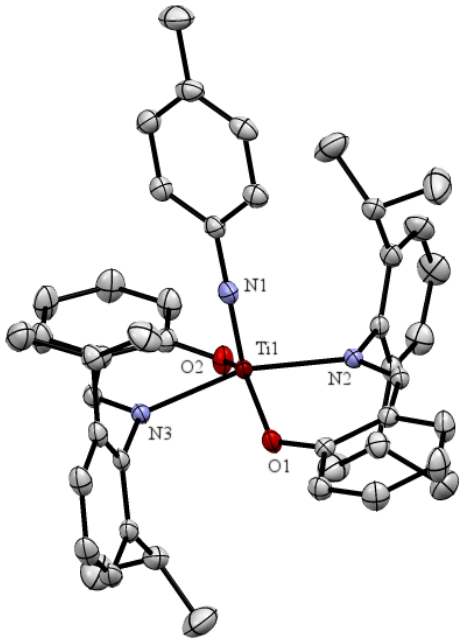

Figure 3.23 50 % thermal ellipsoid drawing of **13**. Hydrogen atoms are omitted for clarity.

Synthesis of 14

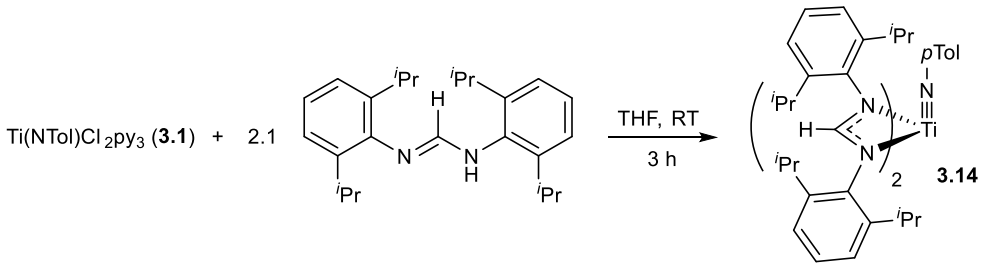

N,N'-(2,6-^{i}Pr$_2$Ph)$_2$formamidine[197] (454 mg, 1.25 mmol, 2.1 equiv), KBn (162 mg, 1.25 mmol, 2.1 equiv) and 2 mL THF were added to a 20 mL scintillation vial equipped with a small stir bar in a N_2-filled glovebox. This was stirred at room temperature for 10 min until a colorless solution formed. The colorless solution was added directly into a suspension of **3.1** (280 mg, 0.607 mmol, 1.0 equiv) and 4 mL THF in a separate 20 mL scintillation vial equipped with a small stir bar. This was then sealed with a Teflon screw cap, stirred at room temperature for 3 h before filtering through a plug of celite and drying the filtrate under vacuum to give a brown solid. 10 mL of ether was added to the solid and the suspension was filtered through a medium frit. The powder residue was dried *in vacuo* for 3 h to give **3.14**. The ether filtrate was further concentrated *in vacuo* to 5 mL, layered with 5 mL hexanes and left to stand at room temperature to yield more of **3.14** as a brown solid

(300 mg, 56 % yield from both the powder and solid). X-ray quality crystals were grown from a 2 : 1 ether : hexanes layering mixture. Elemental analysis was not attempted as complex decomposition would occur under prolonged drying on the vacuum line.

^{1}H NMR (400 MHz, C_6D_6): δ 8.29 (s, 2H, C-*H*), 7.07 (s, 12H, Ar-*H*), 6.94 (d, $^{3}J_{HH}$ = 8.2 Hz, 2H, *m*-NTol-*H*), 6.79 (d, $^{3}J_{HH}$ = 8.1 Hz, 2H, *o*-NTol-*H*), 4.58 (br s, 4H, $^{i}Pr_2C$-*H*), 3.09 (br s, 4H, $^{i}Pr_2C$-*H*), 2.09 (s, 3H, NC_6H_4-C*H*$_3$), 1.01 (br s, 48H, ^{i}Pr).

^{13}C NMR (101 MHz, C_6D_6): δ 164.9, 162.0, 143.6, 131.3, 128.6, 126.0, 124.7, 124.0, 28.2 (^{i}Pr), 25.7 (br, ^{i}Pr-*C*H), 23.4 (br, ^{i}Pr-*C*H), 21.0 (NC_6H_4-*C*H$_3$).

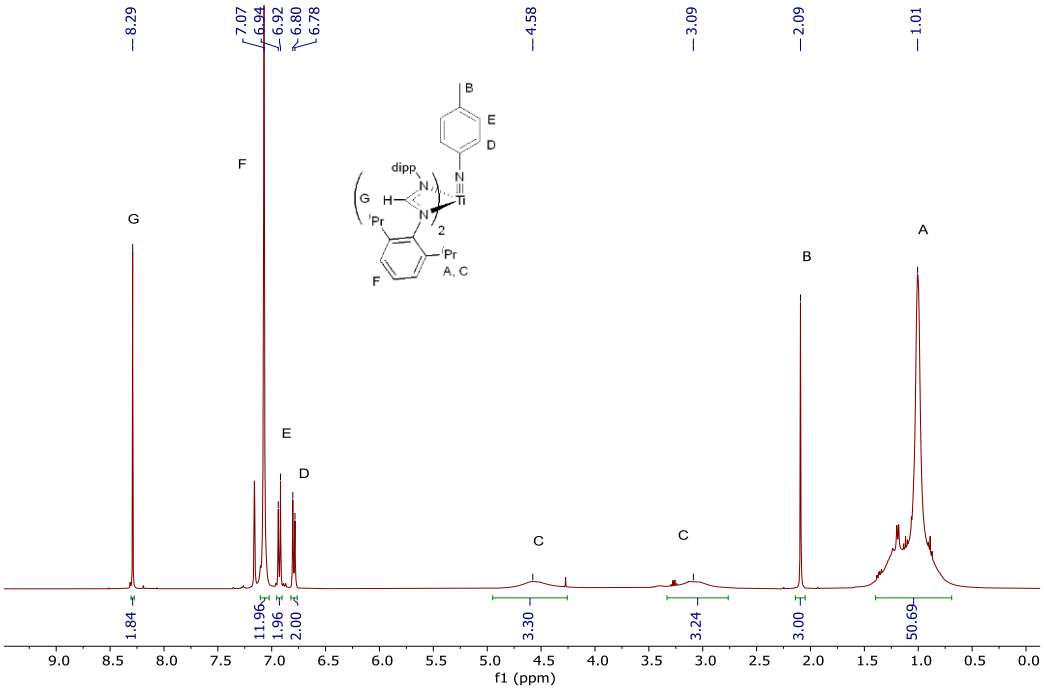

Figure 3.24 ^{1}H NMR spectrum of **3.14** in C_6D_6. *Taken from XYS02026_2H.*

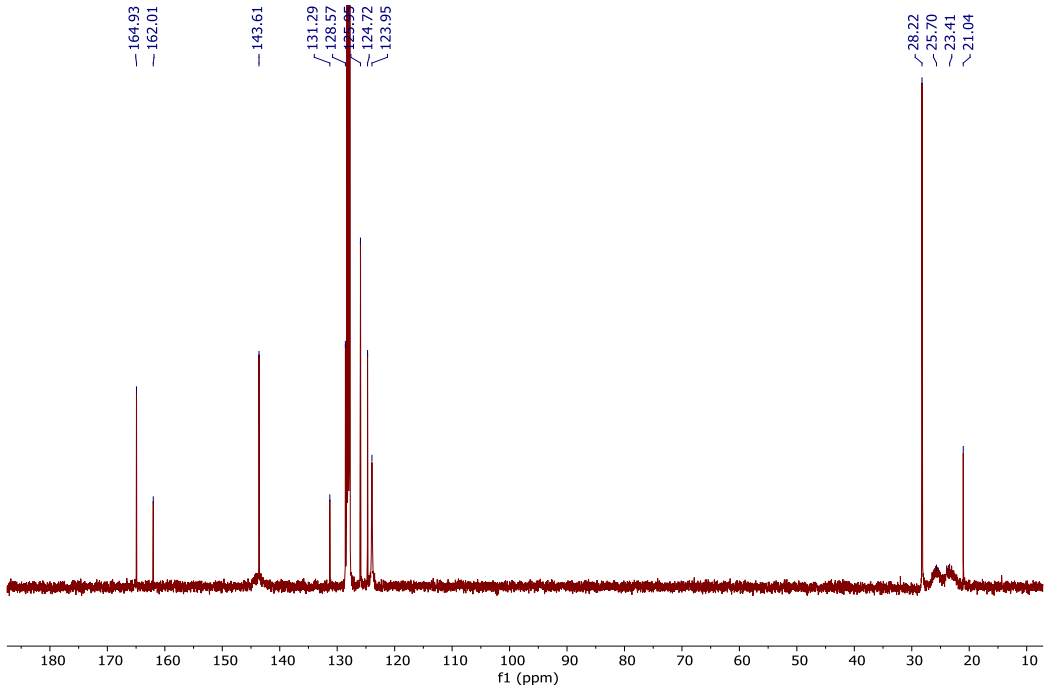

Figure 3.25 ^{13}C NMR spectrum of **3.14** in C_6D_6. *Taken from XYS02026.*

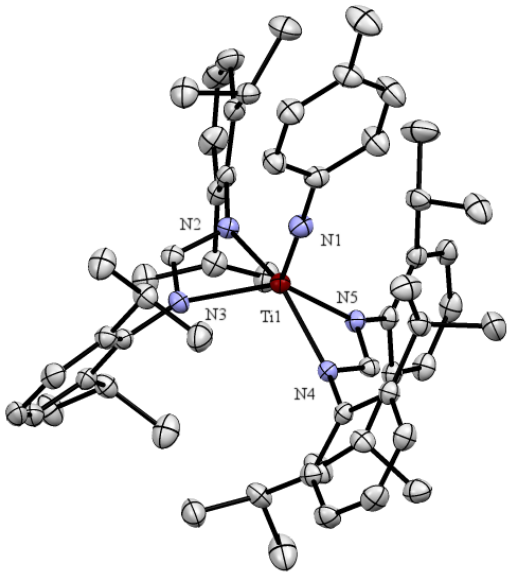

Figure 3.26 50 % thermal ellipsoid drawing of **3.14**. Hydrogen atoms are omitted for clarity.

Synthesis of 3.15

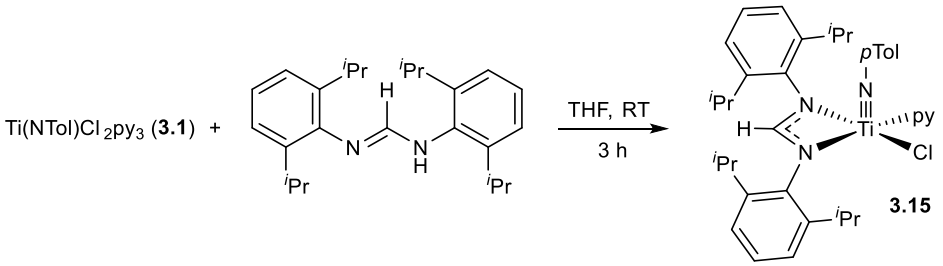

N,N'-(2,6-^{i}Pr$_2$Ph)$_2$formamidine[197] (201 mg, 0.551 mmol, 1.2 equiv), KBn (72 mg, 0.551 mmol, 1.2 equiv) and 4 mL THF were added to a 20 mL scintillation vial equipped with a small stir bar in a N_2-filled glovebox. This was stirred at room temperature for 10 min until a colorless solution formed. The colorless solution was added directly into a suspension of **3.1** (211 mg, 0.457 mmol, 1.0 equiv) and 10 mL THF in a separate 20 mL scintillation vial equipped with a small stir bar. This was then sealed with a Teflon screw cap, stirred at room temperature for 3 h before filtering through a plug of celite and drying *in vacuo* to give a brown solid. The solid was dissolved in 15 mL ether and insoluble material was removed *via* filtration through a glass fibre filter paper fitted in a pipette. 5 mL of hexanes were then layered upon the ether solution and the mixture was left to stand at room temperature to yield X-ray quality brown crystals of **3.15** (133 mg, 46 % yield). Elemental analysis was not attempted as complex decomposition would occur under prolonged drying on the vacuum line.

^{1}H NMR (400 MHz, C_6D_6): δ 8.73 (d, $^{3}J_{HH}$ = 4.9 Hz, 2H, *o*-py-*H*), 8.11 (s, 1H, C-*H*), 7.10 (br s, 5H, Ar-*H*), 7.08 (d, $^{3}J_{HH}$ = 8.4 Hz, 2H, *m*-NTol-*H*), 6.82 (d, $^{3}J_{HH}$ = 8.1 Hz, 2H, *o*-NTol-*H*), 6.53 (t, $^{3}J_{HH}$ = 7.7 Hz, 1H, *p*-py-*H*), 6.23 (t, $^{3}J_{HH}$ = 8.0 Hz, 2H, *m*-py-*H*), 4.03 (br s, 4H, ^{i}Pr$_2$C-*H*), 2.05 (s, 3H, NC$_6$H$_4$-C*H*$_3$), 1.25 (d, $^{3}J_{HH}$ = 6.0 Hz, 24H, ^{i}Pr-*H*).

^{13}C NMR (101 MHz, C_6D_6): δ 164.7, 160.7, 149.9, 144.5, 143.3, 138.6, 131.5, 128.9, 128.6, 126.0, 124.3, 124.1, 123.7, 28.1 (^{i}Pr), 24.8 (br, ^{i}Pr-*C*H), 21.0 (NC$_6$H$_4$-*C*H$_3$).

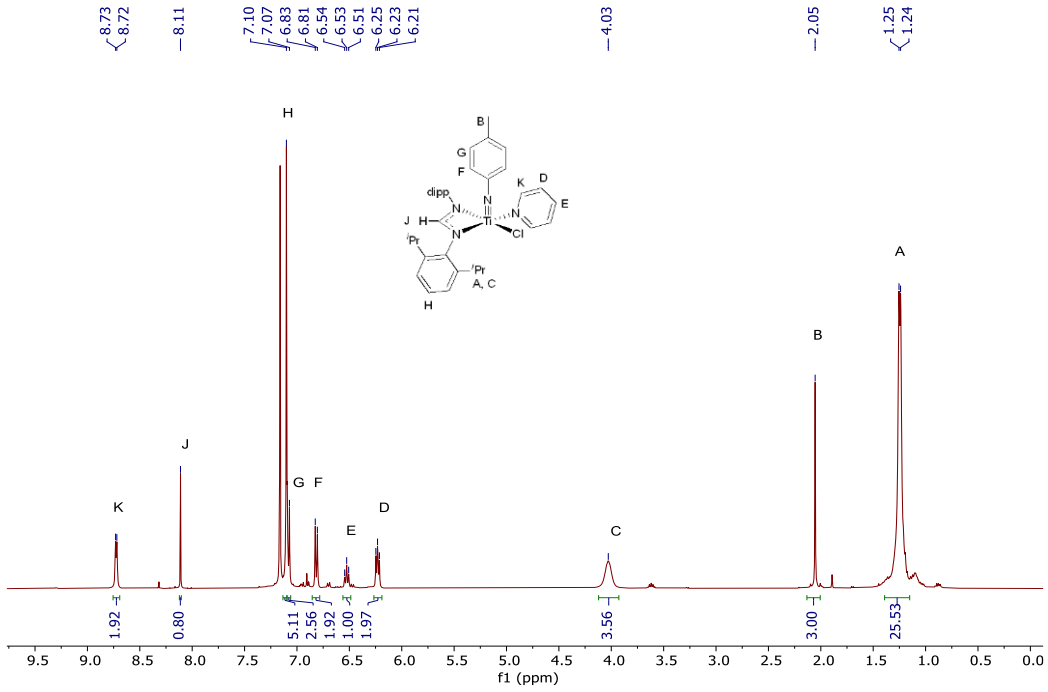

Figure 3.27 ^{1}H NMR spectrum of **3.15** in C_6D_6. *Taken from XYS02053_2H.*

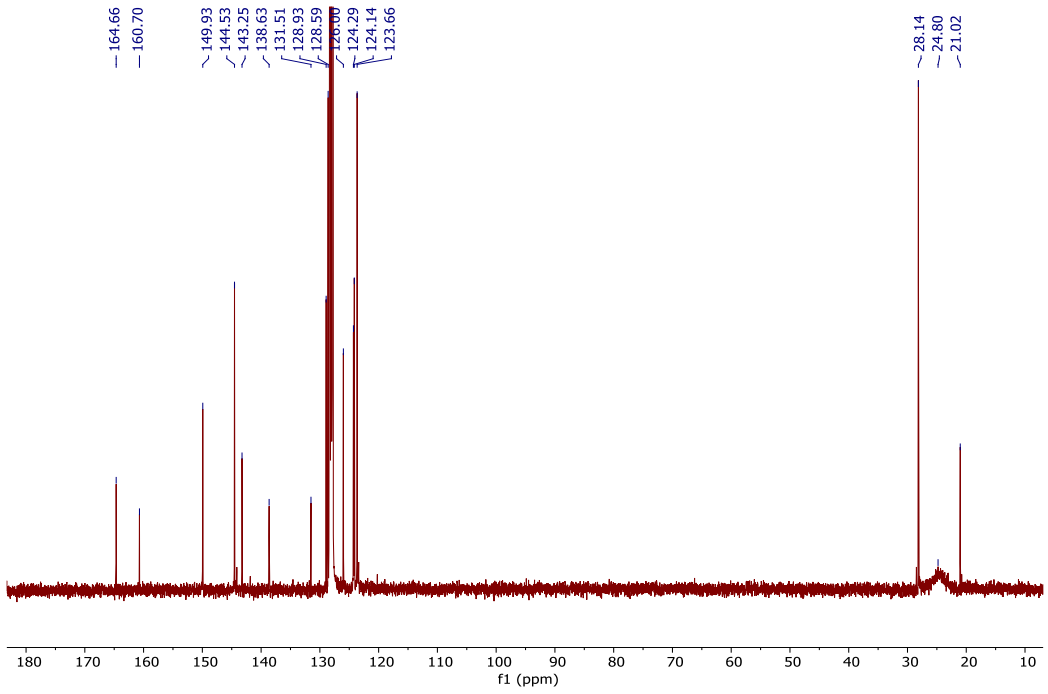

Figure 3.28 ^{13}C NMR spectrum of **3.15** in C_6D_6. *Taken from XYS02053_1C.*

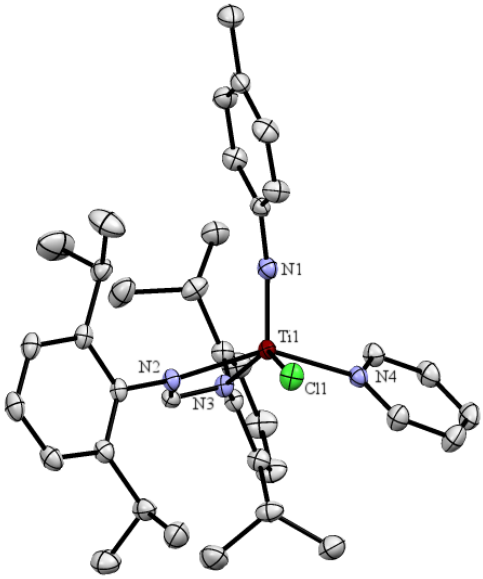

Figure 3.29 50 % thermal ellipsoid drawing of **3.15**. Hydrogen atoms are omitted for clarity.

Synthesis of 3.16

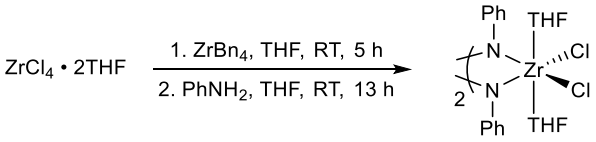

3.16

3.16 was synthesized *via* a modification of the literature procedure, starting from $ZrBn_4$ instead of $Zr(CH_2TMS)_4$.[198] $ZrCl_4(THF)_2$ (4.47 g, 11.8 mmol, 1.0 equiv) and 100 mL THF were added to a 250 mL round-bottom flask equipped with a stir bar in a N_2-filled glovebox. Separately, $ZrBn_4$ (5.40 g, 11.8 mmol, 1.0 equiv) was dissolved in 25 mL THF in a 50 mL round-bottom flask. The $ZrBn_4$ solution was added in dropwise to the THF solution of $ZrCl_4$, with rapid stirring. The flask was sealed, covered in aluminum foil and stirred at room temperature for 5 h to *in situ* generate $ZrCl_2Bn_2$. Afterward, aniline (2.21 g, 23.7 mmol, 2.0 equiv) in 10 mL THF was added dropwise to the reaction mixture. The reaction was stirred for 13 h at room temperature while covered in aluminum foil. Volatiles were then removed under vacuum and the residual brown-yellow solid was dissolved in a minimal amount of 5 : 1 CH_2Cl_2/THF, transferred into two 20 mL vials and layered with

an equal volume of pentane. The solutions were placed in a - 35 °C freezer for three days to afford **3.16** as a yellow crystalline solid (8.68 g, 92 % yield).

^{1}H NMR (400 MHz, $CDCl_3$): δ 7.18 (t, $^{3}J_{HH}$ = 7.8 Hz, 4H, *m*-NPh-*H*), 7.10 (d, $^{3}J_{HH}$ = 7.2 Hz, 4H, *o*-NPh-*H*), 6.76 (t, $^{3}J_{HH}$ = 7.2 Hz, 2H, *p*-NPh-*H*), 3.99 (br s, 16H, 2,5-THF-*H*), 1.71 (br s, 16H, 3,4-THF-*H*).

^{13}C NMR (101 MHz, $CDCl_3$): δ 152.9, 128.5, 121.7, 121.0, 72.8 (br s), 25.5.

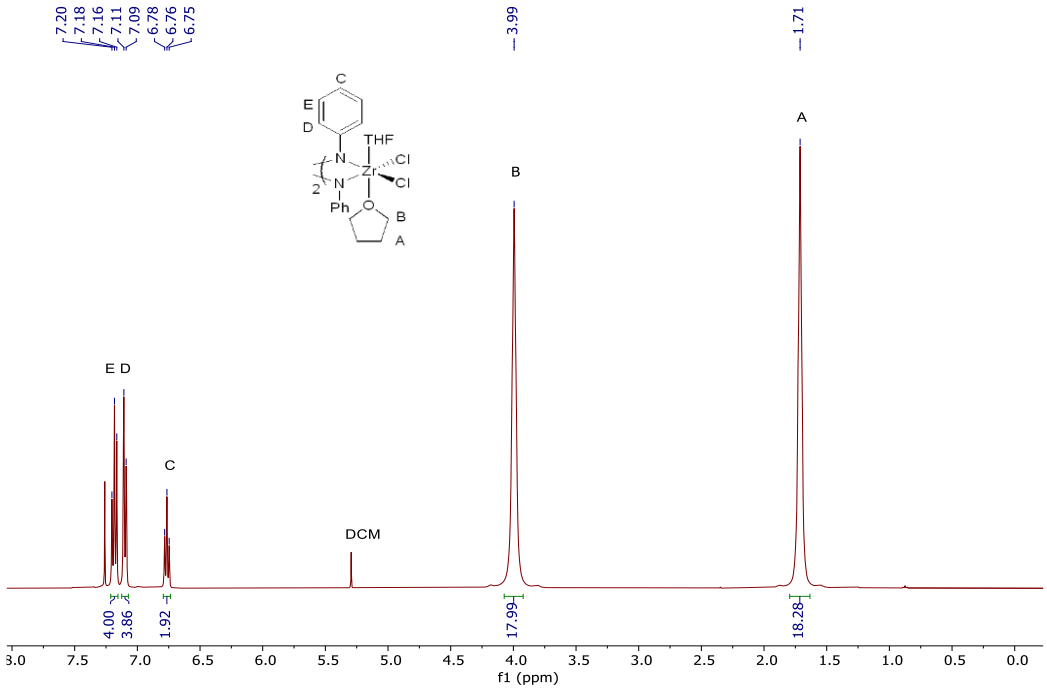

Figure 3.30 ^{1}H NMR spectrum of **3.16** in $CDCl_3$. *Taken from EPB02010.*

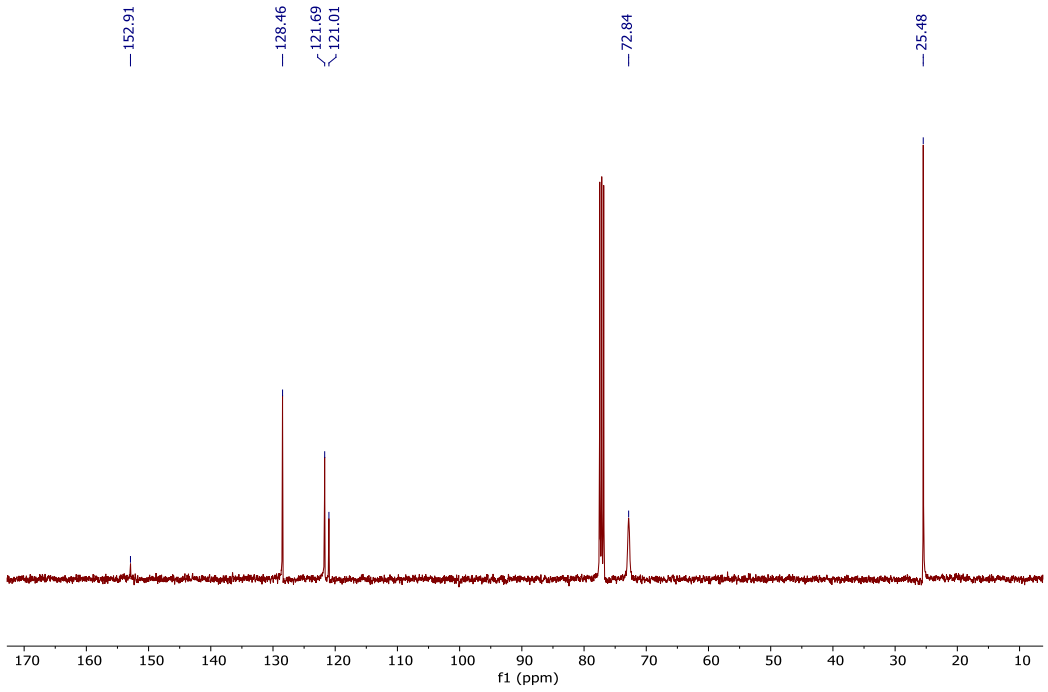

Figure 3.31 ^{13}C NMR spectrum of **3.16** in $CDCl_3$. *Taken from EPB02010.*

Synthesis of 3.17

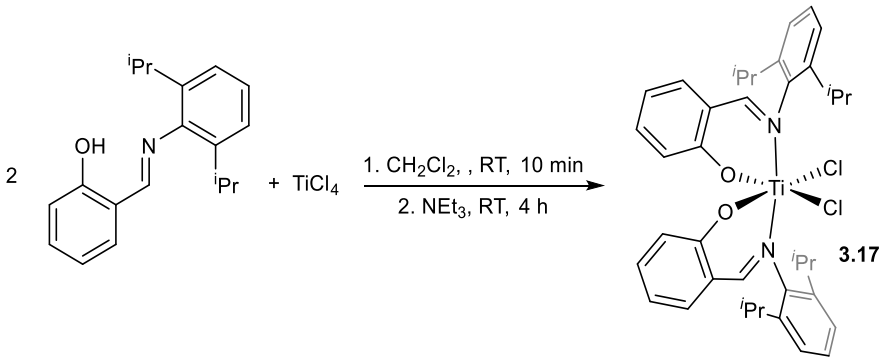

3.17 was synthesized *via* slight modification of literature procedure.[199] N-(2',6'-diisopropylphenyl)(phenoxyimine) ligand (1.49 g, 5.28 mmol, 2.0 equiv)[196] and 20 mL CH_2Cl_2 were added to a 50 mL round-bottom flask equipped with a stir bar in a N_2-filled glovebox. This solution was then added to a stirring solution of $TiCl_4$ (0.50 g, 2.64 mmol, 1.0 equiv) and 30 mL CH_2Cl_2 in a 100 mL round-bottom flask equipped with a stir bar. The orange-red solution was stirred at room temperature for 10 min before addition of NEt_3 (0.53 g, 0.74 mL, 5.28 mmol, 2.0 equiv). The mixture was stirred at room temperature for 4 h before drying under vacuum to give a red solid. 50 mL of toluene was added to the red solid and the suspension filtered to remove NH_4Cl. The filtrate was dried under vacuum

and the remaining orange solid was washed with 2 x 10 mL hexanes and stirred in 10 mL hexanes for two days before filtering to yield **3.17** that matched NMR literature (1.23 g, 69 % yield).

3.5.3 Characterization of substrates and standards in C_6D_5Br

1,3,5-trimethoxybenzene

^{1}H NMR (400 MHz, C_6D_5Br): δ 6.12 (s, 3H, Ar-*H*), 3.51 (s, 9H, C*H*$_3$).

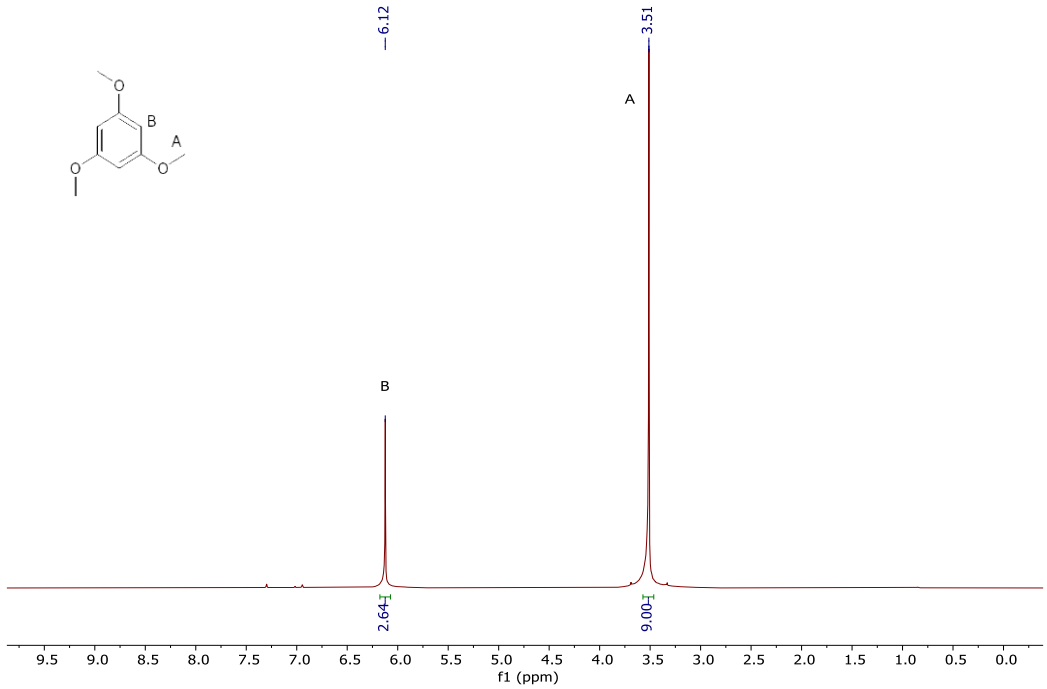

Figure 3.32 ^{1}H NMR spectrum of 1,3,5-trimethoxybenzene in C_6D_5Br.

3-hexyne

^{1}H NMR (400 MHz, C_6D_5Br): δ 2.06 (q, $^3J_{HH}$ = 7.4 Hz, 4H, C*H*$_2$), 1.02 (t, $^3J_{HH}$ = 7.4 Hz, 6H, C*H*$_3$).

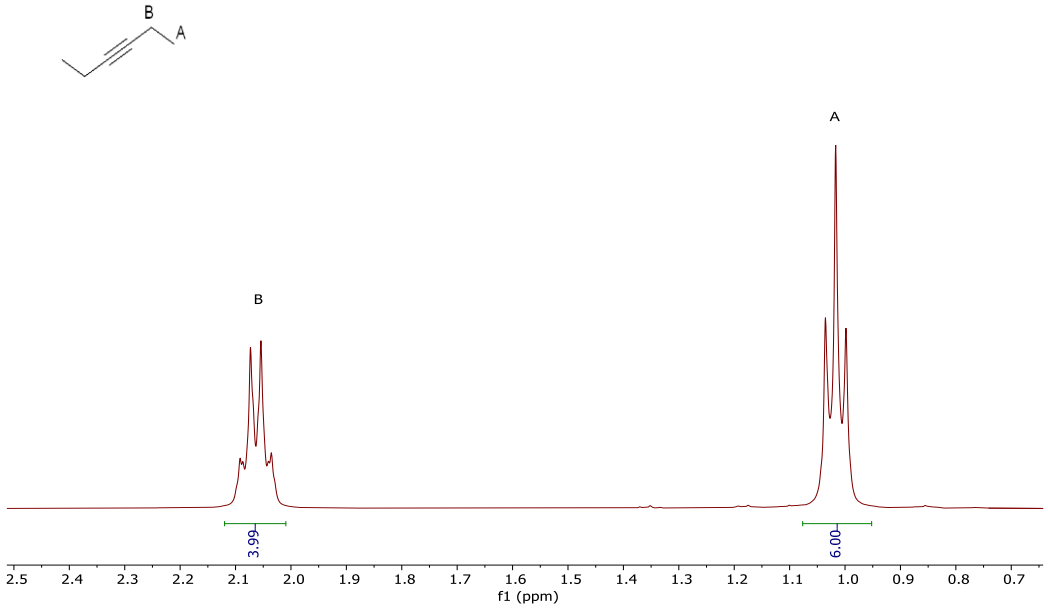

Figure 3.33 ^{1}H NMR spectrum of 3-hexyne in C_6D_5Br.

1-hexyne

^{1}H NMR (400 MHz, C_6D_5Br): δ 2.02 (td, $^{3}J_{HH}$ = 6.9, $^{4}J_{HH}$ = 2.6 Hz, 2H, -C*H*$_2$CH$_2$CH$_2$CH$_3$), 1.89 (t, $^{4}J_{HH}$ = 2.6 Hz, 1H, ^{n}Bu≡*H*), 1.38 – 1.23 (m, 4H, -CH$_2$C*H*$_2$C*H*$_2$CH$_3$), 0.78 (t, $^{3}J_{HH}$ = 7.2 Hz, 3H, -CH$_2$CH$_2$CH$_2$C*H*$_3$).

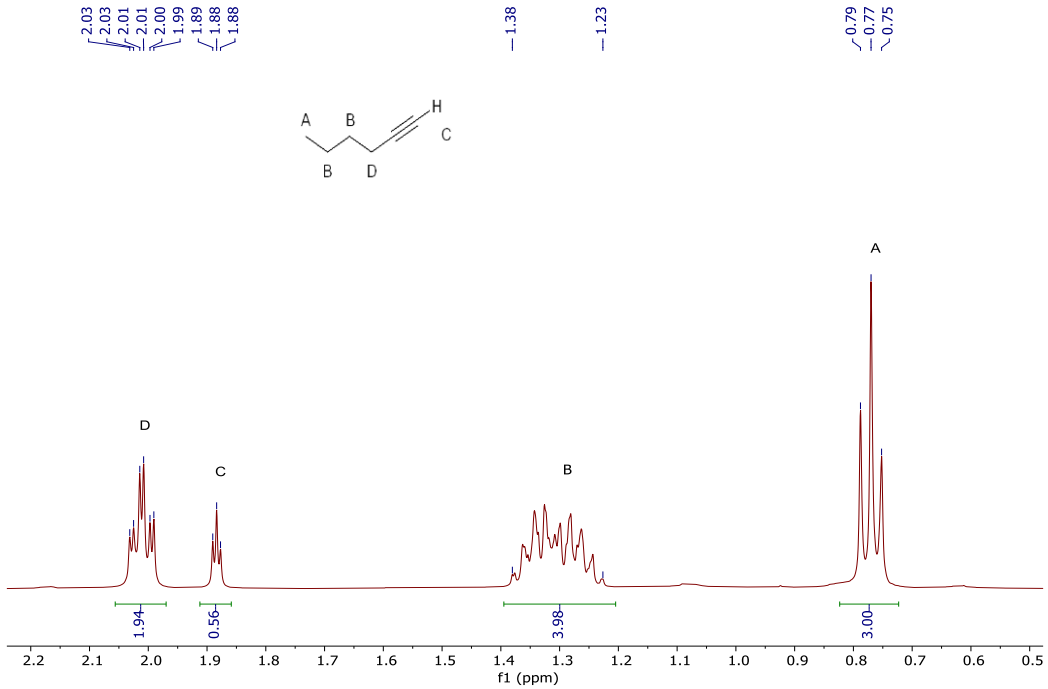

Figure 3.34 ^{1}H NMR spectrum of 1-hexyne in C_6D_5Br.

5,7-dodecadiyne

^{1}H NMR (400 MHz, C_6D_5Br): δ 2.08 (t, $^{3}J_{HH}$ = 6.8 Hz, CH_2CH$_2$CH$_2$CH$_3$), 1.35 – 1.19 (m, 8H, CH$_2$CH_2CH$_2$CH_3 and CH$_2$CH$_2$CH_2CH$_3$), 0.75 (t, $^{3}J_{HH}$ = 7.2 Hz, 6H, CH$_2$CH$_2$CH$_2$CH_3).

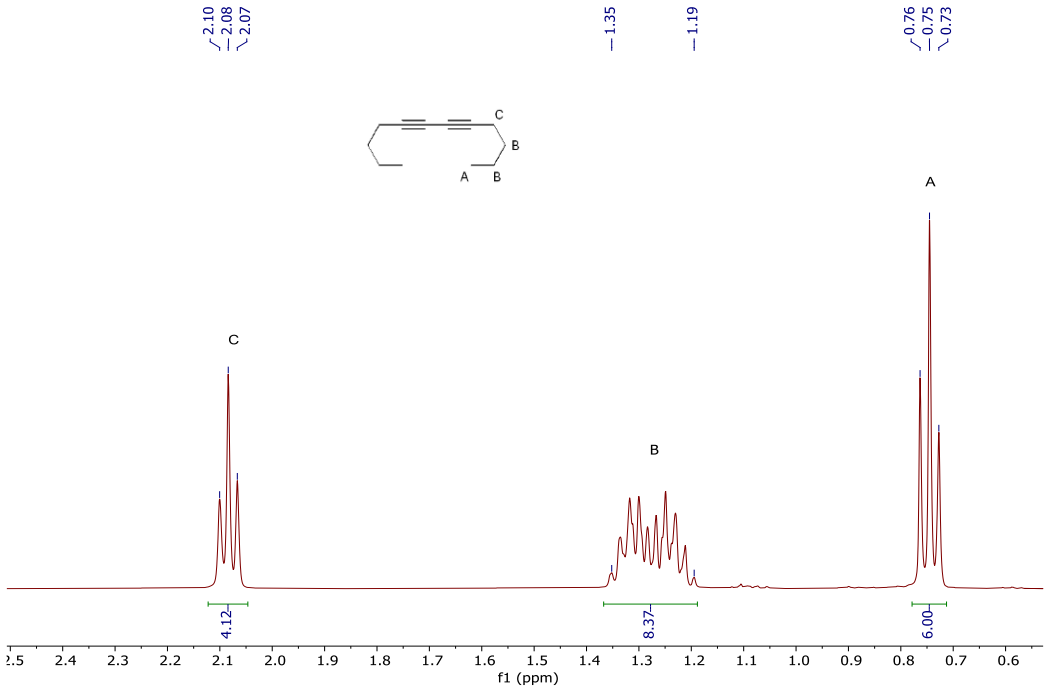

Figure 3.35 ^{1}H NMR spectrum of 5,7-dodecadiyne in C_6D_5Br.

Characterization of 1,3,5-tri-*n*-butyl-benzene (3a) and 1,2,4-tri-*n*-butyl-benzene (3b) in C_6D_5Br

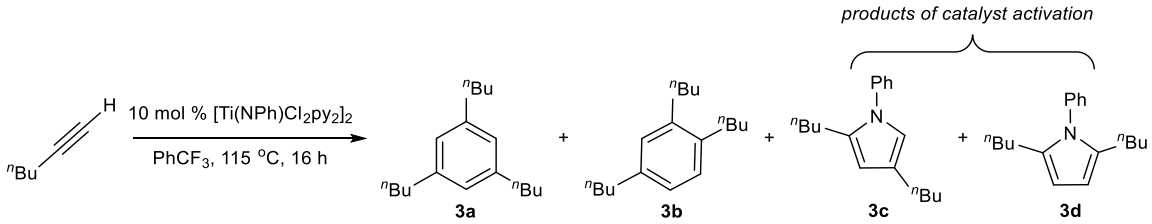

$[Ti(NPh)Cl_2py_2]_2$ (10 mg, 0.01 mmol, 10 mol % of Ti), 1-hexyne (22 mg, 0.268 mmol, 1 equiv) and 1 mL of trifluorotoluene were added to a 20 mL scintillation vial equipped with a small stir bar in a N_2-filled glovebox. This was then sealed with a Teflon screw cap and heated overnight at 115 °C for 16 h. The reaction mixture was then quenched with a solution of 5 mL CH_2Cl_2 : 5 mL H_2O. The organic layer was then washed with 2 x 5 mL H_2O, 5 mL brine, dried over $MgSO_4$, filtered and concentrated to give a yellow oil that contained a mixture of the title compounds (**3a** and **3b**), **3c** and **3d**.

1,3,5-tri-*n*-butyl-benzene (3a)

^{1}H NMR (400 MHz, C_6D_5Br): δ 6.84 (s, 3H, Ar-*H*), 2.60 – 2.51 (m, 6H, C*H*$_2$CH$_2$CH$_2$CH$_3$), 1.58 – 1.50 (m, 6H, CH$_2$C*H*$_2$CH$_2$CH$_3$), 1.38 – 1.27 (m, 6H, CH$_2$CH$_2$C*H*$_2$*C*H$_3$), 0.95 – 0.85 (m, 9H, CH$_2$CH$_2$CH$_2$C*H*$_3$).

1,2,4-tri-*n*-butyl-benzene (3b)

^{1}H NMR (400 MHz, C_6D_5Br): δ 7.06 (d, $^3J_{HH}$ = 7.7 Hz, 1H, C$_6$-Ar-*H*), 6.97 (app d, $^3J_{HH}$ = 7.1 Hz, 2H, C$_3$-Ar-*H* and C$_5$-Ar-*H*), 2.60 – 2.51 (m, 6H, C*H*$_2$CH$_2$CH$_2$CH$_3$), 1.58 – 1.50 (m, 6H, CH$_2$C*H*$_2$CH$_2$CH$_3$), 1.38 – 1.27 (m, 6H, CH$_2$CH$_2$C*H*$_2$*C*H$_3$), 0.95 – 0.85 (m, 9H, CH$_2$CH$_2$CH$_2$C*H*$_3$).

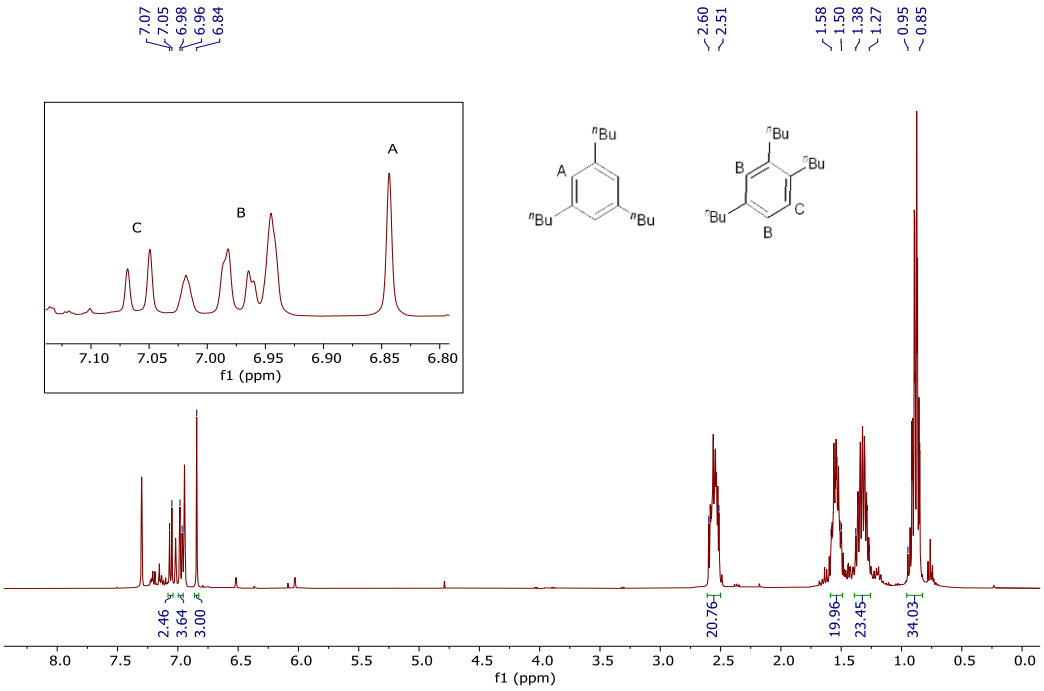

Figure 3.36 ^{1}H NMR spectrum of the mixture of 1,3,5-tri-*n*-butyl-benzene (**3a**) and 1,2,4-tri-*n*-butyl-benzene (**3b**) in C_6D_5Br. *Taken from XYS02044_2H.*

Characterization of hexaethylbenzene (3f) in C_6D_5Br

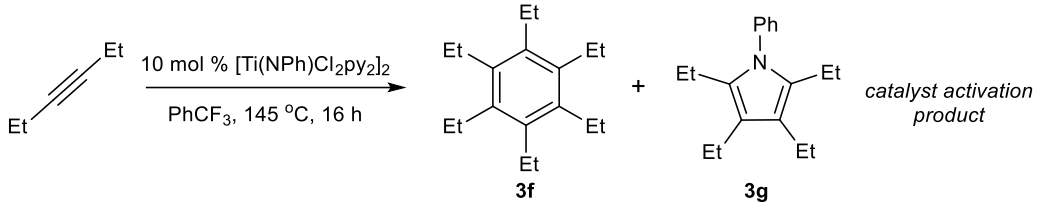

$[Ti(NPh)Cl_2py_2]_2$ (10 mg, 0.0136 mmol, 10 mol % of Ti), 3-hexyne (22 mg, 0.268 mmol, 1 equiv) and 1 mL of trifluorotoluene were added to a 20 mL scintillation vial equipped with a small stir bar in a N_2-filled glovebox. This was then sealed with a Teflon screw cap and heated overnight at 145 °C for 16 h. The reaction mixture was then quenched with a solution of 5 mL CH_2Cl_2 : 5 mL H_2O. The organic layer was washed with 2 x 5 mL H_2O, 5 mL brine, dried over $MgSO_4$, filtered and concentrated to give a pale-yellow solid that contained a mixture of the title compound (**3f**) and **3g**.

^{1}H NMR (400 MHz, C_6D_5Br): δ 2.61 (q, $^3J_{HH}$ = 7.4 Hz, 12H, CH_2), 1.11 ppm (t, $^3J_{HH}$ = 7.4 Hz, 18H, CH_3).

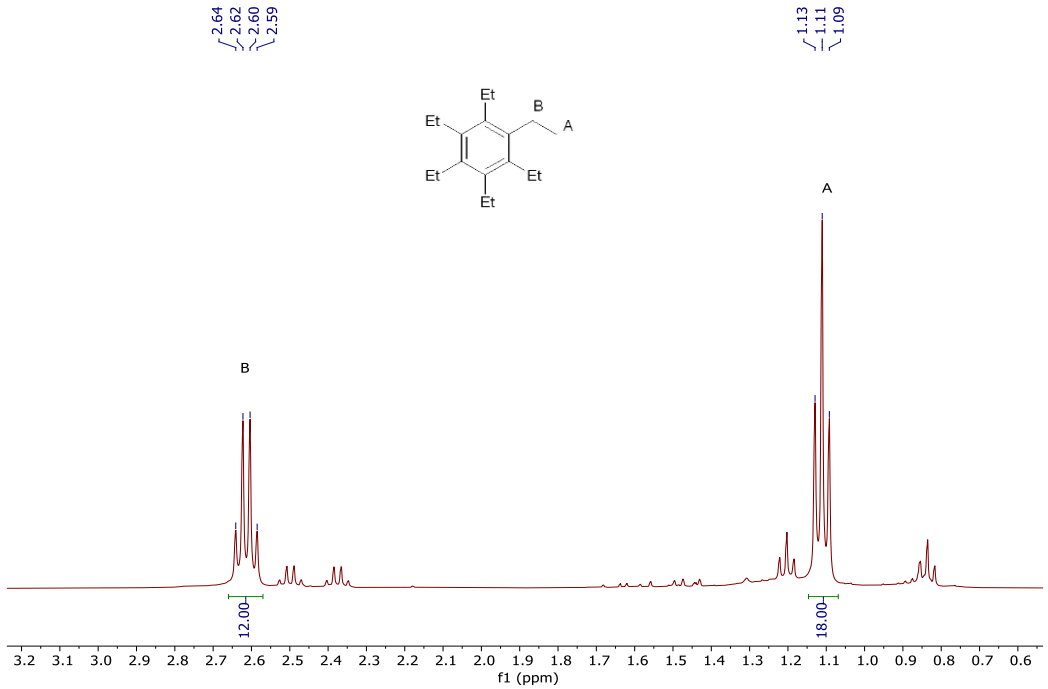

Figure 3.37 ^{1}H NMR spectrum of hexaethylbenzene (**3f**) in C_6D_5Br. Taken from *XYS02045_2H*.

Characterization of 2,5-di-*n*-butyl-1-tolyl-1*H*-pyrrole (3d) in C_6D_5Br

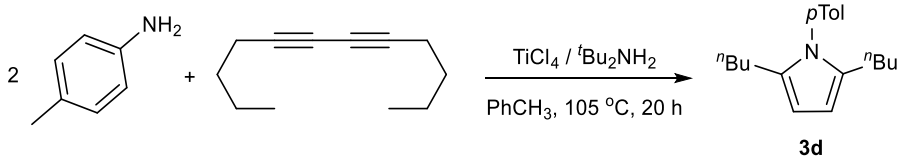

3d

The title compound was prepared *via* slight modification of the literature procedure.[200] *p*-toluidine (159 mg, 1.48 mmol, 2.0 equiv), 5,7-dodecadiyne (121 mg, 0.746 mmol, 1.0 equiv), $TiCl_4$ (34 mg, 0.179 mmol, 24 mol %), *t*-butylamine (70 mg, 0.957 mmol, 1.3 equiv) and 10 mL toluene were added to a 20 mL scintillation vial equipped with a small stir bar in a N_2-filled glovebox. This was then sealed with a Teflon screw cap and heated at 105 °C for 20 h. The reaction mixture was then concentrated *in vacuo* to dryness before dissolving in minimal hexanes. Product was purified with a neutral alumina column using 100 % hexanes as eluent. After the first spot on the TLC was obtained, more polar eluents were used: first 50 % hexanes : 50 % ether to 100 % ether eluent to collect the second spot. The fractions containing the second spot were dried *in vacuo* to give the title compound (**3d**) and starting reagent diyne.

^{1}H NMR (400 MHz, C_6D_5Br): δ 7.02 (d, $^3J_{HH}$ = 7.6 Hz, 2H, *m*-NTol-*H*), 6.97 (d, $^3J_{HH}$ = 8.7 Hz, 2H, *o*-NTol-*H*), 6.08 (s, 2H, C3-*H* and C4-*H*), 2.38 (t, $^3J_{HH}$ = 7.6 Hz, 4H, $CH_2CH_2CH_2CH_3$), 2.14 (s, 3H, NC_6H_4-CH_3), 1.46 (pentet, $^3J_{HH}$ = 7.4 Hz, 4H, $CH_2CH_2CH_2CH_3$), 0.75 (q, $^3J_{HH}$ = 7.3 Hz, 6H, $CH_2CH_2CH_2CH_3$).

Peak for $CH_2CH_2CH_2CH_3$ is hidden beneath the multiplet at δ 1.35 – 1.15. There is also an overlap of the δ 0.75 signal with 5,7-dodecadiyne resulting in an apparent quartet. The NTol signals (δ 6.97 and δ 7.01) overlap with the residual protio impurities of C_6D_5Br.

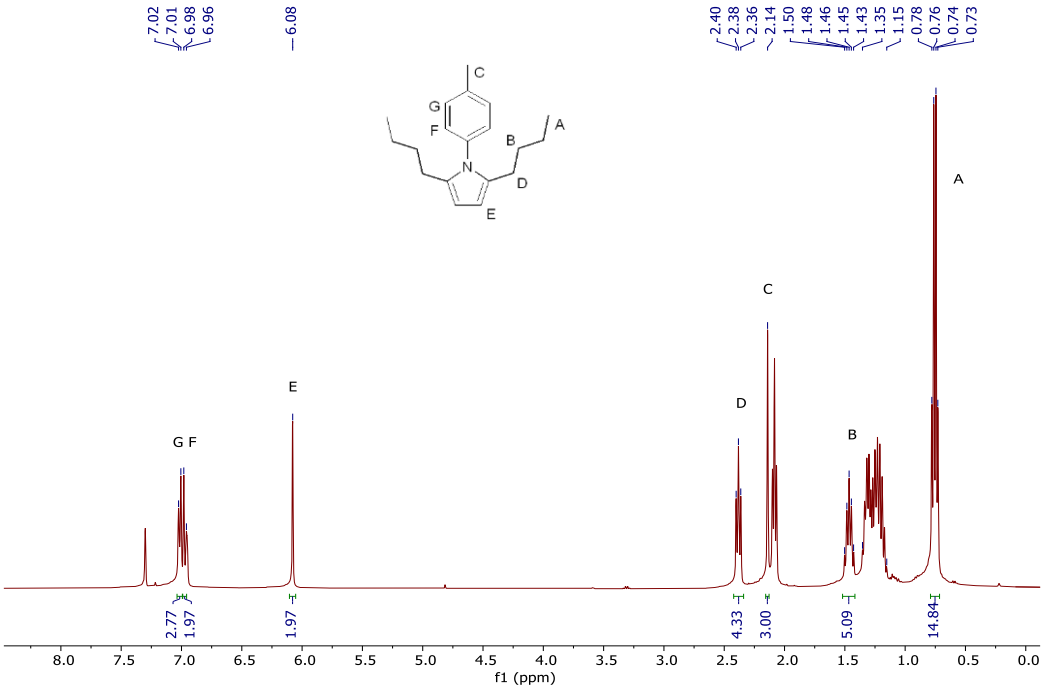

Figure 3.38 ^{1}H NMR spectrum of 2,5-di-*n*-butyl-1-tolyl-1*H*-pyrrole (**3d**) in C_6D_5Br. *Taken from XYS02154_3H.*

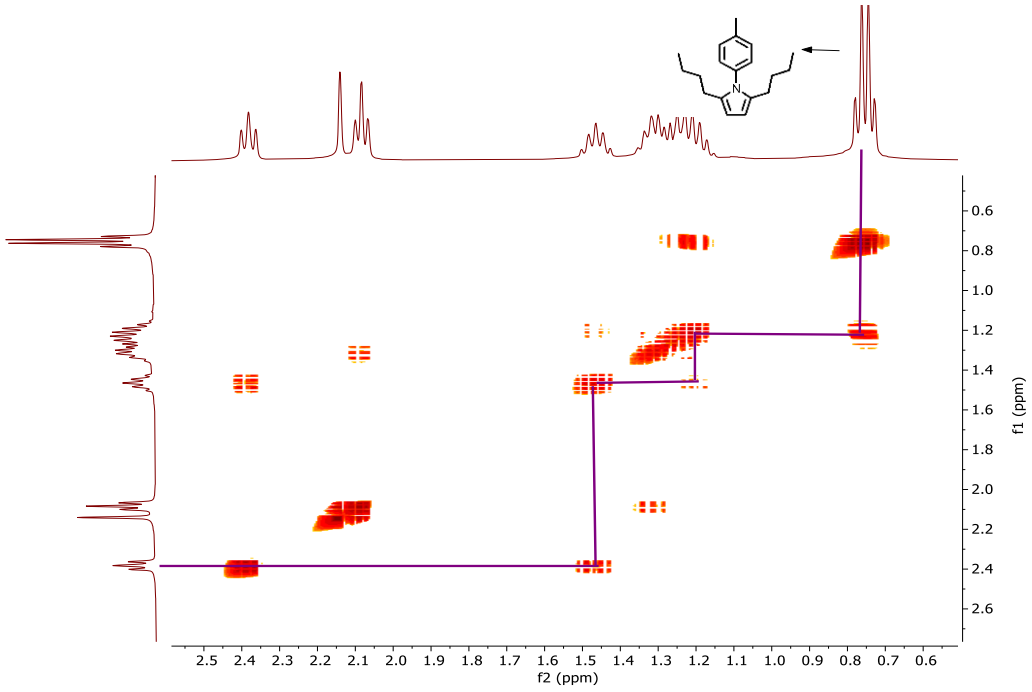

Figure 3.39 Zoom-in ^{1}H-^{1}H COSY NMR spectrum of 2,5-di-*n*-butyl-1-tolyl-1*H*-pyrrole (**3d**) in C_6D_5Br. *Taken from XYS02154_1COSY.*

Characterization of 2,4-di-*n*-butyl-1-*p*-tolyl-1*H*-pyrrole (3c) in C_6D_5Br

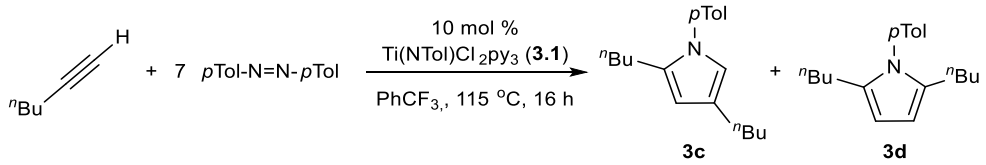

3.1 (10 mg, 0.0217 mmol, 10 mol %), 1,2-di(*p*-tolyl)diazene (306 mg, 1.46 mmol, 7.0 equiv), 1-hexyne (17 mg, 0.207 mmol, 1.0 equiv) and 1 mL of trifluorotoluene were added to a 20 mL scintillation vial equipped with a small stir bar in a N_2-filled glovebox. This was then sealed with a Teflon screw cap and heated overnight at 115 °C for 16 h. The reaction mixture was then concentrated *in vacuo* to dryness and 10 mL of cold hexanes was added to the reaction mixture. Insoluble material was filtered off and the filtrate was concentrated to give a black solid material that contained a mixture of the title compound (**3c**), **3d** and 1,2-di(*p*-tolyl)diazene.

^{1}H NMR (400 MHz, C_6D_5Br): δ 7.06 (d, $^3J_{HH}$ = 8.2 Hz, 2H, *m*-NTol-*H*), 6.99 (d, $^3J_{HH}$ = 8.0 Hz, 2H, *o*-NTol-*H*), 6.54 (s, 1H, C4-*H*), 6.03 (s, 1H, C2-*H*), 2.58 – 2.48 (m, 4H, *o*-C*H*$_2$CH$_2$CH$_2$CH$_3$ and *m*-C*H*$_2$CH$_2$CH$_2$CH$_3$), 2.16 (s, 3H, NC$_6$H$_4$-C*H*$_3$), 1.65 (app quintet, $^3J_{HH}$ = 7.6, *o*-CH$_2$C*H*$_2$CH$_2$CH$_3$), 1.52 – 1.37 (m, 4H, *o*-CH$_2$CH$_2$C*H*$_2$CH$_3$ and *m*-CH$_2$C*H*$_2$CH$_2$CH$_3$), 1.22 (app sextet, $^3J_{HH}$ = 6.8 Hz, 2H, *m*-CH$_2$CH$_2$C*H*$_2$CH$_3$), 0.93 (t, $^3J_{HH}$ = 7.3 Hz, 3H, *o*-CH$_2$CH$_2$CH$_2$C*H*$_3$), 0.77 (t, $^3J_{HH}$ = 7.3 Hz, 3H, *m*-CH$_2$CH$_2$CH$_2$C*H*$_3$).

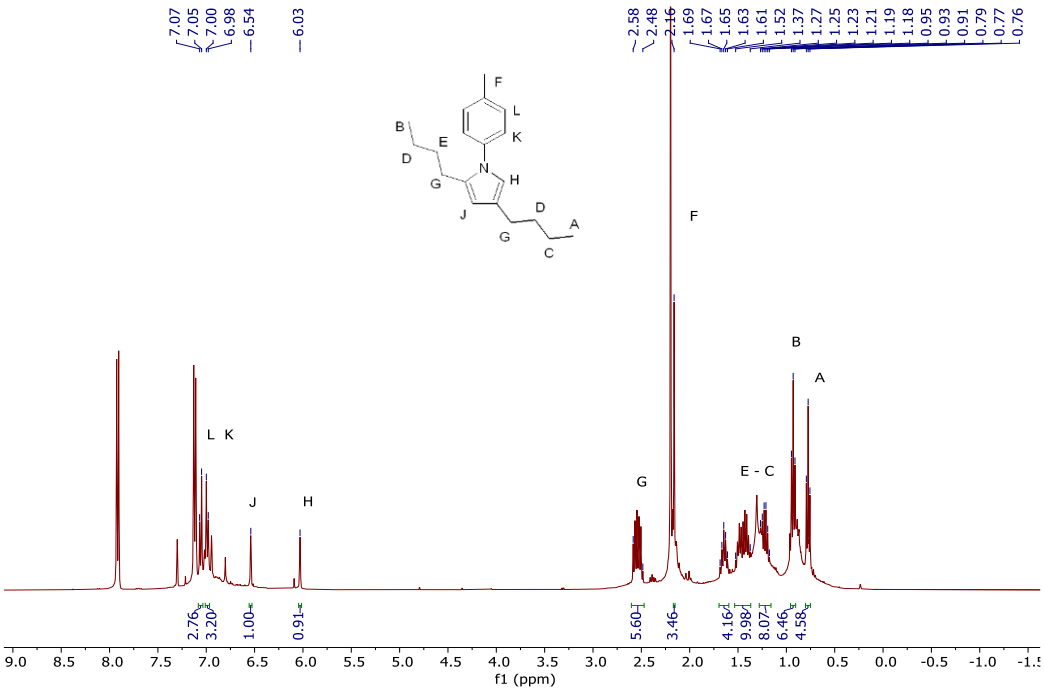

Figure 3.40 ^{1}H NMR spectrum of 2,4-di-*n*-butyl-1-*p*-tolyl-1*H*-pyrrole (**3c**) in C_6D_5Br. *Taken from XYS02041_3H.*

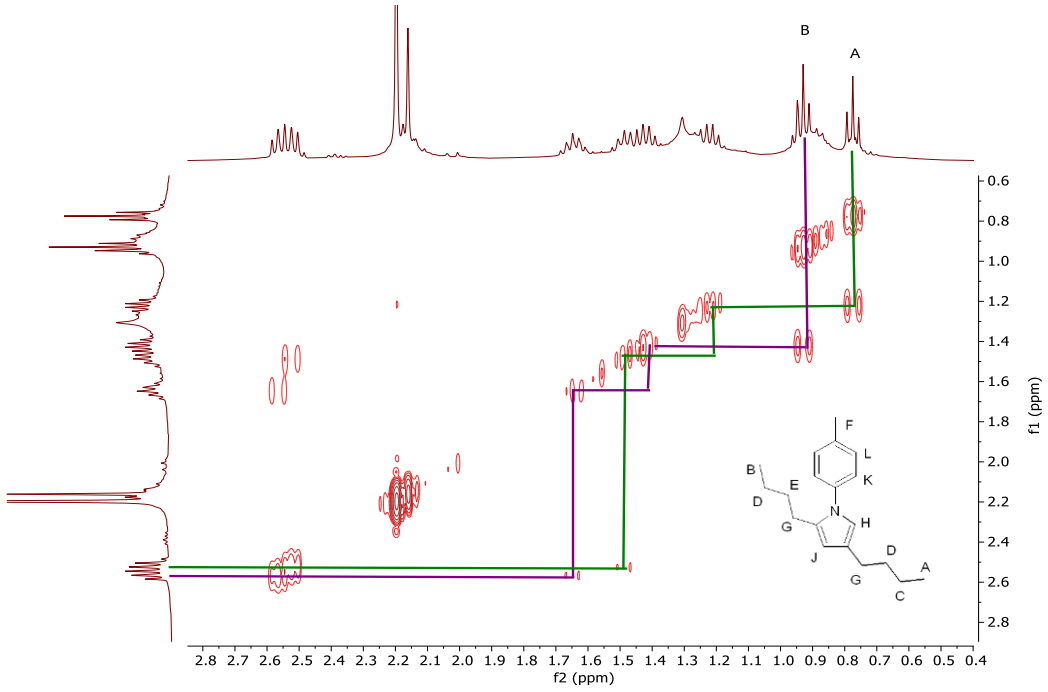

Figure 3.41 Zoom-in ^{1}H-^{1}H COSY NMR spectrum of 2,4-di-*n*-butyl-1-*p*-tolyl-1*H*-pyrrole (**3c**) in C_6D_5Br. *Taken from XYS02041_1COSY.*

Characterization of 2,5-di-*n*-butyl-1-phenyl-1*H*-pyrrole (3d) in C_6D_5Br

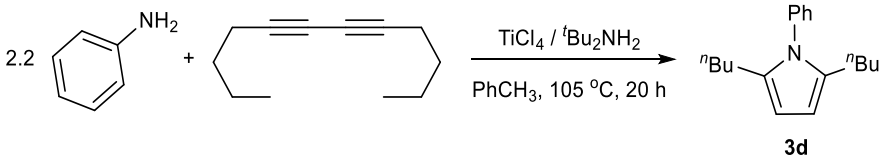

3d

The title compound was prepared *via* slight modification of the literature procedure.[200] Aniline (46 mg, 0.493 mmol, 2.2 equiv), 5,7-dodecadiyne (36 mg, 0.221 mmol, 1.0 equiv), $TiCl_4$ (14 mg, 0.0738 mmol, 33 mol %), *t*-butylamine (31 mg, 0.424 mmol, 1.9 equiv) and 5 mL toluene were added to a 20 mL scintillation vial equipped with a small stir bar in a N_2-filled glovebox. This was then sealed with a Teflon screw cap and heated at 105 °C for 20 h. The reaction mixture was then concentrated *in vacuo* to dryness before dissolving in minimal CH_2Cl_2. The suspension was filtered and dried under vacuum at 65 °C overnight to remove majority of the diyne starting reagent. The product was then dissolved in $CHCl_3$ to form an orange solution that was filtered through a basic alumina plug to give a pale yellow solution. The solution was once again dried under vacuum to give an oil that contained the title compound (**3d**) and starting reagent diyne.

^{1}H NMR (400 MHz, C_6D_5Br): δ 7.23 (t, $^3J_{HH}$ = 7.4 Hz, 2H, *m*-NPh-*H*), 7.15 (t, $^3J_{HH}$ = 7.4 Hz, 1H, *p*-NPh-*H*), 7.07 (d, $^3J_{HH}$ = 7.3 Hz, 2H, *o*-NPh-*H*), 6.08 (s, 2H, C3-*H* and C4-*H*), 2.36 (t, $^3J_{HH}$ = 7.6 Hz, 4H, $CH_2CH_2CH_2CH_3$), 1.44 (pentet, $^3J_{HH}$ = 7.6 Hz, 4H, $CH_2CH_2CH_2CH_3$), 1.18 (sextet, $^3J_{HH}$ = 7.4 Hz, 4H, $CH_2CH_2CH_2CH_3$), 0.75 (t, $^3J_{HH}$ = 7.3 Hz, 6H, $CH_2CH_2CH_2CH_3$).

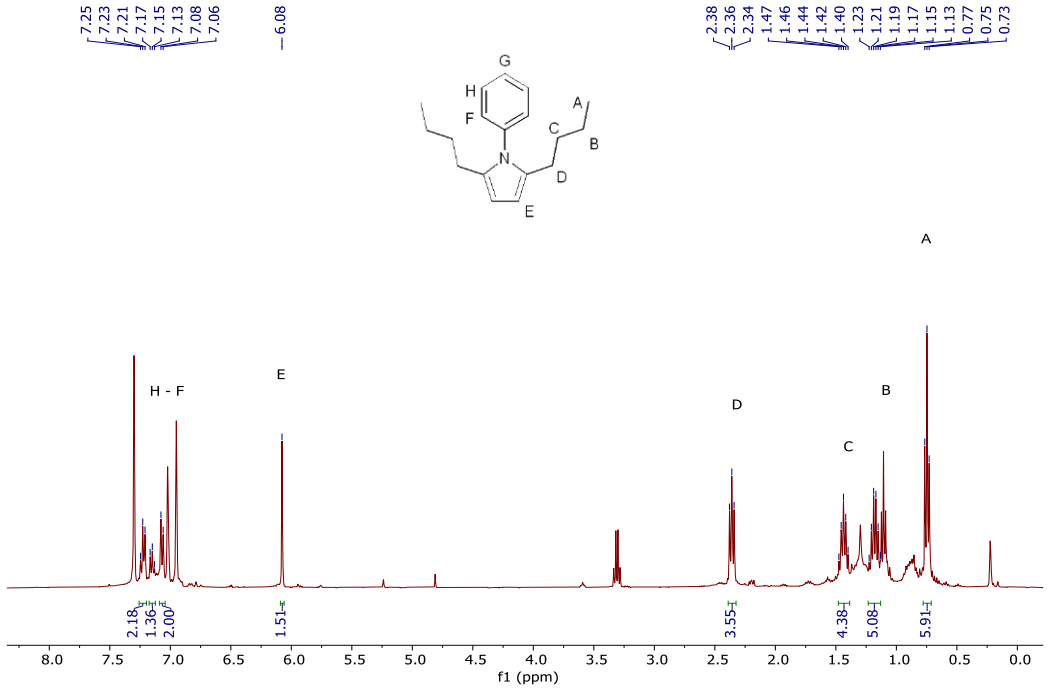

Figure 3.42 ^{1}H NMR spectrum of 2,5-di-*n*-butyl-1-phenyl-1*H*-pyrrole (**3d**) in C_6D_5Br. *Taken from XYS02149_5H.*

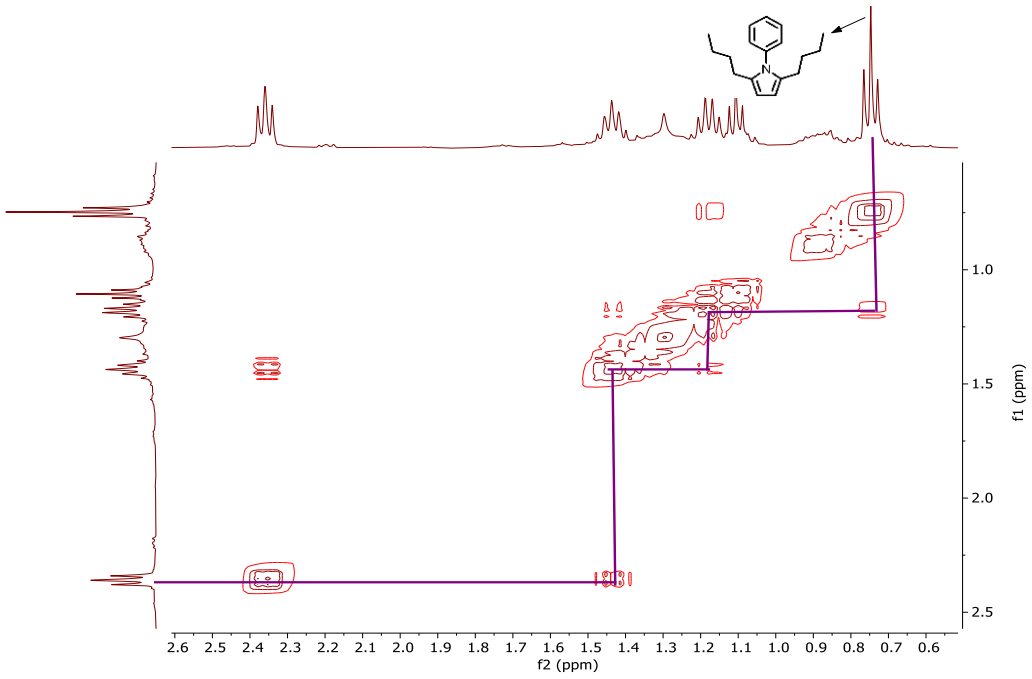

Figure 3.43 Zoom-in ^{1}H-^{1}H COSY NMR spectrum of 2,5-di-*n*-butyl-1-phenyl-1*H*-pyrrole (**3d**) in C_6D_5Br. *Taken from XYS02149_5H_1COSY.*

Characterization of 2,4-di-*n*-butyl-1-phenyl-1*H*-pyrrole (3c) in C_6D_5Br

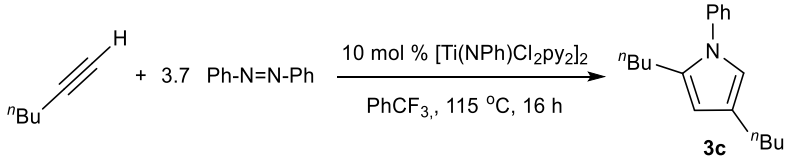

The title compound was prepared *via* slight modification of the literature procedure.[15] $[Ti(NPh)Cl_2py_2]_2$ (47 mg, 0.0638 mmol, 10 mol % of Ti), azobenzene (106 mg, 0.582 mmol, 3.7 equiv), 1-hexyne (13 mg, 0.158 mmol, 1.0 equiv) and 1 mL trifluorotoluene were added to a 20 mL scintillation vial equipped with a small stir bar in a N_2-filled glovebox. This was then sealed with a Teflon screw cap and heated overnight at 115 °C for 16 h. The reaction mixture was then concentrated under vacuum to dryness before dissolving in minimal hexanes. The mixture was purified by neutral alumina column using 100 % hexanes as eluent to give a lightly yellow-colored oil that contained the title compound (**3c**) and some pyrrole decomposition products.

^{1}H NMR (400 MHz, C_6D_5Br): δ 7.22 (t, $^3J_{HH}$ = 7.6 Hz, 2H, *m*-NPh-*H*), 7.15 (d, $^3J_{HH}$ = 7.2 Hz, 2H, *o*-NPh-*H*), 7.10 (app t, $^3J_{HH}$ = 7.2 Hz, 1H, *p*-NPh-*H*), 6.51 (s, 1H, C2-*H*), 6.02 (s, 1H, C4-*H*), 2.57 – 2.49 (m, 4H, *o*-C*H*$_2$CH$_2$CH$_2$CH$_3$ and *m*-C*H*$_2$CH$_2$CH$_2$CH$_3$), 0.93 (t, $^3J_{HH}$ = 7.2 Hz, 3H, *o*-CH$_2$CH$_2$CH$_2$C*H*$_3$), 0.76 (t, $^3J_{HH}$ = 7.3 Hz, 3H, *m*-CH$_2$CH$_2$CH$_2$C*H*$_3$).

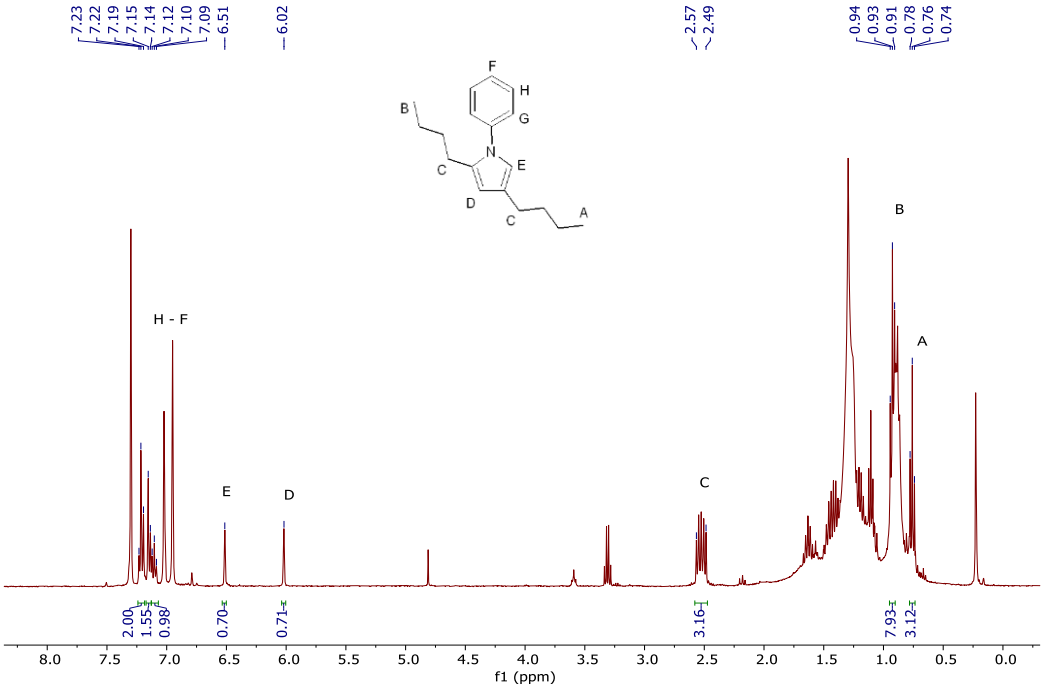

Figure 3.44 ^{1}H NMR spectrum of 2,4-di-*n*-butyl-1-phenyl-1*H*-pyrrole (**3c**) in C_6D_5Br. *Taken from XYS02129_3H.*

Characterization of 2,4-di-*n*-butyl-1-(*t*-butyl)-1*H*-pyrrole (3c) in C_6D_5Br

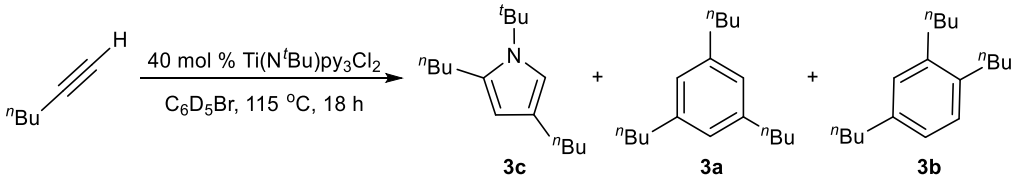

Ti(N^{t}Bu)py$_3$Cl$_2$ (52 mg, 0.122 mmol, 38 mol %), 1-hexyne (26 mg, 0.317 mmol, 1.0 equiv) and 0.8 mL of C_6D_5Br were added to a screw-cap NMR tube in a N_2-filled glovebox. This was then sealed with a Teflon screw cap and heated at 115 °C for 18 h. The mixture was analysed by ^{1}H NMR without any further work-up to give a mixture of the title compound (**3c**), **3a** and **3b**.

^{1}H NMR (400 MHz, C_6D_5Br): δ 6.52 (s, 1H, C2-*H*), 5.94 (s, 1H, C4-*H*), 3.31 (q, $^3J_{HH}$ = 7.0 Hz, 2H, *o*-C*H*$_2$CH$_2$CH$_2$CH$_3$), 2.69 – 2.65 (m, 2H, *p*-C*H*$_2$CH$_2$CH$_2$CH$_3$), 1.36 (s, 9H, ^{t}Bu), 1.10 (t, $^3J_{HH}$ = 7.0 Hz, 3H, *o*-CH$_2$CH$_2$CH$_2$C*H*$_3$).

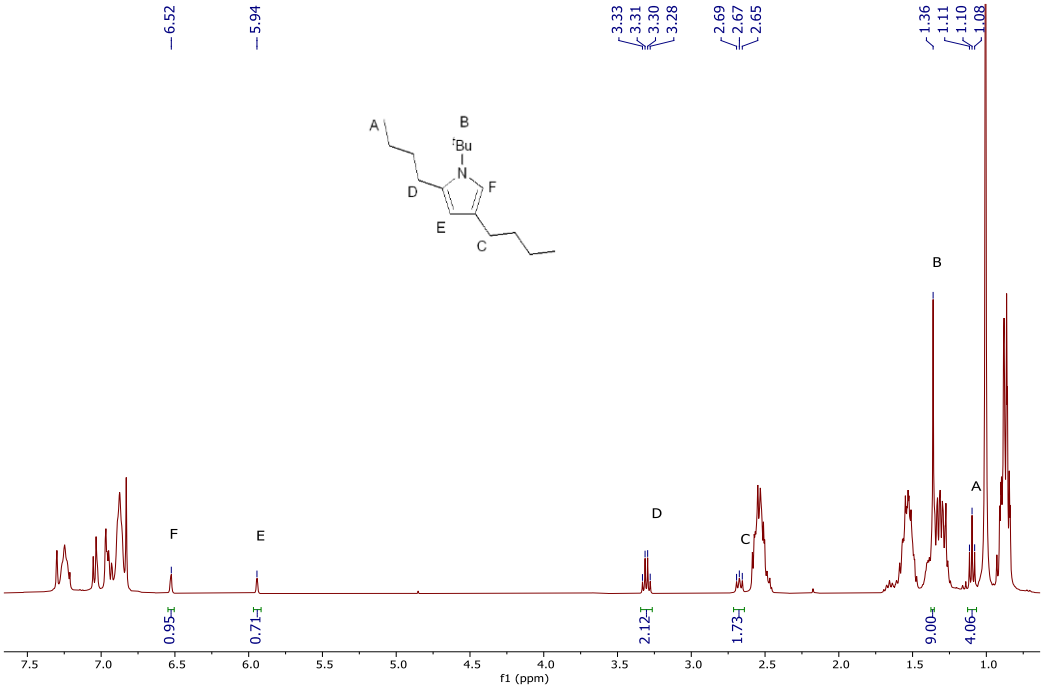

Figure 3.45 ^{1}H NMR spectrum of 2,4-di-*n*-butyl-1-(*t*-butyl)-1*H*-pyrrole (**3c**) in C_6D_5Br. *Taken from XYS02121_2H.*

Characterization of 2,3,4,5-tetraethyl-1-(*p*-tolyl)-1*H*-pyrrole (3g) in C_6D_5Br

The title compound was synthesized following literature procedure[79] in a N_2-filled glovebox to give a dark brown solid that contained a mixture of the title compound (**3g**) and starting material 1,2-di(*p*-tolyl)diazene.

^{1}H NMR (400 MHz, C_6D_5Br): δ 6.97 (app br s, 4H, Ar-*H*), 2.51 (q, $^3J_{HH}$ = 7.5 Hz, 4H, 2,5-C*H*$_2$CH$_3$), 2.40 (q, $^3J_{HH}$ = 7.4 Hz, 4H, 3,4-C*H*$_2$CH$_3$), 2.14 (s, 3H, Ar-C*H*$_3$), 1.21 (t, $^3J_{HH}$ = 7.5 Hz, 6H, 2,5-CH$_2$C*H*$_3$), 0.87 (t, $^3J_{HH}$ = 7.4 Hz, 6H, 3,4-CH$_2$C*H*$_3$).

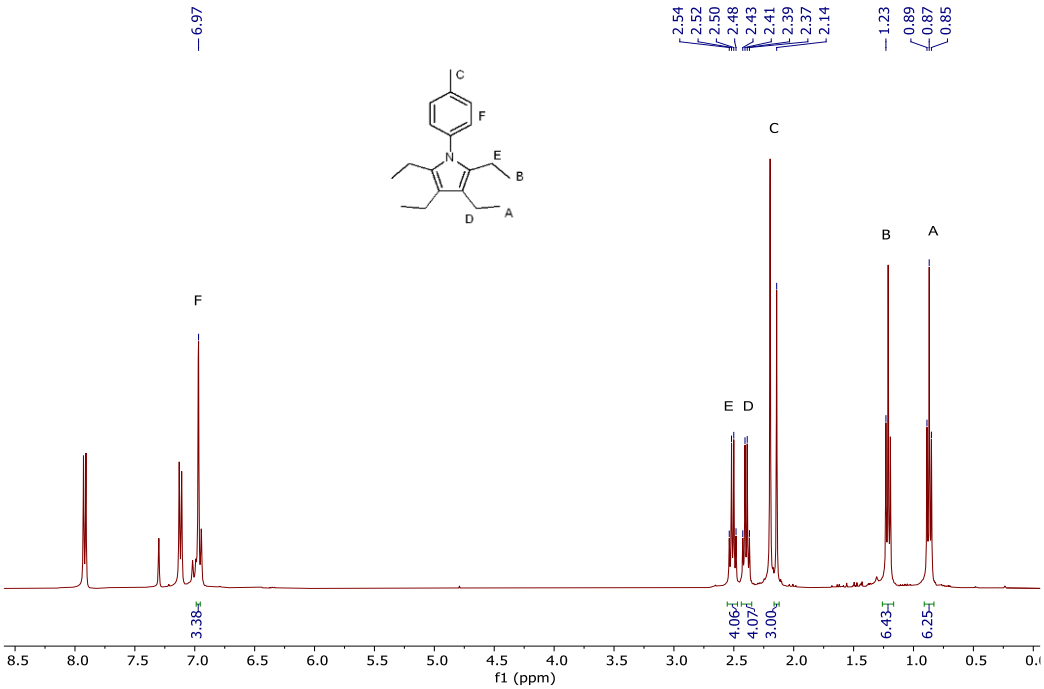

Figure 3.46 ^{1}H NMR spectrum of 2,3,4,5-tetraethyl-1-(*p*-tolyl)-1*H*-pyrrole (**3g**) in C_6D_5Br. *Taken from XYS02042_2H.*

Characterization of 2,3,4,5-tetraethyl-1-phenyl-1*H*-pyrrole (3g) in C_6D_5Br

The title compound was synthesized following literature procedure[79] in a N_2-filled glovebox to give the title compound (**3g**) as a colorless oil.

^{1}H NMR (400 MHz, C_6D_5Br): 7.22 – 7.18 (m, 2H, *m*-NPh-*H*), 7.15 – 7.12 (m, 1H, *p*-NPh-*H*), 7.06 (d, $^{3}J_{HH}$ = 7.0 Hz, 2H, *o*-NPh-*H*), 2.50 (q, $^{3}J_{HH}$ =7.5 Hz, 4H, 3,4-CH_2CH$_3$), 2.37 (q, $^{3}J_{HH}$ = 7.4 Hz, 4H, 2,5-CH_2CH$_3$), 1.20 (t, $^{3}J_{HH}$ = 7.5 Hz, 6H, 2,5-CH$_2$CH_3), 0.83 (t, $^{3}J_{HH}$ = 7.5 Hz, 6H, 3,4-CH$_2$CH_3).

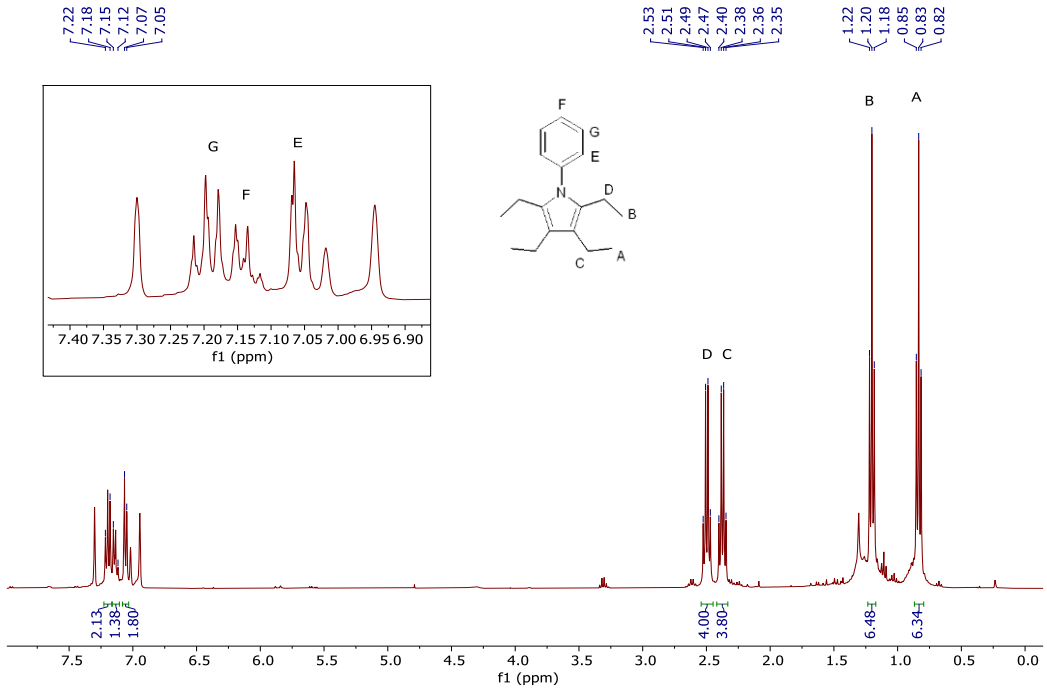

Figure 3.47 ^{1}H NMR spectrum of 2,3,4,5-tetraethyl-1-phenyl-1*H*-pyrrole (**3g**) in C_6D_5Br. *Taken from XYS02091_3H.*

Characterization of 2,3,4,5-tetraethyl-1-(*t*-butyl)-1*H*-pyrrole (3g) in C_6D_5Br

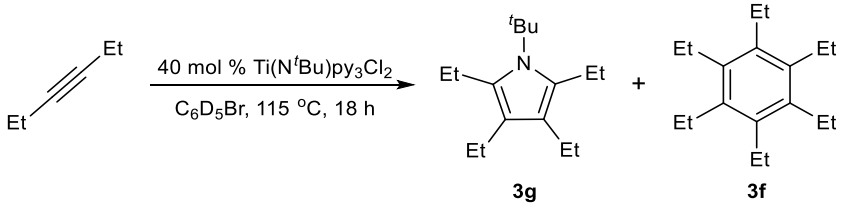

Ti(N^{t}Bu)py$_3$Cl$_2$ (51 mg, 0.119 mmol, 40 mol %), 3-hexyne (26 mg, 0.31 mmol, 1.0 equiv) and 0.5 mL C_6D_5Br were added to a screw-cap NMR tube in a N_2-filled glovebox. This was then sealed with a Teflon screw cap and heated at 115 °C for 18 h. After which, the mixture was analyzed by ^{1}H NMR without any further work-up to give a mixture of the title compound (**3g**), **3f** and 3-hexyne.

^{1}H NMR (400 MHz, C_6D_5Br): δ 2.69 (q, $^{3}J_{HH}$ = 7.1 Hz, 4H, 2,5-CH_2CH$_3$), 2.35 (q, $^{3}J_{HH}$ = 7.1 Hz, 4H, 3,4-CH_2CH$_3$), 1.46 (s, 9H, ^{t}Bu), 1.24 (d, $^{3}J_{HH}$ = 6.8 Hz, 6H, 2,5-CH$_2$CH_3). Peak for 3,4-CH$_2$CH_3 is hidden beneath the multiplet peak of δ 1.10 – 0.98.

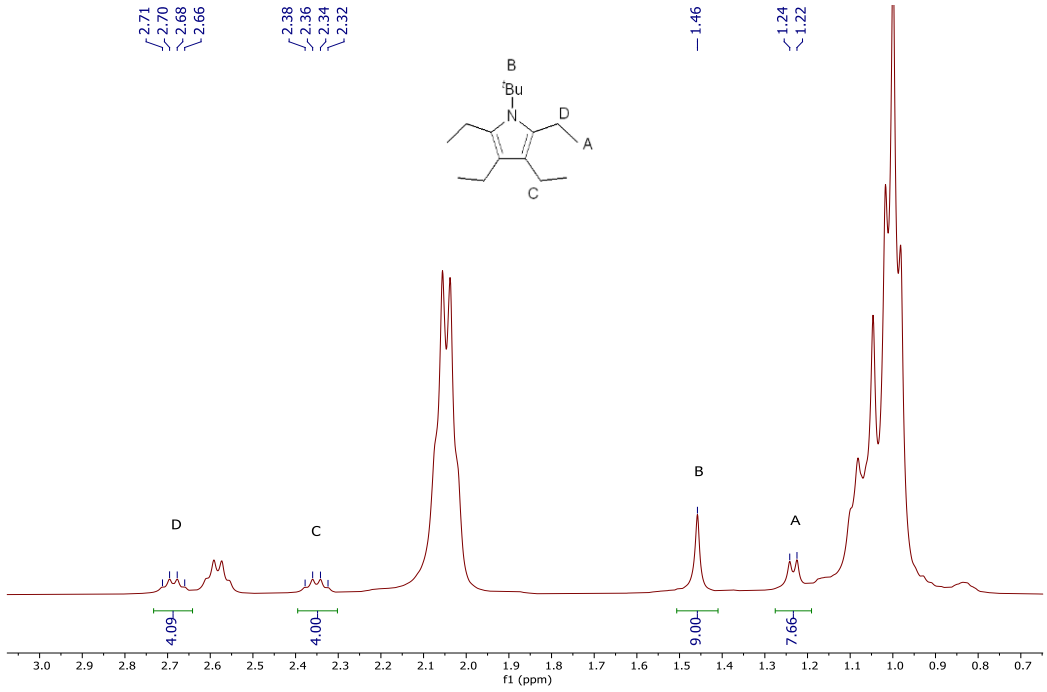

Figure 3.48 ^{1}H NMR spectrum of 2,3,4,5-tetraethyl-1-(*t*-butyl)-1*H*- pyrrole (**3g**) in C_6D_5Br. *Taken from XYS02119_2H.*

3.5.4 General procedure for catalytic alkyne trimerization

Precatalyst (5 mol % Ti, 0.01 mmol, 0.02 M) and 0.5 mL of stock solution were added to a Teflon tape lined screw-cap NMR tube in a N_2-filled glovebox. This was then sealed with a Teflon screw cap and heated at 115 °C for 16 h. The stock solution was prepared by adding either 3-hexyne or 1-hexyne (0.4 M) to C_6D_5Br with 1,3,5-trimethoxybenzene (0.04 M) acting as an internal standard. Quantitative ^{1}H NMR spectra of the catalytic mixture were taken before and after heating on the Bruker Avance III HD 400 and 500 MHz spectrometers (Acquisition time = 5 s; delay time = 30 s; dummy scans = 0; number of scans = 8). 0.01 mmol was used as the initial precatalyst quantity for catalyst activation calculations. Ti(NTol)THF_3I_2 (***3***) was an exception to the general procedure – trimerization of 1-hexyne was completed at room temperature in less than 5 min while 3-hexyne was completed at room temperature over 16 h.

3.5.5 Representative Catalytic Spectra

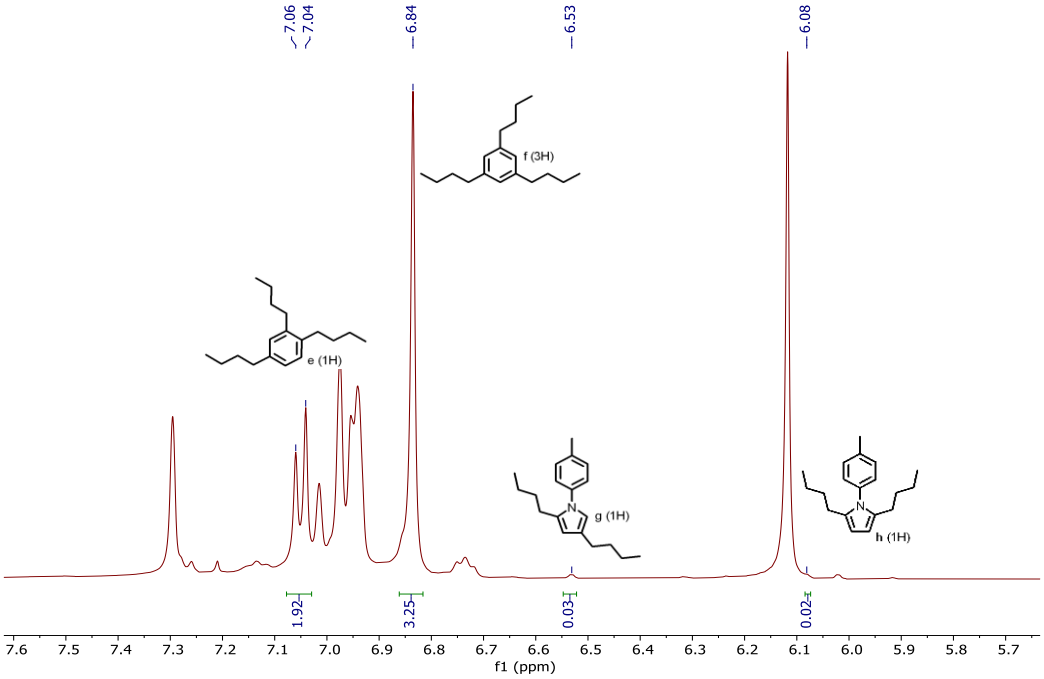

Figure 3.49 Representative zoom-in ^{1}H NMR spectrum of a 1-hexyne catalytic run in C_6D_5Br (115 °C/16 h/Precatalyst **3.2**). *Taken from ZWG04123D.*

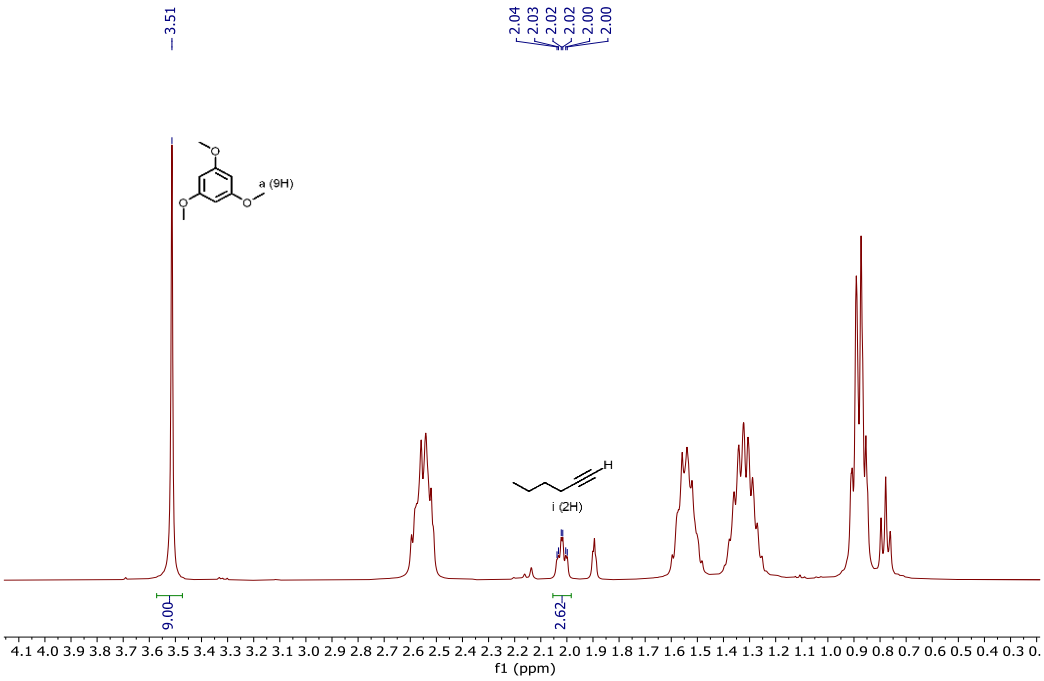

Figure 3.50 Representative zoom-in ^{1}H NMR spectrum of a 1-hexyne catalytic run in C_6D_5Br (115 °C/16 h/Precatalyst **3.2**). *Taken from ZWG04123C.*

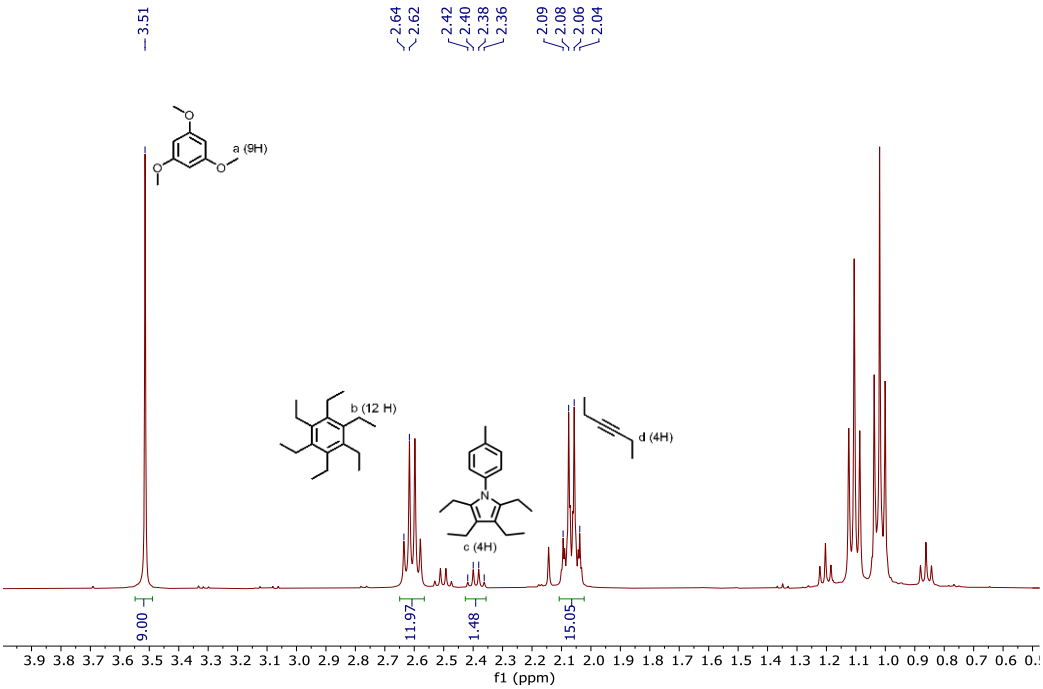

Figure 3.51 Representative zoom-in ^{1}H NMR spectrum of a 3-hexyne catalytic run in C_6D_5Br (115 °C/16 h/Precatalyst **3.2**). *Taken from ZWG04123C.*

3.5.6 Alkyne trimerization mol balance data

Table 3.3 Alkyne trimerization mol balance.

[Ti]	1-Hexyne[a]	3-Hexyne[b]
1	103 ± 8	92 ± 6
2	98 ± 1	81 ± 7
3	96 ± 2[c]	102 ± 3[d]
4	69 ± 1	72 ± 11
5	85 ± 2	95 ± 4
6	101 ± 10	68 ± 17
7	79 ± 8	60 ± 8
8	63 ± 3	84 ± 6
9	62 ± 0	89 ± 0
10	73 ± 2	93 ± 2
11	76 ± 0	59 ± 8
12	74 ± 5	59 ± 13
13	86 ± 9	58 ± 11
14	63 ± 11	83 ± 15
15	91 ± 8	81 ± 6
16	72 ± 3	66 ± 5

[a]Conditions: 5 mol % [Ti], 0.4 M 1-hexyne, C_6D_5Br, 16 h, 115 °C, average of 2 – 4 runs.

[b]Conditions: 5 mol % [Ti], 0.4 M 3-hexyne, C_6D_5Br, 16 h, 115 °C, average of 2 – 4 runs.

[c] < 5 min, room temperature.

[d]16 h, room temperature.

3.5.7 Preliminary kinetic studies

Precatalyst (5 mol %, 0.01 mmol, 0.02 M) and 0.5 mL of stock solution (3-Hexyne or 1-Hexyne) were added to a Teflon tape lined screw-cap NMR tube in a N_2-filled glovebox. This was then sealed with a Teflon screw cap. Quantitative ^{1}H NMR spectra of the catalytic mixture were taken every 5 min (Acquisition time = 5 s, Delay time = 30 s, Dummy Scans = 0, Number of scans = 8) either at room temperature or 115 °C.

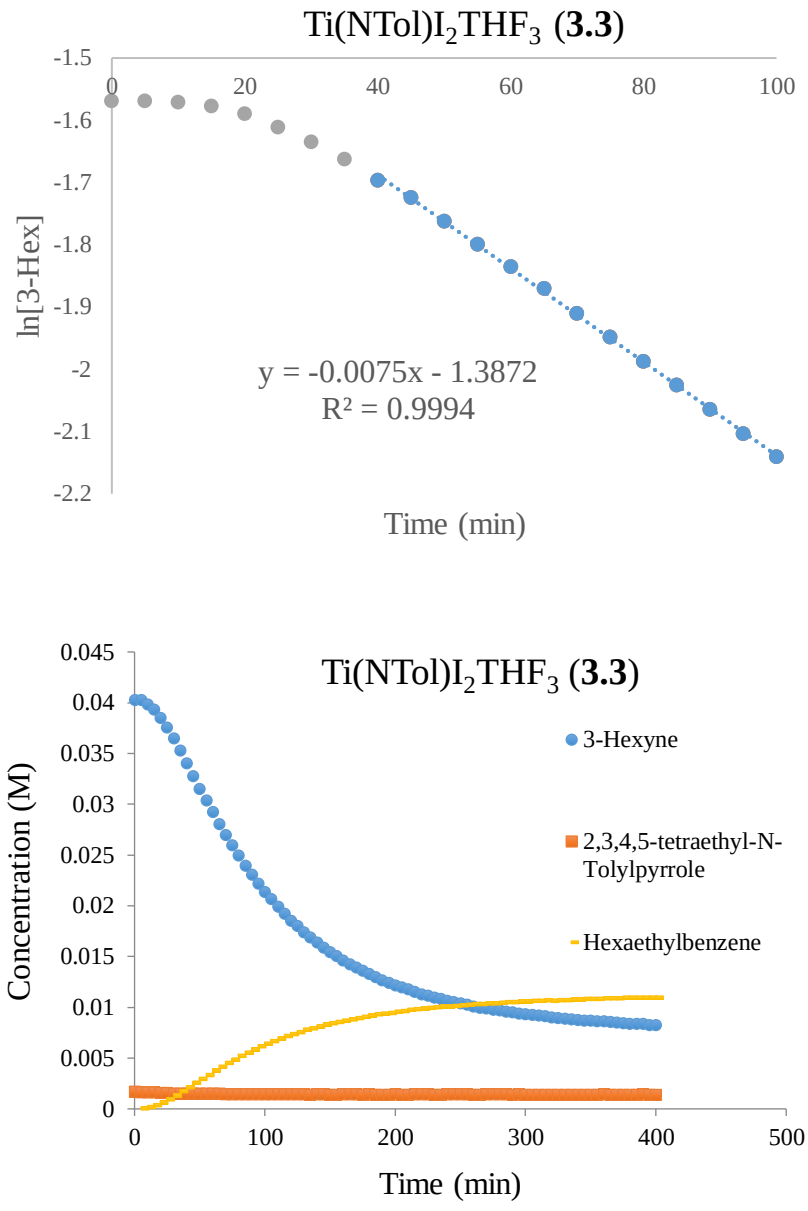

Figure 3.52 ln[Hex] *vs.* time for a 3-hexyne catalytic run in C_6D_5Br (RT/Precatalyst **3.3**).

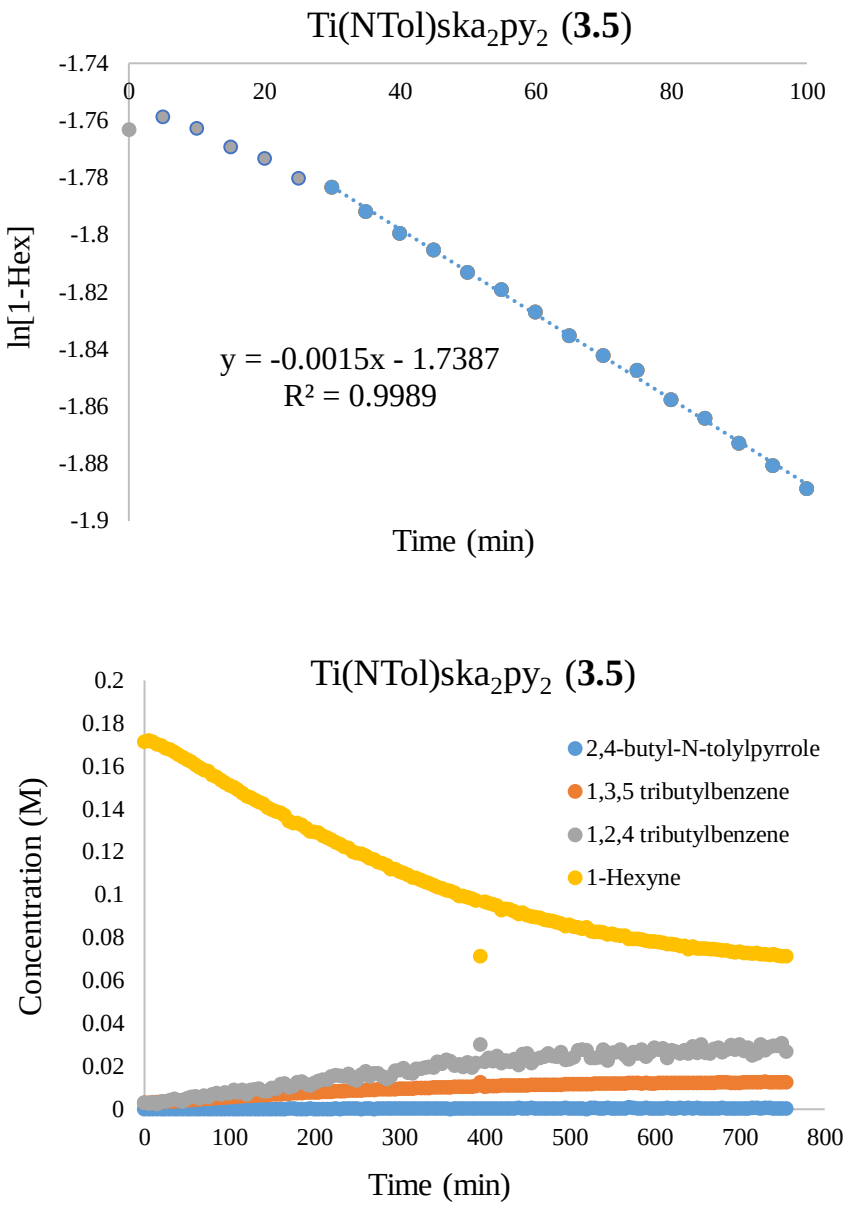

Figure 3.53 ln[Hex] *vs.* time for a 1-hexyne catalytic run in C_6D_5Br (RT/Precatalyst **3.5**).

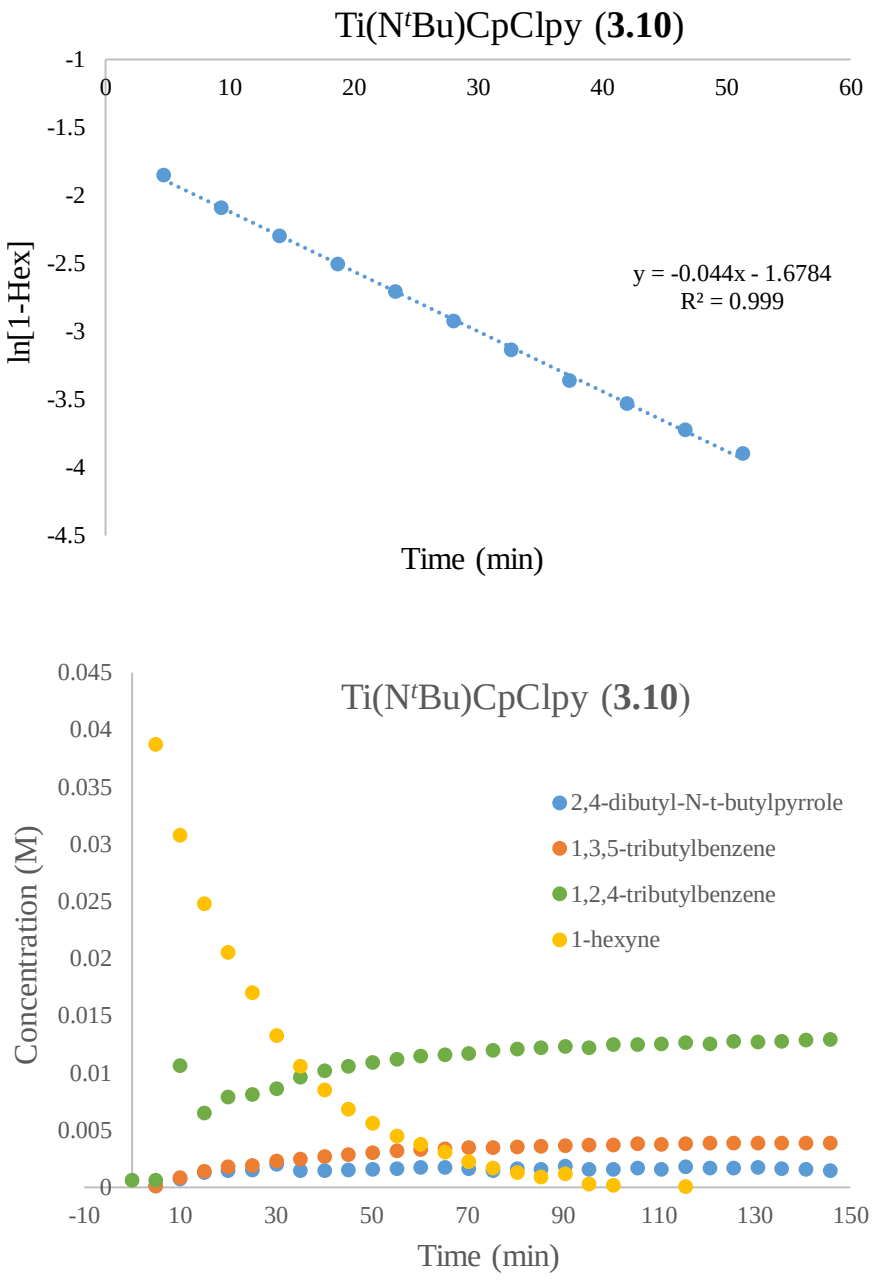

Figure 3.54 ln[Hex] *vs.* time for a 1-hexyne catalytic run in C_6D_5Br (RT/Precatalyst **3.10**).

3.5.8 Control reactions

Precatalyst (5 mol %, 0.01 mmol, 0.02 M) and 0.5 mL of stock solution (3-Hexyne or 1-Hexyne) were added to a Teflon tape lined screw-cap NMR tube in a N_2-filled glovebox. This was then sealed with a Teflon screw cap and heated to 115 °C. Quantitative ^{1}H NMR spectra of the catalytic mixture were taken before and after heating on the Bruker Avance III HD 400 spectrometer (Acquisition time = 5 s, Delay time = 30 s, Dummy Scans = 0, Number of scans = 8).

Table 3.4 Control reactions.

	Precatalyst	**Time (h)**	**Substrate**	**% yield trimer (1,3,5- : 1,2,4-)**
1	none	14	3-Hex	-
2			1-Hex	-
3	**3.17**	14	3-Hex	-
4			1-Hex	-
5[a]	**3.17** + Mg*	16	3-Hex	6%
6[a]			1-Hex	37% (38 : 62)
7	$ZrCl_4$•2THF	16	3-Hex	-
8			1-Hex	-
9	$ZrCl_4$	16	3-Hex	-
10			1-Hex	-
11[b]	$ZrCl_4$ without I.S.	16	3-Hex	Trace
12[b]			1-Hex	Trace
13	TiI_4	16	3-Hex	-
14			1-Hex	-

[a]For entries 5-6, **3.17** (5 mol %, 6.8 mg, 0.01 mmol, 0.02 M), Mg* (6 mol %, 5.0 mg, 0.012 mmol), 1,3,5-trimethoxybenzene (3.4 mg, 0.02 mmol, 0.04 M), 0.5 mL of Tol-d_8 and either 3-hexyne (22.7 μL, 0.2 mmol, 0.4 M) or 1-hexyne (23.0 μL, 0.2 mmol, 0.4 M) were added to the Teflon tape lined screw-cap NMR tube. Assignment of NMR peaks were made based on comparison with known C_6D_5Br spectra.

[b]For entries 11-12, $ZrCl_4$ (10 mol %, 0.01 mmol, 0.02 M), 0.5 mL of C_6D_5Br and either 3-hexyne (11.4 μL, 0.1 mmol, 0.2 M) or 1-hexyne (11.5 μL, 0.1 mmol, 0.2 M) were added to the Teflon tape lined screw-cap NMR tube.

3.5.9 Data for X-ray Structures

Table 3.5 Refined data and cell parameters for X-ray Structures.

	3.3	**3.13**	**3.14**	**3.15**
CCDC Number	1524349	1524350	1524351	1524352
Empirical Formula	$C_{20}H_{29}I_2NO_3Ti$	$C_{45}H_{51}N_3O_2Ti$	$C_{57}H_{77}N_5Ti$	$C_{37}H_{47}ClN_4Ti$, $0.5(C_6H_{14})$
Formula weight	623.14	713.79	880.13	674.22
Temperature (K)	123(2)	123(2)	123(2)	123(2)
a, Å	14.324(5)	9.4769(7)	15.516(2)	11.142(3)
b, Å	10.083(4)	20.5440(13)	14.4749(17)	27.430(5)
c, Å	16.295(6)	20.9582(9)	23.531(5)	12.8602(12)
α, deg	90	90	90	90
β, deg	97.989(7)	95.330(4)	104.510(13)	103.355(12)
γ, deg	90	90	90	90
Volume, $Å^3$	2330.6(15)	4062.8(4)	7135.7(5)	3824.0(13)
Z	4	4	4	4
Crystal System	Monoclinic	Monoclinic	Monoclinic	Monoclinic
Space Group	P 2_1/c	P 2_1/n	P 2_1/c	P 2_1/n
d_{calc}, g/cm^3	1.776	1.167	1.143	1.171
θ range, deg	2.39 to 28.91	3.01 to 74.64	2.94 to 74.75	3.22 to 75.12
μ, mm^{-1}	*3.034*	2.078	1.715	2.768
Abs. Correction	Multi-scan	Multi-scan	Multi-scan	Multi-scan
GOF	1.018	1.056	1.031	1.027
R_1 ,[a]	*R*1 = 0.0273	*R*1 = 0.0319	*R*1 = 0.0386	*R*1 = 0.0412
wR_2 [b] [I>2σ(I)]	*wR*2 = 0.0688	*wR*2 = 0.0919	*wR*2 = 0.1091	*wR*2 = 0.1131

[a] $R_1 = \sum||F_o| - |F_c||/\sum|F_o|$. [b] $wR_2 = [\sum[w(F_o^2-F_c^2)^2]/\sum[w(F_o^2)^2]^{1/2}$.

Chapter 4: Iterative Supervised Principal Component Analysis-Driven Ligand Design for Regioselective Ti-Catalyzed Pyrrole Synthesis

** All Principal Component Analysis work presented in Chapter 4 was performed and is credited to Dr. Benjamin R. Reiner.*

** All computational data presented in Chapter 4 was performed and is credited to Xuelan Wen and Prof. Jason Goodpaster*

4.1 Overview

Rational catalyst design remains a challenging endeavor within the broader chemical community owing to the myriad variables that can influence various aspects of catalytic reactions. Developing predictive structure-activity relationships in an efficient manner is critical in the design and optimization of new catalysts. Herein, we describe the use of iterative supervised principal component analysis (ISPCA) in *de novo* catalyst design. The regioselective synthesis of 2,5-dimethyl-1,3,4-triphenyl-1*H*-pyrrole (**4C**) *via* Ti-catalyzed formal [2+2+1] cycloaddition of phenyl propyne and azobenzene was targeted as a model system. The initial reaction conditions led to an unselective mixture of all possible pyrrole regioisomers. ISPCA was conducted on a training set of catalysts and their performance was regressed against the scores from the top three principal components. Component loadings from this PCA space along with k-means clustering were used to inform the design of new test catalysts. The selectivity of a prospective test set was predicted *in silico* using the ISPCA model and only optimal candidates were synthesized and tested experimentally. This data-driven predictive-modeling workflow was iterated and after only three generations the catalytic selectivity was improved from 0.5 (statistical mixture of products) to over 11 (> 90 % **4C**) by incorporating 2,6-dimethyl-4-(pyrrolidin-1-yl)pyridine as a ligand. The successful development of a highly selective catalyst without resorting to long, stochastic screening processes demonstrates the inherent power of ISPCA in *de novo* catalyst design.

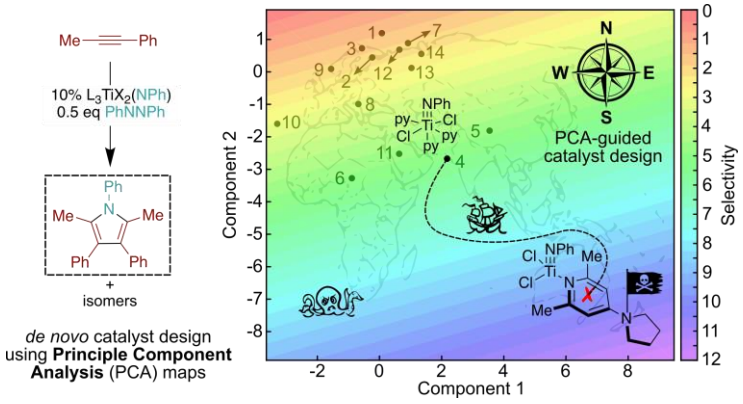

Figure 4.1 Application of ISPCA towards rational catalyst design for a Ti-catalyzed formal [2+2+1] cycloaddition reaction with phenyl propyne and azobenzene.

4.2 Introduction

Rational design of selective catalysts remains an outstanding challenge in organometallic chemistry and the broader synthetic community. Detailed mechanistic understanding can often provide an avenue for improvement, but even for relatively simple systems the number of potential variables that affect catalysis—intermediate and transition state structures, solvent effects, additive effects and more—can be staggering. These can often impact other aspects of catalysis beyond selectivity (rate, yield, etc.) as well.[201-204] Similarly, the mechanisms of many catalytic systems are difficult to interrogate because of experimental, spectroscopic, or computational limitations. Consequently, a variety of strategies have been developed to simplify the search for improved catalysis. For example, design of experiment (DOE)[205-206] and high throughput experimentation (HTE)[207-209] are commonly employed as a route to expedite otherwise long screening processes.

Ultimately, exercising catalyst control over a reaction requires drawing a correlation between catalyst performance and catalyst descriptors to develop structure-activity relationships. Univariate analyses using classical descriptors (e.g., Hammett, Taft, Chartron parameters, Tolman cone angles, etc.)[210-212] are valuable tools for reaction design, but rarely translate across a wide range of ligand archetypes which limits the number of candidates available for a new catalyst screen.[202, 213] To that end, there has been significant effort directed at computer-aided design of selective catalysts.[214-216] Additionally, both machine learning and multivariate regression analysis have emerged as powerful tools for detailed modeling and prediction in chemical catalysis. However, the field of catalysis informatics is still immature[217-218] and any modeling strategy will suffer some inherent drawback (Figure 4.2). Machine learning uses a "top-down" approach where correlations are developed through complex neural networks.[219-223] However, the resulting output often lead to models with high statistical fidelity but little to no interpretation for further intuitive analysis. Moreover, machine learning algorithms can exploit inherent structure to the experimental design which can potentially obscure extraction of chemically meaningful descriptors. Multivariate regression analysis often relies on stepwise forward regression algorithms to build predictive or explanatory models.[204, 213, 224-225] This "bottom-up" approach relies on data inspection and chemical intuition to identify appropriate descriptors that may not be obvious in complex systems.

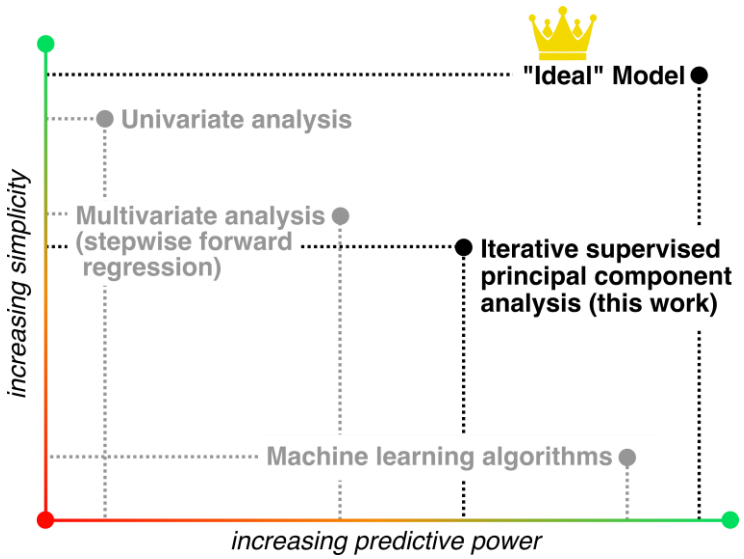

Figure 4.2 Examples of analysis approaches commonly employed in chemical catalysis.

Thus, implementing high-level analysis using computationally low-cost universally translatable descriptors while retaining chemically intuitive information is an ongoing challenge. We were interested in taking a descriptor-agnostic approach to rational catalyst design: how can one pick the best modeling descriptors when there is no obvious choice? Herein, we report an iterative supervised PCA-based strategy (ISPCA) for identifying relevant descriptors for rational catalyst optimization (Figure 4.3) and its implementation in designing regioselective catalysts for Ti-catalyzed [2+2+1] synthesis of substituted pyrroles.

4.3 Approach

We considered principal component analysis (PCA) could be used to direct rational catalyst design. PCA is a statistical procedure that aims to transform a set of possibly correlated variables into a set of linearly orthogonal variables called components. This set of components describes all variance in the original data set; however, a few top components describe *most* of the data variance, ostensibly leading to minimal lossy-type data compression. PCA is commonly used in bioinformatics and chemometrics applications where analysis of an unwieldy number of variables (such as complex metabolite mixtures or numerous spectroscopic peaks) is facilitated by data reduction.[226-

[231] PCA is well poised for use in catalyst design, which similarly suffers from an unwieldy number of variables that may affect catalyst performance.

Despite the success of PCA in other chemical contexts, the use of PCA in chemical catalysis is underexplored. Notably, reports demonstrating extrapolation of PCA-borne structure-activity relationships to practical *de novo* catalyst design are exceedingly rare. The Fey lab has reported the use of PCA ligand maps, denoted "ligand knowledge bases" (LKBs)[201, 232-239] to guide the development of hydroformylation/hydrocyanation catalysts bearing fluorophosphines, however a quantitative regression was not reported.[240] The Rothenberg lab has utilized a similar statistical technique, partial least squares regression (PLSR), to inform the design of olefin isomerization catalysts, however the incorporation of varying experimental conditions likely convolute the regression output due to the inherent sensitivity of catalytic systems to reaction stoichiometry, temperature, catalytic loadings, etc.[241-242]

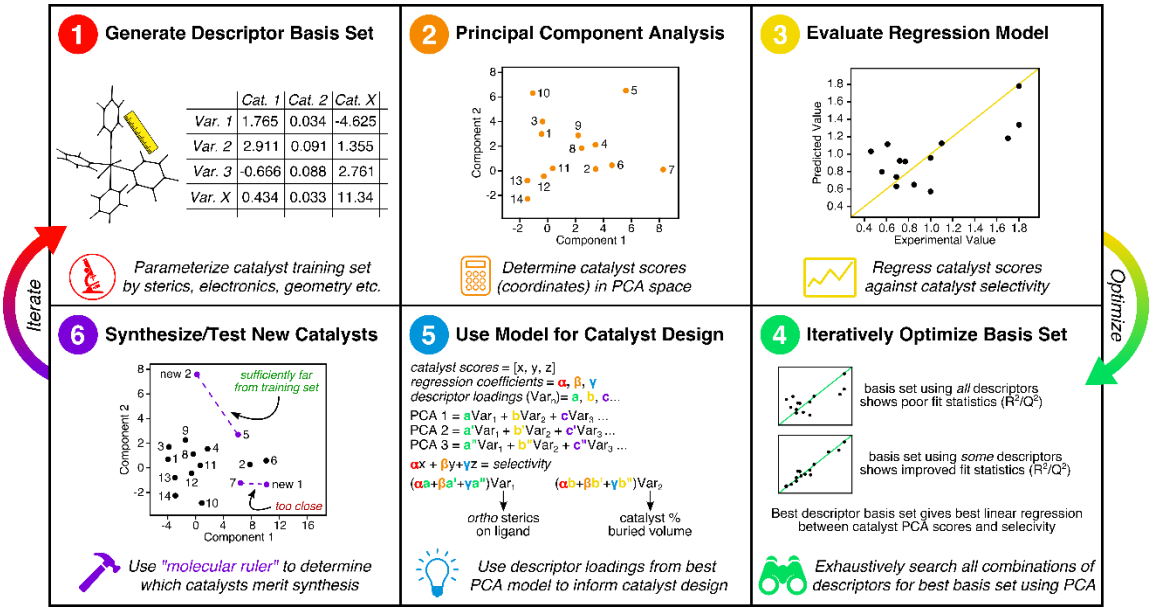

Figure 4.3 Graphical outline of the iterative supervised PCA (ISPCA) strategy.

We have developed an iterative supervised PCA (ISPCA) strategy[231] that exhaustively searches catalyst descriptor combinations, in an effort to provide a model wherein the *least* number of descriptors describes the *most* variance in catalyst performance data (Figure 4.3). First, a basis set of potential descriptors of interest is computed/tabulated

for a catalyst training set (Figure 4.3, Box 1). Principal component analysis of this initial basis set is then carried out to determine the catalyst scores (coordinates) in PCA space (Figure 4.3, Box 2). Next, catalyst scores are linearly regressed against the catalyst performance data and the regression model is evaluated for statistical fit (R^2/Q^2, Figure 4.3, Box 3). Given that the initial basis set may contain redundant, irrelevant, or correlated descriptors the regression fit from C is likely to be poor. As a result, the descriptor basis set is iteratively optimized by exhaustively searching all combinations of descriptors through an automated script (Figure 4.3, Box 4). The ideal basis set will have the best statistical fit for the regression between catalyst PCA scores and catalyst performance, while also utilizing the fewest number of descriptors possible. From this optimized PCA basis set, a predictive and intuitive model for catalyst design can be developed by examining the sum descriptor loadings for the top principal components (Figure 4.3, Box 5). These values are determined by taking the dot product of the PCA regression coefficients and the descriptor loadings. For example, if the descriptor loading for Tolman cone angle was 0.5 in PC1, 0.2 in PC2 and 0.1 in PC3 with accompanying PCA regression coefficients of 2, 4 and 5 respectively, then the sum descriptor loading for Tolman cone angle would be $(0.5 \times 2) + (0.2 \times 4) + (0.1 \times 5) = 2.3$. This sum descriptor loading can then be compared to other loadings in the basis set to determine which descriptor has the greatest impact (and in which direction). Finally, new catalysts can be proposed and modeled against the training set using the optimized basis set (Figure 4.3, Box 6).

Hypothetical new catalysts can be evaluated using a "molecular ruler" (Figure 4.3, Box 6). Changes in catalyst performance are captured as the Euclidean distance between catalyst scores in PCA space. Sufficient distance must be achieved between a training set sample and test sample before a substantial change in catalyst performance is expected – for better or worse. Correlation of pairwise distances between training set catalysts and catalyst performance allows construction of a "molecular ruler" which serves as a statistical gauge to determine if a test catalyst is sufficiently different from the training set to warrant synthesis.

The overall process can then be iterated though several cycles of design/synthesis/analysis as needed. In principle, steps 5 and 6 could be further automated to design and test catalysts *in silico* using established molecular evolution algorithms if

desired.[243] The value of this type of data-driven predictive-modeling workflow has been reviewed previously.[242]

4.4 Results and Discussion

To demonstrate the utility of ISPCA strategies in *de novo* catalyst design, we targeted the development of a regioselective Ti imido catalyst for the intermolecular [2+2+1] synthesis of pyrroles from asymmetric alkynes and azobenzene. Selective intermolecular [2+2+1] formal cycloadditions are uncommon; these types of multicomponent reactions inherently have multiple steps where both chemo- and regioselectivity must be considered, making straightforward design of selective catalysts difficult. Here, the regioselective synthesis of 2,5-dimethyl-1,3,4-triphenyl-1*H*-pyrrole (**4C**) from phenylpropyne and azobenzene (Figure 4.4) was targeted. This reaction was chosen for two reasons: (1) the 3,4-diaryl motif is found in several natural product classes including halitulins[244-246] and lamellarins;[247-249] (2) PhCCMe exhibits a low proclivity toward competitive alkyne trimerization and other side-reactions in Ti-catalyzed [2+2+1] reactions.

Reaction of PhCCMe with PhNNPh catalyzed by Ti(NPh)Cl_2py_3 (**4.1**) was previously shown to generate a 0.45 : 1 : 0.91 mixture of all possible pyrrole regioisomers **4A**, **4B** and **4C** (Figure 4.4). Although there is a substantial thermodynamic bias over the formation of [2+2] cycloadduct regioisomer $\mathbf{IM3_B}$ over $\mathbf{IM3_A}$, this difference is dwarfed by the barriers for rate-determining 2nd alkyne insertion ($\mathbf{TS2_{AC}}$, $\mathbf{TS2_{AD}}$, $\mathbf{TS2_{BE}}$ and $\mathbf{TS2_{BF}}$) leading to the 4 possible azatitanacyclohexadiene intemediates (30.5 ± 1 kcalmol^{-1}).[82] Since [2+2] cycloaddition is reversible, this leads to a mixture of all products. Consequently, PhCCMe, like nearly all internal alkynes examined with catalyst **4.1**, affords a roughly statistical mixture of regioisomers. Since the initial report of Ti-catalyzed pyrrole synthesis and the follow-up detailed mechanistic study,[79, 82-83] significant effort in our lab has been dedicated to the discovery of selective catalysts, including the examination of many successful regioselective alkyne hydroamination platforms reported in the literature (see Supporting Information for additional details). In all cases, Bercaw's Law of Initial Optimization[250-251] appeared in effect: either reaction rates were significantly lowered or there was no significant effect on the reaction regioselectivity (or both).

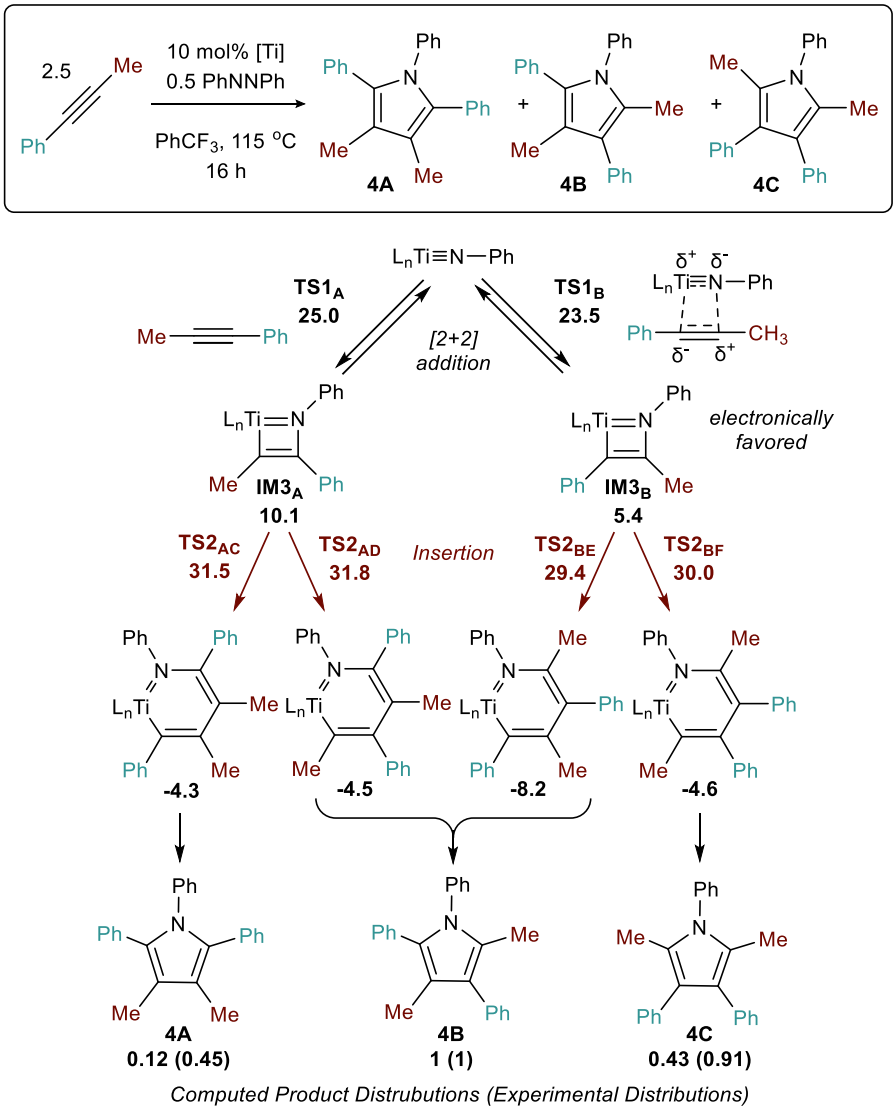

Figure 4.4 Top: Ti-catalyzed [2+2+1] synthesis of regioisomeric pyrroles from PhCCMe. Bottom: computed reaction pathways calculated at M06/6-311G(d,p)/SMD at 110 °C, highlighting rate- and selectivity-determining 2nd alkyne insertion (**TS 2**, maroon) is nonselective with standard catalysts. L_n = Cl_2py. Calculated transition-state and intermediate free energies (kcalmol^{-1}) are presented below each structure. Species labels and calculated product ratios are taken from prior mechanistic work.[82] Experimental ratios are taken from initial discovery.[79]

Based on these initial attempts, a more systematic approach was warranted. Catalysts based on simple halide and N-heterocycle-based X-type[252] ligands and pyridine-based L-type ligands were chosen because they are easy to synthesize, highly modular and the precursors are commercially available. A catalyst screen where these X- and L-type ligands were systematically varied is presented in Figure 4.5. The effects of different L-type ligands are shown in catalysts **4.1**-**4.8**, while the effects of different X-type ligands are shown in catalysts **4.9**-**4.14**. Catalyst selectivity is defined as the ratio of the yield of pyrrole **4C** to the sum of the yields of pyrroles **4A** and **4B**. Triaryl pyrroles were the major reaction product in all cases.

Changing the electronics of the pyridine ring had a minimal effect on selectivity (catalysts **4.1**-**4.3**). In contrast, sterically-encumbered pyridine ligands showed somewhat better selectivity, with both catalysts **4.4** and **4.5** reaching a selectivity of 1.8 for **4C** – a roughly 4-fold increase from **4.1**. Bidentate 4,4'-$^{t}Bu_2$-bpy (**4.7**) results in significantly lower yield (13%), as 2 coordination sites are needed for productive catalysis.[82] The total number of donor pyridines plays a small role (*c.f.* **4.1** and **4.8**) in selectivity, with fewer donors leading to higher selectivity.

Catalysts **4.9**-**4.11** illustrate that lessening the halide donor ability[82] (I < Br < Cl) results in an increase in selectivity for **4C**, culminating in a selectivity of 1.7 for **4.9**. Inspired by Odom's ligand donor parameter (LDP) for early transition metals,[187, 253] several weakly-donating nitrogenous X-type ligands (catalysts **4.11**-**4.14**) were next explored. None of these catalysts resulted in high-yielding reactions and the small differences in reaction selectivity did not correlate to ligand pKa or LDP.

None of the catalysts in Figure 4.5 resulted in synthetically useful selectivity for product **C**. Although both sterically encumbered (**4.4** and **4.5**) and electron deficient (**4.10**) catalysts resulted in a moderate improvement in selectivity (maximum of 1.8 : 1 for **4C**), clear or quantitative trends to further improve selectivity *via* univariate modification were not obvious. Nonetheless, the small spread in the data provided an opportunity to evaluate the data as a training set for ISPCA.

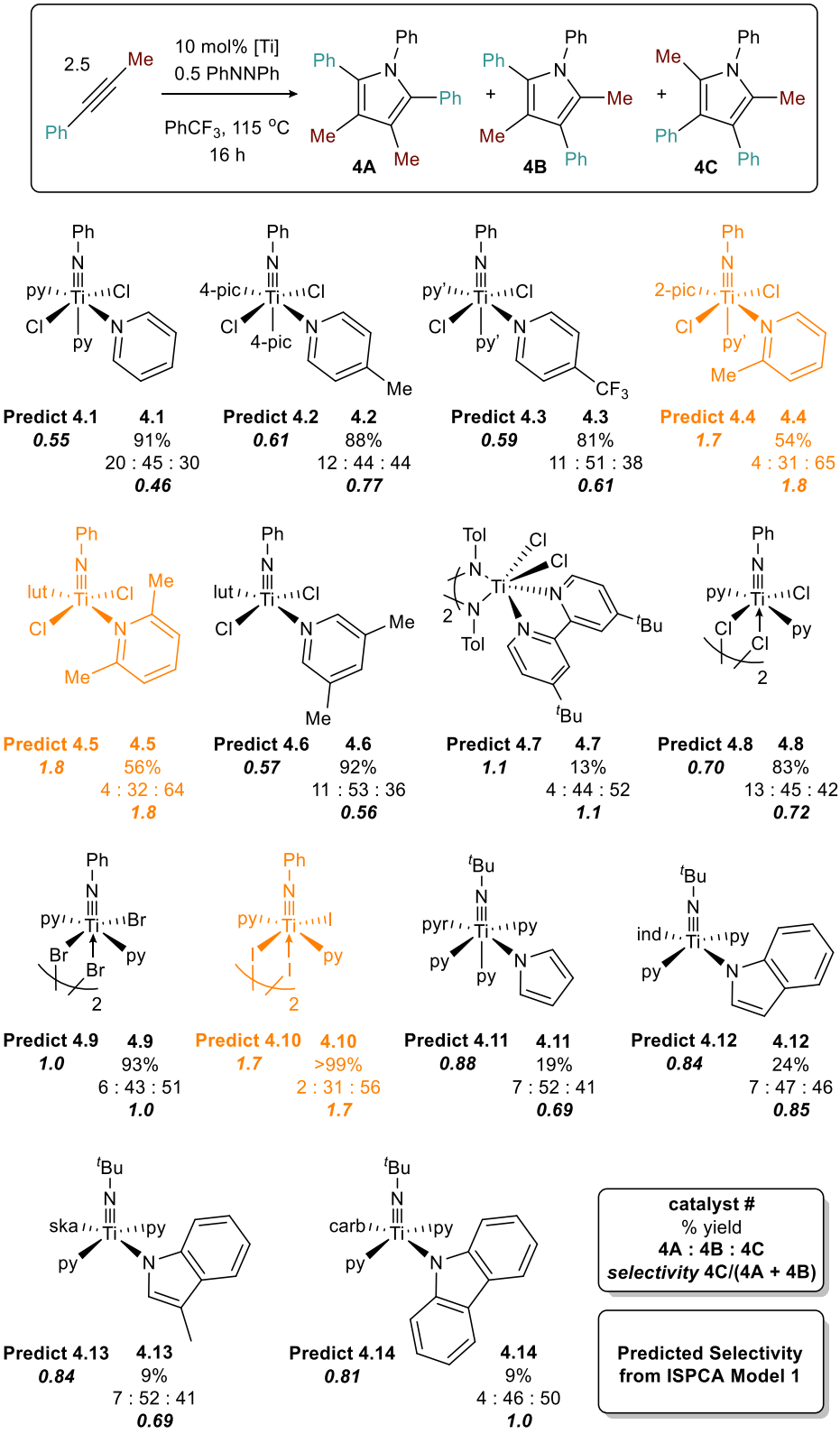

Figure 4.5 Initial catalyst screen (experimental and predicted selectivity) for selective [2+2+1] pyrrole formation from phenylpropyne. The most selective catalysts are drawn in

orange. Predicted values are calculated from ISPCA model 1. Conditions: 0.5 mmol phenyl propyne, 0.1 mmol azobenzene, 10 mol % [Ti], 0.5 mL $PhCF_3$, 115 °C, 16 h, average of 2-3 runs.

ISPCA was performed using catalysts **4.1**-**4.14**. The overall workflow is shown in Figure 2 and the specific details of the analysis for **4.1**-**4.14** are described below. All analysis, data mining and visualization were performed using a Matlab script developed in-house which is provided as supporting information.

Step 1: First, the initial basis set for the analysis was constructed from 22 descriptors spanning a variety of steric, electronic and spectroscopic descriptors for catalysts **4.1-4.14** calculated at the M06/6-311g(d,p) level of theory (see supporting information for additional details). Descriptors for catalysts and free ligands were chosen based on recent work from the Sigman lab detailing the value of catalyst specific descriptors.[213] The full descriptor list can be found in Table 4.1.

Table 4.1 Initial computed and tabulated descriptors used in PCA.[254]

Orbital Energies	**Electronic Descriptors**
Catalyst HOMO	Ti-X donor BDE
Catalyst LUMO	X donor atom Mulliken Electronegativity
Free pyridine HOMO	Free pyridine ligand quadrupole moment
Free pyridine LUMO	Composite donor atom polarizability
	Free pyridine N Mulliken charge
Geometric Descriptors	Catalyst-bound pyridine N Mulliken charge
Imido-Ti-N_{py} angle	Catalyst-bound X donor atom Mullken charge
Ti-imido bond length	Free pyridine proton affinity
Ti-N_{py} bond length	
Ti-X bond length	**NMR Descriptors**
X-Ti-X angle	Catalyst-bound pyridine *p*-^{13}C NMR shift
	Catalyst-bound pyridine *o*-^{13}C NMR shift
Steric Descriptors	Free pyridine *p*-^{13}C NMR shift
% Buried Volume[254]	Free pyridine *o*-^{13}C NMR shift

Step 2: Principal component analysis was conducted on the catalyst training set using the initial basis set and catalyst selectivity was plotted against the scores of the top three principal components. This generated a 3D PCA map[201] populated by the catalyst training set where catalyst scores (coordinates in PCA space) are related to their individual performance (Figure 4.6).

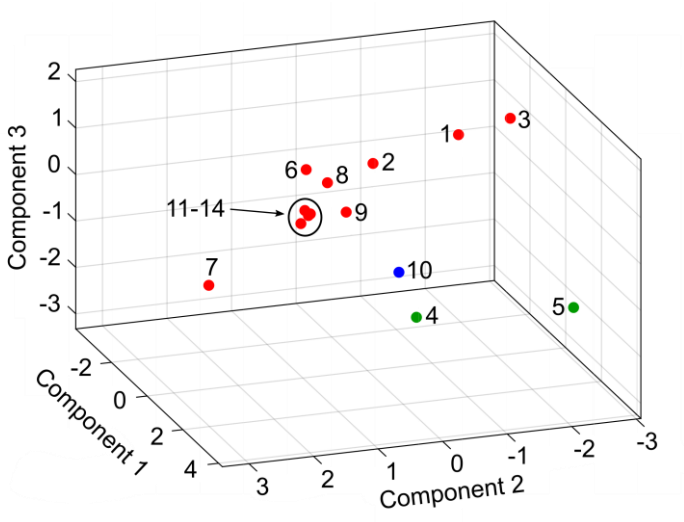

Figure 4.6 Principal component map constructed from the top 3 components of ISPCA model I and populated by the catalyst training set. Coloring is set by a dynamic k-means clustering algorithm (see SI for additional details).

Step 3: Linear least squares fitting was used to regress the catalyst scores against selectivity (Figure 4.7, black). Fit statistics using this unsupervised approach were unsatisfactory ($R^2 < 0.5$) despite the top 3 components accounting for 76 % of the data variance. This is unsurprising considering the low likelihood all descriptors would have a substantial correlation to catalyst performance. This highlights the inherent difficulty in determining descriptors or constructing latent descriptors that are informative in catalyst design. The regression was artificially limited to 3 components to avoid overfitting issues as well as to provide a means of visualizing a chemical space.[201]

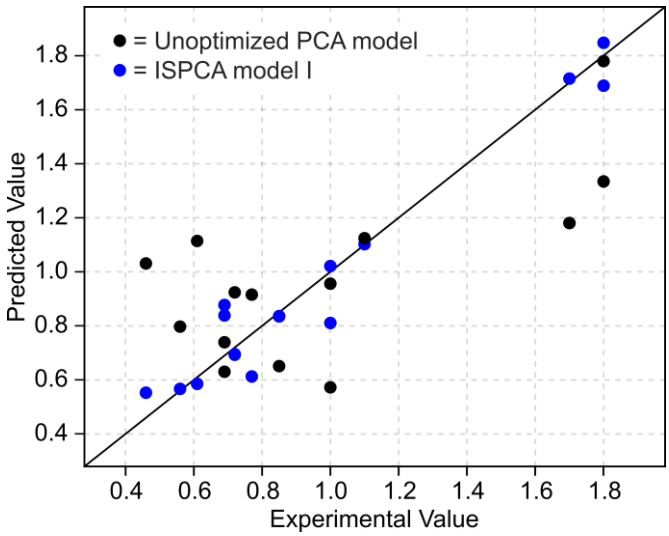

Example Calculation (ISPCA model I):

Selectivity = (regression coefficients × catalyst scores) + c

where c = arithmetic mean of experimental selectivity (0.9821)

Catalyst **6** score [x, y, z] = [-0.8892 -0.7019 0.7936]

PC1, PC2, PC3 regression coefficients = 0.0909, 0.0799, -0.3507

Catalyst **6** predicted selectivity = (0.0909 × -0.8892) + (0.0799 × -0.7019) + (0.3507 × 0.7936) + 0.9821 = **0.57** (exp. selectivity = **0.56**)

Figure 4.7 Unoptimized (black) and ISPCA (blue) model predictions versus experimental plots of reaction selectivity delivered by the catalyst training set.

Step 4: An exhaustive search for an improved basis set was then performed by conducting PCA on all possible descriptor groupings (2.1 million possibilities), using residuals between experimental and predicted selectivity (*via* the top three component approach described above) as the fitness parameter. The grouping delivering the lowest residuals contained 8 descriptors, accounted for 74 % of the data variance and provided the basis set for ongoing analysis (Table 4.2 and Table 4.3). Fit statistics using this supervised approach were considered acceptable (R^2 = 0.95) and the model fit was validated using leave-one-out cross validation (Q^2 = 0.91, Figure 6, blue). The PLSR strategy reported by the Rothenberg lab[241] was also implemented resulting in a worse statistical fit (R^2 = 0.82, Q^2 = 0.58) which supports the merits of the ISPCA method (Figure 4.102).[255]

Table 4.2 Descriptor Contributions to PC1, PC2 and PC3 in optimized ISPCA model 1.

Descriptor	PC1	PC2	PC3
Free pyridine *o*–^{13}C NMR shift	0.474	0.125	-0.387
Ti–X donor BDE	0.418	-0.112	0.558
Free pyridine N Mulliken charge	-0.426	-0.293	0.291
Imido–Ti–N_{py} angle	0.390	0.144	-0.369
Composite donor atom polarizability	-0.336	0.378	-0.345
X–Ti–X angle	0.052	0.511	0.382
Catalyst LUMO	0.267	-0.459	0.071
Ti–N_{py} bond length	0.284	0.501	0.220

Table 4.3 Relative Summed Descriptor Weights from the top 3 components of ISPCA model I.

Descriptor	Relative Weight[a]	Rank
Free pyridine *o*–^{13}C NMR shift	18.9	1
Ti–X donor BDE	-16.7	2
Free pyridine N Mulliken charge	-16.4	3
Imido–Ti–N_{py} angle	15.3	4
Composite donor atom polarizability	12.1	5
X–Ti–X angle	-8.8	6
Catalyst LUMO	-3.7	7
Ti–N_{py} bond length	-1.1	8

Regression coefficients: PC1, PC2, PC3 = 0.0909, 0.0799, -0.3507

[a]*Summed descriptor weights* = regression coefficients × descriptor loadings (Table 4.2).

Step 5: From the optimal ISPCA basis set, relative descriptor weights were determined by regression coefficient weighted summation of the coefficients of all descriptors in the top three principal components (Table 4.3, *c.f.* Approach Section). The relative magnitudes and signs of each descriptor weight were used to understand how tuning electronic or steric parameters would increase catalyst selectivity. For example, the calculated gauge-independent ^{13}C NMR chemical shift of the *o*-C atom on the free pyridine

ligand has a high positive weight in the ISPCA model, suggesting ligands with downfield shifted *o*-^{13}C NMR chemical shifts will have higher selectivity. Similarly, there is a high negative weight associated with Ti-X donor bond dissociation energy (BDE) and a high positive weight for composite donor atom polarizability (number weighted sum of atomic polarizability for donor atoms at Ti) indicating more polarizable X-type ligands are advantageous. The high negative weight associated with free pyridine N Mulliken charge signifies electron rich pyridine ligands are critical to improved selectivity, while a high positive weight of the imido-Ti-N_{py} angle indicates that sterically bulky ligands, which shy away from the imido fragment to minimize steric congestion, are important for engendering regioselective catalysis (Figure 4.8). Conversely, the Ti–N_{py} bond lengths (averaged), X-Ti-X angle and catalyst LUMO have a low weight in the ISPCA model, so tuning these descriptors will likely not result in a substantial change in selectivity. In summary, these quantitative results corroborate chemically intuitive trends: catalysts bearing highly polarizable poorly donating X-type ligands (i.e. iodide) and electron rich sterically encumbered L-type ligands (i.e. lutidine) will be selective catalysts in the pyrrole reaction.

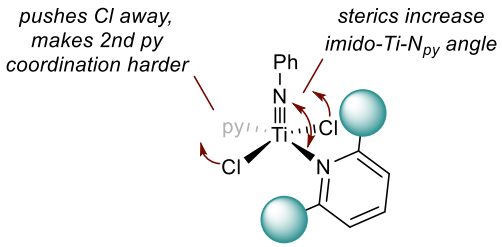

Figure 4.8 Schematic representation of steric effects on the imido-Ti-N_{py} angle.

The generated 3D PCA map shows how traversing PCA space will affect catalyst performance. The coordinates of new catalysts can be determined computationally using the ISPCA regression coefficients. Catalysts that occupy disadvantageous positions in PCA space should not be synthesized in the laboratory. Chemical landscapes often exhibit mathematically complex topologies and therefore a linear regression is unlikely to accurately represent the relationship between PCA space and catalyst position. Moreover, a linear regression is poorly reflective of realities in chemical synthesis – the steric character of bulky ligands cannot be infinitely increased because the resulting

brobdingnagian[256] ligand would be unlikely to bind to any metal center. Therefore, the inherent bias of a linear regression can be tempered by using a "molecular ruler" as a statistical gauge. The "molecular ruler" only considers distance, not direction, in determining the practical value of a test catalyst. Evaluation of the pairwise distances between catalyst scores shows a test catalyst must be 2.7 units in PCA space from the nearest training set neighbor in order to expect a substantial change in selectivity – for better or worse (Δ selectivity = 0.46 or 1 σ).

Step 6: Using the foregoing ISPCA model, potential "2nd generation" catalysts **4.15-4.22** were predicted and synthesized (Figure 4.9), focusing on changing characteristics of the catalyst in accordance with the relative weights of the descriptors in the model. For example, given that the ^{13}C NMR shift of the *ortho*-C on pyridine has a high positive weight in the ISPCA model, we computed *ortho*-halogenated catalyst **4.15**. This catalyst gives comparable predicted (1.2) and experimental (2.0) selectivity to *o*-Me substituted pyridine catalysts **4.4** (1.8) and **4.5** (1.8). Catalysts bearing 2,6-dihalogenated pyridines were considered but could not be synthesized presumably owing to the steric clash between the bulky pyridine ligands and Ti center (see Supporting Information for other catalysts).

Catalyst **4.17** was predicted (3.51) and experimentally confirmed (2.41) to be more selective than any other catalyst in the training set likely owing to the presence of both weak Ti-I bonds and sterically encumbering collidine ligand. **4.17** is a good example of potential additive effects on selectivity: **4.16**, which has stronger Ti-Cl bonds (and is thus less Lewis acidic than **4.17**) and **4.10**, which is similarly Lewis acidic but lacks steric encumbrance on pyridine, each has slightly worse selectivity.

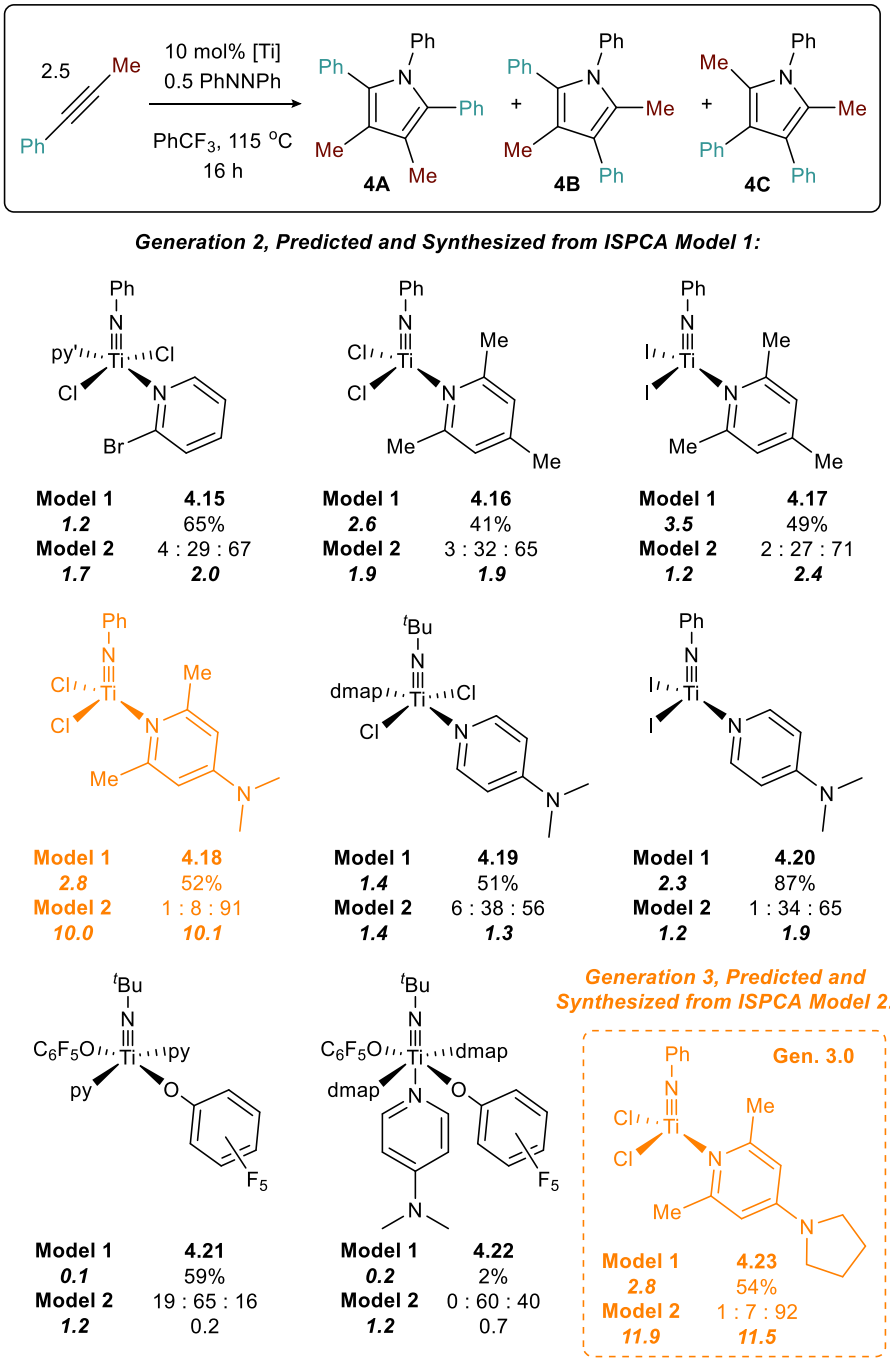

Figure 4.9 Second-generation catalysts predicted and synthesized using ISPCA model I and third-generation catalyst predicted and synthesized using weighted ISPCA model II that incorporates catalysts **4.1-4.22**. The most selective catalysts are drawn in orange. Conditions: 0.5 mmol phenyl propyne, 0.1 mmol azobenzene, 10 mol % [Ti], 0.5 mL $PhCF_3$, 115 °C, 16 h, average of 2-3 runs.

The high relative negative weight of catalyst LUMO in the ISPCA model prompted us to consider facile synthetic avenues to stabilize the LUMO. Orbital calculations showed that the LUMO of the pyridine-based catalysts is almost exclusively localized on the X and L donors while the Ti imido fragment contains the highest population of electron density in the HOMO. We thus turned to catalysts bearing pentafluorophenoxide X-type ligands (**4.21** and **4.22**). The ISPCA model predicted these catalysts would occupy disadvantageous positions in PCA space and should not be highly selective. Indeed, the predicted selectivity for **4.21** (0.11) and **4.22** (0.15) agree with the experimentally determined selectivity of 0.2 and 0.7 for **4.21** and **4.22**, respectively. Catalyst **4.22** is not a competent catalyst for the pyrrole reaction and affords the desired product in low yields. However, catalyst **4.21** provides good yields of product **4B** in unusually high selectivity. Thus, the unique coordinates of catalysts **4.21** and **4.22** in PCA space demonstrate that ISPCA should be an effective method for predicting changes in catalyst performance in a more general context, in this case ultimately allowing for the selective synthesis of any potential pyrrole regioisomer.

Finally, we hypothesized that due to the negative weight associated with free pyridine N Mulliken charge, increasing the electron donating ability of a sterically bulky ancillary pyridine ligand would result in high selectivity. While catalyst **4.18** was predicted to have a good selectivity of 2.8, experimentally **4.18** exhibited a significantly higher selectivity (10.1) than any other catalyst tested to date. This selectivity represents a 20-fold increase in selectivity from the starting catalyst **4.1** and 5-fold increase in selectivity from the initial training set.

Here, the key factors for selectivity are including a sterically encumbered pyridine ligand (correlated to free pyridine *o*-^{13}C NMR shift and imido-Ti-N_{py} angle) *and* strongly donating (correlated to free pyridine N Mulliken charge). When compared to catalysts with only one of these properties, the strength of the multivariate prediction becomes apparent: catalysts **4.5** (sterically encumbered) and **4.19**/**4.20** (strongly donating) each have pedestrian selectivity for **4C** and in a conventional screening endeavor there would be no obvious reason to spend time on the tedious synthesis of 2,6-Me_2-DMAP, which is not commercially available.

Additionally, a "molecular ruler" was used to cull the potential test set *in silico*. For example, catalysts bearing *o*-TMS groups, quinolines, or pendant alkoxides (Figure 4.10**,** catalysts **4.24**-**4.26**) were considered for steric and/or electronic modifications. Catalyst **4.24** was 3.3 units, catalyst **4.25** was 2.6 units and catalyst **4.26** was 4.0 units from the nearest training set neighbors in PCA space (Table 4.15). The "molecular ruler" suggests a value of at least 5.4 units is necessary to expect a 0.9 increase in selectivity, so in combination with the predicted selectivity of ~ 2.0 for the set, these catalysts did not warrant synthesis.

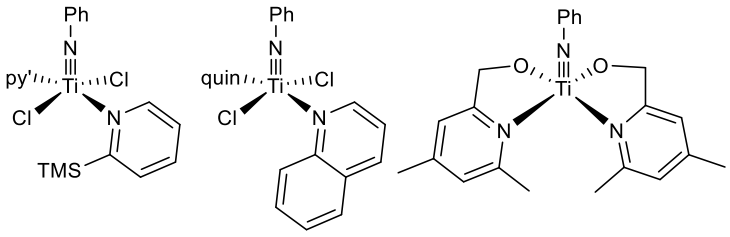

Catalyst 4.24 Predicted *2.6*

Catalyst 4.25 Predicted *1.4*

Catalyst 4.26 Predicted *2.0*

Figure 4.10 Example catalysts deemed not different enough to warrant synthesis *via* prediction from ISPCA model I.

While ISPCA model I led to the synthesis of a highly selective catalyst, the relatively poor predictive power prompted us to more closely examine the accompanying chemical space. Linear regression using ISPCA and catalysts **4.1**–**4.22** as a training set results in relatively poor fit statistics (R^2 = 0.73, Q^2 = 0.14; Figure 4.103). Excluding **4.18** from the training set resulted in good fit statistics (R^2 = 0.89, Q^2 = 0.85; Figure S91). Notably, attempting to fit the PCA subspace surrounding **4.18** using k-means clustering (Figure 4.105) to determine the local nearest neighbors (catalysts **4.4**, **4.5**, **4.8**, **4.16**, **4.19**, **4.20**) resulted in an excellent coefficient of determination (R^2 = 0.99) but a very poor cross validation value (Q^2 = - 0.1). In combination, these modelling attempts suggest catalyst **4.18** may represent an activity cliff. Activity cliffs are commonly found in predictive catalysis and medicinal chemistry[257] where a small modification in a substrate or catalyst results in a dramatic change in performance. Identifying and predicting activity cliffs is an inherent challenge in chemical catalysis. The dramatic increase in performance of catalyst

4.18 is a salient example of how any predictive model must be carefully informed by rigorous experimentation.

In order to effectively model a training set containing catalysts **4.1**–**4.22**, a weighted ISPCA scheme was implemented. Weights were applied to each catalyst based on the pairwise distance from catalyst **4.18** and the following formula:

$$\text{weights} = e^{-\text{distance}/c}$$

where c = 25 and was determined empirically.[258] This modeling strategy resulted in satisfactory fit statistics (R^2 = 0.94, Q^2 = 0.77) and analysis of the relative descriptor weights (Table 4.4 and Figure 4.106) was informative for development of 3rd generation catalysts.

Table 4.4 Relative Summed Descriptor Weights from the top 3 components of weighted ISPCA model II.

Descriptor	Relative Weight	Rank
Free pyridine *p*–^{13}C NMR shift	-25.1	1
Imido–Ti–N_{py} angle	17.6	2
Free pyridine HOMO	13.1	3
Catalyst-bound pyridine *o*–^{13}C NMR shift	10.9	4
Free pyridine *o*–^{13}C NMR shift	6.1	5
Ti–N_{py} bond length	5.0	6

Table 4.4 shows that in this weighted PCA space, the electron donating ability of the ancillary pyridine ligand (correlated to free pyridine *p*–^{13}C NMR shift and free pyridine HOMO) is the most critical factor in determining selectivity. Additionally, maintaining steric bulk around the Ti center (correlated to *o*–^{13}C NMR shifts) is important to selective catalysts. Therefore, we were prompted to synthesize a catalyst bearing a more electron rich 2,6-substituted pyridine. 2,6-dimethyl-4-(pyrrolidin-1-yl)pyridine (Figure 4.9, catalyst **4.23**) was chosen as the optimal ligand owing partially to the synthetic ease in substituting the 4-position on the pyridine ligand in comparison to 2,6-Me_2-DMAP. The weighted ISPCA model (model II) predicted a selectivity of 11.8 which is in good agreement with the experimental value of 11.3. This final generation of catalyst, **4.23**, is nearly 25 times as

selective as the initial catalyst, **4.1**. This reaction was successfully scaled (5 mmol), yielding synthetically useful quantities of **4C** (see Supporting Information for additional details). Other substrates, such as 4-methyl-2-pentyne, resulted in an erosion of selectivity and/or yield, highlighting the multifaceted control elements in this system.

We next were interested in interrogating the origins of the remarkable selectivity of **4.23** and **4.18** relative to **4.1**. DFT calculations were performed on catalysts **4.16**, **4.18** and **4.23**, which all showed improved selectivity compared to **4.1**. These structurally similar catalysts differ only in the *para*-substitution on pyridine, yet the experimental selective ranges from 1.9 to 11.5, thus providing a good benchmark for computational comparison. The free energies of **TS1**, **IM3** and **TS2** were calculated for catalysts **4.1**, **4.16**, **4.18** and **4.23** according to the selectivity manifold in Figure 4.4 (Table 4.5). In the case of **TS2**, there are three possible isomers, named ***cis*-1**, ***cis*-2** and ***trans*** (Figure 4.11) for the relative position of the pyridine ligand to the incoming alkyne. In all cases, the ***cis*-2** structures are lowest in free energy and these structures will be used for discussion below. Free energies of the other isomers are reported in the supporting information. The effects of different L type ligands on the selectivity of phenylpropyne reactions with **4.1** are previously reported.[82]

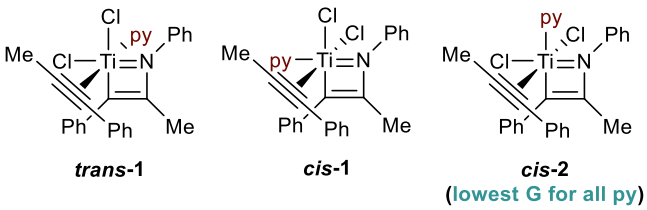

Figure 4.11 Possible isomers of TS2 ($TS2_{BF}$ shown) highlighting different positions of the pyridine ligand—either *trans* to the incoming alkyne (*trans-1*) or *cis* to the incoming alkyne (*cis*-1 and *cis*-2). In all cases the *cis*-2 isomer is lowest in free energy.

In all cases, [2+2] cycloaddition (**TS1**) is significantly lower in energy than rate-determining 2nd alkyne insertion (**TS2**). Thus, cycloaddition (**TS1**) is reversible and insertion (**TS2**) irreversible, indicating that the product distribution is mainly determined by the population of **IM3** (thermodynamically controlled) and the reaction barrier of **TS2** (kinetically controlled). While DFT absolute errors (ΔG) can be on the order of

2 kcalmol^{-1} and the calculated free energies are quite high for **4.16**, **4.18** and **4.23**, DFT can be significantly more accurate for relative differences (thus, ΔΔG) and provide valuable qualitative information for the selectivity.

Table 4.5 DFT-calculated free energies (M06/def2-SVP, SMD $PhCF_3$, 115 °C, kcalmol^{-1}) for select catalysts. All TS2 free energies are reported for the *cis*-2 isomer (Figure 4.11**)**. Schematics of the full selectivity manifolds are shown in Figure 4.107-Figure 4.111.

	4.1	**4.16**	**4.18**	**4.23**
$TS1_A$	25.4	25.1	26.9	26.9
$TS1_B$	23.2	22.7	24.9	25.0
$\Delta\Delta G^{‡}(TS1_A\text{-}TS1_B)$	2.2	2.4	2.0	1.9
$IM3_A$	8.6	6.7	7.8	9.1
$IM3_B$	1.7	3.5	5.7	4.8
$\Delta\Delta G(IM3_A\text{-}IM3_B)$	5.9	3.2	2.1	4.3
$TS2_{AC}$	32.7	43.0	44.5	44.2
$TS2_{AD}$	32.7	40.8	43.4	43.4
$TS2_{BE}$	26.5	40.8	43.0	43.3
$TS2_{BF}$	25.3	37.0	39.6	39.8
$\Delta\Delta G^{‡}(TS2_{BE}\text{-}TS2_{BF})$	**1.2**	**3.8**	**3.4**	**3.5**
Selectivity (Computed[a])	4.9	49	13.3	99
Selectivity (Observed)	0.46	1.9	10.1	11.5

[a]Computed selectivities are determined from the Boltzmann equation and Eyring equation. Details are given in supporting information.

$$\frac{[\mathrm{IM3_A}]}{[\mathrm{IM3_B}]} = \exp\left(\frac{-(\Delta G_{\mathrm{IM3_A}} - \Delta G_{\mathrm{IM3_B}})}{RT}\right) = \exp\left(\frac{-\Delta\Delta G(\mathrm{IM3_A} - \mathrm{IM3_B})}{RT}\right)$$

$$\frac{[\mathrm{TS2_{BE}}]}{[\mathrm{TS2_{BF}}]} = \frac{k_{BE}}{k_{BF}} = \exp\left(\frac{-(\Delta G^{‡}_{\mathrm{TS2_{BE}}} - \Delta G^{‡}_{\mathrm{TS2_{BF}}})}{RT}\right) = \exp\left(\frac{-\Delta\Delta G^{‡}(\mathrm{TS2_{BE}} - \mathrm{TS2_{BF}})}{RT}\right)$$

Comparing **4.1** with **4.16**, **4.18** and **4.23**, the values for $\Delta G^{‡}$(**TS1**) are similar among the four catalysts, ranging from 22.7 kcalmol^{-1} to 26.9 kcalmol^{-1}. By changing pyridine (**4.1**) into 2,6-dimethyl substituted pyridine (**4.16**, **4.18** and **4.23**) the values for

$\Delta\Delta G^{\ddagger}$(**TS1$_A$-TS1$_B$**) all remain ≈ 2 kcalmol^{-1}, suggesting that in all cases **TS1** is still under electronic control for the thermodynamically favored **TS1$_B$**. Thus, there is no major effect of the pyridine on [2+2] cycloaddition. In contrast, $\Delta\Delta G^{\ddagger}$(**TS2$_{BE}$-TS2$_{BF}$**) ≈ 4 kcalmol^{-1} for **4.16**, **4.18** and **4.23** while only 1.2 kcalmol^{-1} for **4.1**. Since **4.16**, **4.18** and **4.23** are electronically different but sterically the same, this result indicates that the steric hindrance of the 2,6-Me$_2$-substituted pyridines is the key factor that leads to the selectivity for **4C** in **TS2** (Figure 4.12) It is worth mentioning that $\Delta\Delta G^{\ddagger}$(**TS2$_{BE}$-TS2$_{BF}$**) may be consistently overestimated for all four catalysts: π-π stacking of adjacent phenyl groups in **TS2$_{BF}$** artificially stabilizes the structure. However, this is only one geometry of the ensemble of transition states and most geometries will not have the additional arene π-stacking interaction.

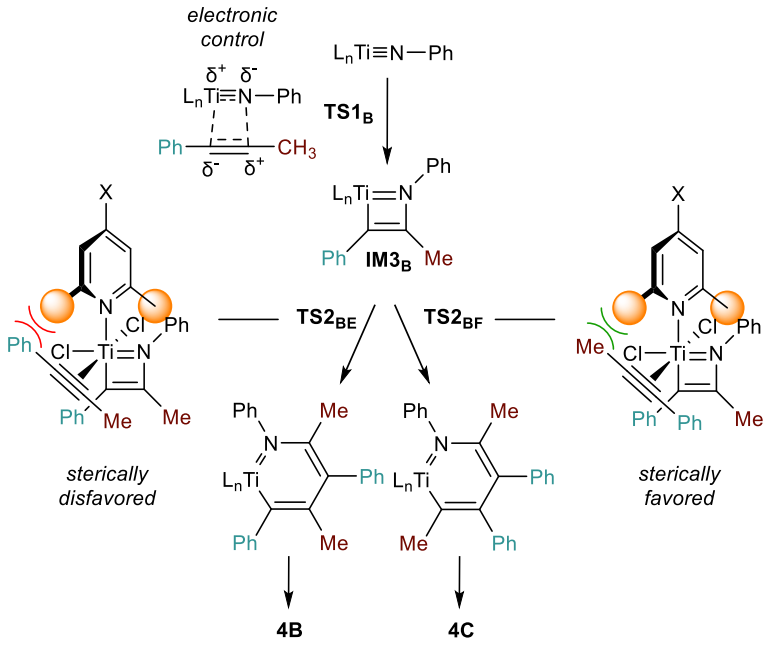

Figure 4.12 Sterically-encumbered pyridine ligands disfavor TS2$_{BE}$, leading to selective formation of **4C** through TS2$_{BF}$.

Given the large positive $\Delta\Delta G$(**IM3$_A$-IM3$_B$**) and $\Delta\Delta G^{\ddagger}$(**TS2$_{BE}$-TS2$_{BF}$**), catalysts **4.16, 4.18** and **4.23** should all produce almost exclusively **4C** through the ***cis*-2** configuration pathway of **TS2$_{BF}$** (Table 4.5). However, **4.18** and **4.23** are significantly more selective than **4.16**. We hypothesize that the difference in observed selectivity may

be correlated to relative ligand lability (Figure 4.13). When uncoordinated $Ti(NPh)Cl_2$ is computed as the catalyst, $\Delta\Delta G^{\ddagger}$(**TS2$_{BE}$-TS2$_{BF}$**) = - 0.7 kcalmol^{-1}, indicating that selectivity favors **4B** over **4C** for the unbound catalyst system (Figure 4.111). Sterically encumbered ligands where the coordination equilibrium favors a bound Ti will be more selective overall, as more of the catalyst will exist in the selective, bound form. Calculation of dissociation free energies is particularly challenging because they are sensitive to the solvation model; however, calculations suggest that dissociation is possible for **4.16**, **4.18** and **4.23** under catalytic conditions.

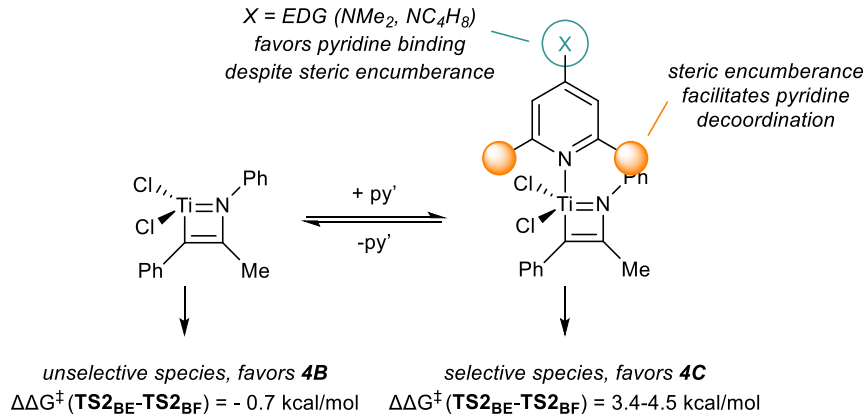

Figure 4.13 Electron-rich, bulky pyridines favor coordinated selective species, while solely sterically encumbered pyridines decoordinate, eroding selectivity.

In sum, calculations indicate that [2+2] cycloaddition is relatively insensitive to ligand effects, as the transition state is not very sterically encumbered and there is already a large intrinsic electronic bias for PhCCMe cycloaddition. However, sterically encumbered catalysts are needed to bias 2nd alkyne insertion to favor product **4C**. These sterically encumbered ligands are more likely to dissociate from Ti, which results in the formation of an unselective naked catalyst. In order to shift the coordination equilibrium to favor bound, selective catalysts, strongly electron donating pyridine groups are needed. Thus, sterically encumbered, electron-rich catalysts such as **4.18** and **4.23** are the most selective catalysts: they are sterically encumbered enough to bias 2nd alkyne insertion, but strong enough donors as to stay bound to Ti throughout catalysis. These observations are consistent with the models derived from ISPCA, where the free pyridine HOMO and *p*-^{13}C

NMR shift (electronic descriptors) and the imido–Ti–N_{py} angle (steric descriptor) are predicted to be the factors most impacting selectivity.

4.5 Conclusion

Iterative supervised principal component analysis (ISPCA) was implemented as a strategy for rational catalyst design. The Ti-catalyzed [2+2+1] synthesis of pentasubstituted pyrroles from phenyl propyne and azobenzene was chosen as a model system to validate the merits of the ISPCA approach, with the aim of controlling the selectivity of the reaction for 2,5-dimethyl-1,3,4-triphenyl-1*H*-pyrrole (**4C**). ISPCA was conducted on a training set of catalysts and their performance was regressed against the scores from the top three principal components. Component loadings from an optimized PCA space were used to inform the design of new test catalysts. Additionally, a "molecular ruler" was used as a statistical gauge to determine if test catalysts warranted synthesis. The selectivity of a prospective test set was predicted *in silico* using the ISPCA model and only optimal candidates were synthesized and tested experimentally. This judicious *in silico* winnowing of test catalysts helped shorten the screening process and after only three generations, the catalytic selectivity improved from 0.5 to over 11 for **4C** – a factor of nearly 25.

DFT calculations demonstrated that the origin of selectivity could be rationalized as a function of the persistence of sterically encumbered pyridine-bound catalyst species. Optimal catalysts are only required to bias the 2nd alkyne insertion, as the initial [2+2] cycloaddition is largely insensitive to ligand effects. Catalyst **4.23** bears a pyridine ligand that is both sterically bulky and highly electron donating. This likely leads to a highly regioselective reaction because the electron donating ability of the ancillary pyridine helps keep the ligand bound to Ti, which creates a sterically encumbered active site that can influence selectivity-determining transition state. ISPCA models corroborate this observation where regression coefficients of descriptors associated with steric bulk and electron donor ability are weighted heavily.

This work serves as a proof of principle that ISPCA and more generally careful analysis of PCA maps is a valuable strategy in *de novo* catalyst design. This ISPCA approach led to models that use relatively sparse training sets (< 20), are reasonably

predictive with out of sample test cases, have sensible interpretations and are constructed from low-computational cost descriptors. ISPCA serves as a way to effectively quantify and complement a researcher's chemical intuition during the catalyst screening process but maintains outputs that are chemically meaningful. Overall, this strategy should be generalizable to any catalyst system and a more widely utilized tool in catalysis informatics.

4.6 Experimental

4.6.1 General considerations for experimental work

All air- and moisture-sensitive reactions were carried out in a nitrogen-filled glovebox. Solvents for air- and moisture-sensitive reactions were prepared in one of three ways: i) predried on a Pure Process Technology solvent purification system (C_6H_6, THF, PhMe, $PhCF_3$, hexanes, pentane, ether), ii) degassed, dried over CaH_2 and stored over molecular sieves prior to use (PhBr) and iii) vacuum transferred from sodium benzophenone ketyl (C_6D_6) or CaH_2 ($CDCl_3$). C_6D_5Br was synthesized following literature procedure,[121] degassed, dried over CaH_2, freeze-pump-thawed thrice , brought into the glovebox, filtered through basic alumina prior to use. Azobenzene was purchased from TCI America (100 g), extracted with hexanes/water to remove residual methanol and dried in *vacuo* before use. Commercial phenyl propyne was used dried over CaH_2, freeze-pump-thawed three times, brought into the glovebox and filtered through basic alumina prior to use.

Solid $[Ti(NPh)Cl_2]_n$[259] and $[Ti(NTol)Cl_2]_n$[119] were synthesized as previously described, dried in *vacuo* and stored in the freezer until use. $[Ti(NPh)Br_2]_n$ and $[Ti(NPh)I_2]_n$ was prepared following a modified procedure using $TiBr_4$ and TiI_4[259] instead. Catalysis results for $Ti(NPh)Cl_2py_3$ (**4.1**) were used directly for comparison from our previous work.[79]

^1H and ^{13}C NMR spectra were recorded on Bruker Avance III HD 400 and 500 MHz and Bruker Avance Neo 600 MHz spectrometers. Chemical shifts are referenced to residual solvent resonances: ^1H (s, 7.26 ppm for $CHCl_3$; s, 7.16 ppm for C_6H_6; s, 7.30 ppm, 7.02 ppm and 6.94 ppm for C_6D_4HBr[194]), ^{13}C (t, 77.2 ppm for $CDCl_3$; t, 128.06 ppm for C_6D_6). Poor solubility of the following complexes required collection of the ^{13}C NMR spectrum *via* indirect detection (^1H – ^{13}C HSQC, HMBC): **4.3**, **4.6**, **4.10**, **4.12**, **4.13**, **4.16**–

4.18, **4.20**, **4.22**, **4.23**, b, d and e. All expected resonances were not observed likely owing to fast T2 relaxation or dynamic ligand exchange occurring at the Larmor frequency. Complexes **4.5**, **4.9** and **4.15** are virtually insoluble which precluded collection of ^{13}C NMR spectra entirely.

4.6.2 Synthesis of compounds

Synthesis of 4.2

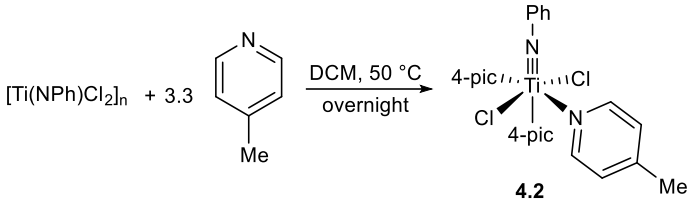

$Ti(NPh)Cl_2(4\text{-picoline})_3$ was synthesized with a slight modification to literature procedure by heating it overnight in CH_2Cl_2.[260]

^{1}H NMR (500 MHz, $CDCl_3$): δ 8.95 (d, $^3J_{HH}$ = 6.0 Hz, 4H, *o*-4-picoline-*H*), 8.63 (br s, 2H, axial *o*-4-picoline-*H*), 7.18 (d, $^3J_{HH}$ = 6.3 Hz, 4H, *o*-NPh-*H*), 7.06 – 7.03 (m, 4H, *m*-NPh-*H* and axial *m*-4-picoline-*H*), 6.91 (d, $^3J_{HH}$ = 7.6 Hz, 2H, *m*-4-picoline-*H*), 6.77 (t, $^3J_{HH}$ = 7.4 Hz, 1H, *p*-NPh-*H*), 2.41 (s, 6H, 4-picoline-CH_3), 2.33 (s, 3H, axial 4-picoline-CH_3).

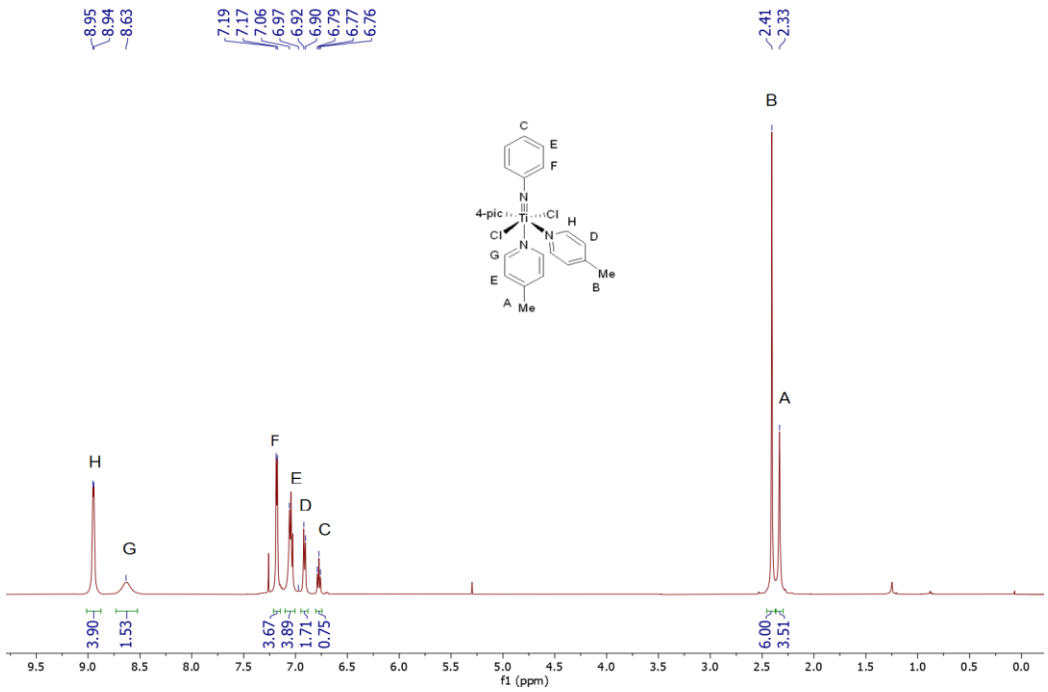

Figure 4.14 ^{1}H NMR spectrum of **4.2** in $CDCl_3$. *Taken from XYS0054B_1H.*

Synthesis of 4.3

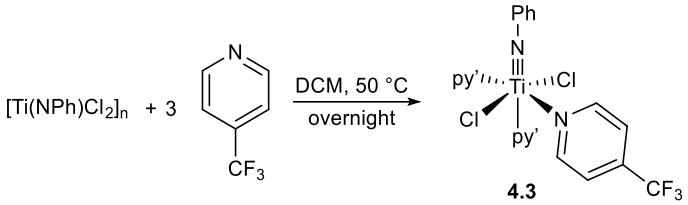

$[Ti(NPh)Cl_2]_n$ (102 mg, 0.49 mmol, 1.0 equiv), 4-(trifluoromethyl)pyridine (214 mg, 1.46 mmol, 3.0 equiv) and 2 mL CH_2Cl_2 were added to a 20 mL scintillation vial equipped with a small stir bar in a N_2-filled glovebox. This was then sealed with a Teflon-lined cap, heated to 50 °C and stirred overnight. After cooling to room temperature, the reaction mixture was filtered through a fine frit and washed with CH_2Cl_2. No visible residue was observed. The filtrate was dried *in vacuo* to give **4.3** as a tan powder (210 mg, 66 % yield).

^{1}H NMR (500 MHz, $CDCl_3$): δ 9.32 (br s, 4H, *o*-4-(trifluoromethyl)pyridine-*H*), 8.97 (br s, 2H, axial *o*-4-(trifluoromethyl)pyridine-*H*), 7.59 (br s, 4H, *m*-4-(trifluoromethyl)pyridine-*H*), 7.53 (br s, 2H, axial *m*-4-(trifluoromethyl)pyridine-*H*), 7.06 (t, $^{3}J_{HH}$ = 7.8 Hz, 2H, *o*-NPh-*H*), 6.88 (d, $^{3}J_{HH}$ = 8.4 Hz, 2H, *m*-NPh-*H*), 6.84 (t, $^{3}J_{HH}$ = 7.4 Hz, 1H, *p*-NPh-*H*).

Hexane impurities are present in the $CDCl_3$ solvent.

^{13}C NMR (126 MHz, C_6D_6): 160.1, 152.1, 139.4 (q), 128.6, 128.0, 124.0, 123.6, 122.9, 120.7, 119.5, 119.5.

This is a partial line-list. Resonances associated with a quaternary C from the CF_3 fragment were not observed.

^{19}F NMR (471 MHz, $CDCl_3$): δ -65.1 (br s, 3F, axial-4-(trifluoromethyl)pyridine-*F*), -65.3 (s, 6F, 4-(trifluoromethyl)pyridine-*F*).

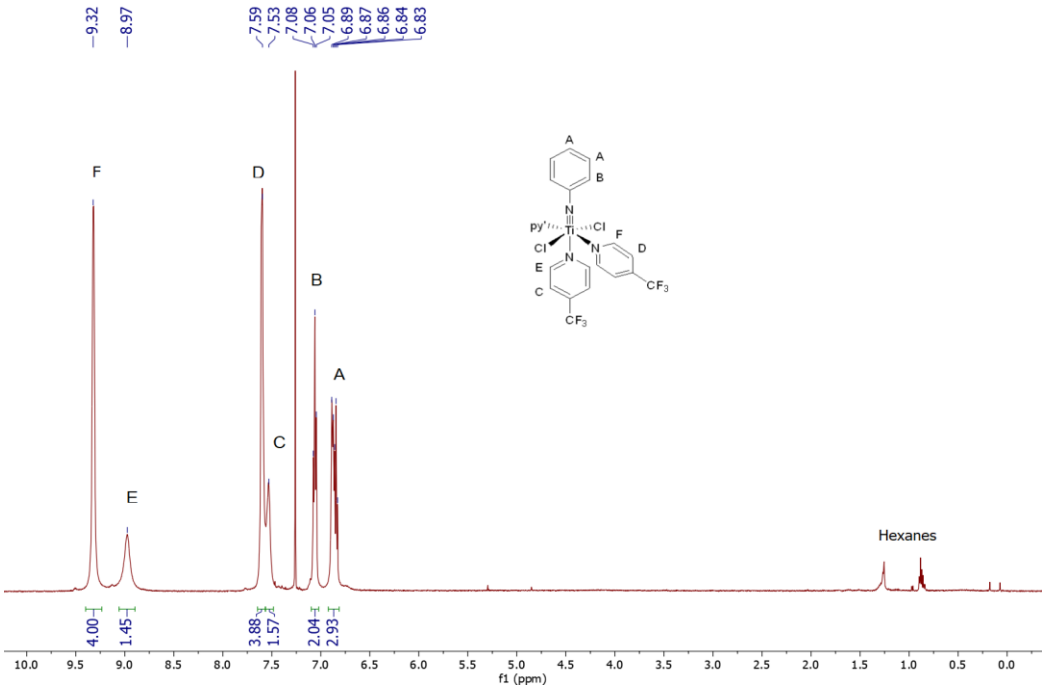

Figure 4.15 ^{1}H NMR spectrum of **4.3** in $CDCl_3$. *Taken from XYS-2019-183_1H.*

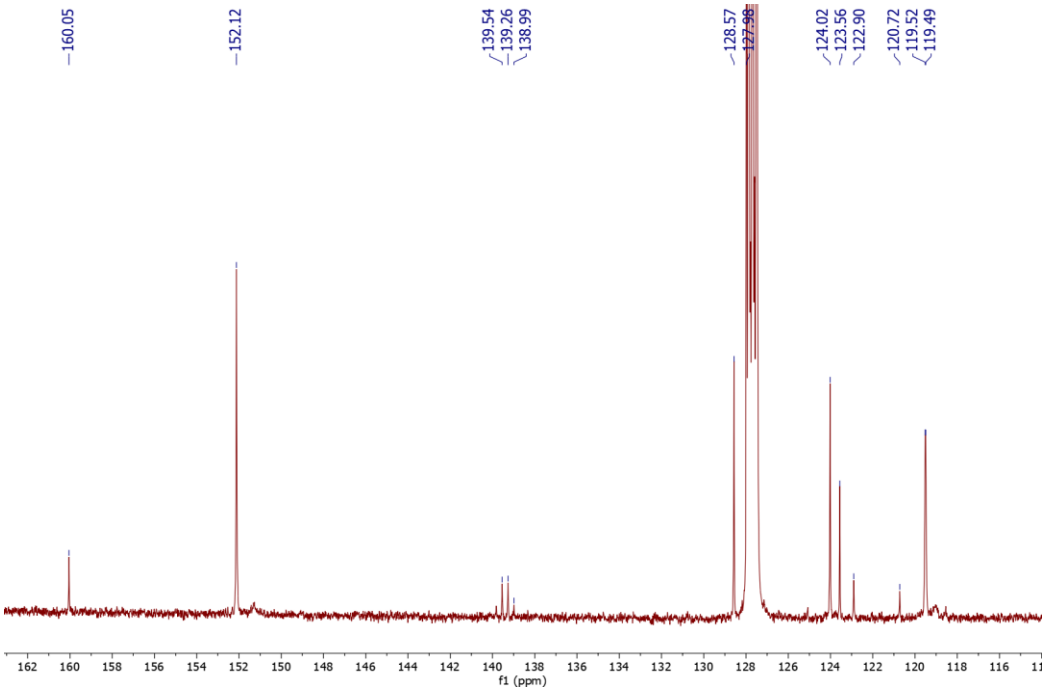

Figure 4.16 ^{13}C NMR spectrum of **4.3** in C_6D_6. *Taken from XYS-2019-183_2C.*

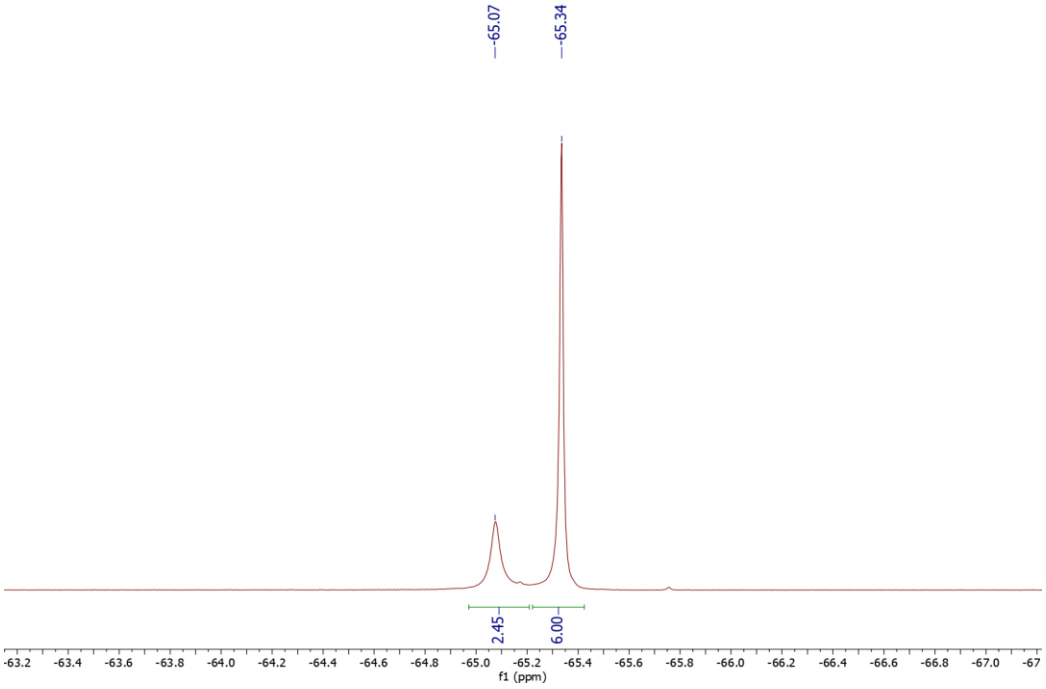

Figure 4.17 ^{19}F NMR spectrum of **4.3** in $CDCl_3$. *Taken from XYS-2019-183_1F.*

Synthesis of 4.4

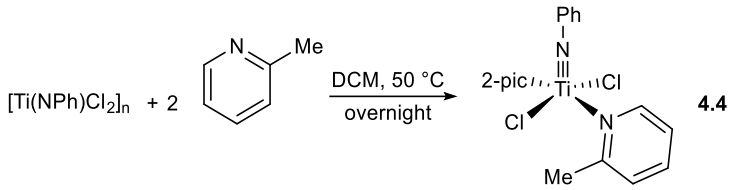

$[Ti(NPh)Cl_2]_n$ (88 mg, 0.42 mmol, 1.0 equiv), 2-picoline (78 mg, 0.84 mmol, 2.0 equiv) and 2 mL CH_2Cl_2 were added to a 20 mL scintillation vial equipped with a small stir bar in a N_2-filled glovebox. This was then sealed with a Teflon-lined cap, heated to 50 °C and stirred overnight. After cooling to room temperature, the reaction mixture was filtered through a fine frit and washed with CH_2Cl_2. The residue was dried *in vacuo* to give **4.4** as a brown powder (125 mg, 75 % yield). Residual CH_2Cl_2 could not be removed despite heating product in *vacuo* at 50 °C for prolonged periods.

^{1}H NMR (500 MHz, $CDCl_3$): δ 9.23 (br s, 2H, *o*-(2-picoline)-*H*), 7.78 (br s, 2H, (2-picoline)-*H*), 7.33 – 7.28 (m, 2H, (2-picoline)-*H*), 7.20 – 7.13 (m, 6H, (2-picoline)-*H* and NPh-*H*), 6.94 (t, $^3J_{HH}$ = 7.2 Hz, 1H, *p*-NPh-*H*), 2.78 (s, 6H, Me-*H*).
Additional peaks in the spectrum belong to rotamers due to restricted rotation around the Ti-N_{py} bond. The peaks are observed to coalesce at 320 K (47 °C) upon heating. Hexane impurities are present in the $CDCl_3$ solvent.

^{13}C NMR (101 MHz, $CDCl_3$): δ 161.0, 157.2, 152.8, 139.6, 130.1, 126.4, 124.9, 123.7, 122.4, 24.7.

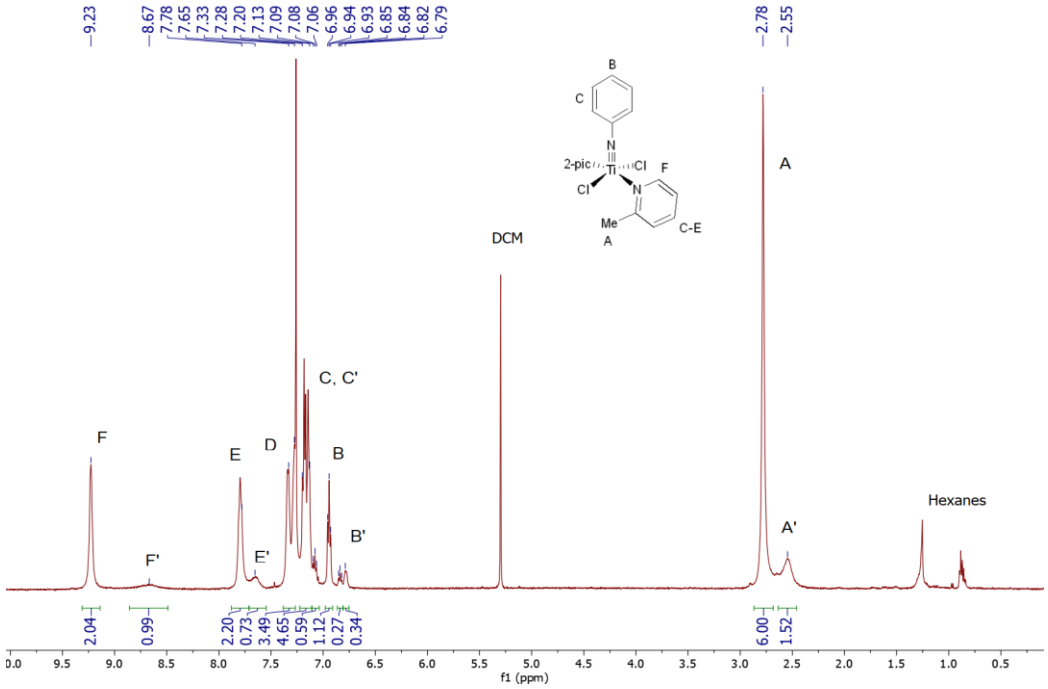

Figure 4.18 ^{1}H NMR spectrum of **4.4** in $CDCl_3$. *Taken from XYS-2020-007_1H.*

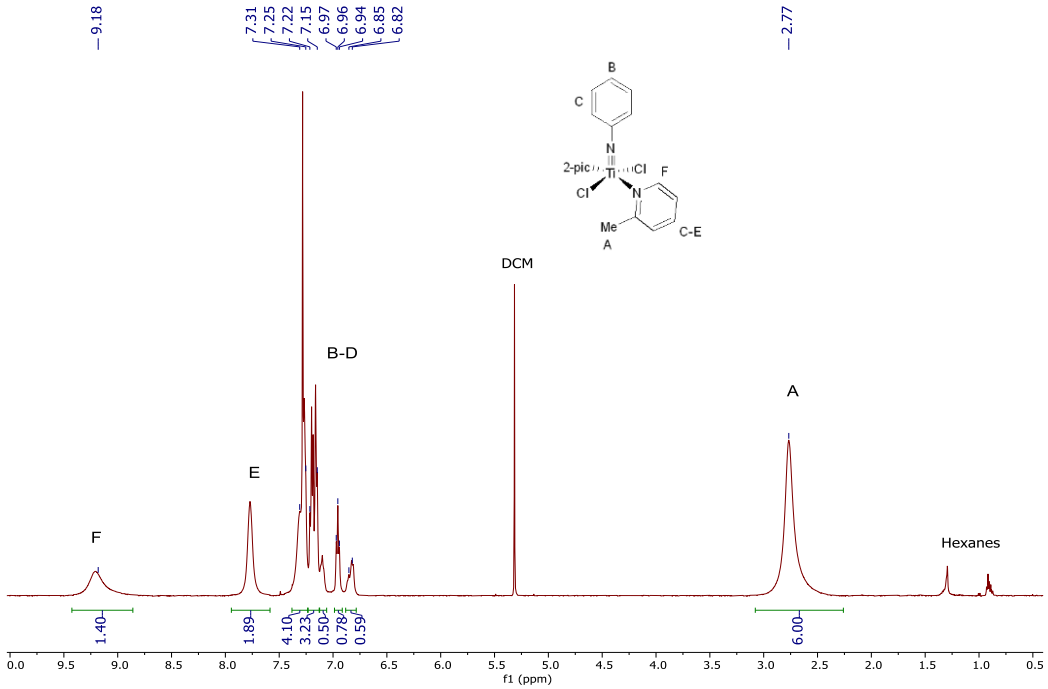

Figure 4.19 ^{1}H NMR spectrum of **4.4** in $CDCl_3$ at 320K. *Taken from XYS-2020-007_320K.*

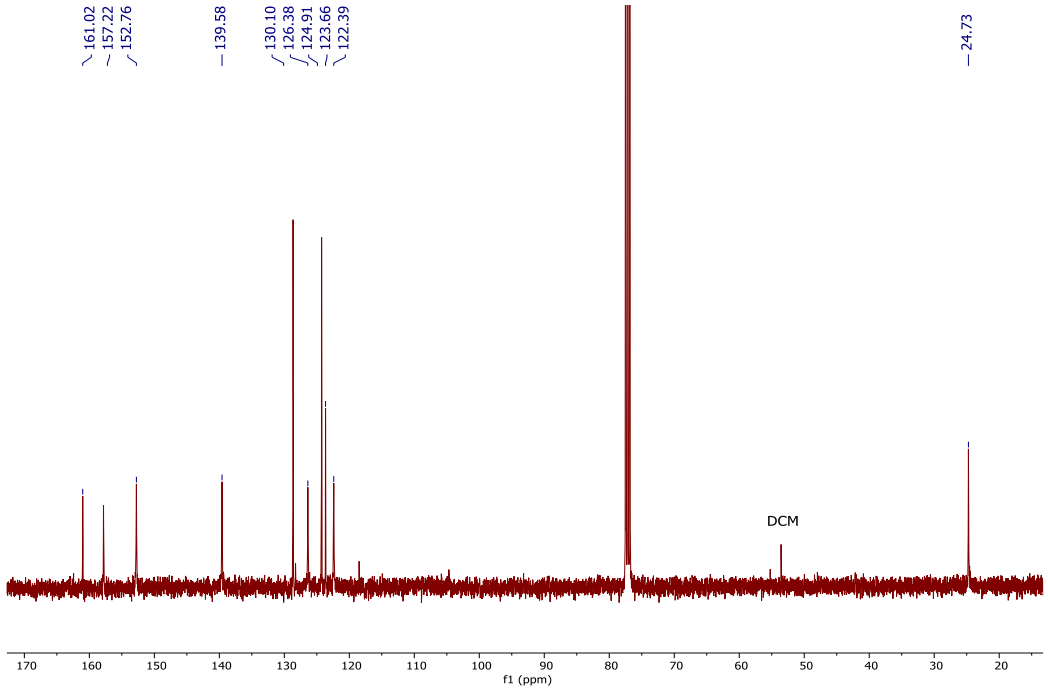

Figure 4.20 ^{13}C NMR spectrum of **4.4** in $CDCl_3$. *Taken from XYS-2020-007_1C.*

Synthesis of 4.5

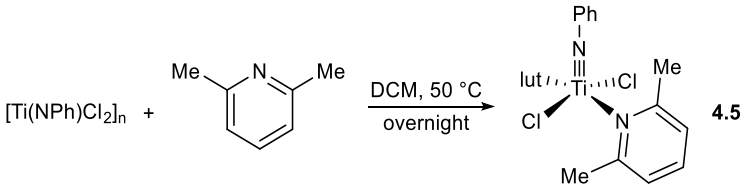

$[Ti(NPh)Cl_2]_n$ (73 mg, 0.37 mmol, 1.0 equiv), 2,6-lutidine (75 mg, 0.7 mmol, 1.9 equiv) and 2 mL CH_2Cl_2 were added to a 20 mL scintillation vial equipped with a small stir bar in a N_2-filled glovebox. This was then sealed with a Teflon-lined cap, heated to 50 °C and stirred overnight. After cooling to room temperature, the reaction mixture was filtered through a fine frit and washed with CH_2Cl_2. The residue was dried *in vacuo* to give **4.5** as a brown powder (97 mg, 75 % yield). **4.5** is highly insoluble in $CDCl_3$ and no ^{13}C NMR spectrum could be obtained.

^{1}H NMR (500 MHz, $CDCl_3$): δ 7.50 (br s, 2H, *o*-NPh-*H*), 7.21 (br s, 2H, *p*-lutidine-*H*), 6.95 (app d, 5H, *m*-lutidine-*H* and *p*-NPh-*H*), 6.85 (br s, 2H, *m*-NPh-*H*), 2.56 (s, 12H, Me-*H*).

Hexane impurities are present in the $CDCl_3$ solvent.

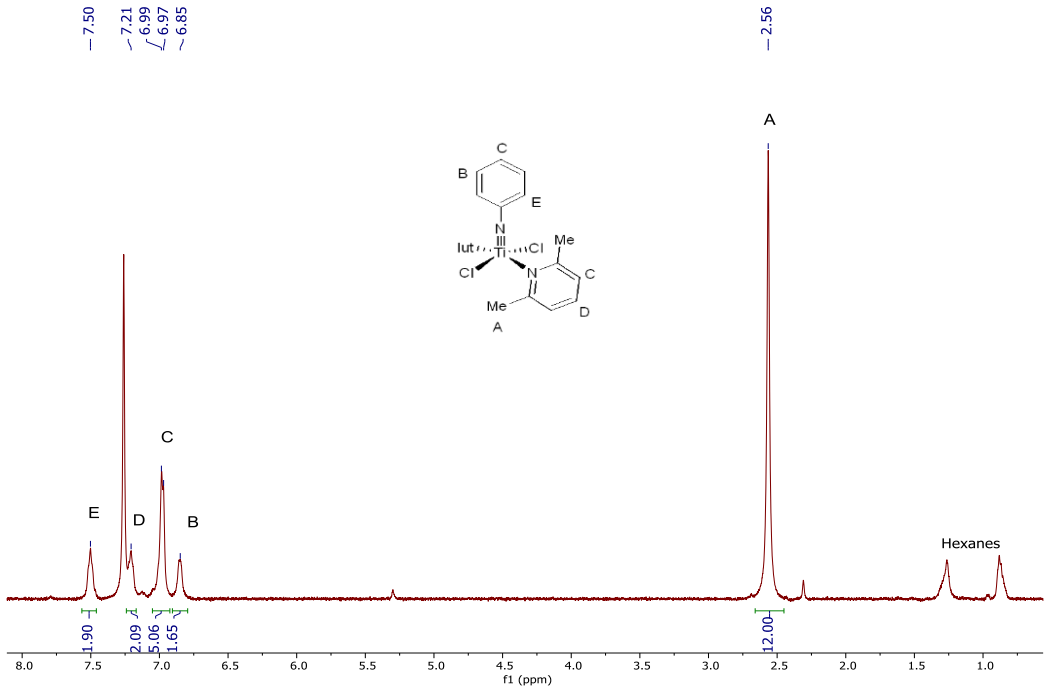

Figure 4.21 ^{1}H NMR spectrum of **4.5** in $CDCl_3$. *Taken from XYS-2019-174B_1H.*

Synthesis of 4.6

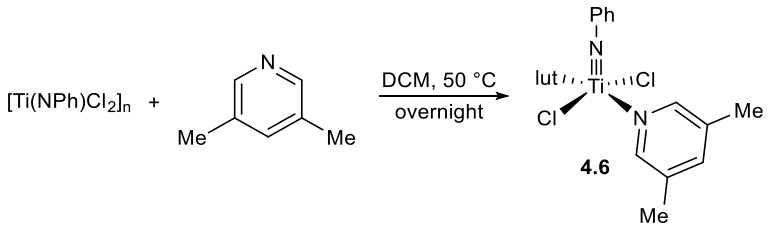

$[Ti(NPh)Cl_2]_n$ (156 mg, 0.75 mmol, 1.0 equiv), 3,5-lutidine (170 mg, 1.65 mmol, 2.2 equiv) and 2 mL CH_2Cl_2 were added to a 20 mL scintillation vial equipped with a small stir bar in a N_2-filled glovebox. This was then sealed with a Teflon-lined cap, heated to 50 °C and stirred overnight. After cooling to room temperature, the reaction mixture was filtered through a fine frit. The residue was dried *in vacuo* to give an impure brown powder that was re-suspended in 2 mL hexanes and stirred over the weekend. The suspension was filtered through a fine frit and washed with hexanes. The residue was dried *in vacuo* to give pure **4.6** as a brown powder (216 mg, 68 % yield).

^{1}H NMR (400 MHz, $CDCl_3$): δ 8.79 (s, 4H, *o*-lutidine-*H*), 7.52 (s, 2H, *p*-lutidine-*H*), 7.10 (t, $^{3}J_{HH}$ = 7.6 Hz, 2H, *o*-NPh-*H*), 6.91 (app d, $^{3}J_{HH}$ = 7.7 Hz, 2H, *m*-NPh-*H*), 6.84 (t, $^{3}J_{HH}$ = 7.8 Hz, 1H, *p*-NPh-*H*), 2.36 (s, 12H, Me-*H*).

Additional peaks in the spectrum belong to the mono-lutidine complex.

^{13}C NMR (126 MHz, $CDCl_3$): δ 148.2, 139.9, 134.1, 128.4, 123.6, 122.9, 18.7

This is a partial line-list. Resonances associated with a quaternary C of the NPh fragment were not observed.

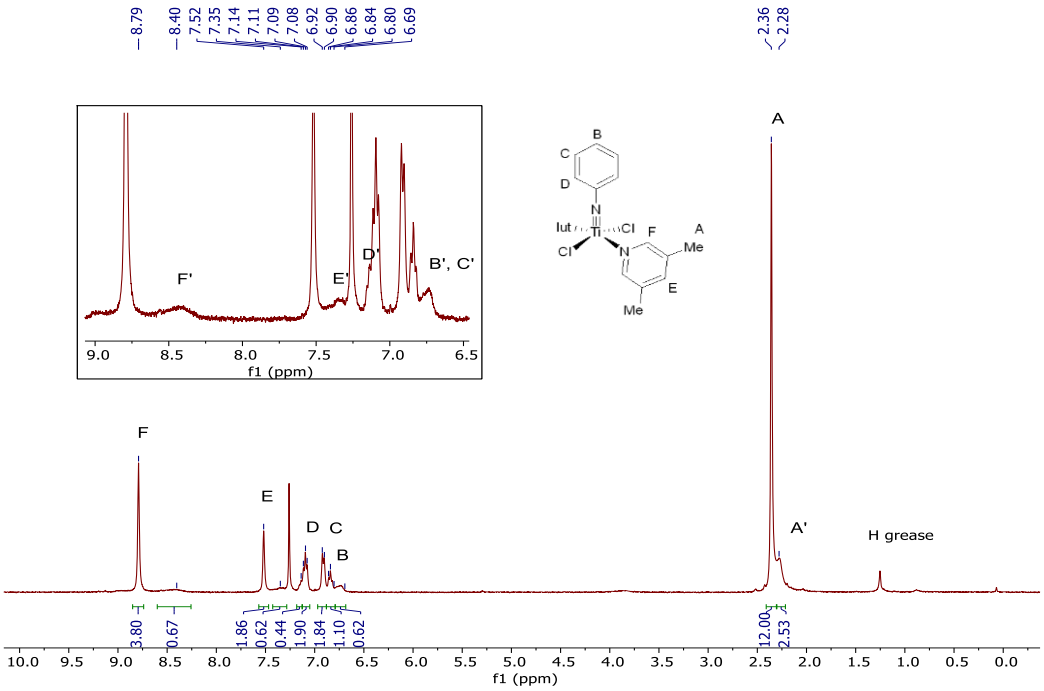

Figure 4.22 ^{1}H NMR spectrum of **4.6** in $CDCl_3$. *Taken from XYS05013-2H.*

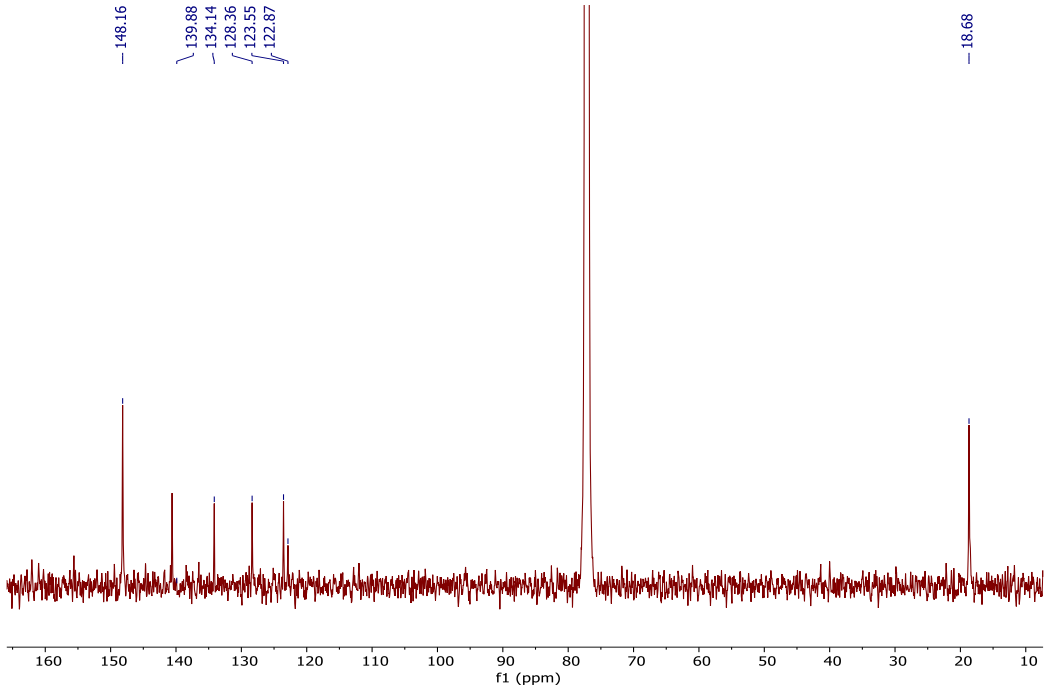

Figure 4.23 ^{13}C NMR spectrum of **4.6** in $CDCl_3$. *Taken from XYS05013-1C.*

Synthesis of 4.7

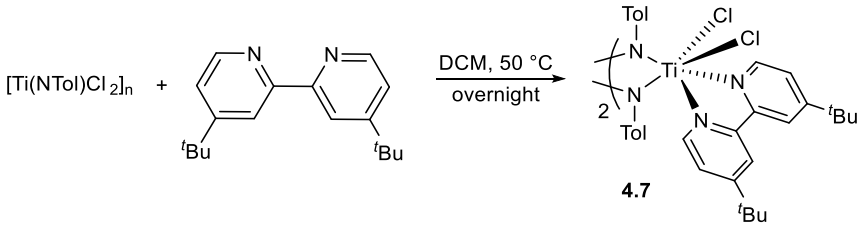

$[Ti(NTol)Cl_2]_n$ (101 mg, 0.45 mmol, 1.0 equiv), 4,4′-di-tert-butyl-2,2′-bipyridine (121 mg, 0.45 mmol, 1.0 equiv) and 2 mL CH_2Cl_2 were added to a 20 mL scintillation vial equipped with a small stir bar in a N_2-filled glovebox. This was then sealed with a Teflon-lined cap, heated to 50 °C and stirred overnight. After cooling to room temperature, this reaction was dried *in vacuo*. The residue was re-dissolved in 2 mL CH_2Cl_2, layered with 2 mL hexanes and cooled in a - 35 °C freezer to yield X-ray quality black crystals which were washed with hexanes to yield pure **4.7** (180 mg, 81 % yield). The crystalline material yielded a complex solution NMR spectrum with peaks appearing to belong to one molecule *via* various NMR experiments.

^{1}H NMR (500 MHz, $CDCl_3$): δ 9.44 – 9.41 (overlapping d, 3H, bipy*-*H*), 9.35 (d, $^{3}J_{HH}$ = 5.5 Hz, 1H, bipy*-*H*), 8.72 (d, $^{3}J_{HH}$ = 6.0 Hz, 2H, bipy*-*H*), 7.92 (s, 2H, bipy*-*H*), 7.80 (s, 2H, bipy*-*H*), 7.72 (app d, $^{3}J_{HH}$ = 5.8 Hz, 3H, bipy*-*H*), 7.62 (s, 2H, bipy*-H), 7.57 (d, $^{3}J_{HH}$ = 8.2 Hz, 2H, *o*-NTol-*H*), 7.46 (s, 1H, bipy*-*H*), 7.23 – 7.20 (overlapping d, 3H, *m*-NTol-*H* and bipy*-*H*), 6.71 (d, $^{3}J_{HH}$ = 6.1 Hz, 2H, bipy*-*H*), 6.55 (br s, 2H, bipy*-*H*), 6.36 (br s, 2H, bipy*-*H*), 6.04 (d, $^{3}J_{HH}$ = 7.9 Hz, 2H, *o*-NTol-*H*), 5.59 (d, $^{3}J_{HH}$ = 8.2 Hz, 2H, *m*-NTol-*H*), 2.36 (s, 3H, NTol-*H*), 2.07 (s, 3H, NTol-*H*), 2.59 (s, 3H, NC_6H_4-CH_3), 1.48 (s, 30H, ^{t}Bu-*H*), 1.28 (s, 11H, ^{t}Bu-*H*), 1.15 (s, 18H, ^{t}Bu-*H*).

^{13}C NMR (101 MHz, $CDCl_3$): δ 164.2, 163.9, 163.0, 154.86, 153.5, 152.4, 152.2, 151.96, 151.0, 134.6, 128.5, 127.5, 126.4, 123.8, 123.0, 122.2, 121.9, 117.3, 117.1, 114.9, 35.7, 35.2, 35.1, 30.6, 30.4, 30.3, 21.3, 21.0, 20.5.

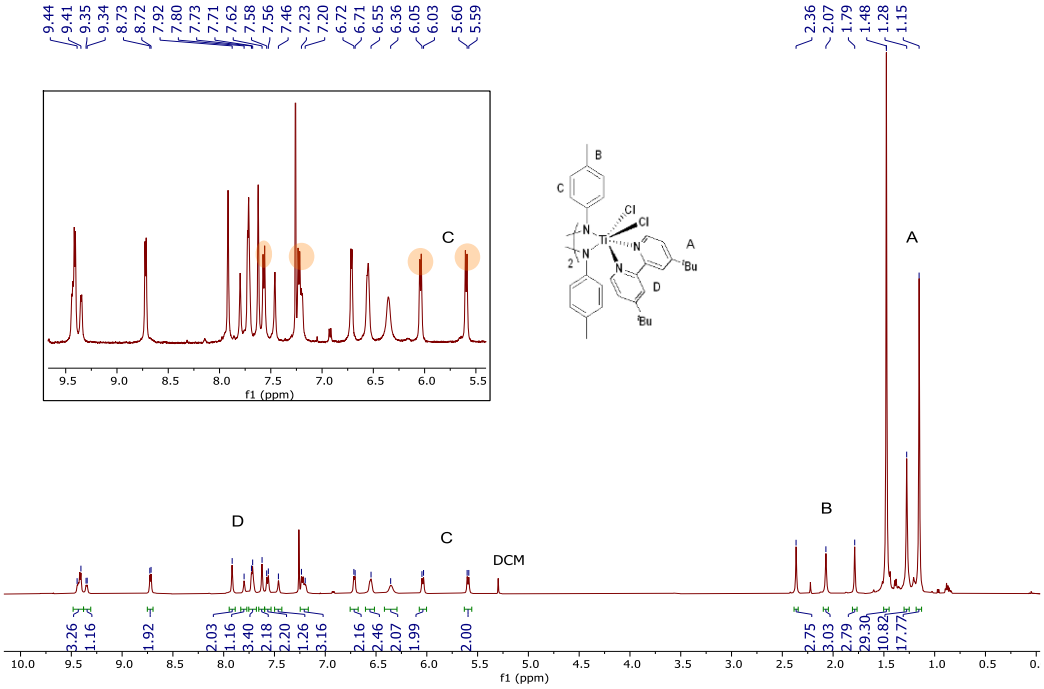

Figure 4.24 ^{1}H NMR spectrum of **4.7** in $CDCl_3$. *Taken from XYS-2019-185-7H.*

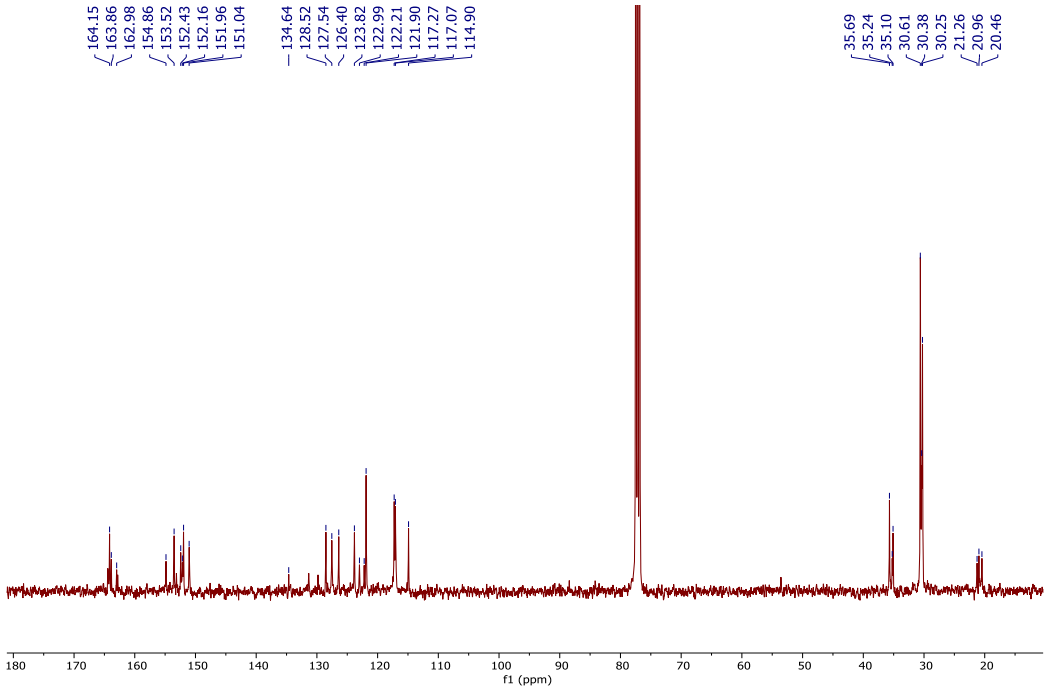

Figure 4.25 ^{13}C NMR spectrum of **4.7** in $CDCl_3$. *Taken from XYS-2019-185-3C.*

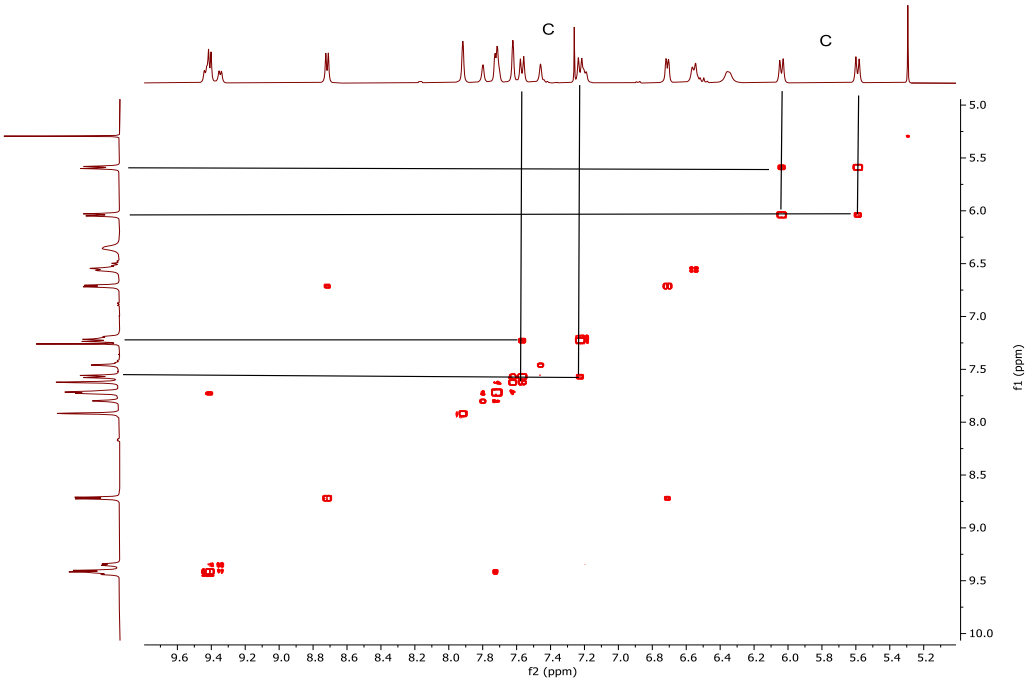

Figure 4.26 Zoom-in ^{1}H-^{1}H COSY NMR spectrum of **4.7** in $CDCl_3$. *Taken from XYS-2019-185-COSY.*

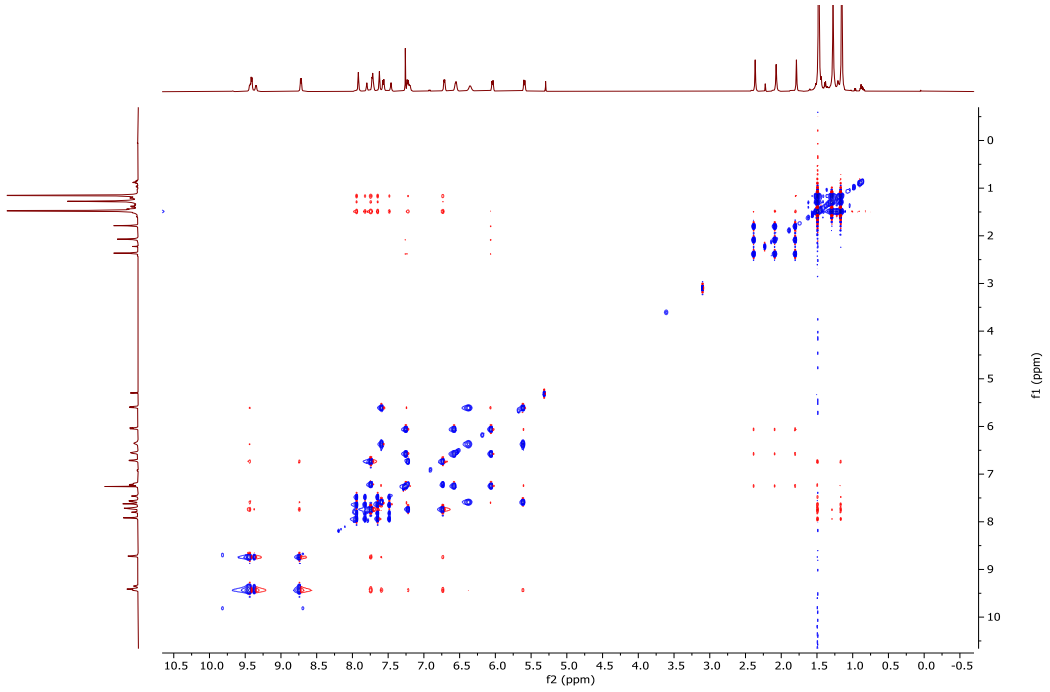

Figure 4.27 ^{1}H-^{1}H NOESY NMR spectrum of **4.7** in $CDCl_3$. *Taken from XYS-2019-185-NOESY.*

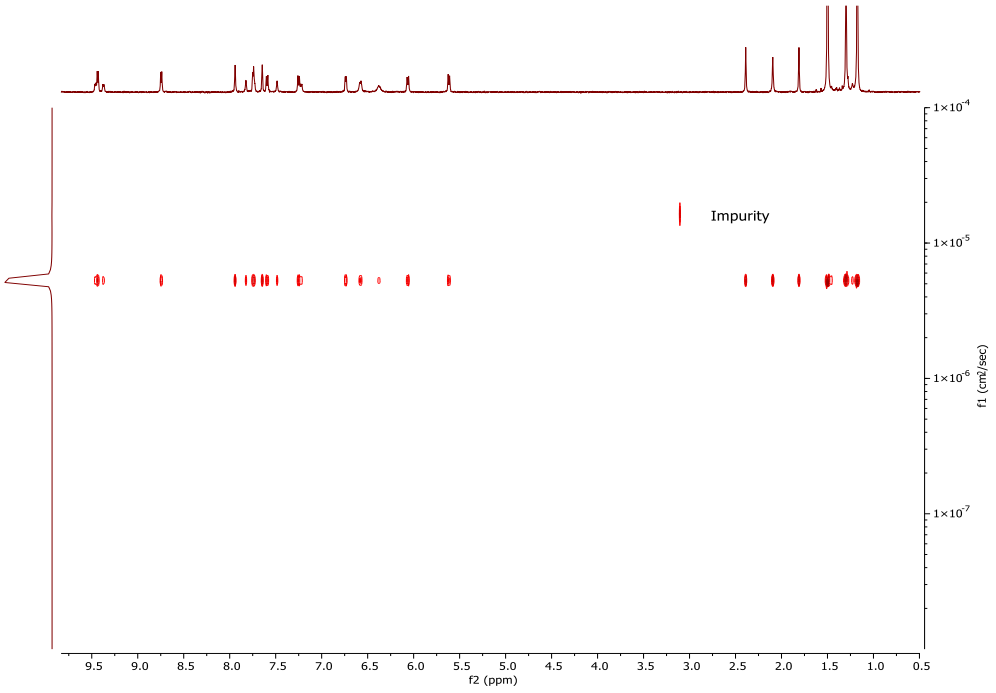

Figure 4.28 DOSY NMR spectrum of **4.7** in $CDCl_3$. *Taken from XYS-2019-185-DOSY6.*

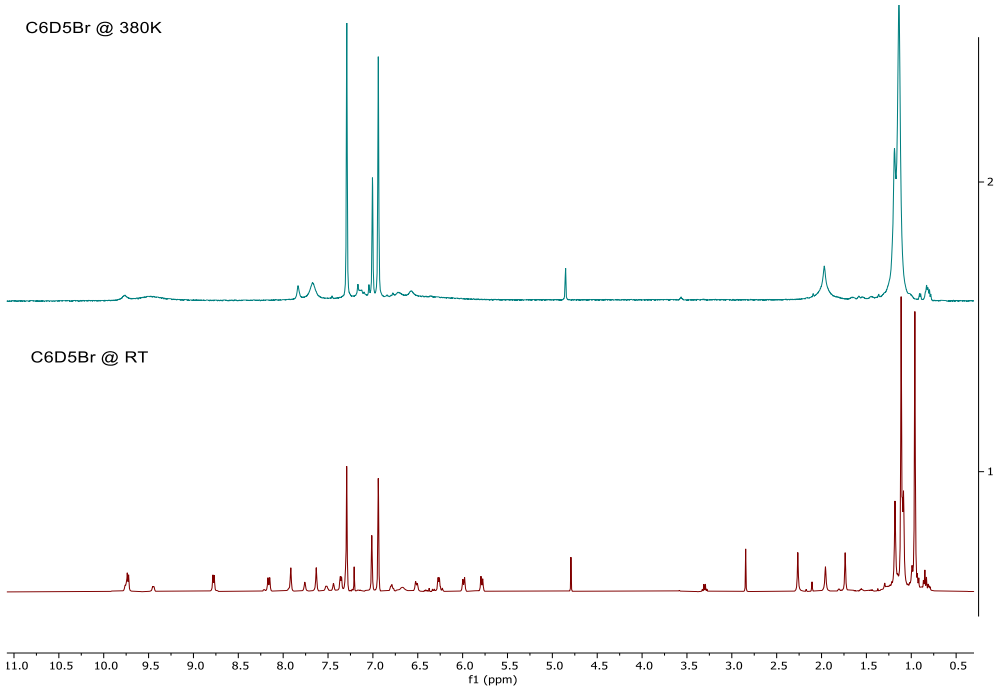

Figure 4.29 Stacked ^{1}H NMR spectrum of **4.7** at 380 K (2) and room temperature (1) in C_6D_5Br. *Taken from XYS-2019-185_380K.*

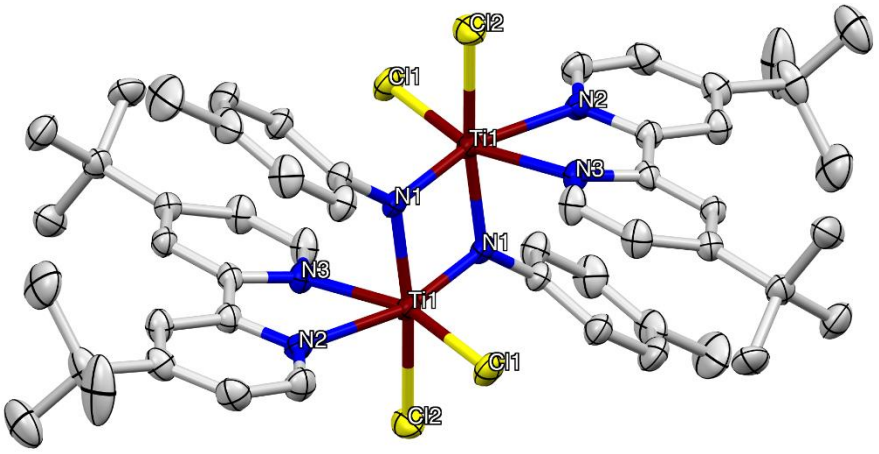

Figure 4.30 50 % thermal ellipsoid drawing of **4.7**. Hydrogen atoms are omitted for clarity.

Synthesis of 4.8

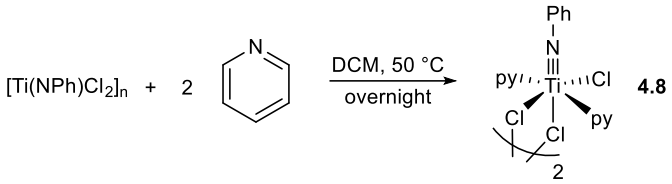

$[Ti(NPh)Cl_2py_2]_2$ (**4.8**) was synthesized with a slight modification to literature procedure by reacting $[Ti(NPh)Cl_2]_n$ with pyridine in the presence of CH_2Cl_2.[119] NMR of complex matches that of reported in literature.

Synthesis of 4.9

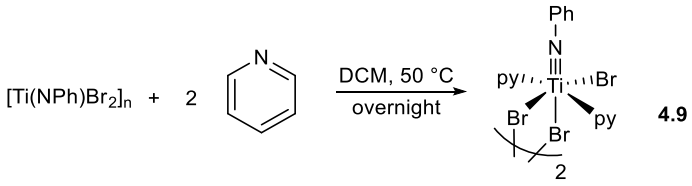

$[Ti(NPh)Br_2]_n$ (658 mg, 2.2 mmol, 1.0 equiv) and 40 mL CH_2Cl_2 were added to a 100 mL round-bottomed flask equipped with a small stir bar in a N_2-filled glovebox. Pyridine (340 mg, 4.4 mmol, 2.0 equiv) was then syringed in all at once into the stirred suspension. The $[Ti(NPh)Br_2]_n$ suspension dissolved and a yellow-brown powder precipitated out shortly after. ~ 40 mL of hexanes were layered to aid in the precipitation. The reaction mixture was filtered through a fine frit and washed with hexanes. The residue was dried *in vacuo* at 40 °C overnight to remove residual CH_2Cl_2 and afford pure **4.9** as a yellow-brown powder (458 g, 55 % yield). **4.9** is highly insoluble in $CDCl_3$ and the ^{13}C NMR spectrum was not obtained.

^{1}H NMR (400 MHz, $CDCl_3$): δ 9.20 (d, $^3J_{HH}$ = 4.9 Hz, 4H, *o*-pyridine-*H*), 7.93 (t, $^3J_{HH}$ = 8.0 Hz, 2H, *p*-pyridine-*H*), 7.51 (t, $^3J_{HH}$ = 6.9 Hz, 4H, *m*-pyridine-*H*), 7.13 (t, $^3J_{HH}$ = 7.6 Hz, 2H, *o*-NPh-*H*), 7.04 (d, $^3J_{HH}$ = 8.3 Hz, 2H, *m*-NPh-*H*), 6.90 (t, $^3J_{HH}$ = 7.0 Hz, 1H, *p*-NPh-*H*).

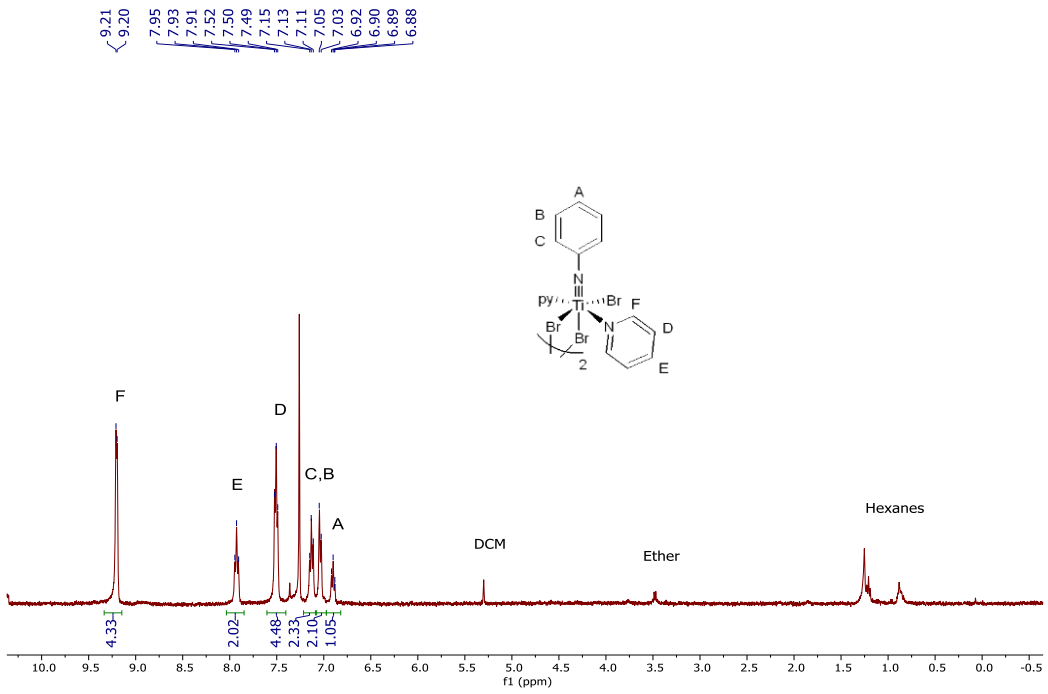

Figure 4.31 ^{1}H NMR spectrum of **4.9** in $CDCl_3$. *Taken from AJP-2019-0003-2H.*

Synthesis of 4.10

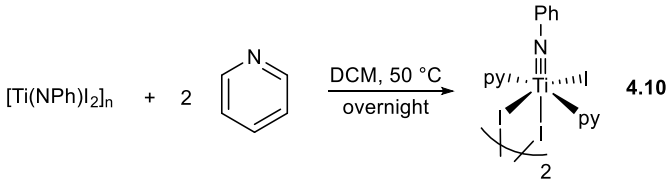

$[Ti(NPh)I_2]_n$ (253 mg, 0.64 mmol, 1.0 equiv), 5 mL CH_2Cl_2 and pyridine (102 mg, 1.29 mmol, 2 equiv) were added to a 20 mL scintillation vial in that order in a N_2-filled glovebox. This was then sealed with a Teflon-lined cap and shaken by hand. The $[Ti(NPh)I_2]_n$ suspension dissolved and a brown powder precipitated out shortly after. The reaction mixture was left to cool in the freezer overnight to facilitate precipitation. Following which, the reaction mixture was filtered through a fine frit, washed with hexanes (2 x 5 mL) and dried *in vacuo* overnight at 50 °C to give pure **4.10** as a brown powder (316 mg, 89 % yield).

^{1}H NMR (400 MHz, $CDCl_3$): δ 9.24 (s, 4H, *o*-pyridine-*H*), 7.95 (s, 2H, *p*-pyridine-*H*), 7.50 (s, 4H, *m*-pyridine-*H*), 7.19 (s, 4H, *o*-NPh-*H* and *m*-NPh-*H*), 6.92 (s, 1H, *p*-NPh-*H*) Hexane impurities are present in the $CDCl_3$ solvent.

^{13}C NMR (101 MHz, $CDCl_3$): δ 151.4, 139.3, 129.2, 125.6, 124.4, 124.0

This is a partial line-list. Resonances associated with a quaternary C of the NPh fragment were not observed.

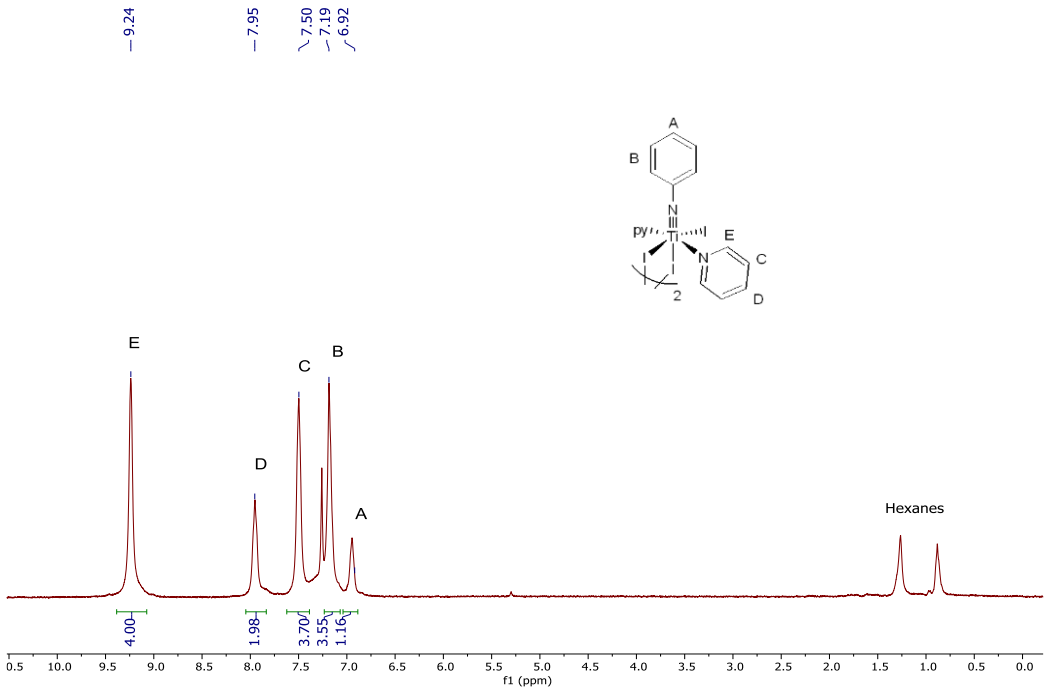

Figure 4.32 ^{1}H NMR spectrum of **4.10** in $CDCl_3$. *Taken from XYS-2019-179-2H.*

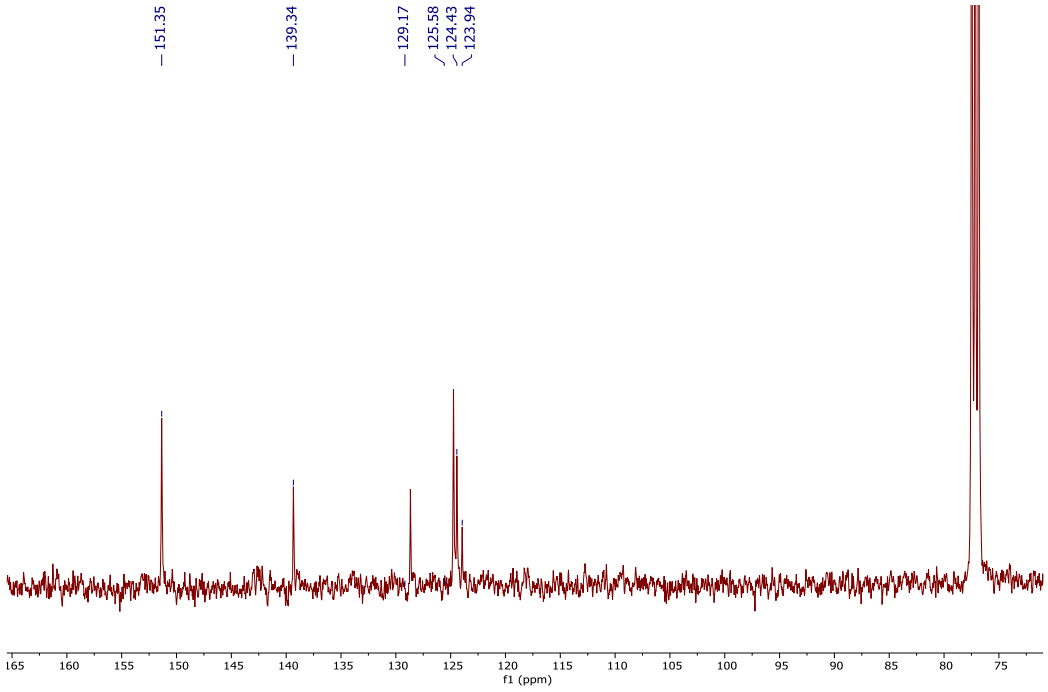

Figure 4.33 ^{13}C NMR spectrum of **4.10** in $CDCl_3$. *Taken from XYS-2019-179-1C.*

Synthesis of 4.11

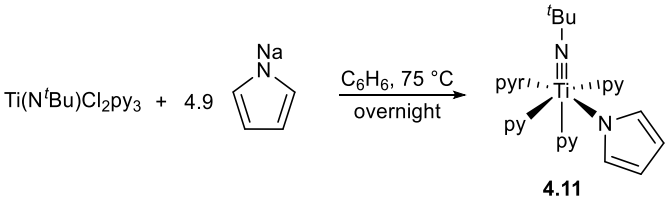

Sodium pyrrolide was prepared beforehand by deprotonating pyrrole (377 mg, 5.6 mmol, 1 equiv) with excess NaH (400 mg, 16.6 mmol, 3 equiv) in 4 mL THF overnight. The suspension was filtered through celite, dried *in vacuo* to yield an off-white solid that was used without further purification.

$Ti(N^tBu)Cl_2py_3$ (382 mg, 0.89 mmol, 1.0 equiv), sodium pyrrolide (391 mg, 4.3 mmol, 4.9 equiv) and 2 mL C_6H_6 were added to a 20 mL scintillation vial equipped with a small stir bar in a N_2-filled glovebox. This was then sealed with a Teflon-lined cap and heated at 75 °C overnight. After cooling to room temperature, the yellow suspension was filtered through a fine frit to remove a sticky brown residue and the yellow filtrate was dried *in vacuo*. The residue was re-dissolved in 5 mL ether, layered with 5 mL hexanes and left to

cool in a - 35 °C freezer to yield pure **4.11** as yellow crystalline material (130 mg, 30 % yield).

^{1}H NMR (400 MHz, $CDCl_3$): δ 8.53 (br s, 2H, axial *o*-pyridine-*H*), 8.01 (app d, $^{3}J_{HH}$ = 4.9 Hz, 4H, *o*-pyridine-*H*), 7.47 (s, 4H, *o*-pyr-*H*), 6.98 (t, $^{3}J_{HH}$ = 7.4 Hz, axial *p*-pyridine-*H*), 6.80 (s, 4H, *m*-pyr-*H*), 6.68 – 6.60 (two overlapping triplets, 4H, axial *m*-pyridine-H and *p*-pyridine-H), 6.33 (t, $^{3}J_{HH}$ = 7.0 Hz, 4H, *m*-pyridine-*H*), 1.12 (s, 9H, ^{t}Bu-*H*).

^{13}C NMR (101 MHz, C_6D_6): δ 151.2, 150.4, 138.1, 135.2, 126.0, 124.1, 123.5, 108.8, 72.8, 31.7.

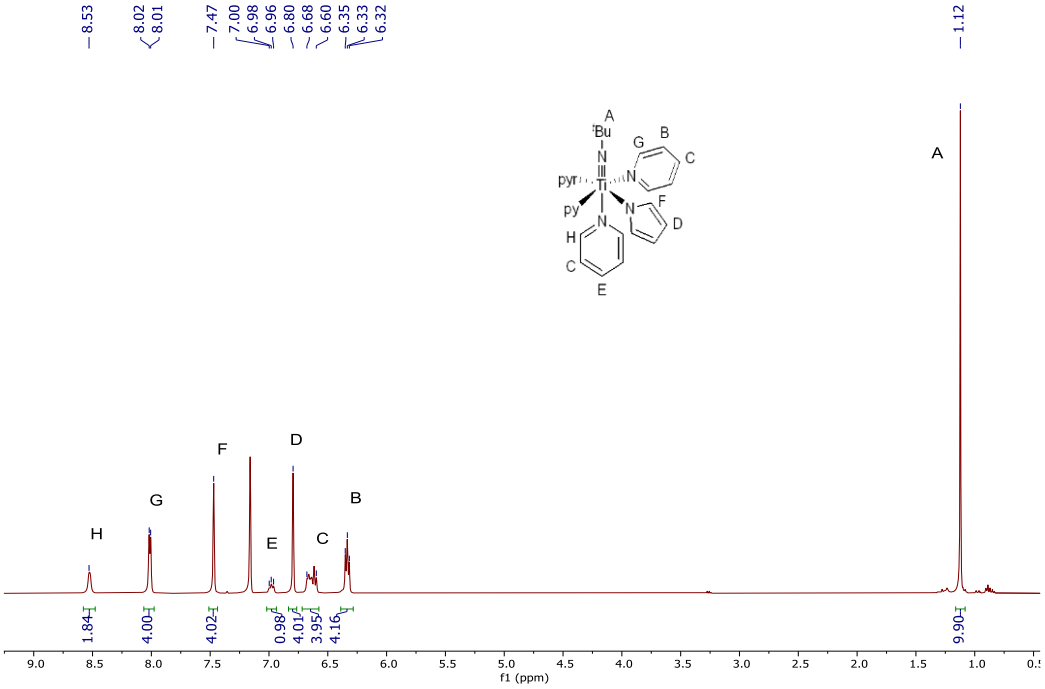

Figure 4.34 ^{1}H NMR spectrum of **4.11** in $CDCl_3$. *Taken from XYS-2019-151B-2H.*

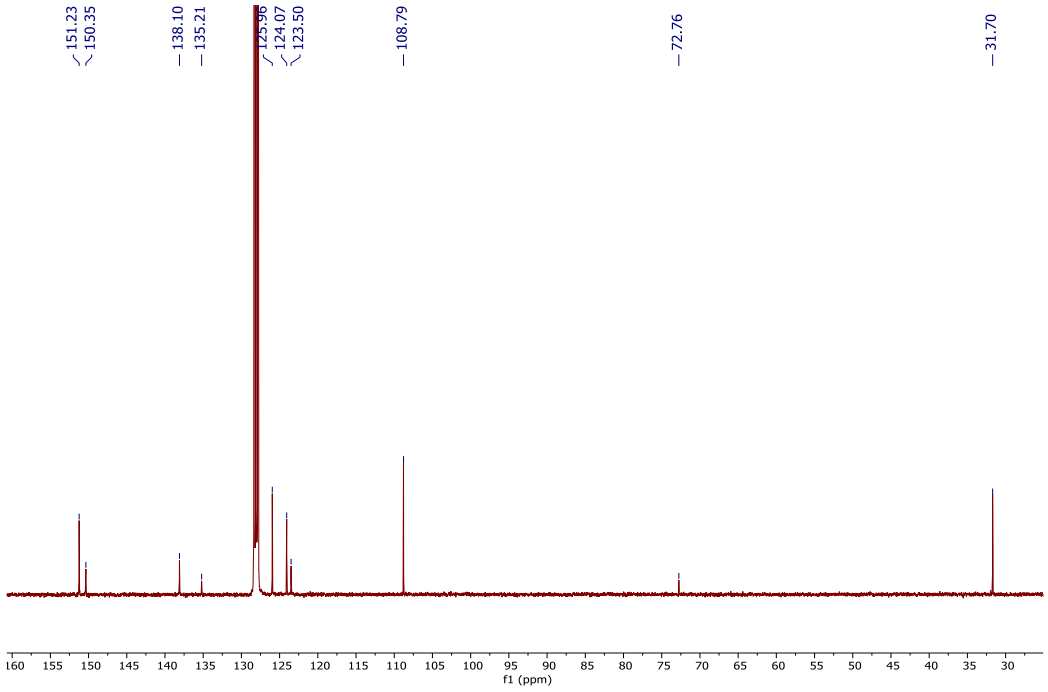

Figure 4.35 ^{13}C NMR spectrum of **4.11** in $CDCl_3$. *Taken from XYS-2019-151B-1C.*

Synthesis of 4.12

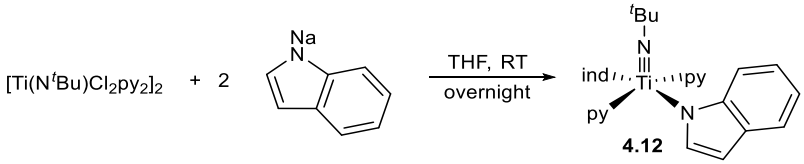

Indole (270 mg, 2.3 mmol, 2.0 equiv), sodium hexamethyldisilazane (480 mg, 2.6 mmol, 2.2 mmol) and 3 mL THF were added to a 20 mL scintillation vial equipped with a small stir bar in a N_2-filled glovebox. This was then sealed with a Teflon-lined cap and stirred overnight at room temperature to generate sodium indolide. In a separate vial, [Ti(N^{t}Bu)Cl$_2$py$_2$]$_2$ (401 mg, 1.15 mmol, 1.0 equiv) was dissolved in 3 mL THF and added to the colourless deprotonated sodium indolide solution. This mixture was stirred overnight at room temperature. Following which, the mixture was dried *in vacuo*, re-dissolved in C_6H_6, filtered through a celite plug and lyophilized *in vacuo*. The crude product was re-dissolved in 6 mL ether and cooled in a - 35 °C freezer to yield orange crystalline blocks that contained residual ether. Dissolution of the blocks in C_6H_6 and lyophilization *in vacuo* yields pure **4.12** as orange powder (176 mg, 15 % yield). X-ray quality crystals were grown

from re-dissolving 20 mg of pure product in 2 mL PhMe, layering with 2 mL hexanes and cooling in a - 35 °C freezer to yield yellow cubes.

^{1}H NMR (400 MHz, C_6D_6): δ 8.75 (br s, 4H, *o*-pyridine-*H*), 8.05 (app d, $^{3}J_{HH}$ = 4.9 Hz, 4H, indole-*H*), 7.99 (d, 2H, indole-*H*), 7.27 (br s, 4H, *m*-pyridine-*H*), 6.96 (br s, 2H, *p*-pyridine-H), 6.44 (app t, $^{3}J_{HH}$ = 7.6 Hz, 2H, indole-*H*), 6.03 (app t, $^{3}J_{HH}$ = 7.0 Hz, 4H, indole-*H*), 1.24 (s, 9H, ^{t}Bu-*H*).

^{13}C NMR (126 MHz, C_6D_6): δ 150.7, 138.2, 130.6, 128.6, 128.4, 124.2, 120.8, 120.5, 119.6, 103.0, 73. 8, 32.0.

This is a partial line-list. Resonances associated with a quaternary C were not observed.

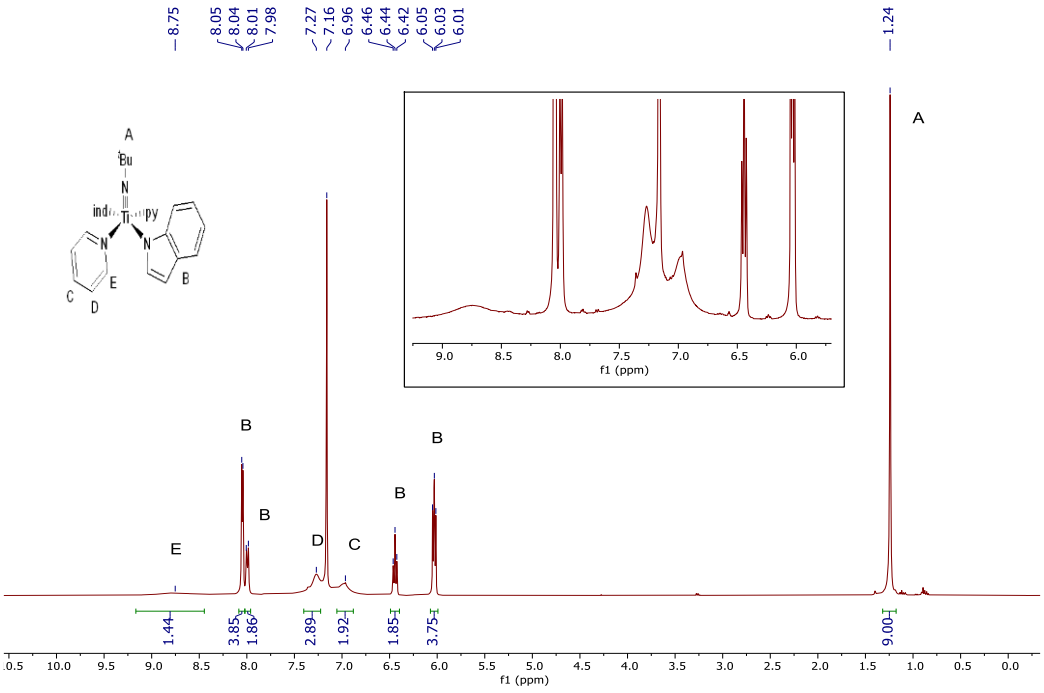

Figure 4.36 ^{1}H NMR spectrum of **4.12** in C_6D_6. *Taken from XYS-2019-162_4H.*

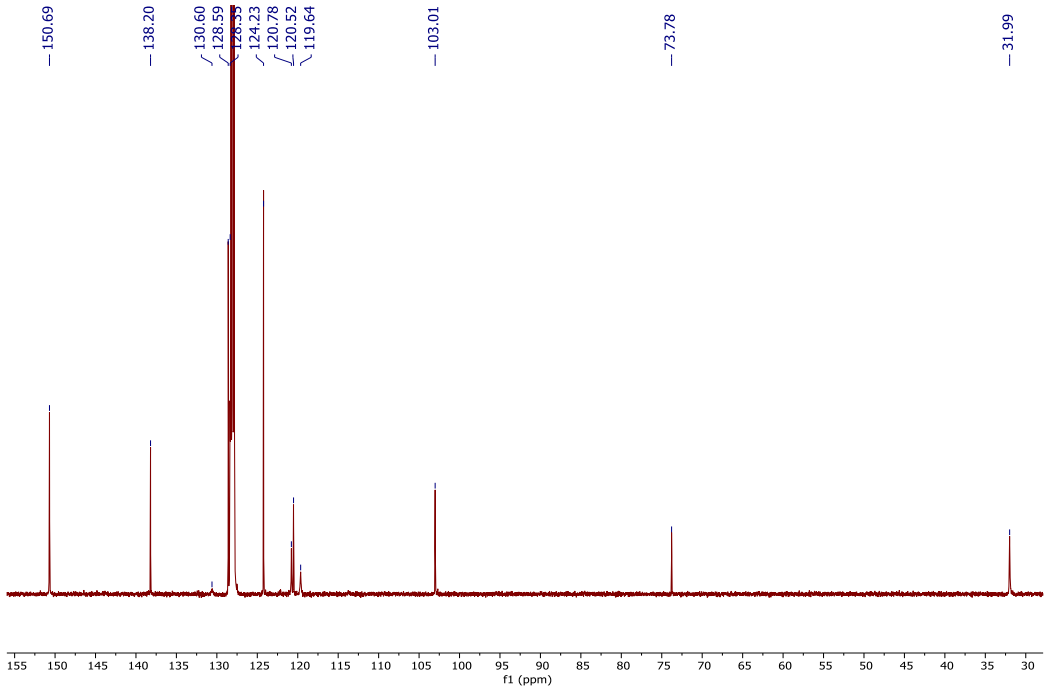

Figure 4.37 ^{13}C NMR spectrum of **4.12** in C_6D_6. *Taken from XYS-2019-162_1C.*

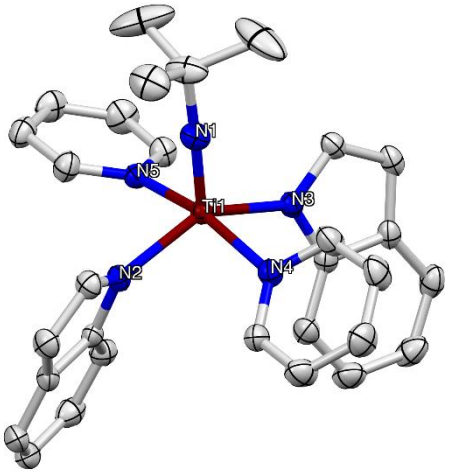

Figure 4.38 50 % thermal ellipsoid drawing of **4.12**. Hydrogen atoms are omitted for clarity.

Synthesis of 4.13

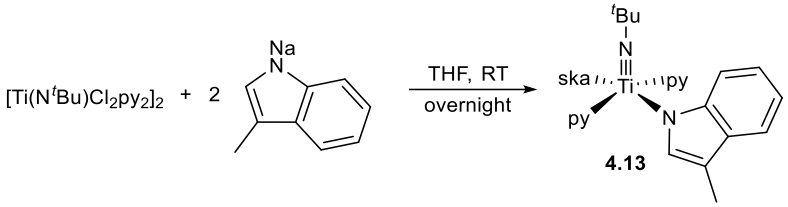

Skatole (200 mg, 1.5 mmol, 2.0 equiv), sodium hexamethyldisilazane (280 mg, 1.5 mmol, 1.5 mmol) and 2 mL THF were added to a 20 mL scintillation vial equipped with a small stir bar in a N_2-filled glovebox. This was then sealed with a Teflon-lined cap and stirred overnight at room temperature to generate sodium skatolide. In a separate vial, $[Ti(N^tBu)Cl_2py_2]_2$ (266 mg, 0.76 mmol, 1.0 equiv) was dissolved in 2 mL THF and then added to the colourless sodium skatolide solution. This mixture was stirred overnight at room temperature. Following which, the mixture was dried *in vacuo*, re-dissolved in C_6H_6, filtered through a celite plug and lyophilised *in vacuo*. The crude product was stirred and washed in 10 mL of pentane overnight and filtered through a fine frit. The sticky solid was washed liberally with more pentane and dried *in vacuo* to yield pure **4.13** as a fluffy, brown powder (178 mg, 33 % yield).

^{1}H NMR (400 MHz, C_6D_6): δ 8.82 – 8.61 (m, 4H, *o*-pyridine-*H*), 8.13 – 8.11 (m, 4H, skatole-*H*), 7.89 – 7.87 (m, 2H, skatole-*H*), 7.29 (br s, 6H, *m,p*-pyridine-*H* (partial overlap with C_6H_6 peak)), 6.43 (app t, $^3J_{HH}$ = 7.6 Hz, 2H, skatole-*H*), 6.03 (app t, $^3J_{HH}$ = 6.9 Hz, 4H, skatole-*H*), 2.65 (br s, 3H, skatole-CH_3), 1.29 (s, 9H, ^{t}Bu-*H*).

^{13}C NMR (101 MHz, C_6D_6): δ 150.8, 138.1, 124.2, 120.8, 119.0, 118.6, 111.3, 73.4, 32.2, 10.6.

This is a partial line-list. Four Cs could not be identified.

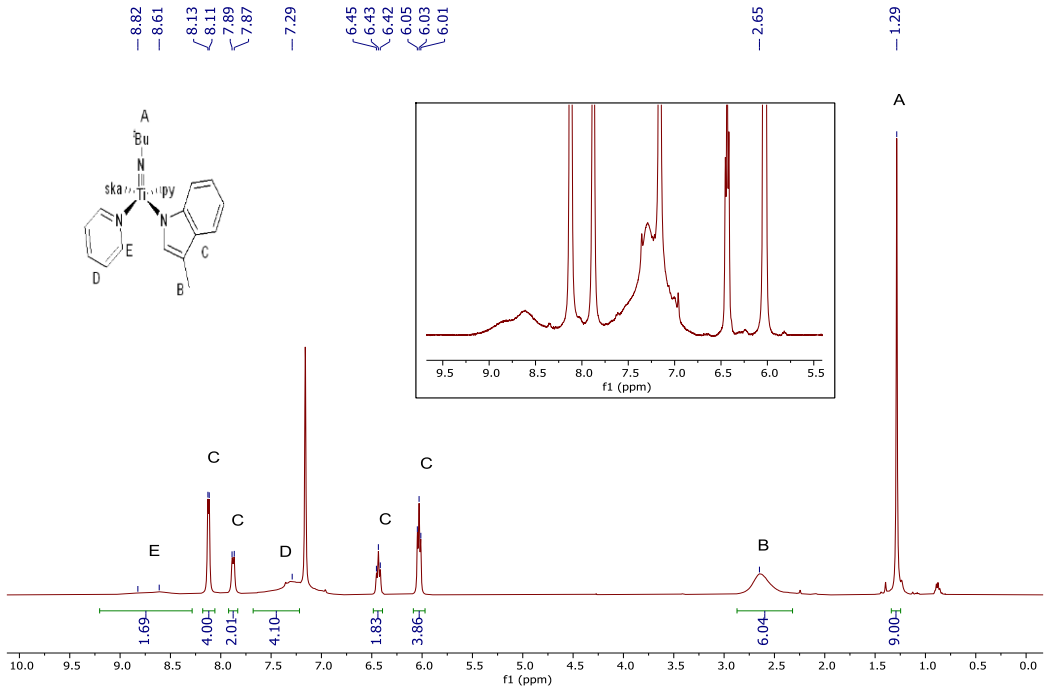

Figure 4.39 ^{1}H NMR spectrum of **4.13** in C_6D_6. *Taken from XYS-2019-159B_5H.*

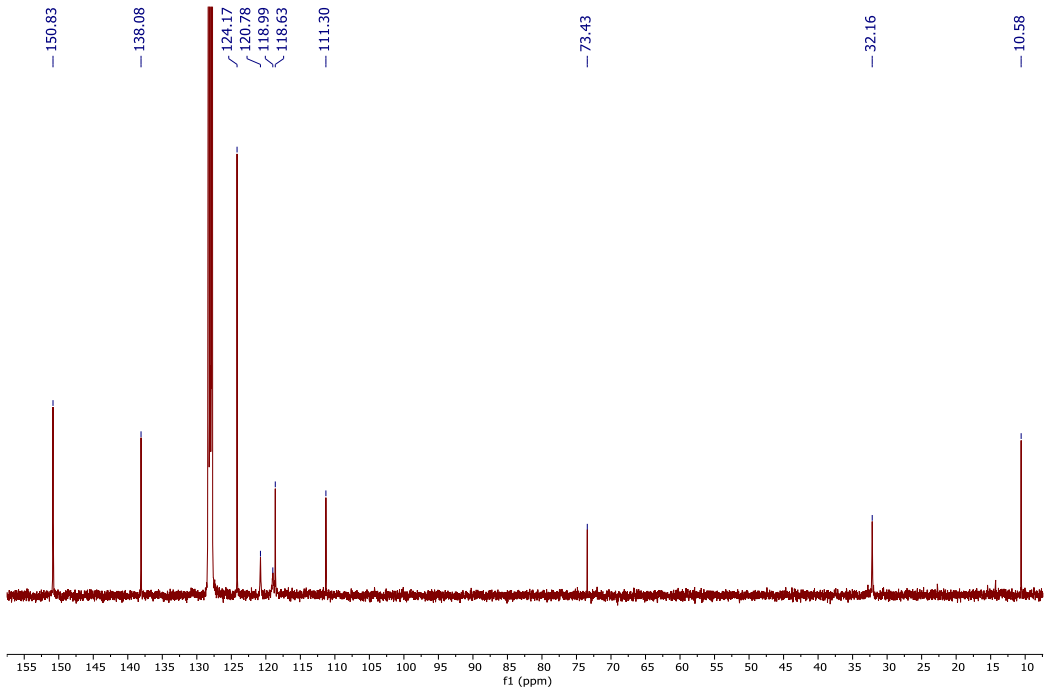

Figure 4.40 ^{13}C NMR spectrum of **4.13** in C_6D_6. *Taken from XYS-2019-159B_1C.*

Synthesis of 4.14

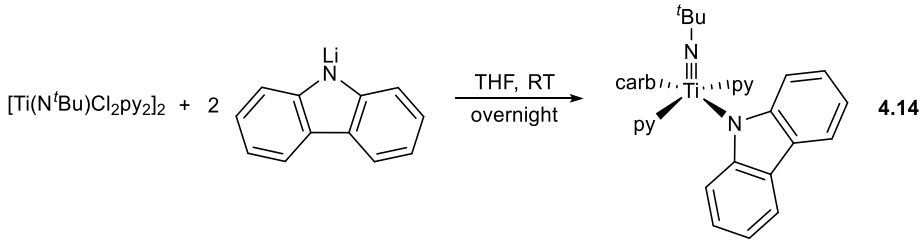

[Ti(N^{t}Bu)Cl$_2$py$_2$]$_2$ (1.01 g, 28.7 mmol, 1.0 equiv), lithium carbazolide (1.0 g, 57.8 mmol, 2.0 equiv) and 10 mL C_6H_6 were added to a 20 mL scintillation vial equipped with a small stir bar in a N_2-filled glovebox. This was then sealed with a Teflon-lined cap and stirred overnight. The resulting suspension was filtered through a celite plug on a coarse frit and the filtrate was dried *in vacuo* to yield pure **4.14** as orange powder (1.50 g, 85 % yield). The powder was re-dissolved in 5 mL ether, layered with 5 mL hexanes and left to cool in a - 35 °C freezer to yield pure **4.14** as yellow crystalline material (1.50 g, 86 % yield). X-ray quality crystals were grown from re-dissolving 100 mg of pure product in 3 mL C_6H_6, layering with 3 mL hexanes at room temperature to yield orange crystals.

^{1}H NMR (400 MHz, $CDCl_3$): δ 8.47 (d, $^3J_{HH}$ = 8.2 Hz, 2H, Ar-*H*), 8.36 (app d, $^3J_{HH}$ = 4.9 Hz, 4H, Ar-*H*), 8.16 (d, $^3J_{HH}$ = 7.7 Hz, 2H, Ar-*H*), 8.06 (d, $^3J_{HH}$ = 7.0 Hz, 2H, Ar-*H*), 7.57 (t, $^3J_{HH}$ = 7.6 Hz, 2H, Ar-*H*), 7.40 (t, $^3J_{HH}$ = 7.6 Hz, 2H, Ar-*H*), 7.26 – 7.23 (m, 2H, Ar-*H*), 7.02 (t, $^3J_{HH}$ = 6.7 Hz, 4H, , Ar-*H*), 6.96 (t, $^3J_{HH}$ = 7.3 Hz, 2H, Ar-*H*), 6.82 (t, $^3J_{HH}$ = 7.6 Hz, 2H, Ar-*H*), 6.68 (d, $^3J_{HH}$ = 8.2 Hz, 2H, Ar-*H*), 1.18 (s, 9H, ^{t}Bu-*H*).

^{13}C NMR (101 MHz, $CDCl_3$): δ 150.9, 149.6, 147.5, 138.7, 126.0, 125.0, 124.9, 124.5, 124.5, 124.1, 120.5, 119.7, 119.6, 119.5, 118.3, 118.0, 117.5, 113.8, 110.7, 75.1, 32.2.

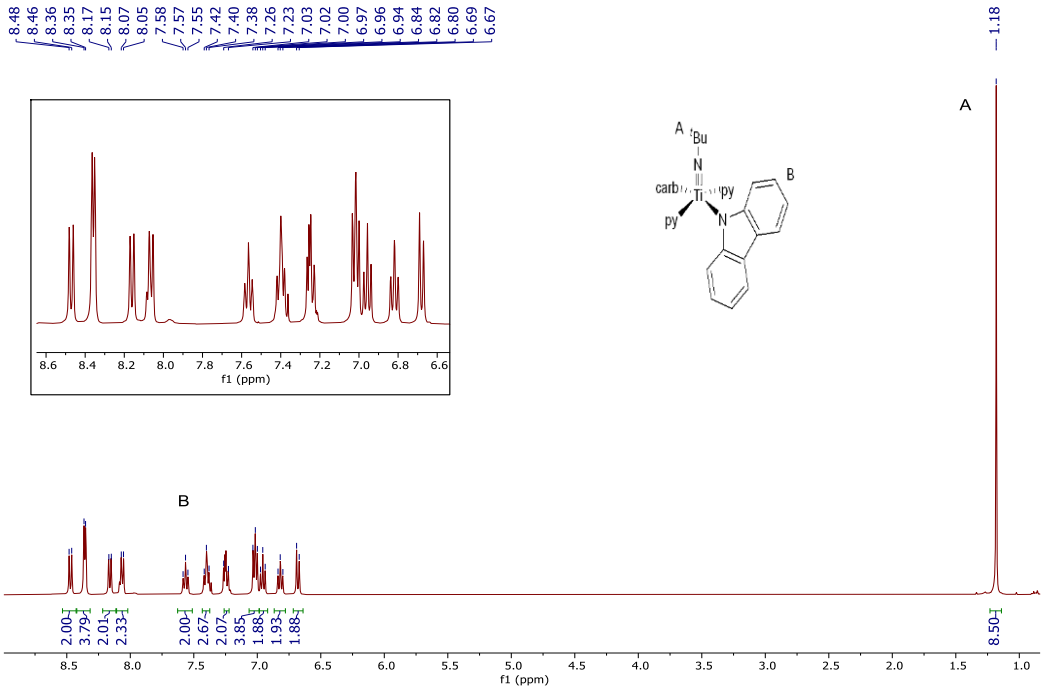

Figure 4.41 ^{1}H NMR spectrum of **4.14** in $CDCl_3$. *Taken from XYS-2019-115C_4H.*

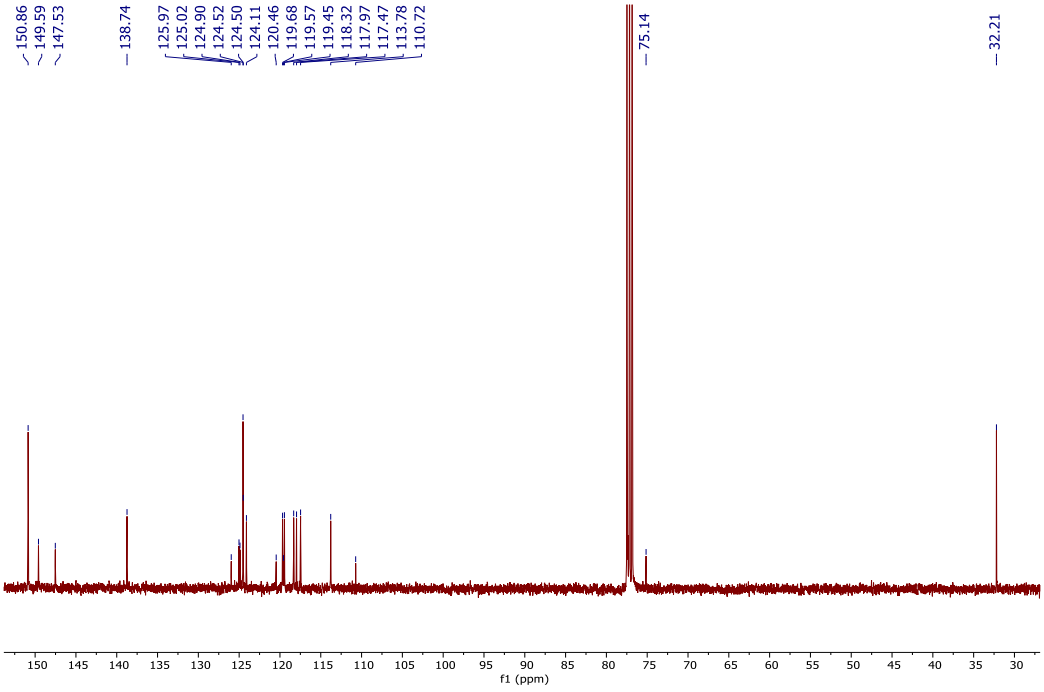

Figure 4.42 ^{13}C NMR spectrum of **4.14** in $CDCl_3$. *Taken from XYS-2019-115C_2C.*

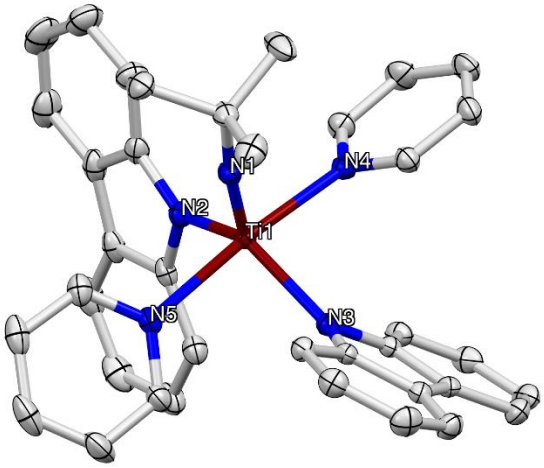

Figure 4.43 50 % thermal ellipsoid drawing of **4.14**. Hydrogen atoms are omitted for clarity.

Synthesis of 4.15

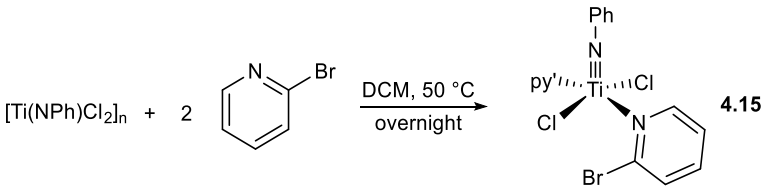

$[Ti(NPh)Cl_2]_n$ (51 mg, 0.24 mmol, 1.0 equiv), 2-bromopyridine (89 mg, 0.56 mmol, 2.3 equiv) and 2 mL CH_2Cl_2 were added to a 20 mL scintillation vial equipped with a small stir bar in a N_2-filled glovebox. This was then sealed with a Teflon-lined cap, heated to 50 °C and stirred overnight. After cooling to room temperature, the reaction mixture was filtered through a fine frit and washed with CH_2Cl_2. The residue was dried *in vacuo* to give **4.15** as a brown powder (70 mg, 55 % yield). Product is highly insoluble in $CDCl_3$ and the ^{13}C NMR spectrum was not obtained.

^{1}H NMR (500 MHz, $CDCl_3$): δ 8.67 (d, $^3J_{HH}$ = 8.2 Hz, 2H, 2-bromopyridine-6*H*), 7.62 – 7.61 (br t, 2H, 2-bromopyridine-4*H*), 7.47 (d, $^3J_{HH}$ = 8.7 Hz, 2H, 2-bromopyridine-3*H*), 7.37 (br s, 2H, 2-bromopyridine-5*H*), 7.17 (br s, 2H, NPh-*H*), 6.93 – 6.91 (m, 3H, NPh-*H*).

Hexane impurities are present in the $CDCl_3$ solvent.

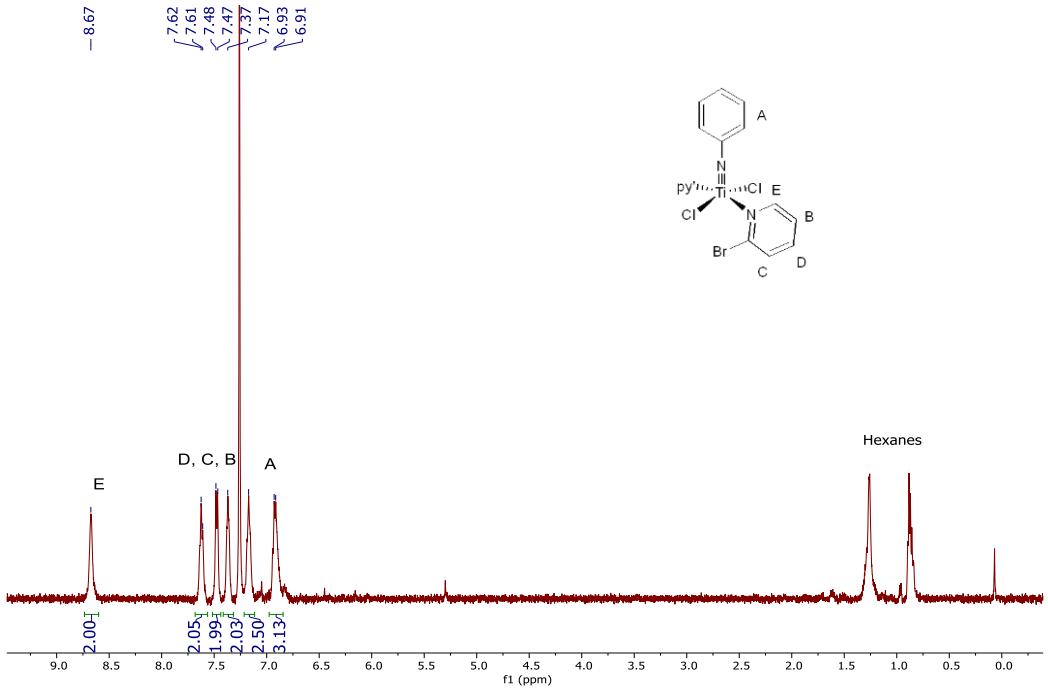

Figure 4.44 ^{1}H NMR spectrum of **4.15** in $CDCl_3$. *Taken from XYS-2020-020B_1H.*

Synthesis of 4.16

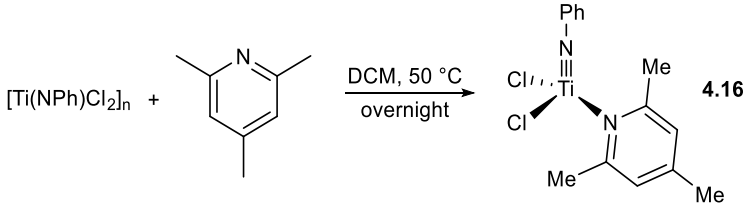

$[Ti(NPh)Cl_2]_n$ (70 mg, 0.33 mmol, 1.0 equiv), 2,4,6-trimethylpyridine (45 mg, 0.37 mmol, 1.1 equiv) and 2 mL CH_2Cl_2 were added to a 20 mL scintillation vial equipped with a small stir bar in a N_2-filled glovebox. This was then sealed with a Teflon-lined cap, heated to 50 °C and stirred overnight. After cooling to room temperature, the reaction mixture was filtered through a fine frit and washed with CH_2Cl_2. The residue was dried *in vacuo* to give **4.16** as a brown powder (83 mg, 75 % yield).

^{1}H NMR (500 MHz, $CDCl_3$): δ 7.16 (t, $^{3}J_{HH}$ = 7.8 Hz, 2H, *o*-NPh-*H*), 6.94 (d, $^{3}J_{HH}$ = 7.5 Hz, 1H, *p*-NPh-*H*), 6.82 – 6.80 (m, 4H, *m*-NPh-*H* and py-*H*), 2.56 (s, 6H, *o*-py-CH_3), 2.29 (s, 3H, *p*-py-CH_3).

Hexane impurities are present in the $CDCl_3$ solvent.

^{13}C NMR (101 MHz, $CDCl_3$): δ 156.2, 133.3, 128.2, 122.9, 117.9, 24.4, 20.8

This is a partial line-list. Due to the insolubility of the material, two Cs could not be identified.

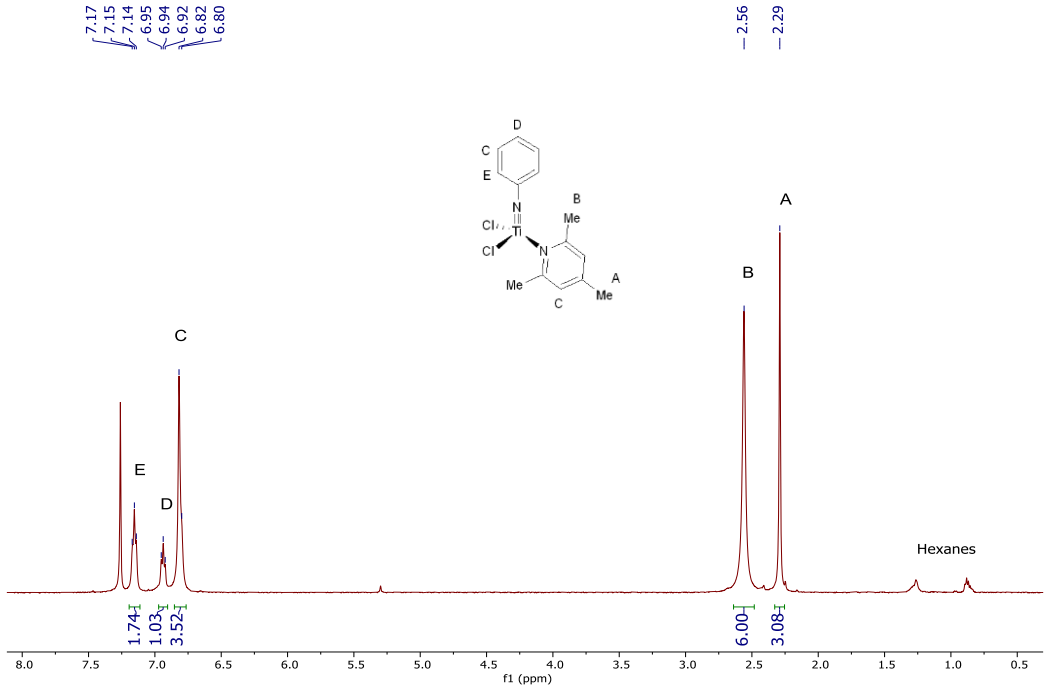

Figure 4.45 ^{1}H NMR spectrum of **4.16** in $CDCl_3$. *Taken from XYS-2019-174A_1H.*

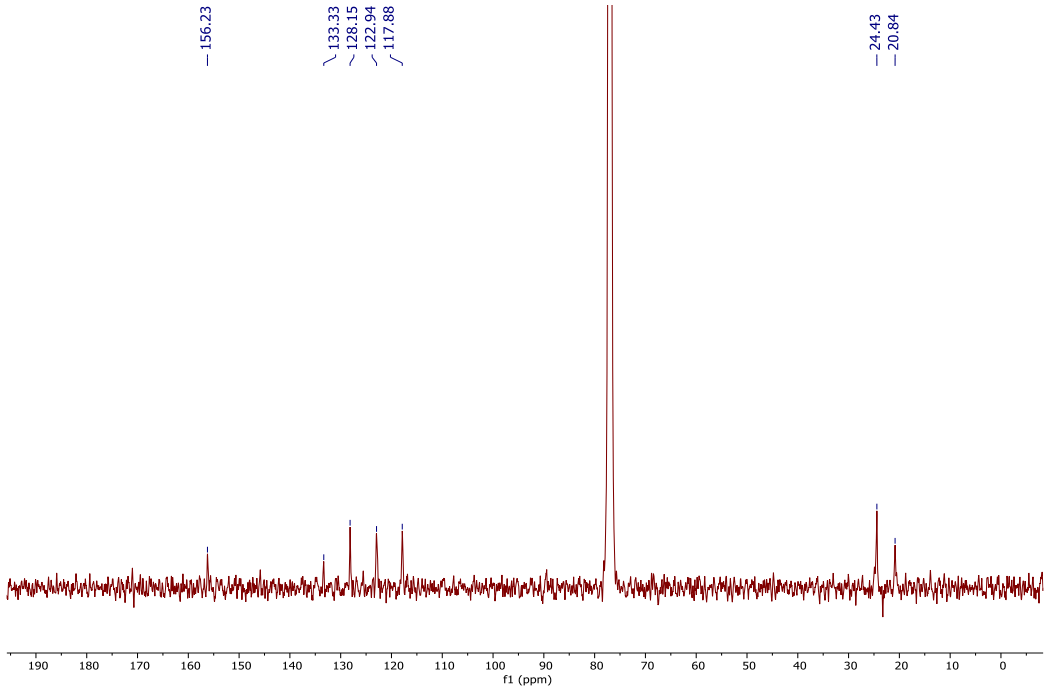

Figure 4.46 ^{13}C NMR spectrum of **4.16** in $CDCl_3$. *Taken from XYS-2019-123A_1C.*

Synthesis of 4.17

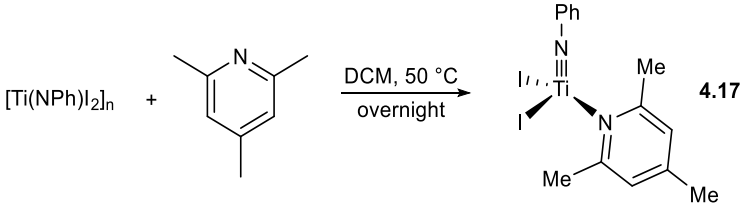

$[Ti(NPh)I_2]_n$ (100 mg, 0.26 mmol, 1.0 equiv), 2,4,6-trimethylpyridine (34 mg, 0.28 mmol, 1.1 equiv) and 2 mL CH_2Cl_2 were added to a 20 mL scintillation vial equipped with a small stir bar in a N_2-filled glovebox. This was then sealed with a Teflon-lined cap, heated to 50 °C and stirred overnight. After cooling to room temperature, the reaction mixture was filtered through a fine frit and washed with CH_2Cl_2. The residue was dried *in vacuo* to give **4.17** as a black powder (74 mg, 57 % yield).

^{1}H NMR (400 MHz, $CDCl_3$): δ 7.29 (br t, 4H, NPh-*H*), 7.11 (br s, 1H, *p*-NPh-*H*), 6.85 (s, 2H, py-*H*), 2.46 (s, 6H, *o*-py-C*H*$_3$), 2.32 (s, 3H, *p*-py-C*H*$_3$).
Hexane impurities are present in the $CDCl_3$ solvent.

^{13}C NMR (101 MHz, $CDCl_3$): δ 129.1, 126.9, 120.4, 24.1, 21.2.

This is a partial line-list. Due to the insolubility of the material, four Cs could not be identified.

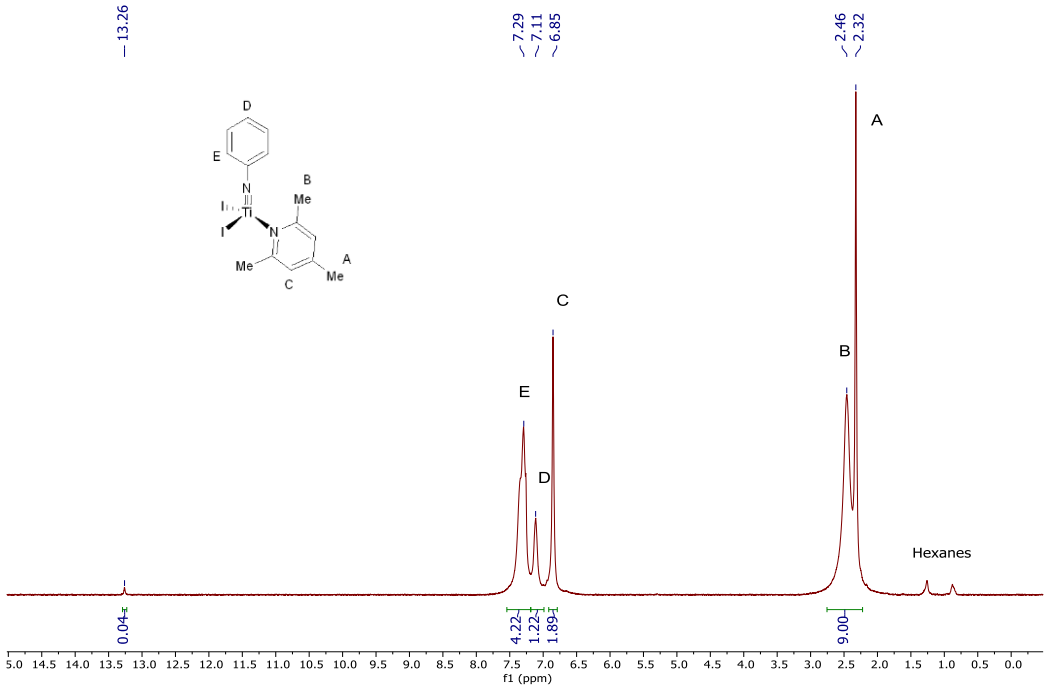

Figure 4.47 ^{1}H NMR spectrum of **4.17** in $CDCl_3$. *Taken from XYS-2019-165A_1H.*

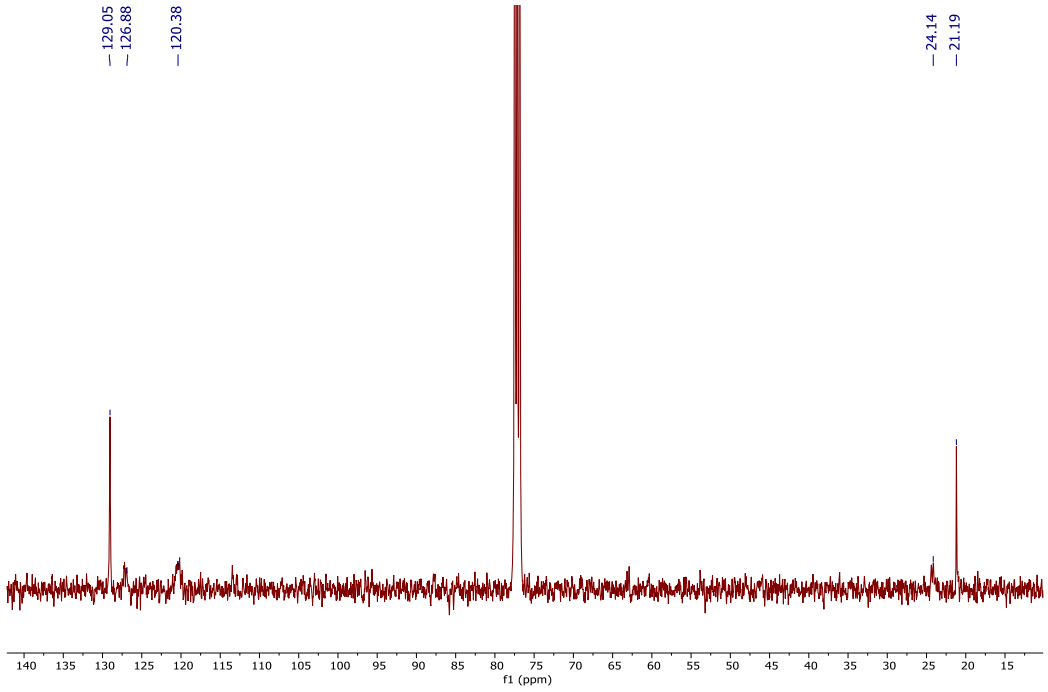

Figure 4.48 ^{13}C NMR spectrum of **4.17** in $CDCl_3$. *Taken from XYS-2019-165A_1C.*

Synthesis of 2,6-dimethyl-4-dimethylaminopyridine

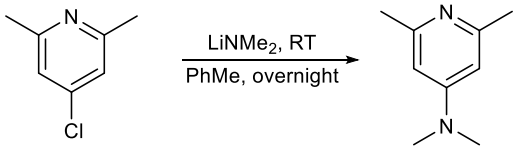

The synthesis of 4-chloro-2,6-lutidine was carried out with slight modifications from previously reported procedure:[261]

1) Post $POCl_3$ quench, the reaction mixture was extracted into $CHCl_3$ instead of CH_2Cl_2.
2) We consistently observe a mixture of oil and solid after the NEt_3 workup step, lowering the overall yield to 40 %. This was purified by filtering through a pipette to remove the solids before using.

$LiNMe_2$ (1.25 g, 24.4 mmol, 2.0 equiv.) was dissolved in PhMe (30 mL) in a 100 mL Schlenk flask in a N_2-filled glovebox. The Schlenk was sealed and removed from the glovebox, attached to a Schlenk line and cooled to - 78 °C. 4-chloro-2,6-lutidine (1.73 g, 12.2 mmol, 1.0 equiv.) was syringed into the cooled solution. The resulting red solution

was stirred for 30 minutes at - 78 °C before warming to room temperature and stirring overnight. The unquenched solution was concentrated *in vacuo*, re-suspended in hexanes (75 mL) and filtered through a fine frit. The yellow filtrate was concentrated *in vacuo*, re-dissolved in CH_2Cl_2 (25 mL), passed through a basic alumina plug and concentrated *in vacuo* a final time to yield pure 2,6-dimethyl-4-dimethylaminopyridine as a thick brown oil (1.0 g, 55 % yield).

^{1}H NMR (400 MHz, $CDCl_3$): δ 6.22 (s, 2H, py-*H*), 2.97 (s, 6H, NMe_2-*H*), 2.42 (s, 6H, *o*-py-C*H*$_3$).

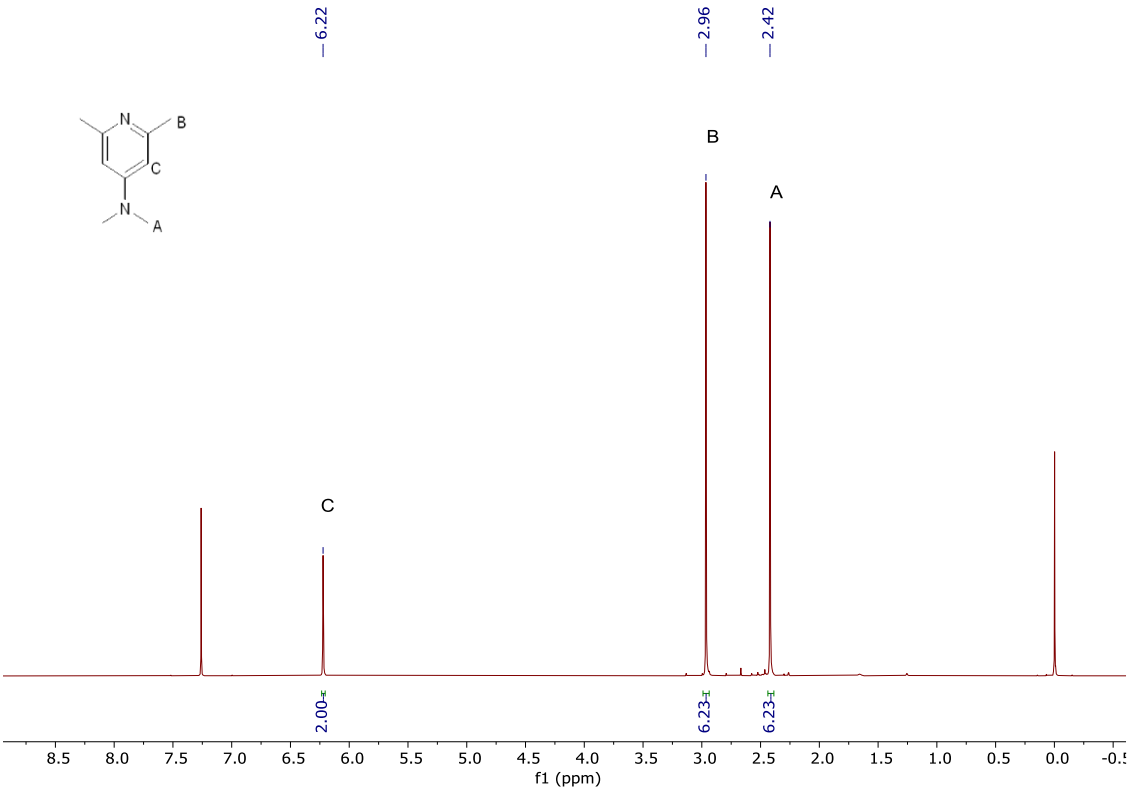

Figure 4.49 ^{1}H NMR spectrum of 2,6-dimethyl-4-dimethylaminopyridine in $CDCl_3$. *Taken from CKK-2020-011_12H.*

Synthesis of 4.18

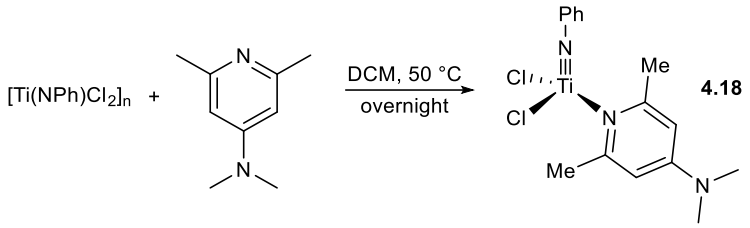

$[Ti(NPh)Cl_2]_n$ (92 mg, 0.44 mmol, 1.0 equiv), 2,6-dimethyl-4-dimethylaminopyridine (66 mg, 0.44 mmol, 1.0 equiv) and 2 mL CH_2Cl_2 were added to a 20 mL scintillation vial equipped with a small stir bar in a N_2-filled glovebox. This was then sealed with a Teflon-lined cap, heated to 50 °C and stirred overnight. After cooling to room temperature, the reaction mixture was filtered through a fine frit and washed with CH_2Cl_2. The residue was dried *in vacuo* to give **4.18** as a highly insoluble brown powder (137 mg, 87 % yield).

^{1}H NMR (400 MHz, $CDCl_3$): δ 7.10 – 6.72 (m, 4H, NPh-*H*), 6.00 (br s, 2H, py-*H*), 3.02 (s, 6H, *o*-py-C*H*$_3$), 2.48 (s, 6H, NMe_2-*H*).
Hexane impurities are present in the $CDCl_3$ solvent.

^{13}C NMR (126 MHz, $CDCl_3$): δ 127.6, 127.9, 124.4, 119.9, 104.7, 39.5.
This is a partial line-list determined with ^{1}H-^{13}C HSQC and HMBC data. Three Cs could not be identified.

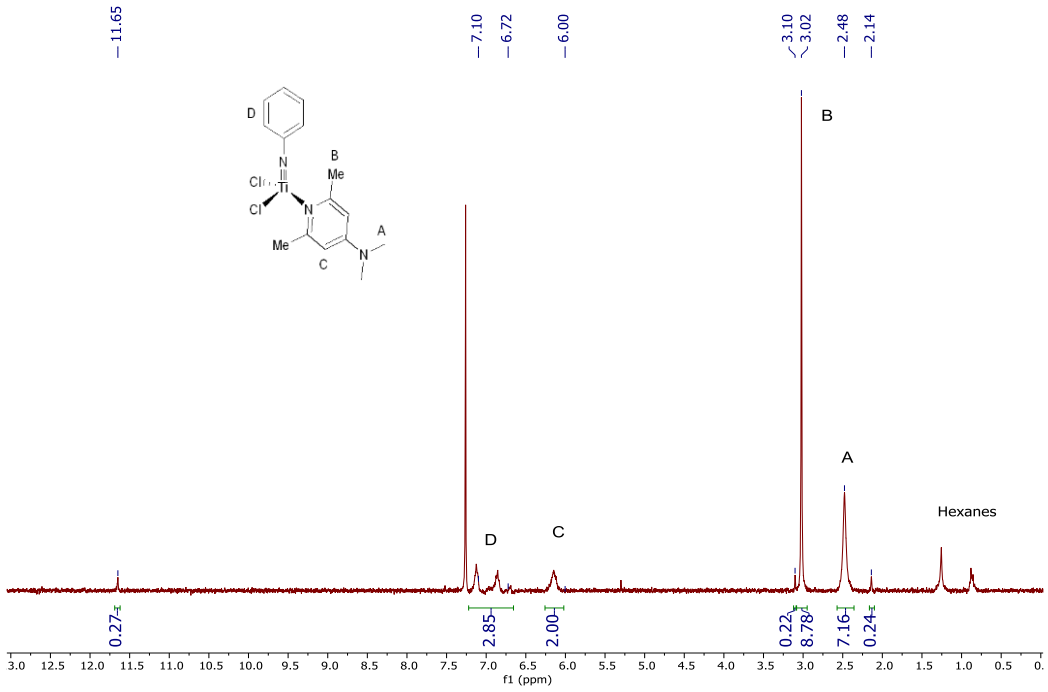

Figure 4.50 ^{1}H NMR spectrum of **4.18** in $CDCl_3$. *Taken from XYS-2020-012A_1H.*

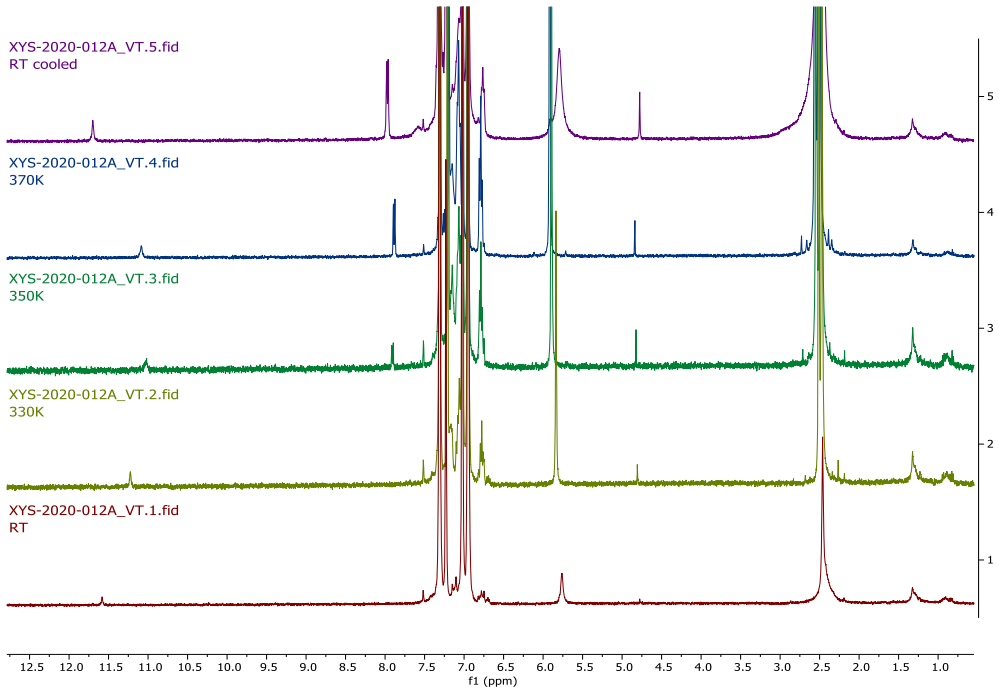

Figure 4.51 Stacked variable temperature ^{1}H NMR spectra of **4.18** in C_6D_5Br. *Taken from XYS-2020-012A_VT.*

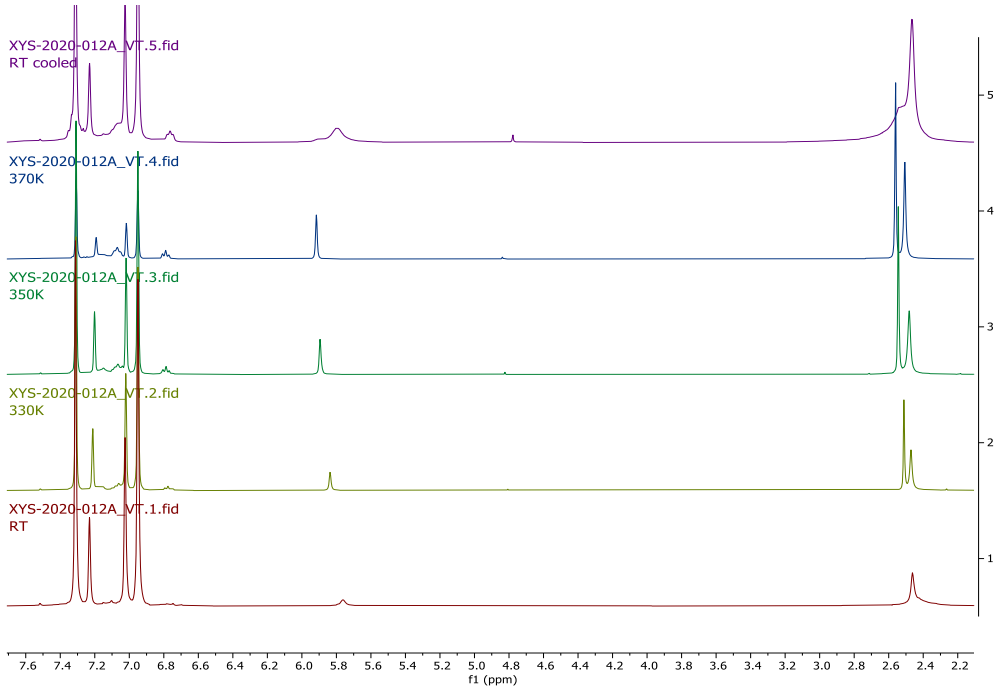

Figure 4.52 Zoom-in stacked variable temperature ^{1}H NMR spectra of **4.18** in C_6D_5Br. *Taken from XYS-2020-012A_VT.*

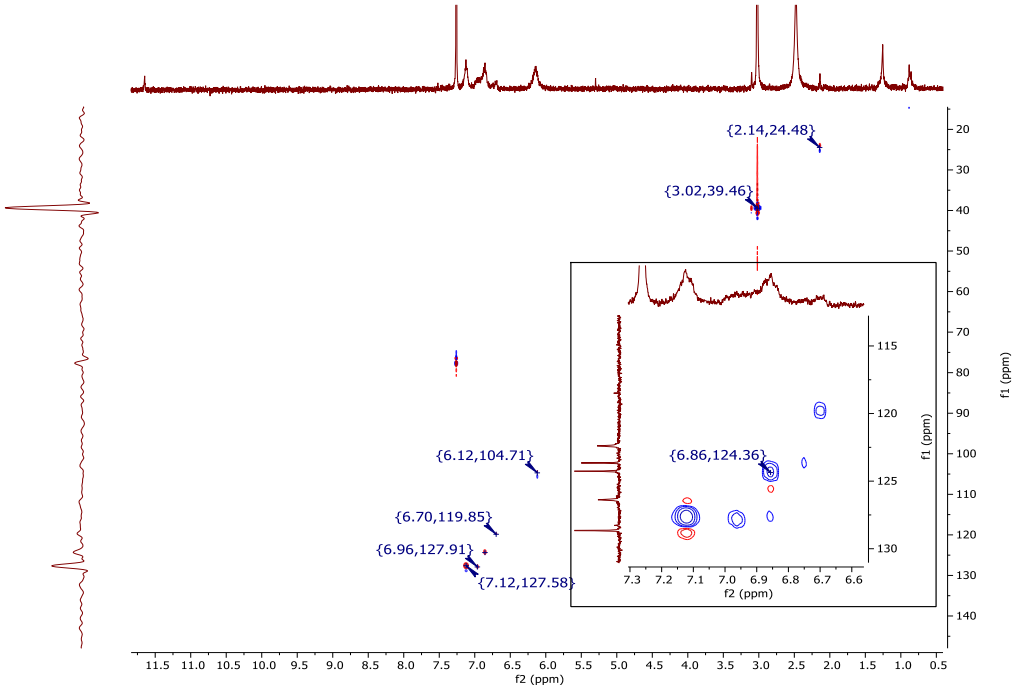

Figure 4.53 ^{1}H-^{13}C HSQC NMR spectrum of **4.18** in $CDCl_3$. *Taken from XYS-2020-012A_HSQC.*

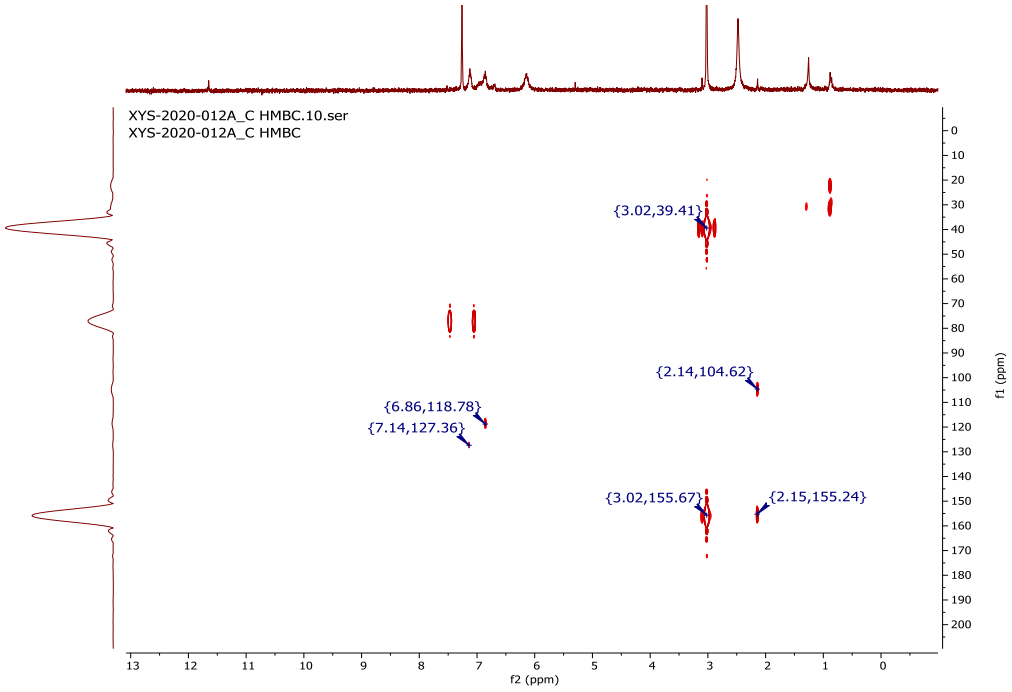

Figure 4.54 ^{1}H-^{13}C HMBC NMR spectrum of **4.18** in $CDCl_3$. *Taken from XYS-2020-012A_C HMBC.*

Synthesis of 4.19

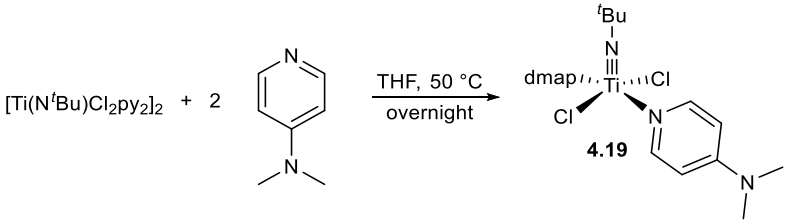

$[Ti(N^tBu)Cl_2py_2]_2$ (137 mg, 0.39 mmol, 1.0 equiv), 4-dimethylaminopyridine (96 mg, 0.79 mmol, 2.0 equiv) and 2 mL THF were added to a 20 mL scintillation vial equipped with a small stir bar in a N_2-filled glovebox. This was then sealed with a Teflon-lined cap, heated to 50 °C and stirred overnight. After cooling to room temperature, yellow suspension was filtered through a fine frit and washed with THF. The residue was dried in *vacuo* to give **4.19** as a yellow powder (120 mg, 71 % yield).

^{1}H NMR (400 MHz, $CDCl_3$): δ 8.83 (d, $^{3}J_{HH}$ = 7.3 Hz, 4H, *o*-dmap-H), 6.53 (d, $^{3}J_{HH}$ = 7.3 Hz, 4H, *m*-dmap-*H*), 3.08 (s, 12H, NMe_2-*H*), 1.03 (s, 9H, ^{t}Bu-*H*).

^{13}C NMR (101 MHz, $CDCl_3$): δ 154.9, 151.1, 105.7, 73.3, 39.3, 31.1

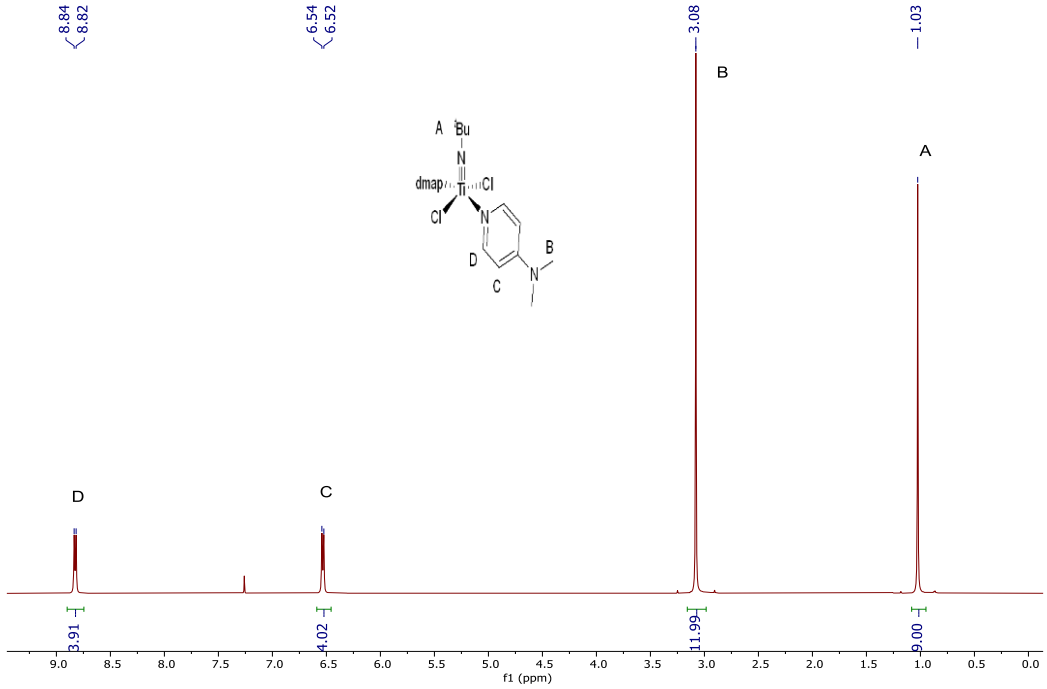

Figure 4.55 ^{1}H NMR spectrum of **4.19** in $CDCl_3$. *Taken from XYS-2019-161_1H.*

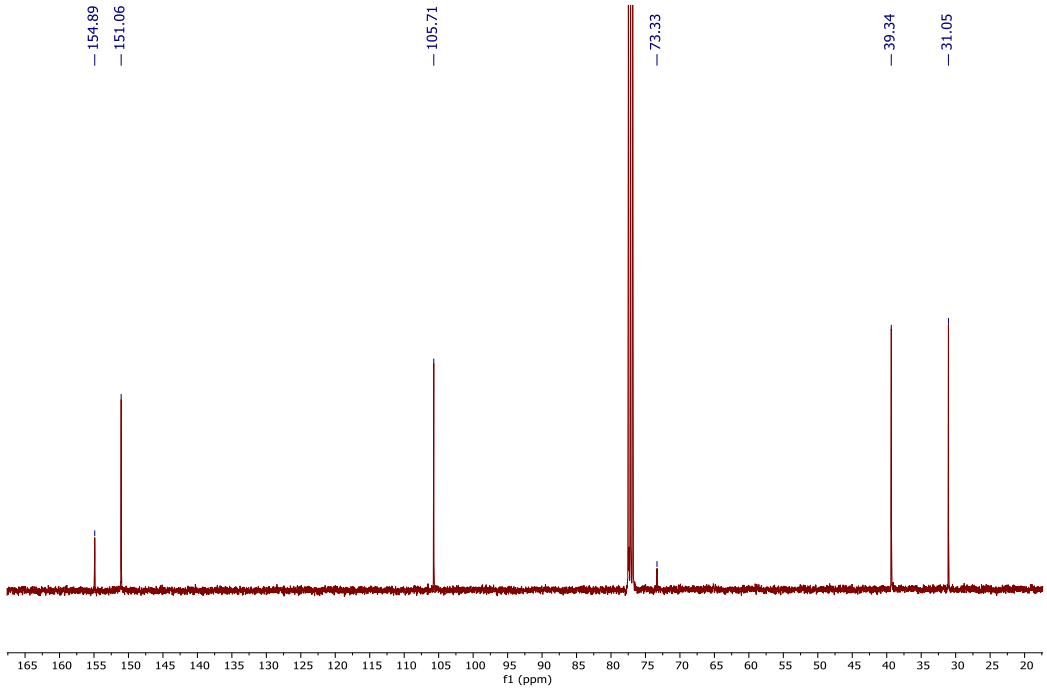

Figure 4.56 ^{13}C NMR spectrum of **4.19** in $CDCl_3$. *Taken from XYS-2019-161_1C.*

Synthesis of 4.20

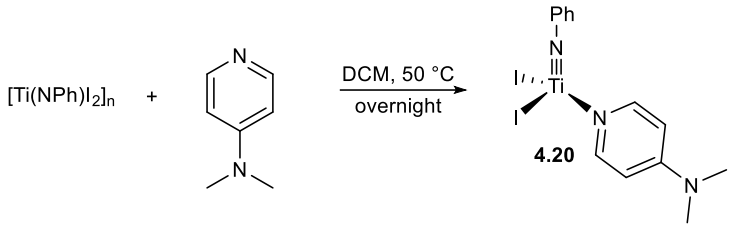

$[Ti(NPh)I_2]_n$ (108 mg, 0.28 mmol, 1.0 equiv), 4-dimethylaminopyridine (37 mg, 0.30 mmol, 1.1 equiv) and 2 mL CH_2Cl_2 were added to a 20 mL scintillation vial equipped with a small stir bar in a N_2-filled glovebox. This was then sealed with a Teflon-lined cap, heated to 50 °C and stirred overnight. After cooling to room temperature, the reaction mixture was dried *in vacuo* to give a black sticky liquid. The crude product was taken up in 5 mL C_6H_6 to form a suspension. Suspension was filtered and washed with more C_6H_6 to give the filtrate as desired product with residual C_6H_6 present. 2 mL of hexanes was added to the product, stirred at room temperature, dried *in vacuo*. This process was repeated three times to give **4.20** as a brown powder (98 mg, 69 % yield).

^{1}H NMR (400 MHz, $CDCl_3$): δ 8.74 (s, 2H, *o*-dmap-*H*), 7.12 (br s, 4H, NPh-*H*), 6.88 (s, 1H, NPh-*H*), 6.52 (s, *m*-dmap-*H*), 3.10 (s, 6H, NMe_2-*H*).

^{13}C NMR (126 MHz, $CDCl_3$): δ 154.9, 150.4, 128.4, 124.1, 122.9, 105.6, 39.5.
This is a partial line-list. Resonances associated with a quaternary C were not observed.

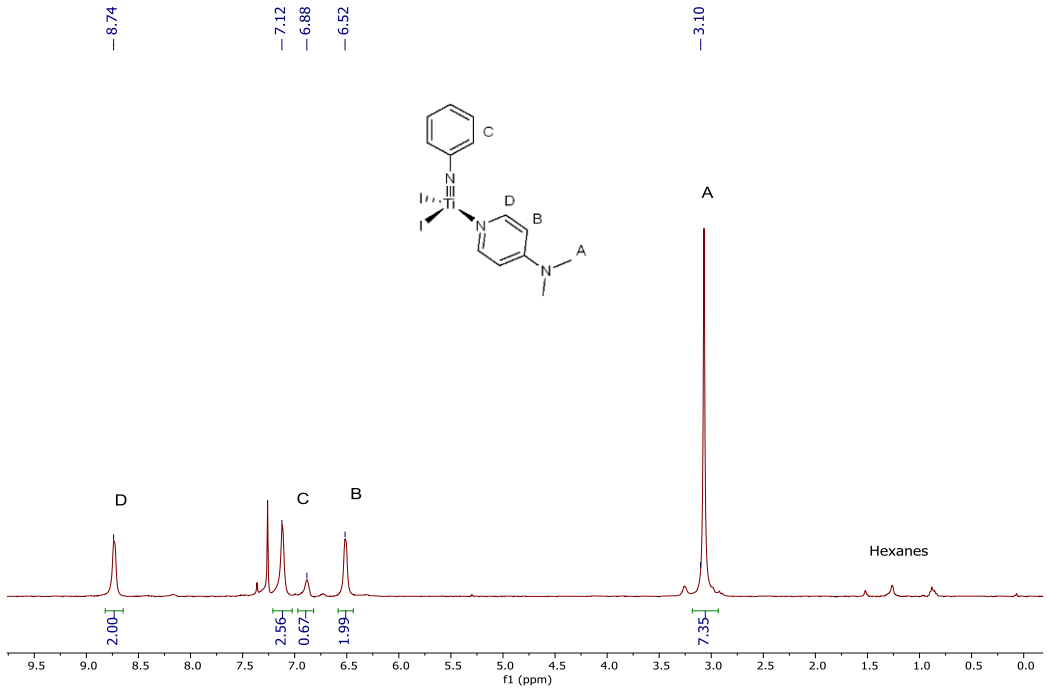

Figure 4.57 ^{1}H NMR spectrum of **4.20** in $CDCl_3$. *Taken from XYS-2019-140A_5H.*

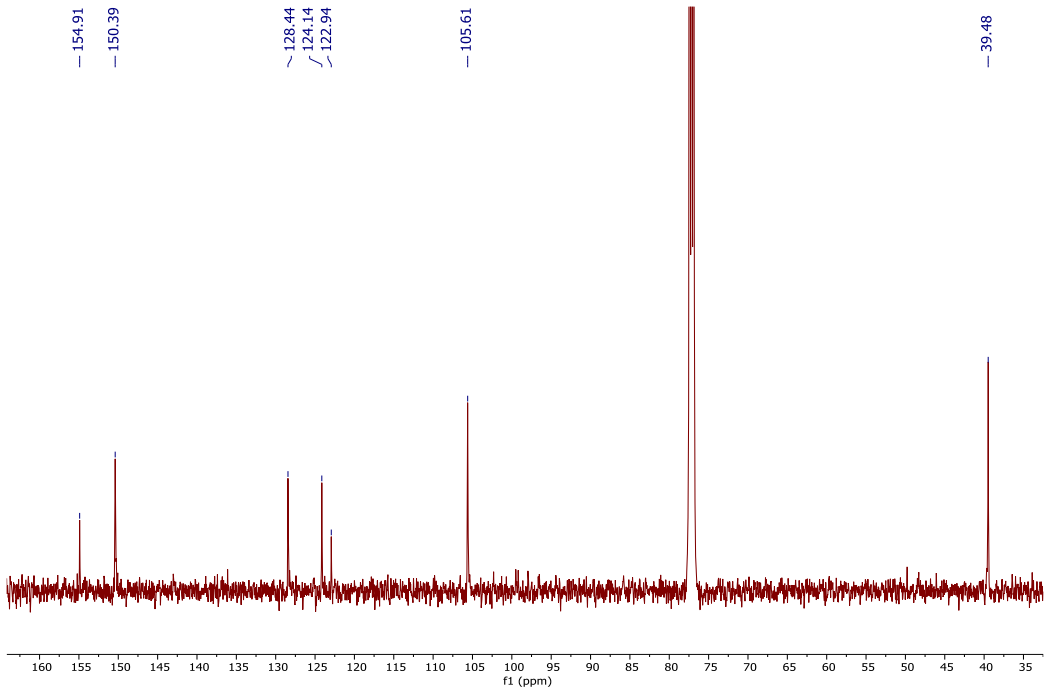

Figure 4.58 ^{13}C NMR spectrum of **4.20** in $CDCl_3$. *Taken from XYS-2019-140A_1C.*

Synthesis of 4.21

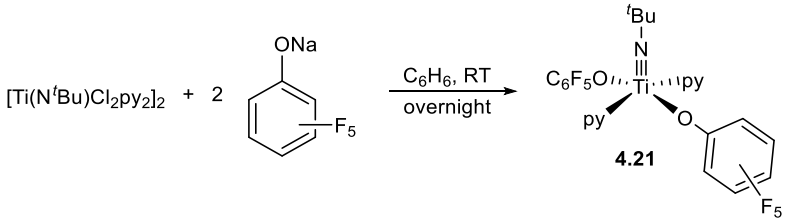

[Ti(N^{t}Bu)Cl$_2$py$_2$]$_2$ (100 mg, 0.29 mmol, 1.0 equiv), sodium pentafluorophenoxide (118 mg, 0.57 mmol, 2.0 equiv) and 2 mL C_6H_6 were added to a 20 mL scintillation vial equipped with a small stir bar in a N_2-filled glovebox. This was then sealed with a Teflon-lined cap and stirred overnight. The suspension was then filtered through a celite plug on a coarse frit and the filtrate was lyophilized *in vacuo* to yield pure **4.21** as an orange powder (110 mg, 86 % yield).

^{1}H NMR (500 MHz, C_6D_6): δ 8.97 (s, 4H, *o*-py-H), 6.84 (t, $^3J_{HH}$ = 7.7 Hz, 2H, *p*-py-*H*), 6.59 (br t, 4H, *m*-py-*H*), 1.06 (s, 9H, ^{t}Bu-*H*).

^{13}C NMR (126 MHz, C_6D_6): δ 150.3, 141.9 (t), 140.0 – 139.7 (m), 138.7, 138.0 – 137.7 (m), 128.6, 124.2, 71.7, 31.2.

^{19}F NMR (471 MHz, C_6D_6): δ -163.3 (dd, $^3J_{FF}$ = 19.9 and $^4J_{FF}$ = 8.7 Hz, *o*-OPh-*F*), -167.6 (app t, $^3J_{FF}$ = 21.2 Hz, *m*-OPh-*F*), -176.6 (tt, $^3J_{FF}$ = 22.6 and $^4J_{FF}$ = 8.2 Hz, *p*-OPh-*F*).

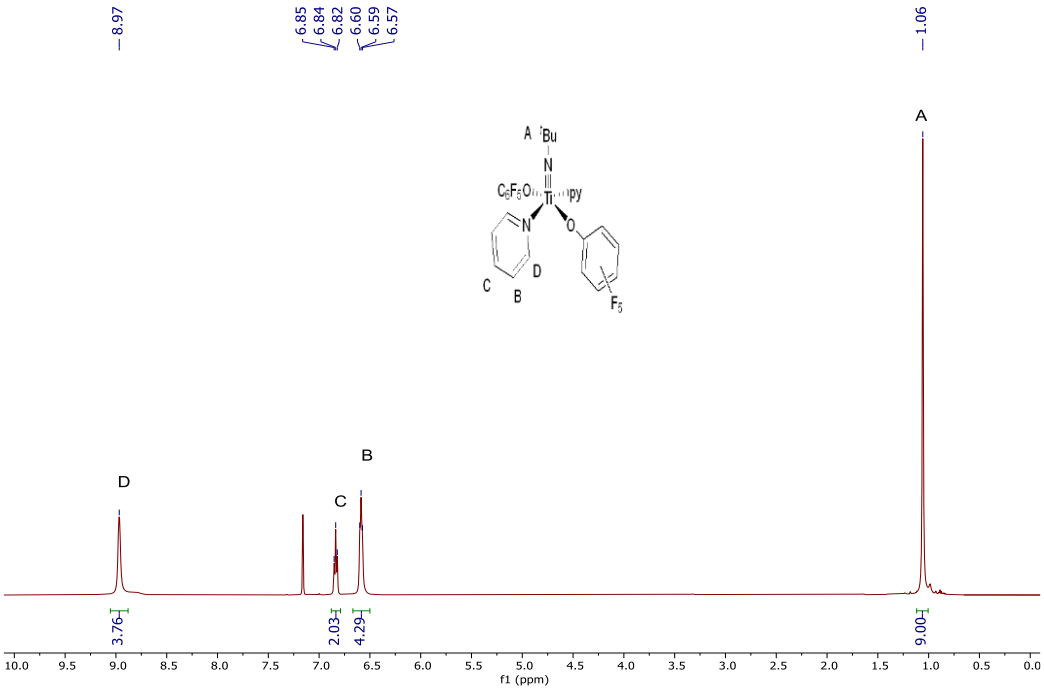

Figure 4.59 ^{1}H NMR spectrum of **4.21** in C_6D_6. *Taken from XYS-2019-159_3H.*

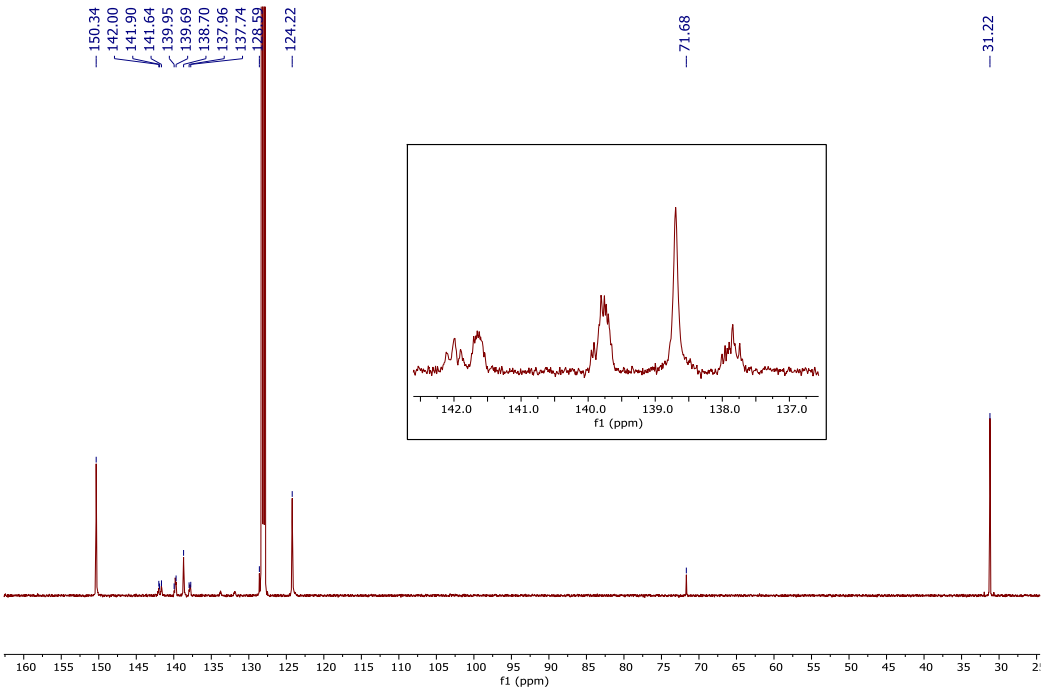

Figure 4.60 ^{13}C NMR spectrum of **4.21** in C_6D_6. *Taken from XYS-2019-169_1C.*

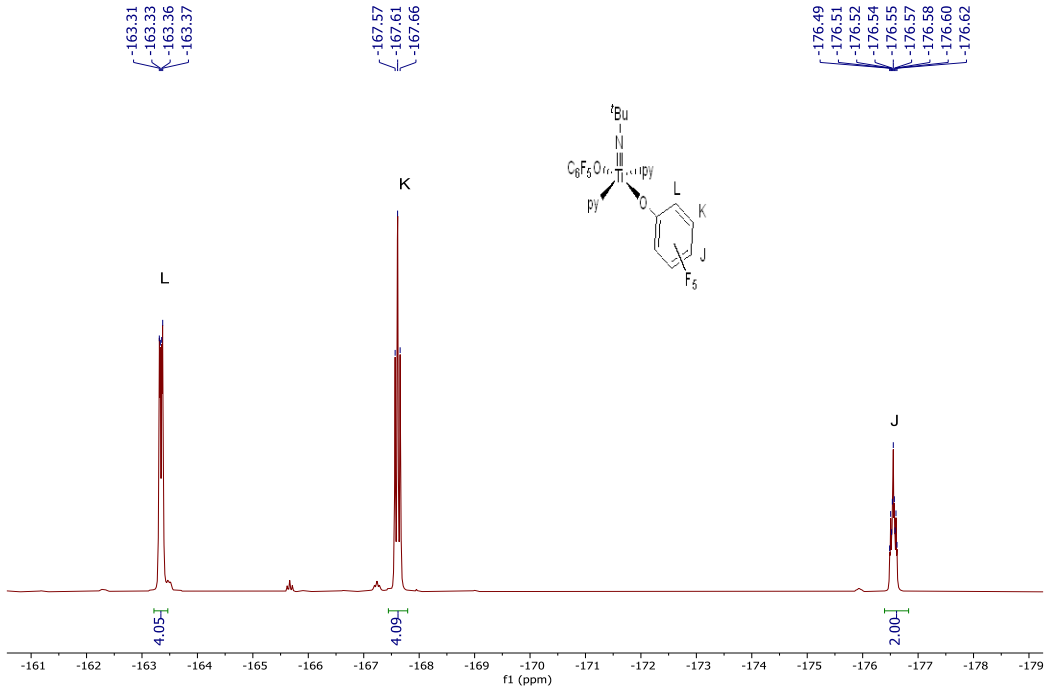

Figure 4.61 ^{19}F NMR spectrum of **4.21** in C_6D_6. *Taken from XYS-2019-169_3F.*

Synthesis of 4.22

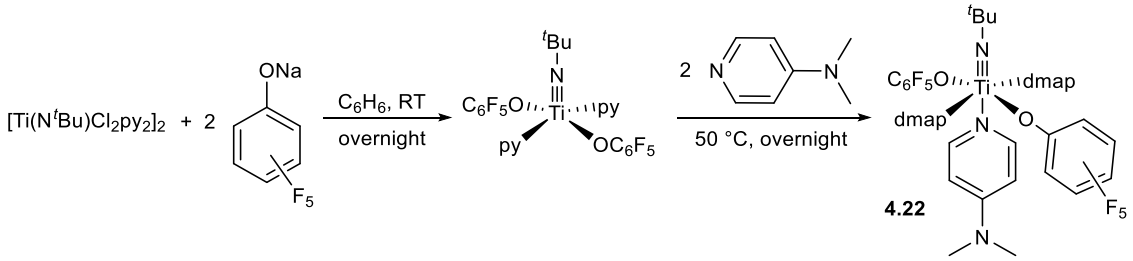

$[Ti(N^tBu)Cl_2py_2]_2$ (100 mg, 0.29 mmol, 1.0 equiv), sodium pentafluorophenoxide (118 mg, 0.57 mmol, 2.0 equiv) and 2 mL C_6H_6 were added to a 20 mL scintillation vial equipped with a small stir bar in a N_2-filled glovebox. This was then sealed with a Teflon-lined cap and stirred overnight. The suspension was filtered through a celite plug on a coarse frit and washed with 1 mL C_6H_6. 4-dimethylaminopyridine (70 mg, 0.57 mmol, 2.0 equiv) was added to the yellow solution, sealed with a Teflon-lined cap and stirred overnight at 50 °C. The solution was cooled in the freezer, lypophilised *in vacuo* to form a crude solid with residual free pyridine. The solid was heated *in vacuo* for several hours at 50 °C to yield pure **4.22** as a pale yellow solid (210 mg, 86 % yield).

^{1}H NMR (500 MHz, C_6D_6): δ 8.83 (d, $^{3}J_{HH}$ = 7.0 Hz, 4H, *o*-dmap-*H*), 8.68 (d, $^{3}J_{HH}$ = 6.0 Hz, 2H, *trans o*-dmap-*H*), 6.02 (d, $^{3}J_{HH}$ = 6.1 Hz, 2H, *trans m*-dmap-*H*), 5.93 (d, $^{3}J_{HH}$ = 7.2 Hz, 4H, *m*-dmap-*H*), 2.14 (s, 6H, *trans* NMe_2-*H*), 2.01 (s, 12H, NMe_2-*H*), 1.25 (s, 9H, ^{t}Bu-*H*).

^{13}C NMR (126 MHz, C_6D_6): δ 154.6, 150.7, 106.5, 105.7, 69.8, 38.1, 31.7.
This is a partial line-list. Due to the insolubility of the material, seven Cs could not be identified.

^{19}F NMR (471 MHz, C_6D_6): δ -162.7 (dd, $^{3}J_{FF}$ = 19.9 and $^{4}J_{FF}$ = 10.0 Hz, *o*-OPh-*F*), -168.7 (app t, $^{3}J_{FF}$ = 21.1 Hz, *m*-OPh-*F*), -179.3 (tt, $^{3}J_{FF}$ = 23.0 and $^{4}J_{FF}$ = 10.0 Hz, *p*-OPh-*F*).

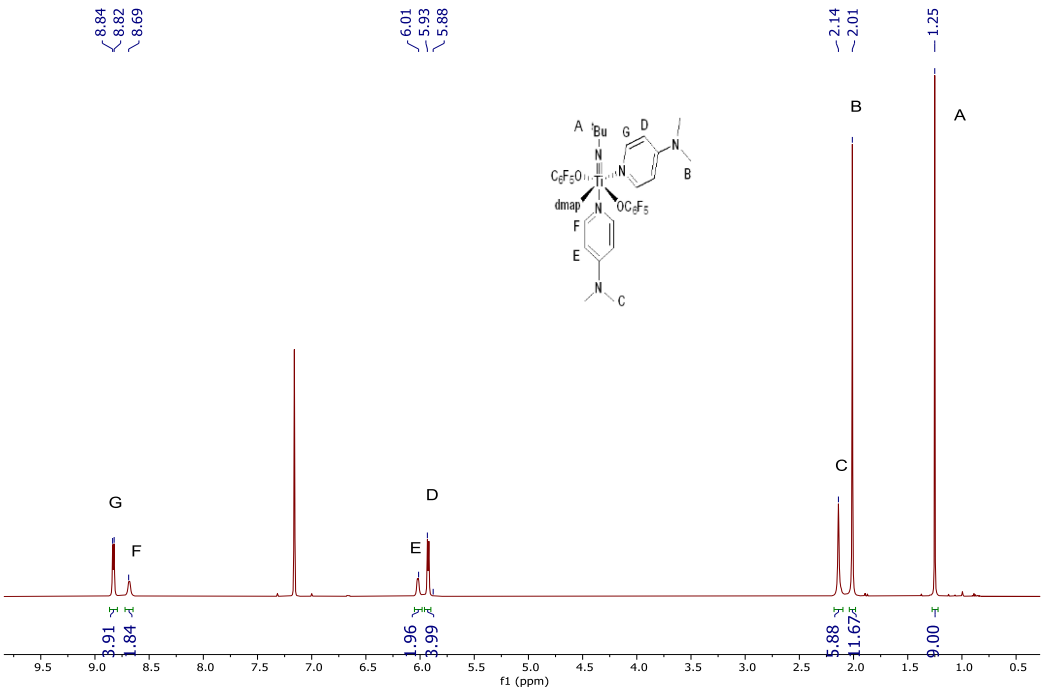

Figure 4.62 ^{1}H NMR spectrum of **4.22** in C_6D_6. *Taken from XYS-2019-178_2H.*

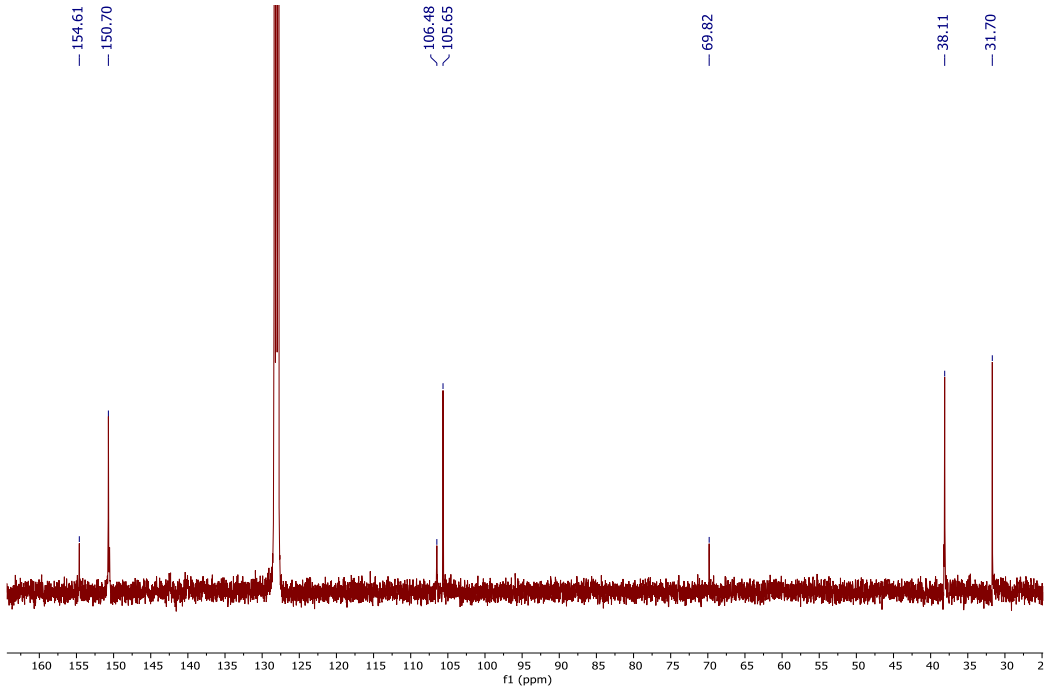

Figure 4.63 ^{13}C NMR spectrum of **4.22** in C_6D_6. *Taken from XYS-2019-178_1C.*

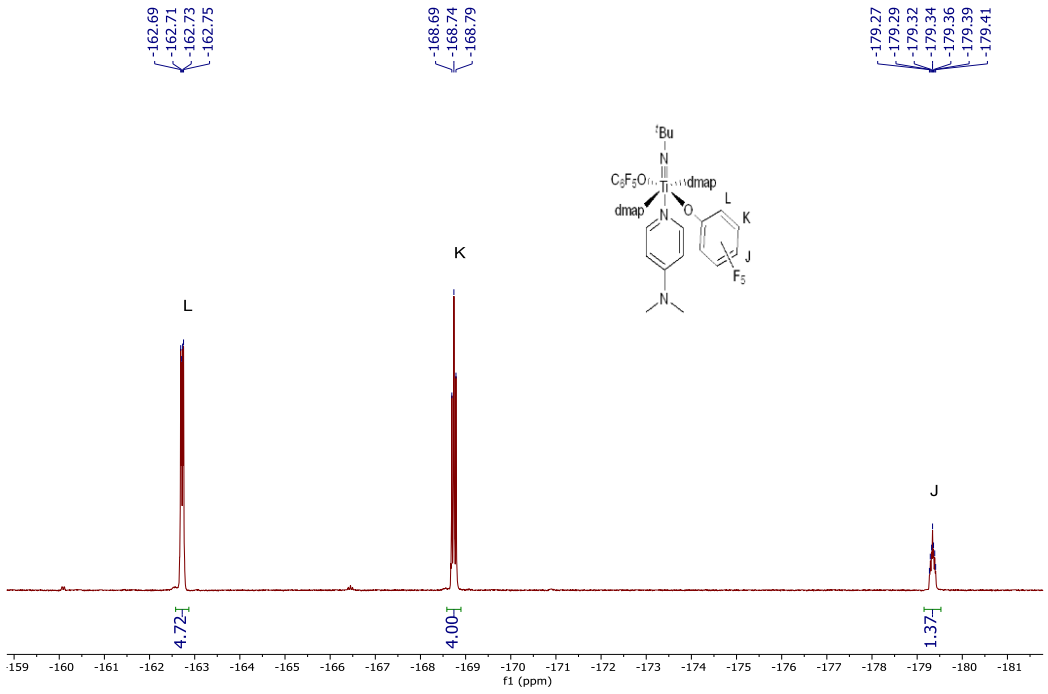

Figure 4.64 ^{19}F NMR spectrum of **4.22** in C_6D_6. *Taken from XYS-2019-178_2F.*

Synthesis of 4.23

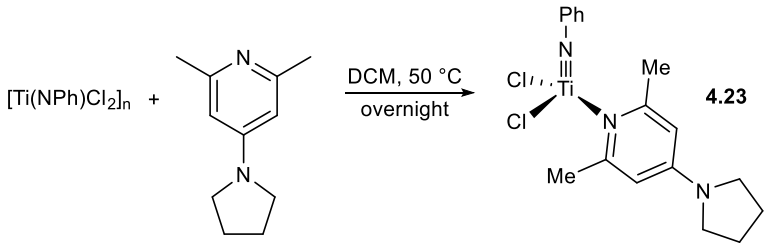

2,6-dimethyl-4-dimethylaminopyridine was synthesized according to literature procedure.[261]

$[Ti(NPh)Cl_2]_n$ (89 mg, 0.42 mmol, 1.0 equiv), 2,6-dimethyl-4-dimethylaminopyridine (78 mg, 0.45 mmol, 1.1 equiv) and 2 mL CH_2Cl_2 were added to a 20 mL scintillation vial equipped with a small stir bar in a N_2-filled glovebox. This was then sealed with a Teflon-lined cap, heated to 50 °C and stirred overnight. After cooling to room temperature, the reaction mixture was filtered through a fine frit and washed with CH_2Cl_2. The residue was dried in *vacuo* to give **4.23** as a highly insoluble brown powder (150 mg, 92 % yield).

^{1}H NMR (400 MHz, $CDCl_3$): δ 7.06 (br s, 1H, NPh-*H*), 6.89 (br s, 2H, NPh-*H*), 6.78 (br s, 1H, NPh-*H*), 6.67 (br s, 1H, NPh-*H*), 6.09 (br s, 2H, py-*H*), 3.26 (br s, 4H, *o*-prl-*H*), 2.41 (br s, 6H, *o*-py-C*H*$_3$), 2.04 (br s, 4H, *m*-prl-*H*).
Hexane impurities are present in the $CDCl_3$ solvent.

^{13}C NMR (151 MHz and 126 MHz, $CDCl_3$): δ 153.5, 148.4, 127.8, 127.5, 124.0, 123.7, 120.0, 104.2, 47.4, 25.4, 22.5.
This is a partial line-list pieced together from ^{13}C data (151 MHz, NS = 15360, AQ = 1 s, d1 = 5 s), ^{1}H-^{13}C HSQC and HMBC data. Resonances associated with a quaternary C of the NPh fragment were not observed.

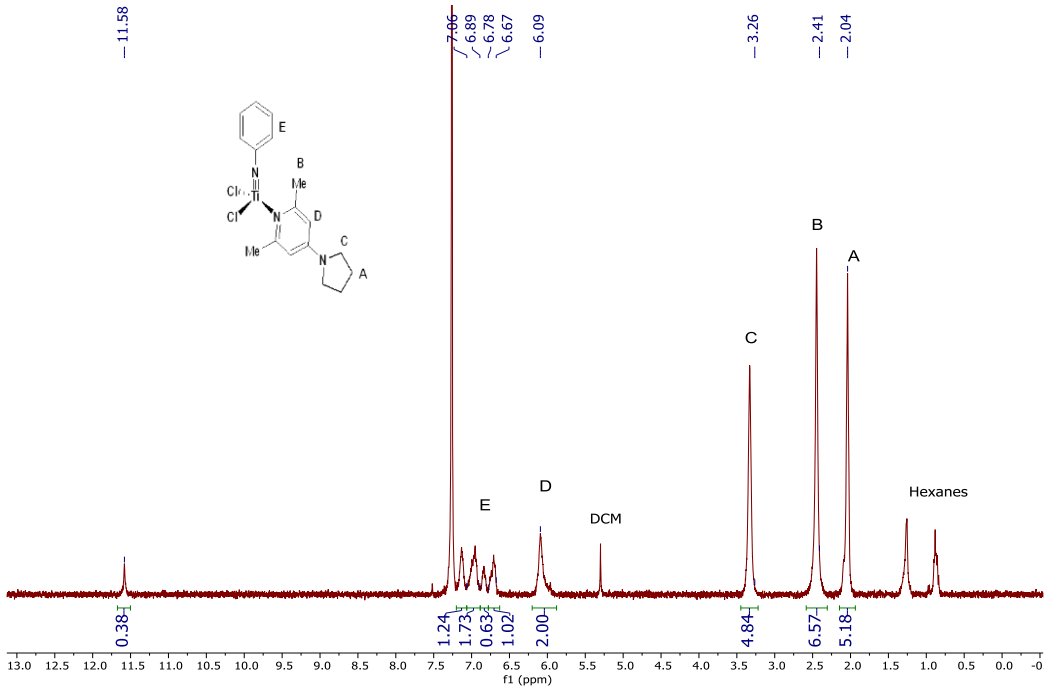

Figure 4.65 ^{1}H NMR spectrum of **4.23** in $CDCl_3$. *Taken from XYS-2020-002_quantH.*

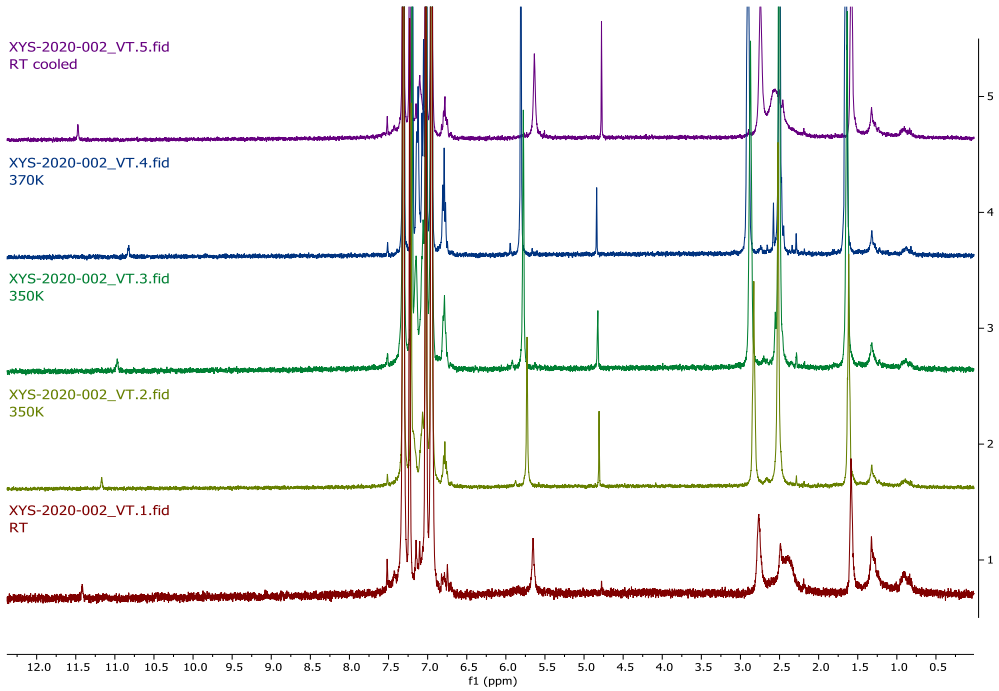

Figure 4.66 Stacked variable temperature ^{1}H NMR spectra of **4.23** in C_6D_5Br. *Taken from XYS-2020-002_VT.*

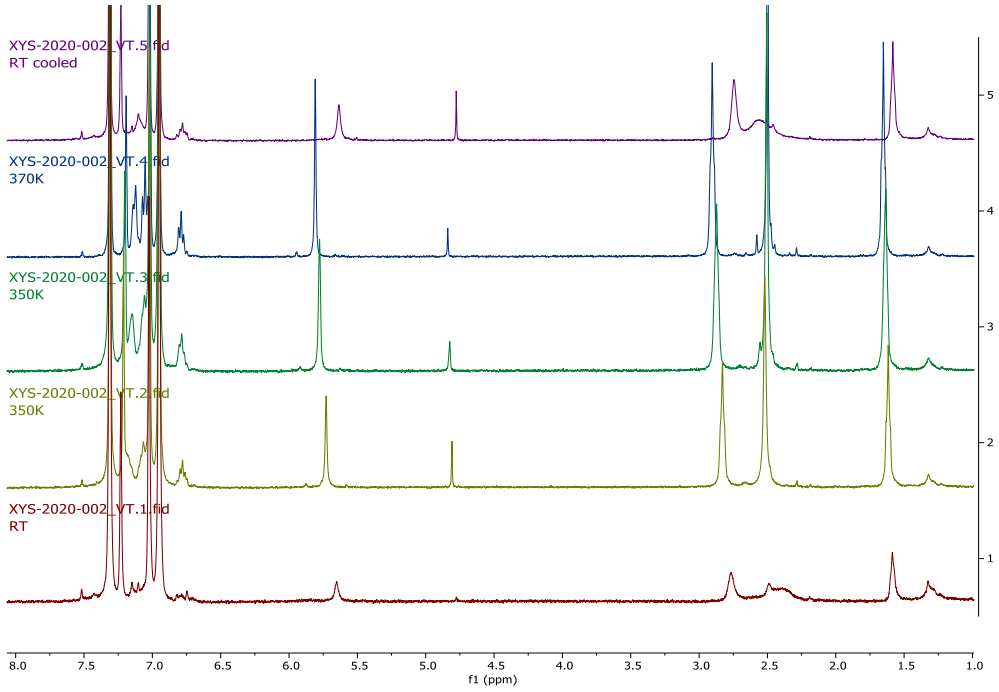

Figure 4.67 Zoom-in stacked variable temperature ^{1}H NMR spectrum of **4.23** in C_6D_5Br. *Taken from XYS-2020-002_VT.*

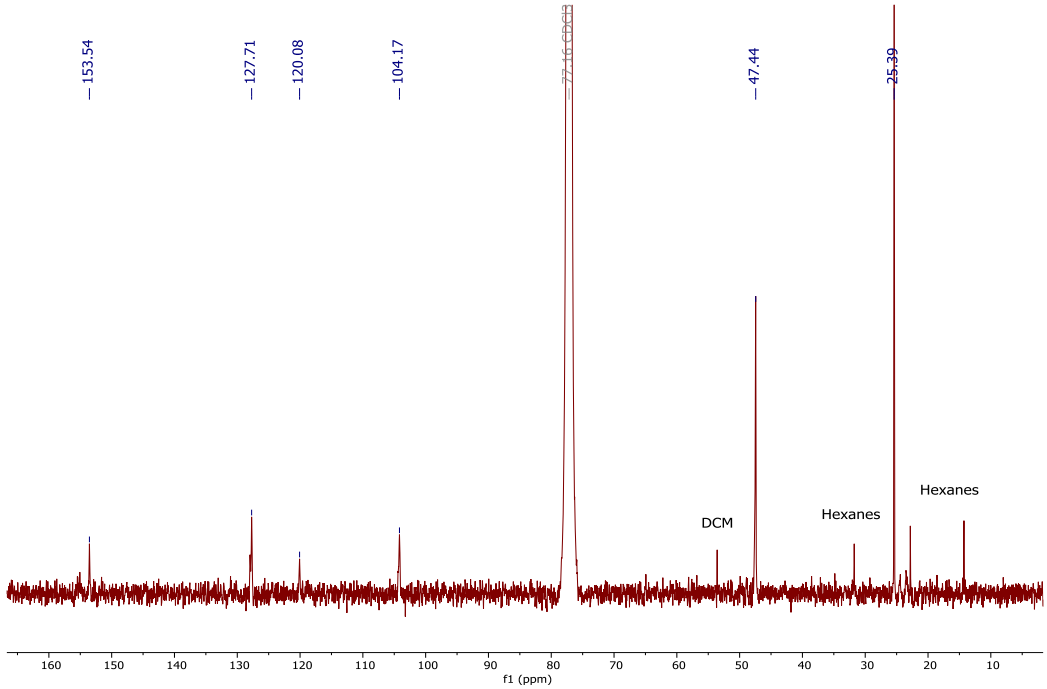

Figure 4.68 ^{13}C NMR spectrum of **4.23** in $CDCl_3$. *Taken from XYS-2020-002_3C.*

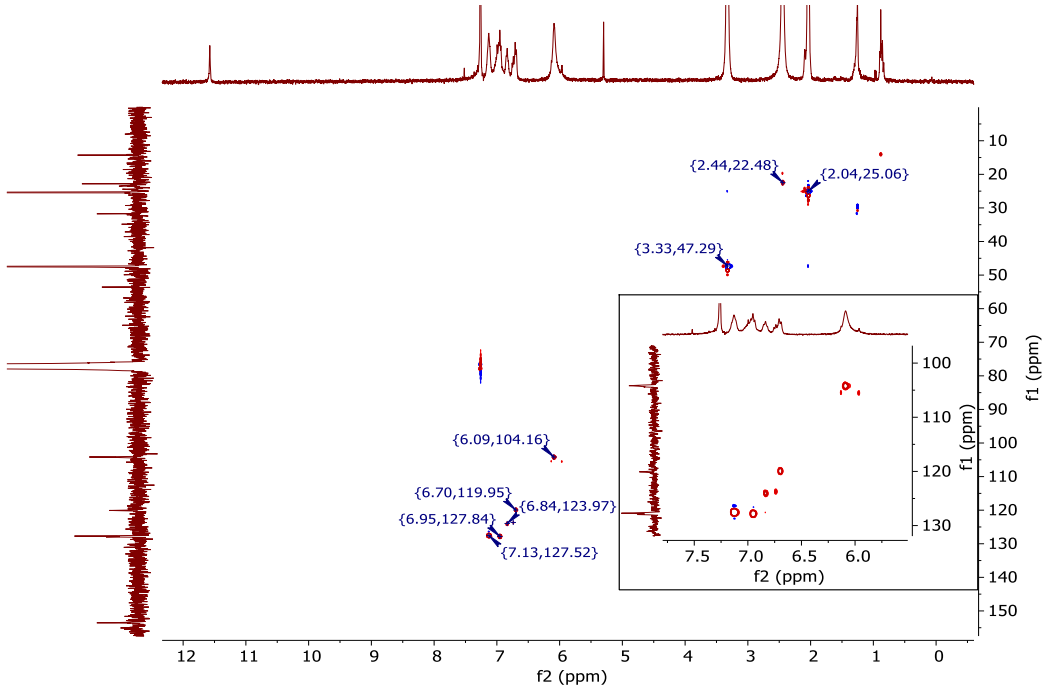

Figure 4.69 ^{1}H-^{13}C HSQC NMR spectrum of **4.23** in $CDCl_3$. *Taken from XYS-2020-002_HSQC.*

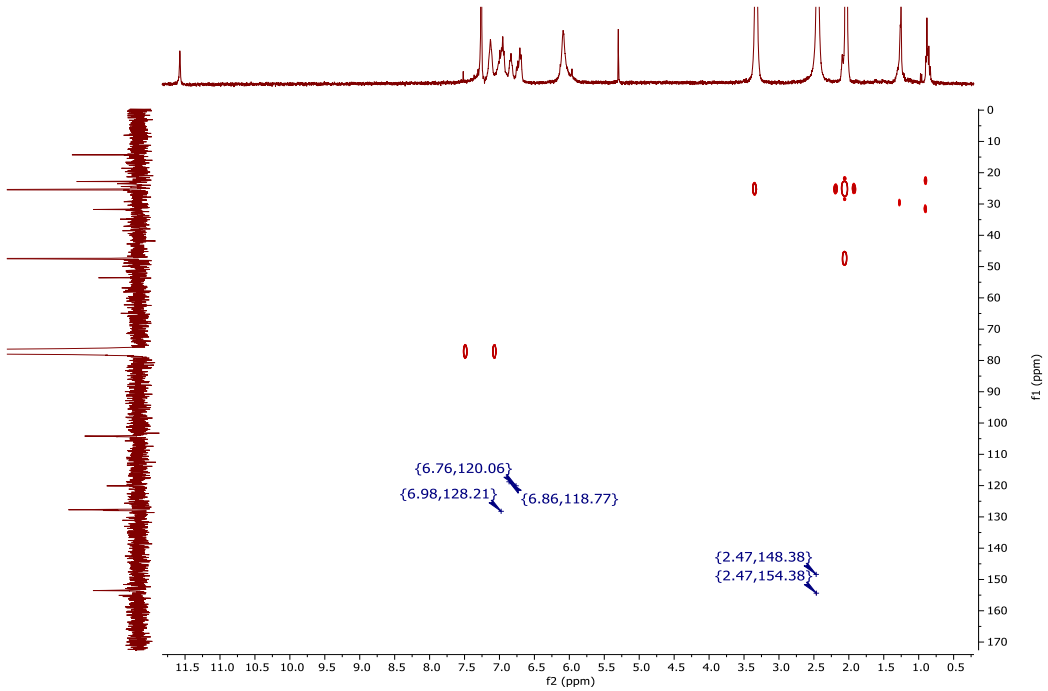

Figure 4.70 ^{1}H-^{13}C HMBC NMR spectrum of **4.23** in $CDCl_3$. *Taken from XYS-2020-002_C HMBC.*

Synthesis of 4.a

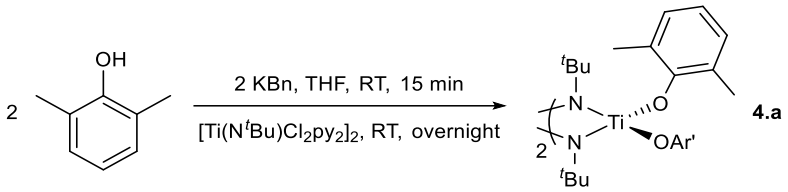

2,6-dimethylphenol (100 mg, 0.82 mmol, 2.0 equiv), KBn (107 mg, 0.82 mmol, 2.0 equiv) and 2 mL THF were added to a 20 mL scintillation vial equipped with a small stir bar in a N_2-filled glovebox. This was then sealed with a Teflon-lined cap and stirred at room temperature for 15 mins to form a deep red solution. In a separate scintillation vial, [Ti(N^{t}Bu)Cl$_2$py$_2$]$_2$ (142 mg, 0.41 mmol, 1.0 equiv) was dissolved in 2 mL THF to form an orange solution. The [Ti] solution was added to the ligand solution and stirred overnight at room temperature. Following which, the reaction mixture was dried *in vacuo*, dissolved in benzene (5 mL), filtered through a celite plug and the filtrate dried *in vacuo*. The crude product was purified by dissolving in ether, layering with the same volume of hexanes and cooling in a - 35 °C freezer to yield X-ray quality brown crystals of pure **4.a**. (14 mg, 9 % yield).

^{1}H NMR (400 MHz, C_6D_6): δ 7.02 (d, $^3J_{HH}$ = 7.6 Hz, 4H, *m*-Ph-*H*), 6.84 (t, $^3J_{HH}$ = 7.5 Hz, 2H, *p*-Ph-*H*), 2.49 (s. 12H, C*H*$_3$), 1.14 (s, 9H, ^{t}Bu-*H*).

^{13}C NMR (101 MHz, C_6D_6): δ 163.3, 128.9, 127.0, 121.5, 73.2, 33.1, 18.2.

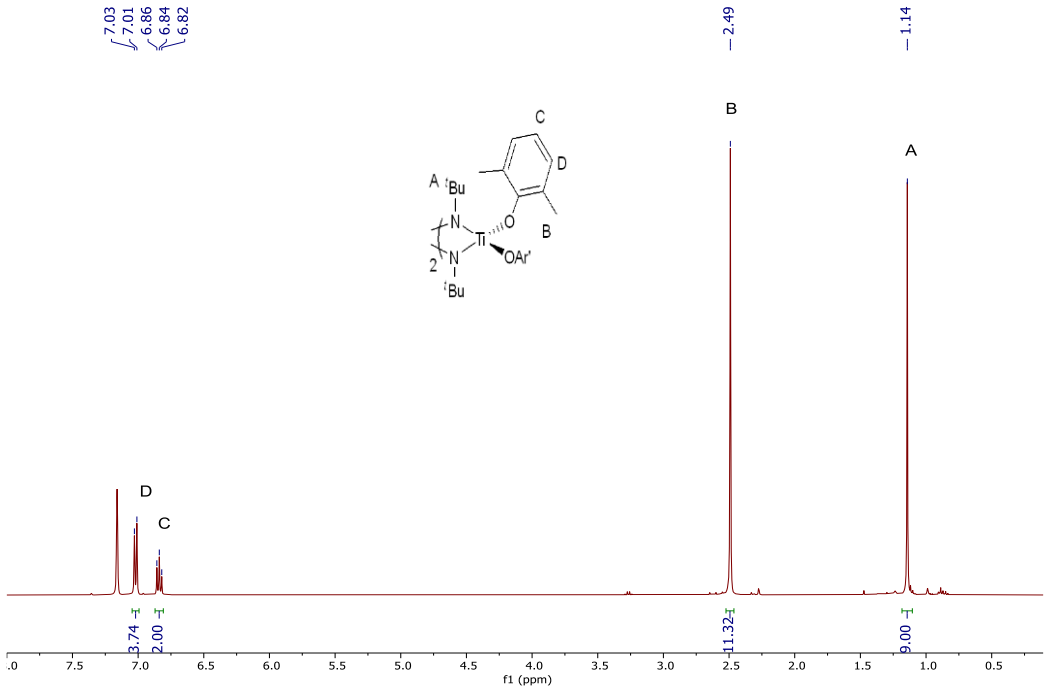

Figure 4.71 ^{1}H NMR spectrum of **4.a** in C_6D_6. *Taken from XYS-2019-160_2H.*

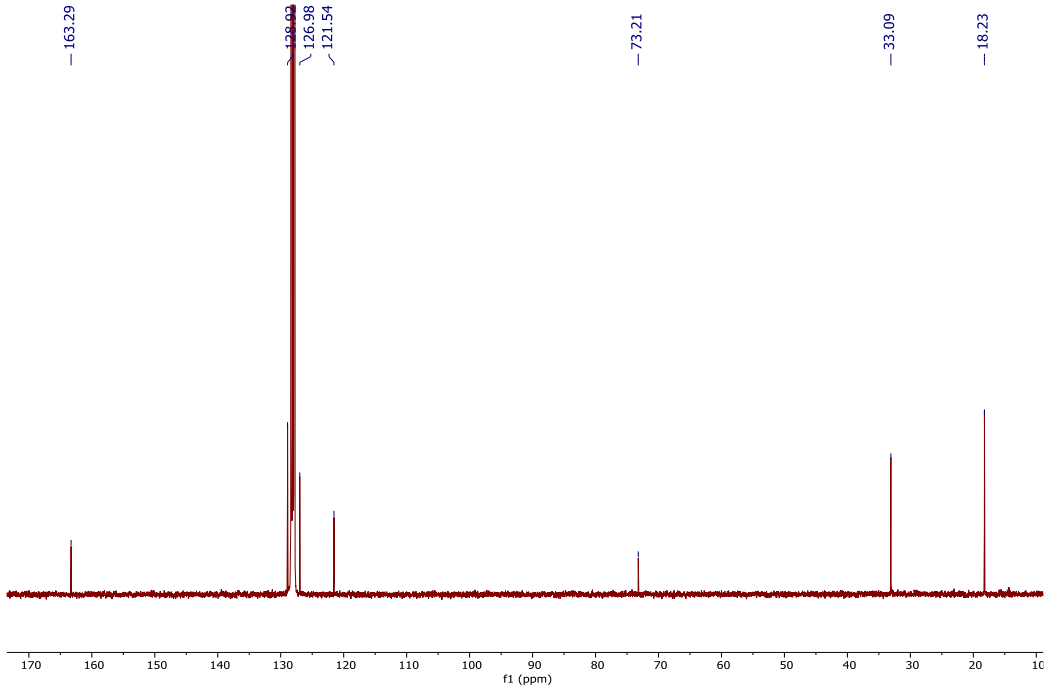

Figure 4.72 ^{13}C NMR spectrum of **4.a** in C_6D_6. *Taken from XYS-2019-160_1C.*

Synthesis of 4.b

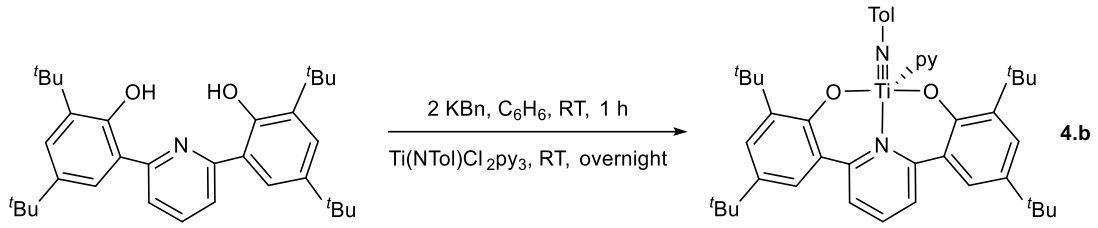

Complex **4.b** was synthesized by modified literature procedure[176] using $(ONO)H_2$ (200 mg, 0.41 mmol, 1.0 equiv), KBn (107 mg, 0.82 mmol, 2.0 equiv) and $Ti(NTol)Cl_2py_3$ (189 mg, 0.41 mmol, 1.0 equiv). Upon benzene lyophilization to form a sticky liquid, 5 mL of hexanes were added to the crude product to crash out an orange powder. The orange powder was dried *in vacuo* for several hours to yield pure **4.b** (100 mg, 34 %).

^{1}H NMR (500 MHz, C_6D_6): δ 8.74 (d, $^3J_{HH}$ = 4.7 Hz, 2H, *o*-py-*H*), 7.83 (app s, 2 H, *m*-OPh-*H*), 7.57 (app s, 2H, *m*-OPh-*H*), 7.40 (d, $^3J_{HH}$ = 7.9 Hz, 2H, *m*-NTol-*H*), 7.12 (t, $^3J_{HH}$ = 8.1 Hz, 1H, Ar-*H*), 6.93 (t, $^3J_{HH}$ = 7.7 Hz, 1H, Ar-*H*), 6.61 – 6.56 (m, 4H, Ar-*H*), 6.31 (d, $^3J_{HH}$ = 7.9 Hz, 2H, *o*-NTol-*H*), 1.92 (s, 3H, NC_6H_4-C*H*$_3$), 1.54 (s, 18H, o-^{t}Bu-*H*), 1.47 (s, 18H, *p*-^{t}Bu-*H*).

^{13}C NMR (101 MHz, C_6D_6): δ 159.8, 159.4, 158.9, 150.5, 140.2, 138.8, 138.5, 137.3, 129.2, 128.5, 127.1, 126.2, 125.6, 124.4, 123.2, 35.4, 34.6, 32.1, 30.1, 21.0.
This is a partial line-list. Resonances associated with a quaternary C were not observed.

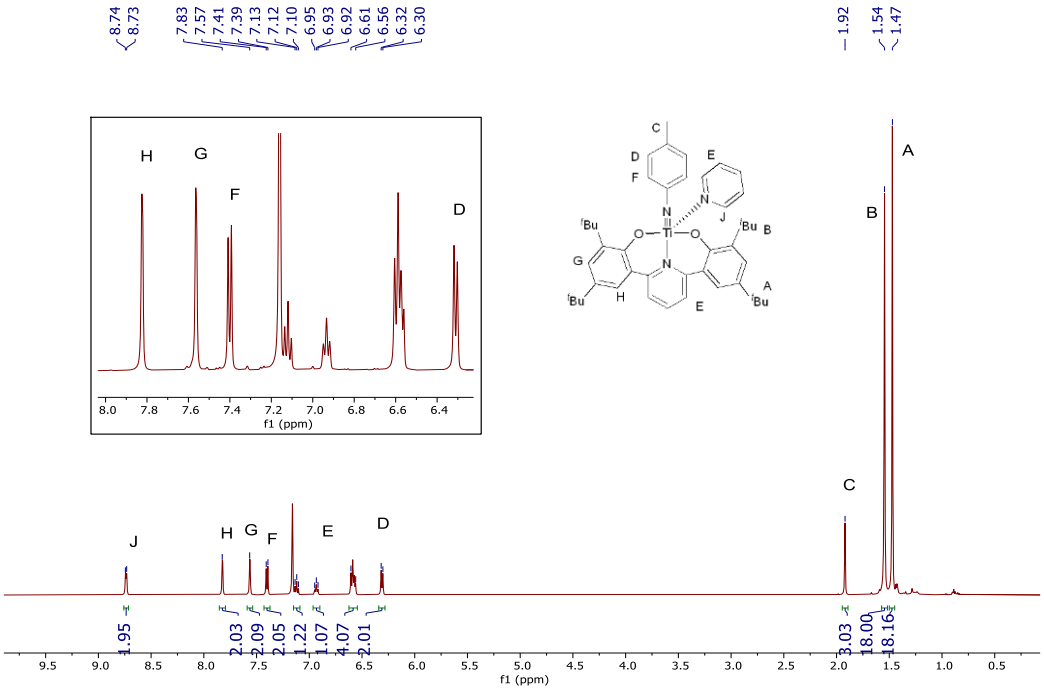

Figure 4.73 ^{1}H NMR spectrum of **4.b** in C_6D_6. *Taken from XYS-2019-138_3H.*

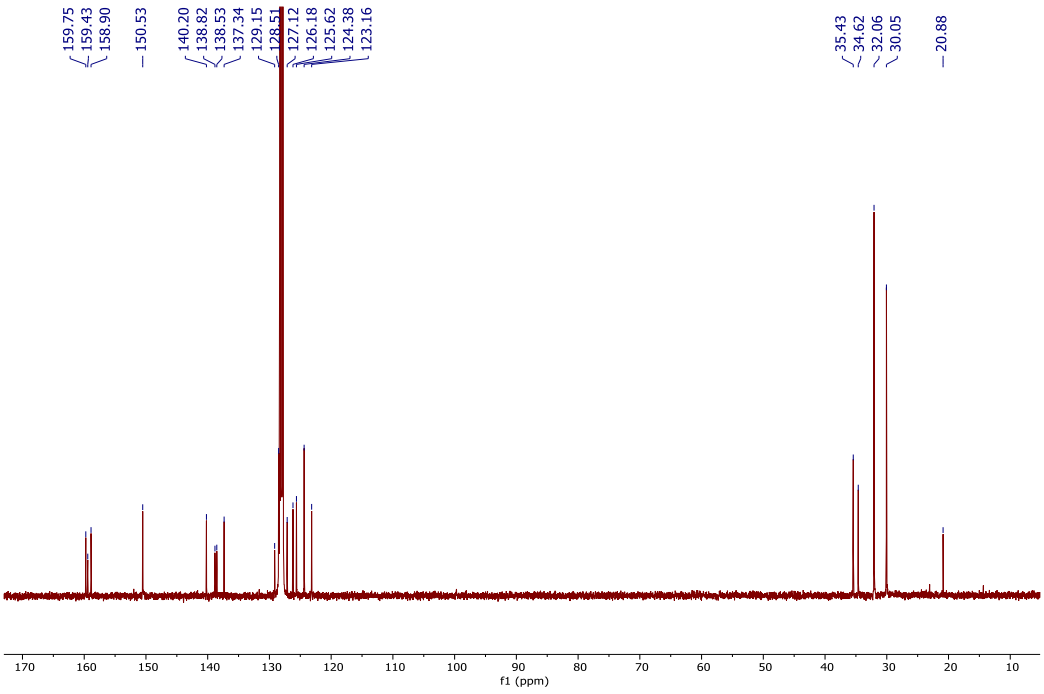

Figure 4.74 ^{13}C NMR spectrum of **4.b** in C_6D_6. *Taken from XYS-2019-138_1C.*

Synthesis of 4.c

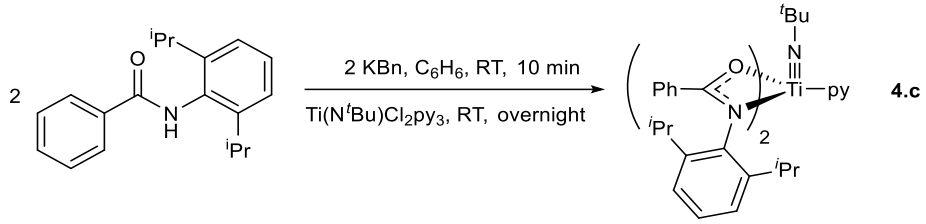

Ti(N^{t}Bu)(amidate)$_2$py (**4.c**) was synthesized with slight modifications to literature procedures.[119] NMR of complex matches that of reported in literature.[167]

Synthesis of 4.d

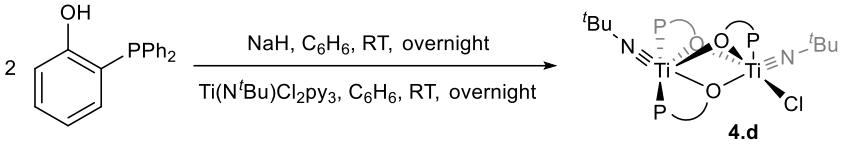

(2-hydroxyphenyl)diphenylphosphine (296 mg, 1.1 mmol, 1 equiv), 5 mL hexanes and NaH (75 mg, 3.1 mmol, 3 equiv) were added in this order to a 20 mL scintillation vial equipped with a small stir bar in a N_2-filled glovebox. Instant evolution of gas was observed. This was then sealed with a Teflon-lined cap about 5 min later and stirred at room temperature overnight. The reaction mixture was filtered through a fine frit and the residue was treated with 2 mL THF to give a fine suspension. The suspension was filtered through a pipette plug and washed with more THF. The filtrate was dried under in *vacuo* for several hours before use to give the ligand Na-salt with one THF bound as a fluffy solid. (337 mg, 85 % yield).

In a separate scintillation vial equipped with a small stir bar, Ti(N^{t}Bu)Cl$_2$py$_2$ (100 mg, 0.23 mmol, 1.0 equiv), Na-OAr' ligand (174 mg, 0.47 mmol, 2.0 equiv) and 5 mL C_6H_6 were added together. The mixture was stirred overnight at room temperature. Following which, the reaction mixture was filtered through a celite plug to remove gelatinous material and the filtrate was dried *in vacuo* to give a sticky orange liquid. The crude product was purified by dissolving in 2 mL C_6H_6 and slow diffusing with pentane to yield X-ray quality orange crystals of pure **4.d**. (34 mg, 13 % yield).

NMR spectra were taken of crystalline material, resulting in highly complex spectra indicative of fluxional species in solution.

^{1}H NMR (400 MHz, $CDCl_3$): δ 8.66 – 8.59 (m, 2H, Ar-*H*), 8.26 (app t, $^{3}J_{HH}$ = 9.6 Hz, 1H, Ar-*H*), 8.04 (app t, $^{3}J_{HH}$ = 9.2 Hz, 1H, Ar-*H*), 7.72 – 7.29 (m, 18H, Ar-*H*), 7.23 – 7.08 (m, 5H, Ar-*H*), 6.96 – 6.42 (m, 14H, Ar-*H*), 6.07 – 5.92 (m, 1H, Ar-*H*), 5.44 – 5.34 (m, 1H, Ar-*H*), 0.87 – 0.79 (m, 15H, ^{t}Bu), 0.18 (s, 3H, ^{t}Bu).

^{13}C NMR (126 MHz, $CDCl_3$): δ 137.5, 137.4, 136.4, 136.3, 135.4, 135.2, 134.2 – 130.7 (m), 129.6, 128.7, 128.1, 127.1, 121.0 – 117.9, 69.6, 68.9, 32.8, 31.9, 30.8.
This is a partial line-list. Many C could not be positively be identified.

^{31}P NMR (162 MHz, $CDCl_3$): δ 7.62, 7.54, 5.44, 5.38, 3.47, 2.58, 2.52, -0.47, -2.73, -2.81.

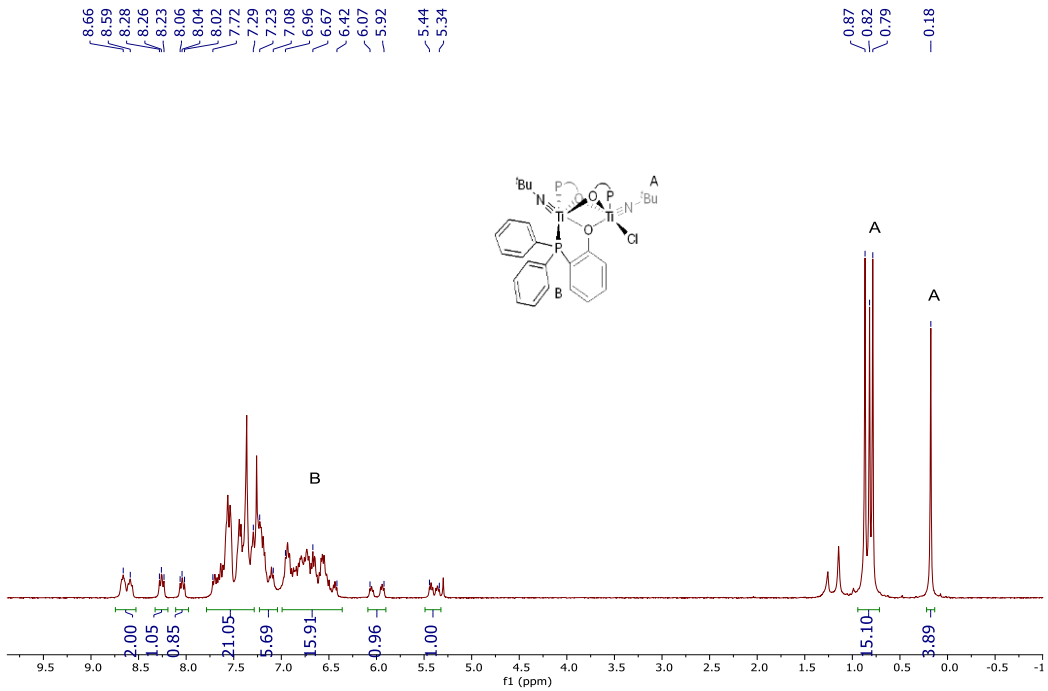

Figure 4.75 ^{1}H NMR spectrum of **4.d** in $CDCl_3$. *Taken from XYS-2019-135B_4H.*

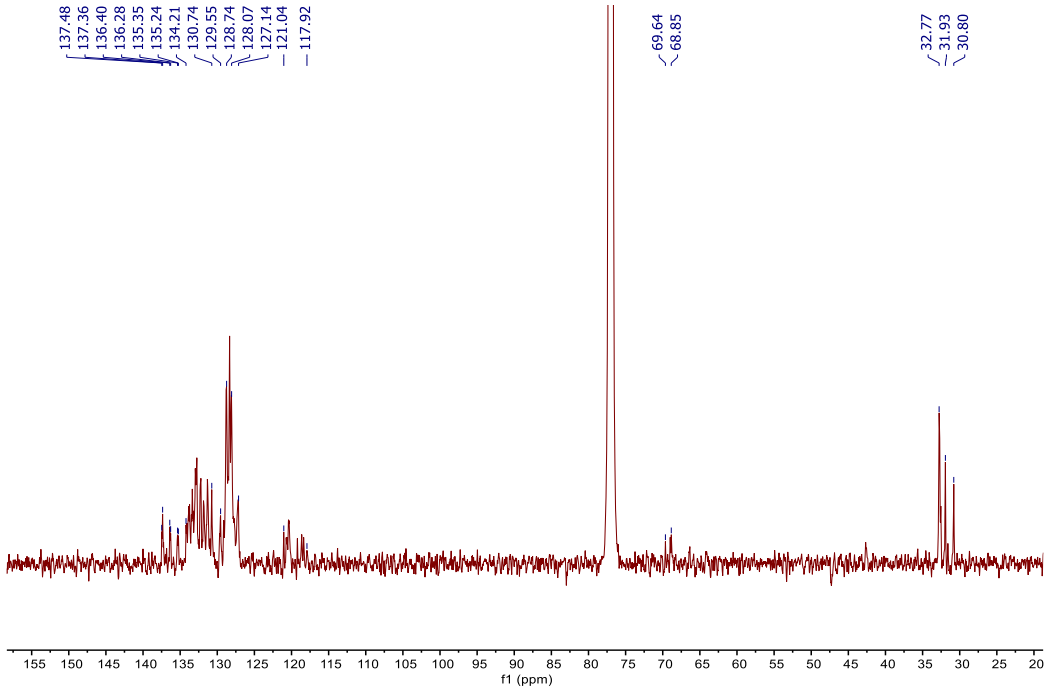

Figure 4.76 ^{13}C NMR spectrum of **4.d** in $CDCl_3$. *Taken from XYS-2019-135B_1C.*

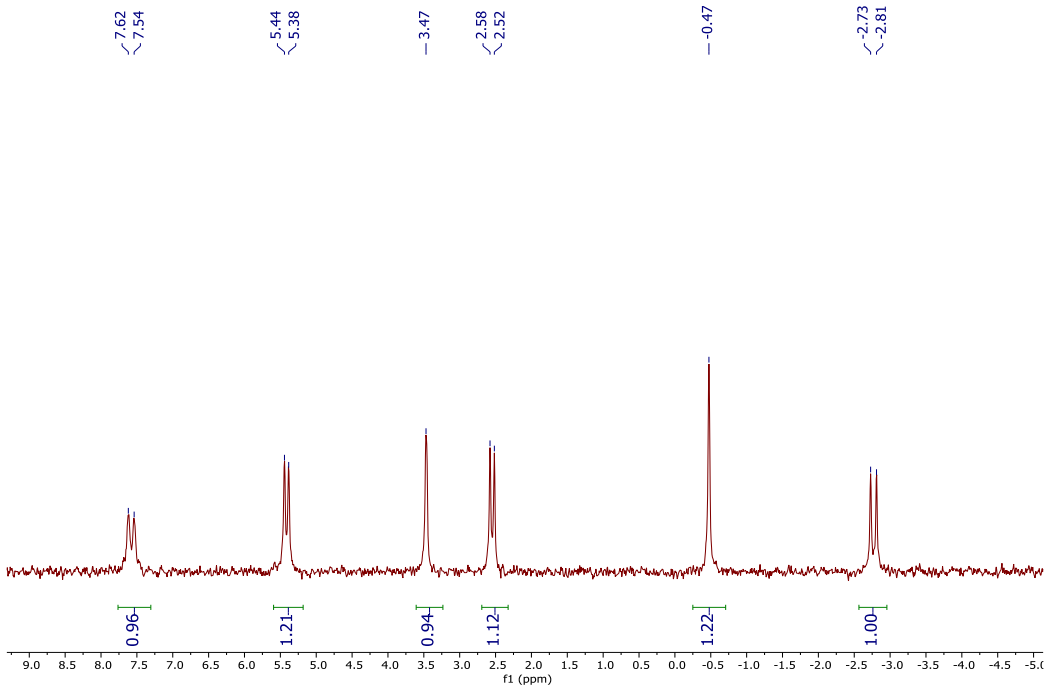

Figure 4.77 ^{31}P NMR spectrum of **4.d** in $CDCl_3$. *Taken from XYS-2019-135B_4P.*

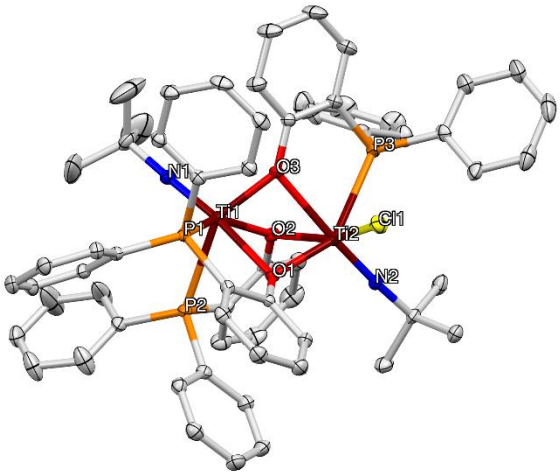

Figure 4.78 50 % thermal ellipsoid drawing of **4.d**. Hydrogen atoms are omitted for clarity.

Synthesis of 4.e

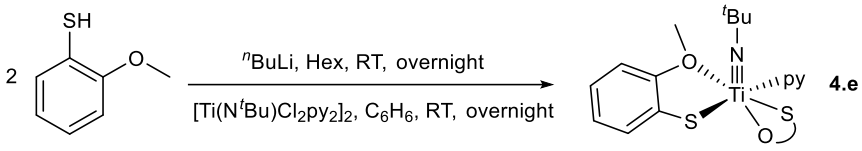

2-methoxythiophenol (1 g, 7.1 mmol, 1.0 equiv), 10 mL hexanes and ^{n}BuLi (3.4 mL, 2.5 M, 8.6 mmol, 1.2 equiv) were added in this order to a 20 mL scintillation vial equipped with a small stir bar in a N_2-filled glovebox in the order. This was then sealed with a Teflon-lined cap and stirred at room temperature overnight. The reaction mixture was filtered, washed with hexanes and the Li-salt residue was dried *in vacuo* for several hours before use (1.03 g, 99 % yield).

In a separate scintillation vial equipped with a small stir bar, [Ti(N^{t}Bu)Cl$_2$py$_2$]$_2$ (206 mg, 0.48 mmol, 1.0 equiv), Li-salt residue (143 mg, 0.98 mmol, 2.0 equiv) and 2 mL C_6H_6 were added to form a deep red solution. The mixture was stirred overnight at room temperature. Following which, the reaction mixture was filtered through a celite plug and the filtrate was dried *in vacuo*. The crude product was purified by dissolving in 1 mL PhMe and cooling in a - 35 °C freezer to yield X-ray quality yellow crystals of pure **4.e**. (75 mg, 33 % yield).

^{1}H NMR (500 MHz, C_6D_6): δ 9.00 (d, $^{3}J_{HH}$ = 4.9 Hz, 2H, *o*-py-*H*), 7.84 (br s, 2H, Ar-*H*), 6.85 (br t, 2H, Ar-*H*), 6.70 – 6.66 (m, 3H, Ar-*H*), 6.35 (app t, $^{3}J_{HH}$ = 7.1 Hz, 2H, Ar-*H*), 6.17 (d, $^{3}J_{HH}$ = 8.0 Hz, 2H), 3.94 (br s, 3H, O-CH_3), 3.24 (br s, 3H, O-CH_3), 1.31 (s, 9H, ^{t}Bu-*H*).

^{13}C NMR (126 MHz, C_6D_6): δ 151.2, 138.0, 137.9, 129.3, 128.6, 128.4, 125.7, 123.8, 70.3, 31.6, 21.4.

This is a partial line-list. Resonances associated with a quaternary C were not observed.

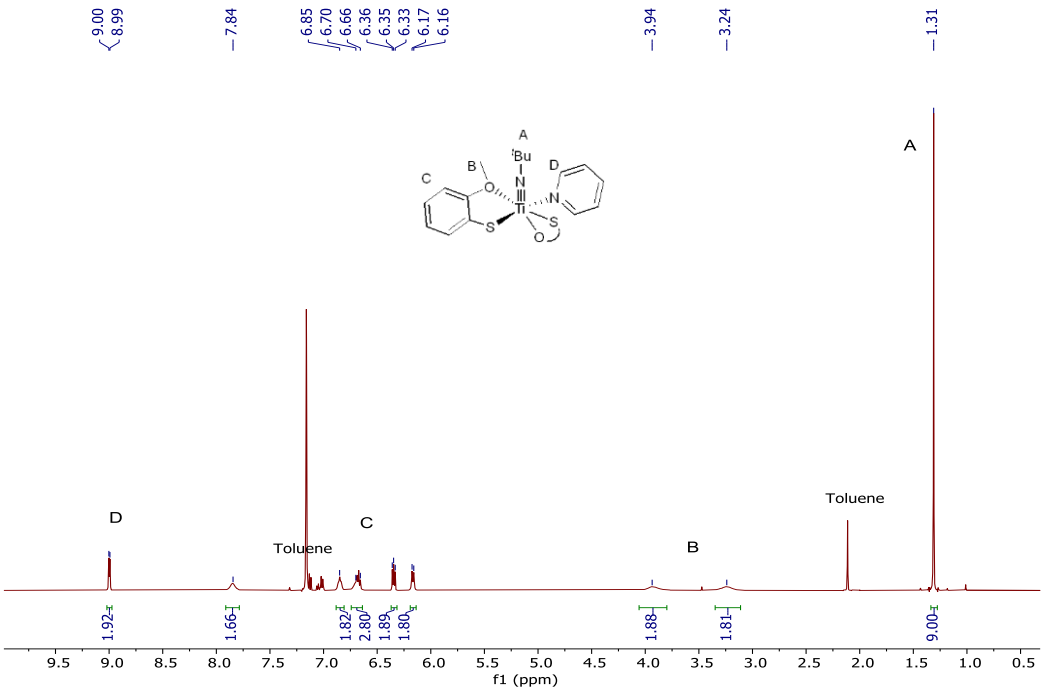

Figure 4.79 ^{1}H NMR spectrum of **4.e** in C_6D_6. *Taken from XYS04078B_3H.*

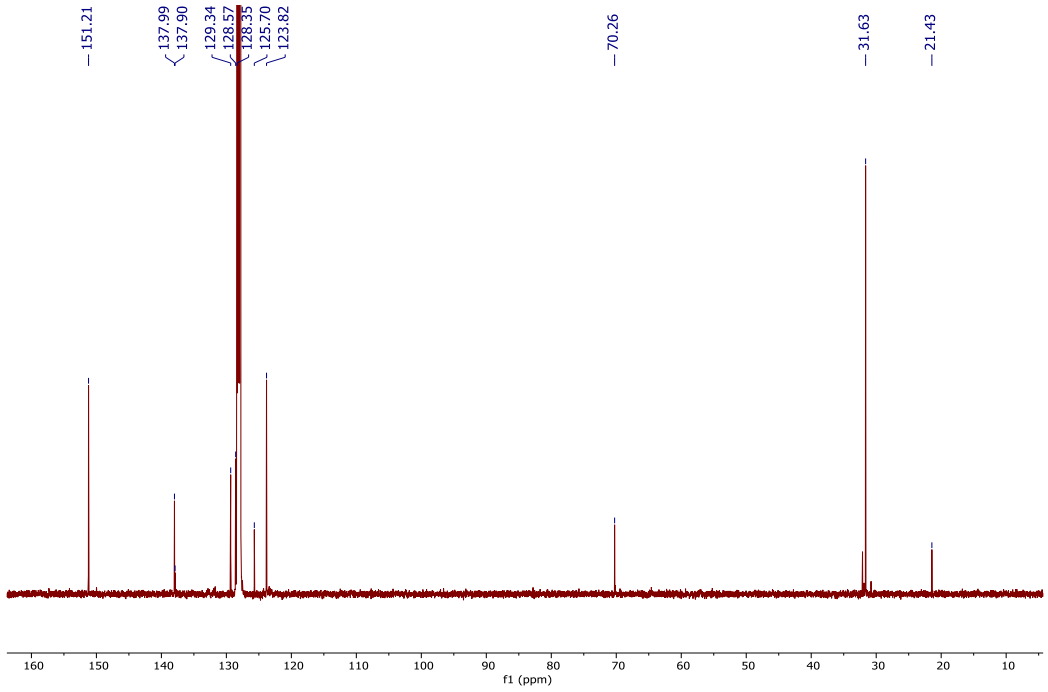

Figure 4.80 ^{13}C NMR spectrum of **4.e** in C_6D_6. *Taken from XYS-2020-024A_1C.*

Synthesis of 4.f

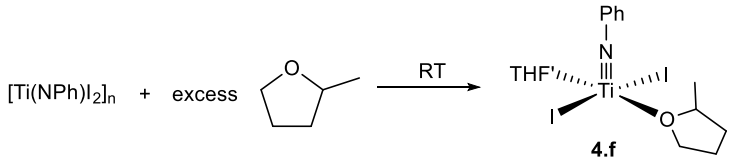

$[Ti(NPh)I_2]_n$ (170 mg, 0.43 mmol, 1.0 equiv) and 2-methyltetrahydrofuran (1 mL, 9.9 mmol, 23.0 equiv) were added to a 20 mL scintillation vial equipped with a small stir bar in a N_2-filled glovebox and stirred to dissolve all solids. 1 mL of hexanes was layered onto the mixture and the mixture was left to cool in a - 35 °C freezer to yield solid material. The reaction mixture was filtered through a fine frit, washed with 5 mL hexanes and dried in *vacuo* for several hours to yield pure **4.f** (60 mg, 25 % yield).

^{1}H NMR (500 MHz, C_6D_6): δ 7.24 (d, $^3J_{HH}$ = 7.9 Hz, 2H, *o*-NPh-*H*), 6.92 (t, $^3J_{HH}$ = 7.7 Hz, 2H, *m*-NPh-*H*), 6.70 (t, $^3J_{HH}$ = 7.5 Hz, 1H, *p*-NPh-*H*), 5.09 (br s, 2H, 2-$C_5H_{10}O$-*H*), 4.24 (br s, 4H, 5-$C_5H_{10}O$-*H*), 1.66 (br s, 2H, $C_5H_{10}O$-*H*), 1.47 (br s, 2H, $C_5H_{10}O$-*H*), 1.37 – 1.29 (m, 2H, $C_5H_{10}O$-*H*), 1.24 – 1.22 (m, 6H, $C_5H_{10}O$-C*H*$_3$), 1.01 – 0.95 (m, 2H, $C_5H_{10}O$-*H*).

^{13}C NMR (101 MHz, C_6D_6): δ 162.1, 128.7, 124.1, 124.1, 86.9, 74.8, 32.2, 24.5, 21.3.

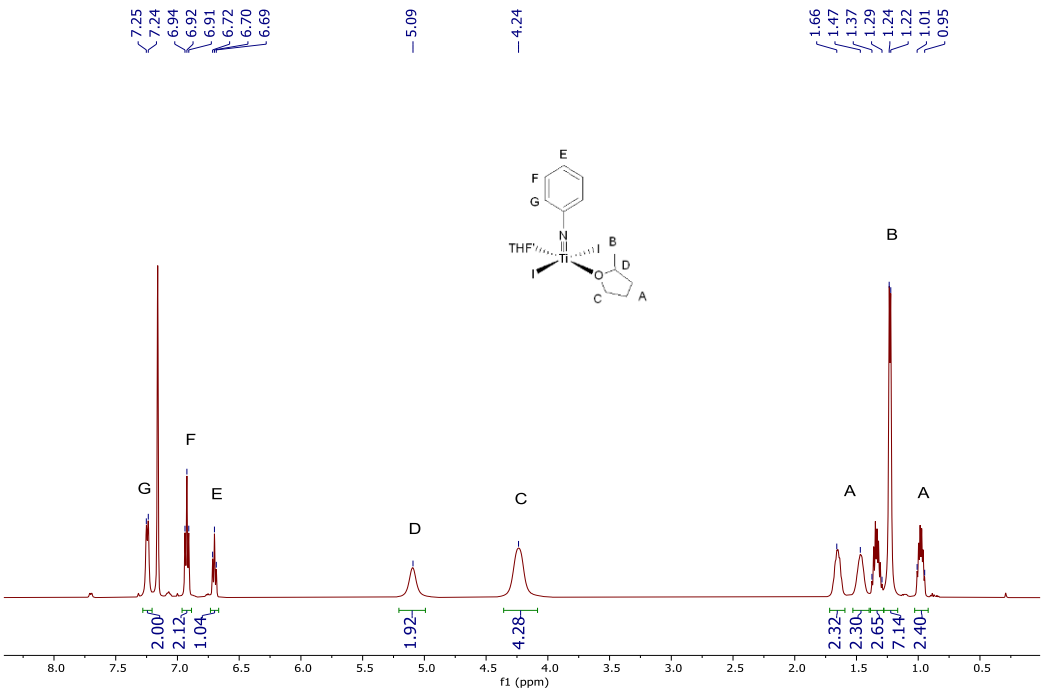

Figure 4.81 ^{1}H NMR spectrum of **4.f** in C_6D_6. *Taken from XYS-2019-123C_2H.*

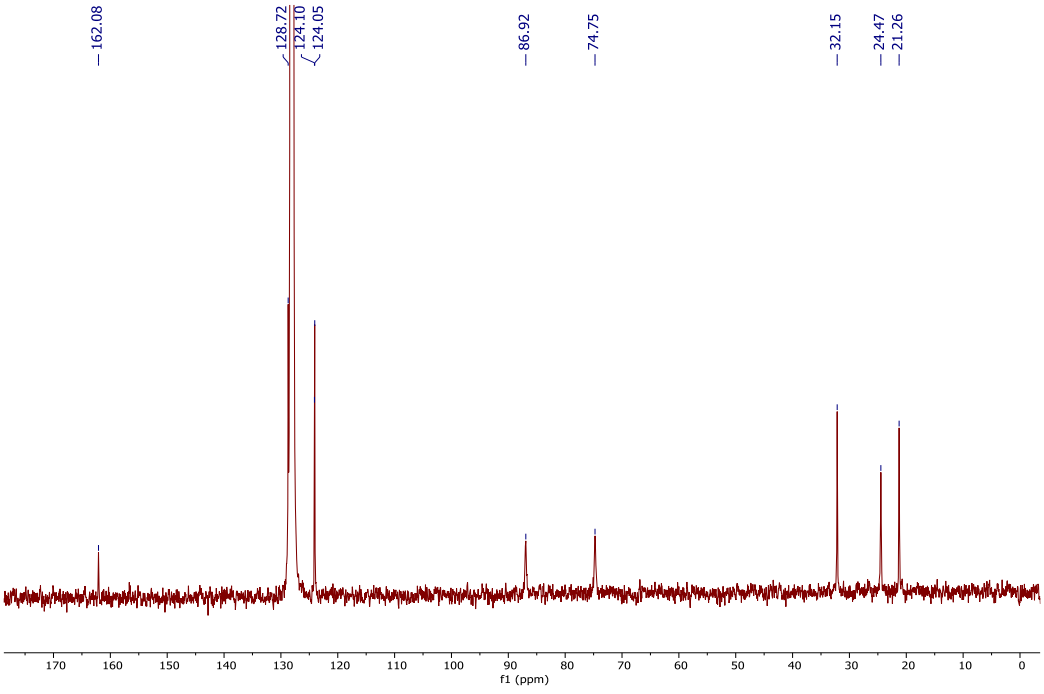

Figure 4.82 ^{13}C NMR spectrum of **4.f** in C_6D_6. *Taken from XYS-2019-123C_1C.*

4.6.3 Representative Ti imido catalysts platforms tested

Over the years, we have also attempted catalysis with other more complex ligand classes that are found widely in Ti-catalyzed hydroamination and polymerization literature, however they often gave poor to moderate yields and selectivity.

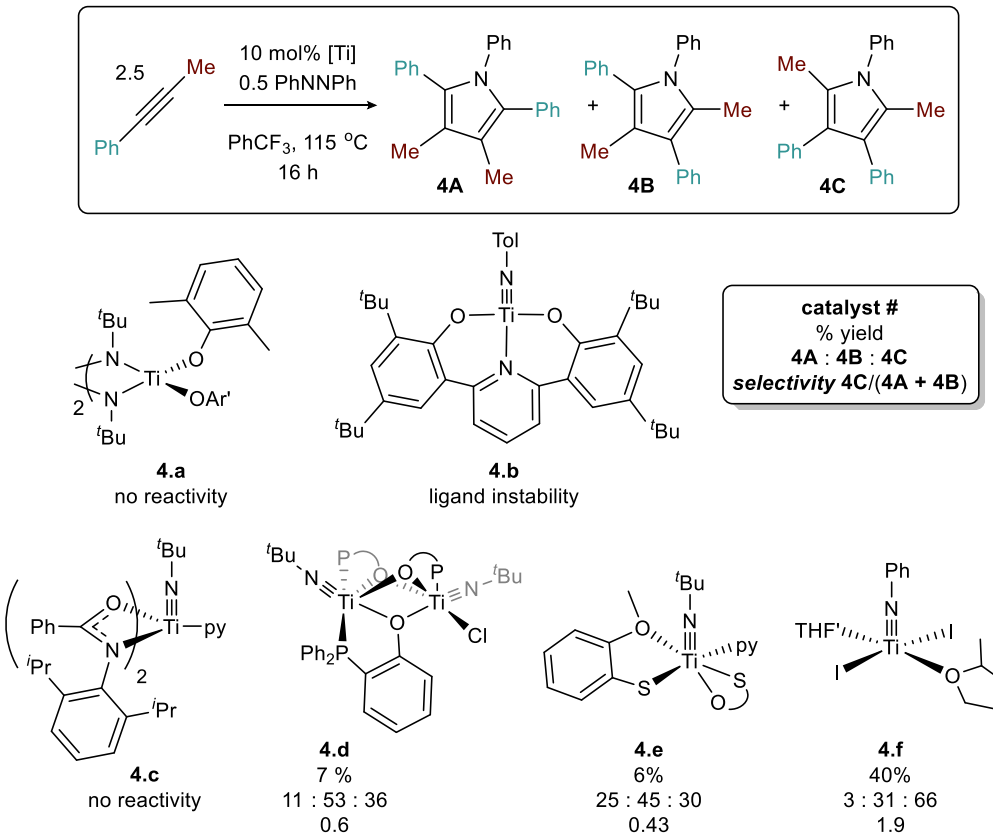

Figure 4.83 Representative ligand scaffolds common in literature tested in catalytic pyrrole formation with PhCCMe. See main text for conditions.

4.6.4 Ligand scaffolds attempted

Represented below are ligands that we attempted but are unable to bind to a Ti imido moiety, presumably due to steric hindrance imposed by the ortho substituents.

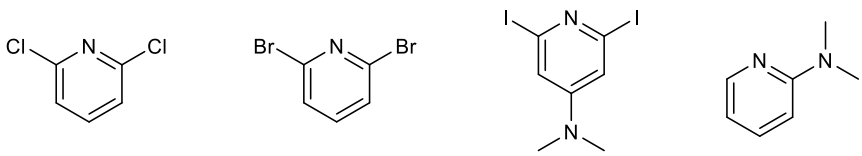

Figure 4.84 Ligand scaffolds that were unsuccessful in coordinating to Ti.

4.6.5 General procedure for catalytic pyrrole formation

Azobenzene (364 mg, 2 mmol), phenyl propyne (1.16 g, 10 mmol) and 1,3,5-trimethoxybenzene (336 mg, 2 mmol, as internal standard) were added to a 10 mL volumetric flask and diluted to 10 mL with $PhCF_3$ to make a stock solution. For each catalytic run, a precatalyst (10 mol % Ti, 0.01 mmol) and 0.5 mL of stock solution were added to a NMR tube in a N_2-filled glovebox. This was then sealed with a NMR cap and electrical tape before heating at 115 °C for 16 h.

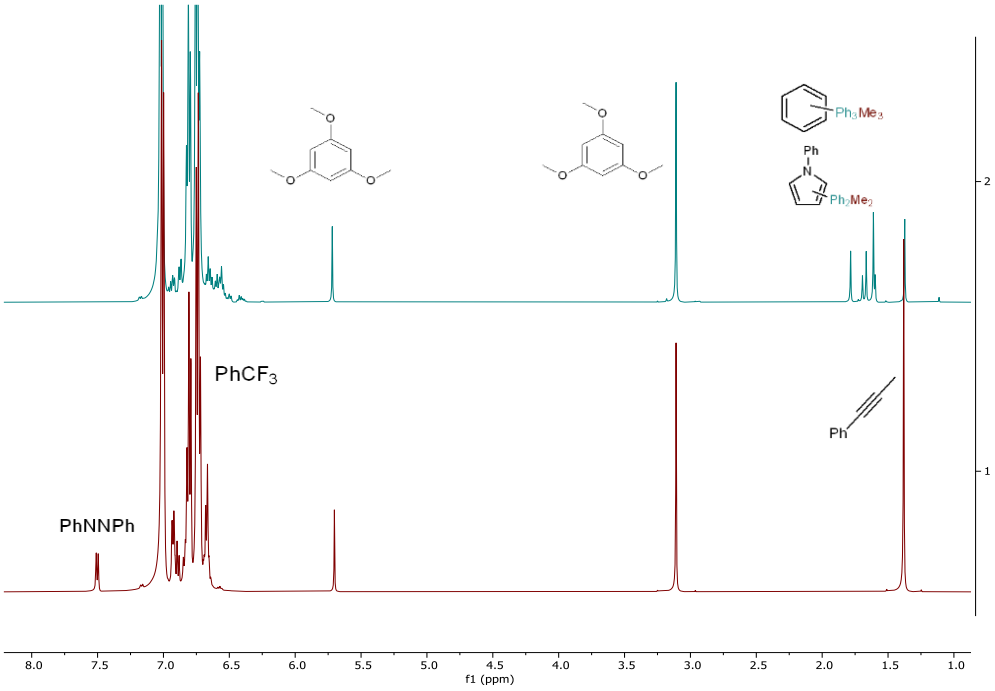

Figure 4.85 Representative stacked catalytic 1H NMR spectra at t = 16 h (2) and t = 0 h (1) in $PhCF_3$ (115 °C/ Precatalyst **4.1**). *Taken from XYS-2020-004F*.

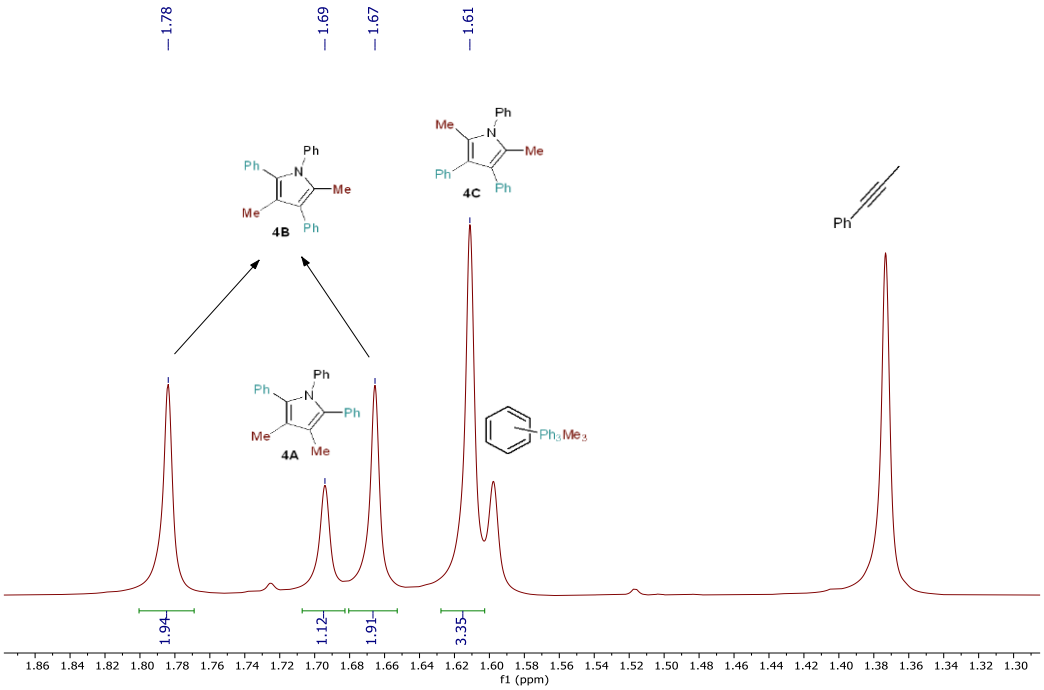

Figure 4.86 Representative zoom-in catalytic ^{1}H NMR spectra at t = 16 h in $PhCF_3$ (115 °C/ Precatalyst **4.1**). *Taken from XYS-2020-004F*.

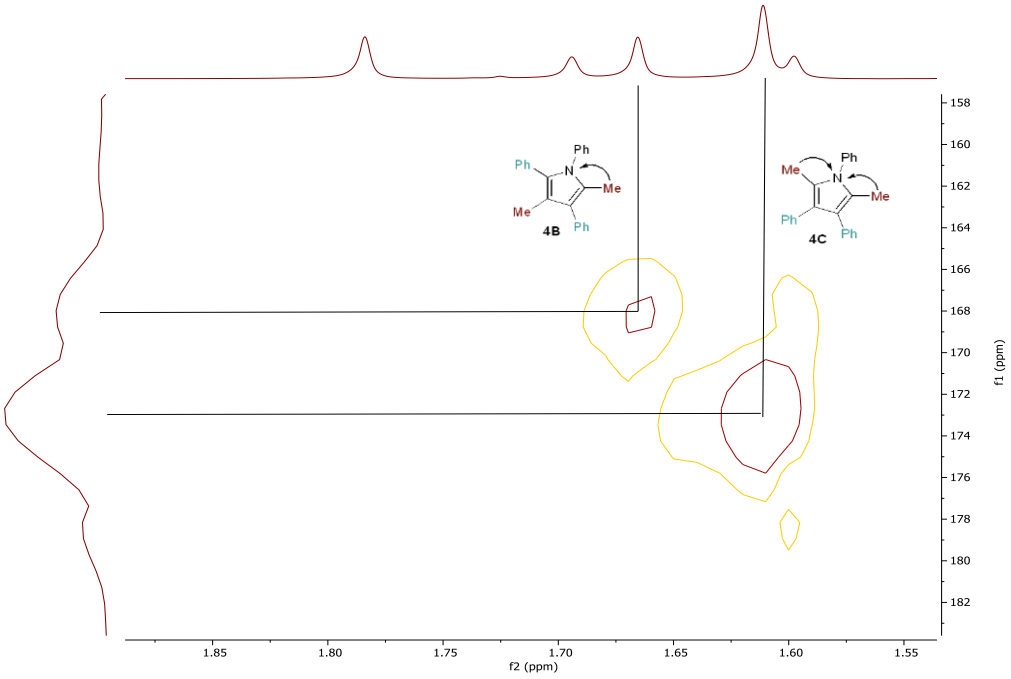

Figure 4.87 Representative catalytic ^{1}H-^{15}N HMBC NMR spectra at t = 16 h in $PhCF_3$ (115 °C/ Precatalyst **4.1**). *Taken from XYS-2020-004F_N HMBC.*

4.6.6 Timepoint studies of catalytic reaction with Precatalyst 4.23

Precatalyst **4.23** (10 mol % Ti, 0.01 mmol, 0.02 M) and 0.5 mL of stock solution were added to a NMR tube in a N_2-filled glovebox. This was then sealed with a NMR cap and electrical tape before heating at 115 °C. Timepoints were taken at regular intervals (hourly for the first 7 hours and then at the end of reaction).

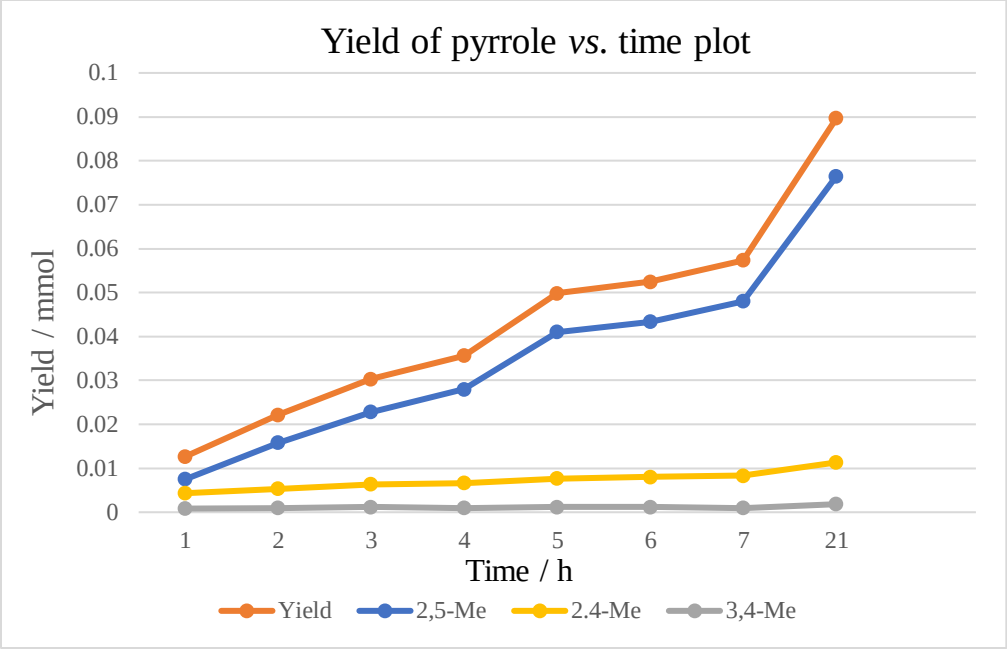

Figure 4.88 Yield of pyrrole *vs.* time for a catalytic reaction with precatalyst **4.23**.

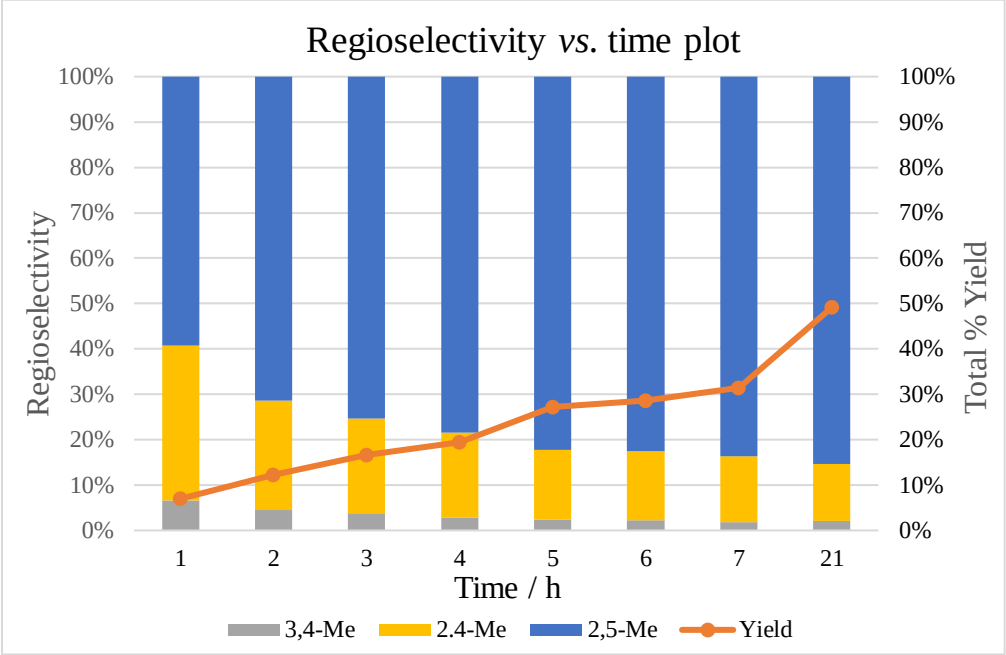

Figure 4.89 Regioselectivity of pyrroles (left axis) and total percent yield of pyrroles (right axis) *vs.* time for a catalytic reaction with precatalyst **4.23**.

4.6.7 Optimization studies with Precatalyst 4.23.

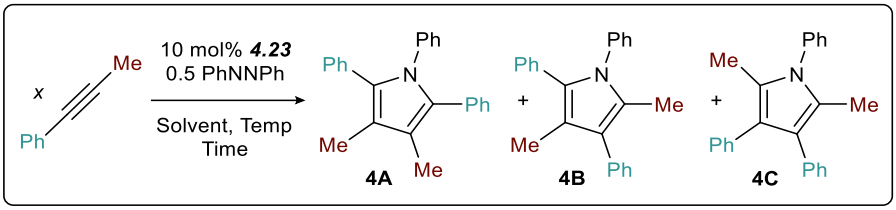

Entry	*x*	Time h	T °C	Solvent	Yield %	Selectivity
1	2.5	16	115	$PhCF_3$	54	11.5
2	2.5	40	100	$PhCF_3$	44	10.1
3	2.5	24	80	$PhCF_3$	7	4.5
4	2.0	16	115	$PhCF_3$	40	9.0
5	2.0	48	100	$PhCF_3$	25	6.6
6[a]	2.5	16	115	$PhCH_3$	35	8.1
7	2.5	16	115	$PhOCH_3$	50	8.1
8	2.5	16	115	PhBr	45	4.9

Conditions: 2.5 equiv (0.5 mmol) or 2.0 equiv (0.4 mmol) phenyl propyne, 0.1 mmol azobenzene, 10 mol % [Ti], 0.5 mL Solvent, Temp °C, Time h.

[a]Due to overlap of product peaks with solvent in ^{1}H NMR, these yields are obtained from quantitative GC-FID. In general, yields observed with GC-FID tend to be lower than NMR.

4.6.8 Isolation attempt of catalytic reaction

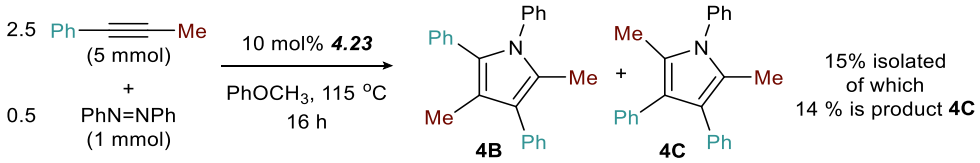

Precatalyst **4.23** (39 mg, 0.1 mmol, 0.1 equiv), azobenzene (182 mg, 1 mmol, 1 equiv), phenyl propyne (0.63 mL, 580 mg, 5 mmol, 5 equiv) and 4.5 mL of anisole were added to a 20 mL scintillation vial equipped with a small stir bar in a N_2-filled glovebox. This was then sealed with a Teflon-lined cap and electrical tape before heating at 115 °C for 16 h. The reaction mixture was dried in *vacuo* while heating at 80 °C for several hours. Crude product was dry loaded under neutral alumina and purified using a long column packed

with neutral alumina using 0 % → 2 % ethyl acetate/hexanes eluent. A mixture of pyrrole regioisomers (Product **4B** and **4C**) was isolated (Mass = 100 mg, 15 % isolated yield).

Product **4C** (2,5-dimethyl-3,4-diphenyl-1-phenyl-1H-pyrrole)

^{1}H NMR (400 MHz, $CDCl_3$): δ 7.43 – 7.39 (m, 2H, *o*-NPh-*H*), 7.34 – 7.31 (m, 2H, *m*-NPh-*H*), 7.28 (br s, 1H, *p*-NPh-*H*), 7.16 – 7.12 (m, 4H, Ar-H), 7.05 – 7.03 (m, 6H, Ar-*H*), 2.00 (s, 6H, *CH_3*).

Peak at 2.05 ppm belongs to product **4B** (2,4-dimethyl-3,5-diphenyl-1-phenyl-1H-pyrrole).

^{13}C NMR (101 MHz, $CDCl_3$): δ 139.0, 136.4, 130.5, 129.3, 128.6, 127.9, 126.0, 125.3, 120.1, 12.1.

Resonances for the last quaternary C could not be positively identified from the rest of the peaks.

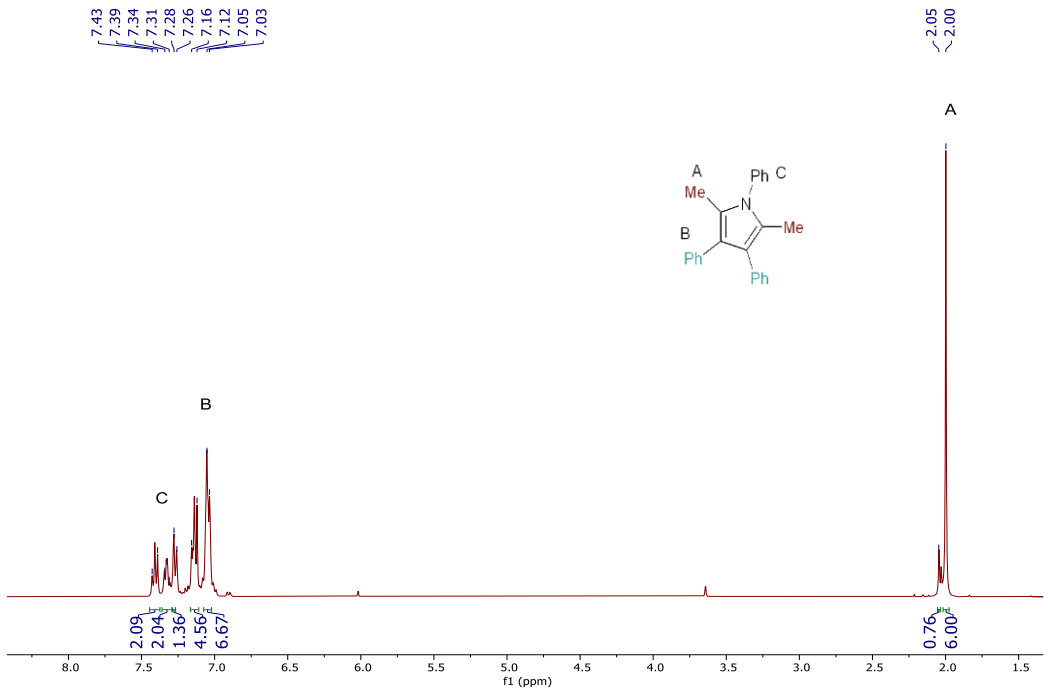

Figure 4.90 ^{1}H NMR spectrum of isolation attempt of product **4C** in $CDCl_3$. *Taken from XYS-2020-022C_Column_F24-51.*

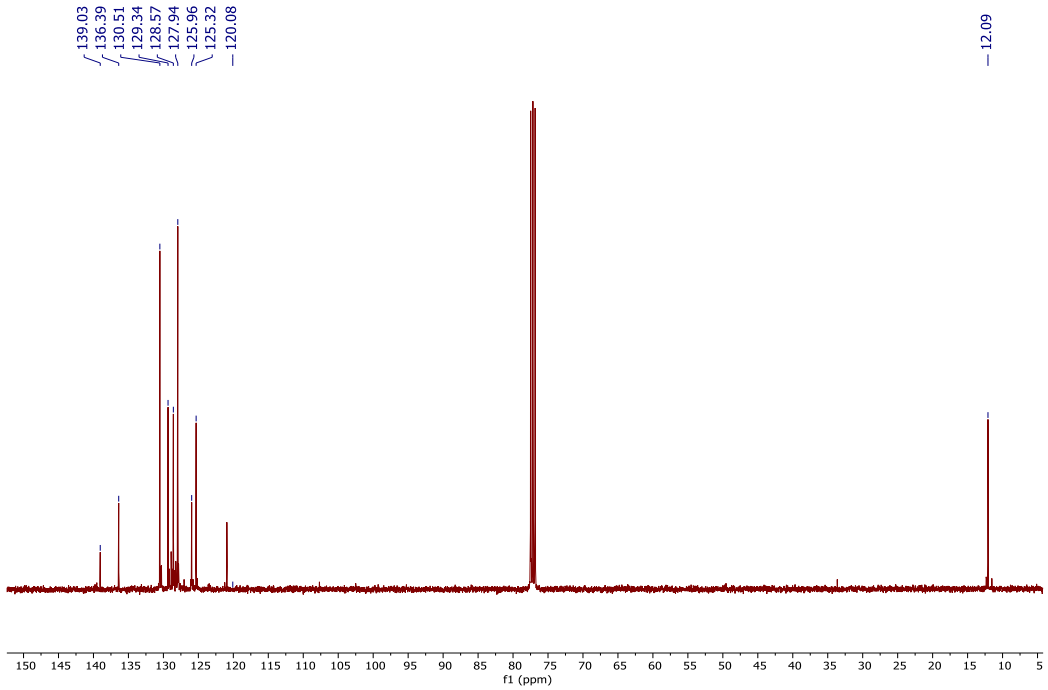

Figure 4.91 ^{13}C NMR spectrum of isolation attempt of product **4C** in $CDCl_3$. *Taken from XYS-2020-022C_Column_F24-51_C.*

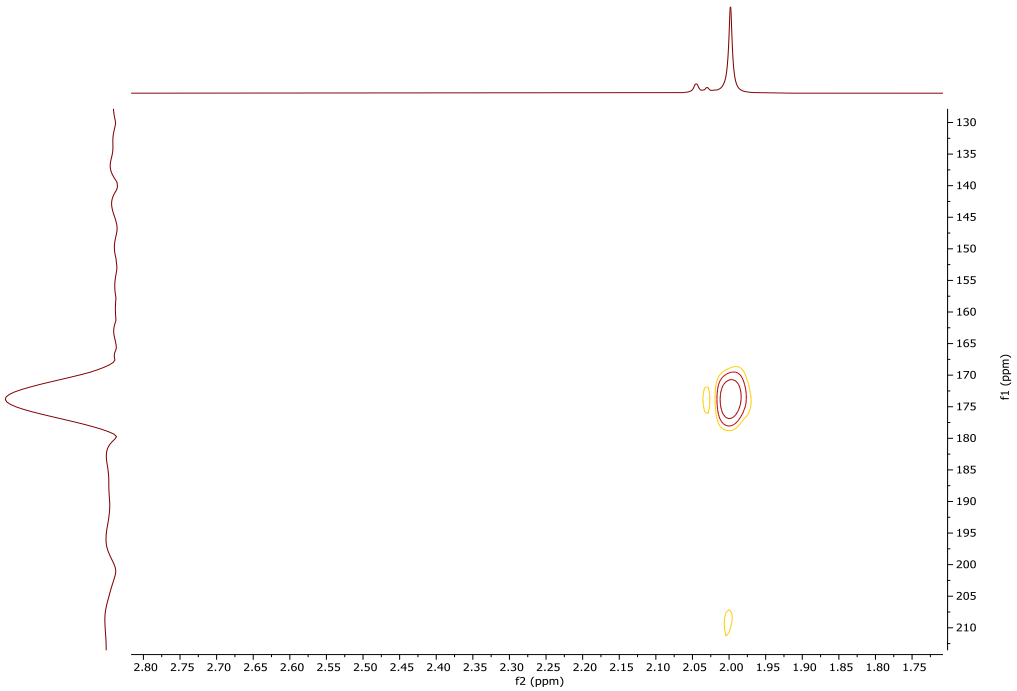

Figure 4.92 ^{1}H-^{15}N NMR spectrum of isolation attempt of product **4C** in $CDCl_3$. *Taken from XYS-2020-022C_Column_F24-51_N HMBC.*

4.6.9 Data for X-ray Structures

Table 4.6 Refined data and cell parameters for X-ray Structures.

	4.7	**4.12**	**4.14**	**4.e**
CCDC Number	1994540	1994543	1994542	1994541
Empirical Formula	$C_{50}H_{62}Cl_4N_6Ti_2$	$C_{30}H_{31}N_5Ti$	$C_{82.52}H_{77.04}N_{10}Ti_2$	$C_{80}H_{78}ClN_2O_3P_3Ti_2$
Formula weight	984.65	509.50	1304.64	1339.60
Temperature (K)	100(2)	125(2)	125(2)	125(2)
a, Å	9.8644(9)	12.9396(11)	9.4737(4)	24.117(3)
b, Å	12.5071(11)	12.9396(11)	36.2928(16)	15.0952(14)
c, Å	12.5128(10)	35.996(4)	19.9562(10)	20.943(2)
α, deg	116.587(2)	90	90	90
β, deg	93.947(3)	90	95.112(2)	114.010(4)
γ, deg	112.994(3)	90	90	90
Volume, Å^3	1213.89(18)	6026.9(12)	6834.2(5)	6964.5(12)
Z	1	8	4	4
Crystal System	Triclinic	Tetragonal	Monoclinic	Monoclinic
Space Group	P -1	P 4_32_12	P $2_1/n$	P $2_1/c$
d_{calc}, gcm^{-3}	1.347	1.123	1.268	1.278
θ range, deg	2.35 to 26.13	2.30 to 26.06	2.37 to 29.93	2.15 to 30.24
μ, mm^{-1}	0.590	0.308	0.288	0.387
Abs. Correction	Multi-scan	Multi-scan	Multi-scan	Multi-scan
GOF	1.058	1.071	1.065	1.227
R_1 ,[a]	$R1$ = 0.0506	$R1$ = 0.0237	$R1$ = 0.1068	$R1$ = 0.1468
wR_2 [b] [I>2σ(I)]	$wR2$ = 0.1390	$wR2$ = 0.0617	$wR2$ = 0.1152	$wR2$ = 0.1525

[a] $R_1 = \sum||F_o| - |F_c||/\sum|F_o|$. [b] $wR_2 = [\sum[w(F_o^2-F_c^2)^2]/\sum[w(F_o^2)^2]^{1/2}$.

4.6.10 General considerations for Principal Component Analysis work

All analysis, data mining and visualization were performed using a Matlab script developed in-house (see supporting information for additional details). The script was performed on a commercial MacBook Air using a 1.8 GHz Intel Core i5 and required a run time of roughly 30-500 s depending on the search method. PCA was performed using the singular value decomposition (SVD) method. Generation of correlation tables, PCA maps and regression statistics were all automated through the script.

4.6.11 Descriptor Set Details methodology

The 22 variables shown below were calculated at the M06/6-311g(d,p) level of theory for each catalyst in accordance with previous computational experiments.[82] Variables denoted with "*catalyst*" were calculated using the monomer of the corresponding N-Ph Ti imido complex. Variables denoted with "*free pyridine*" are calculated for the corresponding free pyridine. "*X*" and "*L*" denotations refer to X- and L-type ligands around the Ti-center.

- Starting points for catalyst geometry optimization were either crystal structures if available or structures modified using the structure viewer, Avogadro. Geometric parameters were averaged when appropriate.
- *% buried volume* was calculated using the online module, SambVca 2.1.[254]
- NMR chemical shifts were calculated using gauge independent atomic orbitals and scaled according to the CHESHIRE CCAT website.[262]
- All ortho atom related shifts were averaged across the relevant positions.
- *Ti-X donor BDE*'s were tabulated from the Lange's Handbook of Chemistry[263] and references therein.
- *Composite donor atom polarizability* were calculated using the static dipole polarizability of the neutral atoms[264] surrounding the Ti center of each catalyst weighted by the number of atoms.
- *Mulliken electronegativities* (EN) were tabulated from Bratsch.[265]
- *Free L ligand quadrupole moment* refers to the Q_{zz} quadrupole vector.

- *Proton affinity* was calculated as the sum of all thermal and free energies using the equation: Proton Affinity = LH – ($L + H^+$).

Table 4.7 List of all descriptors included in initial PCA basis set.

Descriptor Index	Descriptors
1	Catalyst HOMO
2	Catalyst LUMO
3	Free pyridine HOMO
4	Free pyridine LUMO
5	% Buried Volume
6	Free pyridine *p*- ^{13}C NMR shift
7	Free pyridine *o*- ^{13}C NMR shift
8	Catalyst-bound pyridine *p*- ^{13}C NMR shift
9	Catalyst-bound pyridine *p*- ^{13}C NMR shift
10	Composite donor atom polarizability
11	Ti-X donor BDE
12	X donor Mulliken EN
13	Free pyridine quadrupole moment
14	Free pyridine N Mulliken charge
15	Catalyst-bound pyridine N Mulliken charge
16	Catalyst-bound X donor atom Mulliken charge
17	Free pyridine proton affinity
18	Imido-Ti-N_{py} angle
19	Ti-imido bond length
20	Ti- N_{py} bond length
21	Ti-X bond length
22	X-Ti-X angle

4.6.12 Automated Script Details

Overview

A Matlab script called *PCA4U2* was developed in-house in order to facilitate *de novo* catalyst design using principal component analysis (PCA). The script is designed for non-expert end users and uses a series of prompts to direct users. The script presents the option for regression *via* unsupervised principal component analysis (PCA), iterative supervised PCA (ISPCA), weighted PCA, or subspace specific PCA (determined by k-means clustering) and the associated computational costs as well as the option to use a previously determined basis set. Linear regression is conducted against the top 3 components. Data must be inputted as instructed. The catalyst variable matrix should be added as a numeric matrix with each column corresponding to a new variable and each row corresponding to a new catalyst. The script will automatically center and normalize each variable by standard deviation. Observables must be added as a single column vertical vector containing positive values.

Search algorithm details

Unsupervised PCA: Unsupervised PCA conducts PCA on the variable basis set without modification.

ISPCA: ISPCA is conducted with two search options: find the best possible fit or find the best possible fit with the lowest number of variables. Fit in all cases was determined by R^2. While Q^2 is the more desirable statistical parameter for predictive power, computational costs precluded its general use (a 22-variable basis set with a 14-catalyst training set requires ~ 2.1 million calculations for R^2 and ~ 62 million calculation for Q^2). Searches are performed by conducting PCA on each combination of 2 variables and iteratively increasing the group size to the total number of variables. The best fit of each combination is collected and stored in a matrix. Optimization toward the best possible fit was accomplished by searching this matrix for the highest R^2 value. Optimizing toward the lowest number of variables was accomplished by terminating the search loop when R^2 of the current group became lower than the previous group.

Weighted PCA: Weighted PCA was performed by conducting unoptimized PCA on the full variable basis set and determining the pairwise distances between a test catalyst and the remaining training set. These distances were transformed into coefficients for each catalyst by applying the following function: $coefficient = e^{-distance/25}$. ISPCA or unsupervised PCA can be conducted with this weighted catalyst set.

Subspace selective ISPCA: ISPCA performed on a selected PCA subspace was accomplished by conducting unsupervised PCA on the full catalyst/variable set and using a dynamic k-means clustering algorithm (the number of clusters was increased iteratively until intracluster distances no longer decreased substantially) to identify which cluster contains the desired "test" catalyst. This cluster was considered the initial PCA subspace. ISPCA was then conducted on this subspace. The R^2 value of the optimal variable basis set was stored. The next closest catalyst to the subspace was identified using pairwise distances from the initial unsupervised PCA space. This nearest neighbor was added to the subspace and ISPCA was again conducted. This process was iterated until the R^2 of the current subspace fell below an arbitrary cutoff of $R^2 = 0.99$.

Output details

All PCA was conducted using the native Matlab *pca* function. ISPCA was conducted using the native *nchoosek* function and a homebrewed algorithm. The script displays 7 figures for qualitative and quantitative multivariate analysis using PCA.

- *Figure 1* shows a variable Pearson correlation matrix on the left and univariate analysis on the right (See Figure 4.93). An additional figure will appear showing the best univariate fit if the maximum R^2 of the univariate analysis exceeds 0.9.
- *Figure 2* is a Scree-type plot showing each principal component's contribution to the total data variance (See Figure 4.94).
- *Figure 3* shows the data recast over the new PCA axes as a biplot and grouped using k-means clustering (See Figure 4.95). Dynamic k-means clustering is achieved using the native Matlab *ischange* function to determine the proper number of partitions in the corresponding Voronoi cells.

- *Figure 4* shows the model fit as a predicted *vs.* experimental values plot. Script will output basic statistics (including last one out cross validation) and equation to linear least squares fit regression (See Figure 4.96). Note that the regression equation is related to the centered and standard deviation normalized data.
- *Figure 5* shows a color coordinated PCA map in 3 dimensions where the coordinate space is correlated against the entered observable (See Figure 4.97). Color banding is set to the error in the regression and constructed using an interpolated patch object.
- *Figure 6* is a 2D projection of *Figure 5* against desired principal components for publication/presentation purposes (See Figure 4.98).
- *Figure 7* is a plot of pairwise PCA Euclidean distance versus pairwise observable change to demonstrate how different a new catalyst must be from the parent – this metric is an effective molecular ruler for catalyst design (See Figure 4.99). The coloration is based on successively increasing standard deviations (σ) in the pairwise observable change starting from zero (red) to $3\times\sigma$ (green).

Prediction of new data

The final portion of the script is designed to predict new data. The script outputs a variety of scaling vectors and regression coefficients.

- *groups* contains the regression statistics for alternate variable groupings.
- *groupwinner* contains the optimized variable basis set.
- *PCRreal* contains the normalized coefficients of each variable in the chosen principal component regression.
- *PCR* contains the regression coefficients associated with correlating PCA space and observable.
- *meann* and *stdd* are the mean and standard deviation of each column in the supplied data set, respectively.
- *Loadings* are the variable loadings in the displayed components.
- *Yreal* are the model's predicted values for the observable.
- *Scores* are the normalized scores of each observable in PCA space.

- *LOOpredicts* are the prediction values for leave one out cross validation. The corresponding regression coefficients are denoted *LOOCV Qsquared*).

For subspace selective ISPCA the following additional values are generated:

- *Newtrainingset* is the culled catalyst training set.
- *Newobservable* are the observables for the catalysts found in the desired PCA subspace.
- *Neworder* are the indices for *Newobservable*.

The value of any observable (e.g. catalytic selectivity) can be predicted using the following equation, where *predict* is the vector of variables and *observable* is the accompanying observable: ((((predict./stdd)-meann)*loadings)*PCR)+mean(observable).

The end of the script can compute these values for the user. Note the variable vector must be constructed from the appropriate basis set.

Output examples

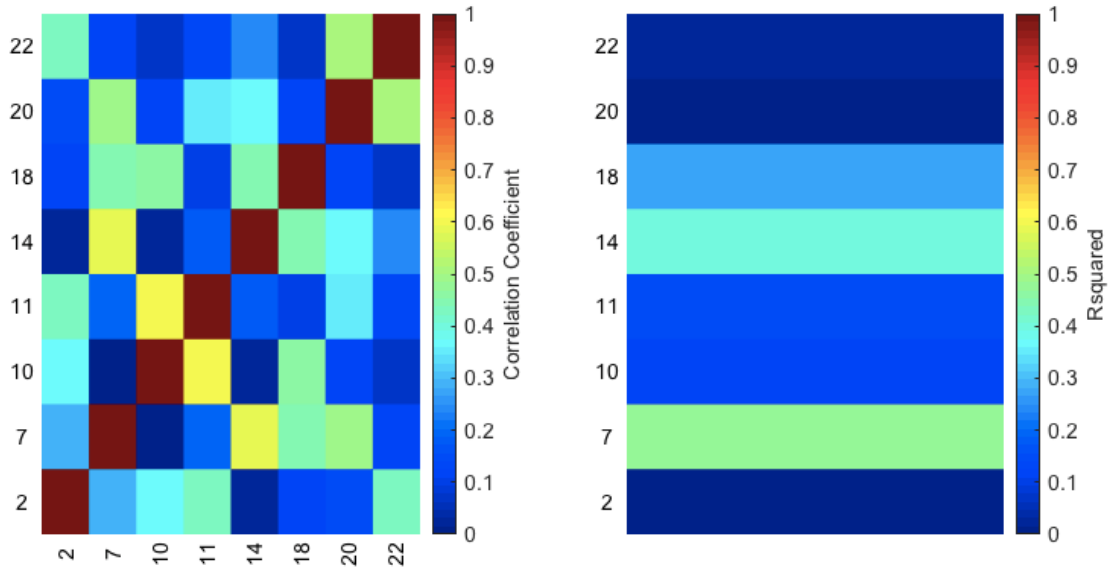

Figure 4.93 Pearson variable correlation matrix (left) and univariate analysis (right); from Figure 1 of *PCA4U2*.

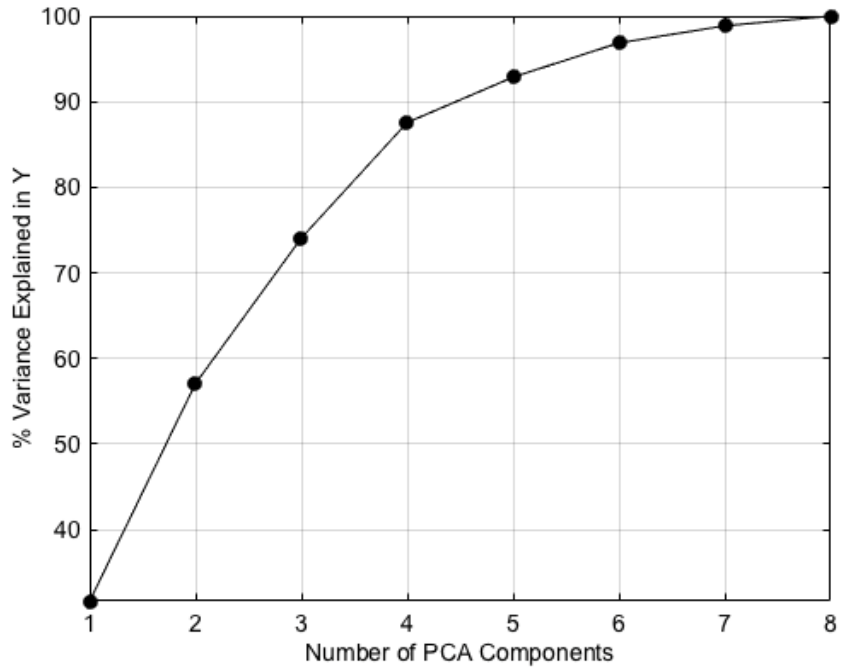

Figure 4.94 Variable Scree-type plot; from Figure 2 of *PCA4U2*.

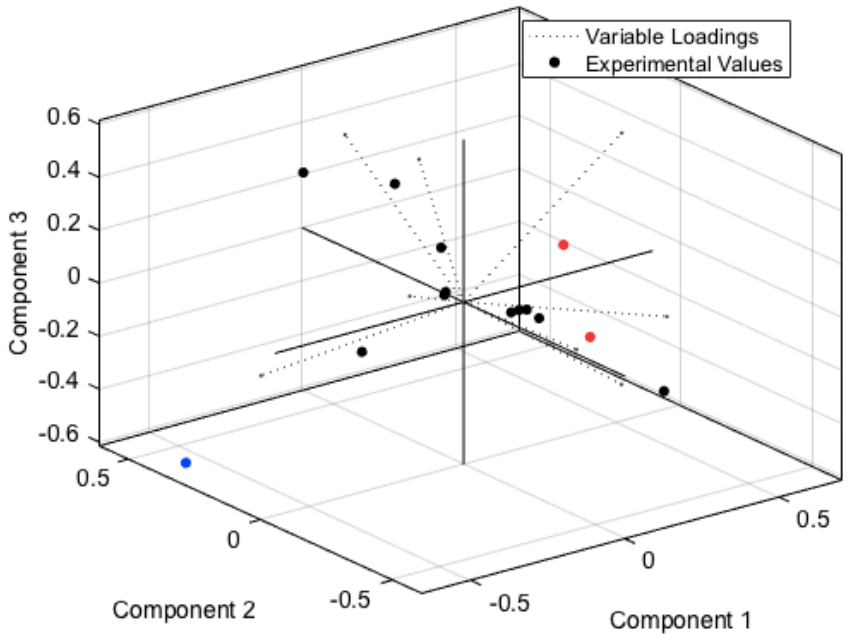

Figure 4.95 PCA-space biplot colored using dynamic k-means clustering; from Figure 3 of *PCA4U2*.

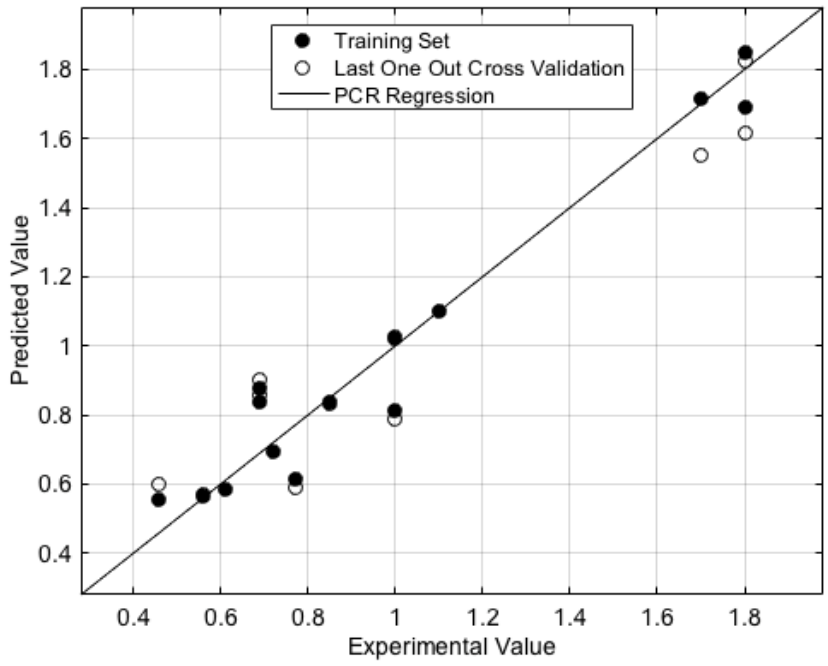

Figure 4.96 Regression fit using linear least squares fitting; from Figure 4 of *PCA4U2*.

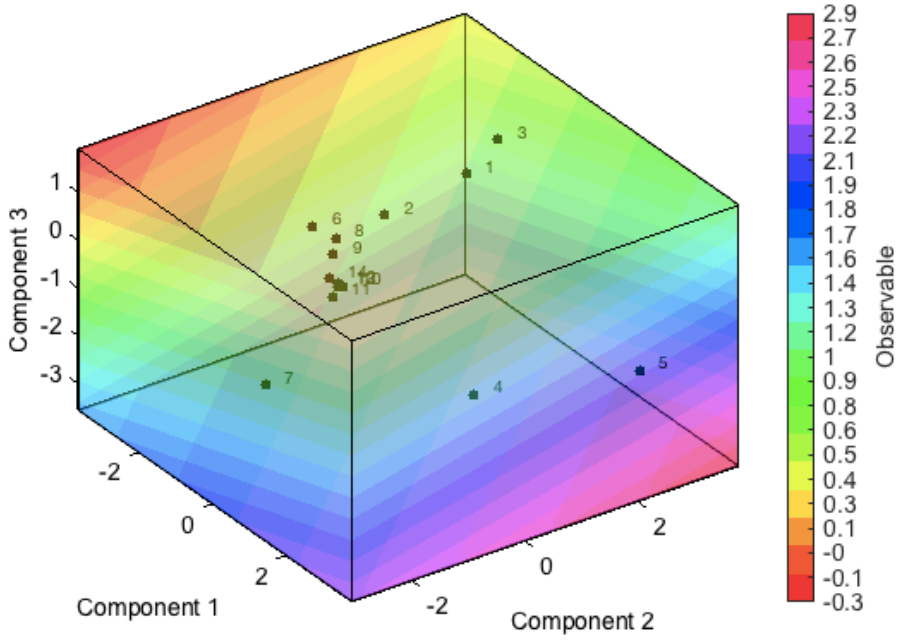

Figure 4.97 3D PCA map colored according to linear regression between catalyst PCA scores and corresponding observable values; from Figure 5 of *PCA4U2*.

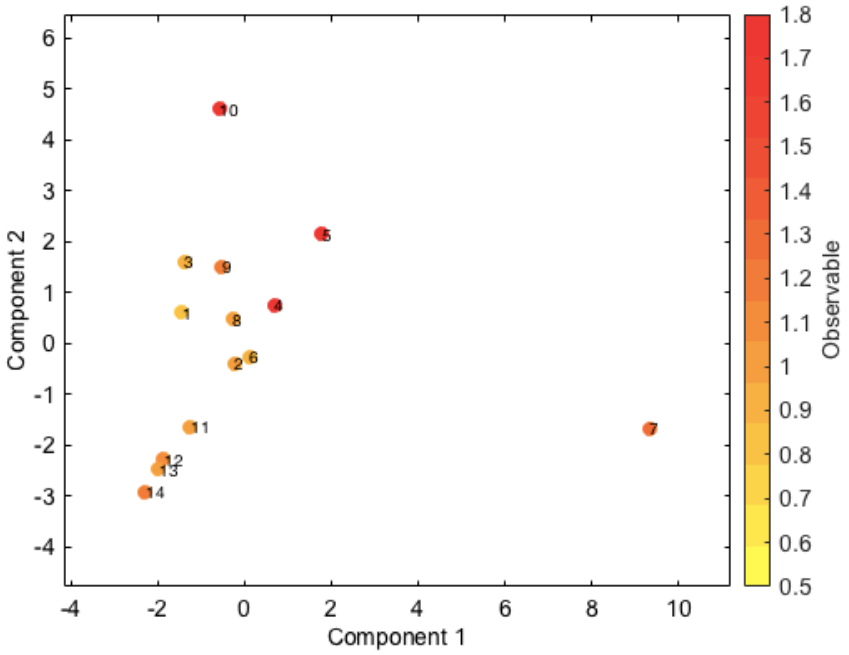

Figure 4.98 2D PCA map projection showing principal component 1 *vs.* 2, colored according to catalyst selectivity; from Figure 6 of *PCA4U2*.

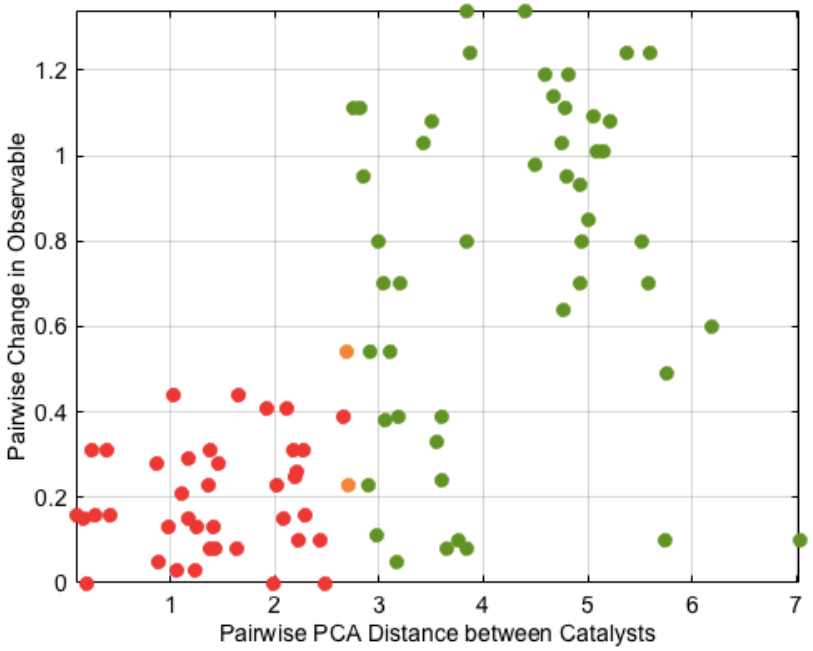

Figure 4.99 "Molecular ruler" plot constructed from pairwise Euclidean distances between catalyst PCA scores and catalyst selectivity; from Figure 7 of *PCA4U2*.

4.6.13 Additional PCA Modelling Data Details

Included below are supplementary principal component-based models and the corresponding fit statistics. Refer to PCAModellingData-SI.exe file for the complete data set.

PCA = Principle component analysis.

ISPCA = Iterative supervised principle component analysis.

PLSR = Partial least squares regression method reported by the Rothenberg lab.[241]

PCA Model IA: Constructed using unoptimized PCA with catalysts **4.1**-**4.14** as the training set.

Table 4.8 Variable loadings in PC1-PC3 and summed regression coefficients in model IA.

Variable Index	Variables	Component 1	Component 2	Component 3	Weights(x 10^3)
1	Catalyst HOMO	-0.295	-0.178	0.053	-28.1
2	Catalyst LUMO	0.232	-0.266	0.033	-14.3
3	Free pyridine HOMO	0.323	-0.109	-0.041	-0.1
4	Free pyridine LUMO	-0.272	0.069	0.105	4.3
5	% Buried Volume	-0.222	-0.126	0.255	-0.2
6	Free pyridine *p*-^{13}C NMR shift	0.305	-0.094	-0.058	-1.0
7	Free pyridine *o*-^{13}C NMR shift	0.198	0.087	0.360	52.2
8	Catalyst-bound pyridine *p*-^{13}C NMR shift	0.305	-0.106	-0.088	-5.0
9	Catalyst-bound pyridine *o*-^{13}C NMR shift	0.094	0.149	0.413	58.8
10	Composite donor atom polarizability	0.038	0.424	-0.174	30.8
11	Ti-X donor BDE	0.066	-0.231	0.246	1.4
12	X donor Mulliken EN	0.133	-0.002	0.205	25.1
13	Free pyridine quadrupole moment	-0.321	0.068	0.041	-4.2
14	Free pyridine N atom Mulliken charge	-0.012	-0.143	-0.407	-53.8
15	Catalyst-bound pyridine N atom Mulliken charge	-0.261	0.024	-0.202	-28.7
16	Catalyst X donor atom Mullken charge	0.162	0.366	-0.100	37.4
17	Free pyridine proton affinity	-0.317	0.089	-0.023	-7.7
18	Imido-Ti-N_{py} angle	0.010	-0.130	0.279	12.6
19	Ti-imido bond length	-0.127	-0.415	-0.137	-63.1
20	Ti-N_{py} bond length	0.018	0.171	0.315	48.4
21	Ti-X donor bond length	0.068	0.431	-0.121	37.9
22	X-Ti-X donor angle	-0.235	0.104	0.213	19.7
				R^2/Q^2	0.49/-0.19

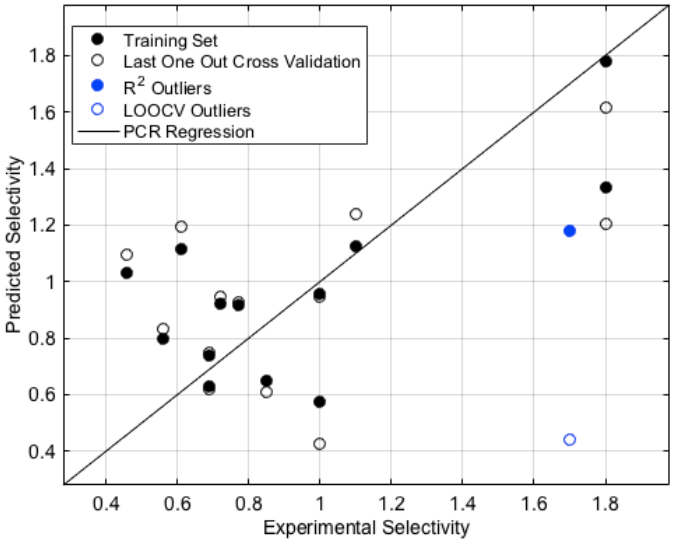

Figure 4.100 Predicted *vs.* experimental selectivity determined by PCA model IA.

PCA Model IB: Constructed using ISPCA with catalysts **4.1**-**4.14** as the training set.

Table 4.9 Variable loadings in PC1-PC3 and summed regression coefficients in model IB.

Variable Index	Variables	Component 1	Component 2	Component 3	Weights(x 10^2)
2	Catalyst LUMO	0.267	-0.459	0.071	-3.7
7	Free ligand: ^{13}C NMR *o*-atom to Ldonor	0.474	0.125	-0.387	18.9
10	Composite donor atom polarizability	-0.336	0.378	-0.345	12.1
11	Ti-Xdonor BDE	0.418	-0.112	0.558	-16.7
14	Free ligand Ldonor atom Mulliken charge	-0.426	-0.293	0.291	-16.4
18	Imido-Ti-Ldonor angle	0.390	-0.144	-0.369	15.3
20	Ti-Ldonor distance	0.284	0.501	0.220	-1.1
22	Xdonor-Ti-Xdonor angle	0.052	0.511	0.382	-8.8
				R^2/Q^2	0.95/0.92

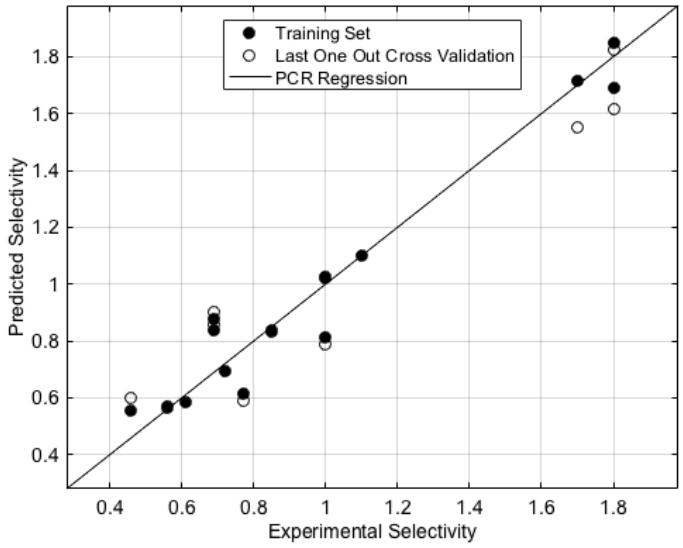

Figure 4.101 Predicted *vs.* experimental selectivity determined by PCA model IB.

PLSR Model IC: Constructed using the PLSR model with catalysts **4.1-4.14** as the training set.

Table 4.10 Variable loadings in PC1-PC3 in model IC.

Variable Index	Variables	Component 1	Component 2	Component 3
7	Free pyridine *o*-^{13}C NMR shift	0.198	0.087	0.360
9	Catalyst-bound pyridine *o*-^{13}C NMR shift	0.094	0.149	0.413
10	Composite donor atom polarizability	0.038	0.424	-0.174
11	Ti-X donor BDE	0.066	-0.231	0.246
18	Imido-Ti-N_{py} angle	0.010	-0.130	0.279
			R^2/Q^2	0.82/0.58

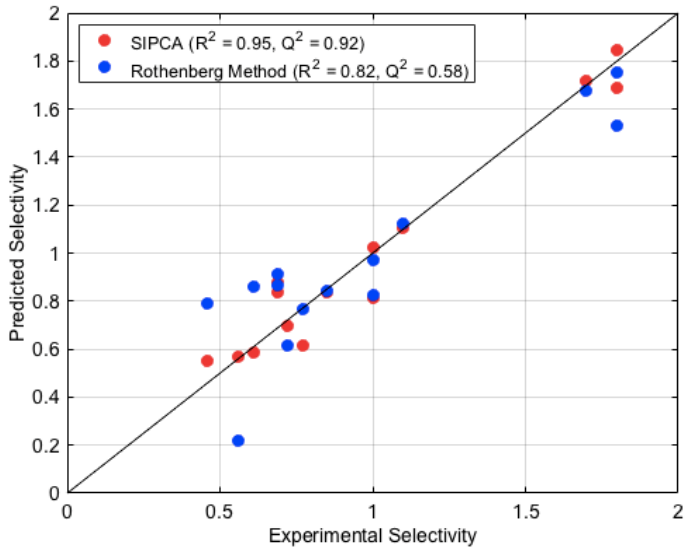

Figure 4.102 Comparison of predicted *vs.* experimental selectivity plots calculated by ISPCA (red) and PLSR model (blue).

PCA Model IIA: Constructed using ISPCA with catalysts **4.1-4.22** as the training set.

Table 4.11 Variable loadings in PC1-PC3 and summed regression coefficients in model IIA.

Variable Index	Variables	Component 1	Component 2	Component 3	Weights
6	Free pyridine *p*-^{13}C NMR shift	0.599	0.416	-0.684	4.4
8	Catalyst-bound pyridine *p*-^{13}C NMR shift	0.609	0.319	0.727	-5.0
15	Catalyst-bound pyridine N atom Mulliken charge	-0.520	0.852	0.062	-2.0
				R^2/Q^2	0.73/0.14

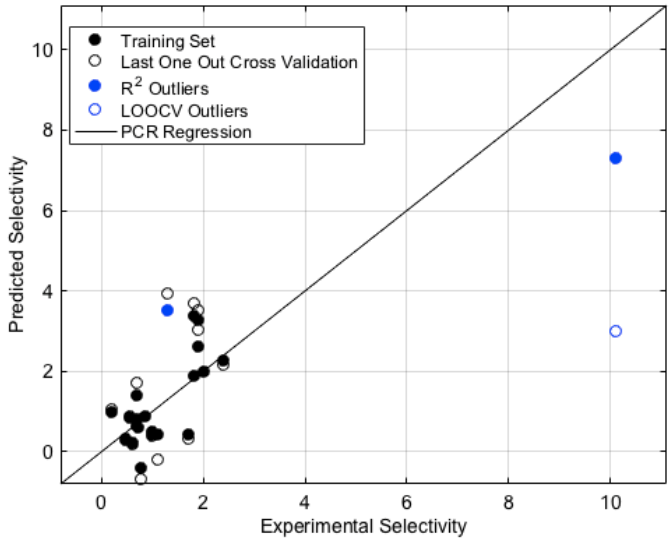

Figure 4.103 Predicted *vs.* experimental selectivity determined by PCA model IIA.

PCA Model IIB: Constructed using ISPCA with catalysts **4.1-4.22**, sans **4.18**, as the training set.

Table 4.12 Variable loadings in PC1-PC3 and summed regression coefficients in model IIB.

Variable Index	Variables	Component 1	Component 2	Component 3	Weights(x 10^2)
1	Catalyst HOMO	-0.482	0.125	0.428	-8.9
4	Free pyridine LUMO	-0.286	-0.346	0.665	12.4
7	Free pyridine *o*-^{13}C NMR shift	0.574	0.029	0.352	21.7
9	Catalyst-bound pyridine *o*-^{13}C NMR shift	0.541	0.060	0.449	21.7
10	Composite donor atom polarizability	0.193	-0.489	-0.126	15.2
12	X donor Mulliken EN	-0.107	0.564	0.178	-13.7
20	Ti-N_{py} bond length	0.122	0.551	-0.040	-10.9
				R^2/Q^2	0.89/0.85

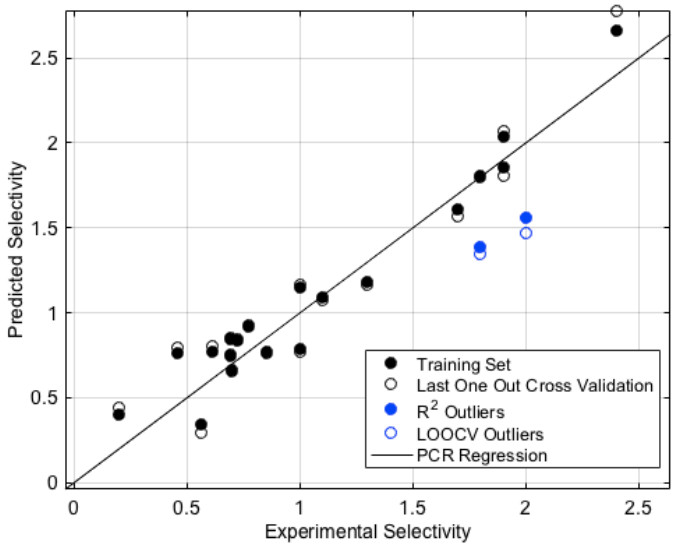

Figure 4.104 Predicted *vs*, experimental selectivity determined by PCA model IIB.

PCA Model IIC: Constructed using ISPCA with catalysts **4.4**, **4.5**, **4.15**, **4.16**, **4.18-4.20** as the training set (determined by a dynamic k-means clustering search algorithm, *vide supra*).

Table 4.13 Variable loadings in PC1-PC3 and summed regression coefficients in model IIC.

Variable Index	Variables	Component 1	Component 2	Component 3	Weights
6	Free pyridine *p*-^{13}C NMR shift	0.566	-0.273	0.778	10.3
8	Catalyst-bound pyridine *p*-^{13}C NMR shift	0.581	-0.086	-0.430	-5.4
18	Imido-Ti-N_{py} angle	0.253	0.955	0.152	3.9
20	Ti-N_{py} bond length	-0.527	0.072	0.433	5.4
				R^2/Q^2	0.99/-0.07

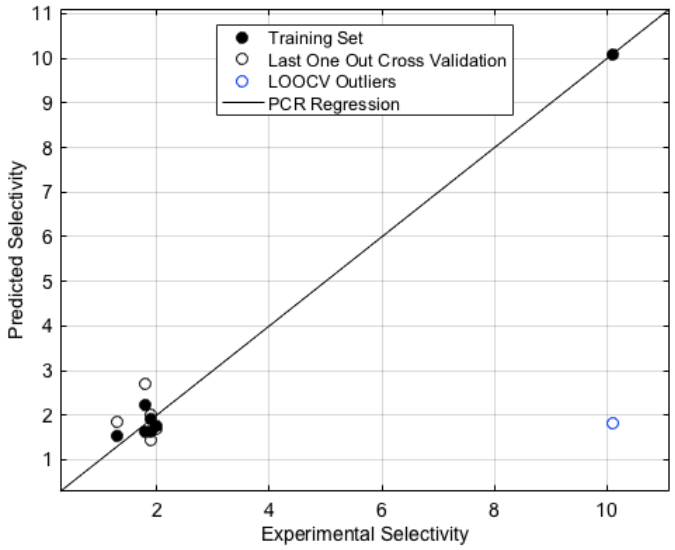

Figure 4.105 Predicted *vs.* experimental selectivity determined by PCA model IIC.

PCA Model IID: Constructed using ISPCA with exponential weighting on catalysts **4.1-4.22** as the training set (weights set according to pairwise distances to catalyst **4.18** in unoptimized PCA space, *vide supra*).

Table 4.14 Variable loadings in PC1-PC3 and summed regression coefficients in model IID.

Variable Index	Variables	Component 1	Component 2	Component 3	Weights
3	Free pyridine HOMO	-0.407	0.877	-0.112	13.1
7	Free pyridine *o*-^{13}C NMR shift	0.409	0.170	-0.118	6.1
8	Catalyst-bound pyridine *p*-^{13}C NMR shift	0.408	0.318	0.840	-25.1
9	Catalyst-bound pyridine *o*-^{13}C NMR shift	0.409	0.155	-0.262	10.9
18	Imido-Ti-N_{py} angle	0.408	0.275	-0.420	17.6
20	Ti-N_{py} bond length	0.409	-0.043	-0.152	5.0
				R^2/Q^2	0.94/0.77

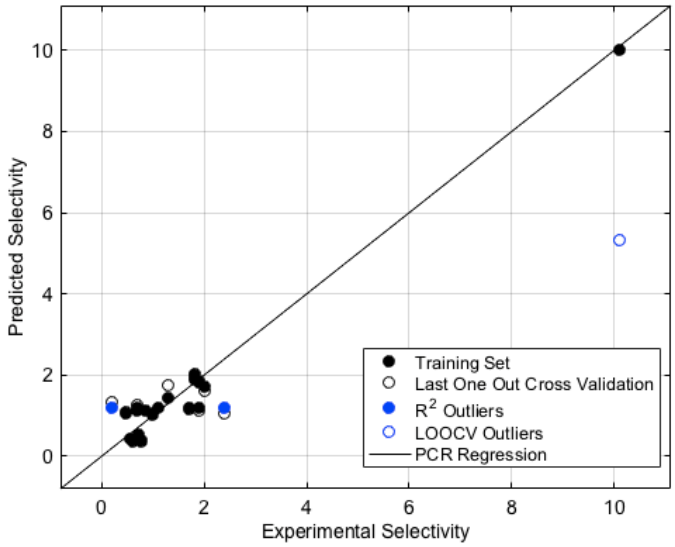

Figure 4.106 Predicted *vs.* experimental selectivity determined by PCA model IID.

Table 4.15 Pairwise Euclidean distances from catalyst **4.1** to all catalysts using different PCA models.

	Model Ia	Model Ib	Model IIa	Model IIb	Model IIc	Model IId
Catalyst ID	Pairwise Distance	Pairwise Distance	Pairwise Distance	Pairwise Distance	Pairwise Distance	Pairwise Distance
4.1	0.00	0.00	0.00	0.00	0.00	0.00
4.2	1.73	1.38	1.82	1.07	1.60	11.80
4.3	1.05	1.17	0.36	1.79	0.35	17.09
4.4	2.93	3.84	1.01	1.60	1.38	23.52
4.5	5.85	4.39	1.43	3.43	0.23	19.54
4.6	2.92	2.43	0.68	2.16	1.39	34.02
4.7	11.20	4.77	4.68	4.65	5.80	114.26
4.8	1.99	2.22	0.40	0.96	1.29	29.57
4.9	2.66	2.92	0.33	1.89	1.35	62.11
4.1	5.34	5.37	0.37	3.60	1.17	187.71
4.11	2.35	2.89	0.51	0.93	1.48	42.45
4.12	2.96	2.66	0.43	0.97	1.30	41.76
4.13	3.17	2.70	0.39	1.02	1.34	41.47
4.14	3.64	2.69	0.39	1.01	1.28	41.68
4.15	2.46	2.41	0.54	2.55	0.51	27.28
4.16	7.39	6.53	3.89	3.27	3.51	56.68
4.17	7.63	8.30	3.78	4.79	4.52	192.77
4.18	9.06	7.54	4.63	4.43	3.87	65.32
4.19	5.91	4.93	3.39	2.29	3.15	58.11
4.2	6.79	7.08	3.30	4.51	3.12	193.48
4.21	3.53	3.28	0.78	0.91	1.16	170.25
4.22	6.11	3.20	2.78	1.94	2.64	170.01
4.23	9.31	7.64	4.46	3.65	4.76	62.28
4.24	5.41	7.01	1.61	2.93	4.62	55.82
4.25	4.23	3.75	2.93	4.13	3.05	174.75
4.26	8.89	7.37	1.74	2.68	1.64	34.60

* Boxes in grey refer to catalysts that were not included in the initial PCA training set.

4.6.14 General considerations for computational work

Geometry optimizations were performed using Gaussian 16 program version c01.[266] All geometry optimizations and frequency calculations were performed using the M06 functional,[267] def2-SVP basis set,[268] and the SMD solvation model[269] with the experimentally used solvent $PhCF_3$ (ε = 9.18) as the solvent. All geometries were characterized by frequency analysis calculations to be local minima (without any imaginary frequency) or transition states (with only one imaginary frequency). All vibrational frequencies below 50 cm^{-1} were replaced with values of 50 cm^{-1} due to the breakdown of the harmonic oscillator model for low frequency vibrational modes. Zero-point vibrational energies and thermal contributions to electronic energy were calculated at 388.15 K and 1 atm. All computational geometries are given in XYZ format as supplementary materials (SelectivityGeometries.xyz, PCAGeometries.xyz). The information of each geometry is given at the line after atom numbers in the following format:
catalyst-configuration-intermediate: free energy before/after frequency correction.

Limited by the size of the systems (78 atoms), a relatively small def2-SVP basis set for all geometry optimization and frequency calculations was used. In Table S10, $\Delta G^{\ddagger}$(TS2) was calculated by summing up the electronic energy at various DFT functionals with def2-TZVPP basis set (otherwise labelled) and thermal free energy correction at M06/def2-SVP level. Although the $\Delta G^{\ddagger}$(TS2) is vastly different depending on the functionals, the $\Delta\Delta G^{\ddagger}(TS2_{BE} - TS2_{BF})$ is very similar for all functionals. Therefore, the $\Delta\Delta G$(IM3) and $\Delta\Delta G^{\ddagger}$(TS2) values calculated by M06/def2-SVP are reliable.

Table 4.16 Gibbs free energies calculated by various DFT functionals with def2-TZVPP basis set.

$E_{high}+\Delta G_{low}^{corr}$	$TS2_{AC}$	$TS2_{AD}$	$TS2_{BE}$	$TS2_{BF}$
BP86	35.1	34.8	34.0	30.7
M06/def2SVP	44.2	43.4	43.3	39.8
MN15L	44.8	44.0	43.9	40.1
M06-D3	47.8	46.9	46.9	43.3
PW6B95D3/def2TZVP	47.5	47.0	47.3	43.9
B3LYP	50.3	49.4	49.7	46.2
M06L-D3	51.3	40.8	49.4	47.0
M06-L	55.4	55.0	53.6	51.3
M06	56.5	55.8	55.9	52.4

4.6.15 Computed reaction pathways for catalysts studied

Dissociation energy of pyridine at intermediate energy IM3 is defined as

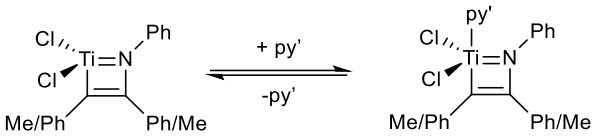

$$\Delta G_{diss} = \Delta G(IM3, L_n = Cl_2) + \Delta G(py') - \Delta G(IM3, L_n = Cl_2py')$$

Six-coordinate TS2 has three possible configurations that were considered in the following reaction pathways. These configurations differ depending on the relative position of the pyridine and attacking alkyne.

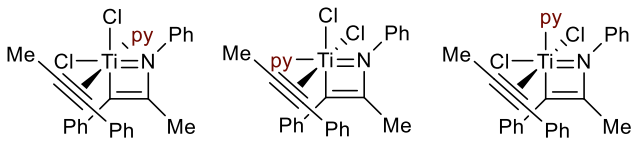

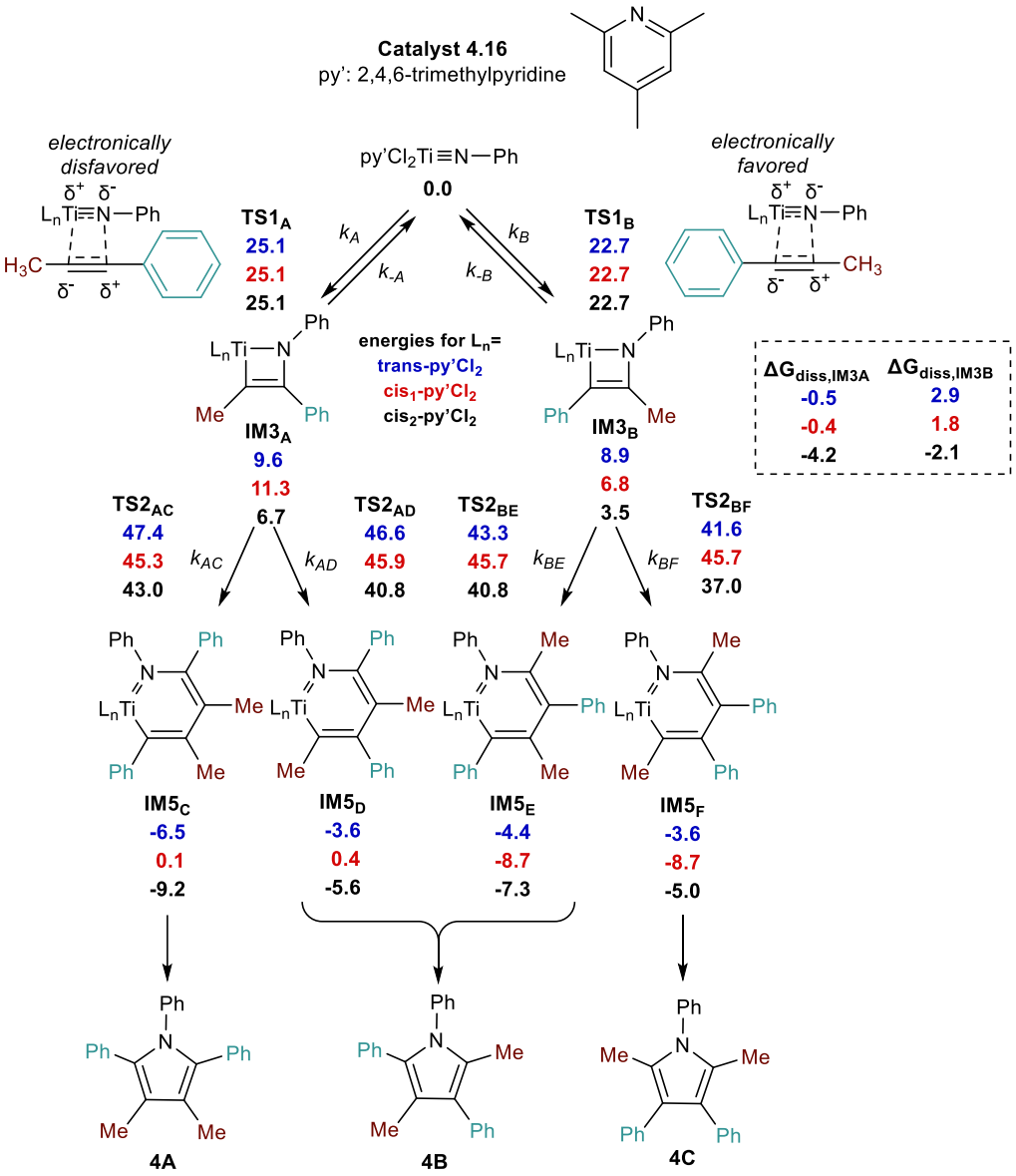

Figure 4.107 Calculated transition state barriers (TS1 and TS2) and intermediate free energies (IM3 and IM5) in kcalmol^{-1} for catalyst **4.16** at *trans*- (blue), *cis*-1 (red) and *cis*-2 (black) configurations. Dissociation energies of pyridine at IM3 are given in the dashed box.

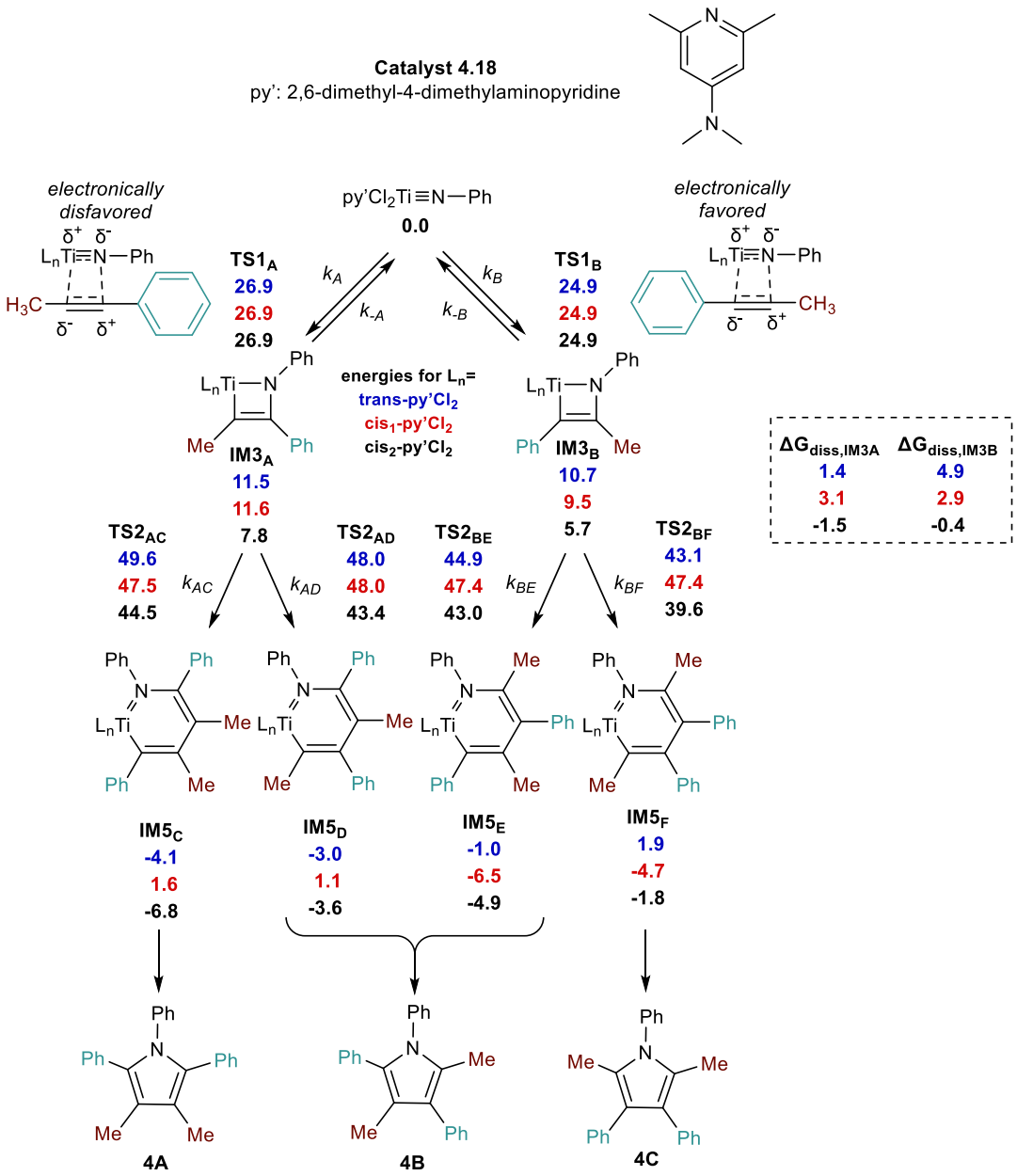

Figure 4.108 Calculated transition state barriers (TS1 and TS2) and intermediate free energies (IM3 and IM5) in kcalmol^{-1} for catalyst **4.18** at *trans*- (blue), *cis*-1 (red) and *cis*-2 (black) configurations. Dissociation energies of pyridine at IM3 are given in the dashed box.

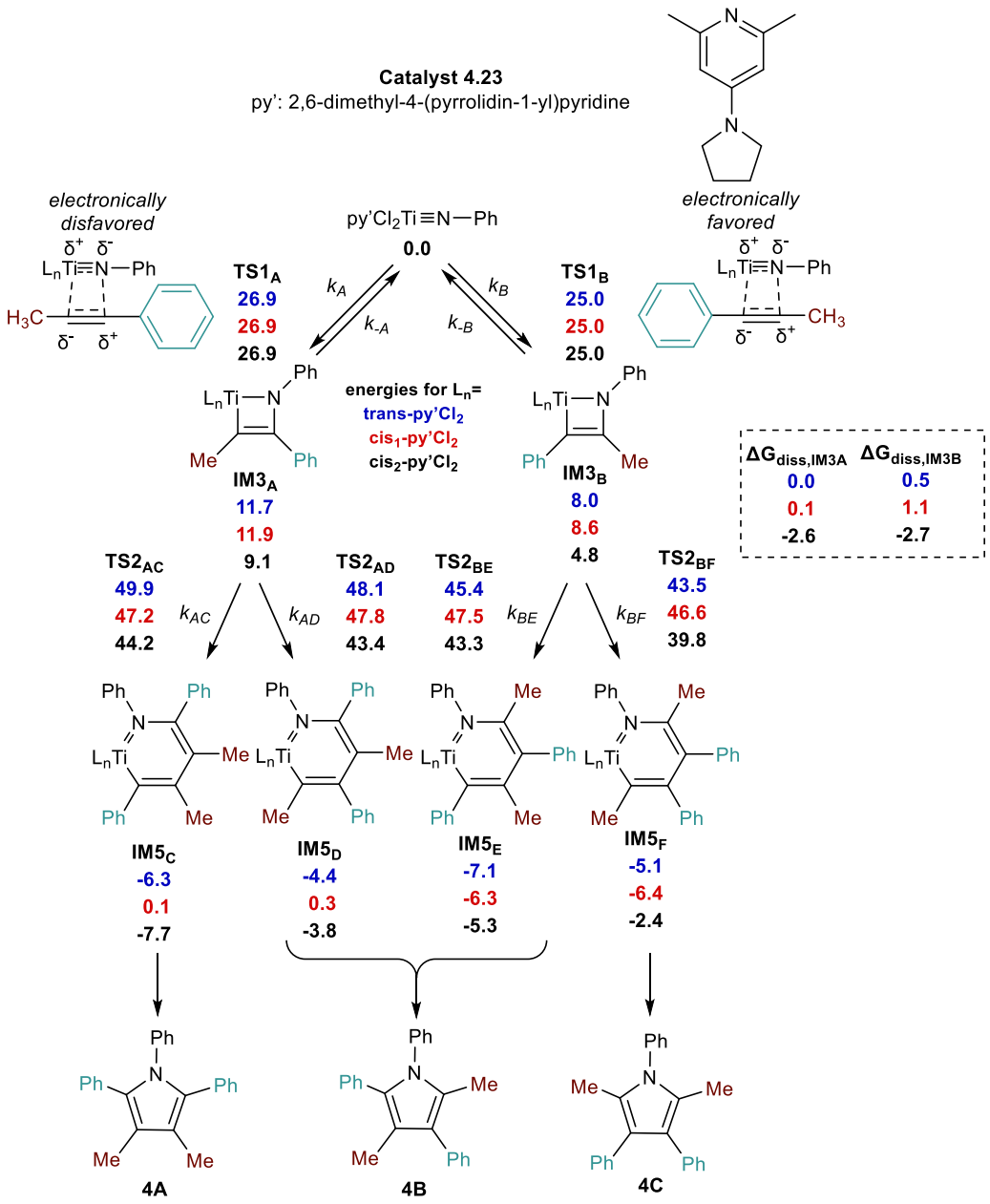

Figure 4.109 Calculated transition state barriers (TS1 and TS2) and intermediate free energies (IM3 and IM5) in kcalmol^{-1} for catalyst **4.23** at *trans*- (blue), *cis*-1 (red) and *cis*-2 (black) configurations. Dissociation energies of pyridine at IM3 are given in the dashed box.

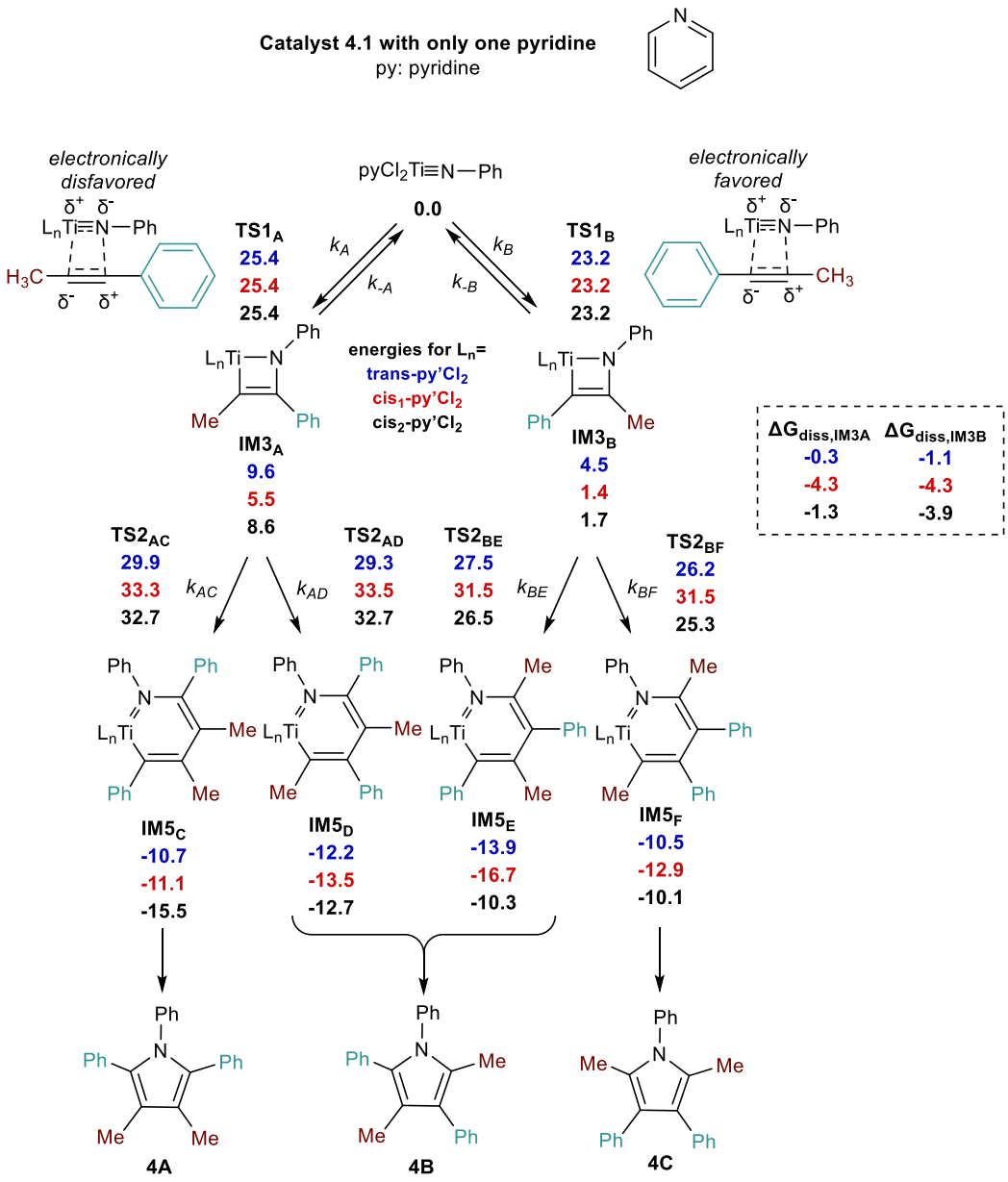

Figure 4.110 Calculated transition state barriers (TS1 and TS2) and intermediate free energies (IM3 and IM5) in kcalmol^{-1} for catalyst **4.1** at *trans*- (blue), *cis*-1 (red) and *cis*-2 (black) configurations. Dissociation energies of pyridine at IM3 are given in the dashed box.

Figure 4.110 is different from Figure 4.4 in three aspects.

1. Figure 4.4 was calculated using M06/6-311G(d,p)/SMD at 110 °C, while Figure 4.110 was calculated using M06/def2-SVP/SMD at 115 °C.
2. Figure 4.4 was calculated using *trans*- configuration, while Figure 4.110 considers *trans*-, *cis*-1 and *cis*-2 configurations.
3. Free energies in Figure 4.4 used the $Ti(NPh)Cl_2py_3$ catalyst as a starting point, while Figure 4.110 used the $Ti(NPh)Cl_2py$ catalyst in order to get directly comparable results to Figures 4.107-4.109.

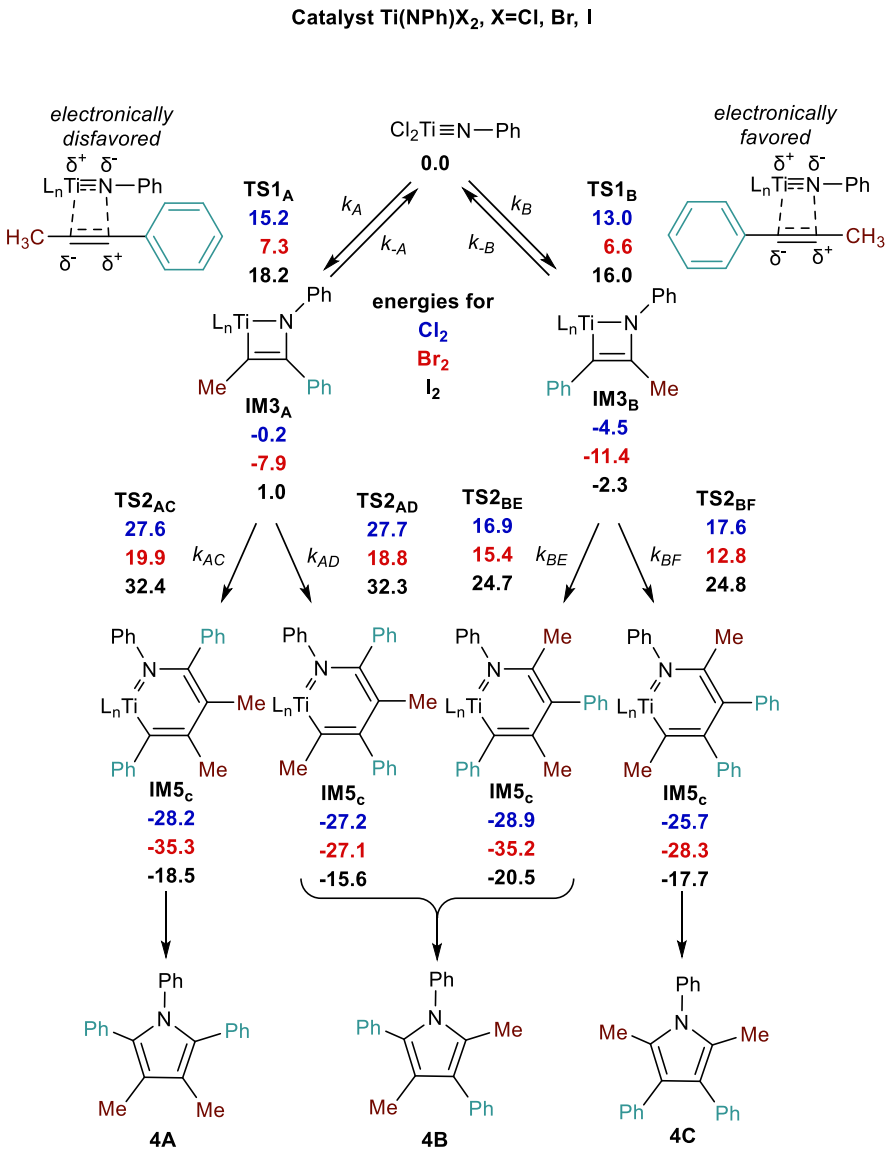

Figure 4.111 Calculated transition state barriers (TS1 and TS2) and intermediate free energies (IM3 and IM5) in kcalmol^{-1} for Ti(NPh)X_2 (X = Cl, Br, I) at *trans*- (blue), *cis*-1 (red) and *cis*-2 (black) configurations.

4.6.16 Computational Regioselectivity

The following procedure was used to obtain the computational product ratio. Since the [2+2] cycloaddition is reversible and not the rate-determining step, the concentration of [IM3$_A$] and [IM3$_B$] are thermodynamically controlled and therefore follow the Boltzmann distribution:

$$\frac{[\mathrm{IM3_A}]}{[\mathrm{IM3_B}]} = \exp\left(\frac{-(\Delta \mathrm{G_{IM3_A}} - \Delta \mathrm{G_{IM3_B}})}{RT}\right) = \exp\left(\frac{-\Delta\Delta \mathrm{G(IM3_A - IM3_B)}}{RT}\right),$$

The following alkyne insertion step is irreversible as well as the rate-determining step, so the rate law is assumed to be:

$$\frac{d[\mathrm{TS2_{AC}}]}{dt} = k_{AC}[\mathrm{IM3_A}][\mathrm{MeCCPh}],$$

$$\frac{d[\mathrm{TS2_{AD}}]}{dt} = k_{AD}[\mathrm{IM3_A}][\mathrm{MeCCPh}],$$

$$\frac{d[\mathrm{TS2_{BE}}]}{dt} = k_{BE}[\mathrm{IM3_B}][\mathrm{MeCCPh}] \text{ and}$$

$$\frac{d[\mathrm{TS2_{BF}}]}{dt} = k_{BF}[\mathrm{IM3_B}][\mathrm{MeCCPh}].$$

where k is the reaction rate from the Eyring equation

$$k = \frac{k_B T}{h} \exp\left(-\frac{\Delta G^{\ddagger}}{RT}\right).$$

therefore, the ratio of the products will be:

$$\frac{[\mathrm{TS2_{BE}}]}{[\mathrm{TS2_{BF}}]} = \frac{k_{BE}}{k_{BF}} = \exp\left(\frac{-(\Delta G^{\ddagger}_{\mathrm{TS2_{BE}}} - \Delta G^{\ddagger}_{\mathrm{TS2_{BF}}})}{RT}\right) = \exp\left(\frac{-\Delta\Delta G^{\ddagger}(\mathrm{TS2_{BE}} - \mathrm{TS2_{BF}})}{RT}\right)$$

where R is the gas constant and T is the temperature. At experimental temperature 115 ℃, RT = 0.77 kcalmol^{-1}. Therefore, a minor change in $\Delta\Delta G^{\ddagger}$ leads to a significant variation in product distribution.

Table 4.17 shows the computationally predicted selectivity. For catalyst **4.16** and **4.18**, we find that our computational prediction matches quantitatively with experimental data, predicting product **4C** to be the dominant product.

Table 4.17 Predicted product ratio using M06/def2-SVP/SMD.

RT (388.15K): 0.77 kcalmol^{-1}	**$\Delta\Delta G(IM3_A - IM3_B)$**	**$\Delta\Delta G^{\ddagger}(TS2_{AC} - TS2_{AD})$**	**$\Delta\Delta G^{\ddagger}(TS2_{BE} - TS2_{BF})$**	**Predicted ratio**	**Experimental ratio**
Catalyst **4.1**	5.77	0.00	1.23	0 : 17 : 83	20 : 45 : 30
Catalyst **4.16**	3.16	2.20	3.78	0 : 2 : 98	3 : 32 : 65
Catalyst **4.18**	2.11	1.12	3.48	1 : 6 : 93	1 : 8 : 91
Catalyst **4.23**	4.30	0.77	3.41	0 : 1 : 99	1 : 7 : 92

Bibliography

1. Hunt, A. J.; Farmer, T. J.; Clark, J. H., CHAPTER 1 Elemental Sustainability and the Importance of Scarce Element Recovery. In *Element Recovery and Sustainability*, First ed.; Hunt, A. J., Ed.; The Royal Society of Chemistry: Cambridge, U.K., 2013; pp 1-28.
2. Earnshaw, N. N. G. A., *Chemistry of the Elements*. Second ed.; Butterworth-Heinemann: Oxford, U.K., 1997.
3. Kepp, K. P., A Quantitative Scale of Oxophilicity and Thiophilicity. *Inorg. Chem.* **2016,** *55*, 9461-9470.
4. Parkin, G., Classification of Organotransition Metal Compounds. In *Comprehensive Organometallic Chemistry III*, Mingos, D. M. P.; Crabtree, R. H., Eds.; Elsevier: Oxford, 2007; Vol. 1, pp 1-57.
5. Gambarotta, S.; Scott, J., Multimetallic Cooperative Activation of N_2. *Angew. Chem., Int. Ed.* **2004,** *43*, 5298-5308.
6. Burford, R. J.; Yeo, A.; Fryzuk, M. D., Dinitrogen activation by group 4 and group 5 metal complexes supported by phosphine-amido containing ligand manifolds. *Coord. Chem. Rev.* **2017,** *334*, 84-99.
7. Hanna, T. E.; Lobkovsky, E.; Chirik, P. J., Dinitrogen Activation by Titanium Sandwich Complexes. *J. Am. Chem. Soc.* **2004,** *126*, 14688-14689.
8. Pun, D.; Lobkovsky, E.; Chirik, P. J., Indenyl Zirconium Dinitrogen Chemistry: N2 Coordination to an Isolated Zirconium Sandwich and Synthesis of Side-on, End-on Dinitrogen Compounds. *J. Am. Chem. Soc.* **2008,** *130*, 6047-6054.
9. Yan, X.; Xi, C., Conversion of Zirconacyclopentadienes into Metalloles: Fagan–Nugent Reaction and Beyond. *Acc. Chem. Res.* **2015,** *48*, 935-946.
10. Micalizio, G. C., Early Transition Metal Mediated Reductive Coupling Reactions. In *Comprehensive Organic Synthesis II*, Second ed.; Knochel, P., Ed.; Elsevier: Amsterdam, 2014; Vol. 5, pp 1660-1737.
11. Xu, S.; Negishi, E.-i., Zirconium-Catalyzed Asymmetric Carboalumination of Unactivated Terminal Alkenes. *Acc. Chem. Res.* **2016,** *49*, 2158-2168.
12. Zweig, J. E.; Kim, D. E.; Newhouse, T. R., Methods Utilizing First-Row Transition Metals in Natural Product Total Synthesis. *Chem. Rev.* **2017,** *117*, 11680-11752.

13. Rosales, A.; Rodríguez-García, I.; Muñoz-Bascón, J.; Roldan-Molina, E.; Padial, N. M.; Morales, L. P.; García-Ocaña, M.; Oltra, J. E., The Nugent Reagent: A Formidable Tool in Contemporary Radical and Organometallic Chemistry. *Eur. J. Org. Chem.* **2015,** *2015*, 4567-4591.

14. McCallum, T.; Wu, X.; Lin, S., Recent Advances in Titanium Radical Redox Catalysis. *J. Org. Chem.* **2019,** *84*, 14369-14380.

15. Grant, L. N.; Miehlich, M. E.; Meyer, K.; Mindiola, D. J., Arrested disproportionation in trivalent, mononuclear, and non-metallocene complexes of Zr(III) and Hf(III). *Chem. Commun.* **2018,** *54*, 2052-2055.

16. Kurogi, T.; Miehlich, M. E.; Halter, D.; Mindiola, D. J., 1,2-CH Bond Activation of Pyridine across a Transient Titanium Alkylidene Radical and Re-Formation of the Ti=CH^{t}Bu Moiety. *Organometallics* **2018,** *37*, 165-167.

17. Perera, T. H.; Lord, R. L.; Heeg, M. J.; Schlegel, H. B.; Winter, C. H., Metallapyrimidines and Metallapyrimidiniums from Oxidative Addition of Pyrazolate N–N Bonds to Niobium(III), Niobium(IV), and Tantalum(IV) Metal Centers and Assessment of Their Aromatic Character. *Organometallics* **2012,** *31*, 5971-5974.

18. Pun, D.; Leopold, S. M.; Bradley, C. A.; Lobkovsky, E.; Chirik, P. J., Bis(indenyl)hafnium Chemistry: Ligand-Induced Haptotropic Rearrangement and Fundamental Reactivity Studies at a Reduced Hafnium Center. *Organometallics* **2009,** *28*, 2471-2484.

19. Chomitz, W. A.; Sutton, A. D.; Krinsky, J. L.; Arnold, J., Synthesis and Reactivity of Titanium and Zirconium Complexes Supported by a Multidentate Monoanionic [N_2P_2] Ligand. *Organometallics* **2009,** *28*, 3338-3349.

20. Figueroa, J. S.; Piro, N. A.; Clough, C. R.; Cummins, C. C., A Nitridoniobium(V) Reagent That Effects Acid Chloride to Organic Nitrile Conversion: Synthesis via Heterodinuclear (Nb/Mo) Dinitrogen Cleavage, Mechanistic Insights, and Recycling. *J. Am. Chem. Soc.* **2006,** *128*, 940-950.

21. Büschel, S.; Bannenberg, T.; Hrib, C. G.; Glöckner, A.; Jones, P. G.; Tamm, M., Adduct formation of [(η^7-C_7H_7)Hf(η^5-C_5H_5)] with isocyanides, phosphines and N-heterocyclic carbenes: An experimental and theoretical study. *J. Organomet. Chem.* **2009,** *694*, 1244-1250.

22. Okamoto, S., Synthetic Reactions Using Low-valent Titanium Reagents Derived from $Ti(OR)_4$ or $CpTiX_3$ (X=O-*i*-Pr or Cl) in the Presence of Me_3SiCl and Mg. *Chem. Rec.* **2016,** *16*, 857-872.

23. Gansäuer, A.; Bluhm, H.; Pierobon, M., Emergence of a Novel Catalytic Radical Reaction: Titanocene-Catalyzed Reductive Opening of Epoxides. *J. Am. Chem. Soc.* **1998,** *120*, 12849-12859.

24. Galindo, A.; Gómez, M.; Gómez-Sal, P.; Martín, A.; del Río, D.; Sánchez, F., Alkyl Alkyne Mono((trimethylsilyl)cyclopentadienyl) Niobium Complexes. Synthesis and Chemical Behavior in Insertion Processes. X-ray Crystal Structures of $[NbCp'(CH_2SiMe_3)_2(Me_3SiCCSiMe_3)]$ and $[NbCp'(NAr)\{\eta^4\text{-}CH(SiMe_3)C(SiMe_3)C(CH_2SiMe_3)CH(SiMe_3)\}]$, (Cp' = $\eta^5\text{-}C_5H_4SiMe_3$, Ar = $2,6\text{-}Me_2C_6H_3$). DFT Studies of the Model Complexes $[Nb(\eta^5\text{-}C_5H_5)R_2(HCCH)]$ (R = Cl, Me). *Organometallics* **2002,** *21*, 293-304.

25. Calderazzo, F.; Pampaloni, G.; Rocchi, L.; Strähle, J.; Wurst, K., The Reduction of the NbX_5/AlX_3 System with Aluminum in the Presence of Aromatic Hydrocarbons: An Approach to Niobium(II), Niobium(I), and Niobium(0) Organometallics. *Angew. Chem., Int. Ed. Engl.* **1991,** *30*, 102-103.

26. Oshiki, T.; Yamada, A.; Kawai, K.; Arimitsu, H.; Takai, K., Alkyne Exchange Reactions of Silylalkyne Complexes of Tantalum: Mechanistic Investigation and Its Application in the Preparation of New Tantalum Complexes Having Functional Alkynes (PhC≡CR (R = COOMe, $CONMe_2$)). *Organometallics* **2007,** *26*, 173-182.

27. Kamitani, M.; Searles, K.; Chen, C.-H.; Carroll, P. J.; Mindiola, D. J., β-Hydrogen Abstraction of an Ethyl Group Provides Entry to Titanium and Zirconium Ethylene Complexes. *Organometallics* **2015,** *34*, 2558-2566.

28. Cavaliere, V. N.; Crestani, M. G.; Pinter, B.; Pink, M.; Chen, C.-H.; Baik, M.-H.; Mindiola, D. J., Room Temperature Dehydrogenation of Ethane to Ethylene. *J. Am. Chem. Soc.* **2011,** *133*, 10700-10703.

29. Crestani, M. G.; Hickey, A. K.; Gao, X.; Pinter, B.; Cavaliere, V. N.; Ito, J.-I.; Chen, C.-H.; Mindiola, D. J., Room Temperature Dehydrogenation of Ethane, Propane, Linear Alkanes C4–C8, and Some Cyclic Alkanes by Titanium–Carbon Multiple Bonds. *J. Am. Chem. Soc.* **2013,** *135*, 14754-14767.

30. Fernández, F. J.; Gómez-Sal, P.; Manzanero, A.; Royo, P.; Jacobsen, H.; Berke, H., *β*-Hydrogen-Containing Zirconium Alkyls with the Doubly-Bridged Bis(dimethylsilanediyl)dicyclopentadienyl Ligand. X-ray Molecular Structures of [Zr{$(SiMe_2)_2(\eta^5\text{-}C_5H_3)_2$}ClEt] and [Zr{$(SiMe_2)_2(\eta^5\text{-}C_5H_3)_2$}Et]$_2(\mu\text{-}CH_2{=}CH_2)$. *Organometallics* **1997,** *16,* 1553-1561.

31. Epstein, O. L.; Savchenko, A. I.; Kulinkovich, O. G., Titanium(IV) isopropoxide-catalysed reaction of alkylmagnesium halides with ethyl acetate in the presence of styrene. Non-hydride mechanism of ligand exchange in the titanacyclopropanes. *Tetrahedron Lett.* **1999,** *40,* 5935-5938.

32. Negishi, E.-i.; Cederbaum, F. E.; Takahashi, T., Reaction of zirconocene dichloride with alkyllithiums or alkyl grignard reagents as a convenient method for generating a "zirconocene" equivalant and its use in zirconium-promoted cyclization of alkenes, alkynes, dienes, enynes, and diynes. *Tetrahedron Lett.* **1986,** *27,* 2829-2832.

33. Negishi, E.-I.; Takahashi, T., Patterns of Stoichiometric and Catalytic Reactions of Organozirconium and Related Complexes of Synthetic Interest. *Acc. Chem. Res.* **1994,** *27,* 124-130.

34. Ei-ichi, N.; Tamotsu, T., Alkene and Alkyne Complexes of Zirconocene. Their Preparation, Structure, and Novel Transformations. *Bull. Chem. Soc. Jpn.* **1998,** *71,* 755-769.

35. Rosenthal, U.; Burlakov, V. V.; Arndt, P.; Baumann, W.; Spannenberg, A., The Titanocene Complex of Bis(trimethylsilyl)acetylene: Synthesis, Structure, and Chemistry. *Organometallics* **2003,** *22,* 884-900.

36. Beweries, T.; Burlakov, V. V.; Bach, M. A.; Arndt, P.; Baumann, W.; Spannenberg, A.; Rosenthal, U., Complexation of Bis(trimethylsilyl)acetylene by Decamethylhafnocene To Give the Hafnacyclopropene $Cp^*_2Hf(\eta^2\text{-}Me_3SiC_2SiMe_3)$: An Unusually Strong Metal−Alkyne Interaction. *Organometallics* **2007,** *26,* 247-249.

37. Beweries, T.; Burlakov, V. V.; Arndt, P.; Baumann, W.; Spannenberg, A.; Rosenthal, U., Synthesis of Hafnacyclopentanes from Hafnocene Alkyne Complexes: Influence of Styrene Substituents on the C–C Coupling Regioselectivity. *Eur. J. Inorg. Chem.* **2009,** *2009,* 1456-1459.

38. Fang, M.; Lee, D. S.; Ziller, J. W.; Doedens, R. J.; Bates, J. E.; Furche, F.; Evans, W. J., Synthesis of the $(N_2)^{3-}$ Radical from Y^{2+} and Its Protonolysis Reactivity To Form $(N_2H_2)^{2-}$ via the $Y[N(SiMe_3)_2]_3/KC_8$ Reduction System. *J. Am. Chem. Soc.* **2011,** *133*, 3784-3787.

39. Fang, M.; Farnaby, J. H.; Ziller, J. W.; Bates, J. E.; Furche, F.; Evans, W. J., Isolation of $(CO)^{1-}$ and $(CO_2)^{1-}$ Radical Complexes of Rare Earths via $Ln(NR_2)_3/K$ Reduction and $[K_2(18\text{-crown-}6)_2]^{2+}$ Oligomerization. *J. Am. Chem. Soc.* **2012,** *134*, 6064-6067.

40. Woen, D. H.; Chen, G. P.; Ziller, J. W.; Boyle, T. J.; Furche, F.; Evans, W. J., Solution Synthesis, Structure, and CO_2 Reduction Reactivity of a Scandium(II) Complex, $\{Sc[N(SiMe_3)_2]_3\}^-$. *Angew. Chem., Int. Ed.* **2017,** *56*, 2050-2053.

41. Woen, D. H.; Chen, G. P.; Ziller, J. W.; Boyle, T. J.; Furche, F.; Evans, W. J., End-On Bridging Dinitrogen Complex of Scandium. *J. Am. Chem. Soc.* **2017,** *139*, 14861-14864.

42. Schmiege, B. M.; Ziller, J. W.; Evans, W. J., Reduction of Dinitrogen with an Yttrium Metallocene Hydride Precursor, $[(C_5Me_5)_2YH]_2$. *Inorg. Chem.* **2010,** *49*, 10506-10511.

43. Demir, S.; Lorenz, S. E.; Fang, M.; Furche, F.; Meyer, G.; Ziller, J. W.; Evans, W. J., Synthesis, Structure, and Density Functional Theory Analysis of a Scandium Dinitrogen Complex, $[(C_5Me_4H)_2Sc]_2(\mu\text{-}\eta^2\text{:}\eta^2\text{-}N_2)$. *J. Am. Chem. Soc.* **2010,** *132*, 11151-11158.

44. Clentsmith, G. K. B.; Cloke, F. G. N.; Green, J. C.; Hanks, J.; Hitchcock, P. B.; Nixon, J. F., Stabilization of Low-Oxidation-State Early Transition-Metal Complexes Bearing 1,2,4-Triphosphacyclopentadienyl Ligands: Structure of $[\{Sc(P_3C_2t\text{Bu}_2)_2\}_2]$; Sc^{II} or Mixed Oxidation State? *Angew. Chem., Int. Ed.* **2003,** *42*, 1038-1041.

45. Wijeratne, G. B.; Zolnhofer, E. M.; Fortier, S.; Grant, L. N.; Carroll, P. J.; Chen, C.-H.; Meyer, K.; Krzystek, J.; Ozarowski, A.; Jackson, T. A.; Mindiola, D. J.; Telser, J., Electronic Structure and Reactivity of a Well-Defined Mononuclear Complex of Ti(II). *Inorg. Chem.* **2015,** *54*, 10380-10397.

46. Zolnhofer, E. M.; Wijeratne, G. B.; Jackson, T. A.; Fortier, S.; Heinemann, F. W.; Meyer, K.; Krzystek, J.; Ozarowski, A.; Mindiola, D. J.; Telser, J., Electronic Structure and Magnetic Properties of a Titanium(II) Coordination Complex. *Inorg. Chem.* **2020**, *59*, 6187-6201.

47. Edema, J. J. H.; Duchateau, R.; Gambarotta, S.; Hynes, R.; Gabe, E., Novel titanium(II) amine complexes L_4TiCl_2[L = 1/2 *N,N,N',N'*-tetramethylethylenediamine (TMEDA), 1/2 *N,N,N'*-trimethylethylenediamine, pyridine, 1/2 2,2'-bipyridine]: synthesis and crystal structure of monomeric trans-$(TMEDA)_2TiCl_2$. *Inorg. Chem.* **1991,** *30,* 154-156.

48. Araya, M. A.; Cotton, F. A.; Matonic, J. H.; Murillo, C. A., An Efficient Reduction Process Leading to Titanium(II) and Niobium(II): Preparation and Structural Characterization of *trans*-$MCl_2(py)_4$ Compounds, M = Ti, Nb, and Mn. *Inorg. Chem.* **1995,** *34*, 5424-5428.

49. Chakarawet, K.; Davis-Gilbert, Z. W.; Harstad, S. R.; Young Jr., V. G.; Long, J. R.; Ellis, J. E., $Ta(CNDipp)_6$: An Isocyanide Analogue of Hexacarbonyltantalum(0). *Angew. Chem., Int. Ed.* **2017,** *56*, 10577-10581.

50. Barybin, M. V.; Brennessel, W. W.; Kucera, B. E.; Minyaev, M. E.; Sussman, V. J.; Young, V. G.; Ellis, J. E., Homoleptic Isocyanidemetalates of 4d- and 5d-Transition Metals: $[Nb(CNXyl)_6]^-$, $[Ta(CNXyl)_6]^-$, and Derivatives Thereof. *J. Am. Chem. Soc.* **2007,** *129*, 1141-1150.

51. Allen, J. M.; Ellis, J. E., Synthesis and characterization of titanium tetraisocyanide complexes, $[CpTi(CNXyl)_4E]$, E = I, $SnPh_3$, and $SnMe_3$. *J. Organomet. Chem.* **2008,** *693*, 1536-1542.

52. Jilek, R. E.; Jang, M.; Smolensky, E. D.; Britton, J. D.; Ellis, J. E., Structurally Distinct Homoleptic Anthracene Complexes, $[M(C_{14}H_{10})_3]^{2-}$, M=Titanium, Zirconium, Hafnium: Tris(arene) Complexes for a Triad of Transition Metals. *Angew. Chem., Int. Ed.* **2008,** *47*, 8692-8695.

53. Sussman, V. J.; Ellis, J. E., From Storable Sources of Atomic Nb^- and Ta^- Ions to Isolable Anionic Tris(1,3-butadiene)metal Complexes: $[M(\eta^4\text{-}C_4H_6)_3]^-$, M=Nb, Ta. *Angew. Chem., Int. Ed.* **2008,** *47*, 484-489.

54. MacDonald, M. R.; Bates, J. E.; Fieser, M. E.; Ziller, J. W.; Furche, F.; Evans, W. J., Expanding Rare-Earth Oxidation State Chemistry to Molecular Complexes of Holmium(II) and Erbium(II). *J. Am. Chem. Soc.* **2012,** *134*, 8420-8423.

55. Arteaga-Müller, R.; Tsurugi, H.; Saito, T.; Yanagawa, M.; Oda, S.; Mashima, K., New Tantalum Ligand-Free Catalyst System for Highly Selective Trimerization of

Ethylene Affording 1-Hexene: New Evidence of a Metallacycle Mechanism. *J. Am. Chem. Soc.* **2009,** *131*, 5370-5371.

56. Tsurugi, H.; Saito, T.; Tanahashi, H.; Arnold, J.; Mashima, K., Carbon Radical Generation by d^0 Tantalum Complexes with α-Diimine Ligands through Ligand-Centered Redox Processes. *J. Am. Chem. Soc.* **2011,** *133*, 18673-18683.

57. Nishiyama, H.; Ikeda, H.; Saito, T.; Kriegel, B.; Tsurugi, H.; Arnold, J.; Mashima, K., Structural and Electronic Noninnocence of α-Diimine Ligands on Niobium for Reductive C–Cl Bond Activation and Catalytic Radical Addition Reactions. *J. Am. Chem. Soc.* **2017,** *139*, 6494-6505.

58. Saito, T.; Nishiyama, H.; Tanahashi, H.; Kawakita, K.; Tsurugi, H.; Mashima, K., 1,4-Bis(trimethylsilyl)-1,4-diaza-2,5-cyclohexadienes as Strong Salt-Free Reductants for Generating Low-Valent Early Transition Metals with Electron-Donating Ligands. *J. Am. Chem. Soc.* **2014,** *136*, 5161-5170.

59. Saito, T.; Nishiyama, H.; Kawakita, K.; Nechayev, M.; Kriegel, B.; Tsurugi, H.; Arnold, J.; Mashima, K., Reduction of (^{t}BuN=)$NbCl_3(py)_2$ in a Salt-Free Manner for Generating Nb(IV) Dinuclear Complexes and Their Reactivity toward Benzo[*c*]cinnoline. *Inorg. Chem.* **2015,** *54*, 6004-6009.

60. Gómez, M.; Hernández-Prieto, C.; Martín, A.; Mena, M.; Santamaría, C., An Effective Route to Dinuclear Niobium and Tantalum Imido Complexes. *Inorg. Chem.* **2017,** *56*, 11681-11687.

61. Klesko, J. P.; Thrush, C. M.; Winter, C. H., Thermal Atomic Layer Deposition of Titanium Films Using Titanium Tetrachloride and 2-Methyl-1,4-bis(trimethylsilyl)-2,5-cyclohexadiene or 1,4-Bis(trimethylsilyl)-1,4-dihydropyrazine. *Chem. Mater.* **2015,** *27*, 4918-4921.

62. Frey, G.; Hausmann, J. N.; Streuff, J., Titanium-Catalyzed Reductive Umpolung Reactions with a Metal-Free Terminal Reducing Agent. *Chem. Eur. J.* **2015,** *21*, 5693-5696.

63. Satoh, Y.; Obora, Y., Active Low-Valent Niobium Catalysts from $NbCl_5$ and Hydrosilanes for Selective Intermolecular Cycloadditions. *J. Org. Chem.* **2011,** *76*, 8569-8573.

64. Paradies, J.; Crudass, J.; MacKay, F.; Yellowlees, L. J.; Montgomery, J.; Parsons, S.; Oswald, I.; Robertson, N.; Sadler, P. J., Photogeneration of titanium(III) from titanium(IV) citrate in aqueous solution. *J. Inorg. Biochem.* **2006,** *100*, 1260-1264.

65. Chong, E.; Xue, W.; Storr, T.; Kennepohl, P.; Schafer, L. L., Pyridonate-Supported Titanium(III). Benzylamine as an Easy-To-Use Reductant. *Organometallics* **2015,** *34*, 4941-4945.

66. Gianetti, T. L.; Nocton, G.; Minasian, S. G.; Tomson, N. C.; Kilcoyne, A. L. D.; Kozimor, S. A.; Shuh, D. K.; Tyliszczak, T.; Bergman, R. G.; Arnold, J., Diniobium Inverted Sandwich Complexes with μ-η^6:η^6-Arene Ligands: Synthesis, Kinetics of Formation, and Electronic Structure. *J. Am. Chem. Soc.* **2013,** *135*, 3224-3236.

67. Plundrich, G. T.; Wadepohl, H.; Clot, E.; Gade, L. H., η^6-Arene-Zirconium-PNP-Pincer Complexes: Mechanism of Their Hydrogenolytic Formation and Their Reactivity as Zirconium(II) Synthons. *Chem. Eur. J.* **2016,** *22*, 9283-9292.

68. Hananouchi, S.; Krull, B. T.; Ziller, J. W.; Furche, F.; Heyduk, A. F., Metal effects on ligand non-innocence in Group 5 complexes of the redox-active [ONO] pincer ligand. *Dalton Trans.* **2014,** *43*, 17991-18000.

69. Munha, R. F.; Zarkesh, R. A.; Heyduk, A. F., Group transfer reactions of d^0 transition metal complexes: redox-active ligands provide a mechanism for expanded reactivity. *Dalton Trans.* **2013,** *42*, 3751-3766.

70. Duan, L.; Jia, Y.-B.; Li, X.-G.; Li, Y.-M.; Hu, H.; Li, J.; Cui, C., Synthesis, Characterization, and Reversible Multielectron Redox Properties of a Biradical Yttrium Complex Containing Bis(2-isopropylaminophenyl)amide. *Eur. J. Inorg. Chem.* **2017,** *2017*, 2231-2235.

71. Heins, S. P.; Wolczanski, P. T.; Cundari, T. R.; MacMillan, S. N., Redox non-innocence permits catalytic nitrene carbonylation by (dadi)Ti=NAd (Ad = adamantyl). *Chem. Sci.* **2017,** *8*, 3410-3418.

72. Roizen, J. L.; Harvey, M. E.; Du Bois, J., Metal-Catalyzed Nitrogen-Atom Transfer Methods for the Oxidation of Aliphatic C–H Bonds. *Acc. Chem. Res.* **2012,** *45*, 911-922.

73. Qin, C.; Davies, H. M. L., Role of Sterically Demanding Chiral Dirhodium Catalysts in Site-Selective C–H Functionalization of Activated Primary C–H Bonds. *J. Am. Chem. Soc.* **2014,** *136*, 9792-9796.

74. Iovan, D. A.; Wilding, M. J. T.; Baek, Y.; Hennessy, E. T.; Betley, T. A., Diastereoselective C−H Bond Amination for Disubstituted Pyrrolidines. *Angew. Chem., Int. Ed.* **2017,** *56*, 15599-15602.

75. Basuli, F.; Wicker, B.; Huffman, J. C.; Mindiola, D. J., Understanding the role of an easy-to-prepare aldimine–alkyne carboamination catalyst, $[Ti(NMe_2)_3(NHMe_2)][B(C_6F_5)_4]$. *J. Organomet. Chem.* **2011,** *696*, 235-243.

76. Fantauzzi, S.; Gallo, E.; Caselli, A.; Ragaini, F.; Macchi, P.; Casati, N.; Cenini, S., Origin of the Deactivation in Styrene Aziridination by Aryl Azides, Catalyzed by Ruthenium Porphyrin Complexes. Structural Characterization of a Δ^2-1,2,3-Triazoline Ru^{II}(TPP)CO Complex. *Organometallics* **2005,** *24*, 4710-4713.

77. King, E. R.; Hennessy, E. T.; Betley, T. A., Catalytic C−H Bond Amination from High-Spin Iron Imido Complexes. *J. Am. Chem. Soc.* **2011,** *133*, 4917-4923.

78. Cramer, S. A.; Jenkins, D. M., Synthesis of Aziridines from Alkenes and Aryl Azides with a Reusable Macrocyclic Tetracarbene Iron Catalyst. *J. Am. Chem. Soc.* **2011,** *133*, 19342-19345.

79. Gilbert, Z. W.; Hue, R. J.; Tonks, I. A., Catalytic formal [2+2+1] synthesis of pyrroles from alkynes and diazenes via Ti^{II}/Ti^{IV} redox catalysis. *Nat. Chem.* **2016,** *8*, 63-68.

80. Chiu, H.-C.; See, X. Y.; Tonks, I. A., Dative Directing Group Effects in Ti-Catalyzed [2+2+1] Pyrrole Synthesis: Chemo- and Regioselective Alkyne Heterocoupling. *ACS Catal.* **2019,** *9*, 216-223.

81. Chiu, H.-C.; Tonks, I. A., Trimethylsilyl-Protected Alkynes as Selective Cross-Coupling Partners in Titanium-Catalyzed [2+2+1] Pyrrole Synthesis. *Angew. Chem., Int. Ed.* **2018,** *57*, 6090-6094.

82. Davis-Gilbert, Z. W.; Wen, X.; Goodpaster, J. D.; Tonks, I. A., Mechanism of Ti-Catalyzed Oxidative Nitrene Transfer in [2+2+1] Pyrrole Synthesis from Alkynes and Azobenzene. *J. Am. Chem. Soc.* **2018,** *140*, 7267-7281.

83. Davis-Gilbert, Z. W.; Yao, L. J.; Tonks, I. A., Ti-Catalyzed Multicomponent Oxidative Carboamination of Alkynes with Alkenes and Diazenes. *J. Am. Chem. Soc.* **2016,** *138*, 14570-14573.

84. Beaumier, E. P.; McGreal, M. E.; Pancoast, A. R.; Wilson, R. H.; Moore, J. T.; Graziano, B. J.; Goodpaster, J. D.; Tonks, I. A., Carbodiimide Synthesis via Ti-Catalyzed Nitrene Transfer from Diazenes to Isocyanides. *ACS Catal.* **2019,** *9*, 11753-11762.

85. Tomson, N. C.; Arnold, J.; Bergman, R. G., Halo, Alkyl, Aryl, and Bis(imido) Complexes of Niobium Supported by the *β*-Diketiminato Ligand. *Organometallics* **2010,** *29*, 2926-2942.

86. Kriegel, B. M.; Bergman, R. G.; Arnold, J., Nitrene Metathesis and Catalytic Nitrene Transfer Promoted by Niobium Bis(imido) Complexes. *J. Am. Chem. Soc.* **2016,** *138*, 52-55.

87. Schmidt, M.; Seitz, A. E.; Eckhardt, M.; Balázs, G.; Peresypkina, E. V.; Virovets, A. V.; Riedlberger, F.; Bodensteiner, M.; Zolnhofer, E. M.; Meyer, K.; Scheer, M., Transfer Reagent for Bonding Isomers of Iron Complexes. *J. Am. Chem. Soc.* **2017,** *139*, 13981-13984.

88. Corbey, J. F.; Fang, M.; Ziller, J. W.; Evans, W. J., Cocrystallization of $(\mu\text{-}S_2)^{2-}$ and $(\mu\text{-}S)^{2-}$ and Formation of an $[\eta^2\text{-}S_3N(SiMe_3)_2]$ Ligand from Chalcogen Reduction by $(N_2)^{2-}$ in a Bimetallic Yttrium Amide Complex. *Inorg. Chem.* **2015,** *54*, 801-807.

89. Fieser, M. E.; Johnson, C. W.; Bates, J. E.; Ziller, J. W.; Furche, F.; Evans, W. J., Dinitrogen Reduction, Sulfur Reduction, and Isoprene Polymerization via Photochemical Activation of Trivalent Bis(cyclopentadienyl) Rare-Earth-Metal Allyl Complexes. *Organometallics* **2015,** *34*, 4387-4393.

90. Camp, C.; Maron, L.; Bergman, R. G.; Arnold, J., Activation of White Phosphorus by Low-Valent Group 5 Complexes: Formation and Reactivity of *cyclo*-P_4 Inverted Sandwich Compounds. *J. Am. Chem. Soc.* **2014,** *136*, 17652-17661.

91. Seitz, A. E.; Eckhardt, M.; Erlebach, A.; Peresypkina, E. V.; Sierka, M.; Scheer, M., Pnictogen–Silicon Analogues of Benzene. *J. Am. Chem. Soc.* **2016,** *138*, 10433-10436.

92. Vogel, U.; Eberl, M.; Eckhardt, M.; Seitz, A.; Rummel, E.-M.; Timoshkin, A. Y.; Peresypkina, E. V.; Scheer, M., Access to Phosphorus-Rich Zirconium Complexes. *Angew. Chem., Int. Ed.* **2011,** *50*, 8982-8985.

93. Cossairt, B. M.; Piro, N. A.; Cummins, C. C., Early-Transition-Metal-Mediated Activation and Transformation of White Phosphorus. *Chem. Rev.* **2010,** *110*, 4164-4177.

94. Cossairt, B. M.; Cummins, C. C., A Niobium-Mediated Cycle Producing Phosphorus-Rich Organic Molecules from White Phosphorus (P_4) through Activation, Functionalization, and Transfer Reactions. *Angew. Chem., Int. Ed.* **2008,** *47*, 8863-8866.

95. Aguilar-Calderón, J. R.; Murillo, J.; Gomez-Torres, A.; Saucedo, C.; Jordan, A.; Metta-Magaña, A. J.; Pink, M.; Fortier, S., Redox Character and Small Molecule Reactivity of a Masked Titanium(II) Synthon. *Organometallics* **2020,** *39*, 295-311.

96. Gómez-Torres, A.; Aguilar-Calderón, J. R.; Saucedo, C.; Jordan, A.; Metta-Magaña, A.; Pinter, B.; Fortier, S., Reversible oxidative-addition and reductive-elimination of thiophene from a titanium complex and its thermally-induced hydrodesulphurization chemistry. *Chem. Commun.* **2020,** *56*, 1545-1548.

97. Davies, H. M. L.; Beckwith, R. E. J., Catalytic Enantioselective C−H Activation by Means of Metal−Carbenoid-Induced C−H Insertion. *Chem. Rev.* **2003,** *103*, 2861-2904.

98. Basuli, F.; Aneetha, H.; Huffman, J. C.; Mindiola, D. J., A Fluorobenzene Adduct of Ti(IV), and Catalytic Carboamination to Prepare *α,β*-Unsaturated Imines and Triaryl-Substituted Quinolines. *J. Am. Chem. Soc.* **2005,** *127*, 17992-17993.

99. Zarkesh, R. A.; Ziller, J. W.; Heyduk, A. F., Four-Electron Oxidative Formation of Aryl Diazenes Using a Tantalum Redox-Active Ligand Complex. *Angew. Chem., Int. Ed.* **2008,** *47*, 4715-4718.

100. Heyduk, A. F.; Zarkesh, R. A.; Nguyen, A. I., Designing Catalysts for Nitrene Transfer Using Early Transition Metals and Redox-Active Ligands. *Inorg. Chem.* **2011,** *50*, 9849-9863.

101. Nguyen, A. I.; Zarkesh, R. A.; Lacy, D. C.; Thorson, M. K.; Heyduk, A. F., Catalytic nitrene transfer by a zirconium(iv) redox-active ligand complex. *Chem. Sci.* **2011,** *2*, 166-169.

102. Huisgen, R., *1,3-Dipolar Cycloaddition Chemistry*. Wiley: New York, 1984.

103. Boren, B. C.; Narayan, S.; Rasmussen, L. K.; Zhang, L.; Zhao, H.; Lin, Z.; Jia, G.; Fokin, V. V., Ruthenium-Catalyzed Azide−Alkyne Cycloaddition: Scope and Mechanism. *J. Am. Chem. Soc.* **2008,** *130*, 8923-8930.

104. Meldal, M.; Tornøe, C. W., Cu-Catalyzed Azide−Alkyne Cycloaddition. *Chem. Rev.* **2008,** *108*, 2952-3015.

105. L'Abbe, G., Decomposition and addition reactions of organic azides. *Chem. Rev.* **1969,** *69*, 345-363.

106. Amarnath, V.; Anthony, D. C.; Amarnath, K.; Valentine, W. M.; Wetterau, L. A.; Graham, D. G., Intermediates in the Paal-Knorr synthesis of pyrroles. *J. Org. Chem.* **1991,** *56*, 6924-6931.

107. Maria Christofi, A.; Garratt, P. J.; Hogarth, G.; Ibbett, A. J.; Ng, Y.-F.; Steed, J. W., Molecular design using electrostatic interactions. Part 4: Synthesis and properties of flexible tetrapodand tetracations derived from naphthalene. Role of structured water in the electrostatic binding of polyanion guests: a model for interactions in biological systems. *Tetrahedron* **2002,** *58*, 4543-4549.

108. Geng, W.; Zhang, W.-X.; Hao, W.; Xi, Z., Cyclopentadiene–Phosphine/Palladium-Catalyzed Cleavage of C–N Bonds in Secondary Amines: Synthesis of Pyrrole and Indole Derivatives from Secondary Amines and Alkenyl or Aryl Dibromides. *J. Am. Chem. Soc.* **2012,** *134*, 20230-20233.

109. Engel, P. S., Mechanism of the thermal and photochemical decomposition of azoalkanes. *Chem. Rev.* **1980,** *80*, 99-150.

110. Harman, W. H.; Lichterman, M. F.; Piro, N. A.; Chang, C. J., Well-Defined Vanadium Organoazide Complexes and Their Conversion to Terminal Vanadium Imides: Structural Snapshots and Evidence for a Nitrene Capture Mechanism. *Inorg. Chem.* **2012,** *51*, 10037-10042.

111. Mankad, N. P.; Müller, P.; Peters, J. C., Catalytic N−N Coupling of Aryl Azides To Yield Azoarenes via Trigonal Bipyramid Iron−Nitrene Intermediates. *J. Am. Chem. Soc.* **2010,** *132*, 4083-4085.

112. Powers, I. G.; Andjaba, J. M.; Luo, X.; Mei, J.; Uyeda, C., Catalytic Azoarene Synthesis from Aryl Azides Enabled by a Dinuclear Ni Complex. *J. Am. Chem. Soc.* **2018,** *140*, 4110-4118.

113. Ju, Y.; Kumar, D.; Varma, R. S., Revisiting Nucleophilic Substitution Reactions: Microwave-Assisted Synthesis of Azides, Thiocyanates, and Sulfones in an Aqueous Medium. *J. Org. Chem.* **2006,** *71*, 6697-6700.

114. Kitamura, M.; Koga, T.; Yano, M.; Okauchi, T., Direct Synthesis of Organic Azides from Alcohols Using 2-Azido-1,3-dimethyl-imidazolinium Hexafluorophosphate. *Synlett* **2012,** *23*, 1335-1338.

115. Smolinsky, G., Notes - The Vapor Phase Pyrolysis of Several Subsituted Azidobenzenes. *J. Org. Chem.* **1961,** *26*, 4108-4110.

116. Walker, P.; Waters, W. A., 314. Pyrolysis of organic azides: a mechanistic study. *J. Chem. Soc.* **1962**, 1632-1638.

117. Lorber, C., Titanium and vanadium imido-bridged complexes. *Coord. Chem. Rev.* **2016,** *308*, 76-96.

118. Heutling, A.; Pohlki, F.; Doye, S., [Ind_2TiMe_2]: A General Catalyst for the Intermolecular Hydroamination of Alkynes. *Chem. Eur. J.* **2004,** *10*, 3059-3071.

119. See, X. Y.; Beaumier, E. P.; Davis-Gilbert, Z. W.; Dunn, P. L.; Larsen, J. A.; Pearce, A. J.; Wheeler, T. A.; Tonks, I. A., Generation of Ti^{II} Alkyne Trimerization Catalysts in the Absence of Strong Metal Reductants. *Organometallics* **2017,** *36*, 1383-1390.

120. Baumann, M.; Baxendale, I. R.; Ley, S. V.; Nikbin, N., An overview of the key routes to the best selling 5-membered ring heterocyclic pharmaceuticals. *Beilstein J. Org. Chem.* **2011,** *7*, 442-495.

121. Whitesides, G. M.; Ehmann, W. J., The Mechanism of Formation of 1,2,3,4-Tetramethylnaphthalene from 2-Butyne and Triphenyltris(tetrahydrofuran)chromium(III). *J. Am. Chem. Soc.* **1970,** *92*, 5625-5640.

122. Blake, A. J.; Collier, P. E.; Dunn, S. C.; Li, W.-S.; Mountford, P.; Shishkin, O. V., Synthesis and imido-group exchange reactions of *tert*-butylimidotitanium complexes. *J. Chem. Soc., Dalton Trans.* **1997**, 1549-1558.

123. Zhou, S.; Liao, H.; Liu, M.; Feng, G.; Fu, B.; Li, R.; Cheng, M.; Zhao, Y.; Gong, P., Discovery and biological evaluation of novel 6,7-disubstituted-4-(2-fluorophenoxy)quinoline derivatives possessing 1,2,3-triazole-4-carboxamide moiety as c-Met kinase inhibitors. *Bioorg. Med. Chem.* **2014,** *22*, 6438-6452.

124. Gannarapu, M. R.; Vasamsetti, S. B.; Punna, N.; Kotamraju, S.; Banda, N., Synthesis of novel 1-substituted triazole linked 1,2-benzothiazine 1,1-dioxido propenone derivatives as potent anti-inflammatory agents and inhibitors of monocyte-to-macrophage differentiation. *Med. Chem. Commun.* **2015,** *6*, 1494-1500.

125. Kim, B. H.; Park, S. M.; Lee, Y. S. 2'-deoxyuridine derivatives and hydrogels formed therewith. US 6884882 B1, Apr 26, 2005.

126. Goswami, P. P.; Suding, V. P.; Carlson, A. S.; Topczewski, J. J., Direct Conversion of Aldehydes and Ketones into Azides by Sequential Nucleophilic Addition and Substitution. *Eur. J. Org. Chem.* **2016,** *2016*, 4805-4809.

127. Zhang, S.-L.; Xue, Z.-F.; Gao, Y.-R.; Mao, S.; Wang, Y.-Q., Triple condensation of aryl methyl ketones catalyzed by amine and trifluoroacetic acid: straightforward access to 1,3,5-triarylbenzenes under mild conditions. *Tetrahedron Lett.* **2012,** *53*, 2436-2439.

128. Rassadin, V. A.; Nicolas, E.; Six, Y., $Ti(O^iPr)_4/^nBuLi$: an attractive reagent system for [2+2+2] cyclotrimerisation reactions. *Chem. Commun.* **2014,** *50*, 7666-7669.

129. McMurry, J. E., Organic chemistry of low-valent titanium. *Acc. Chem. Res.* **1974,** *7*, 281-286.

130. Fürstner, A.; Bogdanović, B., New Developments in the Chemistry of Low-Valent Titanium. *Angew. Chem., Int. Ed.* **1996,** *35*, 2442-2469.

131. Sato, F.; Urabe, H.; Okamoto, S., Synthesis of Organotitanium Complexes from Alkenes and Alkynes and Their Synthetic Applications. *Chem. Rev.* **2000,** *100*, 2835-2886.

132. Vol'Pin, M. E.; Shur, V. B., Nitrogen Fixation by Transition Metal Complexes. *Nature* **1966,** *209*, 1236-1236.

133. Bercaw, J. E.; Marvich, R. H.; Bell, L. G.; Brintzinger, H. H., Titanocene as an intermediate in reactions involving molecular hydrogen and nitrogen. *J. Am. Chem. Soc.* **1972,** *94*, 1219-1238.

134. Fuerstner, A.; Hupperts, A.; Ptock, A.; Janssen, E., "Site Selective" Formation of Low-Valent Titanium Reagents: An "Instant" Procedure for the Reductive Coupling of Oxo Amides to Indoles. *J. Org. Chem.* **1994,** *59*, 5215-5229.

135. Balu, N.; Nayak, S. K.; Banerji, A., Influence of External Ligands and Auxiliaries on the Reactivity of Low-Valent Titanium in McMurry Reaction: Selectivity and Mechanistic Profile. *J. Am. Chem. Soc.* **1996,** *118*, 5932-5937.

136. Yamamoto, K.; Nagae, H.; Tsurugi, H.; Mashima, K., Mechanistic understanding of alkyne cyclotrimerization on mononuclear and dinuclear scaffolds: [4 + 2] cycloaddition of the third alkyne onto metallacyclopentadienes and dimetallacyclopentadienes. *Dalton Trans.* **2016,** *45*, 17072-17081.

137. Morohashi, N.; Yokomakura, K.; Hattori, T.; Miyano, S., Highly regioselective [2+2+2] cycloaddition of terminal alkynes catalyzed by titanium complexes of p-tert-butylthiacalix[4]arene. *Tetrahedron Lett.* **2006,** *47*, 1157-1161.

138. Calderazzo, F.; Marchetti, F.; Pampaloni, G.; Hiller, W.; Antropiusová, H.; Mach, K., Reactivity of titanium(II) Arene derivatives with substituted alkynes. Cyclooligomerization reactions and crystal and molecular structure of $[\eta^4\text{-}C_4(C_6H_5)4]Ti[(\mu\text{-}Br)_2(AlBr_2)]_2$. *Chem. Ber.* **1989,** *122*, 2229-2238.

139. Kablaoui, N. M.; Hicks, F. A.; Buchwald, S. L., Titanocene-Catalyzed Cyclocarbonylation of *o*-Allyl Aryl Ketones to *γ*-Butyrolactones. *J. Am. Chem. Soc.* **1997,** *119*, 4424-4431.

140. Hicks, F. A.; Kablaoui, N. M.; Buchwald, S. L., Scope of the Intramolecular Titanocene-Catalyzed Pauson−Khand Type Reaction1. *J. Am. Chem. Soc.* **1999,** *121*, 5881-5898.

141. Sturla, S. J.; Buchwald, S. L., Monocyclopentadienyltitanium Aryloxide Complexes: Preparation, Characterization, and Application in Cyclization Reactions. *Organometallics* **2002,** *21*, 739-748.

142. Kulinkovich, O. G.; Sviridov, S. V.; Vasilevski, D. A., Titanium(IV) Isopropoxide-Catalyzed Formation of 1-Substituted Cyclopropanols in the Reaction of Ethylmagnesium Bromide with Methyl Alkanecarboxylates. *Synthesis* **1991,** *1991*, 234-234.

143. Kulinkovich, O. G., Titanacyclopropanes as versatile intermediates for carbon-carbon bond formation in reactions with unsaturated compounds. *Pure Appl. Chem.* **2000,** *72*, 1715.

144. Wang, X.; Woo, L. K., Titanium(II) Porphyrin Complexes: Versatile One- and Two-Electron Reducing Agents. Reduction of Organic Chlorides, Epoxides, and Sulfoxides. *J. Org. Chem.* **1998,** *63*, 356-360.

145. Kool, L. B.; Rausch, M. D.; Alt, H. G.; Herberhold, M.; Honold, B.; Thewalt, U., Preparation, characterization and reactivity of $Cp_2M(PMe_3)_2$ complexes (M = Ti, Zr): the molecular structure of $Cp_2Zr(PMe_3)_2$. *J. Organomet. Chem.* **1987,** *320*, 37-45.

146. Lukešová, L.; Horáček, M.; Štěpnička, P.; Fejfarová, K.; Gyepes, R.; Císařová, I.; Kubišta, J.; Mach, K., Synthesis and crystal structures of thermally stable titanocenes. *J. Organomet. Chem.* **2002,** *663*, 134-144.

147. Ladipo, F. T.; Sarveswaran, V.; Kingston, J. V.; Huyck, R. A.; Bylikin, S. Y.; Carr, S. D.; Watts, R.; Parkin, S., Synthesis, characterization, and alkyne cyclotrimerization chemistry of titanium complexes supported by calixarene-derived bis(aryloxide) ligation. *J. Organomet. Chem.* **2004,** *689*, 502-514.

148. Woo, L. K.; Hays, J. A.; Young, V. G.; Day, C. L.; Caron, C.; D'Souza, F.; Kadish, K. M., Synthesis, characterization, substitution, and atom-transfer reactions of (η^2-alkyne)(tetratolylporphyrinato)titanium(II). X-ray structure of *trans*-bis(4-picoline)(tetratolylporphyrinato)titanium(II). *Inorg. Chem.* **1993,** *32*, 4186-4192.

149. Jensen, J. A.; Wilson, S. R.; Schultz, A. J.; Girolami, G. S., Divalent titanium chemistry. Synthesis, reactivity, and X-ray and neutron diffraction studies of $Ti(BH_4)_2(dmpe)_2$ and $Ti(CH_3)_2(dmpe)_2$. *J. Am. Chem. Soc.* **1987,** *109*, 8094-8096.

150. Morris, R. J.; Girolami, G. S., On the π-Donor Ability of Early Transition Metals: Evidence that Trialkylphosphines Can Engage in π-Back-Bonding and X-ray Structure of the Titanium(II) Phenoxide $Ti(OPh)_2(dmpe)_2$. *Inorg. Chem.* **1990,** *29*, 4167-4169.

151. Rosenthal, U., Metallocene-made mad metallacycles in synthesis and catalysis. *Russ. Chem. Bull.* **2014,** *63*, 2577-2582.

152. Haehnel, M.; Ruhmann, M.; Theilmann, O.; Roy, S.; Beweries, T.; Arndt, P.; Spannenberg, A.; Villinger, A.; Jemmis, E. D.; Schulz, A.; Rosenthal, U., Reactions of Titanocene Bis(trimethylsilyl)acetylene Complexes with Carbodiimides: An Experimental and Theoretical Study of Complexation versus C–N Bond Activation. *J. Am. Chem. Soc.* **2012,** *134*, 15979-15991.

153. Rosenthal, U.; Pellny, P.-M.; Kirchbauer, F. G.; Burlakov, V. V., What Do Titano- and Zirconocenes Do with Diynes and Polyynes? *Acc. Chem. Res.* **2000,** *33*, 119-129.

154. Hill, J. E.; Fanwick, P. E.; Rothwell, I. P., Synthesis, structure, and reactivity of a new series of titanium η^2-olefin and η^2-ketone complexes. *Organometallics* **1992,** *11*, 1771-1773.

155. Cohen, S. A.; Auburn, P. R.; Bercaw, J. E., Structure and reactivity of bis(pentamethylcyclopentadienyl)(ethylene)titanium(II), a simple olefin adduct of titanium. *J. Am. Chem. Soc.* **1983,** *105*, 1136-1143.

156. Mullins, S. M.; Duncan, A. P.; Bergman, R. G.; Arnold, J., Reactivity of a Titanium Dinitrogen Complex Supported by Guanidinate Ligands: Investigation of Solution

Behavior and a Novel Rearrangement of Guanidinate Ligands. *Inorg. Chem.* **2001,** *40*, 6952-6963.

157. Graham, T. W.; Kickham, J.; Courtenay, S.; Wei, P.; Stephan, D. W., Reduction of Titanium(IV)-Phosphinimide Complexes: Routes to Ti(III) Dimers, Ti(IV)-Metallacycles, and Ti(II) Species. *Organometallics* **2004,** *23*, 3309-3318.

158. Frazier, B. A.; Wolczanski, P. T.; Keresztes, I.; DeBeer, S.; Lobkovsky, E. B.; Pierpont, A. W.; Cundari, T. R., Synthetic Approaches to (smif)2Ti (smif = 1,3-di-(2-pyridyl)-2-azaallyl) Reveal Redox Non-Innocence and C–C Bond-Formation. *Inorg. Chem.* **2012,** *51*, 8177-8186.

159. Ohkubo, M.; Mochizuki, S.; Sano, T.; Kawaguchi, Y.; Okamoto, S., Selective Cleavage of Allyl and Propargyl Ethers to Alcohols Catalyzed by Ti(O-*i*-Pr)$_4$/MX$_n$/Mg. *Org. Lett.* **2007,** *9*, 773-776.

160. Okamoto, S.; He, J.-Q.; Ohno, C.; Oh-iwa, Y.; Kawaguchi, Y., McMurry coupling of aryl aldehydes and imino pinacol coupling mediated by Ti(O-*i*-Pr)$_4$/Me$_3$SiCl/Mg reagent. *Tetrahedron Lett.* **2010,** *51*, 387-390.

161. Swartz II, D. L.; Staples, R. J.; Odom, A. L., Synthesis and hydroamination catalysis with 3-aryl substituted pyrrolyl and dipyrrolylmethane titanium(iv) complexes. *Dalton Trans.* **2011,** *40*, 7762-7768.

162. Odom, A. L.; McDaniel, T. J., Titanium-Catalyzed Multicomponent Couplings: Efficient One-Pot Syntheses of Nitrogen Heterocycles. *Acc. Chem. Res.* **2015**.

163. Tillack, A.; Khedkar, V.; Jiao, H.; Beller, M., A General Study of Aryloxo and Alkoxo Ligands in the Titanium-Catalyzed Intermolecular Hydroamination of Terminal Alkynes. *Eur. J. Org. Chem.* **2005,** *2005*, 5001-5012.

164. Collier, P. E.; Blake, A. J.; Mountford, P., Mono- and bi-nuclear titanium imido complexes supported by aryloxide ligands: fine control by ortho substituents. *J. Chem. Soc., Dalton Trans.* **1997**, 2911-2920.

165. Dunn, S. C.; Hazari, N.; Jones, N. M.; Moody, A. G.; Blake, A. J.; Cowley, A. R.; Green, J. C.; Mountford, P., Titanium Imido Complexes of Cyclooctatetraenyl Ligands. *Chem. Eur. J.* **2005,** *11*, 2111-2124.

166. Dunn, S. C.; Mountford, P.; Robson, D. A., Cyclopentadienyl, indenyl and bis(cyclopentadienyl) titanium imido compounds. *J. Chem. Soc., Dalton Trans.* **1997**, 293-304.

167. Zhang, Z.; Leitch, D. C.; Lu, M.; Patrick, B. O.; Schafer, L. L., An Easy-To-Use, Regioselective, and Robust Bis(amidate) Titanium Hydroamination Precatalyst: Mechanistic and Synthetic Investigations toward the Preparation of Tetrahydroisoquinolines and Benzoquinolizine Alkaloids. *Chem. Eur. J.* **2007,** *13*, 2012-2022.

168. Yim, J. C. H.; Bexrud, J. A.; Ayinla, R. O.; Leitch, D. C.; Schafer, L. L., Bis(amidate)bis(amido) Titanium Complex: A Regioselective Intermolecular Alkyne Hydroamination Catalyst. *J. Org. Chem.* **2014,** *79*, 2015-2028.

169. Oakes, D. C. H.; Gibson, V. C.; White, A. J. P.; Williams, D. J., Highly Active Titanium-Based Olefin Polymerization Catalysts Supported by Bidentate Phenoxyamide Ligands. *Inorg. Chem.* **2006,** *45*, 3476-3477.

170. Groom, L. R.; Schwarz, A. D.; Nova, A.; Clot, E.; Mountford, P., Synthesis and Reactions of a Cyclopentadienyl-Amidinate Titanium tert-Butoxyimido Compound. *Organometallics* **2013,** *32*, 7520-7539.

171. Elkin, T.; Botoshansky, M.; Waymouth, R. M.; Eisen, M. S., Titanium Bis(amidinates) Bearing Electron Donating Pendant Arms as Catalysts for Stereospecific Polymerization of Propylene. *Organometallics* **2014,** *33*, 840-843.

172. Negishi, E.; Holmes, S. J.; Tour, J. M.; Miller, J. A.; Cederbaum, F. E.; Swanson, D. R.; Takahashi, T., Metal-promoted cyclization. 19. Novel bicyclization of enynes and diynes promoted by zirconocene derivatives and conversion of zirconabicycles into bicyclic enones via carbonylation. *J. Am. Chem. Soc.* **1989,** *111*, 3336-3346.

173. Cotton, F. A.; Kibala, P.; Shang, M.; Wojtczak, W. A., New Compounds of Zirconium(II) and Hafnium(II): Synthesis and X-ray Crystal Structures of Novel Dimers of Formula $M_2X_4(\eta^6\text{-}C_6H_5PMe_2)_2(PMe_2Ph)_2$. *Organometallics* **1991,** *10*, 2626-2630.

174. Müller, T. E.; Hultzsch, K. C.; Yus, M.; Foubelo, F.; Tada, M., Hydroamination: Direct Addition of Amines to Alkenes and Alkynes. *Chem. Rev.* **2008,** *108*, 3795-3892.

175. Vujkovic, N.; Ward, B. D.; Maisse-François, A.; Wadepohl, H.; Mountford, P.; Gade, L. H., Imido-Alkyne Coupling in Titanium Complexes: New Insights into the Alkyne Hydroamination Reaction. *Organometallics* **2007,** *26*, 5522-5534.

176. Tonks, I. A.; Meier, J. C.; Bercaw, J. E., Alkyne Hydroamination and Trimerization with Titanium Bis(phenolate)pyridine Complexes: Evidence for Low-Valent Titanium Intermediates and Synthesis of an Ethylene Adduct of Titanium(II). *Organometallics* **2013,** *32*, 3451-3457.

177. Ladipo, F. T., Synthesis and Reactivity of Well-Characterized Low-Valent Titanium Species. *Comment Inorg. Chem.* **2006,** *27*, 73-102.

178. Ozerov, O. V.; Ladipo, F. T.; Patrick, B. O., Highly Regioselective Alkyne Cyclotrimerization Catalyzed by Titanium Complexes Supported by Proximally Bridged *p*-tert-Butylcalix[4]arene Ligands. *J. Am. Chem. Soc.* **1999,** *121*, 7941-7942.

179. Broere, D. L. J.; Ruijter, E., Recent Advances in Transition-Metal-Catalyzed [2+2+2]-Cyclo(co)trimerization Reactions. *Synthesis* **2012,** *44*, 2639-2672.

180. Diercks, R.; Dieck tom, H., Diazadiene als Steuerliganden in der homogenen Katalyse, IX. Katalytische Cyclotetramerisierung von Propiolsäureestern. *Chem. Ber.* **1985,** *118*, 428-435.

181. Pal, S.; Uyeda, C., Evaluating the Effect of Catalyst Nuclearity in Ni-Catalyzed Alkyne Cyclotrimerizations. *J. Am. Chem. Soc.* **2015**.

182. Roland, C. D.; Li, H.; Abboud, K. A.; Wagener, K. B.; Veige, A. S., Cyclic polymers from alkynes. *Nat Chem* **2016,** *8*, 791-796.

183. Ozerov, O. V.; Patrick, B. O.; Ladipo, F. T., Highly Regioselective [2+2+2] Cycloaddition of Terminal Alkynes Catalyzed by η^6-Arene Complexes of Titanium Supported by Dimethylsilyl-Bridged *p*-tert-Butyl Calix[4]arene Ligand. *J. Am. Chem. Soc.* **2000,** *122*, 6423-6431.

184. Hill, J. E.; Balaich, G.; Fanwick, P. E.; Rothwell, I. P., The chemistry of titanacyclopentadiene rings supported by 2,6-diphenylphenoxide ligation: stoichiometric and catalytic reactivity. *Organometallics* **1993,** *12*, 2911-2924.

185. Troyanov, S., Arene complexes of titanium and zirconium. Synthesis and structure. *J. Organomet. Chem.* **1994,** *475*, 139-147.

186. Bemowski, R. D.; Singh, A. K.; Bajorek, B. J.; DePorre, Y.; Odom, A. L., Effective donor abilities of E-*t*-Bu and EPh (E = O, S, Se, Te) to a high valent transition metal. *Dalton Trans.* **2014,** *43*, 12299-12305.

187. DiFranco, S. A.; Maciulis, N. A.; Staples, R. J.; Batrice, R. J.; Odom, A. L., Evaluation of Donor and Steric Properties of Anionic Ligands on High Valent Transition Metals. *Inorg. Chem.* **2012,** *51*, 1187-1200.

188. Yim, J. C. H.; Schafer, L. L., Efficient Anti-Markovnikov-Selective Catalysts for Intermolecular Alkyne Hydroamination: Recent Advances and Synthetic Applications. *Eur. J. Org. Chem.* **2014,** *2014*, 6825-6840.

189. Musso, F.; Solari, E.; Floriani, C.; Schenk, K., Hydrocarbon Activation with Metal Halides: Zirconium Tetrachloride Catalyzing the Jacobsen Reaction and Assisting the Trimerization of Alkynes via the Formation of η^6-Arene−Zirconium(IV) Complexes. *Organometallics* **1997,** *16*, 4889-4895.

190. Kozhushkov, S. I.; Yufit, D. S.; Ackermann, L., Ruthenium-Catalyzed Hydroarylations of Methylenecyclopropanes: Mild C−H Bond Functionalizations with Conservation of Cyclopropane Rings. *Org. Lett.* **2008,** *10*, 3409-3412.

191. Yu, B.-C.; Shirai, Y.; Tour, J. M., Syntheses of new functionalized azobenzenes for potential molecular electronic devices. *Tetrahedron* **2006,** *62*, 10303-10310.

192. Zheng, Q.; Hua, R.; Wan, Y., An alternative CuCl–piperidine-catalyzed oxidative homocoupling of terminal alkynes affording 1,3-diynes in air. *Appl. Organomet. Chem.* **2010,** *24*, 314-316.

193. Bigelow, H. E.; Robinson, D. B., Azobenzene. *Org. Synth.* **1942,** *22*, 28.

194. Hayes, P. G.; Piers, W. E.; Parvez, M., Arene Complexes of β-Diketiminato Supported Organoscandium Cations: Mechanism of Arene Exchange and Alkyne Insertion in Solvent Separated Ion Pairs. *Chem. Eur. J.* **2007,** *13*, 2632-2640.

195. Sheldrick, G. M., *Acta Cryst.* **2008**, 112-122.

196. Chang, S.; Jones, L.; Wang, C.; Henling, L. M.; Grubbs, R. H., Synthesis and Characterization of New Ruthenium-Based Olefin Metathesis Catalysts Coordinated with Bidentate Schiff-Base Ligands. *Organometallics* **1998,** *17*, 3460-3465.

197. Elkin, T.; Kulkarni, N. V.; Tumanskii, B.; Botoshansky, M.; Shimon, L. J. W.; Eisen, M. S., Synthesis and Structure of Group 4 Symmetric Amidinate Complexes and Their Reactivity in the Polymerization of α-Olefins. *Organometallics* **2013,** *32*, 6337-6352.

198. Dubberley, S. R.; Evans, S.; Boyd, C. L.; Mountford, P., New and versatile routes to zirconium imido dichloride compounds. *Dalton Trans.* **2005**, 1448-1458.

199. Strauch, J.; Warren, T. H.; Erker, G.; Fröhlich, R.; Saarenketo, P., Formation and structural properties of salicylaldiminato complexes of zirconium and titanium. *Inorg. Chim. Acta* **2000,** *300–302*, 810-821.

200. Ackermann, L.; Born, R., $TiCl_4/^tBuNH2$ as the sole catalyst for a hydroamination-based Fischer indole synthesis. *Tetrahedron Lett.* **2004,** *45*, 9541-9544.

201. Fey, N., Lost in chemical space? Maps to support organometallic catalysis. *Chem. Cent. J.* **2015,** *9*, 38.

202. Wu, K.; Doyle, A. G., Parameterization of phosphine ligands demonstrates enhancement of nickel catalysis via remote steric effects. *Nat. Chem.* **2017,** *9*, 779-784.

203. Toste, F. D.; Sigman, M. S.; Miller, S. J., Pursuit of Noncovalent Interactions for Strategic Site-Selective Catalysis. *Acc. Chem. Res.* **2017,** *50*, 609-615.

204. Sigman, M. S.; Harper, K. C.; Bess, E. N.; Milo, A., The Development of Multidimensional Analysis Tools for Asymmetric Catalysis and Beyond. *Acc. Chem. Res.* **2016,** *49*, 1292-1301.

205. Weissman, S. A.; Anderson, N. G., Design of Experiments (DoE) and Process Optimization. A Review of Recent Publications. *Org. Process Res. Dev.* **2015,** *19*, 1605-1633.

206. Murray, P. M.; Bellany, F.; Benhamou, L.; Bučar, D.-K.; Tabor, A. B.; Sheppard, T. D., The application of design of experiments (DoE) reaction optimisation and solvent selection in the development of new synthetic chemistry. *Org. Biomol. Chem.* **2016,** *14*, 2373-2384.

207. Isbrandt, E. S.; Sullivan, R. J.; Newman, S. G., High Throughput Strategies for the Discovery and Optimization of Catalytic Reactions. *Angew. Chem., Int. Ed.* **2019,** *58*, 7180-7191.

208. Robbins, D. W.; Hartwig, J. F., A Simple, Multidimensional Approach to High-Throughput Discovery of Catalytic Reactions. *Science* **2011,** *333*, 1423-1427.

209. McNally, A.; Prier, C. K.; MacMillan, D. W. C., Discovery of an α-Amino C–H Arylation Reaction Using the Strategy of Accelerated Serendipity. *Science* **2011,** *334*, 1114-1117.

210. Hammett, L. P., The Effect of Structure upon the Reactions of Organic Compounds. Benzene Derivatives. *J. Am. Chem. Soc.* **1937,** *59*, 96-103.

211. Tolman, C. A., Steric effects of phosphorus ligands in organometallic chemistry and homogeneous catalysis. *Chem. Rev.* **1977,** *77*, 313-348.

212. Clavier, H.; Nolan, S. P., Percent buried volume for phosphine and N-heterocyclic carbene ligands: steric properties in organometallic chemistry. *Chem. Commun.* **2010,** *46*, 841-861.

213. Harper, K. C.; Bess, E. N.; Sigman, M. S., Multidimensional steric parameters in the analysis of asymmetric catalytic reactions. *Nat. Chem.* **2012,** *4*, 366-374.

214. Raugei, S.; DuBois, D. L.; Rousseau, R.; Chen, S.; Ho, M.-H.; Bullock, R. M.; Dupuis, M., Toward Molecular Catalysts by Computer. *Acc. Chem. Res.* **2015,** *48*, 248-255.

215. Wheeler, S. E.; Seguin, T. J.; Guan, Y.; Doney, A. C., Noncovalent Interactions in Organocatalysis and the Prospect of Computational Catalyst Design. *Acc. Chem. Res.* **2016,** *49*, 1061-1069.

216. Reid, J. P.; Sigman, M. S., Comparing quantitative prediction methods for the discovery of small-molecule chiral catalysts. *Nat. Rev. Chem.* **2018,** *2*, 290-305.

217. Toyao, T.; Maeno, Z.; Takakusagi, S.; Kamachi, T.; Takigawa, I.; Shimizu, K.-i., Machine Learning for Catalysis Informatics: Recent Applications and Prospects. *ACS Catal.* **2020,** *10*, 2260-2297.

218. Gromski, P. S.; Henson, A. B.; Granda, J. M.; Cronin, L., How to explore chemical space using algorithms and automation. *Nat. Rev. Chem.* **2019,** *3*, 119-128.

219. Ahneman, D. T.; Estrada, J. G.; Lin, S.; Dreher, S. D.; Doyle, A. G., Predicting reaction performance in C–N cross-coupling using machine learning. *Science* **2018,** *360*, 186-190.

220. Estrada, J. G.; Ahneman, D. T.; Sheridan, R. P.; Dreher, S. D.; Doyle, A. G., Response to Comment on "Predicting reaction performance in C–N cross-coupling using machine learning". *Science* **2018,** *362*, eaat8763.

221. Chuang, K. V.; Keiser, M. J., Comment on “Predicting reaction performance in C–N cross-coupling using machine learning”. *Science* **2018,** *362*, eaat8603.

222. Nielsen, M. K.; Ahneman, D. T.; Riera, O.; Doyle, A. G., Deoxyfluorination with Sulfonyl Fluorides: Navigating Reaction Space with Machine Learning. *J. Am. Chem. Soc.* **2018,** *140*, 5004-5008.

223. Zahrt, A. F.; Henle, J. J.; Rose, B. T.; Wang, Y.; Darrow, W. T.; Denmark, S. E., Prediction of higher-selectivity catalysts by computer-driven workflow and machine learning. *Science* **2019,** *363*, eaau5631.

224. Reid, J. P.; Sigman, M. S., Holistic prediction of enantioselectivity in asymmetric catalysis. *Nature* **2019,** *571*, 343-348.

225. Reid, J. P.; Proctor, R. S. J.; Sigman, M. S.; Phipps, R. J., Predictive Multivariate Linear Regression Analysis Guides Successful Catalytic Enantioselective Minisci Reactions of Diazines. *J. Am. Chem. Soc.* **2019,** *141*, 19178-19185.

226. Kowalski, B. R., Chemometrics: Views and Propositions. *J. Chem. Inf. Comput. Sci.* **1975,** *15*, 201-203.

227. Lourenço, N. D.; Lopes, J. A.; Almeida, C. F.; Sarraguça, M. C.; Pinheiro, H. M., Bioreactor monitoring with spectroscopy and chemometrics: a review. *Anal. Bioanal. Chem.* **2012,** *404*, 1211-1237.

228. Macnaughtan, D.; Rogers, L. B.; Wernimont, G., Principal-component analysis applied to chromatographic data. *Anal. Chem.* **1972,** *44*, 1421-1427.

229. Bro, R.; Smilde, A. K., Principal component analysis. *Anal. Methods* **2014,** *6*, 2812-2831.

230. García-Muelas, R.; López, N., Statistical learning goes beyond the d-band model providing the thermochemistry of adsorbates on transition metals. *Nat. Commun.* **2019,** *10*, 4687.

231. Piironen, J.; Vehtari, A. In *Iterative Supervised Principal Components*, International Conference on Artificial Intelligence and Statistics, Proceedings of Machine Learning Research, Playa Blanca, Lanzarote, Canary Islands, April 9-11, 2018; Storkey, A.; Perez-Cruz, F., Eds.; PMLR: 2018.

232. Fey, N.; Orpen, A. G.; Harvey, J. N., Building ligand knowledge bases for organometallic chemistry: Computational description of phosphorus(III)-donor ligands and the metal–phosphorus bond. *Coord. Chem. Rev.* **2009,** *253*, 704-722.

233. Fey, N.; Harvey, J. N.; Lloyd-Jones, G. C.; Murray, P.; Orpen, A. G.; Osborne, R.; Purdie, M., Computational Descriptors for Chelating P,P- and P,N-Donor Ligands[1]. *Organometallics* **2008,** *27*, 1372-1383.

234. Durand, D. J.; Fey, N., Computational Ligand Descriptors for Catalyst Design. *Chem. Rev.* **2019,** *119*, 6561-6594.

235. Fey, N.; Tsipis, A. C.; Harris, S. E.; Harvey, J. N.; Orpen, A. G.; Mansson, R. A., Development of a Ligand Knowledge Base, Part 1: Computational Descriptors for Phosphorus Donor Ligands. *Chem. Eur. J.* **2006,** *12*, 291-302.

236. Jover, J.; Fey, N.; Harvey, J. N.; Lloyd-Jones, G. C.; Orpen, A. G.; Owen-Smith, G. J. J.; Murray, P.; Hose, D. R. J.; Osborne, R.; Purdie, M., Expansion of the Ligand Knowledge Base for Chelating P,P-Donor Ligands (LKB-PP). *Organometallics* **2012,** *31*, 5302-5306.

237. Jover, J.; Fey, N.; Harvey, J. N.; Lloyd-Jones, G. C.; Orpen, A. G.; Owen-Smith, G. J. J.; Murray, P.; Hose, D. R. J.; Osborne, R.; Purdie, M., Expansion of the Ligand Knowledge Base for Monodentate P-Donor Ligands (LKB-P). *Organometallics* **2010,** *29*, 6245-6258.

238. Fey, N.; Haddow, M. F.; Harvey, J. N.; McMullin, C. L.; Orpen, A. G., A ligand knowledge base for carbenes (LKB-C): maps of ligand space. *Dalton Trans.* **2009**, 8183-8196.

239. Mansson, R. A.; Welsh, A. H.; Fey, N.; Orpen, A. G., Statistical Modeling of a Ligand Knowledge Base. *J. Chem. Inf. Model.* **2006,** *46*, 2591-2600.

240. Fey, N.; Garland, M.; Hopewell, J. P.; McMullin, C. L.; Mastroianni, S.; Orpen, A. G.; Pringle, P. G., Stable Fluorophosphines: Predicted and Realized Ligands for Catalysis. *Angew. Chem., Int. Ed.* **2012,** *51*, 118-122.

241. Landman, I. R.; Paulson, E. R.; Rheingold, A. L.; Grotjahn, D. B.; Rothenberg, G., Designing bifunctional alkene isomerization catalysts using predictive modelling. *Catal. Sci. Technol.* **2017,** *7*, 4842-4851.

242. Maldonado, A. G.; Rothenberg, G., Predictive modeling in homogeneous catalysis: a tutorial. *Chem. Soc. Rev.* **2010,** *39*, 1891-1902.

243. Chu, Y.; Heyndrickx, W.; Occhipinti, G.; Jensen, V. R.; Alsberg, B. K., An Evolutionary Algorithm for *de Novo* Optimization of Functional Transition Metal Compounds. *J. Am. Chem. Soc.* **2012,** *134*, 8885-8895.

244. Heinrich, M. R.; Steglich, W.; Banwell, M. G.; Kashman, Y., Total synthesis of the marine alkaloid halitulin. *Tetrahedron* **2003,** *59*, 9239-9247.

245. Kashman, Y.; Koren-Goldshlager, G.; Gravalos, M. D. G.; Schleyer, M., Halitulin, a new cytotoxic alkaloid from the marine sponge Haliclona tulearensis. *Tetrahedron Lett.* **1999,** *40*, 997-1000.

246. Banwell, M. G.; Bray, A. M.; Edwards, A. J.; Wong, D. J., Rapid and convergent assembly of the polycyclic framework assigned to the cytotoxic marine alkaloid halitulin. *J. Chem. Soc., Perkin Trans. 1* **2002**, 1340-1343.

247. Young, I. S.; Thornton, P. D.; Thompson, A., Synthesis of natural products containing the pyrrolic ring. *Nat. Prod. Rep.* **2010,** *27*, 1801-1839.

248. Imbri, D.; Tauber, J.; Opatz, T., Synthetic approaches to the lamellarins--a comprehensive review. *Mar. Drugs* **2014,** *12*, 6142-6177.

249. Bailly, C., Anticancer properties of lamellarins. *Mar. Drugs* **2015,** *13*, 1105-1123.

250. Behenna, D. C.; Stoltz, B. M., Natural Products as Inspiration for Reaction Development: Catalytic Enantioselective Decarboxylative Reactions of Prochiral Enolate Equivalents. In *Inventing Reactions. Topics in Organometallic Chemistry*, Gooßen, L., Ed.; Springer, Berlin, Heidelberg: 2012; Vol. 44, pp 281-313.

251. Jansen, K. Chemists share their lab superstitions. https://cen.acs.org/people/Chemists-share-lab-superstitions/96/i44 (accessed April 8, 2020).

252. Green, M. L. H., A new approach to the formal classification of covalent compounds of the elements. *J. Organomet. Chem.* **1995,** *500*, 127-148.

253. Billow, B. S.; McDaniel, T. J.; Odom, A. L., Quantifying ligand effects in high-oxidation-state metal catalysis. *Nat. Chem.* **2017,** *9*, 837-842.

254. Falivene, L.; Cao, Z.; Petta, A.; Serra, L.; Poater, A.; Oliva, R.; Scarano, V.; Cavallo, L., Towards the online computer-aided design of catalytic pockets. *Nat. Chem.* **2019,** *11*, 872-879.

255. Bair, E.; Hastie, T.; Paul, D.; Tibshirani, R., Prediction by Supervised Principal Components. *J. Am. Stat. Assoc.* **2006,** *101*, 119-137.

256. Swift, J., *Gulliver's Travels*. Harper: New York, 1950.

257. Stumpfe, D.; Hu, H.; Bajorath, J., Evolving Concept of Activity Cliffs. *ACS Omega* **2019,** *4*, 14360-14368.

258. Delchambre, L., Weighted principal component analysis: a weighted covariance eigendecomposition approach. *Mon. Not. R. Astron. Soc.* **2014,** *446*, 3545-3555.

259. Pennington, D. A.; Horton, P. N.; Hursthouse, M. B.; Bochmann, M.; Lancaster, S. J., Synthesis and catalytic activity of dinuclear imido titanium complexes: the molecular structure of $[Ti(NPh)Cl(\mu\text{-}Cl)(THF)_2]_2$. *Polyhedron* **2005,** *24*, 151-156.

260. Davis-Gilbert, Z. W.; Kawakita, K.; Blechschmidt, D. R.; Tsurugi, H.; Mashima, K.; Tonks, I. A., In Situ Catalyst Generation and Benchtop-Compatible Entry Points for Ti^{II}/Ti^{IV} Redox Catalytic Reactions. *Organometallics* **2018,** *37*, 4439-4445.

261. Obligacion, J. V.; Semproni, S. P.; Pappas, I.; Chirik, P. J., Cobalt-Catalyzed $C(sp^2)$-H Borylation: Mechanistic Insights Inspire Catalyst Design. *J. Am. Chem. Soc.* **2016,** *138*, 10645-10653.

262. Tantillo, D. J. Chemical Shift Repository for computed NMR scaling factors, with Coupling Constants Added Too. http://cheshirenmr.info/index.htm (accessed 2020).

263. Dean, J. A., Table 4.11 Bond Dissociation Energies. In *Lange's Handbook of Chemistry*, Fifteenth ed.; Esposito, R., Ed.; McGraw-Hill Education: 2005; Vol. 1, pp 4.41 - 4.53.

264. Schwerdtfeger, P.; Nagle, J. K., 2018 Table of static dipole polarizabilities of the neutral elements in the periodic table. *Mol. Phys.* **2019,** *117*, 1200-1225.

265. Bratsch, S. G., Revised Mulliken electronegativities: I. Calculation and conversion to Pauling units. *J. Chem. Educ.* **1988,** *65*, 34.

266. Frisch, M. J.; Trucks, G. W.; Schlegel, H. B.; Scuseria, G. E.; Robb, M. A.; Cheeseman, J. R.; Scalmani, G.; Barone, V.; Petersson, G. A.; Nakatsuji, H.; Li, X.; Caricato, M.; Marenich, A. V.; Bloino, J.; Janesko, B. G.; Gomperts, R.; Mennucci, B.;

Hratchian, H. P.; Ortiz, J. V.; Izmaylov, A. F.; Sonnenberg, J. L.; Williams; Ding, F.; Lipparini, F.; Egidi, F.; Goings, J.; Peng, B.; Petrone, A.; Henderson, T.; Ranasinghe, D.; Zakrzewski, V. G.; Gao, J.; Rega, N.; Zheng, G.; Liang, W.; Hada, M.; Ehara, M.; Toyota, K.; Fukuda, R.; Hasegawa, J.; Ishida, M.; Nakajima, T.; Honda, Y.; Kitao, O.; Nakai, H.; Vreven, T.; Throssell, K.; Montgomery Jr., J. A.; Peralta, J. E.; Ogliaro, F.; Bearpark, M. J.; Heyd, J. J.; Brothers, E. N.; Kudin, K. N.; Staroverov, V. N.; Keith, T. A.; Kobayashi, R.; Normand, J.; Raghavachari, K.; Rendell, A. P.; Burant, J. C.; Iyengar, S. S.; Tomasi, J.; Cossi, M.; Millam, J. M.; Klene, M.; Adamo, C.; Cammi, R.; Ochterski, J. W.; Martin, R. L.; Morokuma, K.; Farkas, O.; Foresman, J. B.; Fox, D. J. *Gaussian 16 Rev. C.01*, Wallingford, CT, 2016.

267. Zhao, Y.; Truhlar, D. G., The M06 suite of density functionals for main group thermochemistry, thermochemical kinetics, noncovalent interactions, excited states, and transition elements: two new functionals and systematic testing of four M06-class functionals and 12 other functionals. *Theor. Chem. Acc.* **2008,** *120*, 215-241.

268. Weigend, F.; Ahlrichs, R., Balanced basis sets of split valence, triple zeta valence and quadruple zeta valence quality for H to Rn: Design and assessment of accuracy. *Phys. Chem. Chem. Phys.* **2005,** *7*, 3297-3305.

269. Marenich, A. V.; Cramer, C. J.; Truhlar, D. G., Universal Solvation Model Based on Solute Electron Density and on a Continuum Model of the Solvent Defined by the Bulk Dielectric Constant and Atomic Surface Tensions. *J. Phys. Chem. B* **2009,** *113*, 6378-6396.